

Dilip Kumar Sarkar  
Pradip Kumar Sadhu  
Sunandan Bhunia  
Jagannath Samanta  
Suman Paul *Editors*

# Proceedings of the 4th International Conference on Communication, Devices and Computing

ICCDC 2023

# Lecture Notes in Electrical Engineering

## Volume 1046

### Series Editors

- Leopoldo Angrisani, Department of Electrical and Information Technologies Engineering, University of Napoli Federico II, Napoli, Italy
- Marco Arteaga, Departament de Control y Robótica, Universidad Nacional Autónoma de México, Coyoacán, Mexico
- Samarjit Chakraborty, Fakultät für Elektrotechnik und Informationstechnik, TU München, München, Germany
- Jiming Chen, Zhejiang University, Hangzhou, Zhejiang, China
- Shanben Chen, School of Materials Science and Engineering, Shanghai Jiao Tong University, Shanghai, China
- Tan Kay Chen, Department of Electrical and Computer Engineering, National University of Singapore, Singapore, Singapore
- Rüdiger Dillmann, University of Karlsruhe (TH) IAIM, Karlsruhe, Baden-Württemberg, Germany
- Haibin Duan, Beijing University of Aeronautics and Astronautics, Beijing, China
- Gianluigi Ferrari, Dipartimento di Ingegneria dell'Informazione, Sede Scientifica Università degli Studi di Parma, Parma, Italy
- Manuel Ferre, Centre for Automation and Robotics CAR (UPM-CSIC), Universidad Politécnica de Madrid, Madrid, Spain
- Faryar Jabbari, Department of Mechanical and Aerospace Engineering, University of California, Irvine, CA, USA
- Limin Jia, State Key Laboratory of Rail Traffic Control and Safety, Beijing Jiaotong University, Beijing, China
- Janusz Kacprzyk, Intelligent Systems Laboratory, Systems Research Institute, Polish Academy of Sciences, Warsaw, Poland
- Alaa Khamis, Department of Mechatronics Engineering, German University in Egypt El Tagamoa El Khames, New Cairo City, Egypt
- Torsten Kroeger, Intrinsic Innovation, Mountain View, CA, USA
- Yong Li, College of Electrical and Information Engineering, Hunan University, Changsha, Hunan, China
- Qilian Liang, Department of Electrical Engineering, University of Texas at Arlington, Arlington, TX, USA
- Ferran Martín, Departament d'Enginyeria Electrònica, Universitat Autònoma de Barcelona, Bellaterra, Barcelona, Spain
- Tan Cher Ming, College of Engineering, Nanyang Technological University, Singapore, Singapore
- Wolfgang Minker, Institute of Information Technology, University of Ulm, Ulm, Germany
- Pradeep Misra, Department of Electrical Engineering, Wright State University, Dayton, OH, USA
- Subhas Mukhopadhyay, School of Engineering, Macquarie University, NSW, Australia
- Cun-Zheng Ning, Department of Electrical Engineering, Arizona State University, Tempe, AZ, USA
- Toyoaki Nishida, Department of Intelligence Science and Technology, Kyoto University, Kyoto, Japan
- Luca Oneto, Department of Informatics, Bioengineering, Robotics and Systems Engineering, University of Genova, Genova, Italy
- Bijaya Ketan Panigrahi, Department of Electrical Engineering, Indian Institute of Technology Delhi, New Delhi, Delhi, India
- Federica Pascucci, Department di Ingegneria, Università degli Studi Roma Tre, Roma, Italy
- Yong Qin, State Key Laboratory of Rail Traffic Control and Safety, Beijing Jiaotong University, Beijing, China
- Gan Woon Seng, School of Electrical and Electronic Engineering, Nanyang Technological University, Singapore, Singapore
- Joachim Speidel, Institute of Telecommunications, University of Stuttgart, Stuttgart, Germany
- Germano Veiga, FEUP Campus, INESC Porto, Porto, Portugal
- Haitao Wu, Academy of Opto-electronics, Chinese Academy of Sciences, Haidian District, Beijing, China
- Walter Zamboni, Department of Computer Engineering, Electrical Engineering and Applied Mathematics, DIEM—Università degli studi di Salerno, Fisciano, Salerno, Italy
- Junjie James Zhang, Charlotte, NC, USA
- Kay Chen Tan, Department of Computing, Hong Kong Polytechnic University, Kowloon Tong, Hong Kong

The book series *Lecture Notes in Electrical Engineering* (LNEE) publishes the latest developments in Electrical Engineering—quickly, informally and in high quality. While original research reported in proceedings and monographs has traditionally formed the core of LNEE, we also encourage authors to submit books devoted to supporting student education and professional training in the various fields and applications areas of electrical engineering. The series cover classical and emerging topics concerning:

- Communication Engineering, Information Theory and Networks
- Electronics Engineering and Microelectronics
- Signal, Image and Speech Processing
- Wireless and Mobile Communication
- Circuits and Systems
- Energy Systems, Power Electronics and Electrical Machines
- Electro-optical Engineering
- Instrumentation Engineering
- Avionics Engineering
- Control Systems
- Internet-of-Things and Cybersecurity
- Biomedical Devices, MEMS and NEMS

For general information about this book series, comments or suggestions, please contact [leontina.dicecco@springer.com](mailto:leontina.dicecco@springer.com).

To submit a proposal or request further information, please contact the Publishing Editor in your country:

#### **China**

Jasmine Dou, Editor ([jasmine.dou@springer.com](mailto:jasmine.dou@springer.com))

#### **India, Japan, Rest of Asia**

Swati Meherishi, Editorial Director ([Swati.Meherishi@springer.com](mailto:Swati.Meherishi@springer.com))

#### **Southeast Asia, Australia, New Zealand**

Ramesh Nath Premnath, Editor ([ramesh.premnath@springernature.com](mailto:ramesh.premnath@springernature.com))

#### **USA, Canada**

Michael Luby, Senior Editor ([michael.luby@springer.com](mailto:michael.luby@springer.com))

#### **All other Countries**

Leontina Di Cecco, Senior Editor ([leontina.dicecco@springer.com](mailto:leontina.dicecco@springer.com))

**\*\* This series is indexed by EI Compendex and Scopus databases. \*\***

Dilip Kumar Sarkar · Pradip Kumar Sadhu ·  
Sunandan Bhunia · Jagannath Samanta ·  
Suman Paul  
Editors

# Proceedings of the 4th International Conference on Communication, Devices and Computing

ICCDC 2023



Springer

*Editors*

Dilip Kumar Sarkar  
Department of Applied science  
Aluminum Research Center REGAL  
University of Quebec at Chicoutimi  
Chicoutimi, QC, Canada

Sunandan Bhunia  
Department of Electronics  
and Communication Engineering  
Central Institute of Technology  
Kokrajhar, Assam, India

Suman Paul  
Department of Electronics  
and Communication Engineering  
Haldia Institute of Technology  
Haldia, West Bengal, India

Pradip Kumar Sadhu  
Indian Institute of Technology (ISM)  
Dhanbad, Jharkhand, India

Jagannath Samanta  
Department of Electronics  
and Communication Engineering  
Haldia Institute of Technology  
Haldia, West Bengal, India

ISSN 1876-1100                   ISSN 1876-1119 (electronic)  
Lecture Notes in Electrical Engineering  
ISBN 978-981-99-2709-8       ISBN 978-981-99-2710-4 (eBook)  
<https://doi.org/10.1007/978-981-99-2710-4>

© The Editor(s) (if applicable) and The Author(s), under exclusive license to Springer Nature  
Singapore Pte Ltd. 2023

This work is subject to copyright. All rights are solely and exclusively licensed by the Publisher, whether the whole or part of the material is concerned, specifically the rights of translation, reprinting, reuse of illustrations, recitation, broadcasting, reproduction on microfilms or in any other physical way, and transmission or information storage and retrieval, electronic adaptation, computer software, or by similar or dissimilar methodology now known or hereafter developed.

The use of general descriptive names, registered names, trademarks, service marks, etc. in this publication does not imply, even in the absence of a specific statement, that such names are exempt from the relevant protective laws and regulations and therefore free for general use.

The publisher, the authors, and the editors are safe to assume that the advice and information in this book are believed to be true and accurate at the date of publication. Neither the publisher nor the authors or the editors give a warranty, expressed or implied, with respect to the material contained herein or for any errors or omissions that may have been made. The publisher remains neutral with regard to jurisdictional claims in published maps and institutional affiliations.

This Springer imprint is published by the registered company Springer Nature Singapore Pte Ltd.  
The registered company address is: 152 Beach Road, #21-01/04 Gateway East, Singapore 189721,  
Singapore

# **Committee**

## **Chief Patron**

Dr. Lakshman Chandra Seth, D.Lit., Hon'ble Chairman, Haldia Institute of Technology, Haldia, India

## **General Chair**

Prof. (Dr.) Chanchal Kumar De, Haldia Institute of Technology, Haldia, India  
Prof. (Dr.) Pradip Kumar Sadhu, Indian Institute of Technology (ISM), Dhanbad, India

## **Program Chair**

Dr. Avisankar Roy, Haldia Institute of Technology, Haldia, India  
Mr. Tirthadip Sinha, Haldia Institute of Technology, Haldia, India

## **Organizing Chair**

Dr. Banibrata Bag, Haldia Institute of Technology, Haldia, India  
Dr. Avishek Das, Haldia Institute of Technology, Haldia, India  
Mr. Surajit Mukherjee, Haldia Institute of Technology, Haldia, India

## Publication Chair

Dr. Jagannath Samanta, Haldia Institute of Technology, Haldia, India  
Dr. Suman Paul, Haldia Institute of Technology, Haldia, India

## Finance Chair

Mr. Dibyendu Chowdhury, Haldia Institute of Technology, Haldia, India

## International Advisory Committee

### Members, Organization

Prof. Honkala Iiro, University of Turku, Finland.  
Prof. S. M. Abdur Razzak, Rajshahi University of Engineering and Technology, Bangladesh  
Prof. Dilip Sarkar, University of Miami, Florida, United States of America  
Prof. Mohammad S. Obaidat, University of Sharjah, UAE  
Prof. Arokiaswami Alphones, School of Electrical and Electronics Engineering, Nanyang Technological University, Singapore  
Prof. (Dr.) Nemai Chandra Karmakar, Director, Monash Microwave, Antenna, RFID and Sensor Laboratory (MMARS), Department of Electrical and Computer Systems Engineering, Monash University, Australia  
Prof. Kamla Prasan Ray, Defence Institute of Advanced Technology, India  
Prof. Sukumar Nandi, India Institute of Technology, Guwahati, India  
Prof. Animesh Maitra, University of Calcutta, India  
Prof. J. P. Bandopadhyay, University of Calcutta, India  
Prof. C. K. Sarkar, Jadavpur University, Kolkata, India  
Prof. Sanjay Dhar Roy, National Institute of Technology Durgapur, India  
Prof. Sourangshu Mukhopadhyay, University of Burdwan, India  
Prof. Abhijit Biswas, University of Calcutta, Kolkata, India  
Prof. Debashis De, Maulana Abul Kalam Azad University of Technology, Kolkata, India  
Prof. Malay Kumar Pandit, Haldia Institute of Technology, Haldia, India  
Prof. Kisalaya Chakrabarti, Haldia Institute of Technology, Haldia, India  
Prof. Jaydeb Bhaumik, Jadavpur University, Kolkata, India.  
Prof. Sunandan Bhunia, Central Institute of Technology, Kokrajhar, India  
Dr. Manu Malek, Editor-in-Chief, *Journal of Computer and Electrical Engineering*, Elsevier

## Technical Program Committee Members

### TPC Members, Organization

- Dr. Huang Sunan, National University of Singapore, Singapore  
Dr. Jishan-E-Giti, Rajshahi University of Engineering and Technology, Bangladesh  
Dr. Gandeva Bayu Satrya, Telkom University, Indonesia  
Dr. P. Karuppanan, Motilal Nehru National Institute of Technology, Allahabad, India  
Dr. Angshuman Majumdar, Brainware University, Kolkata, India  
Dr. Saptarshi Ghosh, Indian Institute of Technology, Indore, India  
Dr. Sumit Gautam, Indian Institute of Technology, Indore, India  
Dr. Debasish Maji, Vellore Institute of Technology, Vellore, India  
Dr. Mauparna Nandan, Haldia Institute of Technology, Haldia, India  
Dr. Sudip Roy, Indian Institute of Technology Roorkee, India  
Dr. Prabir Kumar Saha, National Institute of Technology, Meghalaya, India  
Dr. Chiranjib Goswami, Asansol Engineering College, India  
Dr. Sudipta Sahana, University of Engineering and Management, Kolkata, India  
Dr. Swarup Kumar Mitra, MCKV College of Engineering, Kolkata, India  
Dr. Alok Saha, Dr. B. C. Roy College of Engineering, Durgapur, India  
Dr. Somnath Ghosh, Indian Institute of Technology Jodhpur, India  
Dr. Sudipta Das, IMPS College of Engineering and Technology, Malda, India  
Dr. Shampa Chatterjee, Haldia Institute of Technology, Haldia, India  
Dr. Dharmpal Singh, JIS College of Engineering, Kalyani, India  
Prof. Sunil Lavadiya, Marwadi University, India  
Dr. Prasun Chowdhury, St. Thomas College of Engineering and Technology, Kolkata, India  
Prof. (Dr.) Surjeet Dalal, College of Computing Sciences and IT, Moradabad, Uttar Pradesh, India  
Dr. Partha Pratim Sarkar, UIT, Burdwan University, India  
Dr. Soma Barman Mandal, Institute of Radio Physics and Electronics, University of Calcutta, India  
Dr. Sanjeev Kumar Metya, National Institute of Technology, Arunachal Pradesh, India  
Dr. Santigopal Pain, Haldia Institute of Technology, India  
Dr. Hemant Patidar, Oriental University, Madhya Pradesh, India  
Dr. Sumalya Ghosh, Lead Engineer, Sankalp Semiconductor (An HCL Technologies Company)  
Dr. Amol C. Adamuthe, Rajarambapu Institute of Technology, India  
Dr. Abhik Gorai, Kalinga Institute of Industrial Technology, Bhubaneswar, India  
Dr. Tanmoy Sarkar, Radionics Laboratory, University of Burdwan, India  
Dr. Kaushik Mandal, Institute of Radio Physics and Electronics, University of Calcutta, Kolkata, India  
Dr. Bidhan Malakar, JIS College of Engineering, Kalyani, India  
Dr. Surajit Kundu, National Institute of Technology, Sikkim, India  
Dr. Chandrima Mondal, Jadavpur University, India

- Dr. Sapana Ranwa, National Institute of Technology, Durgapur, India  
Dr. Wasim Arif, National Institute of Technology, Silchar, India  
Dr. T. Satyanarayana, Lakireddy Bali Reddy College of Engineering, Andhra Pradesh, India  
Dr. Ivy Majumdar, B. P. Poddar Institute of Engineering and Technology, Kolkata, India  
Dr. Pratyusha Rakshit, Jadavpur University, India  
Dr. Soumojit Shee, ITER, SOA DU, Bhubaneswar  
Dr. Partha Sarathi Pal, CSIR-Central Mechanical Engineering Research Institute  
Dr. Rajesh Bera, Gayatri Vidya Parishad College of Engineering, Visakhapatnam  
Dr. Sudipta Das, National Institute of Technology, Sikkim  
Dr. Chaitali Koley, National Institute of Technology, Mizoram  
Dr. Soumen Mallick, Dr. B. C. Roy Engineering College, Durgapur  
Dr. Madhusudan Maiti, C. V. Raman Global University, Odisha, India  
Dr. Sudhendu Das Mahapatra, Manipal University, Jaipur, Rajasthan, India  
Dr. Bidesh Chakraborty, Assansol Engineering College, Assansol, India  
Dr. Subhankar Joardar, Haldia Institute of Technology, Haldia, India  
Dr. Dheeraj K. Agarwal, MNIT, Bhopal, India  
Dr. Samiran Chatterjee, Amrita Sai Institute of Science and Technology, Andhra Pradesh, India.  
Dr. Santanu Koley, Haldia Institute of Technology, Haldia, India  
Dr. Avishek Chakraborty, SR University, Warangal, Telangana, India  
Dr. Premangsu Mukhopadyay, Haldia Institute of Technology, Haldia, India  
Dr. Gopi Ram, National Institute of Technology, Warangal, India  
Dr. Soumya Roy, Haldia Institute of Technology, Haldia, India  
Dr. Arnab De, K. K. Group of Institutions, Jharkhand, India  
Dr. Bappaditya Roy, VIT Andhra Pradesh, India  
Dr. Radhakrishna Bhat, Manipal Institute of Technology, Manipal Academy of Higher Education, Manipal, India  
Dr. Sita Kondamadugula, Alabama A&M University, USA  
Dr. Anup Karak, Vidyasagar University, India  
Dr. Sanchita Pramanik, Vidyasagar University, India

## **Local Advisory Committee**

- Mr. Sayantan Seth, Vice Chairman, Haldia Institute of Technology, Haldia, India  
Mr. Asish Lahiri, Secretary, Haldia Institute of Technology, Haldia, India  
Prof. (Dr.) Subrata Mandal, Principal, Haldia Institute of Technology, Haldia, India  
Dr. A. Mishra, Registrar, Haldia Institute of Technology, Haldia, India  
Prof. (Dr.) A. B. Maity, Dean, SAS and H, Haldia Institute of Technology, Haldia, India  
Prof. (Dr.) T. K. Jana, Dean, SECI, Haldia Institute of Technology, Haldia, India

Mr. S. K. Basu, Finance Manager, Haldia Institute of Technology, Haldia, India  
Dr. D. Das, Manager Administration, Haldia Institute of Technology, Haldia, India

## **Local Organizing Committee**

Mr. Asim Kumar Jana, Haldia Institute of Technology, Haldia, India  
Mr. Kushal Roy, Haldia Institute of Technology, Haldia, India  
Mr. Amit Bhattacharyya, Haldia Institute of Technology, Haldia, India  
Mr. Rajkumar Maity, Haldia Institute of Technology, Haldia, India  
Mr. Akinchan Das, Haldia Institute of Technology, Haldia, India  
Mr. Pinaki Satpathy, Haldia Institute of Technology, Haldia, India  
Mr. Santanu Maity, Haldia Institute of Technology, Haldia, India  
Mr. Tilak Mukherjee, Haldia Institute of Technology, Haldia, India  
Mr. Dipak Samanta, Haldia Institute of Technology, Haldia, India  
Mr. Jayanta Kumar Bag, Haldia Institute of Technology, Haldia, India  
Dr. Sudipta Bardhan, Haldia Institute of Technology, Haldia, India  
Mrs. Pallabi Pahari, Haldia Institute of Technology, Haldia, India  
Mrs. Razia Sultana, Haldia Institute of Technology, Haldia, India  
Mrs. Moumita Jana, Haldia Institute of Technology, Haldia, India  
Ms. Sayani Ghosh, Haldia Institute of Technology, Haldia, India  
Mr. Sachindeb Jana, Haldia Institute of Technology, Haldia, India  
Mr. Sourav Das, Haldia Institute of Technology, Haldia, India  
Mr. Tapan Maity, Haldia Institute of Technology, Haldia, India  
Mr. Atanu Pradhan, Haldia Institute of Technology, Haldia, India  
Mr. Asim Kuila, Haldia Institute of Technology, Haldia, India  
Mr. Pulak Maity, Haldia Institute of Technology, Haldia, India  
Mr. Shubhendu Barman, Haldia Institute of Technology, Haldia, India  
Mrs. Ira Samanta, Haldia Institute of Technology, Haldia, India  
Ms. Sunetra Maity, Haldia Institute of Technology, Haldia, India  
Mrs. Parswati Banerjee, Haldia Institute of Technology, Haldia, India

# Preface

The 4th International Conference on Communication, Devices and Computing (ICCDC 2023) was held at Haldia Institute of Technology, Haldia, from March 1 to 3, 2023. Haldia is a city in Purba Medinipur district of Indian state West Bengal. Haldia Institute of Technology is dedicated to the objectives of creating highly trained professional manpower in various disciplines of engineering. It has gained reputation through institutional dedication to teaching and research.

In response to call for papers of ICCDC 2023, a total of 136 papers were submitted for presentation and inclusion in proceedings of conference. These papers were evaluated and ranked based on their novelty, significance and technical quality by at least two reviewers per paper. After a careful and blind refereeing process, 55 papers were selected for inclusion in the proceeding. These papers cover current research in communication, signal processing, image processing, wireless network, semiconductor devices, VLSI design, antenna design and machine learning. The conference hosted three offline talks by Prof. Arokiaswami Alphones, Nanyang Technological University, Singapore, Prof. Chinmoy Saha, Indian Institute of Space Science and Technology, Kerala, India, and Prof. Md. Saidur Rahman, Bangladesh University of Engineering and Technology, Bangladesh. The conference also hosted three virtual invited talks by Prof. Shaibal Mukherjee, Indian Institute of Technology Indore, India, Prof. (Dr.) Durbadal Mandal, National Institute of Technology Durgapur, India, and Prof. Ramesh Bansal, University of Sharjah, UAE.

A conference of this kind would not be possible without the full support from different committee members. The organizational aspects were looked after by the organizing committee members who spent their time and energy in making the conference a reality. We also thank all the technical program committee members and additional reviewers for thoroughly reviewing the papers submitted to the conference and sending their constructive suggestions to improve the quality of papers. Our hearty thanks to Springer for agreeing to publish the conference proceedings.

Special thanks to the Defence Research and Development Organisation (DRDO), Government of India, for their financial support to conduct the conference for grant success.

We are indebted to Haldia Institute of Technology for sponsoring and supporting the event. Last but not the least, our sincere thanks go to all speakers, participants all authors who have submitted papers to ICCDC 2023. We sincerely hope that the readers will find the proceedings stimulating and inspiring.

Chicoutimi, Canada  
Dhanbad, India  
Kokrajhar, India  
Haldia, India  
Haldia, India

Prof. Dilip Kumar Sarkar  
Prof. Pradip Kumar Sadhu  
Dr. Sunandan Bhunia  
Dr. Jagannath Samanta  
Dr. Suman Paul

# **Message from the Volume Editors**

It is a great pleasure for us to organize the 4th International Conference on *Communication, Devices and Computing* (ICCDC 2023) held from March 1 to 3, 2023 at the Haldia Institute of Technology, Purba Medinipur, West Bengal, India. Our main goal is to provide an opportunity to the participants to learn about contemporary research in communication, devices and computing and exchange ideas among themselves and with experts present in the conference as invited speakers. It is our sincere hope that the conference will help the participants in their research and training and open new avenues for work for those who are either starting their research or are looking for extending their area of research to a different area of current research in *communication, devices and computing*.

After an initial call for papers, 136 papers were submitted for presentation at the conference. All submitted papers were sent to external referees, and after refereeing, 55 papers were recommended for publication for the conference proceedings that will be published by Springer in its Lecture Notes on Electrical Engineering (LNEE) series.

Special thanks to the Defence Research and Development Organisation (DRDO), Government of India, for their financial support to conduct the conference for grant success.

We are grateful to the speakers, participants, reviewers, organizers, sponsors, and Haldia Institute of Technology for their support and help, without which it would have been impossible to organize the conference. We express our gratitude to the organizing committee members who work behind the scene tirelessly in taking care of the details in making this conference a success.

Prof. Dilip Kumar Sarkar  
Prof. Pradip Kumar Sadhu  
Dr. Sunandan Bhunia  
Dr. Jagannath Samanta  
Dr. Suman Paul

# Contents

<b>Crop Yield Prediction Based on Weather and Soil Parameters Using Regression Tree Model .....</b>	1
Kandi Venkata Narasimha Reddy and Evuri Brahma Reddy	
<b>A Gray Wolf Optimization-Inspired Hybrid Method for Disease Identification .....</b>	11
Emon Asad and Ayatullah Faruk Mollah	
<b>Automated Retinal Blood Vessel Segmentation Using Modified U-Net Architecture .....</b>	23
Debasis Maji, Souvik Maiti, Ashis Kumar Dhara, and Gautam Sarkar	
<b>Design of 1-DOF Integer and Fractional-Order PID Controllers Using an Ensemble Differential Evolution for a Magnetic Levitation System .....</b>	33
Mou Das Mahapatra, Shibendu Mahata, Ritu Rani De, Rajani Kanta Mudi, and Chanchal Dey	
<b>Substrate Integrated Waveguide H-Plane Horn MIMO Antenna Design for mW Applications .....</b>	43
Mantar Singh Mandloi, Ujjwal Tripathi, Ajay Parmar, and Leeladhar Malviya	
<b>BSVM: A BERT-Based Support Vector Machine for Hindi Hostile Content Detection .....</b>	57
Angana Chakraborty, Subhankar Joardar, and Arif Ahmed Sekh	
<b>Residual Convolutional Neural Network Models for COVID-19 Detection from Chest X-Ray: A Comparative Study .....</b>	69
Saikat Acharyya, Sourav Mandal, and Rohini Basak	

<b>Prediction of Client Term Deposit Subscription Using Machine Learning .....</b>	83
Muskan Singh, Namrata Dhanda, U. K. Farooqui, Kapil Kumar Gupta, and Rajat Verma	
<b>Real Estate Price Prediction Using Machine Learning .....</b>	95
Shilpa Yadav, Namrata Dhanda, Archana Sahai, Rajat Verma, and Sakshi Pandey	
<b>A Comparative Study to Detect Cervical Dysplasia by Using Pap Smear Images .....</b>	113
Jheelam Mondal and Subhankar Joardar	
<b>Design of a Cost-Effective Remote Health Monitoring System Using IoT .....</b>	125
Subhadeep Paul, Madhusudan Maiti, Dibyendu Chowdhury, and Subhas Chandra Saha	
<b>Current Exploration in Microfluidics-Based Point-Of-Care Biosensor Applications: A Review .....</b>	139
Pitam Chakrabarti, Sucheta Das, and Shamba Chatterjee	
<b>A Review on Memristor-Based Reactance-Less Relaxation Oscillator .....</b>	149
Rajesh Dutta, Amiya Karmakar, and Sudakshina Kundu	
<b>Optimal Control and Voltage Sag Compensation in a PV/FC Integrated Microgrid Through Biography Based Optimization Technique .....</b>	159
Gagan Kumar Sahoo, Subham Mohanty, and Subhashree Choudhury	
<b>Performance Comparisons of MPEDE-Based Integer and Fractional-Order PID Controllers for a Cruise Control System .....</b>	177
Mou Das Mahapatra, Shibendu Mahata, Ritu Rani De, Rajani Kanta Mudi, and Chanchal Dey	
<b>Novel CMOS 1-Digit BCD-Adder Correction Circuit .....</b>	189
Shatabhisa Goswami, Ananya Mandal, Aishikée Mishra, Joyoshri Goswami, and Aloke Saha	
<b>Digital Image Tampering Detection Using Deep Learning: A Survey .....</b>	197
Sunen Chakraborty, Paramita Dey, and Kingshuk Chatterjee	
<b>Nanorod Shaped TiO<sub>2</sub> Photoanode and Mixed Halide Absorber-Based Perovskite Solar Cell Device Fabrication .....</b>	217
Anitesh Anand, Niranjan Polai, Madhu Paswan, Manas Mishra, Chanchal Kumar De, and Debasis De	

<b>GA-Based IMC Fractional PI Controller Design for Dissolved Oxygen Control with a Non-integer Order Biological Wastewater Treatment Plant .....</b>	229
Indranil Dey, Sridhar Pilli, and Seshagiri Rao Ambati	
<b>A Comprehensive Study for Maximum Power Point Tracking Methodologies for Wind Power Systems .....</b>	245
Ahmed G. Abo-Khalil, Ramesh C. Bansal, and Nsilulu T. Mbungu	
<b>Deep Learning Approach to Recognize Yoga Posture for the Ailment of the Low Back Pain .....</b>	263
Katta Uday Kiran, Manvendra Singh, Md. Sarfaraj Alam Ansari, and Mahesh Chandra Govil	
<b>Multicrops Disease Identification and Classification System Using Deep MobileNetV2 CNN Architecture .....</b>	275
R. Ramya, N. Deepikasri, T. Madhubala, and A. Manikandan	
<b>Machine Learning and Deep Learning-Based Smart City Infrastructure to Connect Intelligent Domain Using Internet of Things .....</b>	289
Shiplu Das, Srinjoy Sarkar, Subhadip Dutta, Sohini Ghosh, Sudipto Dhar, Buddhadeb Pradhan, and Sudipta Sahana	
<b>Experimental Investigation on Spectrum Sensing Testbed Using GNU Radio and SDR .....</b>	303
Manas Pandey, Anjali Chauhan, Dibyendu Chowdhury, and Suddhendu DasMahapatra	
<b>Harris Hawks Optimization-Based Multilevel Thresholding Segmentation of Magnetic Resonance Brain Images .....</b>	309
Elisabeth Thomas and S. N. Kumar	
<b>Applications in Medical Technology for Optimized Convolutional Neural Network Using Differential Evolutionary Algorithm .....</b>	323
Vanita S. Buradkar and Asha Ambhaikar	
<b>Optimization of Different Parameters of One Bit Full Adder Using QCA Technology .....</b>	333
Sachindeb Jana, Kisalaya Chakrabarti, and Angsuman Sarkar	
<b>A Robust PID Design for Load Frequency Control Using AEPSO Algorithm with Changing Loads .....</b>	347
Souvik Dutta, Alpana Barman, Santigopal Pain, and Parimal Acharjee	
<b>Bilayer Graphene Nanoribbon Transistor for Butane Gas Detection .....</b>	359
S. K. Tripathy, J. K. Singh, and G. M. Prasad	

<b>Prediction of Far-Field Profile in Optical Kerr Type Nonlinear Triangular Index Profile Fiber of LP<sub>11</sub> Mode Using Simple and Accurate Chebyshev Technique .....</b>	367
Kushal Roy, Tilak Mukherjee, and Angshuman Majumdar	
<b>Design and Fabrication of High-Gain Array Antenna for 5G Communication and Wireless Applications .....</b>	379
Arun Raj and Durbadal Mandal	
<b>An Efficient SEC-DAEC Code for Protecting Data Bits in IoT Devices .....</b>	391
Sweta Bijali Maity, Raj Kumar Maity, Jagannath Samanta, and Chanchal Kumar De	
<b>Evaluation of Water Quality Index Using Machine Learning Approach .....</b>	401
Moupali Sen, Shreya Basu, Arijit Chatterjee, Anwesha Banerjee, Saheli Pal, Pritam Kumar Mukhopadhyay, Sudipta Sahana, and Stobak Dutta	
<b>Governance of Water and Electricity Sectors in Developing Countries: A Review .....</b>	409
Tsongo P. Kamabu, Eyul'Anki D. Musibono, Banza B. Banza, Mowene G. Mayobo, Mukwanga W. Siti, J. Sumaili, Ramesh C. Bansal, Ahmed G. Abo-Khalil, Mwana W. K. Mbukani, Diambomba H. Tungadio, Kiseya F. Tshikala, T. Madiba, and Nsilulu T. Mbungu	
<b>Far-Field Radiation Pattern Synthesis of Elliptical Antenna Arrays Using GA and PSO .....</b>	427
Satish Kumar, Gopi Ram, Durbadal Mandal, and Rajib Kar	
<b>CVD-Grown MoS<sub>2</sub> Nanosheets-Based Gas Sensor for Low-Limit Detection of NO<sub>2</sub> Gas .....</b>	439
Shreerupa Biswas and Sapana Ranwa	
<b>A Linear Array of Dropper-Shaped Wideband Printed Radiators for Ku-band Applications .....</b>	449
Kalyan Sundar Kola and Anirban Chatterjee	
<b>Sentiment-Based Simplification of Legal Text .....</b>	463
Cinu C. Kiliroor, Som Sagar, and Swani Sundara Didde	
<b>Prediction of Dew Point Temperature and Relative Humidity for Nashik Region Using LSTM .....</b>	477
Mandal Nabanita and Sarode Tanuja	
<b>Optimization in the Method of Choosing Quasi-Optimal Values of the Regularization Parameter .....</b>	491
Van Huyen Le	

<b>Analysis and Comparison of Real-Time Data Set with Generation of Networks for Underwater Wireless Sensor Networks .....</b>	<b>503</b>
D. Ruby, J. Jeyachidra, T. Logesh, P. Ranjani, G. Umamaheswari, and K. Nandhini	
<b>Deep Ear Biometrics for Gender Classification .....</b>	<b>521</b>
Ritwiz Singh, Keshav Kashyap, Rajesh Mukherjee, Asish Bera, and Mamata Dalui Chakraborty	
<b>Design of Smart IoT-Based Gas Leakage Detection and Prevention Devices for Hydrogen Station .....</b>	<b>531</b>
Tapan Maity, Pranabendu Giri, Rohit Sasmal, Niladri Biswas, Sourav Das, Raj Kumar Maity, Prabir Saha, and Jagannath Samanta	
<b>Efficient and Novel Architecture of Golay Encoder and Decoder for McEliece Cryptosystem .....</b>	<b>547</b>
Tirthadip Sinha and Jaydeb Bhaumik	
<b>Blockchain-Based Dynamic Pricing Framework for Electric Vehicle Charging .....</b>	<b>563</b>
Brijmohan Lal Sahu and Preeti Chandrakar	
<b>Movie's-Emottracker: Movie Induced Emotion Detection by Using EEG and AI Tools .....</b>	<b>583</b>
Sima Das, Siddhartha Chatterjee, Sutapa Bhattacharya, Solanki Mitra, Arpan Adhikary, and Nimay Chandra Giri	
<b>Models for Analysis of Factors Influencing Economic Development .....</b>	<b>597</b>
Dung Nguyen Thi Thu and V. Chernenkaya Ludmila	
<b>Password Scheme: Amalgamation of Characters with Picture .....</b>	<b>609</b>
Sk Sahnawaj and Apratim Mitra	
<b>Performance Analysis of Energy Harvesting-Based CR Network Assisted by Full-Duplex Relays Under Joint Underlay/Overlay Mode .....</b>	<b>617</b>
Dipak Samanta, Chanchal Kumar De, and Abhijit Chandra	
<b>Secure Sharing of Student Credentials Using Blockchain .....</b>	<b>633</b>
Puja Sarkar, Psarag Jyoti Kalita, Mugdhatanu Dev Goswami, Sanchita Saha, and Amitava Nag	
<b>An Optimal Circular Antenna Array Design for an Efficient 5G Communication System Using Krill Herd Optimization .....</b>	<b>647</b>
Rajrup Saha, Avishek Das, Durbadal Mandal, and Rajib Kar	
<b>Impact of Stress Concentrated Region on MEMS-Based Piezoelectric Energy Harvester .....</b>	<b>657</b>
Satyanarayana Talam, Ayesha Begum, M. B. Chakravarthi, Tilak Mukherjee, Poornaiah Billa, and Rambabu Busi	

<b>Color based Classification of Products Using Internet of Things .....</b>	<b>665</b>
Meenaxi M. Raikar, S. M. Meena, Siddaraj Hubballi, Anirudh Kulkarni, Vinayak Merawade, and Yash Deshpande	
<b>Design of a Compact Dual-Band Antenna with Meandered Slotted Patch and U-slotted Defected Ground Plane .....</b>	<b>677</b>
Avisankar Roy, Surajit Mukherjee, Tapas Tewary, Smarajit Maity, and Sunandan Bhunia	
<b>Performance Analysis of Energy Harvesting-Based Relay-Assisted CR Network Under Co-channel Interference Environment .....</b>	<b>685</b>
Dipak Samanta, Jayanta Kumar Bag, Chanchal Kumar De, and Abhijit Chandra	
<b>Author Index .....</b>	<b>707</b>

## About the Editors

**Dilip Kumar Sarkar** is a professor in the Department of Applied Sciences, University of Quebec at Chicoutimi, Canada. He received his Ph.D. from Kalyani University, India, in 1999. He has received various awards and worked in different international institution. He had completed more than 15 research projects, and few are ongoing. He has published three books and more than 100 research articles in various national and international conferences and journals. His areas of interest are nanostructured super-hydrophobic thin films surfaces, energy storage system, advanced surface structure for metal, etc.

**Pradip Kumar Sadhu** received his Bachelor, Postgraduate and Ph.D. (Engineering) degrees from Department of Electrical Engineering, Jadavpur University, Kolkata, West Bengal, India. Currently, he is working as a professor (HAG) and the ex-head of Electrical Engineering Department of Indian Institute of Technology (ISM), Dhanbad, India. Also, he served B.I.T., Mesra, Ranchi, as a faculty member of Electrical and Electronics Engineering Department. Prior to join B.I.T. Mesra, also he served the different industries for twelve years. He has total experience of 35 years, out of which 23 years in teaching and 12 years in industry. He has thirteen (13) Granted Patents. In addition, nineteen (19) more patents in his name are under process. He has several journal and conference publications in national and international levels including *IEEE Transactions on Industrial Electronics*, *IEEE transactions on Power Systems*, *IEEE Transactions on Instrumentation and Measurement*, *IEEE Sensors Journal*, *IEEE Access*, *Solar Energy*, *Renewable Energy*, *Building and Environment*, *Renewable and Sustainable Energy Reviews*, *IET Generation, Transmission and Distribution*, *IET Science Measurement and Technology*, *IET Smart Grid*. He is a principal investigator of few government-funded projects. He has developed hybrid charging system for e-vehicles that allows charging in static as well as dynamic condition; technology for which the patent application has been filed can herald a new era for adoption of electric vehicles as principal mode of road transport. He is a reviewer of various international journals like *IEEE Transaction on Power Electronics*, *IEEE Transactions on Industrial Electronics*, *Solar Energy*, *Renewable*

*Energy*, etc. He has guided 19 numbers of doctoral candidates and a large number of M.Tech. students.

**Sunandan Bhunia** is an associate professor in the Department of Electronics and Communication Engineering, Central Institute of Technology, BTAD, Assam. He has obtained his B.Tech. and M.Tech. from Institute of Radiophysics and Electronics, Calcutta University, in 2002 and 2004, respectively. He has obtained Ph.D. degree in engineering from Jadavpur University in 2009. He was awarded gold medal from Vidyasagar University for first class first in Physics (H) in 1999. He has published about 50 research articles in reputed international and national journals and conferences. His area of research interest includes microstrip antenna, microstrip filter, frequency selective surfaces, VLSI, etc.

**Jagannath Samanta** is an associate professor in the Department of Electronics and Communication Engineering at the Haldia Institute of Technology, Haldia, West Bengal, India. He received the B.Tech. and M.Tech. degree in Electronics and Communication Engineering from West Bengal University of Technology, West Bengal, India, in 2005 and 2008, respectively. He received Gold Medal during M.Tech. degree. He received his Ph.D. (Tech) degree from the Institute of Radio Physics and Electronics, University of Calcutta, in 2018. His research interests include digital VLSI design, error-correcting codes, and IoT in emerging applications. He has published more than 50 research papers in international journals that include IEEE Transactions, Springer, and international conferences. He is the reviewer of referred journals like IEEE Transactions, Springer, Elsevier, etc.

**Suman Paul** is currently an assistant professor in the Department of Electronics and Communication Engineering at the Haldia Institute of Technology, West Bengal, India, and interests in scheduling, QoS/QoE in communication networks, and applications of soft computing techniques in networking and IoT. Professor Paul worked as an associate researcher in the Indian Institute of Management (IIM), Calcutta, in a project on ZigBee-based wireless sensor network, funded by DIT, Government of India. He is a regular reviewer of SCIE/Scopus-indexed journals. Dr. Paul has published books on mobile ad hoc network, edited books on Springer Series, research articles in science citation indexed, Scopus-indexed journals of repute, chapters of Springer and presented papers in IEEE international conferences and filed patents to his credit. He was the joint convener of the International Conference, ICCDC 2019, Haldia, India, and a member of ACM, Machine Intelligence Research Labs, USA, and qualified Cisco Certified Network Associate.

# Crop Yield Prediction Based on Weather and Soil Parameters Using Regression Tree Model



Kandi Venkata Narasimha Reddy and Evuri Brahma Reddy

**Abstract** The development of artificial intelligence and advances in computer science have provided a significant impetus for progress in the field of machine learning. In recent years, machine learning algorithms have been used effectively in the sector of agriculture with the purpose of accurately estimating the amount of crop output. The process of estimating the yield of crops using accessible historical data, such as characteristics relating to the weather and soil, as well as previous crop yields, is known as crop yield prediction. A function of machine learning known as regression makes predictions about a number. The use of regression methods may be highly beneficial when attempting to forecast the yield of crops. The development of regression methods applicable to the agricultural industry is the primary emphasis of this research. When attempting to estimate the amount of wheat, maize, and cotton that will be harvested, many types of regression analysis, including quadratic, pure-quadratic, interactions, and polynomial, are used. Finally, a regression tree model has been suggested that is capable of reliably predicting the yields of cotton, maize, and wheat. The metrics of Root Mean Squared Error (RMSE), R<sup>2</sup>, and Mean Percentage Prediction Error (MPPE) are used in the decision-making process to predict the yield in an effective way.

**Keywords** Crop yield · Machine learning · Regression · Agriculture

---

K. V. Narasimha Reddy (✉)

Assistant Professor, Department of Computer Science and Engineering, Narasaraopeta Engineering College, Narasaraopeta, Guntur, India  
e-mail: [narasimhareddy03@gmail.com](mailto:narasimhareddy03@gmail.com)

E. Brahma Reddy

Department of Computer Science and Engineering, Narasaraopeta Engineering College, Narasaraopeta, Guntur, India

## 1 Introduction

Agriculture [1] is a significant industry since it is the major means through which people across the globe get their food. As a result of the demand to produce more food that is of higher quality, the industry confronts a number of issues. A digital revolution is now taking place in the agricultural industry, which presents an opportunity to solve some of these problems. The translation of data into knowledge is playing a crucial role in this move from conventional skill-based activities to digital practices, which are becoming more prevalent. Because machine learning is one of the most common techniques used to transform data and make sense of it so that users can make better decisions, it is an essential enabler for the agricultural digital revolution. Wheat, maize, and cotton are three of the most important crops that are grown on a commercial scale all over the world. Wheat, maize, and cotton production together accounted for 87 million tonnes throughout the globe in 2019 (FAO 2021). In the context of India, wheat, maize, and cotton are three of the most significant deciduous agricultural crops when accounting for foreign currency revenues, job generation, and activities secondary to agriculture. In 2019, India produced 900,000 tonnes of wheat, maize, and cotton. The agricultural sector employed 30,213 people and generated around R6 billion in revenue. The agricultural yield, which is the quantity and quality of the product that is harvested, is one of the most important factors that determine whether or not an orchard can remain economically viable. “To declare something will happen in the future,” as defined by the Oxford dictionary, is the definition of the verb “to predict.” The yield prediction is an estimate of the yield [2] that will be achieved after a certain amount of time has passed. The estimate is computed via the use of machine learning by using a model that is predicated on a collection of predictor variables. The accurate forecasting of yield in the agricultural sector is essential because it serves as the basis for the planning and decision-making processes that occur throughout the agricultural supply chain. In order to achieve sustainability, it is also necessary to guarantee that natural resources are used effectively. The projections of crop [3] output have an effect on resource choices such as the number of employees to hire, the quantity of packaging material to acquire, and the sales programmes to be implemented. The accurate forecasting of crop output requires not only the collection of pertinent data but also the development of a model that is tailored to the specifics of the issue at hand. The selection of data requires first and foremost a comprehensive comprehension of the factors that influence the yield. The use of approaches based on machine learning is regarded as a suitable factor for modelling apple yield prediction. This is due to the fact that machine learning approaches have been demonstrated to be beneficial in a variety of sectors and have also been successfully used in other research in order to accurately estimate agricultural production. These approaches may be used to describe the connection between input and output properties. They are particularly useful for modelling non-linear, complicated relationships, such as the one involved in yield prediction, because of their ability to provide more accurate results (Fig. 1).

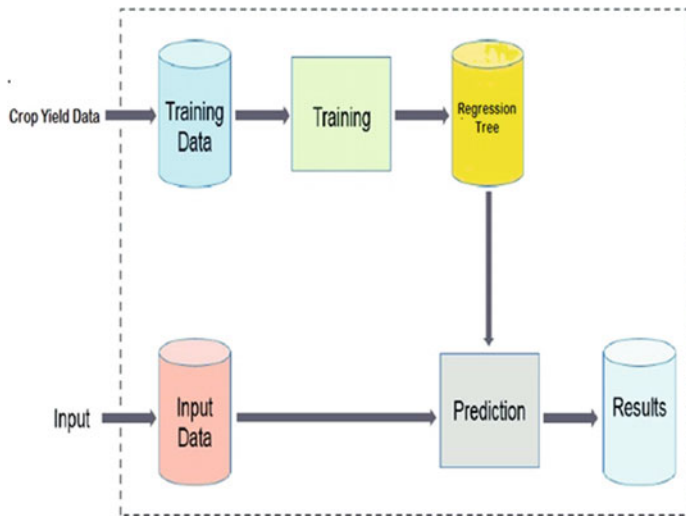


**Fig. 1** Crop-yield prediction using decision tree regression

Predicting yield [4–7] is difficult because yield is influenced by a variety of qualitative and quantitative elements that are associated with one another. These factors include the kind of agriculture, weather patterns, the area of growth, and the quality of the soil. In addition, the yield is also affected by choices made in agricultural practices, such as the amount of irrigation [8–12] and fertilizer that is used. In actuality, the majority of forecasts are made utilizing either the in-depth expertise of specialists or straightforward estimators that are derived from previous results. Because of the complicated interplay that exists between input and output parameters, it is necessary to have an analytical model that is objectively driven by data and can forecast yield. Analytical models have been of use to a wide variety of businesses since they can take into account a large number of interconnected aspects. In particular, the use of machine learning approaches to the process of problem-solving in business is becoming more popular and widespread. The topic of agricultural yield prediction has seen a great deal of research over the years, the majority of which has focussed on using machine learning in some capacity to the research. However, the majority of research has only looked at one or two different approaches to apple yield prediction [13–15]. It has been shown that yield prediction studies for different kinds of crops may benefit from an objective assessment of the various methodologies. These studies have also shown that there is no one machine learning approach that performs better than the others and that the method and model that are most suited to a particular issue are contingent on the nature of that problem. In addition, the majority of the studies that have been done focus on a rather short forecast interval, which ranges from two to five months before the harvest. This strategy makes use of the improved quality and increased quantity of data that are accessible closer to the time of harvest. For the sake of resource planning and budgeting, however, early yield

projection, which is defined as occurring four to six months ahead to harvest, is essential. As a result of this, the apple business presents an opportunity to construct a model that can assist with making predictions of this kind. The rest of the paper is organized as follows: Sect. 2 describes literature review, Sect. 3 describes proposed model, Sect. 4 details the experimental results, and Sect. 5 concludes the article.

## 2 Literature Survey

In spite of the futility of such an endeavour, many individuals all around the globe continue to invest significant effort into making predictions about next crops. Youn et al. [1] proposed utilizing deep learning to predict crop yields using satellite images. For most developing nations, annual agricultural output projections were produced using a CNN. This method was implemented on a soybean dataset using information from three separate sources (a soybean dataset, a soil dataset, and a climate dataset from the United States). Their technique is based on a Gaussian approach, as shown by the reduction in RMSE from an average of 6.3 to 5.9 with the LSTM model and from 5.8 to 5.6 with the CNN model. These improvements were accomplished using a Gaussian method. Paudel et al. [2] produced a complementary piece that similarly integrated agronomic crop modelling. The crop yields of soft wheat, spring barley, sunflowers, sugar beets, and potatoes in the Netherlands, Germany, and France were predicted using three different machine learning methods. Sun et al. [3] introduced a unique multilevel deep learning model for predicting agricultural production by combining RNN and CNN to extract both spatial and temporal information. Mainly, they wanted to see how various datasets affected the prediction process and how well the suggested method worked for predicting yields in the Corn Belt of the United States. The inputs consisted of time-series information from satellite data and data on soil properties. Their goal was to utilize the data from these experiments to make county-level projections for US Maize Belt yields in the years 2013–2016. In their paper [4], Shahhosseini and colleagues stated that further study was needed to demonstrate how combining crop modelling and machine learning may enhance forecasts of maize output in the Corn Belt of the United States. Khaki and Wang [5] devised a system based on a Deep Neural Network for estimating the yield, verifying the yield, and identifying the yield difference across corn hybrids based on genotype and environmental (weather and soil) data. Through the use of this method, we were able to anticipate, verify, and analyse yield gaps in corn hybrids. Participation in the 2018 Syngenta Crop Challenge allowed for the execution of this investigation. Their model was shown to have a high degree of accuracy in its predictions, with a RMSE of 12% of the annualized rate and 50% of the standard error for the test data utilizing forecasted weather information. Abbas et al. [6]’s research is another factor in determining the estimated yield of potato tubers. Forecasts of potato tuber yield are calculated using four separate machine learning techniques. Some common algorithms. The data needed to create these predictions comes from proximal sensing, which is used to gather information on soil and agricultural properties. Recent recommendations by

Kaneko et al. [7] advised focussing research on agricultural output in Africa. They predicted maize yields at the district level across six African nations using a deep learning architecture trained on data from satellite images. These computer simulations allowed them to calculate a probability of 0.56. We use a novel methodology that incorporates concepts from meteorology, chemistry, and agriculture. Agriculture production is the best indication of the impacts of climate change on farmers and consumers. Paudel and colleagues [8] have used machine learning to estimate agricultural production on a wide scale by combining agronomic crop modelling techniques with statistical analysis. This study appeared in the journal Agricultural and Biological Engineering. The method used places an early emphasis on accuracy, flexibility, and reusability. Features were developed using data from the MCYFS database, which includes observations on weather, satellite photography, and soil conditions. Three machine learning algorithms are used in their proposed procedure to provide regionally specific predictions about crop yields in different crops in the UK and across Europe. These techniques include GBR, SVR, and KNN. Also, it is worth noting that Farhat et al. [9] have done some work predicting tuber yields in potatoes. LR, elastic net, KNN, and are the four machine learning techniques used to predict potato (*Solanum tuberosum*) tuber production using proximal sensed information of soil and crop factors. Six field's electrical conductivity, moisture content, slope, normalized difference vegetation index (NDVI), and soil chemistry were measured over the course of two growing seasons in Atlantic Canada (2017 and 2018). Support Vector Regression was shown to be the most effective model. Estimates are needed for the wheat crop in northern India.

### 3 Proposed Work

By reusing historical data and information to “train” a model with fresh information, machine learning allows machines to learn and improve over time. It is this model’s job to predict future production. The higher the quality of the datasets used to train the classifier, the better it will perform. Machine learning methods, including regression and classification, have been shown to outperform several common statistical methods. The chemical composition of the soil, the quantity of precipitation, the temperature, etc., are all crucial factors in crop production. These factors greatly contribute to a noticeable rise in agricultural output. Which crops are best to grow depending on market conditions?

**Algorithm** Regression tree for Crop-yield prediction based on weather and soil parameters

Data: Set of training samples  $D_0$ .

Result: Binary Decision Tree

1. Create root node  $r_0$  associated with  $D_0$ .

2. While  $\exists$  non-pure leaf node  $r$ ; and a split is possible do
  - a. Determine the best bivariate oblique split
  - b.  $a * X_i + b < X_i$  on 4; according to a prior defined
  - c. impurity measure.
  - d. Partition  $D_i$ ; into two new subsets  $D_{i1}$  and  $D_{i2}$
  - e. according to the split.
    - i. Split  $r_i$ ; into two new nodes  $r_{i1}$  and  $r_{i2}$  associate
    - ii. each  $r_{ij}$ , with a new leaf node with the
    - iii. corresponding subset  $i j$  for  $j = 1, 2$ .
3. end
4. for all the leaf nodes  $r_i$ ; do
 

Assign the most frequent class label in  $D_i$  to  $r_i$
5. end

Classifying decisions using decision trees is the purpose of decision tree classifiers. To create a class label (discrete) prediction, decision tree classifiers, just like any other kind of classifier, consider the values of the characteristics and features of the data. Classifiers based on decision trees have the same organizational structure as decision trees, in which straightforward constraints on a single attribute are used to mark the connection between an intermediate node and the offspring of that node. Class label predictions are used to label the individual leaves. Many different approaches to learning have been suggested as possible approaches for decision tree classifiers. Most techniques include both a “tree growth” and “pruning” phase. The process of the tree developing is called recursion, and it consists of choosing an attribute to split on and then repeating the actual splitting criteria on the offspring until the data corresponding to that route is either pure or too tiny in size. During the pruning phase, a portion of the bottom of the tree that has learnt noise from the data is removed to increase the accuracy of the model.

$$\text{Mean Absolute Error} = (1/n)^* \sum |y_i - x_i|$$

The algorithm 1 gives the general design that was used for the regression tree model for the prediction of crop yields. Because it gives the anticipated entity as a function of the dependent entities, regression analysis is most often used for the purpose of prediction. In certain circumstances, it reveals the connections between the variables that are independent and those that are dependent. The actions required to construct a regression model for the accurate forecasting of crop production.

$$\text{RMSE} = \text{SD}_y \sqrt{(1 - r^2)}$$

## 4 Results and Discussions

The Food and Agriculture Organization (FAO) and the World Data Bank are the sources of all of the datasets that are accessible to the public on this website [20]. The challenge of accurately predicting crop yields is a significant one in the agriculture industry. It is crucial to have correct knowledge about the history of crop yield when making choices pertaining to agricultural risk management and making forecasts about the future. Agricultural output is mostly dependent on weather patterns (rain, temperature, etc.) and herbicides.

Here, Figs. 2 and 3 describe the R, Max, MAE, and RMSE between existing regression tree model and existing models. The figures show that the proposed model is better compared to existing models.

Here, Fig. 4 describes the regression comparison between existing regression tree model and existing models. The figure shows that the proposed model is better compared to existing models. Table 1 shows the performance of proposed and existing models.

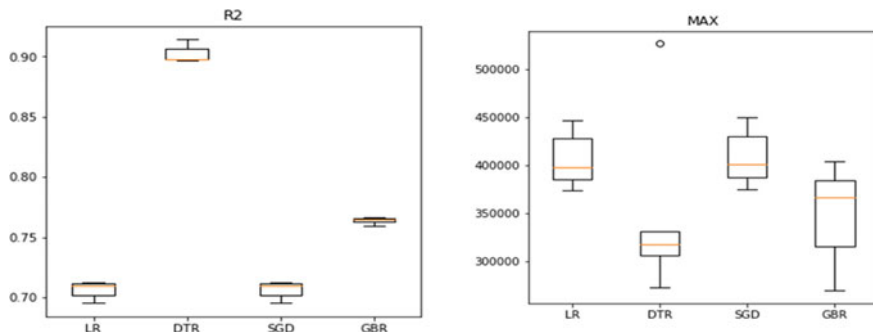


**Fig. 2** Squared value of R and MAX comparison

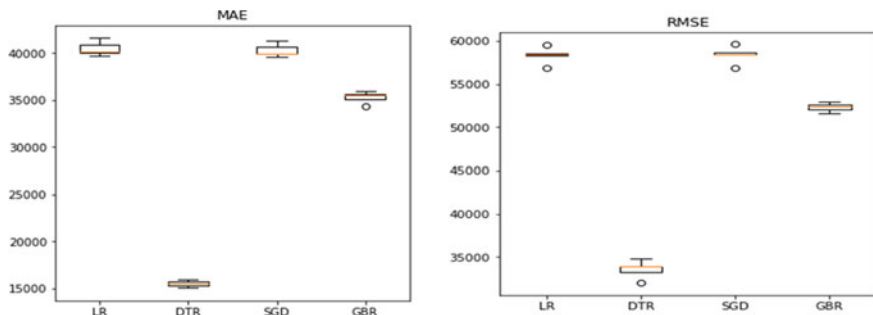


**Fig. 3** MAE and RMSE comparison

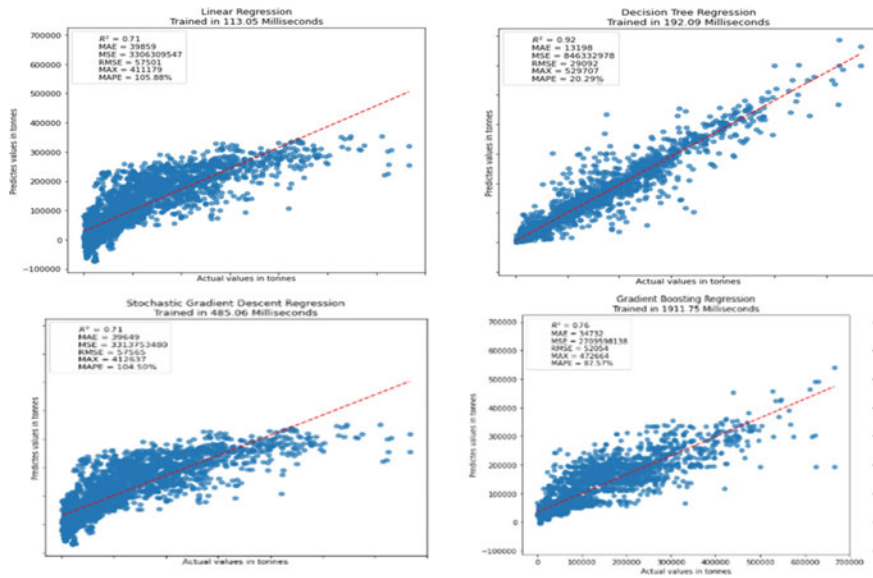


**Fig. 4** Regression of proposed regression tree and existing models

**Table 1** Different metric for evaluation

Models	$R^2$	MAX	MAE	RMSE
Linear regression	0.71	411,179	39,859	57,501
Decision tree regression	0.92	529,707	13,198	29,092
Stochastic gradient descent regression	0.71	412,637	39,649	57,565
Gradient boosting regression	0.76	472,664	34,732	52,054

## 5 Conclusion

The ability to accurately forecast crop production is one of the most important considerations for farmers. The work showed that regression approaches may be used for yield prediction for the region with good results, which is something that was proved by the endeavour. The utilization of wheat, maize, and cotton is visible extensively in several parts of our country. India is a standout amongst the majority of countries in Asia when it comes to producing yields, and this can be noticed everywhere. Therefore, an attempt was made to forecast the production of such in India. In order to make an accurate forecast of the yield, a regression model is used as a prediction tool, and some of the most significant contributing components to yield production are chosen. The information that was acquired, in addition to the various characteristics, was included in the regression model in the capacity of input variables. Following these steps allows for the identification of the most appropriate regression model for the yield. Each model is executed a number of times so that a range of

possible estimates of root mean square and R2 statistics values may be considered. The projection of the amount of wheat, maize, and cotton that will be produced in selected years is carried out with the use of a regression tree model for the purpose of yield prediction. The findings indicate that the regression model that was suggested is an appropriate way for forecasting the amount of yield that would be produced. The root mean square, R2 statistics, and percentage prediction error are the metrics that are used to evaluate and contrast the outcomes of the various models. The most accurate model for estimating crop output is one that has a lower root mean square, a higher percentage prediction error, and a higher R2 statistic value.

## References

1. Li JYX, Low M, Lobell D, Ermon S (2017) Deep gaussian process for crop yield prediction based on remote sensing data. In: The thirty-first AAAI conference on artificial intelligence
2. Paudel D, Boogaard H, de Wit A, Anssen S, Osinga S, Pylianidis C, Athanasios IN (2021) Machine learning for large scale crop yield forecasting. Agric Syst 187:103016. <https://doi.org/10.1016/j.agry.2020.103016>
3. Gopi AP, Naik KJ (2021) A model for analysis of IoT based aquarium water quality data using CNN model. In: 2021 international conference on decision aid sciences and application (DASA), December, IEEE, pp 976–980
4. Sun J, Lai Z, Di L, Sun Z, Tao J, Shen Y (2020) Multi level deep learning network for county level corn yield estimation in the u.s. corn belt. IEEE J Sel Top Appl Earth Obs Remote Sens 13:5048–5060. <https://doi.org/10.1109/JSTARS.2020.3019046>
5. Shahhosseini M, Hu G, Huber I, Archontoulis S (2021) Coupling machine learning and crop modelling improves crop yield prediction in the US cornbelt. Sci Rep 11. <https://doi.org/10.1038/s41598-020-80820-1>
6. Khaki S, Wang L (2019) Crop yield prediction using deep neural networks. Front Plant Sci 10. <https://doi.org/10.3389/fpls.2019.00621>
7. Abbas F, Afzaal H, Farooque AA, Tang S (2020) Crop yield prediction through proximal sensing and machine learning algorithms. A gronomy 10(7). <https://doi.org/10.3390/agronomy10071046>
8. Kaneko A, Kennedy T, Mei L, Sintek C, Burke M, Ermon S, Lobell D (2019) Deep learning for crop yield prediction in Africa
9. Paudel D, Boogaard H, de Wit A, Janssen S, Osinga S, Pylianidis C, Athanasios's IN (2021) Machine learning for large-scale crop yield forecasting. Agricul Syst 187:103016
10. Abbas A, Afzaal H, Farooque AA, Tang S (2020) Crop yield prediction through proximal sensing and machine learning algorithms. Agronomy 10(7)
11. Camacho DM, Collins KM, Powers RK, Costello JC, Collins JJ (2018) Next-generation machine learning for biological networks. Cell 173(7):1581–1592
12. Gopi AP, Jyothi RNS, Narayana VL, Sandeep KS (2020) Classification of tweets data based on polarity using improved RBF kernel of SVM. Int J Inform Technol 1–16
13. Aziz S, Dowling MM, Hammami H, Piepenbrink A (2019) Machine learning in finance: a topic modeling approach. SSRN
14. van Kloppenburg T, Kassahun A, Catal C (2020) Crop yield prediction using machine learning: a systematic literature review. Comput Electron Agric 177:105709
15. Kaneko A, Kennedy T, Mei L, Sintek C, Burke M, Ermon S, Lobell D (2016) Deep learning for crop yield prediction in Africa
16. Vander Plas J (2016) In: Python data science handbook, essential tools for working with data. O'reilly edition

17. Truong Q, Nguyen M, Dang H, Mei B (2020) Housing price prediction via improved machine learning techniques. *Proc Comput Sci* 174:433–442; In: 2019 international conference on identification, information and knowledge in the internet of things
18. Arepalli PG, Akula M, Kalli RS, Kolli A, Popuri VP, Chalichama S (2022) Water quality prediction for salmon fish using gated recurrent unit (GRU) model. In: 2022 second international conference on computer science, engineering and applications (ICCSEA), September, IEEE, pp 1–5
19. Gopi AP, Gowthami M, Srujana T, Gnana Padmini S, Durga Malleswari M (2022) Classification of denial-of-service attacks in IoT networks using AlexNet. In: Human-centric smart computing: proceedings of ICHCSC 2022, Singapore, Springer Nature Singapore, pp 349–357
20. <https://www.kaggle.com/datasets/patelris/crop-yield-prediction-dataset>

# A Gray Wolf Optimization-Inspired Hybrid Method for Disease Identification



Emon Asad and Ayatullah Faruk Mollah

**Abstract** Disease identification from gene expression microarray data is an extremely important research problem. Analysis of microarray data helps to accurately diagnose the disease types, finds therapeutic plans for that disease, helps to gain insight into molecular mechanisms of that genetic disease and many more. In this work, a filter-wrapper-based disease identification technique inspired by gray wolf optimization (GWO) algorithm is proposed. In the first stage, mutual information-based filter method is used to discard irrelevant genes. Then, the rest of the genes are passed to GWO embedded with support vector machine to detect the most relevant genes and corresponding disease types. Nearly 100% accuracy is obtained with an average of 3.9 genes on three microarray datasets. On another dataset, 91.66% accuracy is obtained with an average of 4.6 genes only. The comparative results with other state-of-the-art methods confirm the superiority of this proposed method.

**Keywords** Disease identification · Gray wolf optimization · Microarray data · Hybrid feature selection · Cancer classification

## 1 Introduction

Cancer is a major health problem across the world. Almost 10 million people succumbed to cancer in 2020 [1]. Many cancers can be cured if detected and treated early. Microarray data contain gene expression profile of thousands of genes, and analysis of such data may help us to identify the disease type (i.e., what type of cancer) and to find therapeutic plans for the disease. Accurately detecting a disease or detecting any abnormality in health or finding any interesting pattern from these

---

E. Asad (✉) · A. F. Mollah

Department of Computer Science and Engineering, Aliah University, IIA/27 New Town, Kolkata 700160, India

e-mail: [mailto:emonasad@gmail.com](mailto:mailto:emonasad@gmail.com)

A. F. Mollah

e-mail: [afmollah@aliah.ac.in](mailto:afmollah@aliah.ac.in)

microarray datasets is quite a challenging task to accomplish because those datasets have large dimensions and small samples, which decrease classification accuracy and increase computational complexity. Also, those datasets contain irrelevant information, noise and redundant information that may mislead the classifiers [2]. To tackle those problems, feature selection is one of the most sought-after data preprocessing techniques which can reduce the computational complexity by reducing the number of dimensions and removing the redundant, irrelevant features, or noise [3]. Mainly, there are four types of feature selection methods available—filter, wrapper, ensemble or hybrid and embedded techniques [2, 4]. Among them, ensemble or hybrid technique is the most popular due to its high accuracy in prediction and low computational complexity [5]. Hybrid machine learning methods have been applied by many researchers to solve feature selection, disease identification and gene selection problems from microarray datasets [2, 6–8]. Recently, in a number of works, a population-based heuristic algorithm called gray wolf optimization (GWO) [9] has been applied, which mimics the hunting behavior of gray wolf. Due to its simplicity and fast convergence nature, GWO is extremely popular among research community. Therefore, GWO has been applied on various fields to solve different problems such as: feature selection [9], intrusion detection in networks [10], scheduling [11], biomedical data analysis [12], image analysis [13] and many more.

In this work, a hybrid disease detection technique for biomedical microarray data based on mutual information and gray wolf optimization (MIGWO) is presented. In the first stage of this method, we have applied mutual information (MI)-based gene selection technique to reduce the number of dimensions and to select varying numbers of most informative genes from the datasets. The prospective features are then passed to GWO algorithm with support vector machine (SVM) classifier to select optimal subset of features and to detect the disease type. In our study, we have tested the MIGWO algorithm with four microarray datasets, i.e., mixed-lineage leukemia (MLL), leukemia, colon cancer and central nervous system (CNS). Comparative results show that MIGWO method has excelled over many existing state-of-the-art methods in terms of classification accuracy and numbers of genes obtained for CNS, MLL and colon cancer datasets, and for the leukemia data, it has achieved competitive results.

## 2 Related Works and Motivation

Disease identification from microarray data is a well-studied problem, and recently, studies on various aspects of this problem are being carried out. In [6], Alomari et al. have presented a gene selection technique by combining robust minimum redundancy maximum relevancy (rMRMR) with modified gray wolf optimizer (MGWO) and have applied the rMRMR-MGWO method over nine datasets. The proposed rMRMR-MGWO method has obtained 100% accuracy for five datasets with only few genes. Kundu et al. [7] adopted a filter-wrapper-based gene selection technique which implements Pasi Luukka's filter-based method followed by altruistic whale

optimization algorithm (AltWOA) wrapper method for biomarker identification from eight high-dimensional microarray datasets. Their method has produced an average of 100% classification accuracy with an average of 24.5 genes for seven datasets. In [14], Ghosh et al. have proposed a quantum squirrel-inspired gene selection technique and tested their model on prostate cancer's gene expression and methylation data. The proposed algorithm exhibits a steady 100% classification accuracy with only around four genes and surpassed other existing state-of-the-art methods. Additionally, they have biologically validated the selected genes by incorporating Kyoto encyclopedia of genes' and genomes' (KEGGs) pathway and gene ontologies' (GOs) terms for the selected genes.

Lately, a number of studies have involved GWO algorithm to solve a variety of optimization problems. Chakraborty et al. [12] have adopted an integrative technique with enhanced gray wolf optimization (E-GWO) feature selection algorithm to apply over five biomedical heart disease datasets. Their method has achieved the highest accuracy of 99.26% with random forest bagging technique (RFBT) classifier. In [10], Alzubi et al. have introduced a hybrid intrusion detection method by applying modified binary gray wolf optimization and binary particle swarm optimization over two different benchmark attack datasets, i.e., NSL KDD'99 and UNSW-NB15. By applying this intrusion detection approach, the detection accuracy has been improved by 0.3–12%, and the detection rate has been improved by 2–12% in contrast with other state-of-the-art algorithms. Hu et al. [9] implemented an improved binary gray wolf optimization algorithm for feature selection from popular UCI datasets and achieved very low classification error with low features.

In this work, we have applied a filter-wrapper-based disease identification technique over microarray datasets. Information theoretic feature selector, i.e., mutual information is applied to calculate the score of each feature. The features are then ranked in descending order according to their computed scores. Sequentially, top 100, 200 and 300 features are then selected from the sorted array for evaluation and detection of diseases by applying GWO algorithm combined with SVM classifier. The performance of the MIGWO method has been determined by observing the maximum accuracy achieved with the least number of genes selected by this method.

### 3 Materials and Methods

In this work, a two-step disease detection technique called MIGWO for biomedical microarray datasets has been presented. In the first step of this method, we have normalized the data, and then, the scores of the features/genes are computed using MI filter-based technique. Subsequently, the genes are ranked in descending order according to their MI scores and top-ranked genes are passed through the GWO for evaluation and detection of diseases.

### 3.1 Normalization of Data

Data normalization or data scaling technique scales data within a specified range of values. Data normalization removes the outliers in data and enhances model's power of prediction. In this work, a min–max normalization technique is utilized as it is extensively used by researchers. Min–max scaler projects the data within the range 0 and 1 [4].

### 3.2 Mutual Information

Mutual information (MI) is a widely used filter-based feature selection technique [15–18]. Mutual information is a measure for a random variable when other's information is given. It also can be thought of as the reduction of uncertainty of a random variable when knowledge of another one is given. The MI is derived from the idea of Shannon's entropy and conditional entropy. MI between two random variables  $A$  and  $B$  is shown in Eq. 1 as follows [19]:

$$\begin{aligned} MI(A, B) &= H(A) - H(A|B) \\ \text{Or} \\ MI(A, B) &= H(B) - H(B|A) \end{aligned} \quad (1)$$

The entropy  $H(A)$  of a random variable  $A$  having a probability density function  $p$  is calculated as shown in Eq. 2.

$$H(A) = - \sum_i p(a_i) * \log_2 p(a_i). \quad (2)$$

Also, the conditional entropy  $H(A|B)$  of two random variables  $A$  and  $B$  with  $p$  as the probability density function can be calculated by Eq. 3 as follows [4]:

$$H(A|B) = - \sum_{a \in A} p(a, b) \sum_{b \in B} p(a, b) * \log_2 \frac{P(A, B)}{g(a)}. \quad (3)$$

Here,  $p(a, b)$  signifies the joint probability distribution at  $(a, b)$  between the variables  $a$  and  $b$ , and  $g(a)$  is the marginal probability of  $a$ .

### 3.3 Ranking of Features

After calculating the MI score for each feature/gene, all the genes are arranged in descending order according to their MI scores. This technique ranks the features

or genes according to their informative values, and the most informative genes are found at the top of the sorted array, whereas the least informative ones are at the bottom of the array. Sequentially, top 100, 200 and 300 genes from the sorted array are then selected for evaluation by the GWO. The genes are sorted according to Eq. 4 as shown below.

$$g_1, g_2, g_3 \dots, g_n, \quad (4)$$

whereas  $\text{score}(g_1) > \text{score}(g_2) > \text{score}(g_3) > \dots > \text{score}(g_n)$ .

Here, a microarray dataset  $D_{m \times n}$  contains  $m$  samples and  $n$  features or genes. The gene set  $F = \{f_1, f_2, \dots, f_n\}$  has  $n$  genes. Also,  $g_i (i = 1, \dots, n)$  denotes the genes after sorting.

### 3.4 Gray Wolf Optimization

A novel type of swarm intelligence-based and population strategy-dependent meta-heuristic algorithm, i.e., gray wolf optimization [6] mimics the hunting behavior of gray wolves in the wild. A gray wolf gang mainly consists of four types of gray wolves according to their social dominant hierarchy. Alpha ( $\alpha$ ) wolves are the supreme ones which are responsible for decision-making for hunting, sleeping place, controlling the pack, etc. The beta wolves ( $\beta$ ) are second in command after the alphas. Beta wolves help the alphas to control or manage the pack. The beta wolves take charge after the alpha dies. The delta wolves ( $\delta$ ) live at the third dominant level of hierarchy. They obey the  $\alpha$ 's and  $\beta$ 's. They work as sentinels, scouts, hunters and as caretakers. The omegas ( $\omega$ ) are lowest level of wolves' pack. They obey  $\alpha$ ,  $\beta$  and  $\delta$  and back up the pack in  $\alpha$ ,  $\beta$  and  $\delta$  levels of wolves for hunting the prey. In GWO, the mathematical replica of the wolves and their social hierarchy, encircling, hunting, tracking and attacking the prey of the wolves are implemented. Also, in the GWO,  $\alpha$  contains the best solution,  $\beta$  has the second best solution and  $\delta$  has the third best solutions, respectively. The rest of the possible solutions is possessed by the  $\omega$  wolves. The encircling behavior of the wolves is mathematically represented by Eqs. 5–6 as below.

$$\vec{G} = \left| \vec{C} \cdot \vec{Y}_p(t) - \vec{R}(t) \right|, \quad (5)$$

$$\vec{R}(t+1) = \vec{Y}_p(t) - \vec{A} \cdot \vec{G}. \quad (6)$$

Here, the position vector of the prey and position vector of the wolf at  $t^{\text{th}}$  iteration are denoted by  $\vec{Y}_p(t)$  and  $\vec{R}(t)$ , respectively.  $\vec{A}$  and  $\vec{C}$  are the coefficient vectors, and they can be calculated by Eqs. 7–8 as given below.

$$\vec{A} = 2\vec{b} \cdot \vec{q}_1 - \vec{b}, \quad (7)$$

$$\vec{C} = 2 \cdot \vec{q}_2, \quad (8)$$

where  $b$  is a variable, and it linearly decreases from 2 to 0 over iterations, and  $q_1, q_2$  are random vectors and their values lie in between  $[0, 1]$ .

To update the positions of the  $\alpha$ ,  $\beta$  and  $\delta$  wolf which have the best, second best and the third best solutions, respectively, we can use Eqs. 9–15 as presented below.

$$\vec{G}_\alpha = \left| \vec{C}_1 \cdot \vec{X}_\alpha - R \right|, \quad (9)$$

$$\vec{G}_\beta = \left| \vec{C}_2 \cdot \vec{X}_\beta - R \right|, \quad (10)$$

$$\vec{G}_\delta = \left| \vec{C}_3 \cdot \vec{X}_\delta - R \right|, \quad (11)$$

$$\vec{X}_1 = \vec{X}_\alpha - A_1 \cdot (\vec{G}_\alpha), \quad (12)$$

$$\vec{X}_2 = \vec{X}_\beta - A_2 \cdot (\vec{G}_\beta), \quad (13)$$

$$\vec{X}_3 = \vec{X}_\delta - A_3 \cdot (\vec{G}_\delta), \quad (14)$$

$$\vec{R}(t+1) = \frac{(\vec{X}_1 + \vec{X}_2 + \vec{X}_3)}{3}. \quad (15)$$

$\vec{X}_1$ ,  $\vec{X}_2$  and  $\vec{X}_3$  are the three best solutions in the swarm,  $A$  and  $C$  are calculated using Eqs. 7–8. In the GWO, the exploration of the search space is controlled by the parameter  $A$ , whereas the exploitation is guided by the parameter  $C$ . When  $|A| < 1$ , the wolf attacks the prey, and when  $|A| > 1$ , then the wolf diverges away from the prey to find much better prey or the solution. Also, the stochastic value of  $C$  ( $C > 1$  or  $C < 1$ ) places the prey in random positions in determining the distance as it can be seen in Eq. 5. The working of the MIGWO is depicted in Fig. 1.

### 3.5 Fitness Function

The above-described filter-wrapper-based optimization algorithm seeks to identify the disease with maximum classification accuracy, whereas it selects less numbers of features or genes, and hence, it falls under multi-objective optimization problem. The fitness function for this MIGWO algorithm is defined as follows in Eq. 16.

$$F = p \cdot A_c + q \cdot \frac{M}{N}, \quad (16)$$

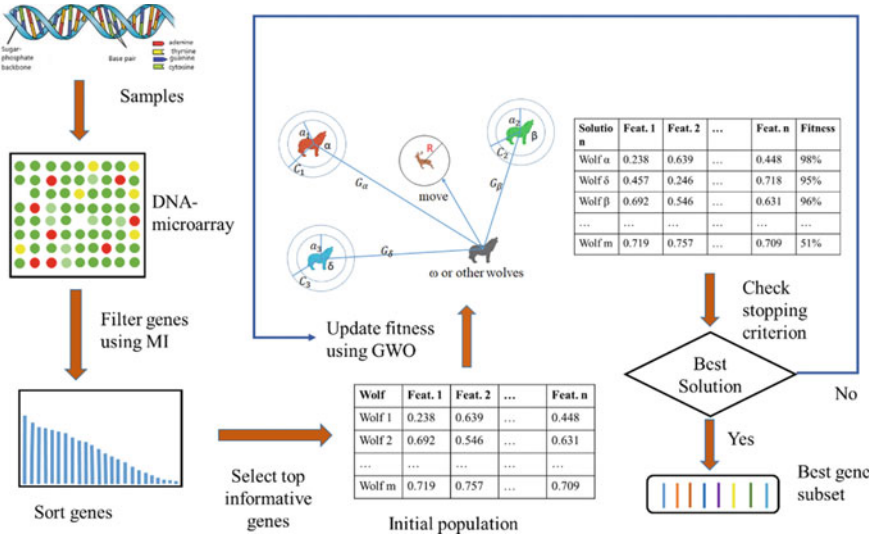


**Fig. 1** Two-step workflow diagram of the MIGWO. The first step filters out irrelevant genes from computation, and the GWO-powered second stage selects the most informative genes and detects diseases

where  $A_c$  is the accuracy obtained by the classifier,  $M$  is the numbers of selected features and  $N$  is the total numbers of features or genes. Also,  $p$  and  $q$  are weights to counter the balance between  $A_c$  and  $\frac{M}{N}$ .

## 4 Results and Discussion

The MIGWO method has been applied on four microarray datasets, i.e., mixed-lineage leukemia (MLL) [20], leukemia [21], colon cancer [22] and central nervous system (CNS) [23]. The number of features and samples of these datasets varies from 2000 to 12,582 and 60 to 72, respectively. The experiments were conducted on an Intel Core i5 processor and 8 GB RAM machine and Python 3.9 environment. SVM [24] with train-test split was used for performance measure. Training was conducted in order to maximize the test accuracy while minimizing the number of selected genes. Also, computation time (in seconds) was considered as a performance measure, as the results is portrayed in Table 1.

The MIGWO method has sequentially selected top 100, 200 and 300 most informative genes from the four microarray datasets to reduce the complexity in computation. From Table 1, it is observed that the average accuracy and average number of genes selected from MLL dataset are 97.77% and 3, respectively. From the leukemia dataset, the average classification accuracy obtained is 100% with an average of 3.33 number of genes. For the colon cancer dataset, the average accuracy is 100%, whereas

**Table 1** Observed results for the four microarray datasets applying MIGWO

Dataset	No. of features	No. of samples	No. of features by MI	Accuracy	No. of features selected	Computation time (s)
MLL [20]	12,582	72	100	1.0	3	125.7
			200	0.9333	4	447.0
			300	1.0	2	819.0
Leukemia [21]	7129	72	100	1.0	4	136.7
			200	1.0	2	796.0
			300	1.0	4	1219.0
Colon cancer [22]	2000	62	100	1.0	3	1406.8
			200	1.0	7	1518.5
			300	1.0	6	2480.0
CNS [23]	7129	60	100	0.9166	3	658.4
			200	0.9166	4	1427.6
			300	0.9166	7	1151.6

average number of gene is 5.33. Also, from the CNS dataset, average accuracy obtained is 91.66% and the average number of gene selected is 4.66.

For the top 300 genes, the MIGWO method has achieved high accuracy with less number of genes as this can be observed from Table 1. It is seen from the table that 100% accuracy was achieved with only two genes from MLL data. For leukemia data, 100% accuracy was obtained with four genes, and from colon cancer data, 100% accuracy was obtained only with six genes. For CNS data, 91.66% accuracy was achieved with only seven features. However, the highest accuracy can be observed with lower number of genes for leukemia data, colon cancer data and CNS data when number of selected genes, respectively, are 200, 100 and 100. In that case, the MIGWO method has shown 100% accuracy for leukemia and colon cancer datasets with only two and three genes, respectively. For the CNS dataset, 91.66% accuracy can be observed with only three features. The fitness graph for top 300 genes for all datasets is shown in Fig. 2.

Comparison of the MIGWO method with other state-of-the-art methods shows the superiority of this proposed method over others, as it is portrayed in Table 2. The comparison has been done considering higher accuracy obtained and lower number of features selected by the methods. Also, it can be noted that the comparison has been done considering the top 300 most informative genes in evaluation by the MIGWO. The proposed MIGWO method has outperformed other state-of-the-art methods for CNS, MLL and colon cancer microarray datasets as it can be observed from Table 2. For leukemia dataset, MIGWO shows very competitive results. Our work is highlighted in italics in Table 2.

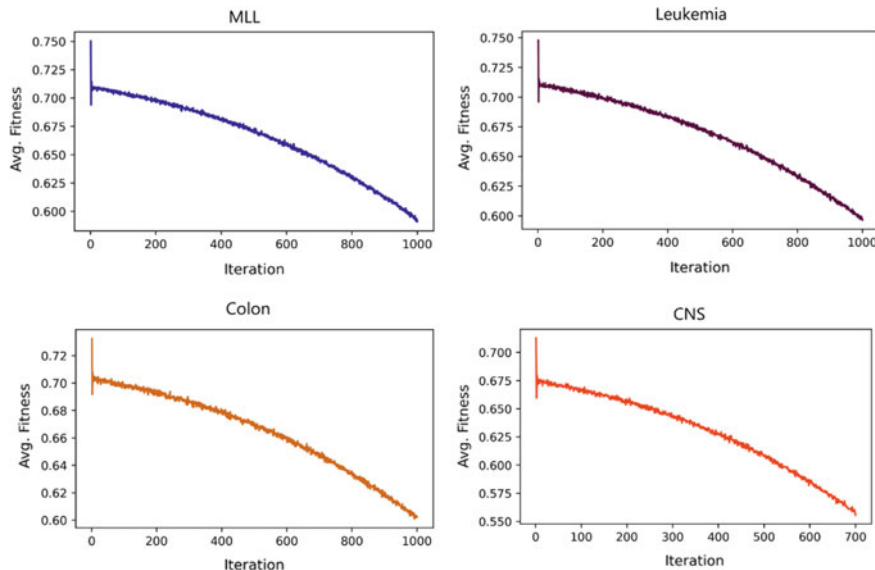


**Fig. 2** Average fitness value with respect to iterations of the MIGWO algorithm for top 300 features for MLL, leukemia, colon cancer and CNS datasets

## 5 Conclusion and Future Work

In this work, a hybrid disease identification method using mutual information and the gray wolf optimization algorithm has been presented and evaluated on four microarray datasets representing different diseases. This method has achieved high accuracy with a low number of genes for all four datasets (97.36% accuracy with 4.08 genes on average), which suggests the potency of the proposed MIGWO method. Comparison with other state-of-the-art methods suggests the superiority of this method over many others. In future, the proposed MIGWO method can be applied to other microarray datasets for gene selection and also can be applied on a wide variety of datasets for feature selection and thereby disease identification.

**Table 2** Comparison of the MIGWO with other state-of-the-art methods

Dataset	Method name	No. of genes	Accuracy (%)	Precision	Recall	F-score	Time (sec.)
MLL [20]	Shreem et al. [25]	10	98.97	–	–	–	–
	Jain et al. [26]	30.8	100	–	–	–	245.7
	Sharbaf et al. [27]	18.70	97.55	–	–	–	–
	Pashaei et al. [28]	5	98.61	–	–	–	–
	<i>MIGWO</i>	2	100	–	–	–	819.0
Leukemia [21]	Alshamlan et al. [29]	4	100	–	–	–	–
	Aziz et al. [8]	12	98.68	–	–	–	–
	Jain et al. [26]	4	100	–	–	–	141.4
	Dashtban et al. [2]	15	100	–	–	–	–
	Shreem et al. [25]	26.4	100	–	–	–	–
	Moradi et al. [30]	100	89.86	–	–	–	–
	<i>MIGWO</i>	4	100				136.7
Colon cancer [22]	Jain et al. [26]	4	94.89	–	–	–	39.27
	Aziz et al. [8]	16	98.14	–	–	–	–
	Alshamlan et al. [29]	10	98.38	–	–	–	–
	Basavegowda et al. [3]	–	96.00	–	96.00	–	–
	Shreem et al. [25]	9	87.53	–	–	–	–
	Alomari et al. [6]	9.8	95.86	96.83	94.09	96.80	–
	<i>MIGWO</i>	6	100	–	–	–	2480.0
CNS [23]	Kilicarslan et al. [23]	–	83.95	–	–	–	–
	Jain et al. [26]	10.5	95.84	–	–	–	78.43
	Basavegowda et al. [3]	–	96.00	96.00	96.00	96.00	–
	Salem et al. [31]	38	86.67	–	–	–	–
	Pashaei et al. [28]	2	86.66	–	–	–	–
	<i>MIGWO</i>	7	91.66	–	–	–	1151.6

## References

1. Ferlay J, Colombet M, Soerjomataram I, Parkin DM, Piñeros M, Znaor A, Bray F (2021) Cancer statistics for the year 2020: an overview. *Int J Cancer* 149(4):778–789
2. Dashtban M, Balafar M (2017) Gene selection for microarray cancer classification using a new evolutionary method employing artificial intelligence concepts. *Genomics* 109(2):91–107
3. Basavegowda HS, Dagnew G (2020) Deep learning approach for microarray cancer data classification. *CAAI Trans Intell Technol* 5(1):22–33
4. Asad E, Mollah AF (2021) Biomarker identification from gene expression based on symmetrical uncertainty. *Int J Intell Inf Technol* 17(4):19–37
5. Alhenawi E, Al-Sayed R, Hudaib A, Mirjalili S (2021) Feature selection methods on gene expression microarray data for cancer classification: a systematic review. *Comput Biol Med* 140:105051
6. Alomari OA, Makhadmeh SN, Al-Betar MA, Alyasseri ZAA, Doush IA, Abasi AK, Awadallah MA, Zitar RA (2021) Gene selection for microarray data classification based on gray wolf optimizer enhanced with TRIZ-inspired operators. *Knowl-Based Syst* 223:107034
7. Kundu R, Chattopadhyay S, Cuevas E, Sarkar R (2022) AltWOA: altruistic whale optimization algorithm for feature selection on microarray datasets. *Comput Biol Med* 144:105349
8. Aziz R, Verma C, Srivastava N (2017) A novel approach for dimension reduction of microarray. *Comput Biol Chem* 71:161–169
9. Hu P, Pan JS, Chu SC (2020) Improved binary grey wolf optimizer and its application for feature selection. *Knowl-Based Syst* 195:105746
10. Alzubi QM, Anbar M, Sanjalawe Y, Al-Betar MA, Abdullah R (2022) Intrusion detection system based on hybridizing a modified binary grey wolf optimization and particle swarm optimization. *Expert Syst with Appl* 204:117597
11. Lu C, Gao L, Li X, Xiao S (2017) A hybrid multi-objective grey wolf optimizer for dynamic scheduling in a real-world welding industry. *Eng Appl Artif Intell* 57:61–79
12. Chakraborty C, Kishor A, Rodrigues JJ (2022) novel enhanced-grey wolf optimization hybrid machine learning technique for biomedical data computation. *Comput Electri Eng* 99:107778
13. Mohakud R, Dash R (2022) Designing a grey wolf optimization based hyper-parameter optimized convolutional neural network classifier for skin cancer detection. *J King Saud Univer—Comput Inform Sci* 34(8(B)):6280–6291
14. Ghosh M, Sen S, Sarkar R, Maulik U (2021) Quantum squirrel inspired algorithm for gene selection in methylation and expression data of prostate cancer. *Appl Soft Comput* 105:107221
15. Zhou H, Wang X, Zhu R (2022) Feature selection based on mutual information with correlation coefficient. *Appl Intell* 52:5457–5474
16. Hassan KM, Islam MR, Nguyen TT, Molla MKI (2022) Epileptic seizure detection in EEG using mutual information-based best individual feature selection. *Expert Syst with Appl* 193:116414
17. Gavel S, Raghuvanshi AS, Tiwari S (2022) Maximum correlation based mutual information scheme for intrusion detection in the data networks. *Expert Syst with Appl* 189:116089
18. Hoque N, Bhattacharyya D, Kalita J (2014) MIFS-ND: a mutual information-based feature selection method. *Expert Syst Appl* 41(14):6371–6385
19. Beraha M, Metelli AM, Papini M, Tirinzoni A, Restelli M (2019) Feature selection via mutual information: new theoretical insights. In: International joint conference on neural networks, Budapest
20. Zhu Z, Ong YS, Dash M (2007) Markov blanket-embedded genetic algorithm for gene selection. *Pattern Recogn* 49(11):3236–3248
21. Golub TR, Slonim D, Tamayo P, Huard C, Gaasenbeek M, Mesirov J, Coller H, Loh ML, Downing JR, Caligiuri MA, Bloomfield CD, Lander E (1999) Molecular classification of cancer: class discovery and class prediction by gene expression monitoring. *Science* 286(5439):531–537
22. Alon U, Barkai N, Notterman DA, Gish K, Ybarra S, Mack D, Levine AJ (1999) Broad patterns of gene expression revealed by clustering analysis of tumor and normal colon tissues probed

- by oligonucleotide arrays. In: Proceedings of the national academy of sciences of the United States of America, pp 6745–6750
- 23. Kilicarslan S, Adem K, Celik M (2020) Diagnosis and classification of cancer using hybrid model based on ReliefF and convolutional neural network. *Med Hypotheses* 137:109577–109587
  - 24. Guyon I, Weston J, Barnhill S, Vapnik V (2002) Gene selection for cancer classification using support vector machines. *Machine Language* 46(1–3):389–422
  - 25. Shreem SS, Abdullah S, Nazri MZA (2016) Hybrid feature selection algorithm using symmetrical uncertainty and a harmony search algorithm. *Int J Syst Sci* 47(6):1312–1329
  - 26. Jain I, Jain VK, Jain R (2018) Correlation feature selection based improved-binary particle swarm optimization for gene selection and cancer classification. *Appl Soft Comput* 62:203–215
  - 27. Sharbaf FV, Mosafer S, Moattar MH (2016) A hybrid gene selection approach for microarray data classification using cellular learning automata and ant colony optimization. *Genomics* 107(6):231–238
  - 28. Pashaei E, Ozen M, Aydin N (2016) Gene selection and classification approach for microarray data based on random forest ranking and BBHA. In: IEEE-EMBS international conference on biomedical and health informatics, Las Vegas, pp 308–311
  - 29. Alshamlan HM, Badr GH, Alohalil YA (2015) Genetic bee colony (GBC) algorithm: a new gene selection method for microarray cancer classification. *Comput Biol Chem* 56:49–60
  - 30. Moradi P, Gholampour M (2016) A hybrid particle swarm optimization for feature subset selection by integrating a novel local search strategy. *Appl Soft Comput* 43:117–130
  - 31. Salem H, Attiya G, El-Fishawy N (2017) Classification of human cancer diseases by gene expression profiles. *Appl Soft Comput* 50:124–134

# Automated Retinal Blood Vessel Segmentation Using Modified U-Net Architecture



Debasis Maji, Souvik Maiti, Ashis Kumar Dhara, and Gautam Sarkar

**Abstract** Robotized tracking of vein structures is becoming a crucial aspect for better analysis of vascular ailment. Diabetes is an internationally predominant illness. The retinal images of diabetic patients are used for determining the severity level. This work utilizing profound learning procedure could significantly benefit in effective identification. In spite of the fact that we utilize just a little part of pictures (1/4) in preparing however are helped with higher picture goals. An essential aspect in determining the existence of many eye disorders and heart issues is the status of the blood vessels in the retina. The segmentation of blood vessels in fundus pictures has become quite popular for this reason. This study suggests a method for segmenting blood vessels using a modified U-net architecture. These outcomes propose that a profound learning framework could expand the expense adequacy of screening.

**Keywords** Fundus image · Diabetic retinopathy · Blood vessels segmentation

## 1 Introduction

Diabetic retinopathy, which causes the structure of the retinal blood vessels to alter and results in blindness, is one of the most frequent disorders. A cataract is the maximum broadly diagnosed purpose for visible debilitation with inside the industrialized global that represents the extra a part of visible deficiency [1]. The early locating hold a strategic distance from proper affects consisting of visible deficiency.

---

D. Maji (✉)

Department of Electrical Engineering, Haldia Institute of Technology, Haldia, West Bengal 721657, India

e-mail: [hitdebasis@gmail.com](mailto:hitdebasis@gmail.com)

S. Maiti · G. Sarkar

Department of Electrical Engineering, Jadavpur University, Kolkata 700032, India

A. K. Dhara

Department of Electrical Engineering, National Institute of Technology, Durgapur, West Bengal 713209, India

A cataract is a thick, cloudy quarter that systems with inside the focal factor of the attention. A cataract starts while proteins in the attention form packs that maintain the point of interest from sending clean photos to the retina. Air conditioning cording to the study, there might be approximately 0.1/2 billion visually impaired people in 2020 [2, 3]. There are essentially two types of previous work on segmenting retinal blood vessels. The initial group employed conventional machine learning techniques, such as support vector machines [4, 28]. Early conclusion and cure can decline the suffering of cataract patients and keep visual weakening from visual weakness. The most effective thanks to acknowledge retinal ailments is thru retinal vessel division, but it needs retinal specialists for manual vessel recognition and division. Cataract recognition and classification is extremely dependent upon the vein subtleties and optic circle. The manual vessel division and identification is a repetitive methodology [5, 6]. Besides, manual division is price avid and time requiring sweat because it needs retinal eyes professional for the division procedure [6, 7]. During this way, the automatic extraction and division of the vessels are extraordinarily basic for early location of a cataract by utilizing AI ideas. This exam demonstrates a unique blood vessel segmentation procedure for image of the retina. In this inspection, we tried to cover the entire content of ongoing and past retinal cleavage investigations. According to the brief, we classify as directed and independent strategies. In addition, there are vector machine-based ancillary technologies, neural system-based technologies, various technologies, coordinated filtering strategies, numerical morphology technologies, and model-based technologies, ship monitoring method and strategy. The retinal fundus photograph, the preparation and processing steps, the dataset used, and the evaluation method are also presented into reduce the higher complexity and lower noise level. Suarez and others, Soares et al. [7, 8] proposed a technique that uses classification to classify pixels as vascular or avascular. Here, the Gabor change of differential update is applied. Lupa,scu et al. [9, 29]. Use there have been a lot of new semantic segmentation techniques developed recently. The most illustrative networks among them are U-net. The filter reaction demonstrates how close the elements are in a given position and direction. Chaudhuri et al. [10, 30] Probably the most vascular frame robot segmentation method. They proposed a format with Gaussian contours to identify straight segmented fragments of blood vessels. The filtered reaction image is thresholdized and further processed to obtain the final split. (Kov'acs and Hajdu [11, 12]) By summarizing Gabor's design and then reconstructing the shape of the blood vessel, the centerlines of blood vessels were extracted, because lesions may present local features similar to blood vessels, the appearance of may be effected to blood vessel segmentation. Annunziata et al. [13, 14] proposed a strategy to solve the tightness of exudate. After preparation, the exudate is separated and stained. In this article, we propose a novel method to the track retinal blood vessels. For each application, we compare the pre-trained model's performance fine-tuned by and the performance of the model fully trained

from scratch based on medical imaging data. The contribution of the article is as follows:

- (a) In order to properly explore the feature interdependence of spatial and channel dimension, we apply FCN module several times in the feature extraction network to extract picture features from low dimensional to high dimensional.
- (b) The proposed network outperforms the other six recently developed fundus vessel segmentation networks on dataset.
- (c) The proposed method can achieve up to 95.68 segmentation accuracy for DRIVE data

## 2 Related Works

Artificial neural network (ANN)-based automated DR severity level monitoring is described in [15, 32]. From retinal fundus pictures, pathological abnormalities such AM, blood vessels, hemorrhage, and exudate can be identified. The DR is then divided into mild, moderate, and severe by adding the lesion into a multilayer feedforward neural network. The proposed method used in [16, 33] small vessel segmentation. Here, retinal damaged vessels segmentation a challenging task. Retinal image were coded using to categories DR as mild, moderate, or severe. The verified red lesion detection method's results are used to generate the automated categorization in [17, 34]. The public database is evaluated by the checkout method of leaving one out. They made an effort to evaluate if DR might be automatically detected. Retinal fundus is categorized as diabetic or nondiabetic in [18]. There are four smaller versions of the main picture. The Haar wave transform is then used once the characteristics have been retrieved. Principal component analysis was performed to choose the best characteristics (PCA). The classification procedure is then carried out using a rule classifier and a backpropagation neural network. A pre-trained the model was suggested by Sunil et al. [18, 19] to segment blood vessels from fundus pictures. The Microsoft COCO dataset [20] was used to pre-train the DEEPLAB-COCO-LARGEFOV [21] model. Following the pre-trained model's training, 800 image patches taken from 66 fundus pictures were used. The model's patchy outputs were then merged to create the necessary segmented blood vessels. When Sunil et al. evaluated their model on 23 fundus pictures. Before blood vessel segmentation can be performed, fundus pictures must first be pre-processed, according to a method Sonro et al. [22] suggested 75% accuracy rate was achieved on 5000 verified images. presented a pipeline employing the U-net architecture for the fundus blood vessel segmentation. The fundus pictures were initially pre-processed in order to do this, and the U-net was then trained using patches of the pre-processed images in order to improve the architecture's accuracy. 190,000 patches in all were taken out of the DRIVE database [23]. In [24], they took out the texture, entropy, hard exudate region, blood vessel area, and bifurcation sites.

### 3 Methodology

We created an optimal learning strategy to categorize fundus photos using our suggested methodology. The likelihood of blindness increases with level. The method can be used to detect such symptoms early. It should be mentioned that one of the crucial places used to level the eye is the blood vessel. Establishing a deep learning model for the classification of vessels in fundus pictures is the goal of this test. For U-net, we proposed U-net for the task of retinal vessel division. U-net adds a consideration module to the first U-net. In the element layer, convolution is replaced by severe convolution, and two alternating paths are added to the element layer, so that the model separates pixels from the fundus image and better distinguishes the subtleties of blood vessels. The general method is shown in Fig. 1. U-net's structure is comparable to FCN's [25]. The distinction is that U-net [39] employs a symmetric encoder structure, which includes development and pressure techniques. The pressure approach uses layers of convolution and clustering to implement the standard CNN model. A blurry picture with a size of  $572 \times 572$  serves as the message. The expansion method includes CNN layer, so the channels of element are reduced to 1 channel, and the map is included to reset a single image size [26]. The missing association between the compressed method and the developed method led the globalization model to and neighborhood data.

The used model  $1 \times 1$  convolution divides component vectors into the needed number of classes and associates the Softmax layers to classify severity of DR in order and target probability estimates to complete the division. Such a simple U-net equilibrium the structure has realized astonishing performance in various applications in the biomedical sector.

## 4 Experimental Results and Discussion

### 4.1 Database

The majority of cutting-edge datasets are segmentation-focused. Here, we suggest an alternative technique to the binary classification seen in the most recent datasets for grading health conditions. This approach requires a dataset that has been graded according to various health conditions. There are 40 fundus photographs in the DRIVE [27]. We select 20 images for practice, while the remaining 20 images are used for the testing. These retinal fundus images were captured with a camera at a 45-degree angle. The dimensions of each image are  $584 \times 565$ . The Eye Images dataset, which is open to the public, is largely used to determine an image's tortuosity. The dataset, which consists of 120 retinal pictures, is utilized to verify the suggested methodology. Each image is  $584 \times 565$  pixels in size. CHASEDB1 [27] contains of 28 fundus retinal photographs acquired from the fundus image. We have enhanced the photographs as previously said in order to train.

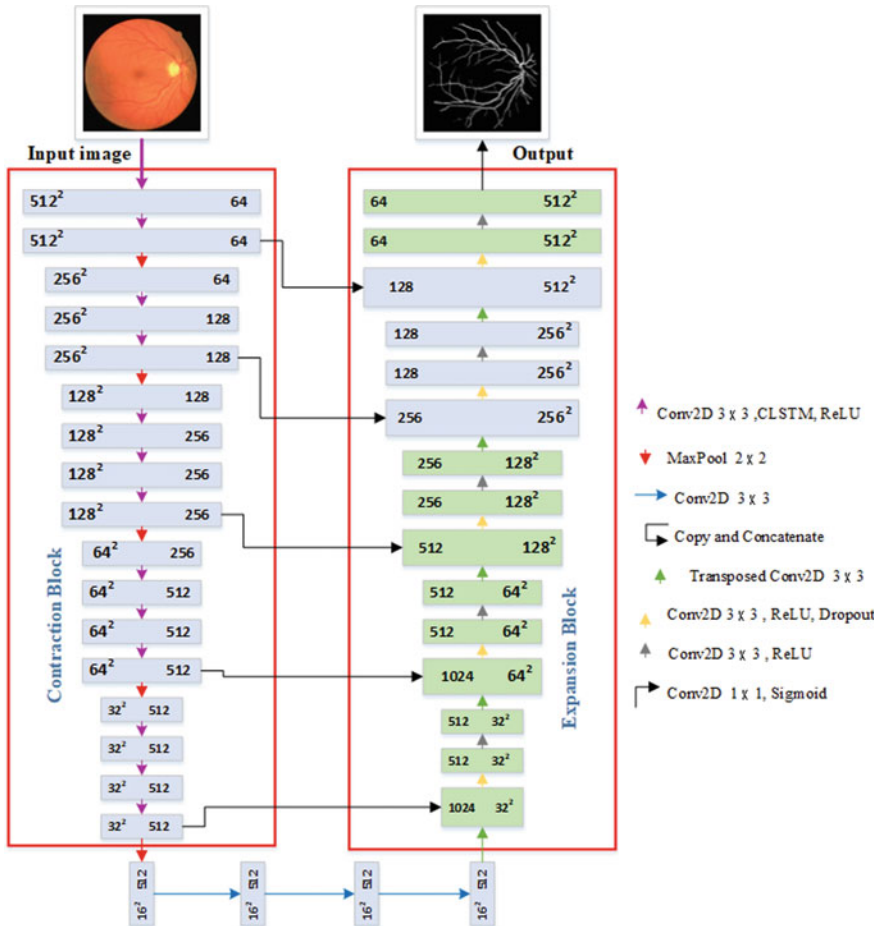


**Fig. 1** Segmentation result from DRIVE dataset with model can locate tiny blood vessels and keep better vascular connection using modified U-net

## 4.2 Experimental Outcomes

We have contrasted our suggested method with the most recent neural network-based grading system. Table 1 provides a summary of the findings. Here, we conducted a critical analysis outputs of the recommended strategy as well as the benchmarked results. The information includes hand assigned grades from various experts. Vessel segmentation has been shown in Fig. 2. Segmentation results of two retinal images: (p), (t) the color retinal images; (m), (q). Accuracy, specificity, and sensitivity are taken into account as the criteria for evaluating the performance of the suggested network. The fraction of accurately foreseen events is the accuracy. While the sensitivity shows the likelihood of correctly identifying ill patients, the specificity

**Table 1** Performance analysis of the suggested technique and the other existing approaches on DRIVE database

Methodology	Sensitivity	Specificity	Accuracy
Roychowdhury [35]	0.7249	0.9830	0.9520
Qiaoliang Li [36]	0.7406	0.9807	0.9527
Residual U-net [37]	0.7332	0.9782	0.9553
Recurrent U-net [37]	0.7569	0.9830	0.9556
R2U-net [37]	0.7520	0.9806	0.9556
DEU-net [38]	0.8039	0.9804	0.9567
Proposed	0.8209	0.9731	0.9568

shows the likelihood of correctly identifying healthy persons. The following are the mathematical expressions:

$$\text{Accuracy} = \frac{\text{TP} + \text{TN}}{\text{TP} + \text{FP} + \text{TN} + \text{FN}} \quad (1)$$

$$\text{Specificity} = \frac{\text{TN}}{\text{TN} + \text{FP}} \quad (2)$$

$$\text{Sensitivity} = \frac{\text{TP}}{\text{TP} + \text{FN}}, \quad (3)$$

where FN and FP stand for the improperly detected background pixels and object pixels, respectively, while TN and TP represent the background and object pixels that were correctly identified.

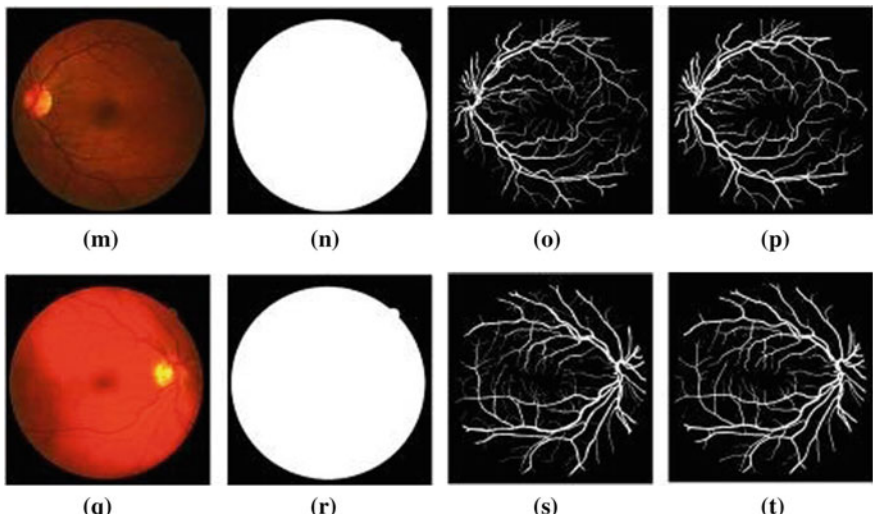
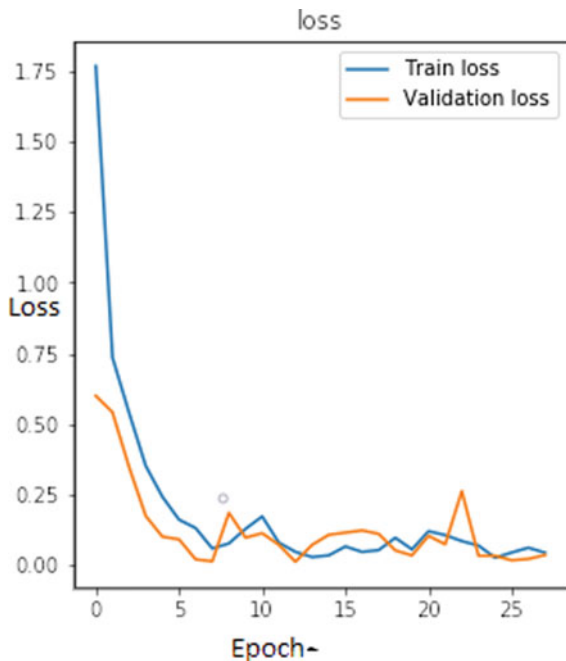


**Fig. 2** Segmentation results of two retinal images: (p), (t) the color retinal images; (m), (q)

**Fig. 3** Training and validation loss during training using modified U-net segmentation results



25 number of epochs are used to train the modified U-net model and the DRIVE database are used 40 fundus photos; 20 images for the training and 20 images for testing. Each fundus picture is a certain size of  $584 \times 768$  pixels. The loss is shown in Fig. 3. The training and validation loss during training using modified U-net segmentation results.

The 20 fundus photos used in our experiment are the divided into four training and testing folds. As a result, all 20 photos are used to the train and test the experimental model. Using 14 GPUs and 2 CPU cores, the model is trained. Figure 4 displays the outcome of vessel segmentation and visualization of vessel tortuosity, with red denoting the tortured section of vessels and blue denoting the vessel index number. The recommended approach appears to make judgments based on the vasculature, which is by far the most important signal for evaluating vascular tortuosity. 1 NVIDIA Tesla K80 GPU, GB RAM, and a batch size of 4 is utilized on both DRIVE [40] fundus photos because some of the fundus images in the database include blood vessels that have been severely damaged by the ocular illness, causing score much below average.

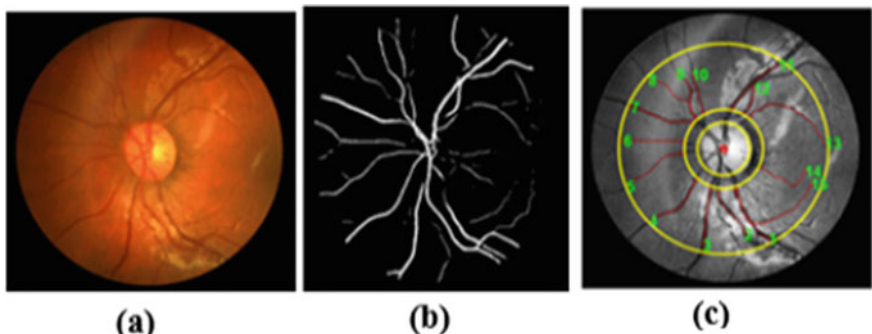


**Fig. 4** **a** Test image from CHASEDB1(02\_test\_img.png) dataset; **b** segmentation result by modified U-net; **c** tortuosity measurement result

## 5 Conclusion

For the vessels segmentation of retinal image, a modified U-net architecture was put out in this paper. In the DRIVE database, it outperformed a qualified ophthalmologist and produced superior results. According to Table 1 and when compared to the other picture vessel segmentation methods, the accuracy of the approach suggested in this work on DRIVE is 0.9568. That is to say, when various approaches are compared, our way comes out on top. While the outcomes in the actual fundus photos are not as good as those in the DRIVE database. The ophthalmologist's photographs would have some sounds in them, which is why. We can promise that the results will be substantially better if the noise-removal preprocessing is done using the raw photos.

## References

- Pascolini D, Mariotti SP (2012) Global estimates of visual impairment: 2010. *Br J Ophthalmol* 96(5):614–618
- Mitchell P, Cumming RG, Attebo K, Panchapakesan J (1997) Prevalence of cataract in Australia: the Blue Mountains eye study. *Ophthalmology* 104(4):581–588
- Congdon N, Vingerling JR, Klein BE, West S, Friedman DS, Kempen J, O'Colmain B, Wu S-Y, Taylor HR (2004) Prevalence of cataract and pseudophakia/aphakia among adults in the United States. *Arch Ophthalmol (Chicago, Ill 1960)* 122(4):487–494
- Kanski JJ, Kubicka-Trzáska A (2007) Clinical ophthalmology: a self-assessment companion. Elsevier Churchill Livingstone
- Vinogradov SV, Kohli E, Zeman AD (2005) Cross-linked polymeric nanogel formulations of 5'-triphosphates of nucleoside analogues: role of the cellular membrane in drug release. *Mol Pharm* 2(6):449–461
- Klein BEK, Klein R, Linton KLP, Magli YL, Neider MW (1990) Assessment of cataracts from photographs in the Beaver Dam eye study. *Ophthalmology* 97(11):1428–1433
- Soares JVB, Leandro JJJG, Cesar RM, Jelinek HF, Cree MJ (2006) Retinal vessel segmentation using the 2-D Gabor wavelet and supervised classification. *IEEE Trans Med Imaging* 25(9):1214–1222

8. Kotyk T, Chakraborty S, Dey N, Gaber T, Hassanien AE, Snasel V (2016) Semi-automated system for cup to disc measurement for diagnosing glaucoma using classification paradigm. In: Proceedings of the second international Afro-European conference for industrial advancement AECIA 2015. Springer, pp 653–663
9. Lupascu CA, Tegolo D, Trucco E (2010) FABC: retinal vessel segmentation using AdaBoost. *IEEE Trans Inf Technol Biomed* 14(5):1267–1274
10. Memari N, Ramlı AR, Bin Saripan MI, Mashohor S, Moghbel M (2017) Supervised retinal vessel segmentation from color fundus images based on matched filtering and AdaBoost classifier. *PLoS ONE* 12(12):e0188939
11. Fraz MM, Remagnino P, Hoppe A, Velastin S, Uyyanonvara B, Barman SA (2011) A supervised method for retinal blood vessel segmentation using line strength, multiscale Gabor and morphological features. In: 2011 IEEE international conference on signal and image processing applications (ICSIPA). IEEE, pp 410–415
12. Moraru L, Obreja CD, Dey N, Ashour AS (2018) Dempster-shafer fusion for effective retinal vessels' diameter measurement. In: Soft computing based medical image analysis. Elsevier, pp 149–160
13. Lennon R (2002) Remote sensing digital image analysis: an introduction. United States, Esa/Esrin
14. Maji D, Sekh AA (2020) Automatic grading of retinal blood vessel in deep retinal image diagnosis. *J Med Syst* 44(10):1–14
15. James J, Sharifahmadian E, Shih L (2018) Automatic severity level classification of diabetic retinopathy. *Int J Comput Appl* 180:30–35
16. Yang Y, Li T, Li W, Wu H, Fan W, Zhang W (2017) Lesion detection and grading of diabetic retinopathy via two-stages deep convolutional neural networks. In: International conference on medical image computing and computer-assisted intervention. Springer, pp 533–540
17. Paing MP, Choomchuay S, Yodprom MDR (2016) Detection of lesions and classification of diabetic retinopathy using fundus images. In: 2016 9th Biomedical engineering international conference (BMEiCON). IEEE, pp 1–5
18. Seoud L, Chelbi J, Cheriet F (2015) Automatic grading of diabetic retinopathy on a public database. In: Ophthalmic medical image analysis international workshop. University of Iowa
19. Prasad DK, Vibha L, Venugopal KR (2015) Early detection of diabetic retinopathy from digital retinal fundus images. In: 2015 IEEE recent advances in intelligent computational systems (RAICS). IEEE, pp 240–245
20. Roychowdhury S, Koozekanani DD, Parhi KK (2013) DREAM: diabetic retinopathy analysis using machine learning. *IEEE J Biomed Heal Inform* 18(5):1717–1728
21. Gayathri S, Krishna AK, Gopi VP, Palanisamy P (2020) Automated binary and multiclass classification of diabetic retinopathy using haralick and multiresolution features. *IEEE Access* 8:57497–57504
22. Akram MU, Khalid S, Tariq A, Khan SA, Azam F (2014) Detection and classification of retinal lesions for grading of diabetic retinopathy. *Comput Biol Med* 45:161–171
23. Pratt H, Coenen F, Broadbent DM, Harding SP, Zheng Y (2016) Convolutional neural networks for diabetic retinopathy. *Proc Comput Sci* 90:200–205
24. Mookiah MRK, Acharya UR, Martis RJ, Chua CK, Lim CM, Ng EYK, Laude A (2013) Evolutionary algorithm based classifier parameter tuning for automatic diabetic retinopathy grading: a hybrid feature extraction approach. *Knowledge-based Syst* 39:9–22
25. Long J, Shelhamer E, Darrell T (2015) Fully convolutional networks for semantic segmentation. In: Proceedings of the IEEE conference on computer vision and pattern recognition. pp 3431–3440
26. Lian S, Luo Z, Zhong Z, Lin X, Su S, Li S (2018) Attention guided U-net for accurate iris segmentation. *J Vis Commun Image Represent* 56:296–304
27. Bansal N, Dutta M (2013) Retina vessels detection algorithm for biomedical symptoms diagnosis. *Int J Comput Appl* 71(20)
28. Staal J, Abràmoff MD, Niemeijer M, Viergever MA, Van Ginneken B (2004) Ridge-based vessel segmentation in color images of the retina. *IEEE Trans Med Imaging* 23(4):501–509

29. Hoover AD, Kouznetsova V, Goldbaum M (2000) Locating blood vessels in retinal images by piecewise threshold probing of a matched filter response. *IEEE Trans Med Imaging* 19(3):203–210
30. Fraz MM, Remagnino P, Hoppe A, Uyyanonvara B, Rudnicka AR, Owen CG, Barman SA (2012) An ensemble classification-based approach applied to retinal blood vessel segmentation. *IEEE Trans Biomed Eng* 59(9):2538–2548
31. Budai A, Bock R, Maier A, Hornegger J, Michelson G (2013) Robust vessel segmentation in fundus images. *Int J Biomed Imaging*
32. Prentašić P, Lončarić S, Vatavuk Z, Benčić G, Subašić M, Petković T, Dujmović L, Malenica-Ravlić M, Budimlija N, Tadić R (2013) Diabetic retinopathy image database (DRiDB): a new database for diabetic retinopathy screening programs research. In: 2013 8th international symposium on image and signal processing and analysis (ISPA). IEEE, pp 711–716
33. Estrada R, Allingham MJ, Mettu PS, Cousins SW, Tomasi C, Farsiu S (2015) Retinal artery-vein classification via topology estimation. *IEEE Trans Med Imaging* 34(12):2518–2534
34. Holm S, Russell G, Nourrit V, McLoughlin N (2017) DR HAGIS—a fundus image database for the automatic extraction of retinal surface vessels from diabetic patients. *J Med Imaging* 4(1):14503
35. Roychowdhury S, Koozekanani DD, Parhi KK (2014) Blood vessel segmentation of fundus images by major vessel extraction and subimage classification. *IEEE J Biomed Heal Inform* 19(3):1118–1128
36. Li Q, Feng B, Xie L, Liang P, Zhang H, Wang T (2015) A cross-modality learning approach for vessel segmentation in retinal images. *IEEE Trans Med Imaging* 35(1):109–118
37. Alom MZ, Hasan M, Yakopcic C, Taha TM, Asari VK (2018) Recurrent residual convolutional neural network based on U-net (R2U-net) for medical image segmentation
38. Wang B, Qiu S, He H (2019) Dual encoding U-net for retinal vessel segmentation. In: International conference on medical image computing and computer-assisted intervention. Springer, pp 84–92
39. Maiti S, Maji D, Dhara AK, Sarkar G (2022) Automatic detection and segmentation of optic disc using a modified convolution network. *Biomed Signal Process Control* 76:103633
40. Maji D, Maiti S, Dhara AK, Sarkar G (2022) Biomedical signal processing and control 74 (2022); Automatic grading of retinal blood vessel tortuosity using Modified CNN in deep retinal image diagnosis. *Biomed Signal Process Control* 74:103514

# Design of 1-DOF Integer and Fractional-Order PID Controllers Using an Ensemble Differential Evolution for a Magnetic Levitation System



**Mou Das Mahapatra, Shibendu Mahata, Ritu Rani De, Rajani Kanta Mudi, and Chanchal Dey**

**Abstract** A time-domain-based metaheuristic design approach employing a high-level ensemble of three variants of differential evolution algorithms is presented for an optimal control of magnetic levitation system. Traditional and fractional-order proportional-integral-derivative (FOPID) controllers of one degree-of-freedom, that optimally minimizes the step response error, are designed. Comparisons with the published models highlight the improved transient behavior for both the proposed controllers. Results also demonstrate a significantly smaller settling time for the designed FOPID-based-controlled system compared to the classical one.

**Keywords** Ensemble differential evolution · Fractional order PID controller · Magnetic levitation · Metaheuristic optimization

## 1 Introduction

The idea of fractional calculus (FC), the generalized version of classical calculus, germinated around the end of seventeenth century. However, the first comprehensive compendium on FC was available only around the 1970s [1]. The application domains of FC have subsequently proliferated and now encompass diverse fields such as circuit

---

M. Das Mahapatra (✉) · S. Mahata · R. Rani De

Department of Electrical Engineering, Dr. B. C. Roy Engineering College, Durgapur, India  
e-mail: [mou.dasmahapatra@bcrc.ac.in](mailto:mou.dasmahapatra@bcrc.ac.in)

S. Mahata

e-mail: [shibendu.mahata@bcrc.ac.in](mailto:shibendu.mahata@bcrc.ac.in)

R. Rani De

e-mail: [riturani.de@bcrc.ac.in](mailto:riturani.de@bcrc.ac.in)

R. Kanta Mudi

Department of Instrumentation and Electronics Engineering, Jadavpur University, Kolkata, India

C. Dey

Department of Applied Physics, University of Calcutta, Kolkata, India

e-mail: [cdaphy@caluniv.ac.in](mailto:cdaphy@caluniv.ac.in)

theory, robotics, automatic control, economics, nanotechnology, signal processing, medical science, mechanics, bio-engineering, and system identification [2–5].

The definition of  $\alpha$ th-order derivative ( $n - 1 < \alpha < n$ ) of function  $f(t)$  is given by (1).

$${}_a D_t^\alpha f(t) = \frac{1}{\Gamma(n-\alpha)} \frac{d^n}{dt^n} \int_a^t (t-\tau)^{n-\alpha-1} f(\tau) d\tau \quad (1)$$

The Laplace transformation of (1) is given according to (2).

$$L \left\{ {}_0 D_t^\alpha f(t) \right\} = s^\alpha F(s) - \sum_{k=0}^{n-1} s^k D^{\alpha-k-1} f(0+), \quad (2)$$

where the Laplacian operator is symbolized by  $L\{\cdot\}$ .

A major application of FC in control theory results from the generalization of integer-order proportional-integral-derivative (IOPID) controller to the fractional domain, namely the fractional-order PID (FOPID) controller [6]. Ongoing research studies include the implementation of effective and optimal FOPID tuning methodology. For example, Mughees et al. used an ant colony optimizer algorithm and Ziegler-Nichols method for fine tuning the FOPID controller parameters for a magnetic levitation (Maglev) system [7]. Ziegler-Nichols, Cohen-Coon and Nelder-Mead optimization algorithm-based tuning of FOPID controller for a furnace to achieve maximum heating utilization with minimum risk of explosion was reported by Basu et al. [8]. Bingi et al. proposed a 2-DOF (degree-of-freedom) controller for a pressure control system. The designed controller efficiently rejects load disturbances [9]. In [10], a neural network-based FOPID tuning technique for a radar-guided missile tracker was reported. In addition, within the neural network framework, the  $H_2/H_\infty$  optimization was applied to improve the stability and performance. A discrete-time GA-based controller was introduced to stabilize idle speed of an internal combustion engine under external load disturbance [11]. Optimization of FOPID parameters for applications related to heat pumps, electric vehicles, and automatic generation control, was attained through a metaheuristic approach [12].

In this paper, the focus is on designing optimal 1-DOF IOPID and FOPID controllers for an inherently unstable and nonlinear plant, namely the Maglev system. The cost function is formulated to reduce the quadratic error in unit step response. A multi-population-based framework comprising an ensemble of different differential evolution (DE) variants is employed here to solve the formulated problems. Comparisons with the published literature demonstrate that both the designed controllers improve the system's transient characteristic. It is also demonstrated that the settling time can benefit from the incorporation of the FOPID controller as compared to the classical one.

## 2 The Magnetic Levitation (Maglev) System

Maglev is an electro-mechanical system that includes an electromagnetic coil wound about a core, a steel ball, and an infrared (IR) position sensor (see Fig. 1). The sensor continuously measures the position of the ball and separates the ball's vertical movement from its horizontal one. The sensor converts the position of the ball to an equivalent sensor voltage  $x_v$  by considering the sensor gain  $k_2$  as the proportionality factor. To calculate the error signal,  $x_v$  is fed to an analog-to-digital converter (ADC). Then, the ADC's output and the reference input are compared to yield an error signal, which on application to a controller results in an output signal  $u(t)$ . The digital-controlled output is then converted to an analog form by the digital-to-analog converter. The analog control output is then fed through a current amplifier that provides the coil current, considering the coil current gain  $k_1$  as the proportionality factor. Thus, the ball's position can be controlled by the coil current. The electromagnetic coil's current depends on the applied voltage, that in-turn, depends on the ball's position. For a stable system, the gravitational pull of the ball should be counterbalanced by the magnetic force generated by the coil current. The gravitational and electromagnetic force experienced on the metal ball is expressed as per (3).

$$m\ddot{x} = mg - f_e \quad (3)$$

where the ball has a mass  $m$  and position  $x$ ;  $g$  denotes the gravitational constant; and  $f_e$  is the rate of change of stored energy. The magnetic force  $f_e$  is directly proportional to the coil current and varies inversely with the ball's position, as given by (4).

$$f_e = \frac{ki^2}{x^2} \quad (4)$$

where  $k$  is dependent on the coil.

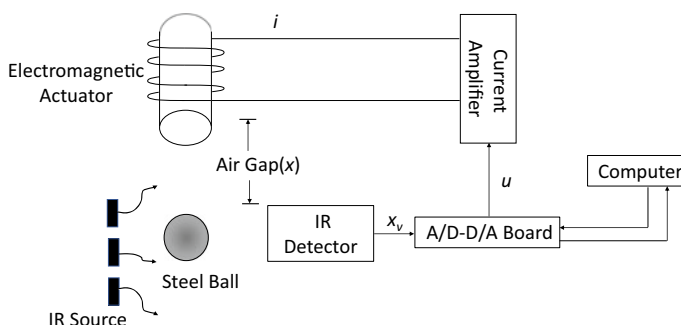


**Fig. 1** Block diagram of Maglev system

Thus, from (3) and (4), we obtain (5).

$$m\ddot{x} = mg - \frac{ki^2}{x^2} \quad (5)$$

For the ease of system analysis, the nonlinear Maglev system needs linearization. Assume  $x = x_0 + \Delta x$ ,  $i = i_0 + \Delta i$ , where  $x_0$  and  $i_0$  are the equilibrium position and equilibrium coil current, respectively;  $\Delta x$  and  $\Delta i$  are minor variations from the equilibrium condition for the respective variables. The standard procedure for linearization may be carried out; the values of  $x_0$  and  $i_0$  are obtained as  $-1.5$  V ( $0.009$  m) and  $0.8$  A, respectively, by evaluating  $\dot{x} = 0$ . Evaluation of the partial derivative (first-order) followed by application of Laplace transformation will lead to the transfer function given by (6).

$$\frac{\Delta x}{\Delta i} = \frac{-\frac{2g}{i_0}}{s^2 - \frac{2g}{x_0}} \quad (6)$$

Since the ball's position and current are proportional to sensor voltage ( $x_v$ ) and controlled output ( $u$ ), the Maglev system's transfer function is modified by accounting for  $k_1$  and  $k_2$ , as per (7).

$$G(s) = \frac{\Delta x_v}{\Delta u} = \frac{-2k_1 k_2 g / i_0}{(s^2 - (2g/x_0))} \quad (7)$$

The linearized Maglev, with parameter values presented in Table 1 of [13], is modeled by (8).

$$G(s) = \frac{-3518.85}{s^2 - 2180} \quad (8)$$

The plant has poles at  $\pm 46.69$ , which implies that it is an unstable system. Therefore, the designed controller must ensure closed loop stability.

Applications of Maglev can be found in trains, magnetic bearings, radical-ride roller coasters, contactless melting, etc. Due to highly nonlinear characteristics, uncertainty, and instability of Maglev system, it is time consuming to design the control law. Various research exposes different methods to design the controller for these systems. Lin et al. proposed an adaptive PID controller that guarantees the system's stability for an unknown system model [14]. For the stabilization and trajectory tracking of the Maglev system, linear quadratic regulator [15] and particle swarm optimization [16]-based controllers were reported. Internal model control-based PID controller [17], digital FOPID based on optimal pole-zero approximation [18], robust PID controllers designed in the frequency domain [19], decentralized PID control [20], fractional sliding mode controller [21], and 2-DOF PID controller [22] have also been reported for enhancing the performance of Maglev system. To obtain the optimal performance indices of Maglev, a GA-based tuned PID controller was reported by Ahmad et al. [23]. The high nonlinearity, plant parameter uncer-

tainty, and open loop instability have been overcome by model reference adaptive PID controller [24], FOPID controller using the simplex algorithm [25], and PID controller using a gray wolf optimizer [26]. The problem of state observation-based sensor-less control has been addressed by Bobtsov et al. [27] for a 2-DOF system, which is also applicable for 1-DOF model. For the nonlinear model, a sliding mode controller was proposed where the neural network estimator further modified the control characteristics to mitigate external disturbances [28].

### 3 Proposed Method

Due to simplicity of design, faster response, and better performance, the PID controller has ruled control engineering for decades [29]. The combination of FC and classical PID control theory results in the theoretical premise of the FOPID-based control. The FOPID is a generalized PID controller, whose transfer function is given by (9).

$$G_{FOPID}(s) = \frac{U(s)}{E(s)} = k_p + k_i s^{-\lambda} + k_d s^{\beta}; \lambda, \beta \in (0, 2) \quad (9)$$

where the error  $E(s)$  is the controller input,  $U(s)$  is the controller output and  $k_p$ ,  $k_i$ , and  $k_d$  are the respective gain terms. If  $\lambda = \beta = 1$ , the PID controller is modeled as  $G_{PID}(s) = k_p + k_i s^{-1} + k_d s$ . To reduce the step response error of the unity-feedback Maglev system, the cost function is formulated according to (10).

$$f = \sum_{t=0}^{t_f} [r(t) - y(t, X_P)]^2 \quad (10)$$

where the unit step input and its response from the closed loop system are, respectively, denoted by  $r(t)$  and  $y(t)$ ;  $X_P = [k_p \ k_i \ k_d]$  or  $X_P = [k_p \ k_i \ k_d \ \lambda \ \beta]$  depending on whether the proposed controller is integer or fractional type; and 501 sample points between 0 s (sec) and  $t_f$  s are considered for evaluating the time response error.

To solve various optimization problems, the DE algorithm is a powerful tool. Proper conglomeration of multiple strategies integrated into one DE variant is gaining impetus in the evolutionary algorithm (EA) community. This paper employs a multi-population EA-based ensemble of multiple DE algorithms (EDEV) [30]. EDEV integrates the complimentary search characteristics of three efficient and popular DE variants, namely the self-adaptive DE (JADE), the composite DE (CoDE), and DE with ensemble of parameters (EPSDE).

The population of EDEV has several same-sized indicator sub-populations and one reward sub-population. After a fixed number of generations, reward sub-population gets re-allocated to the recent best performing DE variant evaluated on the basis of fitness improvements. Thus, the most efficient DE variant adaptively acquires more computational resources. JADE is applicable for solving unimodal optimization problems, whereas CoDE and EPSDE are efficient for simple multimodal and

highly complex optimization problems, respectively. The detailed structure of EDEV is available in [30]. The EDEV control parameters used in this work are the same as reported in [31].

## 4 Simulation Results

In this work,  $t_f$  is chosen as 5 s; the lower boundary for  $X_P$  is set as  $[-20 -20 -20]$  and  $[-20 -20 -20 0 0]$ , respectively, for the PID and FOPID design cases, whereas the corresponding upper boundaries are  $[0 0 0]$  and  $[0 0 0 2 2]$ . Comparisons are highlighted between the proposed and reported systems about the well-known time-integral errors, namely IAE, ISE, ITAE, and ITSE [32]. All the simulations are conducted in MATLAB.

### 4.1 Performance Analysis of the Proposed IOPID Controller

The proposed 1-DOF EDEV-based IOPID controller is determined as per (11).

$$G_{PID} = -6.1148 - \frac{6.2108}{s} - 1.3302s \quad (11)$$

The poles of the proposed controller-based closed loop system transfer function lie at  $\{-4.6767, -0.0021+0.0006j, -0.0021-0.0006j\}$ ; the zeros are located at  $\{-1.5150, -3.0818\}$ . Thus the closed loop system has stable and minimum-phase behavior.

The interior point optimization algorithm-based IOPID controller is given by (12) [13].

$$G_{PID} = -2.3973 - \frac{2.7749}{s} - 0.4451s \quad (12)$$

The step response comparisons between the IOPID controller-based closed loop systems for the proposed and reported [13] approaches are illustrated in Fig. 2. Maximum peak overshoot ( $M_p$ ) of 23.7% occurs at 0.403 s for [13], whereas  $M_p$  for the proposed system is much lower (8.2%) and occurs at 0.435 s; though, improvements in settling time is insignificant. Results presented in Table 1 shows that the proposed approach achieves significantly lower error indices as compared to [13].

### 4.2 Performance Analysis of the Proposed FOPID Controller

The transfer function of the EDEV-based proposed FOPID controller for the suggested Maglev system is given by (13).

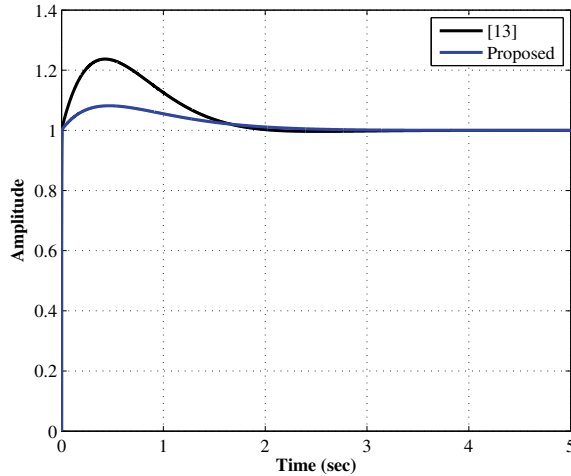


**Fig. 2** Step responses of proposed and reported 1-DOF PID-controlled Maglev system

**Table 1** Performance comparison of IOPID controller-based Maglev system

Model	IAE	ISE	ITAE	ITSE
[13]	0.2313	0.0394	0.3928	0.0616
Present work	0.0988	0.0055	0.1825	0.0081

$$G_{FOPID} = -14.8389 - \frac{15.1923}{s^{1.0676}} - 0.5903s^{1.6675} \quad (13)$$

The interior point search technique-based FOPIID controller reported in [13] is given as per (14).

$$G_{FOPID} = -3.50 - \frac{4.0}{s^{0.8750}} - 0.20s \quad (14)$$

The derivative term in (14) is of integer-order, instead of the fractional one. This occurs due to the saturation of the  $\beta$  value to the considered upper limit in [13]. The proposed and published [13] system's time responses are compared in Fig. 3. Results demonstrate that  $M_p = 5.8\%$  at 0.350 s is attained by the proposed, whereas a much larger overshoot ( $M_p = 17.6\%$  at 0.157 s) is exhibited by the FOPIID-based system in [13]. Of particular interest is the 2% settling time ( $t_s$ ), where the proposed system ( $t_s = 0.699$  s) comprehensively outperforms the cited literature [13] ( $t_s = 2.309$  s). Table 2 shows time-domain error performances, which highlight the lower error achieved by the proposed FOPIID-controlled Maglev system as compared to that of [13].

Finally, the time responses of the proposed IOPID and FOPIID-based Maglev are compared in Fig. 4. Though the overshoot behaviors of the two systems are comparable, the settling time of the FOPIID-controlled system ( $t_s = 0.699$  s) is markedly lower as compared to that of the IOPID-based system ( $t_s = 1.666$  s).

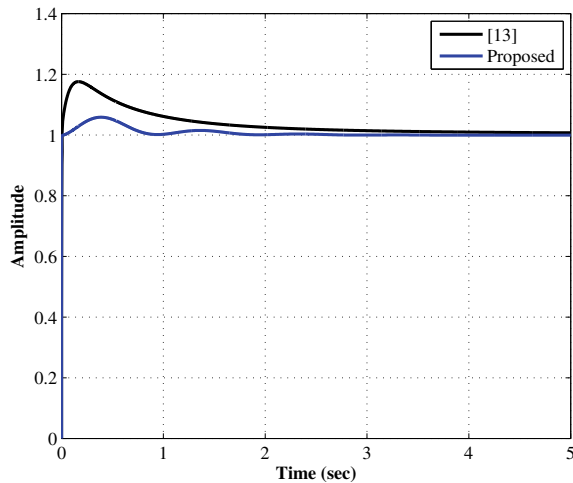
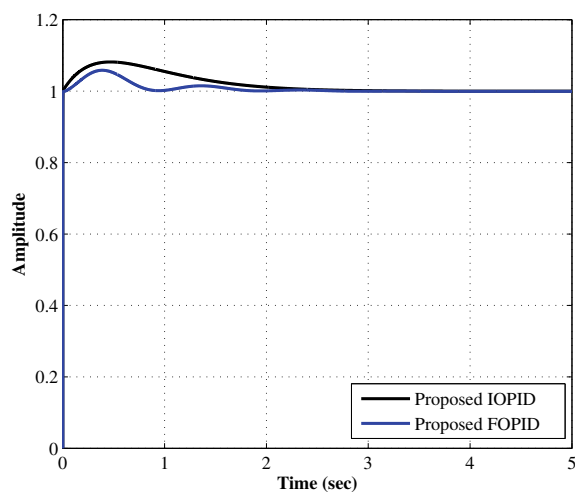


**Fig. 3** Step responses of proposed and reported 1-DOF FOPID-controlled Maglev system

**Table 2** Performance comparison of FOPID controller-based Maglev system

Model	IAE	ISE	ITAE	ITSE
[13]	0.1946	0.0155	0.5147	0.0235
Present work	0.0399	0.0012	0.0831	0.0019

**Fig. 4** Step responses of proposed IOPID and FOPID-controlled Maglev system



## 5 Conclusion

Optimal control of Maglev using an evolutionary method is presented. As compared to published literature, the EDEV-based proposed IOPID controller achieves smaller overshoot (8.2 vs. 23.7%), whereas the fractional PID helps attain lower overshoot (5.8 vs. 17.6%) and a faster settling time (0.699 vs. 2.309 s). Comparisons also reveal that the linearized Maglev system based on the proposed FOPID can achieve a faster transient than the proposed classical controller; though, the overshoot characteristics are similar.

## References

1. Oldham KB, Spanier J (1974) Fractional calculus. Academic Press, New York, USA
2. Sun H, Zhang Y, Baleanu D, Chen W, Chen Y (2018) A new collection of real-world applications of fractional calculus in science and engineering. *Commun Nonlinear Sci Numer Simul* 64:213–231
3. Tarasov VE (2019) On history of mathematical economics: application of fractional calculus. *Mathematics* 7(6):509
4. Zhang Y, Sun H, Stowell HH, Zayernouri M, Hansen SE (2017) A review of applications of fractional calculus in Earth system dynamics. *Chaos Solitons Fract* 102:29–46
5. Mahata S, Saha SK, Kar R, Mandal D (2018) Optimal design of wideband fractional order digital integrators using symbiotic organisms search algorithm. *IET Circuits Devices Syst* 12(4):362–373
6. Shah P, Agashe S (2016) Review of fractional PID controller. *Mechatron* 38:29–41
7. Mughees A, Mohsin SA (2020) Design and control of magnetic levitation system by optimizing fractional order PID controller using ant colony optimization algorithm. *IEEE Access* 8:116704–116723
8. Basu A, Mohanty S (2017) Tuning of FOPID ( $PI^{\lambda}D^{\mu}$ ) controller for heating furnace. *Int J Electron Eng Res* 9:1415–1437
9. Bingi K, Ibrahim R, Karsiti MN, Hassan SM, Harindran VR (2019) Real-time control of pressure plant using 2DOF fractional-order PID controller. *Arabian J Sci Eng* 44(3):2091–2102
10. Yaghi M, Efe MÖ (2019)  $H_{\infty}$ -Neural-based FOPID controller applied for radar-guided missile. *IEEE Trans Indus Electron* 67(6):4806–4814
11. Yang Y, Zhang HH, Yu W, Tan L (2020) Optimal design of discrete-time fractional-order PID controller for idle speed control of an IC engine. *Int J Powertrains* 9(1–2):79–97
12. Khezri R, Oshnoei A, Tarafdar HM, Muyeen SM (2018) Coordination of heat pumps, electric vehicles and AGC for efficient LFC in a smart hybrid power system via SCA-based optimized FOPID controllers. *Energies* 11(2):420
13. Swain SK, Sain D, Mishra SK, Ghosh S (2017) Real time implementation of fractional order PID controllers for a magnetic levitation plant. *AEU-Int J Electron Commun* 78:141–156
14. Lin CM, Lin MH, Chen CW (2011) SoPC-based adaptive PID control system design for magnetic levitation system. *IEEE Syst J* 5(2):278–287
15. Anurag K, Kamlu S (2018) Design of LQR-PID controller for linearized magnetic levitation system. In: 2018 2nd International conference inventive system control (ICISC), January, IEEE, pp 444–447
16. Varshney A, Bhushan B (2020) Trajectory tracking and ball position control of magnetic levitation system using swarm intelligence technique. In: 2020 International conference electronics sustainable communications systems (ICESC), July, IEEE, pp 29–35

17. Duka AV, Dulău M, Oltean SE (2016) IMC based PID control of a magnetic levitation system. *Procedia Tech* 22:592–599
18. Chopade AS, Khubalkar SW, Junghare AS, Aware MV, Das S (2016) Design and implementation of digital fractional order PID controller using optimal pole-zero approximation method for magnetic levitation system. *IEEE/CAA J Automatica Sinica* 5(5):977–989
19. Hypiusová M, Kozáková A (2017) Robust PID controller design for the magnetic levitation system: frequency domain approach. In: 2017 21st International conference process control (PC), June, IEEE, pp 274–279
20. Chen Q, Tan Y, Li J, Mareels I (2017) Decentralized PID control design for magnetic levitation systems using extremum seeking. *IEEE Access* 6:3059–3067
21. Pandey S, Dourla V, Dwivedi P, Junghare A (2019) Introduction and realization of four fractional-order sliding mode controllers for nonlinear open-loop unstable system: a magnetic levitation study case. *Nonlinear Dyn* 98(1):601–621
22. Ghosh A, Krishnan TR, Tejaswy P, Mandal A, Pradhan JK, Ranasingh S (2014) Design and implementation of a 2-DOF PID compensation for magnetic levitation systems. *ISA Trans* 53(4):1216–1222
23. Ahmad I, Shahzad M, Palensky P (2014) Optimal PID control of magnetic levitation system using genetic algorithm. In: 2014 IEEE International energy conference (ENERGYCON), May, IEEE, pp 1429–1433
24. Singh B, Kumar V (2015) A real time application of model reference adaptive PID controller for magnetic levitation system. In: 2015 IEEE Power, communication information technology conference (PCITC), October, IEEE, pp 583–588
25. Verma SK, Yadav S, Nagar SK (2015) Optimal fractional order PID controller for magnetic levitation system. In: 2015 39th National systems conference (NSC), December, IEEE, pp 1–5
26. Yadav S, Verma SK, Nagar SK (2016) Optimized PID controller for magnetic levitation system. *IFAC-PapersOnLine* 49(1):778–782
27. Bobtsov AA, Pyrkin AA, Ortega RS, Vedyakov AA (2018) A state observer for sensorless control of magnetic levitation systems. *Automatica* 97:263–270
28. Sun Y, Xu J, Qiang H, Chen C, Lin G (2019) Adaptive sliding mode control of maglev system based on RBF neural network minimum parameter learning method. *Measurement* 141:217–226
29. Borase RP, Maghade DK, Sondkar SY, Pawar SN (2021) A review of PID control, tuning methods and applications. *Int J Dyn Control* 9(2):818–827
30. Wu G, Shen X, Li H, Chen H, Lin A (2018) Ensemble of differential evolution variants. *Inf Sci* 423:172–186
31. Mahata S, Kar R, Mandal D (2020) Comparative study of nature-inspired algorithms to design  $(1+\alpha)$  and  $(2+\alpha)$ -order filters using a frequency-domain approach. *Swarm Evol Comput* 55(100685):1–24
32. Mahata S, Herencsar N, Alagoz BB, Yeroglu C (2021) A robust frequency-domain-based order reduction scheme for linear time-invariant systems. *IEEE Access* 9:165773–165785

# Substrate Integrated Waveguide H-Plane Horn MIMO Antenna Design for mW Applications



Mantar Singh Mandloi, Ujjwal Tripathi, Ajay Parmar,  
and Leeladhar Malviya

**Abstract** The high gain, wide bandwidth, extremely high data rate, and high capacity are the necessities of the current and next generations of wireless and vehicular applications like high-speed trains, aeroplanes, satellite communication, and in underground moving vehicles. The present research proposes an optimum H-plane horn MIMO antenna using SIW technology for 5G millimetre wave (mmW) to solve the problem of reliability, gain, and to overcome the effects of penetration losses. MIMO antenna consisting of two H-plane horns is designed on multilayer substrates (Rogers RT5880(thickness = 0.79 mm) and Rogers RO3003 (thickness = 0.75 mm) of size  $56.31 \times 35.06$  mm $^2$ ). The proposed SIW MIMO horn antenna covers a wide band of 26.27–35.53 GHz frequency range (bandwidth 9.26 GHz). The SIW MIMO antenna radiation efficiency ranges between 96.16–97.87%, and the gain between 6.9–8.8 dBi in the whole 2:1 VSWR ( $-10$  dB return loss) frequency band. The ECC in the proposed band is between 0 and 0.0011.

**Keywords** Horn antenna · MIMO · SISO · SIW · Slow wave structure

## 1 Introduction

To fulfil the requirement of today's wireless communication like high data rate and low latency, 5G technology is getting more attention [1]. 5G technologies have advanced mobile broadband at 10 Gbps, massive machine type communication at 1 million per km and have highly reliable low latency communications at 1 ms as compared to the previous technologies like 3G and 4G. In vehicular communication 5G or millimetre-wave transmission becomes a difficult task due to high penetration losses [2–6]. To solve this problem, an antenna can be placed upon the roof of the moving vehicle to connect with network stations and another high directive antenna can be placed inside the fast moving vehicle for the coverage of the users [7].

---

M. S. Mandloi · U. Tripathi · A. Parmar · L. Malviya (✉)  
Shri G. S. Institute of Technology and Science, Indore, M.P 452003, India  
e-mail: [ldmalviya@gmail.com](mailto:ldmalviya@gmail.com)

To achieve wide operating bandwidth, high gain and high directivity in moving vehicles, rectangular shaped waveguide horn antennas are widely considered in mmW applications. Substrate integrated waveguide (SIW) technology can be used to limit the use of bulky and large structure regular metallic H-plane horn antennas. The SIW planar technology on the microwave dielectric substrates includes the advantages of low loss, low profile, wide bandwidth, miniaturization and high gain and has propagation properties similar to air filled metallic waveguides [8–11]. Substrate integrated waveguide antennas can operate only in transverse electric  $\text{TE}_{m0}$  mode (the electric and magnetic field components are perpendicular to each other), where the cut-off frequencies of  $\text{TE}_{m0}$  mode is given by [12, 13].

$$F_c = \frac{nc}{2W\sqrt{\Delta_r}} n = 1, 2, 3 \dots \quad (1)$$

Here,  $m$  represents the number of half wavelengths in  $x$ -direction,  $\epsilon_r$  is the permittivity of the dielectric material,  $c$  = speed of light ( $3 \times 10^8$  m/s), and  $W$  is the spacing between holes in SIW.

## 2 SISO Antenna Design

The design steps of single input single output (SISO) antenna and analysis of H-plane SIW horn antenna is presented in this section of the paper. Firstly, a linear SIW antenna is designed on Rogers RT5880 ( $\epsilon_r = 2.2$ , height = 0.79 mm,  $\tan(\delta) = 0.0009$ ) with a size of  $14.98 \times 19.06$  mm $^2$ . In the design, only upper conductor and substrate are having SIW structures with full ground on back. This SISO antenna covered three bands with respect to VSWR 2:1 and return loss of  $-10$  dB of 26.14–27.19 GHz (BW = 1.05 GHz), 29.51–29.92 GHz (BW = 0.413 GHz), and 31.34–32.11 GHz (BW = 0.77 GHz). The front and back schematic views of the design are shown in the Fig. 1.

To increase the gain, horn structures are added to the first step. It covers 2:1 VSWR bands 29.88–31.42 GHz (BW = 1.54 GHz) and 34.28–34.97 GHz (BW = 0.69 GHz). The schematic views of the step 2 are shown in the Fig. 2. The presented SISO antenna of step 2 is further updated by using combination of two substrates Rogers RT5880 ( $\epsilon_r = 2.2$ , height = 0.79 mm,  $\tan(\delta) = 0.0009$ )(top), and Rogers RO3003 ( $\epsilon_r = 3$ , height = 0.75,  $\tan(\delta) = 0.0010$ )(bottom) having dimensions of  $35.06 \times 27.67 \times 1.732$  mm $^3$ . The slow wave structures are created on the back side of the perfect electric conductor (PEC) and bottom substrate in the aperture area of design and it covered 3 bands of 27.26–27.87 GHz (BW = 0.61 GHz), 29.65–30.88 GHz (BW = 1.18 GHz), and 32.96–34.07 GHz (BW = 1.12 GHz). The front and back views of step 3 SISO antenna without the curved patches and two tapered slots are shown in the Fig. 3.

To increase the bandwidth and minimize the return loss, curved patches at the top of the substrate integrated waveguide structure are added in design step 3. In design

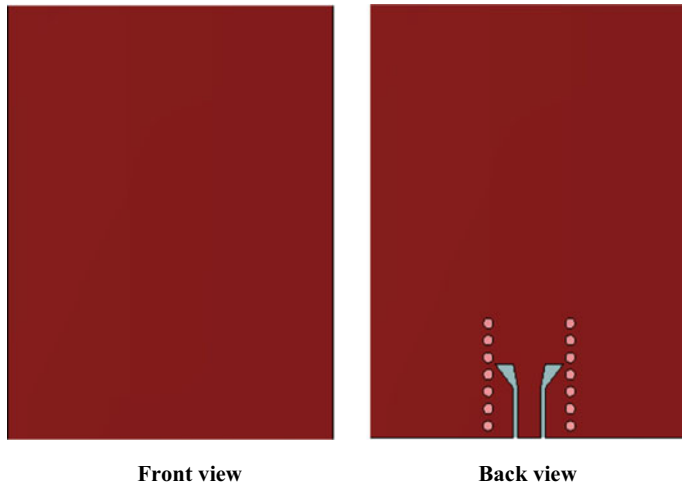


**Fig. 1** Schematic views of step 1 of SISO antenna

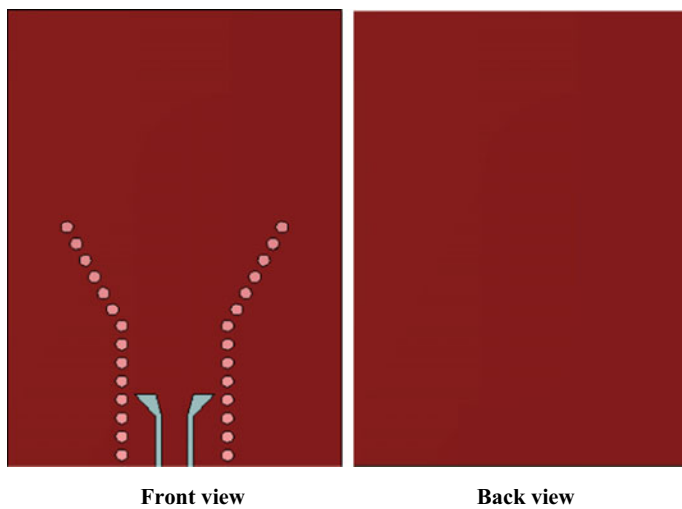


**Fig. 2** Schematic views of step 2 of SISO antenna

step 4, capacitance is calculated using the parallel plate given in the Eq. 2.

$$C = \frac{\varepsilon A}{d} \quad (2)$$

where  $A$  is the area and the  $d$  is the separation between the two PEC plates.

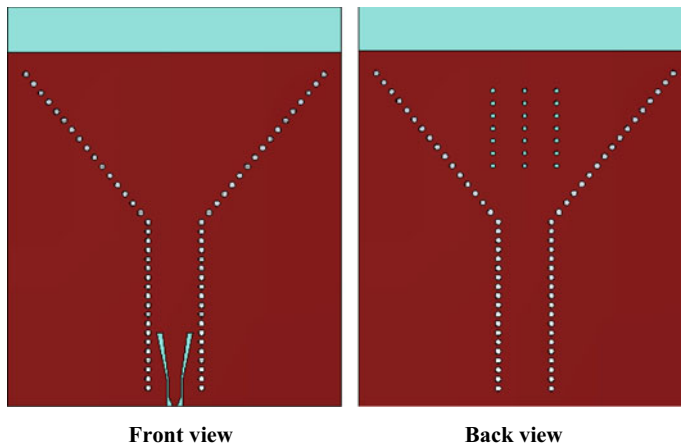


**Fig. 3** Schematic views of step 3 of SISO antenna (without patches)

The designed SISO antenna covers a wide band of 26.33–35.55 GHz (BW = 9.22 GHz) with radiation efficiency of 96.25–98.2% and the achieved gain ranges between 6.07–9.62 dBi. The front and back views of step 4 SISO antenna with the curved patches and two tapered slots are shown in the Fig. 4.

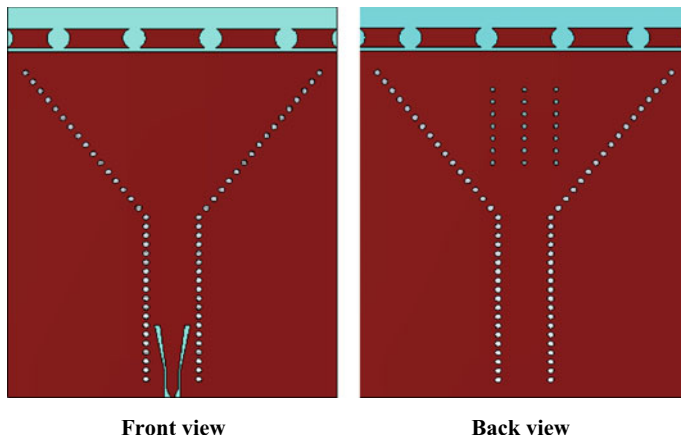


**Fig. 4** Schematic views of step 4 of SISO antenna (with patches)

### 3 Design of SIW H-Plane MIMO Antenna

The single input single output antennas suffer from low reliability due to signal loss in penetration and high signal to noise ratio (SNR) in frequency band FR2(24.25–52.6 GHz). At the transmitter and receiver end, if we use multiple antenna elements or antenna arrays then it becomes multiple input multiple output technology (MIMO). For non-line of sight (NLOS) wireless communication, MIMO antennas offer better performance due to high channel capacity and boosted spectral efficiency. The channel capacity of SISO and MIMO antennas are given by the following equations, respectively [14–18].

$$C = B \log_2 \left( 1 + \frac{S}{N} \right) \quad (3)$$

$$C = \log_2 \left[ \det \left( I_{Nr} + \frac{\rho}{NN_t} HH^* \right) \right] \quad (4)$$

where  $\rho$  is the signal,  $N$  is the noise,  $I_{Nr} = N_r \times N_r$  identity matrix,  $H$  is the channel matrix and its transpose is  $H^*$ ,  $N_r$ , and  $N_t$  are the number of receiving and transmitting antenna elements.

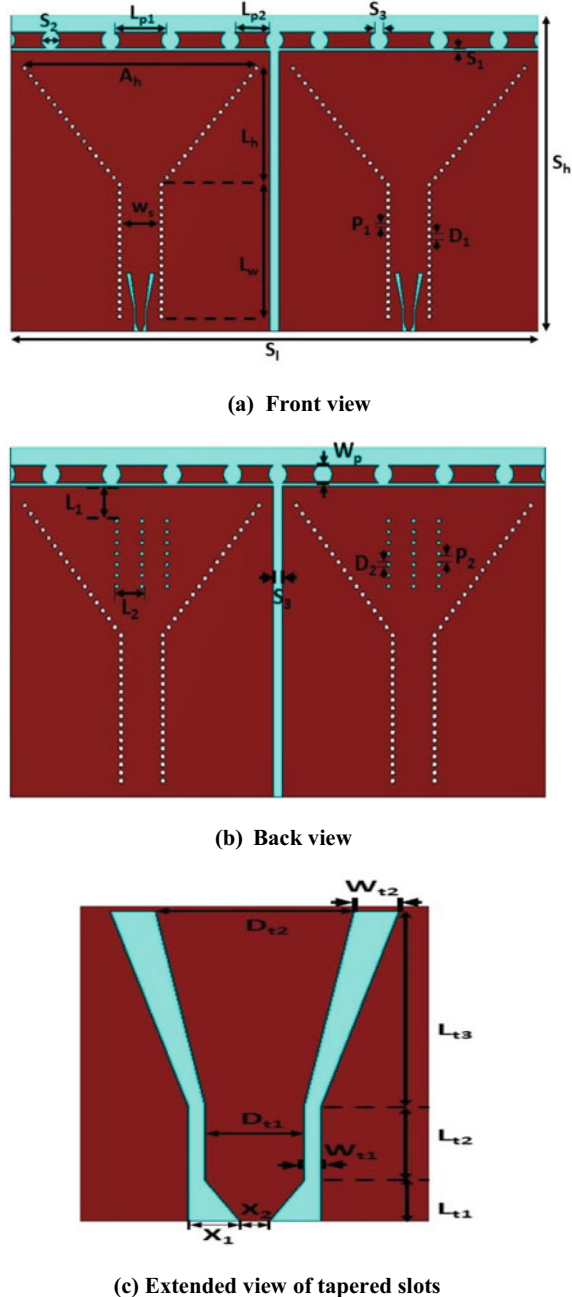
In design step 5, a wideband SIW H-plane horn antenna which consists of two slow waves are designed on  $56.31 \times 35.06 \times 1.732$  mm<sup>3</sup> multilayer dielectric substrate as indicated in previous section. The proposed SIW H-plane horn MIMO antenna with respect to 2:1 VSWR covers 26.27–35.53 GHz (BW = 9.26 GHz) which is declared by the federal communications commission (FCC) as FR2 band of frequency. The front and back views of step proposed SIW H-plane horn antenna with the curved patches and two tapered slots are shown in the Fig. 5a–c, and the dimensional parameters are given in the Table 1.

### 4 Results and Discussion

The simulated results of S-parameters for different design steps are compared in Fig. 6. The simulated S-parameters of the proposed SIW H-plane horn MIMO antenna covers 2:1 VSWR ( $S_{11} = S_{22} - 10$  dB) band of 26.27–35.53 GHz. The returns loss  $S_{11}$  is  $-49.54$  dB at 27.35 GHz and the isolation is  $|S_{12}| = |S_{21}| > 15.65$  dB in the complete operating band and are shown in Fig. 7.

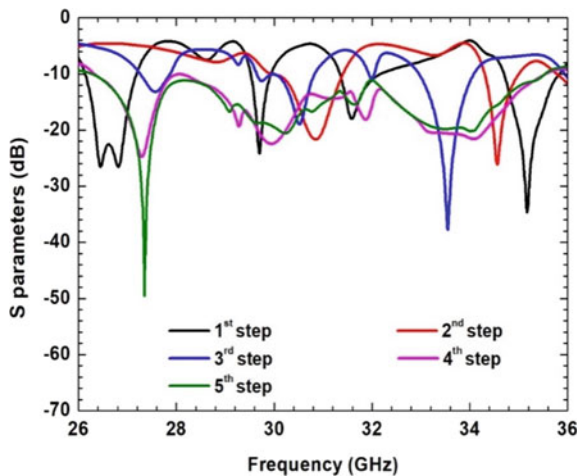
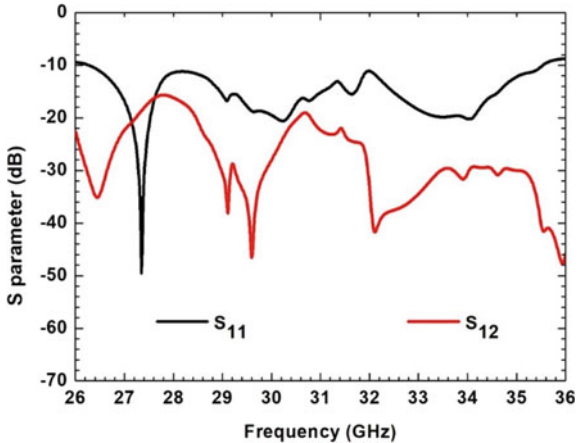
The proposed SIW H-plane horn MIMO antenna is designed for the 2:1 VSWR, i.e.  $-10$  dB return loss at the ports with 89% transmission of power and 11% reflection and is shown in Fig. 8. The following formula is used to calculate VSWR w. r. t. return loss as [19],

**Fig. 5** Schematic views of SIW H-plane horn MIMO antenna



**Table 1** Dimensional parameters of SIW H-plane horn MIMO antenna

Variable	Value (mm)						
$S_1$	56.31	$L_W$	15.06	$W_s$	3.9	$X_1$	0.53
$S_h$	35.06	$L_H$	12.93	$W_p$	1.74	$X_2$	0.315
$S_1$	0.317	$L_1$	3.26	$P_1$	0.287	$L_{t1}$	0.84
$S_2$	1.97	$L_2$	2.23	$P_2$	0.68	$L_{t2}$	1.55
$S_3$	0.978	$L_{P1}$	5.39	$D_1$	0.52	$L_{t3}$	4.06
$A_h$	24.7	$L_{P2}$	3.788	$D_2$	0.40	$W_{t1}$	0.176
$D_{t1}$	1.02	$D_{t2}$	2.05	$W_{t2}$	0.465		

**Fig. 6**  $S_{11}$  parameter of design steps of SIW H-plane horn antenna**Fig. 7** S-parameters of SIW H-plane horn MIMO antenna

$$\text{VSWR} = \frac{10^{\frac{\text{Return Loss}(dB)}{20}} + 1}{10^{\frac{\text{Return Loss }(dB)}{20}} - 1} \quad (5)$$

The gain and efficiency graphs of the proposed SIW H-plane horn MIMO antenna are presented in Fig. 9, respectively. It is observed that gain varies from 6.9–8.8 dBi in the operating frequency band and the maximum gain is 8.8 dBi at 27 GHz. The radiation efficiency lies between 96.16–97.87% and the total efficiency lies between 86.6–96.67% in the presented operating band.

Envelope correlation coefficient (ECC) is the diversity parameter which includes all the return loss and isolation parameters of the proposed SIW H-plane horn MIMO antenna. The international telecommunication union (ITU) has given the maximum value of ECC equals 0.5. The ECC can be calculated with the help of the following

**Fig. 8** VSWR of SIW H-plane horn MIMO antenna

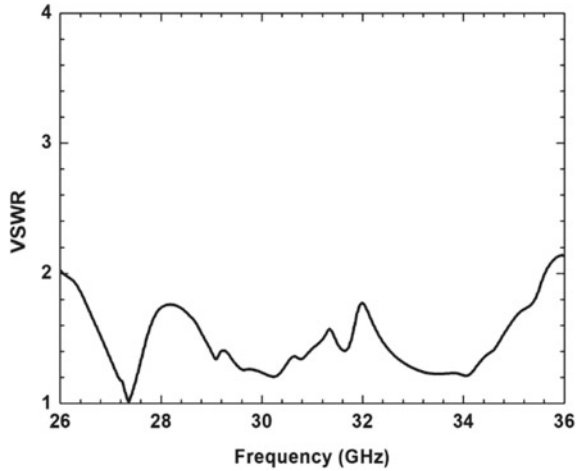


**Fig. 9** Gain and efficiencies of SIW H-plane horn MIMO antenna

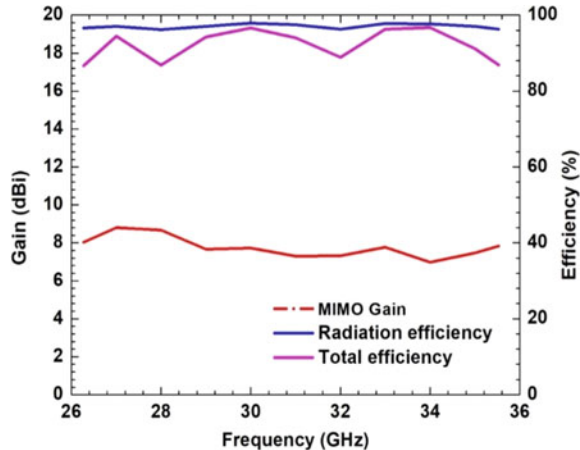
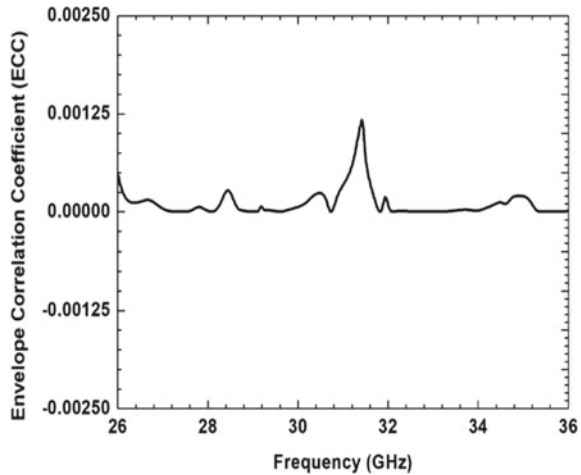


**Fig. 10** ECC of SIW H-plane horn MIMO antenna



formula [20]

$$\text{ECC} = \frac{\left| \sum_{n=1}^N S_{i,j}^* S_{n,j}^* \right|}{\sqrt{\left| \prod_{k=(i,j)} \left[ 1 - \sum_{n=1}^N S_{i,n}^* S_{n,k}^* \right] \right|}} \quad (6)$$

In the operating band of proposed MIMO, ECC is less than 0.0012 and is shown in Fig. 10. The another diversity performance metrics of the proposed SIW H-plane horn MIMO antenna is the diversity gain. Its maximum value is 10. The diversity gain can be obtained in terms of ECC. The proposed SIW H-plane horn MIMO antenna achieves approximately 10 dB in design and is shown in Fig. 11.

The normalized far-field radiation patterns of E-field and H-field of the proposed SIW H-plane horn MIMO antenna at the different frequencies in the presented band are shown in Figs. 12a-c and 13a-c, respectively. The cross-polarization values in the given radiation patterns of the proposed SIW H-plane horn antenna can be controlled using the thin dielectric substrates/laminates or by etching a rectangular/square/triangular slot of appropriate dimension at the mid of the SIW layer slots. Also, the side lobe and back lobe levels can be minimized to enhance the gain and front to back lobe ratio (FBR) by using the metallic reflector of appropriate dimensions and proper separation from the proposed ground plane of the presented MIMO [21].

The proposed SIW H-plane horn MIMO antenna with the existing designs is compared in the Table 2. The proposed structure exhibits better performance as compared to the existing designs in terms of data rate, gain, efficiency, and reliability, etc.

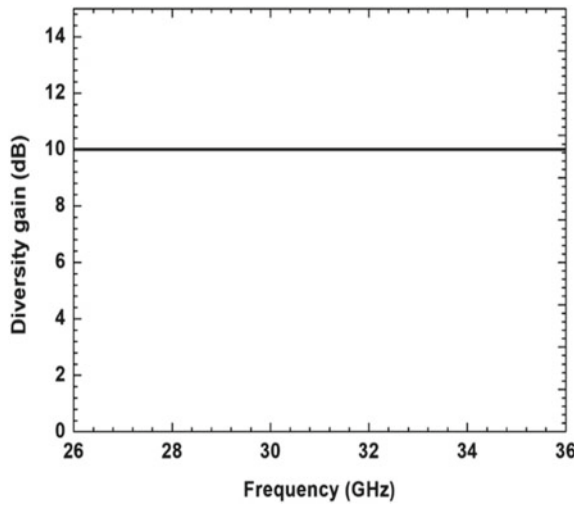


**Fig. 11** Diversity gain of SIW H-plane horn MIMO antenna

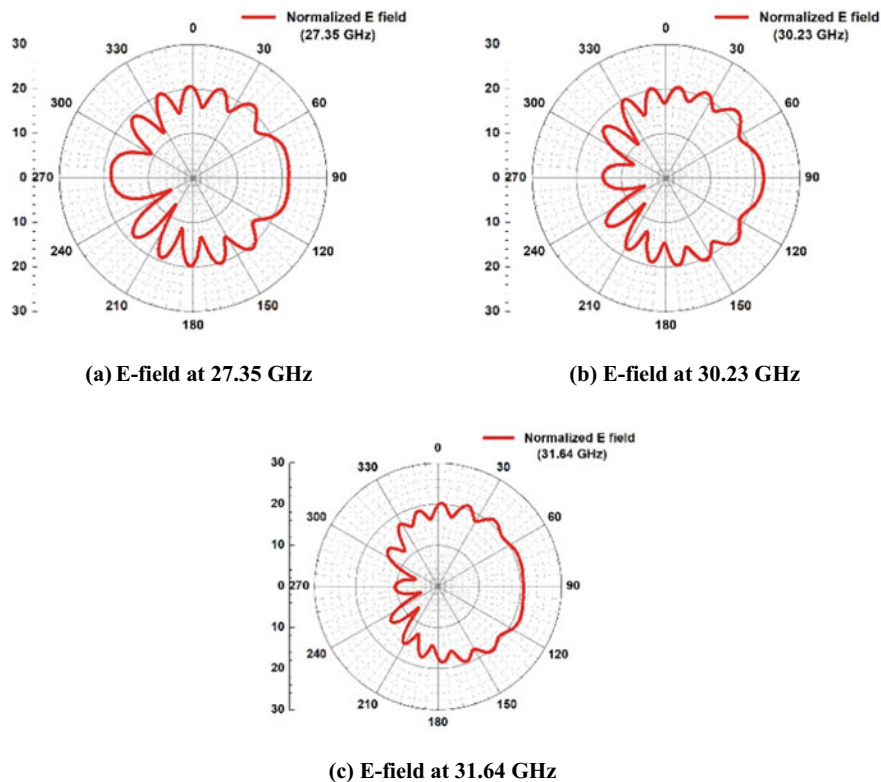


**Fig. 12** E-fields of SIW H-plane horn MIMO antenna

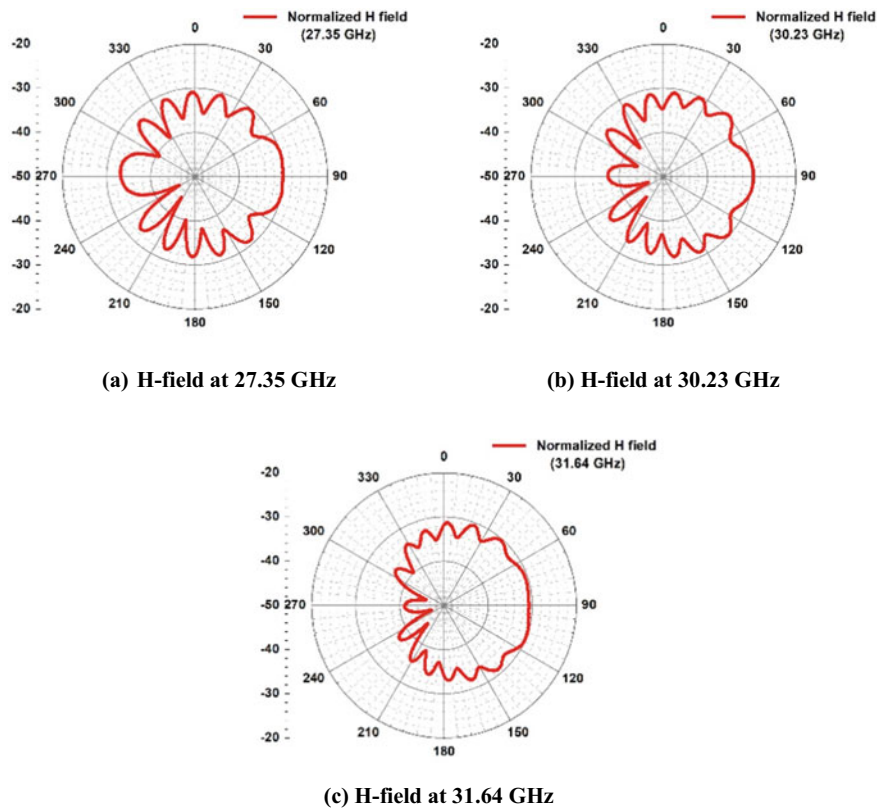


**Fig. 13** H-fields of SIW H-plane horn MIMO antenna

**Table 2** Comparison of existing designs with proposed SIW MIMO antenna

Ref. No.	Frequency/ band (GHz)	Dimension (mm <sup>3</sup> )	No. of elements	Gain (dBi)	Application
7	27.5–28.5	$23.96 \times 29.74 \times 1.49$	1	5.1–5.5	5G mmW
9	18–40	$69.2 \times 39.2 \times 2.54$	1	5–5.1	5G
10	16.6	$32.4 \times 58.68 \times 1.44$	1	4–5.5	5G
11	35	$19.55 \times 37.4 \times 1.44$	1	5.4–6.8	5G
Proposed work	26.27–35.53	$56.31 \times 35.06 \times 1.73$	2	6.9–8.8	5G mmW

## 5 Future Scope

The presented design is used to reduce losses above the 10 GHz frequency and can be extended for the filter designs and multiport and multi-element antennas. The range can be further extended as per the direction of ITU [22–24].

## 6 Conclusion

The high gain and high data rate SIW H-plane horn MIMO antenna design has been presented for vehicular applications. In this research, for the high-speed moving objects for 5G mmW to solve the problem of multipath propagation like reliability, signalling, and to overcome the effects of penetration losses. The multilayer Roger's dielectric substrate of dimension  $56.31 \times 35.06 \text{ mm}^2$  has been used for the slow wave SIW MIMO horn to cover 26.27–35.53 GHz frequency range (bandwidth 9.26 GHz). The SIW MIMO antenna radiation efficiency was 96.16–97.87%, and the gain was 6.9–8.8 dBi in the whole 2:1 VSWR frequency band. The ECC in the proposed band was between 0 and 0.0011 and the diversity gain was very close to the 10 dB in whole band.

## References

1. Ozpinar H, Aksimsek S, Tokan NT (2020) A novel compact, broadband, high gain millimeter-wave antenna for 5G beam steering applications. *IEEE Trans Veh Tech* 69:2389–2397
2. Pant M, Malviya L (2022) Design, developments, and applications of 5G antennas: a review. *Int J Microwave Wireless Technol* 1–27
3. Liu Y, Wang C, Huang J, Sun J, Zhang W (2019) Novel 3-D nonstationarymmwave massive MIMO channel models for 5G high-speed train wireless communications. *IEEE Trans Veh Technol* 68(3):2077–2086
4. Leevanshi R, Mohit P, Leeladhar M, Ajay P, Charhate SV (2021) 5G beamforming techniques for the coverage of intended directions in modern wireless communication: in-depth review. *Int J Microw Wirel Technol* 13:1039–1062
5. Sanjay C, Leeladhar M (2021) Multi-element wideband planar antenna for wireless applications. *Wireless Personal Commun* 1–13
6. Leeladhar M, Parul G (2021) Millimeter wave high-gain antenna array for wireless applications. *IETE J Res* 1–10
7. Zhang Y, Deng JY, Sun D, Yin JY, Guo XL (2021) Compact slow-wave SIW H-plane horn antenna with increased gain for vehicular millimeter wave communication. *IEEE Trans Veh Technol* 70(7):7289–7293
8. Cheng X (2018) Millimeter-wave frequency beam scanning array with a phase shifter based on substrate-integrated-waveguide. *IEEE Access* 6:47408–47414
9. Mallahzadeh AR, Esfandiarpour S (2018) Wideband H-plane horn antenna based on ridge substrate integrated waveguide (RSIW). *IEEE Antennas Wireless Propag Lett* 11:85–88
10. Liu L (2020) Substrate integrated waveguide filtering horn antenna facilitated by embedded via-hole arrays. *IEEE Antennas Wireless Propag Lett* 19(7):1187–1191

11. Wang L, Esquius-Morote M, Qi H, Yin X, Mosig JR (2017) Phase corrected H-plane horn antenna in gap SIW technology. *IEEE Trans Antennas Propag* 65(1):347–353
12. Xu F, Wu K (2005) Guided-wave and leakage characteristics of substrate integrated waveguide. *IEEE Trans Microw Theory Tech* 53(1):66–73
13. Cassivi Y, Perregini L, Arcioni P, Bressan KW, Conciauro G (2002) Dispersion characteristics of substrate integrated rectangular waveguide. *IEEE Microwave Wireless Compon Lett* 12(9):333–335
14. Malviya LD, Panigrahi R, Kartikeyan MV (2017) MIMO antennas with diversity and mutual coupling reduction techniques: a review. *Int J Microw Wirel Technol* 9(8):1763–1780
15. Khan MU, Sharawi MS (2015) A dual-band micro-strip annular slot-based MIMO antenna system. *Microw Opt Technol Lett* 57(2):360–364
16. Malviya LD, Panigrahi RK, Kartikeyan MV (2016) A  $2 \times 2$  dual band MIMO antenna with polarization diversity for wireless applications. *Progress in Electromagnet Res C* 61:91–103
17. Mei X, Wu KL (2020) Envelope correlation coefficient for multiple MIMO antennas of mobile terminals. In: 2020 IEEE international symposium on antennas and propagation and North American radio science meeting, (2020), pp 1597–1598
18. Malviya L, Kartikeyan MV, Panigrahi RK (2020) MIMO antennas for wireless communication: theory and design. CRC Press, Taylor & Francis
19. Balanis CA (2005) In: Antenna theory: analysis and design. Wiley-Interscience
20. Malviya LD, Panigrahi RK, Kartikeyan MV (2018) Offset planar MIMO antenna for omnidirectional radiation patterns. *Int J RF Microwave Comput Aided Eng* 28:1–9
21. Milligan T, Schejbal V, Kovarik V (2006) A method of cross-polarization reduction. *IEEE Antennas and Propag Magazine* 48(5): 108–111. <https://doi.org/10.1109/MAP.2006.277163>
22. Mandloi M, Gupta P, Parmar A, Malviya P, Malviya LD (2022) Beamforming MIMO array antenna for 5G-millimetre-wave applications. *Wireless Personal Commun*. 1–20. <https://doi.org/10.1007/s11277-022-10090-9>
23. Yadav R, Parmar A, Malviya L, Nitnaware D (2022) 28 GHz inset feed circular shaped compact patch antenna arrays for 5G wireless communications. In: 10th IEEE international conference on communication systems and network technologies, pp 1–4. <https://doi.org/10.1109/CSNT.2021.01>
24. Pant M, Malviya M (2022) Fifth generation MIMO antenna array with diversity and mutual coupling reduction technique. In: IEEE 11th international conference on communication systems and network technologies (CSNT), pp 36–41. <https://doi.org/10.1109/CSNT54456.2022.9787609>

# BSVM: A BERT-Based Support Vector Machine for Hindi Hostile Content Detection



Angana Chakraborty , Subhankar Joardar , and Arif Ahmed Sekh

**Abstract** Social media platforms are increasingly providing hostile content. This has caused a requirement for accurate hostile post detection so that appropriate countermove can be made. Increasingly hostile content in various electronic media has created new obstacles for language comprehension. Regional languages make it more challenging. Despite being a good number of studies have been done in the English language, there has not been much progress in Regional languages because the appropriate datasets and tools are not yet available. Hindi is the native language of 615M persons. This research offers a Bidirectional Encoder Representations from Transformers (BERT)-based contextual embedding approach with a combination of Support Vector Machine (SVM) in order to categorize social media posts in Hindi Devanagari script as hostile or non-hostile using the Constraint 2021 Hindi Dataset. Offensive, fake, defamatory, and hateful posts are further evaluated to determine their status. In this research work, several SOTA BERT-based techniques are also subjected to comparative analysis. Our proposed model is found to perform better than the baseline model for all the hostile subclasses (defamation, fake, hate, and offensive).

**Keywords** Natural language processing · Social media · Hostility detection · Hindi language · BERT · SVM

## 1 Introduction

Platforms for Social media like Twitter, Facebook, Instagram, WhatsApp, etc., have significantly impacted how we live, enabling us to interact with individuals around the world and share knowledge in a fraction of a second. This is accompanied by

---

A. Chakraborty · S. Joardar  
Haldia Institute of Technology, Haldia, India  
e-mail: [angana.chakraborty9@gmail.com](mailto:angana.chakraborty9@gmail.com)

A. Ahmed Sekh  
XIM University, Bhubaneswar, India

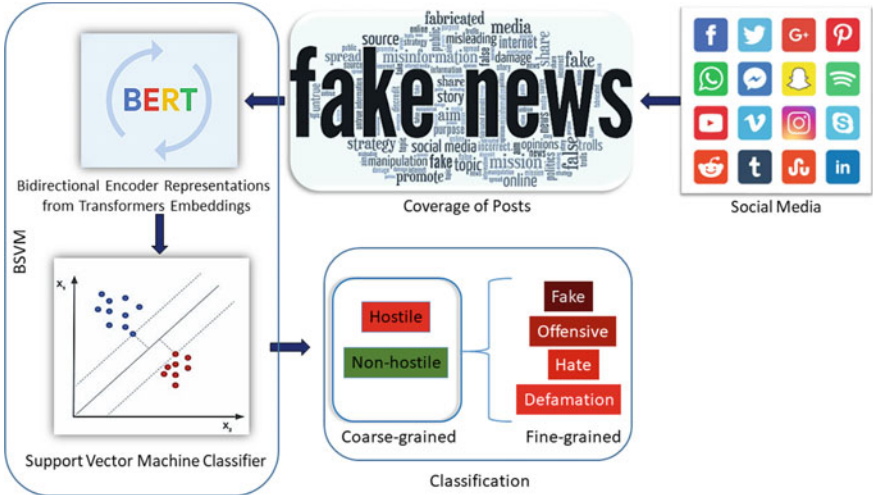


**Fig. 1** The proposed workflow for detecting hostile content from social media posts

an increase in social media usage, cheaper cellphones, and the accessibility of the Internet, all of which have contributed to social media's explosive expansion [23]. By October 2021, there were 4.55 billion social media users worldwide [13]. User-generated material is continuously growing as people spend increasingly more time with social media. These user-generated contents have given birth to hostile social media posts, including the dissemination of untrue stories, death threats trolling, and hateful and offensive content, among other things. According to the Social Hostilities Index, India is rated fourth [29], demonstrating the urgent need to monitor abusive online comments. The biggest issue nowadays is figuring out what information on social media is real and what is fraudulent (Fig. 1).

It has become difficult to accurately sub-categorize content that is fake, hateful, offensive, defamatory, etc. [9]. The approach is even more difficult when the post is in a regional language like Hindi [11]. With 615 million native speakers, Hindi ranks third among all languages used worldwide [24]. The study of the language is crucial because many people interact using the Devanagari (Hindi) script. Hindi is a language with few resources, since it lacks the necessary datasets and tools for the aforementioned activities [34].

In this research, we use different pre-trained feature embedding mechanisms (HindiBERTa [28], ROBERTa Hindi [3], and Indic-Transformers Hindi XLM-RoBERTa [5], HindiBERT [4], TinyBERT [6], SpanBERT [7], Indic-BERT [22]) with machine learning algorithm like SVM to identify hostile posts on social media in the Hindi language. Two classification phases have been used to detect hostility, notably discussed below:

**Coarse-grained classification:** In this phase, every post is classified as hostile or non-hostile. As a result, it is also regarded as a problem of binary classification [15].

**Fine-grained classification:** It comes after the first stage of classification. If the post is labeled as hostile, then a more fine-grained classification of hostile classes has been made. The hostile classes have been categorized using multiple labels and multiple classes. Every hostile post is sub-classified as defamatory, fake, hateful, or otherwise offensive [31].

This article has explored the Hindi Constraint 2021 dataset and has also offered some solution to several problems relating to the identification of hostile content in Hindi. The key difficulties are the lack of dataset and tools for the task because Hindi is a low-resource language. Apart from that, content classification in a multi-class, multi-label arrangement is challenging. Our contribution consists of the following upgrades above the Baseline [10]:

- Proposed a fine-tuning method of pre-trained language models that improve the baseline for Hindi.
- Proposed a BERT-based contextual embeddings combined with SVM namely BERT-SVM (BSVM), that improve one of a baseline models.

The article is structured as follows: Sect. 2 includes a review of the research on hostile language detection. The dataset used for our research is described in Sect. 3 of the article. Proposed methodology is explained in Sect. 4. Section 5 includes the experimental setup. We have presented and discussed our findings in Sect. 6. In Sect. 7, we have discussed conclusion.

## 2 Related Works

Regarding the detection of hostile language in social media posts, we looked into the following literature.

**Hostile Languages, Data, and Labeling:** As part of the CONSTRAINT-2021 shared task on hostile post detection in Hindi, Bhardwaj et al. [10] proposed a new multidimensional hostility detection dataset in the Hindi language. The authors categorized 8200 messages on Facebook and Twitter as hostile or not hostile. Additionally, they gave each of the hostile posts a fine-grained hostile label, such as fake, hate, offensive, and defamation. Despite the fact that hostile posts tend to have lower average word counts than non-hostile posts, it is interesting to note that hostile postings have a greater average number of letters each post. The dataset was then benchmarked using traditional binary classification algorithms, and the weighted F1-scores were reported. In order to address bias and imbalance present in the most of existing natural language datasets, Mollas et al. [26] and Moon et al. [27] discussed the development of new datasets in the English and Korean languages, respectively. They tested them using cutting-edge algorithms and provided a detailed explanation of the dataset development process. Bias and hatred are interwoven, as demonstrated by Moon et al. [27] found that trained models with a bias label were more effective at detecting hate speech. They used a dataset for Korean language. A dataset in Bengali language

was proposed by Hossain et al. [19] to categorize various news categories into real and fake classes. Due to their inability to differentiate between offensive language and hate speech, lexical detection approaches have been shown to have low precision for hate speech tasks in the English language by Davidson et al. [14]. From tweets, they generated a dataset with three labels: hate, offensive, and neither. They highlighted the distinction between hate speech and offensive language by assessing it using widely used algorithms. For efficient classification, Zhang et al.’s [37] attention was on semantics. They asserted that hateful content exhibits a “long tail” trend in comparison with non-hateful text because it lacks distinctive linguistic elements that help with classification. The majority of information is therefore classified as non-hate by current standards. They suggest models based on CNN to categorize English-language tweets that lack discriminative features and outperformed others. However, it is still difficult to identify hate speech based only on linguistic substance. The Marathi language dataset HASOC 2021 was presented by Velnkar et al. [35] to categorize tweets into hate and non-hate classes. Using machine learning techniques, Canhasi et al. [12] presented a publicly available dataset in Albanian to categorize news into true and fake classes. Fawaid et al. [17] used the BERT approach with Transformer Network to do fake news detection in the Bahasa Indonesia language, outperforming other deep learning techniques (BiLSTM, CNN, Hybrid CNN-BiLSTM).

**Neural Architectures for Hostile Language Detection:** According to Badjatiya et al. [8], an English-language tweet can be categorized as either racist, sexist, or neither. Badjatiya et al.’s comparison of various deep learning algorithms for hate speech multi-class detection. The study by Koratana et al. [25] discussed toxic speech and methods for overcoming difficulties when applying a model to identify hate speech in English. They made advantage of the dataset “Toxic Comment Classification Challenge” that Google Jigsaw posted on Kaggle. GloVe embedding vectors are used by Roy et al. [32].’s proposed classifier using CNN to gather semantic data. The issue at hand is to anticipate hate speech in an English-language tweet as soon as the user posts it. According to the size of the kernel, they proposed a CNN system that serves as an n-gram feature extractor from end-to-end. Emojis and hashtags postings on social media in English can be presented uniquely, according to Roy et al. [33]. A multitask learning framework in Arabic that uses CNN, max-pooling, and bi-LSTM layers was provided in the publication of Abu-Farha et al. [16]. Shekhar et al. [34] used deep neural networks and XGBoost-based models for coarse-grained and fine-grained categorization of hostile posts for Indic languages, with Hindi specifically. Devanagari Hindi Offensive Tweets (DHOT) dataset was suggested by Jha et al. [21] to categorize tweets in Hindi into abusive and non-abusive categories using a fast-Text-based model.

### 3 Dataset Description

Using the dataset in [10], which is made available to the public on the CONSTRAINT-2021 shared task website [31], we evaluated our proposed methodology. This dataset

**Table 1** Summary of the CONSTRAINT-2021 Hindi Dataset

Split	Defamation	Fake	Hate	Offensive	Total hostile	Non-hostile
Train (70%)	564	1144	792	742	2678	3050
Validation (20%)	77	160	103	110	376	435
Test (10%)	169	334	237	219	780	873
Overall	810	1638	1132	1071	3834	4358

comprises of 8192 Hindi (Devanagari script) social media postings, of which 4358 posts fall into the non-hostile category and the remaining 3834 posts fall into several hostile categories (such as “defamation,” “fake,” “hate,” and “offensive”). For the categories of defamation, fake, hate, and offensive content, the annotated dataset contains 810, 1638, 1132, and 1071 posts, respectively. For the train, validation, and test sets, we split the dataset into proportions of 70%, 20%, and 10%, respectively. The following explanations are provided for the various classes of the dataset [1, 10]:

- **Defamation:** Inaccurate information that is intended to harm an individual or group’s public reputation.
- **Fake:** Information that is proven to be false.
- **Hate:** A post intended to provoke violence or hatred toward a specific group of people because of their religion, ethnicity, race, or geographic location.
- **Offensive:** Post that criticizes a specific person or group and uses crude, vulgar language to do it.
- **Non-hostile:** A post which is free from hostility.

The description of the Constraint 2021 Hindi Dataset is shown in Table 1.

## 4 Methodology

The goal of the research is to determine whether a post uses hostile language or not. We have accomplished two classifications of hostile posts: binary (hostile/non-hostile) classification and multi-label multi-class classification. In multi-label multi-class classification, hostile posts are further categorized into fake, hate, offensive, and defame classes. Various pre-trained feature embedding mechanisms (HindiBERTa, ROBERTa Hindi, and Indic-Transformers Hindi XLMRoBERTa, HindiBERT, Tiny-BERT, SpanBERT, Indic-BERT) are used to improve the result obtained by Baseline [10]. Finally, traditional machine learning classifier (SVM) is used for suitable classification of hostile posts. We employ a linear kernel for SVM using  $c = 0.01$  and  $\gamma = 1$ . All of our coarse-grained and fine-grained models are trained using the one versus all technique. We set the class weight parameter in SVM to “balanced” so that the model can determine the appropriate weights for classes that have imbalances. Proposed flow of our methodology is depicted in Fig. 2.

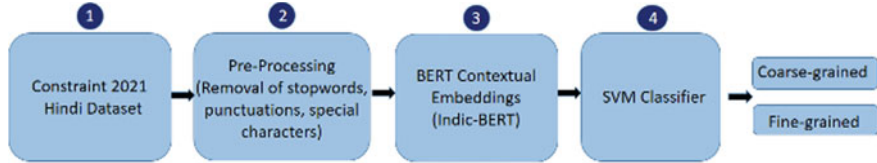


**Fig. 2** Proposed flow of the methodology

## 5 Experiment

Here, we go into great depth on the experimental setup and pre-processing procedures.

**Data pre-processing:** The original dataset is comprised of raw social media posts and is labeled with a string of different classes/labels. Every post is given a binary label (hostile/non-hostile) and a multi-class label (hostile, defame, fake, hatred, and offensive). This way, the post is mapped to five different label for coarse-grained and fine-grained tasks. Stop words, special characters, and punctuations were removed from all posts to make them cleaner. We made the decision to keep URLs in place since we saw improved performance when they were present. We believe that URLs enhance semantic value and make categorization tasks easier.

### 5.1 Experimental Setup

For all of our tests, we used a Tesla P100-PCIE GPU. The code base is created using frameworks for deep learning like PyTorch [30] and Hugging Face transformers [36]. Macro-F1 score is the evaluation metric employed [2]. Macro-F1-score is tested for hostile and non-hostile classes for coarse-grained task, whereas it is tested for four hostile classes for fine-grained tasks. The macro-F1-score is calculated as the mean of the F1-scores for each class:

$$F1 = \frac{1}{N} \sum_{i=0}^N F1_i \quad (1)$$

In this case,  $i$  stands for the class index and  $N$  for the total number of classes/labels. By changing the batch size, learning rate and number of epochs, etc., we have experimented with various hyperparameter combinations.

For this purpose, pre-trained language models from seven various BERT models HindiBERTa, ROBERTa Hindi, Indic-Transformers Hindi XLMRoBERTa, HindiBERT, TinyBERT, SpanBERT, and Indic-BERT are employed. With AdamW [18] acting as the optimizer and a learning rate of  $1e-5$ , the fine-tuning procedure involved 15 epochs.

**Table 2** Coarse-grained task F1-scores (classification in binary)

Model	Coarse grained
Baseline [10]	84.11
BERT+SVM (HindiBERTa)	94.79
BERT+SVM (RoBERTa Hindi)	94.97
BERT+SVM (Indic-Transformers Hindi XLMRoBERTa)	93.58
BERT+SVM (HindiBERT)	93.89
BERT+SVM (TinyBERT)	93.40
BERT+SVM (SpanBERT)	95.13
Proposed BERT+SVM (Indic-BERT)	96.49

**Table 3** Fine-grained tasks F1-scores (Classification using multiple labels and classes)

Model	Defamation	Fake	Hate	Offensive
Baseline [10]	43.57	68.15	47.49	41.98
BERT+SVM (HindiBERTa)	35.76	74.96	55.14	56.87
BERT+SVM (RoBERTa Hindi)	40.12	73.65	50.23	61.09
BERT+SVM (XLMRoBERTa)	36.55	68.23	52.61	57.19
BERT+SVM (HindiBERT)	36.46	72.57	42.12	58.13
BERT+SVM (TinyBERT)	32.19	61.44	44.75	51.40
BERT+SVM (SpanBERT)	43.72	75.23	55.31	61.13
Proposed BERT+SVM (Indic-BERT)	44.63	76.00	56.93	61.80

## 6 Results and Discussion

Here, we go over the findings of various experiments as well as a discussion of the findings. Using machine learning algorithm SVM, we conducted a comparative evaluation of seven various BERT architectures: HindiBERTa, ROBERTa Hindi, Indic-Transformers Hindi XLMRoBERTa, HindiBERT, TinyBERT, SpanBERT, and Indic-BERT. We focused on reporting results from two experiments: a binary classification task (Coarse grained) and a multi-class multi-label test (Fine grained). The findings for coarse-grained tasks and fine-grained tasks, respectively, are summarized in Tables 2 and 3.

Table 2 makes clear that the Indic-BERT+SVM model performs better on the coarse-grained tasks than the baseline model.

Table 3 shows that the Indic-BERT + SVM model performs better for all the fine-grained tasks (Defamation, Fake, Hate, Offensive) than the baseline model.

**Table 4** Classification report of the proposed method (Indic-BERT+SVM) for coarse-grained task

	Precision	Recall	F1-score	Support
Non-hostile	0.96	0.96	0.96	873
Hostile	0.96	0.96	0.96	780
Accuracy			0.96	1653
Macro avg	0.96	0.96	0.96	1653
Weighted avg	0.96	0.96	0.96	1653

**Table 5** Classification report of the proposed method (Indic-BERT+SVM) for fine-grained tasks

	Precision	Recall	F1-score	Support
Defamation	0.88	0.86	0.87	1042
Fake	0.71	0.74	0.72	309
Hate	0.43	0.55	0.48	185
Offensive	0.30	0.20	0.24	117
Accuracy			0.75	1653
Macro avg	0.58	0.58	0.58	1653
Weighted avg	0.75	0.75	0.75	1653

## 6.1 Classification Report

We have also evaluated the performances of our proposed methods for coarse-grained task and fine-grained tasks with other performance metrics (i.e., precision, recall, accuracy, etc.). Tables 4 and 5 represent classification report of our proposed method (Indic-BERT+SVM) for coarse-grained task(Non-hostile/Hostile) and fine-grained tasks (Defamation, Fake, Hate, Offensive), respectively.

## 6.2 Confusion Matrix

See Fig. 3.

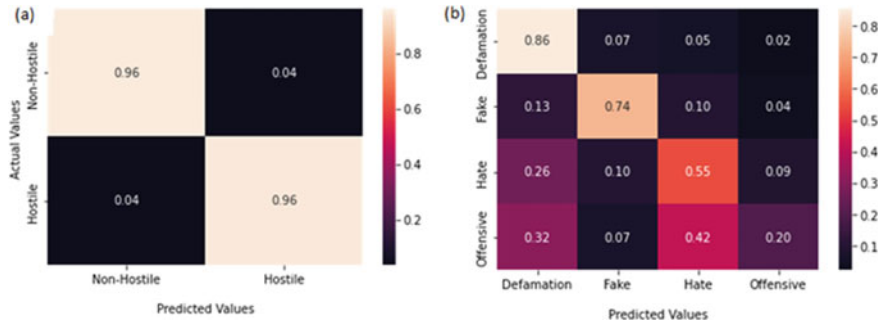


**Fig. 3** The coarse-grained confusion matrix of the proposed method is presented in (a), and the fine-grained confusion matrix of the proposed method is presented in (b)

**Table 6** Incorrectly classified posts from the dataset

Post	GT	PL
अंडरवर्ट्ट डॉन छोटा राजन के भाई को बीजेपी द्वारापहली सरकार है	Not Hate	Hate
हमारे हिन्दू जाट भाई ओपर बोला गह लोत देख लो।		
और वो टदो जाट भाई ओये साले किसी के सगे नहीं है।	Fake	Hate
बंगाल के डायन के ग्रास हैं ये बेचारे, मास्टर साहब और उनका परिवार	Defamation	Fake
सबको पता है कश्मीरियों के ऊपर जुल्म हो रहा है पर उनके लिए कोई आवाज़ नहीं उठाता	Offensive	Hate

GT Ground truth, PL Predicted label

### 6.3 Analysis of Errors

Nearly all of the social media posts in the dataset that were part of our proposed model (Indic-BERT+SVM) performed well, but there were a few posts for which our model fell short. Table 6 presents the true labels and predicted labels for posts from the dataset that were incorrectly categorized using the proposed model for various tasks (Defamation, Fake, Hate, and Offensive).

## 7 Conclusion

In this research, we have proposed a model which is a combination of Indic-BERT-based contextual embeddings and machine learning algorithm SVM for coarse-grained and fine-grained classification of hostile posts. We have made a comparative analysis of four different BERT architectures HindiBERTa, ROBERTa Hindi, Indic-Transformers Hindi XLMRoBERTa, HindiBERT, TinyBERT, SpanBERT, and Indic-BERT using SVM. The evaluation findings show that our final approach (Indic-BERT+SVM) performs significantly better than the baseline in all dimensions. Both coarse- and fine-grained tasks benefit from using comments on a tweet as additional

data. For the coarse-grained task, comments that share the same emotion should not be hostile; however, a hostile post may express opposing and strongly held opinions. It is possible for comments to mention the emotion for fine-grained tasks. On a fake post, for example, someone might comment that it is fake. Finally, we think that an end-to-end pipeline for hostile language detection on social media may be created using our proposed model. We will eventually expand our efforts to include other languages with few resources, such as Bengali and Marathi. We have already reviewed some papers on Bengali, Marathi, etc. Detailed discussion is given in Sect. 2 (Related Works). More over 200 million people worldwide talk in Bengali, which is also their primary form of communication [20]. So, hostile content detection in Bengali language is also very challenging due to low resources and unavailability of datasets. We have observed that maximum researchers have done binary classification on Bengali language (Fake/Authentic). Our future plan is to implement multi-label multi-class classification in Bengali language. Marathi is the state of Maharashtra's official language in India. It is the third most widely used language in India and is spoken by 83 million people nationwide [35]. Detection of hostile information is difficult in Marathi language due to lack of resources. Our long-term goal is to detect hostile information in Marathi language using multi-class multi-label classification because maximum researchers have done binary classification.

## References

1. Shared task @ constraint 2021 (2021). <https://constraint-shared-task-2021.github.io/>
2. Documentation/evaluation view/classification loss metrics/macro f1-score (2022). <https://peltarion.com/knowledge-center/documentation/evaluation-view/classification-loss-metrics/macro-f1-score>
3. flax-community/roberta-hindi (2022). <https://huggingface.co/flax-community/roberta-hindi>
4. monsoon-nlp/hindi-bert (2022). <https://huggingface.co/monsoon-nlp/hindi-bert>
5. neuralspace-reverie/indic-transformers-hi-xlmroberta (2022). <https://huggingface.co/neuralspace-reverie/indic-transformers-hi-xlmroberta>
6. sentence-transformers/paraphrase-tinybert-l6-v2 (2022). <https://huggingface.co/sentence-transformers/paraphrase-TinyBERT-L6-v2>
7. Spanbert/spanbert-base-cased (2022). <https://huggingface.co/SpanBERT/spanbert-base-cased>
8. Badjatiya P, Gupta S, Gupta M, Varma V (2017) Deep learning for hate speech detection in tweets. In: Proceedings of the 26th international conference on World Wide Web companion, pp 759–760
9. Bagora A, Shrestha K, Maurya K, Desarkar MS (2022) Hostility detection in online hindi-english code-mixed conversations. In: 14th ACM web science conference 2022, pp 390–400
10. Bhardwaj M, Akhtar MS, Ekbal A, Das A, Chakraborty T (2020) Hostility detection dataset in hindi. ArXiv preprint [arXiv:2011.03588](https://arxiv.org/abs/2011.03588)
11. Bhatnagar V, Kumar P, Bhattacharyya P (2022) Investigating hostile post detection in hindi. Neurocomputing 474:60–81
12. Canhasi E, Shijaku R, Berisha E (2022) Albanian fake news detection. Transactions on Asian and low-resource language information processing (2022)
13. Chaffey D (2022) Global social media statistics research summary 2022 (2022). <https://www.smartinsights.com/social-media-marketing/social-media-strategy/new-global-social-media-research>

14. Davidson T, Warmsley D, Macy M, Weber I (2017) Automated hate speech detection and the problem of offensive language. Proceedings of the international AAAI conference on web and social media 11:512–515
15. De A, Elangoan V, Maurya KK, Desarkar MS (2021) Coarse and fine-grained hostility detection in hindi posts using fine tuned multilingual embeddings. In: International workshop on combating on line hostile posts in regional languages during emergency situation. Springer, pp 201–212
16. Farha IA, Magdy W (2020) Multitask learning for arabic offensive language and hate-speech detection. In: Proceedings of the 4th workshop on open-source Arabic corpora and processing tools, with a shared task on offensive language detection, pp 86–90
17. Fawaid J, Awalina A, Krisnabayu RY, Yudistira N (2021) Indonesia's fake news detection using transformer network. In 6th International conference on sustainable information engineering and technology 2021, pp 247–251
18. Graetz FM (2018) Why adamw matters. <https://towardsdatascience.com/why-adamw-matters-736223f31b5d>
19. Hossain MZ, Rahman MA, Islam MS, Kar S (2020) Banfakenews: a dataset for detecting fake news in bangla. ArXiv preprint [arXiv:2004.08789](https://arxiv.org/abs/2004.08789)
20. Islam F, Alam MM, Hossain SS, Motaleb A, Yeasmin S, Hasan M, Rahman, R.M.: Bengali fake news detection. In: 2020 IEEE 10th international conference on intelligent systems (IS). IEEE, pp 281–287
21. Jha VK, Hrudya P, Vinu P, Vijayan V, Prabaharan P (2020) Dhot-repository and classification of offensive tweets in the Hindi language. Proced Comput Sci 171:2324–2333
22. Kakkani D, Kunchukuttan A, Golla S, Gokul N, Bhattacharyya A, Khapra MM, Kumar P (2020) Indicnlpsuite: monolingual corpora, evaluation benchmarks and pre-trained multilingual language models for indian languages. Findings of the association for computational linguistics: EMNLP 2020:4948–4961
23. Kamal O, Kumar A, Vaidhya T (2021) Hostility detection in hindi leveraging pre-trained language models. In: International workshop on combating on line Hostile posts in regional languages during emergency situation. Springer, pp 213–223
24. Klappenbach A (2022) The 12 most spoken languages in the world. <https://blog.busuu.com/most-spoken-languages-in-the-world/>
25. Koratana A, Hu K (2018) Toxic speech detection. In: Proceedings of the 32nd international conference on neural information processing systems, pp 1–9
26. Mollas I, Chrysopoulou Z, Karlos S, Tsourmakas G (2020) Ethos: an online hate speech detection dataset. ArXiv preprint [arXiv:2006.08328](https://arxiv.org/abs/2006.08328)
27. Moon J, Cho WI, Lee J (2020) Beep! korean corpus of online news comments for toxic speech detection. ArXiv preprint [arXiv:2005.12503](https://arxiv.org/abs/2005.12503)
28. Romero M (2022) mrm8488/hindiberta (2022). <https://huggingface.co/mrm8488/HindiBERTa>
29. Nazareth S (2019) Removed from reality. <https://www.thehindu.com/opinion/op-ed/removed-from-reality/article26272904.ece?homepage=true>
30. Paszke A, Gross S, Massa F, Lerer A, Bradbury J, Chanan G, Killeen T, Lin Z, Gimelshein N, Antiga L et al (2019) Pytorch: an imperative style, high-performance deep learning library. Advances in Neural Inf Proc Syst 32
31. Patwa P, Bhardwaj M, Guptha V, Kumari G, Sharma S, Pykl S, Das A, Ekbal A, Akhtar MS, Chakraborty T (2021) Overview of constraint 2021 shared tasks: detecting english covid-19 fake news and hindi hostile posts. In: International workshop on combating on line hostile posts in regional languages during emergency situation. Springer, pp 42–53
32. Roy PK, Tripathy AK, Das TK, Gao XZ (2020) A framework for hate speech detection using deep convolutional neural network. IEEE Access 8:204951–204962
33. Roy SG, Narayan U, Raha T, Abid Z, Varma V (2021) Leveraging multilingual transformers for hate speech detection. ArXiv preprint [arXiv:2101.03207](https://arxiv.org/abs/2101.03207)
34. Shekhar C, Bagla B, Maurya KK, Desarkar MS (2021) Walk in wild: an ensemble approach for hostility detection in hindi posts. ArXiv preprint [arXiv:2101.06004](https://arxiv.org/abs/2101.06004)

35. Velankar A, Patil H, Gore A, Salunke S, Joshi R (2021) Hate and offensive speech detection in hindi and marathi. ArXiv preprint [arXiv:2110.12200](https://arxiv.org/abs/2110.12200)
36. Wolf T, Debut L, Sanh V, Chaumond J, Delangue C, Moi A, Cistac P, Rault T, Louf R, Funtowicz M et al (2020) Huggingface's transformers: state-of-the-art natural language processing. Arxiv 2019. arXiv preprint [arXiv:1910.03771](https://arxiv.org/abs/1910.03771) (2020)
37. Zhang Z, Luo L (2019) Hate speech detection: a solved problem? the challenging case of long tail on twitter. Semantic Web 10(5):925–945

# Residual Convolutional Neural Network Models for COVID-19 Detection from Chest X-Ray: A Comparative Study



Saikat Acharyya , Sourav Mandal , and Rohini Basak

**Abstract** Early COVID-19 research revealed that people with COVID have anomalies on chest radiographs. However, correct diagnosis of COVID-positive patients requires experienced radiotherapists, who may not always be readily available. Therefore, to address this issue, we proposed a model that automatically distinguishes between COVID and non-COVID X-Rays without the assistance of a qualified radiologist. By employing pre-trained convolutional neural networks (CNN) models on image datasets and learning various features, matrices, and deep learning techniques, image classification has demonstrated significant success. We create a new model using the residual network of layer 40 (accuracy 94.12%) because we have access to a larger dataset for training and testing. We develop and validate our model to classify the images into four categories: COVID, Viral Pneumonia, Lung Opacity, and Normal. The goal of the work provided here is to identify the best residual network that converges quickly while also offering the best accuracy. It compares several residual CNN pre-trained models with various optimizers with the newly constructed models.

**Keywords** Residual convolutional neural network · COVID-19 detection · Image classification · ResNet-40 · CNN

## 1 Introduction

Since December 2019, coronavirus, one of the worst human catastrophes ever, has killed billions of individuals worldwide and infected numerous people. The largest issue in combating the coronavirus is to stop its rapid spread. Thus, researchers and public health professionals are constantly looking for improved methods to stop the

---

S. Acharyya · R. Basak  
Jadavpur University, Kolkata, India

S. Mandal ()  
XIM University, Bhubaneswar, India  
e-mail: [sourav.mandal@ieee.org](mailto:sourav.mandal@ieee.org)

virus's transmission and identify it as accurately as possible with the least amount of work and time. The limited supply of test kits and the length of time it takes to generate the results overshadow the great sensitivity of RT-PCR testing (few hours to a day or two) [1]. The urgent need is to comprehend the new virus known as SARS-CoV-2, or severe acute respiratory syndrome coronavirus 2, and how it affects the human body. As it is an RNA virus with the ability to mutate, it is not only necessary to comprehend the same concepts more than often; but we also need to be informed about how they are evolving. Since its appearance in Wuhan, China in December 2019, the severe acute respiratory syndrome coronavirus 2 (SARS-CoV-2), the virus that causes COVID-19, has spread worldwide [2].

Chest X-Rays are a great alternative for early COVID identification since the virus spreads from the lungs [3]. Chest X-Rays can be a very good alternative in terms of cost, time, and availability as using chest X-Rays we can lower cost and get results in time [4]. It was discovered in early research that COVID patients display abnormalities in chest radiographs [3]. Radiation is used in X-Rays (radiography) to provide a two-dimensional image of the structure and organs of any part of the human body. It contains all of the tiniest information on those components, and COVID can be found if it is properly analyzed and investigated. Typically, a skilled radiologist needs to properly evaluate the X-Ray plate even though there is a chance of human error owing to poor vision, poor lighting, or other variables.

Figure 1 is clearly labeled as COVID and Non-COVID, but without a specialist it is impossible to tell them apart. This is where deep neural networks come into play. An image used for feature extraction undergoes a convolution operation, producing multiple distinct feature maps from the same image by performing a convolution operation with different configurations. It learns the kernels or configurations necessary to classify the image into one of four categories with the use of a neural network. As an illustration, suppose we have an image that is  $30 \times 30 \times 1$  (where 1 represents only 1 channel in RGB), without reducing the size, the total number of inputs for the fully connected layer will be  $30 \times 30 = 900$ . Similarly, if the image size is  $100 \times 100$ , we have 10,000 inputs for the completely connected layer, where it was quite challenging to build a deep network with that many parameters in the first layer. The convolutional and pooling layers in convolutional neural networks (CNN) allow us to minimize the number of input parameters needed to learn while maintaining the performance of a feedforward neural network [27].

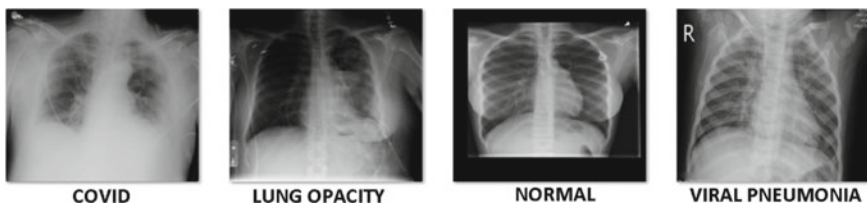


**Fig. 1** Sample X-Ray images of COVID, Lung Opacity, Normal and Pneumonia categories

Because of the change in the COVID virus's shape and its influence, it has always been difficult for the radiologist to spot the tiny change in the chest X-Ray images which can be resolved utilizing the deep neural network. However, in order for that to happen, the network must be trained on a large number of COVID-impacted X-Ray pictures that contain a variety of variances. Researchers in the deep learning community have noted that there is a lack of data available for training and that it is difficult to reduce bias when training with an imbalanced number of images.

It has already been established from earlier studies (see following section) that pre-trained CNN models perform admirably in the case of the COVID-19 identification job utilizing the chest X-Ray when the sample size is modest. In our study, we employed a sizable dataset of 21,165 photos, divided into four categories: COVID, Viral Pneumonia, Lung Opacity, and Normal, 3616 of which are for COVID-19. We create ResNet-40, a novel layer 40 network that is built on residual neural networks [12]. It uses convolution operations with different kernels serially or in parallel to reduce the number of parameters that must be learned without sacrificing learning the maximum features, max pooling layer, avgpool layer, fully connected layer, "Relu" activation function, and "softmax" output activation function for classifying those images across four categories. In our example, the image of Fig. 1 with a size of (224 × 224) is the input. Utilizing the gradient descent approach, weights and biases are updated until network convergence to minimize the cost function. We divided our input data into three subsets, trained our model using several optimizers, and were able to obtain test accuracy, precision, and recall for COVID classification of 95%, 98%, and 98%, respectively. Additionally, we used the X-Ray pictures to train pre-trained ResNet networks, such as ResNet-18, 50, and 101 [4], and then, we compared the results. The best performance we achieved is 97% for ResNet-101 when trained with SGD optimizer, where the total number of epochs is fixed.

We would like to express our gratitude to Kaggle [6, 7] for making this large dataset available to the public, which has enabled us to carry out the tasks listed below to solve this issue.

- We created a brand-new model called ResNet-40, a convolutional residual neural network with forty layers.
- Three portions of the data set were randomly assigned. SGD optimizer with momentum of 0.9 was used to train the model using subset 1, and the parameter was saved. With the Adagrad optimizer, subsets 1 and 2 were used to train the model, saved the parameter, then. The model was finally trained using subsets 1, 2, and 3 using Adam Optimizer.

The remainder of the paper is structured as follows. In Sect. 2, we reviewed a few pertinent works reported in the literature. In Sect. 3, we provided our proposed techniques. In Sect. 4, we assessed our findings. We concluded in Sect. 5.

## 2 Related Work

The field of image recognition and classification has seen a great amount of research. In this section, some of the earlier methods for image classification using machine learning as well as deep learning approaches are covered. Nowadays, AI is widely employed in the medical industry to address a variety of issues, including the detection of tumors and other diseases as well as breast cancer. Naturally, the research community has also employed it for COVID detection. Using a pre-trained deep neural network, Apostolopoulos et al. [8] were able to detect COVID with an accuracy of 96.78% on a set of 1427 X-Ray images, of which 228 images were from COVID-19, 714 images are from viral pneumonia, and the remaining images are normal. For the classification of COVID-19 chest X-Ray pictures, Abbas et al. [19] employed a CNN network Decompose, Transfer, and Compose, also known as DeTraC, and were able to reach an accuracy of 93.1%. In order to train the network utilizing pre-trained CNN-based ResNet-18, ResNet-50, etc., Shervin et al. [20] produced a dataset of 5000 chest X-Ray pictures. They were successful in achieving a high sensitivity and specificity rate of about 98% and 90%, respectively. To capture the inherent ambiguities in radiograph interpretation, Jeremy et al. [21] worked on a sizable dataset of 224,316 chest radiographs of 65,240 individuals and categorized those pictures based on 14 distinct observations. In order to automatically detect COVID-19 infection, Asif et al. [22] propose a deep CNN model CoroNet based on Xception architecture pre-trained on ImageNet dataset. This network was then trained on COVID-19 and other X-Ray images, and it was successful in achieving an overall accuracy of 89.6%. Elisha et al. [23] employed a pre-trained deep learning network (ReNet50) to detect COVID-19, which they claimed had an accuracy of 89.7%, and improved the frontal CXR image data by data augmentation and lung segmentation. Another architecture, called ECOVNet, was proposed by Nihad et al. [24]. It is based on EfficientNet architecture and was pre-trained on the ImageNet dataset before being trained on chest X-Ray images. It was claimed to have an accuracy of 97% and a precision and recall rate of 100% when detecting COVID. Another piece of work by Parnian et al. [25] suggested COVID-CAPS, an alternating modeling framework. It is built on the idea that capsule networks can handle small datasets and claims to have a 95.7% accuracy rate for COVID identification. By using the network CheXNet and a dataset of 6200 X-Ray pictures, of which 462 were for COVID-19 patients, Mehmet et al. [26] were able to detect COVID with 98% sensitivity and 95% specificity. To identify X-Ray images between normal and COVID-19 using a pre-trained deep neural network and image augmentation, Muhammad et al. [6] demonstrated 99.7% accuracy. Before feeding the image to a neural network, Tawsifur et al. [7] utilized a new image enhancement technique and proposed a novel U-net model and were able to achieve an accuracy of 98.6%. The dependability of network performance for the segmented lung images is greatly increased when utilizing the visualization technique, according to a comparison of the results with six other conventional pre-trained models.

Based on various deep learning techniques, a variety of image recognition model architectures have been created like Alexnet [9], ZFNet [10], VGGNet [13], GoogLeNet [11], Inception V2, V3 [14], and Xception [15]. With the introduction of new models, errors reduced drastically and finally reduced to 3.5% using ResNet.

ImageNet large-scale visual recognition contests were won by ResNet [12] introduced by Microsoft Corporation in 2015. ResNet models like ResNet-50 have already been found to work effectively for identifying COVID-19 using transfer learning algorithms [4, 5, 5]. The addition of skip connections is the principal underpinning ResNet, which helps to reduce training error and resolve exploding/vanishing gradient issues using a highly deep convolutional neural network that lowers the error to 3.57%.

### 3 Proposed Methodology

The goals of the proposed work are listed below. Here, residual convolutional neural network (RCNN) is utilized as a model to train the network. SGD, Adagrad, and Adam optimizers are also used, and step LR is used as part of hyper-parameter tuning.

- To investigate the convolutional neural network to distinguish the normal, pneumonia, opacity, and COVID X-Rays.
- To reach the highest level of COVID detection accuracy.

The primary tools utilized in this work are Python, PyTorch [23], and ResNet Models [12].

**The dataset** A total of 21,165 images from each of the four classes—COVID, Lung Opacity, Pneumonia, and Normal—make up the dataset utilized in this model, which was downloaded from Kaggle [6, 7]. The dataset is divided into a train dataset and a test dataset in a 4:1 ratio. The data is stored in two folders called train and test. Four child folders for four separate courses, each with the class name, make up each folder. The folder with that name contains images for that specific genre. Lung Opacity (Train-4807, Test-1205), Viral Pneumonia (Train-1058, Test-287), COVID-19 (Train-2888, Test-728), and Normal (Train-8105, Test-2087) are the categories of illness.

#### Methodology

**Data pre-processing.** By removing unused border pixels, images are center cropped to reduce their size from  $299 \times 299 \times 3$  (RGB) to  $224 \times 224 \times 3$ . After that, horizontal flips are used to introduce some outliers, which help to reduce training bias. Next, the image dataset is converted to a torch tensor, and finally, the dataset is normalized to have zero mean and unit variance.

**Training Method.** We experimented with the different network-training architectures listed below, of which Architecture I is the model we have proposed.

### Architecture I

Our first architecture was a layer 40 residual network, which we developed and used. Convolutional layer, max pooling layer, residual blocks, Avg pool, and FC layer make up this design. Figure 2 represents the architectures of normal CNN block and residual block side by side.

Table 1 describes the entire configuration of the network with Activation function—“Relu”, Loss Function—“Cross Entropy”, Output activation function—“Softmax”. Residual blocks can be distinguished based on the number of operations, 2 operations—Basic Block and 3 operations-Bottleneck Block. The operation performed for each block is ( $3 \times 3$  convolution + batch normalization + activation function (Relu) +  $3 \times 3$  convolution + batch normalization). The difference is, in case of basic block input is directly added after the operation, whereas for Bottleneck block,  $1 \times 1$  convolutions are performed before addition. Figure 3 represents the architecture of the basic residual block and bottleneck residual block.

All the input was separated into three groups for the network’s training, and the model was run using the setup listed below.

**Input set 1** (One third randomly selected image, Optimizer- SGD with momentum 0.9, Learning rate 0.1, Epoch-20) is used for training, and once the training loop is completed, model parameters are saved.

The model is loaded with the saved parameters and used **input set 2** (Input set 1 + half of the rest of the images, Optimizer-Adagrad, Learning rate 0.001, Epoch-20) for training, and once the training loop is completed, updated model parameters are saved.

The model is loaded with the saved parameters and used **input set 3** (Input set 1 + set 2 + rest of the images, all saved parameters loaded, Optimizer—Adam

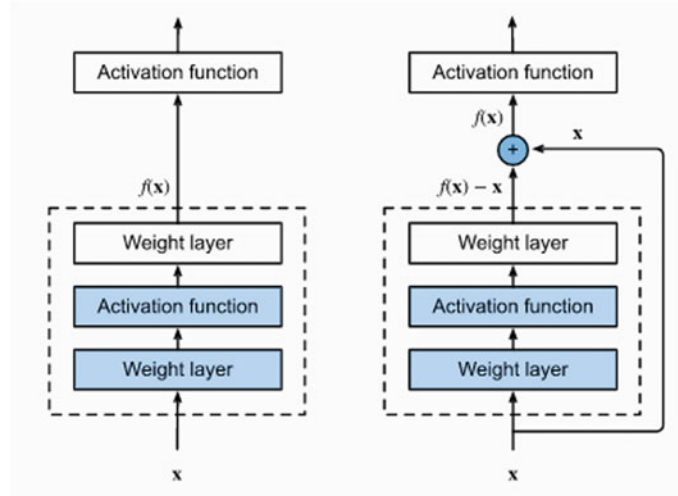


**Fig. 2** Normal CNN and with residual block

**Table 1** Configurations of kernels and in/out size

Layer name	Basic/ Residual bock	Input size	Kernel size	Feature map	Strides	Output size
Conv + Max pool	NA	224 × 224 × 3	5 × 5	64	2	112 × 112
		112 × 112 × 64	3 × 3	64	2	56 × 56
Conv 2	Basic × 4	56 × 56 × 64	3 × 3	64	1	56 × 56
Conv 3	Residual × 1 + Basic × 4	56 × 56 × 64	3 × 3	128	2	28 × 28
		28 × 28 × 128	3 × 3	128	1	28 × 28
Conv 4	Residual × 1 + Basic × 5	28 × 28 × 128	3 × 3	256	2	14 × 14
		14 × 14 × 256	3 × 3	256	1	14 × 14
Conv 5	Residual × 1 + Basic × 3	14 × 14 × 512	3 × 3	512	2	7 × 7
		7 × 7 × 512	3 × 3	512	1	7 × 7
AvgPool	NA	7 × 7 × 512	7 × 7	512	1	1 × 1
FC layer	NA	512	NA	NA	NA	4

[18], Learning rate 0.0001, Epoch -40) for training, and once the training loop is completed, updated model parameters are saved and used for testing.

Instead of using a single optimizer and running the model on the full dataset, we trained the same model with increasing input using three separate optimizers. Our goal was to increase the performance of training, and we saw a sizable improvement. Following that, we discuss a few of the additional architectures we tested and contrast them with our proposed model architecture I (see Arch1 in Table 2).

### Architecture II

Utilizing the pre-trained neural network ResNet-18, transfer learning is the second architecture that has been deployed. The configuration that yields the best results for us is provided below. We trained the network using the complete input image and various optimizers with varying learning rates like using Adam optimizer (Batch Size-150, Epoch-40, Learning rate = 0.01, Step Lr-0.1 after 15 steps, using Adagrad (Batch Size-150, Epoch-40, Learning rate = 0.01, Step Lr-0.1 after 15 steps), using SGD optimizer (Batch Size-150, Epoch-40, Momentum-0.9. Learning rate = 0.01, Step Lr-0.1 after 15 steps) (see Arch2, Arch3, and Aech4 in Table 2 for details).

### Architecture III

The pre-trained neural network ResNet-50 has been employed as the third architecture. We trained the network using the complete input image and the same

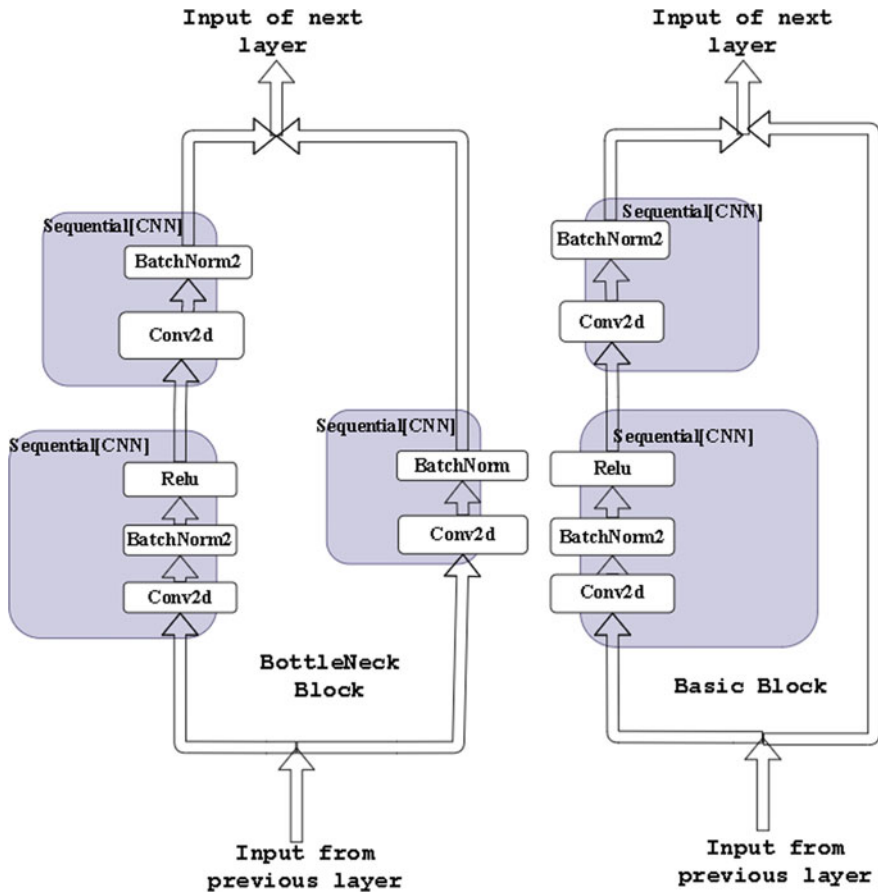


**Fig. 3** Detailed view of bottleneck and basic residual block

Architecture-II-inspired optimizers with the same set of hyperparameters (see Arch5, Arch6, and Aech7 in Table 2 for details).

#### Architecture IV

The only difference is the usage of ResNet-101. We trained the network using the same input image and the same Architecture-II-inspired optimizers with the same set of hyperparameters (see Arch8, Arch9, and Aech10 in Table 2 for details).

## 4 Model Performance and Results

Here, we discuss our research on the effectiveness of various architectural designs before making a comparison to our proposed models.

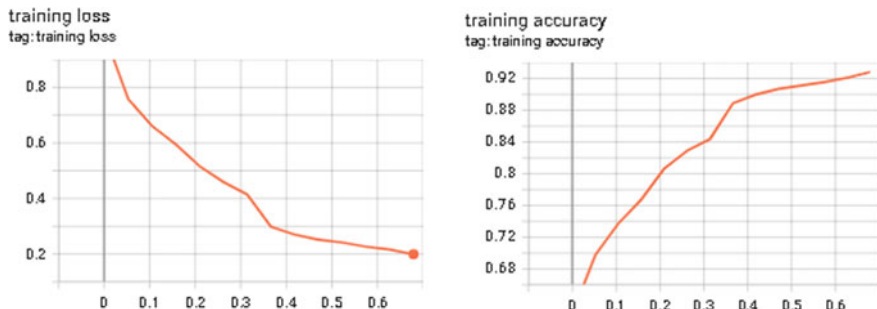
**Table 2** Comparison of training accuracy and training loss for different models

Architecture	Name	Training loss (%)	Training accuracy (%)	Testing loss (%)	Testing accuracy (%)
Arch1	ResNet-40	0.10	99.98	32.13	94.89
Arch2	ResNet-18 Adam	6.18	97.91	27.76	92.36
Arch3	ResNet-18 Adagrad	46.98	85.13	47.01	84.10
Arch4	ResNet-18 SGD 0.9	12.88	95.63	16.01	93.92
Arch5	ResNet-50 Adam	15.94	94.22	21.06	92.29
Arch6	ResNet-50 Adagrad	8.66	97.12	12.99	95.19
Arch7	ResNet-50 SGD 0.9	0.96	99.74	13.88	96.54
Arch8	ResNet-101 Adam	15.94	94.22	21.06	92.29
Arch9	ResNet-101 Adagrad	8.60	96.89	13.64	95.43
Arch10	ResNet-101 SGD 0.9	0.89	99.78	12.36	96.94

#### 4.1 Performance of Proposed Architecture I

We achieved the final testing accuracy of 94.12% using Architecture I for this classification problem of Covid detection.

Figures 4 and 5 show how, for Architecture I, training, and test loss have lowered, and accuracy has increased.

**Fig. 4** Training loss and accuracy curve for Architecture I

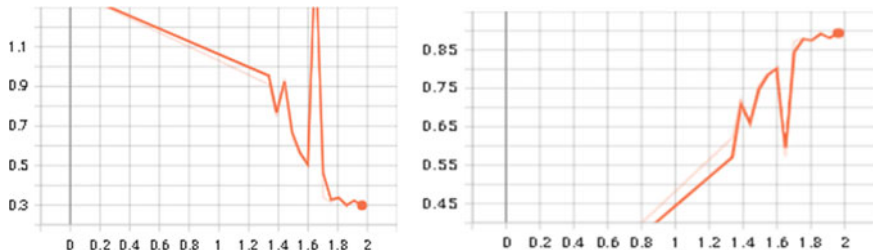


**Fig. 5** Validation loss and accuracy curve of Architecture I

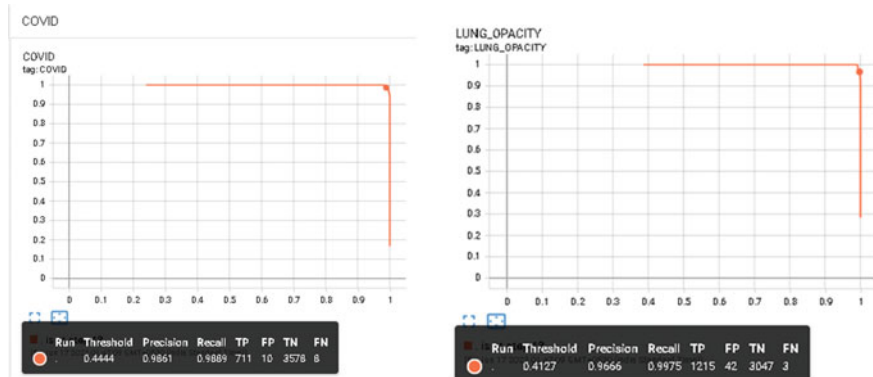


**Fig. 6** PR curve for COVID and Lung Opacity categories

#### 4.2 Precision and Recall (PR) Curve for Each Class

The PR curve for the COVID class is shown in Fig. 6 on the left. Out of Total Sample-4307, it is noticed that TP (True Positive)-711, TN (True Negative)-3578, FP (False Positive)- 10, and FN (False Negative)-8. The PR curve for Lung Opacity class is shown in Fig. 6 (right). Out of Total Sample-4307, it is noticed that TP-1215, TN-3047, FP-42, and FN-3.

Figure 7s (left) PR curve for the Normal class is shown. Out of Total Sample-4307, TP-2094, TN-2189, FP-0, and FN-24 can be seen here. The PR curve for the class of viral pneumonia is shown in Fig. 7 (right). Out of Total Sample-4307, TP-251, TN-4048, FP- 7 and FN-1 can be seen here.

#### 4.3 Performance Analysis of Different Architectures

The training loss and training accuracy for various topologies are compared in Table 2. It can be shown that architecture I has converged quickly for the same number

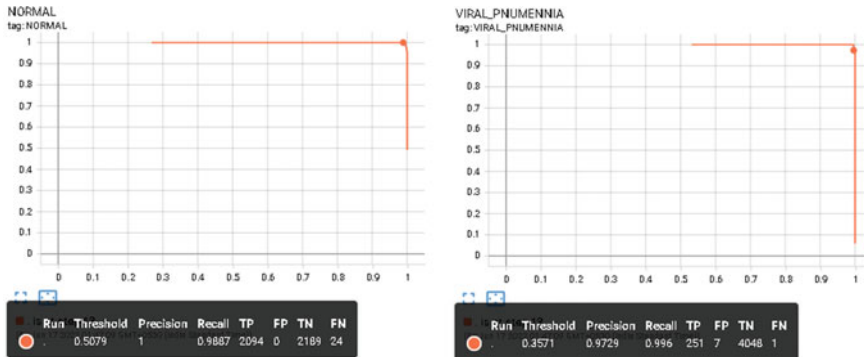


**Fig. 7** PR curve for Normal and Viral Pneumonia categories

of epochs, with training error and loss displaying a good figure for all pre-trained models (ResNet-18, ResNet-50, and ResNet-101). It also performed better with SGD with momentum 0.9 for all pre-trained models.

The testing loss and testing accuracy for various topologies are compared in Table 2. Architecture I is performing well in this area as well, while ResNet-101 with SGD outperformed the competition.

Based on the above results in Table 2 we can analyze as listed below.

1. All architectures analyze chest X-Rays and classify the images according to the disease fairly well.
2. For the same number of epochs, pre-trained models with SGD and momentum of 0.9 converge quickly and provide the best accuracy.
3. Our proposed model performed extremely well, providing training accuracy of about 99.98% and testing accuracy of about 95%.
4. Architecture IV ResNet-101 provides the best accuracy, with a training accuracy of 99.78% and a testing accuracy of 97%.

Table 3 compares the performances of similar systems and methods on the same dataset. It can be observed that our method performs well.

The sample size is most likely the cause of Gamma [7]s lower accuracy for ResNet-18,50 and 101 compared to us. The samples in this open dataset are always being updated by the author. They employed a total sample size of 18,479 for their research;

**Table 3** Comparison of different methods on same dataset

Methodology	Technique	Accuracy (%)
Gamma [7]	DenseNet-201	95.11
Gamma [7]	ResNet-18	93.31
Gamma [7]	ResNet-50	93.24
Gamma [7]	ResNet-101	93.13
Our proposed method	ResNet-40	94.89

in our instance, it is 21,165. When we used ResNet-18, 50, and 101, validation accuracy improved as the train sample size grew.

## 5 Conclusions and Future Work

We can conclude that when it comes to the task of identifying COVID-19 utilizing chest X-Ray, our proposed approach with ResNet-40 performs on par with the pre-trained model. By incorporating regularization/dropouts, which can allow us to lower overfitting and enhance generalization error, we can further improve our network. Adding more samples and retraining our network on top of them is an alternative that will help our model learn new parameters and enhance testing accuracy. Further in the future, we can create a web page or a web/mobile app that the whole public can utilize. We can also employ GradCam [16, 17] methods to visually identify the COVID-infected area and use a professional option to confirm that it is identifying the proper area of impact for COVID identification. convolutional neural networks can perform well in a variety of other medical applications, as this model indicates.

## References

1. Shan F, Gao Y, Wang J, Shi W, Shi N, Han M, Xue Z, Shen D, Shii Y (2020) Lung infection quantification of COVID-19 in CT images with deep learning. arXiv
2. Wang L, Wong A (2020) COVID-Net: A tailored deep convolutional neural network design for detection of COVID-19 cases from chest X-Ray images. arXiv
3. Ai T, Yang Z, Hou H, Zhan C, Chen C, Lv W, Tao Q, Sun Z, Xia L (2020) Correlation of chest CT and RT-PCR testing in coronavirus disease 2019 (COVID-19) in China: a report of 1014 cases. Radiology:200642
4. Kumar QP, Kumari S (2020) Detection of coronavirus disease (COVID-19) based on deep features, preprints.org, p 9
5. Maghdid HS, Asaad AT, Ghafoor KZ, Sadiq AS, Khan MK (2020) Diagnosing COVID-19 Pneumonia from X-Ray and CT images using deep learning and transfer learning algorithms. arXiv
6. Chowdhury MEH, Rahman T, Khandakar A, Mazhar R, Kadir MA, Mahbub ZB, Islam KR, Khan MS, Iqbal A, Al-Emadi N, Reaz MBI, Is-lam MT (2020) Can AI help in screening Viral and COVID-19 Pneumonia? IEEE Access 8:132665–132676
7. Rahman T, Khandakar A, Qiblawey Y, Tahir A, Kiranyaz S, Kashem SBA, Islam MT, Al Maadeed S, Zughaiher SM, Khan MS, Chowdhury MEH, Exploring the effect of image enhancement techniques on COVID-19 detection using chest X-Ray images
8. Apostolopoulos ID, Bessiana T (2020) COVID-19: Automatic detection from X-Ray images utilizing transfer learning with convolutional neural networks. Phys Eng Sci Med
9. Krizhevsky A, Krizhevsky A, Sutskever I, Hinton GE (2012) Imagenet classification with deep convolutional neural networks. Adv Neural Inf Process Syst
10. Zeiler MD, Fergus R (2014) Visualizing and understanding convolutional networks. In: Lecture notes in computer science (including subseries lecture notes in artificial intelligence and lecture notes in bioinformatics), vol 8689 LNCS, no. PART 1, pp 818–833

11. Szegedy C, Liu W, Jia Y, Sermanet P, Reed S, Anguelov D, Erhan D, Vanhoucke V, Rabinovich A (2015) Going deeper with convolutions. In: Proceedings of the IEEE computer society conference on computer vision and pattern recognition, vol 07–12 June 2015, pp 1–9
12. He K, Zhang X, Ren S, Sun J (2016) Deep residual learning for image recognition. In: Proceedings of the IEEE computer society conference on computer vision and pattern recognition, vol 2016, pp 770–778
13. Simonyan K, Zisserman A (2015) Very deep convolutional networks for large-scale image recognition
14. Szegedy C, Vanhoucke V, Ioffe S, Shlens J, Wojna Z (2016) Rethinking the inception architecture for computer vision. In: Proceedings of the IEEE computer society conference on computer vision and pattern recognition, vol 2016, pp 2818–2826
15. Chollet F (2016) Xception: deep learning with depth wise separable convolutions. In: Proceedings 30th IEEE conference on computing vision pattern recognition, CVPR, vol 2017, pp 1800–1807
16. Selvaraju RR, Cogswell M, Das A, Vedantam R, Parikh D, Batra D (2016) Grad-CAM: visual explanations from deep networks via gradient-based localization. *Int J Comput Vis* 128(2):336–359
17. Zhou B, Khosla A, Lapedriza A, Oliva A, Torralba A (2016) Learning deep features for discriminative localization. In: CVPR, pp 2921–2929
18. Kingma DP, Ba JL (2015) Adam: a method for stochastic optimization. In: 3rd International conference on learning representations, ICLR 2015—conference track proceedings
19. Abbas A, Abdelsamea MM, Gaber MM (2021) Classification of COVID-19 in chest X-Ray images using DeTraC deep convolutional neural network. *Appl Intell* 51(2021):854–864
20. Minaee S, Kafieh R, Sonka M, Yazdani S, Jamalipour Soufi G (2020) Deep-COVID: predicting COVID-19 from chest X-Ray images using deep transfer learning. *Med Image Anal* 65(2020):101794
21. Irvin J, Rajpurkar P, Ko M, Yu Y, Ciurea-Ilcus S, Chute C, Marklund H, Haghgoor B, Ball R, Shpanskaya K, Seekins J, Mong DA, Halabi SS, Sandberg JK, Jones R, Larson DB, Langlotz CP, Patel BN, Lungren MP, Ng AY (2019) CheXpert: a large chest radiograph dataset with uncertainty labels and expert comparison. In: Proceedings of the AAAI conference on artificial intelligence, pp 590–597
22. Khan AI, Shah JL, Bhat MM (2020) Coronet: a deep neural network for detection and diagnosis of COVID-19 from chest X-Ray images. *Comput Meth Programs Biomed*:105581
23. The PyTorch team. Torch Script. <https://pytorch.org/docs/stable/jit.html>
24. Goldstein E, Keidar D, Yaron D, Shachar Y, Blass A, Charbinsky L, Aharony I, Lifshitz L, Lumelsky D, Neeman Z, Mizrahi M, Hajouj M, Eizenbach N, Sela E, Weiss CS, Levin P, Benjaminov O, Bachar GN, Tamir S, Rapson Y, Suhami D, Dror AA, Bogot NR, Grubstein A, Shabshin N, Elyada YM, Eldar YC (2020) COVID-19 classification of X-Ray images using deep neural networks. arXiv preprint [arXiv:2010.01362](https://arxiv.org/abs/2010.01362)
25. Chowdhury NK, Rahman M, Rezoana N, Kabir MA (2020) ECOWNet: An ensemble of deep convolutional neural networks based on efficientNet to detect COVID-19 from chest X-Rays. arXiv preprint [arXiv:2009.11850](https://arxiv.org/abs/2009.11850)
26. Afshar P, Heidarian S, Naderkhani F, Oikonomou A, Plataniotis KN, Mohammadi A (2020) COVID-CAPS: A capsule network-based framework for identification of COVID-19 cases from X-Ray images. *Pattern Recogn Lett* 138:638–643
27. Yamac M, Ahishali M, Degerli A, Kiranyaz S, Chowdhury ME, Gab-bouj M (2020) Convolutional sparse support estimator based COVID-19 recognition from X-Ray images. arXiv preprint [arXiv:2005.04014](https://arxiv.org/abs/2005.04014)

# Prediction of Client Term Deposit Subscription Using Machine Learning



**Muskan Singh, Namrata Dhanda, U. K. Farooqui, Kapil Kumar Gupta, and Rajat Verma**

**Abstract** The majority of the banking industry's income is often derived from long-term deposits which are subscribed by the clients. Understanding clients' behaviour and attributes is crucial for banks for their growth in sales. To help with this, marketing tactics are used to target new clients producing a lot of information about client traits and other important features. In recent years, it has been found that a variety of data analysis techniques can be used to analyse the customer's traits along with the factors that have a big impact on consumers' decisions to subscribe to term deposits. Bank deposits are among the important challenges faced by a financial institution. It can be challenging to anticipate a customer's likelihood of becoming a depositor by analysing associated data. According to current estimates, the finance and business sector has suffered as a result of the crisis economic and the economy's ongoing collapse. As a result, banks are struggling to attract consumers because of the economic crisis. Marketing is regarded as a practical tool. The banking sector is trying to get customers to consider term deposits. Recognizing the objective of the company. The main aim is to predict a term deposit subscription by a customer according to the history data analysis of the client's behaviour. The data has been explored thoroughly and then a model in been built using ML Algorithms to predict the desired subscription. The algorithms are being compared, and the best accuracy given by the algorithm has been proposed as the best for prediction.

**Keywords** Machine learning · Exploratory data analysis · Logistic regression · Accuracy

---

M. Singh · N. Dhanda · K. K. Gupta

Department of Computer Science and Engineering, Amity University Uttar Pradesh, Lucknow Campus, Lucknow, India

U. K. Farooqui

Amity Institute of Information Technology, Amity University, Lucknow, Uttar Pradesh, India

R. Verma (✉)

Department of Computer Science and Engineering, Pranveer Singh Institute of Technology, Kanpur, India

e-mail: [rajatverma310795@gmail.com](mailto:rajatverma310795@gmail.com)

## 1 Introduction

As we know, the success of the nation's economy depends on banks. The numerous tasks that bank complete have made them vital and popular in today's society. The services provided by banks include money borrowing and lending, collecting deposits from customers in exchange for periodic interest payments, providing financial help through providing a range of loans, and protecting consumer funds. Banks have consistently been reliable to their clients. Security and economic confidence are considered the goals of the financial system. If banks are allowed to fail, consumers will lose their money because it would trigger a great financial panic and many people will take back their funds and retain them as cash. A withdrawal of funds would decrease the funds which are available for lending. As a consequence, there are a lot of problems that come with investing in banks.

As a result, bank deposits are regarded as a funding source for economic expansion. In addition, customer details have various aspects that have a significant impact on a customer's potential. However, for a human professional is not simple to search through a customer's database. Only if there are notable input attributes that can be detected will this be easily accomplished [1]. Data mining is a process for locating hidden information in various datasets. Recently, this technique is used to create incredibly effective categorization models in several areas, including banking and finance. There are a lot of techniques in data mining that can be used to classify data in the bank. Because there are not enough human specialists and important qualities may have been missed, predicting probable depositors can be done by automated methods by looking at raw data [2].

## 2 Literature Survey

In [5] paper, the author discusses how a DM implementation based on the CRISP-DM approach was put into practice. Real-world data were acquired from a Portuguese marketing effort promoting bank deposit subscriptions. The goal of the business is to develop a model that can explain why a contact is successful or whether a client subscribes to a deposit. By identifying the critical elements that determine campaign success, assisting with improved resource management (such as human effort, phone calls, and time), and assisting in the selection of premium and affordable groups of potential buying clients, such a model can increase campaign effectiveness.

In [2], the paper contends that to comprehend German moral hazard concerns, it is important to look beyond, particularly in the light of German Ordo-liberalism-related worries, and to concentrate on the existing national institutional structures that the German Government aimed to safeguard. German moral hazard worries were a result of the worry that adequately financed German deposit guarantee schemes (DGS)—could be used to make up for underfunded (and mostly ex-post funded) DGS in other

member states. Thus, they show that the shortcomings of the previously agreed-upon harmonization of national DGS are to blame for the challenges facing the development of an EDIS. A study that is centred on national systems can explain this difficulty to unify schemes above a modest minimal threshold. In [7], for the success of telemarketing calls in long-term deposits, the author suggests a (DM) approach. Data gathered from 2008 to 2013 were used to examine a Portuguese retail bank, taking the impacts of the current financial crisis into account. A sizable collection of 150 characteristics linked to social-economic, product, and bank client attributes were examined.

In the modelling phase, a semi-automatic feature selection method that was used with data collected before July 2012 and enabled the selection of a smaller set of 22 features was investigated. Additionally, the authors contrasted four DM models: SVM, neural network, decision trees, and logistic regression.

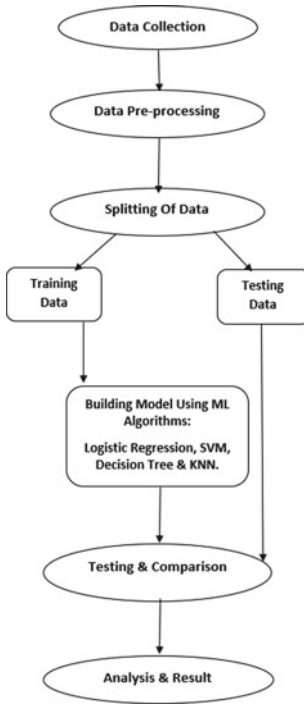
In the research paper, identifying long-term deposit customers, the authors have done a study in which to better understand how business processes might be enhanced by utilizing techniques of data mining to uncover intriguing trends, by using R programming to analyse bank transaction data. To analyse the given dataset statistically, employed, principal component analysis (PCA), factor analysis, and correlations. The paper's objective is to create models for prediction for clients signing up for long-term deposits using classification algorithms, including Logistic Regression, Random Forest, Support Vector Machine, and K-nearest neighbors. The best accuracy obtained in logistic regression was 90.64%, while the sensitivity was 99.05%.

The author Sergio Moro in his research paper enhanced the concept of Bank direct marketing through Data Mining and studied the financial crisis in Portuguese due to credit restrictions, increased competition for deposit retention, and demands direct marketing campaign efficiency improvements, the financial crisis put pressure on banks. Utilizing recent data from a Portuguese retail bank, our study ran a data mining implementation on direct marketing campaigns for deposit subscriptions. For modelling, he employed the Support Vector Machine (SVM) data mining technique and assessed it using a sensitivity analysis. The findings provided previously undiscovered relevant information, including the ideal call duration and the best months to run advertising. Such information can be used to increase the effectiveness of campaigns.

### 3 Proposed Methodology

To divide the customer list, this study tries to discover the key features and construct an ML model. Sampling strategies can correct the class imbalance due to the difficulties of the dataset. When the label of the training tuple is known, supervised learning is the best method of choice for classification issues or classification problem statements. Our research primarily focuses on anticipating customer reactions to bank applications for long-term deposits [2]. To create a flow for our system, the authors first need to define the model. The problem can be solved by using supervised learning

**Fig. 1** Methodology of the implementation



algorithms for the classification problem statement. The algorithms used are Random Forest, Logistic Regression, and Decision Tree. The algorithms are used to build up the ML model, and then, accuracy is compared to decide upon which algorithm is best to predict the desired outcome. Correlation analysis has also been performed obtained by the customers to predict who will likely subscribe. The data which is considered are customers' age, marital status, job, qualification, and other factors. The proposed methodology is shown in Fig. 1.

## 4 Dataset Overview

For this implementation, the dataset on bank telemarketing was taken from Kaggle website [20]. When Portuguese banks wanted to grow their business, they employed their call centre to run campaigns to attract people. 17 campaigns which happened between May and November 2010 are included in the dataset. Throughout the campaign, a compelling online application for long-term deposits with reasonable interest rates was made accessible. Consumer's past data traits, characteristics, and other behaviour were found to influence their response [8, 9].

**Fig. 2** Variables of the dataset

```
out[45]: ID          int64
          age         int64
          job          object
          marital      object
          education    object
          default      object
          balance      int64
          housing      object
          loan          object
          contact      object
          day           int64
          month         object
          duration     int64
          campaign     int64
          pdays         int64
          previous     int64
          poutcome      object
          subscribed   object
          dtype: object
```

## 5 Collection of Data

In the procedure of prediction, this is the initial step for collecting data regarding the problem statement. Here, the prediction is done on the historical data collected from the customers after analysing them for some time. So, here the features include such as his ID, age, job status, default balance, loan, contact, marital status and education, and other personal information as well [3]. Below are the features of the customer datasets collected. Also, the duration of the phone calls made to the clients is assessed and calls are made for the specific client in the campaign. The variable of the dataset is illustrated in Fig. 2.

## 6 Data Preprocessing

It is the most important process. Data pre-processing is the process of cleaning the data from unwanted data attributes and other impurities. Usually, datasets gathered from medical patients have null values or missing values and other impurities which cause an error in the computation of the data. Also, unwanted data affects the quality. So, the data pre-processing process is done to improve data quality and effectiveness [7]. This process is necessary so that machine learning algorithms could be applied effectively to the datasets for accurate results and successful prediction. Missing value removal is the process in, which data having the value of 0 (zero) as the worth

is eliminated. Other unwanted data is also removed in this process. Doing so helps to work faster and it also reduces the rate of error in the analysis of the data.

## 7 Exploratory Data Analysis

This is the step where the data features are taken into consideration and analysis has been done to give out some desirable relationship among the features of the data collected by clients or customers. Making correlation between variables gives us an idea of the relationship between the variables and extract meaningful information from the analysis. This focuses on summarizing the huge number of datasets accumulated and making inferences from them.

The information set contains categorical as well as numerical values. Here, the datasets have already been divided into train datasets and test datasets. The training file contains the dependent variables and the target variable, i.e. subscribed. The training data file is the one on which the model is been trained and makes it learn so that when the model is been provided with the unknown datasets that are testing data files, it can predict the training provided [4].

Univariate analysis is the analysis which is done on a specific independent variable in the given datasets while bivariate analysis is done between the independent and the target variable to see how both are correlated to each other. In the given information set, the authors will look at the distribute of the age variable to see most of the people belonging to which group of age. The Distribution of the Age variable is highlighted in Fig. 3.

The figure given above shows that a lot of people belonging to the age group of 20 to 60 are likely to subscribe to a term deposit. Now, consider the different types of jobs the clients for exploring. The Types of Job is highlighted in Fig. 4.

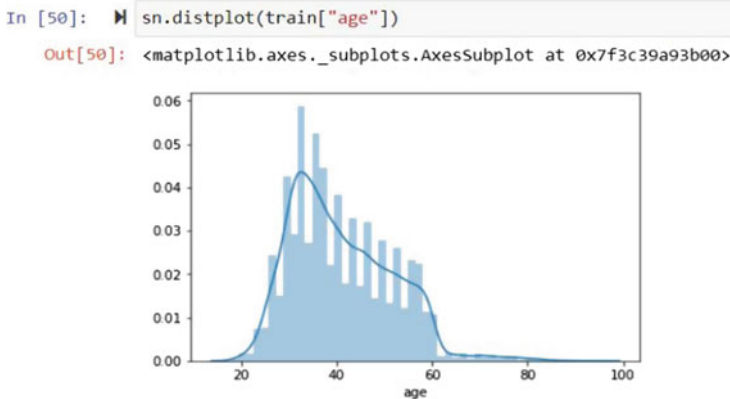


**Fig. 3** Distribution of age variable

```
In [51]: train['job'].value_counts().plot.bar()  
Out[51]: <matplotlib.axes._subplots.AxesSubplot at 0x7f3c3d9256a0>
```

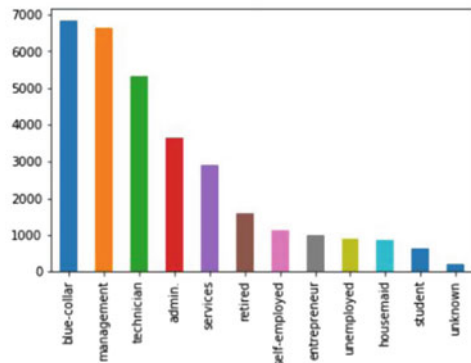


**Fig. 4** Types of jobs

The authors can visualize that most of the customers belong to a blue collared job for subscribing to term deposit and the least no. is students. The Default history analysis is shown in Fig. 5.

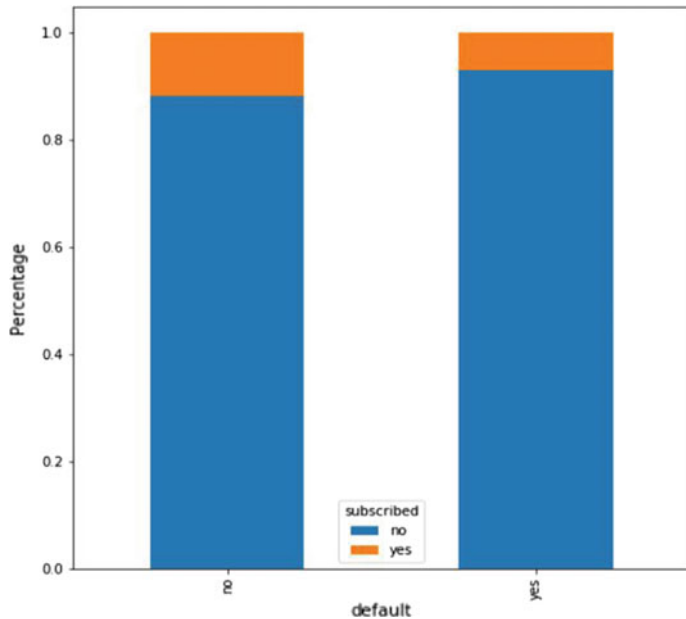


**Fig. 5** Default history analysis

From the above graph, the authors can infer that the clients having no default history are more prone to subscribe as compared to clients having a default history.

## 8 Model Building

When the data is been ready, in prediction. Machine learning algorithms are applied to the datasets to build up the model. Different techniques of machine learning algorithms will be used to build up the model to analyse the data and then for prediction of the results or consequences with great accuracy and precision. Also, different packages and libraries are used to complete the entire process of prediction.

## 9 Logistic Regression

This is a predictive analysis algorithm. Additionally, supervised learning is used. The idea of probability is the foundation of this method. One of the simplest algorithms, logistic regression, is utilized in a variety of classification problems, including the identification of cancer, diabetes, spam, heart illness, and liver disease. This algorithm assumes that the input and output variables have a linear relationship [5]. When it comes time to categorize or separate data objects into categories, the authors employ this algorithm. Logistic regression, which simply divides data into binary forms of 0 and 1, is based on a linear regression model.

## 10 Random Forest Algorithm

Another supervised learning-based machine learning method is the Random Forest algorithm. This is used to address classification and regression issues. It employs the ensemble learning approach, which combines several learning algorithms to address any complicated issue. Compared to other algorithms, this learning offers better and more accurate predictions or results. The ensemble approach is used to minimize the noise and variance mistakes that frequently occur in models. [6] An ensemble learning technique known as the Random Forest algorithm is frequently employed to handle huge datasets. Leo Bremen invented this algorithm. Using this Random Forest model, Decision tree performance also becomes better.

## 11 Decision Tree

This is another important ML algorithm used to build up a model to predict desirable outcomes with great accuracy and precision. Tree-based approaches are a different category which is a widely used machine learning model. A decision tree is the most basic and important tree-based algorithm. The training model is used to forecast the value based on the decision rules from the training data. One benefit of using a tree-based method is that they can discover non-linearity or non-linear effects with sufficient tree depth and do not make any assumptions about the structure of the data [10, 11].

## 12 Support Vector Machine

A supervised ML model, or SVM, is used to solve two-group classification problems using classification techniques. When labelled data has been provided, SVM will classify new text. It is used to solve linear and non-linear problems along with practical problems as well. This learning is used for classification and regression problems. It creates a line or hyperplane which divides the data into classes. The most popular technique of machine learning algorithms is SVM. The algorithms follow as: Firstly, the authors will select that hyperplane or line which divides the class better [12]. Compute the distance between the line and data which is called the margin to find a better plane. The chances of miss conception will be high if the distance between the two classes is low. Choose the class with the high margin [13–19].

## 13 Results and Discussion

When the model is been trained on the training dataset, accuracy is been calculated for the algorithms and a comparison is been done to choose the best algorithm for better prediction with great accuracy and without errors. As the authors can infer from the table, Random Forest Classifier is the best model giving a higher accuracy score than the other ML models. The problem statement was a classification problem which uses a supervised learning algorithm. The accuracy results given by different ML models are shown in Fig. 6.

	Model	Testing Accuracy %
0	Logistic Regression	89.083728
1	Support Vector Machine	88.593997
2	Random Forest Classifier	90.726698
3	Decision Tree Classifier	90.426540

**Fig. 6** Accuracy results of different models

## 14 Conclusion and Future Scope

To predict clients' subscriptions made for a term deposit and to comprehend probable client behaviour to support bank marketing activities was the main aim of the implementation. For this investigation, a recent and real-world dataset from a Portuguese bank was employed. The most effective method for building the model with strong predictive capabilities was found to be Random Forest. Managers can utilize the accuracy score, responsiveness, and specificity analysis the authors performed to analyse the input value in the model to improve campaigns. Decision-makers may get an advantage from the clarity as it reduces management risk and makes it simpler for them to quickly and precisely decide whether to authorize a loan. Better and more advanced classification methods can be adopted for making predictions on such problem statements. With the use of ML, there is a high scope of predictions like this in different business problems other than banking and will be advantageous for the upcoming generation and business.

## References

1. Howarth D, Quaglia L (2018) The difficult construction of a European Deposit Insurance Scheme: a step too far in Banking Union? *J Econ Policy Reform* 21(3):190–209
2. Rony MAT, Hassan MM, Ahmed E, Karim A, Azam S, Reza DA (2021) Identifying long-term deposit customers: a machine learning approach. In: 2021 2nd international informatics and software engineering conference (IISSEC). IEEE, pp 1–6
3. Vitorio A, Marques G (2021) Impact of imbalanced data on bank telemarketing calls outcome forecasting using machine learning. In: 2021 international conference on data analytics for business and industry (ICDABI). IEEE, pp 380–384
4. Guo J, Hou H (2019) Statistical decision research of long-term deposit subscription in banks based on decision tree. In: 2019 International conference on intelligent transportation, big data and smart city (ICITBS). IEEE, pp 614–617
5. Kumar NST, Reddy DS (2021) Bank marketing data classification using machine learning algorithms. *Central Asian J Math Theory Comput Sci* 2(9):31–36
6. Wisaeng K (2013) A comparison of different classification techniques for bank direct marketing. *Int J Soft Comput Eng (IJSCSE)* 3(4):116–119

7. Moro S, Cortez P, Rita P (2014) A data-driven approach to predict the success of bank telemarketing. *Decis Support Syst* 62:22–31
8. Elsalamony HA (2014) Bank direct marketing analysis of data mining techniques. *Int J Comput Appl* 85(7):12–22
9. Verma R, Dhanda N, Nagar V (2022) Security concerns in IoT systems and its blockchain solutions. In: *Cyber intelligence and information retrieval: proceedings of CIIR 2021*. Springer Singapore, pp 485–495
10. Verma R, Dhanda N, Nagar V (2022) Enhancing & optimizing security of IoT systems using different components of industry 4.0. *Int J Eng Trends Technol* 70(7):147–157. <https://doi.org/10.14445/22315381/ijett-v70i7p216>
11. Varma M, Zisserman A (2004) Unifying statistical texture classification frameworks. *Image Vis Comput* 22(14):1175–1183
12. Wang H, Ullah MM, Klaser A, Laptev I, Schmid C (2009) Evaluation of local spatio-temporal features for action recognition. In: *Bmvc 2009-british machine vision conference*. BMVA Press, pp 124–1
13. Verma R, Dhanda N, Nagar V (2022) Application of truffle suite in a blockchain environment. In: *Proceedings of third international conference on computing, communications, and cyber-security: IC4S 2021*. Springer Nature Singapore, Singapore, pp 693–702
14. Verma R, Dhanda N, Nagar V (2022) Towards a secured IoT communication: a blockchain implementation through APIs. In: *Proceedings of third international conference on computing, communications, and cyber-security: IC4S 2021*. Springer Nature Singapore, Singapore, pp 681–692
15. Verma R, Dhanda N, Nagar V (2022) Enhancing Security with in-depth analysis of brute-force attack on secure hashing algorithms. In: *Proceedings of trends in electronics and health informatics: TEHI 2021*. Springer Nature Singapore, Singapore, pp 513–522
16. Verma R, Dhanda N, Nagar V (2023) Analysing the security aspects of IoT using blockchain and cryptographic algorithms. *Int J Recent Innov Trends Comput Commun* 11(1s):13–22. <https://doi.org/10.17762/ijritcc.v11i1s.5990>
17. Verma R, Dhanda N, Nagar V (2020) Addressing the issues & challenges of internet of things using blockchain technology. *Int J Adv Sci Technol* 29(05):10074–10082
18. Verma R, Nagar V, Mahapatra S (2021) Introduction to supervised learning. *Data Analytics Bioinf: Mach Learn Perspect*, pp1–34
19. Verma R, Mishra PK, Nagar V, Mahapatra S (2021) Internet of things and smart homes: a review. *Wirel Sens Netw Internet of Things*:111–128
20. Bank Marketing Dataset (2007) Kaggle, 1

# Real Estate Price Prediction Using Machine Learning



Shilpa Yadav, Namrata Dhanda, Archana Sahai, Rajat Verma, and Sakshi Pandey

**Abstract** Real estate is a type of property that includes both land and structures as well as access to water, minerals, and other natural resources. The following paper provides an example of how a price forecasting implementation for the housing market and real estate market was carried out. There are numerous algorithms available for price prediction. Real estate price is important to both buyers and sellers. The usual methods of the quantifying price of real estate are cumbersome. Today, machine learning models are important tools to replace human work with models that can predict the price of real estate. This paper examines which characteristics of real estate property determine the price and provides insight into each of these characteristics. It is well known that many economic parameters can affect property price developments to a greater or lesser extent. In addition, it will be interesting for bankers and investors to know the future development of real estate prices. A key indicator of the economy is the price of real estate. In this study, some ML algorithms like linear regression have been used to predict the cost of a house from given attributes in the housing information set downloaded from Kaggle for Bangalore. The dataset has information about the location of the house, cost, square feet, etc. To reduce the risk of bias, hyperparameters were chosen optimally and the data set was cleaned up before being divided using k-fold cross-validation. Explanatory variables will be used to predict the price that covers many aspects of real estate. The objective of the study is to build a model that can predict the price given the features.

**Keywords** Linear regression · Hyperparameters · Cross-validation · Price prediction · Explanatory variables

---

S. Yadav · N. Dhanda · S. Pandey

Department of Computer Science and Engineering, Amity University, Lucknow, Uttar Pradesh, India

A. Sahai

Amity Institute of Information Technology, Amity University, Lucknow, Uttar Pradesh, India

R. Verma (✉)

Department of Computer Science and Engineering, Pranveer Singh Institute of Technology, Kanpur, India

e-mail: [rajatverma310795@gmail.com](mailto:rajatverma310795@gmail.com)

## 1 Introduction

Real estate has such a huge amount of potential because there is a lot of impact of professionals connected to buildings and their surroundings, which indirectly provides rich information about the buildings and their surroundings [1]. This real estate implementation aims to perform data visualization techniques to understand insights into the real estate dataset by using statistical analysis. ML algorithms are used to understand the dataset and its insights. Some Python tools are used for getting the visual understanding and cleaning it to make it ready to apply regression models. The challenge of accurately evaluating the value of real estate influences a wide run of parties, including property owners, purchasers, agents, creditors, and investors. It is also a challenging one [2]. Different elements in the dataset determine price, including size, the number of rooms, and location. Prices are additionally vulnerable to fluctuations in the market, need, also according to the circumstance at that point of time, such as when a property needs to be sold quickly. For most people, buying and selling a home will be a lifelong goal; therefore, the authors need to have realistic expectations about the homes that infuse all the properties. A set of data that includes details of the address, cost, and other features like house size, etc., of a house. While working on this type of dataset, the authors must determine which column is crucial to us and which is not. Building a regression model that can accurately estimate the price of the house based on various considerations is a major objective for this implementation [3]. For this dataset, the authors are going to utilize linear regression to see whether it provides us with good accuracy or not. Regression analysis is often used to predict price of property even when there are many other options. A single target variable serves as the output for each regression technique, and one or more predictor variables serve as the input. The usefulness of several machine learning techniques in determining the selling price of homes based on a variety of factors, including size, the number of bedrooms and bathrooms, and the location, has been assessed in this research files at a later stage.

## 2 Literature Survey

A literature review is necessary since various preliminary tasks must be completed before beginning the implementation. The authors have looked at a lot of articles that discuss how to estimate prices in the housing market and other marketplaces. The main goal is to obtain better accuracy than the earlier studies conducted. The passages that follow will give an overview of past prediction work carried out by various researchers and will be useful for putting the related implementation into practice.

Real estate has changed significantly in the twenty-first century from being a necessity, not only for individuals desiring to buy real estate but also for the companies that advertise these assets [4, 5, 6]. Nowadays, in addition to being a man's

fundamental need, real estate property also functions as a prestige symbol. Due to the properties' values' slow decline, these investments frequently seem to be profitable. Changes in the price of real estate may have an impact on a wide range of household investors, bankers, policymakers, and other individuals. Prices in a daily market are determined by underlying elements such as income, demographic trends, and global economic conditions. When buying a house, the buyer has some anticipations regarding the property. Instead of genuine fundamentals, expectations are built based on prior price movements [7, 8]. The price variation from year to year may be the short-term anticipation. One of the major contributing factors to the high levels of the housing bubble may be long-term expectations. By communicating with consumers, the seller attempts to market the property by learning about their interests and wants. On the sales floor, sellers advertise their goods and act as the first point of contact for inquiries and sales opportunities. It appears that investing in real estate is a popular choice. Estimating the value of a real estate is therefore an important economic indicator. To complete the task, Scikit Learn library of Python is utilized in this implementation. The availability and price of residences in the city can be predicted by users using this work. While experimenting with different machine learning algorithms has shown, in conclusion, that the linear regression model performs better with a higher accuracy % and fewer error values.

In [1], the SVC with linear kernel is the model that performs the best for classification problems, with an accuracy of 0.6740; with PCA preprocessing, the accuracy can be enhanced in comparison with all other techniques with PCA preprocessing, and 0.6913 is the best. The best-performing model for a regression problem is SVR with a Gaussian kernel, which has an RMSE of 0.5271. However, due to SVR's large dimensionality, visualization is challenging. However, the lasso regression model can offer insights into specific properties, which is useful in helping us understand the relationships between housing characteristics and sale prices. In [9], the paper describes about how houses in rural areas with limited facilities are affordable rather than the houses in urban areas having all facilities. The paper addressed various attributes used by the previous researchers to forecast prices using various algorithms. The research paper was made in order to help other researchers in building the real-world model. In [10], various machine learning regression techniques like linear regression, polynomial regression, decision tree, and random forest have been implemented and when all the above techniques are compared, it is found that polynomial regression with all the features gives the best results. In [11], the paper explains about how IMAS outperforms many alternatives. It can achieve 78% accuracy and an F1 score of 50% and one of the best alternative methods obtained 75% accuracy and F1 score of 43%. In this, more focus is given on the difficult and minority classes by compromising the overall performance of the model. Thamarai and Malarvizhi [12] experimented with basic ML techniques and implementation done using scikit learn python library. It helps to check the availability of the houses and prices of those houses in a particular region [13]. In this study, the authors discovered that neighborhood and total square footage (TOTAL BSMT SF + GR LIV AREA) of the home can account for around 80% of the difference in residential sales price. On the

other hand, they have also developed a model that accounts for 92% of the variation in sales and has 36 variables that are all significant at the 0.05 level.

By reading all these research papers, it provides a clear idea and serves as the starting point for the implementation. While most authors have concluded that the linear regression algorithm has the most influence on prediction, other algorithms should also be considered in the real world. By doing this study, the authors were able to effectively complete the implementation and learn more about the implementation's benefits and drawbacks.

### 3 Proposed Work

The goal of this system is to establish a model for price prediction by evaluating the numerous features that the user enters. These features are fed into the ML model, which then predicts based on how they affect the label. After the dataset is complete, it will go through the data cleaning procedure, where any unnecessary material is removed and the raw data is transformed into a .csv file. Additionally, the data will undergo data preprocessing, during which any missing data will be resolved and, if necessary, label encoding will be performed. Additionally, this will go through data transformation and be turned into a NumPy array before being sent to train the model. Several machine learning techniques will be employed to train the model, and when they are applied, their error rates will be retrieved. A final algorithm and model for precise predictions will be created as a result. After logging in, users and businesses can fill out a form with details about the many features of their property that they want to assess the value of. The model will then receive the user's information and display the estimated price of the property in a matter of seconds. The flow chart of the implementation is shown in Fig. 1.

### 4 Implementation

The primary goal of this implementation is to accurately anticipate the future price of real estate. The following section summaries will provide an overall understanding of the implementation's procedure. Below is a step-by-step procedure for the implementation:

- The Scientific Setting.
- Information's source.
- Excel.
- Normalizing the data.
- Identifying Outliers.

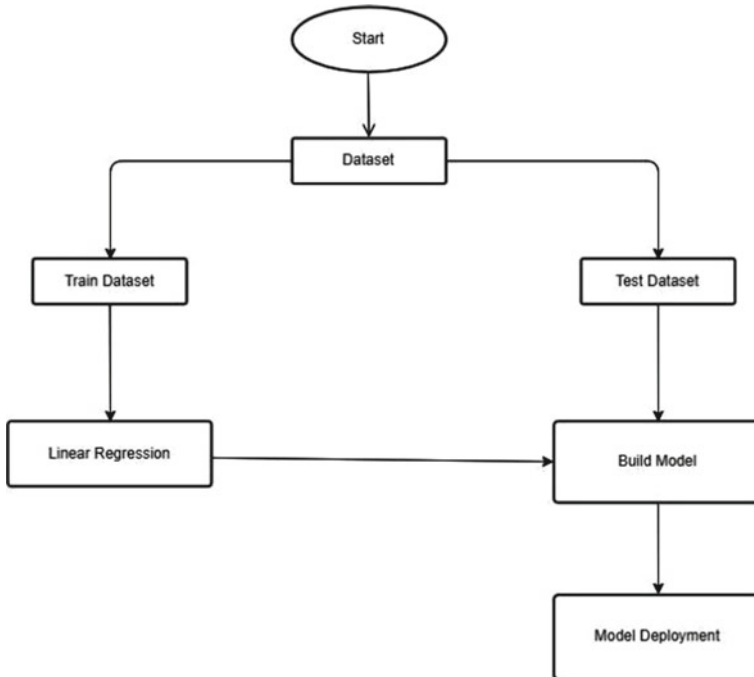


**Fig. 1** Flow chart of implementation

- Used Jupyter Notebook for analysis and visualization.

As stated in the methodology, machine learning models are constructed using linear regression and various prediction algorithms.

Dividing the data sets into training and test sets for the cross-validation procedure.

The model is built for the prediction.

The UI is built, and the python flask server is written to serve HTTP requests.

The dataset is downloaded from kaggle.com [14] and then built the model after performing data cleaning, feature engineering, dimensionality reduction, outlier removal, etc. Once, the model is ready then exported to a pickle file, then wrote python flask file that can consume the pickle file and do the price prediction of the real estate. For different requests, Python Flask will provide HTTP endpoints, and the user interface written in HTML, CSS, and JS will make HTTP get and post calls. Python is used for programming, pandas are used for data manipulation, matplotlib is used for data visualization, sklearn is used for model development, and python flask is used for the backend server. For creating the front end of the websites, use HTML, CSS, and JS. Using supervised learning and in this, the authors need to tag all datasets which means they have input and output values and based on those, tried to build an ML model.

## 4.1 Linear Regression

This method of supervised machine learning predicts an output that is continuous and has a constant slope [9]. It is employed to predict values within a continuous range. Using linear regression, it is possible to carry out a variety of tasks, including predicting housing prices. Predictions of house prices will likely be helpful to those who want to buy a property since they will be able to better organize their finances if they are aware of the price range in the future.

- **k-fold cross-validation model**—One of the most well-known methods widely used by data scientists is k-fold cross-validation. With this data-splitting technique, the authors may maximize the use of our dataset when building larger models. The development of a more comprehensive model that can perform well with unknown input is the main objective of all machine learning techniques. With k-fold cross-validation, the data-splitting process can be completed more successfully.
- **GridSearchCV**—By modifying hyperparameters, GridSearchCV is a technique for determining the appropriate parameters for a particular model. A technique called GridSearchCV is part of the Scikit (or Sk-learn) model selection package. It is important to note that the Scikit Learn library needs to be set up on the computer system. This function uses a loop over predefined hyperparameters to help fit our model to the training set. As a result, the authors can select the ideal parameters from the list of hyperparameters.

Cleaning the errors of the dataset and removing invalid values is the next step. Replacing range values with the average of numbers. Handling these non-uniformities is an important part of data cleaning.

## 4.2 Description of Dataset

The dataset has been downloaded from Kaggle.com [14]. It is used to anticipate prices using a variety of machine learning methods, and it is taken from Kaggle.com [14]. It has 13,320 rows and nine attributes. Fig. 2 shows sample (20 rows) of the dataset. The detailed information about each attribute is given in Table 1.

First, the authors imported the dataset in pandas in CSV format from kaggle.com. The dataset for the analysis contains dependent variables and independent variables. The price is a dependent variable which is needed to predict this implementation. Used Jupyter notebook for writing the code, and imported a few basic libraries like pandas, NumPy, matplotlib, and sklearn which are needed for building the model. Once imported, now read the CSV file for performing data cleaning. Describe function is used to see the statistics related to the data. Examined various features and attributes of the dataset using the head method. Figure 3 demonstrates the reading of the dataset.

1	area_type	availability	location	size	society	total_sqft	bath	balcony	price
2	Super built	19-Dec	Electronic	2 BHK	Coomee	1056	2	1	39.07
3	Plot Area	Ready To Move	Chikka Tirupathi	4 Bedroom	Theanmp	2600	5	3	120.00
4	Built-up	A Ready To Move	Uttarahalli	3 BHK		1440	2	3	62.00
5	Super built	Ready To Move	Lingadheeranahalli	3 BHK	Soiewre	1521	3	1	95.00
6	Super built	Ready To Move	Kothanur	2 BHK		1200	2	1	51.00
7	Super built	Ready To Move	Whitefield	2 BHK	DuenaTa	1170	2	1	38.00
8	Super built	18-May	Old Airport	4 BHK	Jaades	2732	4		204.00
9	Super built	Ready To Move	Rajaji Nagar	4 BHK	Brway G	3300	4		600.00
10	Super built	Ready To Move	Marathahalli	3 BHK		1310	3	1	63.25
11	Plot Area	Ready To Move	Gandhi Ba	6 Bedroom		1020	6		370.00
12	Super built	18-Feb	Whitefield	3 BHK		1800	2	2	70.00
13	Plot Area	Ready To Move	Whitefield	4 Bedroom	Prrry M	2785	5	3	295.00
14	Super built	Ready To Move	7th Phase	2 BHK	Shncyes	1000	2	1	38.00
15	Built-up	A Ready To Move	Gottigere	2 BHK		1100	2	2	40.00
16	Plot Area	Ready To Move	Sarjapur	3 Bedroom	Skityer	2250	3	2	148.00
17	Super built	Ready To Move	Mysore Rc	2 BHK	PrntaEn	1175	2	2	73.5.00
18	Super built	Ready To Move	Bisuvanahalli	3 BHK	Prtyel	1180	3	2	48.00
19	Super built	Ready To Move	Raja Rajeswari	3 BHK	GrrvaGr	1540	3	3	60.00
20	Super built	Ready To Move	Ramakrishna Nagar	3 BHK	PeBayle	2770	4	2	290.00

**Fig. 2** Figure shows first 20 rows of dataset**Table 1** Demonstrates the attributes of the dataset

Attributes	Description
area_type	Type of plot-super built, plot area, built-up area
Availability	Date when the property will be available for buying
Location	Name of the property's place
Size	BHK
Society	A society where the property is available
total_sqft	Area of land
Bath	No. of bathrooms
Balcony	No. of balconies
Price	Price for the property

```
#reading dataset
df1 = pd.read_csv("realestateDataset.csv")
df1.head()
```

	area_type	availability	location	size	society	total_sqft	bath	balcony	price
0	Super built-up Area	19-Dec	Electronic City Phase II	2 BHK	Coomee	1056	2.0	1.0	39.07
1	Plot Area	Ready To Move	Chikka Tirupathi	4 Bedroom	Theanmp	2600	5.0	3.0	120.00
2	Built-up Area	Ready To Move		Uttarahalli	3 BHK	NaN	1440	2.0	3.0
3	Super built-up Area	Ready To Move	Lingadheeranahalli	3 BHK	Soiewre	1521	3.0	1.0	95.00
4	Super built-up Area	Ready To Move		Kothanur	2 BHK	NaN	1200	2.0	1.0

**Fig. 3** Reading of the dataset

```
#drop certain columns(not considering them as an important factor for predicting the price)
df2= df1.drop(['area_type','society','balcony','availability'],axis='columns')
df2.head()
```

	location	size	total_sqft	bath	price
0	Electronic City Phase II	2 BHK	1056	2.0	39.07
1	Chikka Tirupathi	4 Bedroom	2600	5.0	120.00
2	Uttarahalli	3 BHK	1440	2.0	62.00
3	Lingadheeranahalli	3 BHK	1521	3.0	95.00
4	Kothanur	2 BHK	1200	2.0	51.00

**Fig. 4** Dropping of certain columns

### 4.3 Data Cleaning

Data cleaning is the process of removing inaccurate, damaged, badly structured, duplicate, or incomplete data from a dataset. A few important methods for cleaning data are as follows:

- Removal of duplicates.
- Delete any information that is no longer relevant.
- Make sure capitalization is uniform.
- Transform the data type.
- Simple demonstration.
- Fix errors.
- Translation of languages.
- Add any missing values.

### 4.4 Dropping Attributes and Handling Null Values

Rows or columns with null values can be removed to manage missing values. Columns can be completely dropped if more than half of their rows are null. The authors can also remove the rows with one or more columns with null values. Hence, dropping certain columns which are unimportant for the prediction and dropping these leads to better results. After dropping, data cleaning needs to be done and the process starts with handling null values. `isnull ()` function is used for checking null values, and these values can be either dropped or replaced with the median value of that column. Figure 4 demonstrates the dropping of certain columns.

### 4.5 Convert the Data Type

In the size attribute, there are two types of values (2 bhk or 2 bedroom) which have the same meaning so this problem can be solved by taking the string and tokenizing

```
def convert_sqft_to_num(x):
    tokens= x.split('-')
    if len(tokens)==2:
        return(float(tokens[0])+float(tokens[1]))/2
    try:
        return float(x)
    except:
        return None

convert_sqft_to_num('2100')
2100.0

convert_sqft_to_num('1195 - 1440')
1317.5
```

**Fig. 5** Conversion of data type

it with the first token using the lambda function. It will transform the size column, and one new column will be created containing only numeric value (e.g., 2). Figure 5 demonstrates the conversion of data type.

## 4.6 Removing Outliers and Data Types

Outlier detection and removal are the next steps, and outliers are data errors or extreme variations in the dataset. There will be single observations which, at the first glance, appear to not match the information the authors are examining. The performance of the data the authors are working with will be improved if the authors can delete an outlier for a valid reason, such as incorrect data entry [11, 15]. The authors should eliminate an outlier if it turns out to be inaccurate or irrelevant to the analysis. These are simply data points or observations that deviate from the expected range or pattern. Outliers can be found through visualization, applying formulas to the dataset, or using statistical methods. The techniques like standard deviation and simple domain knowledge are used to remove and detect these. Examined the dataset and removed these data points if there is any bedroom of less than 300 ft<sup>2</sup>. Removed data points having the price per ft<sup>2</sup> extremely high or extremely low. Figures 6 and 7 demonstrate cleaning errors and removing outliers of the dataset, respectively.

```
#clean errors
df3['bhk']= df3['size'].apply(lambda x: int(x.split(' ')[0]))
C:\Users\SHILPI YADAV\AppData\Local\Temp\ipykernel_16612\2290192944.py:2: SettingWithCopyWarning:
A value is trying to be set on a copy of a slice from a DataFrame.
Try using .loc[row_indexer,col_indexer] = value instead
See the caveats in the documentation: https://pandas.pydata.org/pandas-docs/stable/user_guide/indexing.html#returning-a-view-versus-a-copy
df3['bhk']= df3['size'].apply(lambda x: int(x.split(' ')[0]))

df3.head()

  location      size  total_sqft  bath   price  bhk
0  Electronic City Phase II    2 BHK     1056    2.0  39.07    2
1  Chikka Tirupathi 4 Bedroom    2600    5.0 120.00    4
2  Uttarahalli    3 BHK     1440    2.0  62.00    3
3  Lingadheeranahalli    3 BHK     1521    3.0  95.00    3
4  Kothanur        2 BHK     1200    2.0  51.00    2
```

**Fig. 6** Cleaning errors

```
#removing data errors and outliers
def is_float(x):
    try:
        float(x)
    except:
        return False
    return True

df3[~df3['total_sqft'].apply(is_float)].head(10)

  location      size  total_sqft  bath   price  bhk
30  Yelahanka    4 BHK     2100 - 2850    4.0 186.000    4
122  Hebbal        4 BHK     3067 - 8156    4.0 477.000    4
137  8th Phase JP Nagar    2 BHK     1042 - 1105    2.0  54.005    2
165  Sarjapur    2 BHK     1145 - 1340    2.0  43.490    2
188  KR Puram    2 BHK     1015 - 1540    2.0  56.800    2
410  Kengeri      1 BHK  34.46Sq. Meter    1.0  18.500    1
549  Hennur Road    2 BHK     1195 - 1440    2.0  63.770    2
648  Arekere      9 Bedroom  4125Perch    9.0 265.000    9
661  Yelahanka    2 BHK     1120 - 1145    2.0  48.130    2
672  Bettahalsoor  4 Bedroom    3090 - 5002    4.0 445.000    4
```

**Fig. 7** Removing outlier

## 4.7 Feature Engineering

After cleaning the data errors and outliers, dimensionality reduction is important. To select the crucial features for the model's construction, feature engineering should be done. Feature engineering is the process of extracting relevant features from the data to train machine learning algorithms. Data science depends on feature engineering because it generates accurate and reliable data. Achieving the best outcomes from the algorithms is the main goal of feature engineering. Created a new feature price\_per\_sqft, it would also help in outlier detection and reducing dimensionality. Figure 8 demonstrates the creation new feature.

```
#now data cleaning done. feature engineering and dimensionality reduction are next
```

```
#create new feature price_per_sqft
df5= df4.copy()
df5['price_per_sqft']= df5['price']*100000/df5['total_sqft']
df5.head()
```

	location	size	total_sqft	bath	price	bhk	price_per_sqft
0	Electronic City Phase II	2 BHK	1056.0	2.0	39.07	2	3699.810606
1	Chikka Tirupathi	4 Bedroom	2600.0	5.0	120.00	4	4615.384615
2	Uttarahalli	3 BHK	1440.0	2.0	62.00	3	4305.555556
3	Lingadheeranahalli	3 BHK	1521.0	3.0	95.00	3	6245.890861
4	Kothanur	2 BHK	1200.0	2.0	51.00	2	4250.000000

**Fig. 8** Creating new features

## 4.8 Dimensionality Reduction

Explored location column which is a categorical feature and it is a high dimensional problem as it contains 1304 places. There are numerous ways for reducing the dimensionality of the dataset. One of the effective techniques is to make a new category to see the number of data points for every location. Then, the category is named other for the data points that have a value lesser than the threshold [10]. Applied lambda function for converting the locations that have less than 10 data points to others and it has reduced the dimensionality to some extent. Figure 9 demonstrates dimensionality reduction.

```
#Locations that has data points less than 10
location_stats_less_than_10= location_stats[location_stats<=10]
location_stats_less_than_10

location
Basapura          10
1st Block Koramangala    10
Gunjur Palya       10
Kalkere           10
Sector 1 HSR Layout  10
...
1 Giri Nagar        1
Kanakapura Road,      1
Kanakapura main Road  1
Karnataka Shabrimala  1
whitefield          1
Name: location, Length: 1052, dtype: int64

len(df5.location.unique())
1293

df5.location= df5.location.apply(lambda x: 'other' if x in location_stats_less_than_10 else x)
len(df5.location.unique())
```

**Fig. 9** Dimensionality reduction

```
#getting some basic insights from visualization
def plot_scatter_chart(df,location):
    bhk2= df[(df.location==location) & (df.bhk==2)]
    bhk3= df[(df.location==location) & (df.bhk==3)]
    matplotlib.rcParams['figure.figsize']= (15,10)
    plt.scatter(bhk2.total_sqft, bhk2.price, color= 'blue', label='2 BHK', s=50)
    plt.scatter(bhk3.total_sqft, bhk3.price, marker= '+', color= 'green', label='3 BHK', s=50)
    plt.xlabel("Total Square Feet Area")
    plt.ylabel("Price Per Square Feet")
    plt.title(location)
    plt.legend()

plot_scatter_chart(df7, "Rajaji Nagar")
```

**Fig. 10** Data visualization function

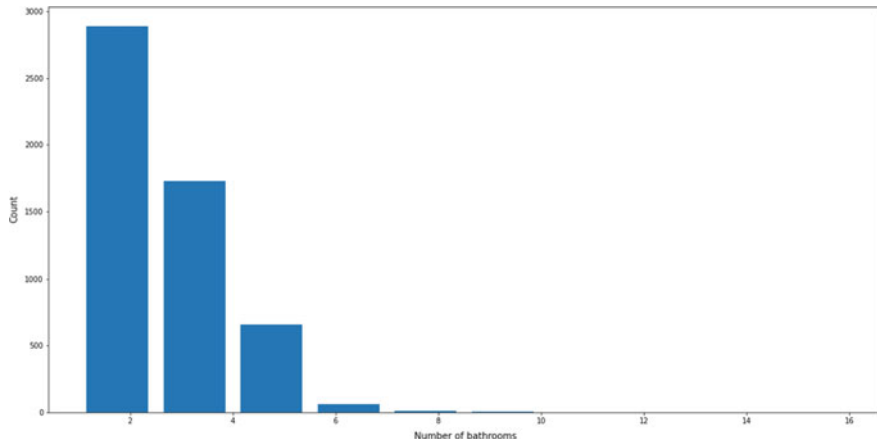


**Fig. 11** Scatter plot which shows the price per ft<sup>2</sup> of 2 bhk and 3 bhk in Rajaji Nagar

## 4.9 Data Visualization

Visualized the dataset for getting better insights and understanding of the data. With the help of data visualization, the authors can see that a variety of factors, including square feet area and location, have an impact on home pricing. The Visualization Function and Scatter plots for 2-bedroom and 3-bedroom apartments are shown in Figs. 10 and 11, respectively. Figure 12 demonstrates the count of bathrooms.

## 4.10 Model Building

For building the model, there is a need to convert the text data into numeric so that model can interpret that easily using 1 hot encoding (also called dummies). The dataset was divided into train and test for effective model training and testing, and

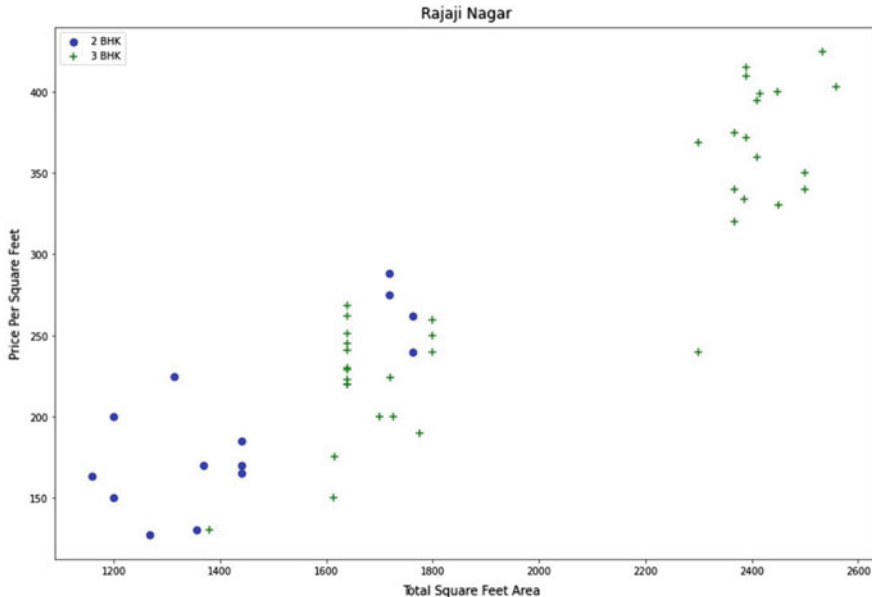


**Fig. 12** Graph showing count of records having  $n$  number of bathrooms

dependent ( $X$ ) and independent ( $Y$ ) variables were created. Our machine is trained using train data, and the authors use test data to determine how effectively it has learned the data. Using the scikit learn library, one can import the train and test strategy. The linear regression model is created first which gives a score of approx. 85% which is quite okay. Now, for optimality, tried k-fold cross-validation model gives a score of around 80%. Lasso regression, Decision Tree, and GridSearchCV are some of another regression techniques for the prediction. All the model prediction techniques are checked to check for overfitting by evaluating the values using the cross-validation technique. Linear regression gives the highest score. Then, built the python function for predicting the price. After building the model, there is a need to export the model and the related artifacts that are needed for the python flask server. The pickle file contains coefficients, and intercepts but not actual data. Figures 13 and 14 demonstrate the prediction function and validation model, respectively.

#### 4.11 Web Interface of Model

For the backend, the flask framework of python is used to write a python service that can serve HTTP requests. After writing the python flask server, there is a need to test the written code. For this, the authors have used the postman application to test HTTP request calls. After building the backend, there is a need to build the frontend UI application using frontend technologies like HTML, CSS, and JS. If a simple

```

def predict_price(location,sqft,bath,bhk):
    loc_index= np.where(X.columns==location)[0][0]

    x= np.zeros(len(X.columns))
    x[0]= sqft
    x[1]= bath
    x[2]= bhk
    if loc_index>=0:
        x[loc_index]= 1

    return lr_clf.predict([x])[0]

predict_price('1st Phase JP Nagar', 1000, 2, 2)
C:\Users\SHILPI YADAV\AppData\Local\Programs\Python\Python310\lib\site-packages\sklearn\base.py:450: UserWarning: X does not have valid feature names, but LinearRegression was fitted with feature names
  warnings.warn(
83.63367364122013

```

**Fig. 13** Prediction function

```

#k fold cross validation model
from sklearn.model_selection import ShuffleSplit
from sklearn.model_selection import cross_val_score

cv= ShuffleSplit(n_splits=5, test_size=0.2, random_state=0)

cross_val_score(LinearRegression(), X, Y, cv=cv)

array([ 8.16684136e-01, -3.12450749e+14, -7.01586116e+13,  8.46447691e-01,
       8.51547439e-01])

```

**Fig. 14** Validation model

user interface is developed, people who have little to no understanding will be able to predict prices for their dream homes with ease. The users can use UI to enter the features of their property and predict the price at their convenience. Then, it is hosted using Amazon Web Services (AWS) and it can be accessed by anyone to check the price of real estate.

## 5 Findings

The findings show that the use of various machine learning algorithms can change the accuracy tremendously. The linear regression model gives a score of approximately 85%. For optimality, k-fold cross-validation model gives a score of around 80%. The best score achieved is 85% of linear regression. As the model is based on the dataset fed to it, poor dataset can decrease the accuracy or affect the prediction negatively. Using the above model, people can easily buy houses and real estate at their rightful prices [16]. It also ensures that people do not get tricked by sketchy agents. Also, an Amazon EC2 connection has taken the implementation even further and increased the ease of use.

## 6 Conclusion and Future Scope

Because real estate pricing drives the market, the authors want to ensure that this model is utilized. The system can self-train using the algorithms and price prediction by using the supplied raw data or attributes [17]. After reviewing numerous academic papers, blogs, and articles, a collection of potential methods was selected. The authors are tasked with forecasting pricing, which the authors have already done with the use of several machine learning techniques, including linear regression. This research also helps us to learn how attributes affect predictions. Linear regression has a higher prediction accuracy than the other methods but in the future ensemble techniques can be applied for better accuracy. Based on the data that is already accessible, the authors can create models for the prediction of potential problems, and occasionally data science can help prevent problems by identifying outliers. The model can be used by big organizations to set the pricing and save a lot of valuable price and time. The authors can ensure the buyers to the correct prices as it is the essence of the market. The implementation is quite time-saving and user-friendly.

Every system, including modern software, can aid in predicting future prices. The accuracy of this price estimate can be increased by including additional information about the homes' surroundings, markets, and other relevant factors. To give consumers a quick notion and help them invest their money more safely, the forecasted information may be stored in databases and made into an application. If real-time data is possible, it is possible to connect the data to ML algorithms directly, allowing for the demonstration of an application environment [15]. The dataset contains the data of Bangalore but in the future, it can be fed with more data, and hence, it can anticipate the cost for more areas. For adding numerous locations, supplementary features can be added to this proposed implementation to avail users of a fully fledged system that contains multiple functionalities for the buyers to use with the ML model. The website can provide the users with the option to select the various ML algorithms but the best one is selected by default. The score can be improved through feature selection or using other regression models [18, 19, 20, 21, 22, 23, 24, 25, 26].

## References

1. Yu H, Wu J (2016) Real estate price prediction with regression and classification. CS229 (Machine Learning) Final Project Reports
2. Ghosalkar NN, Dhage SN (2018) Real estate value prediction using linear regression. In: 2018 fourth international conference on computing communication control and automation (ICCUBEA). IEEE, pp 1–5
3. Manjula R, Jain S, Srivastava S, Kher PR (2017) Real estate value prediction using multivariate regression models. IOP Conf Ser Mater Sci Eng 263(4):042098. IOP Publishing
4. Caiyu S, Jinri W, Jie D, Yuan L (2022) Mining potential 5G mobile users based on logistic regression and random forest. In: 2022 IEEE 5th international conference on information systems and computer aided education (ICISCAE). IEEE, pp 351–356

5. Anand S, Yadav P, Gaur A, Kashyap I (2021) Real estate price prediction model. In: 2021 3rd International conference on advances in computing, communication control and networking (ICAC3N). IEEE, pp 541–543
6. Durganjali P, Pujitha MV (2019) House resale price prediction using classification algorithms. In: 2019 International conference on smart structures and systems (ICSSS). IEEE, pp 1–4
7. Sin E, Wang L (2017) Bitcoin price prediction using ensembles of neural networks. In: 2017 13th International conference on natural computation, fuzzy systems and knowledge discovery (ICNC-FSKD). IEEE, pp 666–671
8. Phan TD (2018) Housing price prediction using machine learning algorithms: the case of Melbourne city, Australia. In: 2018 International conference on machine learning and data engineering (iCMLDE). IEEE, pp 35–42
9. Zulkifley NH, Rahman SA, Ubaidullah NH, Ibrahim I (2020) House price prediction using a machine learning model: a survey of literature. *Int J Mod Educ Comput Sci* 12(6)
10. Khare S, Gourisaria MK, Harshvardhan GM, Joardar S, Singh V (2021) Real estate cost estimation through data mining techniques. *IOP Conf Ser Mater Sci Eng* 1099(1):012053. IOP Publishing
11. Li Y, Branco P, Zhang H (2022) Imbalanced multimodal attention-based system for multiclass house price prediction. *Mathematics* 11(1):113
12. Thamarai M, Malarvizhi SP (2020) House price prediction modeling using machine learning. *Int J Inf Eng Electron Bus* 12(2)
13. Mohd T, Jamil NS, Johari N, Abdullah L, Masrom S (2020) An overview of real estate modelling techniques for house price prediction. In: Charting a sustainable future of asean in business and social sciences: proceedings of the 3rd international conference on the future of ASEAN (ICoFA) 2019, vol 1. Springer Singapore, pp 321–338
14. Bangalore House Price Prediction (2021) Kaggle, 1
15. Rizun N, Baj-Rogowska A (2021) Can web search queries predict prices change on the real estate market? *IEEE Access* 9:70095–70117
16. Madhuri CR, Anuradha G, Pujitha MV (2019) House price prediction using regression techniques: a comparative study. In: 2019 International conference on smart structures and systems (ICSSS). IEEE, pp 1–5
17. Pai PF, Wang WC (2020) Using machine learning models and actual transaction data for predicting real estate prices. *Appl Sci* 10(17):5832
18. Verma R, Dhanda N, Nagar V (2022) Security concerns in IoT systems and its blockchain solutions. In: Cyber intelligence and information retrieval: proceedings of CIIR 2021. Springer Singapore, pp 485–495
19. Verma R, Dhanda N, Nagar V (2022) Enhancing & optimizing security of IoT systems using different components of industry 4.0. *Int J Eng Trends Technol* 70(7):147–157. <https://doi.org/10.14445/22315381/ijett-v70i7p216>
20. Verma R, Dhanda N, Nagar V (2022) Application of truffle suite in a blockchain environment. In: Proceedings of third international conference on computing, communications, and cyber-security: IC4S 2021. Springer Nature Singapore, Singapore, pp. 693–702
21. Verma R, Dhanda N, Nagar V (2022) Towards a secured IoT communication: a blockchain implementation through APIs. In: Proceedings of third international conference on computing, communications, and cyber-security: IC4S 2021. Springer Nature Singapore, Singapore, pp 681–692
22. Verma R, Dhanda N, Nagar V (2022) Enhancing security with in-depth analysis of brute-force attack on secure hashing algorithms. In: Proceedings of trends in electronics and health informatics: TEHI 2021. Springer Nature Singapore, Singapore, pp 513–522
23. Verma R, Dhanda N, Nagar V (2023) Analysing the security aspects of IoT using blockchain and cryptographic algorithms. *Int J Recent Innov Trends Comput Commun* 11(1s):13–22. <https://doi.org/10.17762/ijritcc.v11i1s.5990>
24. Verma R, Dhanda N, Nagar V (2020) Addressing the issues and challenges of internet of things using blockchain technology. *Int J Adv Sci Technol* 29(05):10074–10082

25. Verma R, Nagar V, Mahapatra S (2021) Introduction to supervised learning. *Data Analytics Bioinf: Mach Learn Perspect*:1–34
26. Verma R, Mishra PK, Nagar V, Mahapatra S (2021) Internet of things and smart homes: a review. *Wirel Sens Netw Internet of Things*:111–128

# A Comparative Study to Detect Cervical Dysplasia by Using Pap Smear Images



Jheelam Mondal and Subhankar Joardar

**Abstract** Neoplasia is a process that produces abnormal as well as excessive growth of tissue. It persists in this manner after caseation of the stimuli which evoked the change. Cervical cancer or neoplasm (squamous cell carcinoma) is the fourth most common cause among the different types of cancers present worldwide. However, cervical cancer can be effectively prevented by routine screening by taking cervical smears and staining by Papanicolaou stain and reporting them according to the Bethesda system 2001 of cervicovaginal cytology. Due to the ever-increasing awareness, increasing workload and paucity of trained pathologists, AI and machine learning are increasingly used for reporting of Pap smear. Despite years of research in this field, precise segmentation of cervical image cells remains a challenge since there can be presence of cluster of cells. Here, we are going to discuss the comparative study of the traditional classification methods which are mainly dependent on main features like morphology, texture, and size of nucleus in the cell. This analysis is quite helpful for developing an automated classification of cells which helps in initial cervical screening.

**Keywords** Pap smear images · Image classification · Cervical cancer · Image segmentation

## 1 Introduction

### 1.1 Background Study

Cancer is the most feared disease, and it accounts for nearly 10 million deaths worldwide every year. Cancer involves growth of cells abnormally and spread of the same to different parts of the body. According to a report by Indian Council for Medical

---

J. Mondal (✉) · S. Joardar  
Haldia Institute of Technology, Haldia, India  
e-mail: [jheelam.cse@gmail.com](mailto:jheelam.cse@gmail.com)

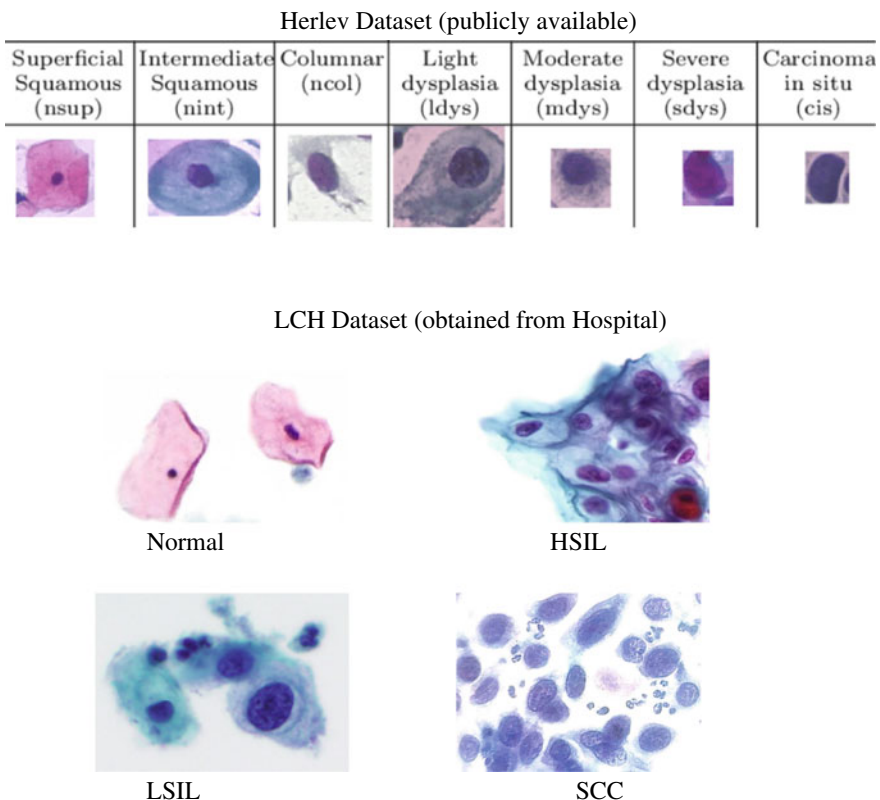
Research on the burden of cancers in India, cervical cancer (4.3%) is one of the total seven cancers which comprise the total burden. Since there are no early symptoms or signs for cervical cancer, conventional pap smear test is the widely used as screening test to detect cervical cancer cells [1] at early stage and prevent it as well. However, this test is still unavailable in under-developed countries. The cause is complexity, time-consuming process, and tedious manual screening of cells having abnormal growth from a specimen. Sometimes, images have uneven layering or overlapping of cells. In this test, the sample of cells is collected and is then placed on a glass slide and stained them with a Papanicolaou stain (a combination of stains). Then, this slide is placed under a microscope to find out the abnormal cells. Since the entire process is costly, time-consuming as well as it involves human error, so the automation process of checking a pap smear image will be very useful for doing the preliminary screening for a skilled pathologist if not replaced completely.

Image analysis literature can be a single-cell level or smear level, second one is some types of segmentation algorithms for identifying the region of interest, and third one is types of features observed and lastly analysis of classification processes. Previous study is typically done on two types of image analysis, i.e., cell level [2] and smear level [3, 4]. Each image is either a single cell that can be abnormal or normal cervical cell in the cell level study. Whereas in case of smear level study, the image contains more than one cervical cell and also contains unwanted debris in the background.

Classification is the most vital stage in making a decision. Literature involving two types of Pap smear classification can be categorized either cell classification or smear classification. Different researches of single-cell classification are classified into Normal class (can be Normal Intermediate (NI), Normal Superficial (NS), Normal Columnar (NC), Abnormal class, Severe dysplasia (SD), Moderate dysplasia (MD), and Carcinoma in situ (CS)). Again, according to the Bethesda system, pap smear image is classified into normal, low-grade (LSIL), high-grade (HSIL), and squamous cell carcinoma (SCC). Also, it was found that researches on smear level cell classification are comparatively difficult (Fig. 1).

## 1.2 *Literature Survey*

The motivation of this project is to find out presence of cancer cells or not in the image sample. Over the past few decades, researchers have done extensive study in this area to build an automated image analysis method. A pap smear image contains 100–10,000 cells, and it is a difficult as well as time-consuming task for a pathologist to check the image manually under a microscope. This screening of the image has three distinct tasks—segmentation, feature extraction or selection, and classification. Along with cervical cells, there can be different kinds of other cells like RBCs which form the debris in a digitized image. To study the image properly, we need to remove such debris present in the image. Proper cell segmentation plays a vital role in classification of cervical cells. Presence of clusters in cell is also a problem in



**Fig. 1** Sample cervical cells of Herlev and LCH pap smear datasets

segmentation of cytoplasm and nuclei of a pap smear image. Some other problems that are encountered in cell segmentation phase are poor staining quality and poor contrast quality of the sample image. Another major problem in analyzing medical sample is unavailability of real image data. Hence, a large number of researchers have carried out their research work on limited data available publicly. So, the automated system should be robust enough so that it performs well not only on the public data available but on real-time data as well. For instance, the Herlev dataset [5] has a total of 917 images (675 abnormal cells and 242 normal cells). Using this dataset, the attained nucleus segmentation accuracy ranged between 0.85 [6] and 0.92 [7]. Using an overlapping cervical cell dataset [8], the cytoplasm segmentation accuracy ranges from 0.87 to 0.89 [8]. However, most cell classification researches assume that proper segmentations of cytoplasm and nucleus are readily present [9, 10]. High accuracy classification (e.g., 96.8%) is achieved on the Herlev dataset from the segmented cytoplasm and nucleus, using fivefold cross validation [10, 11]. Among various multi-class SVM classifiers, polynomial SVM classifier resulted in an accuracy of 0.95 for classification [14] (Table 1).

**Table 1** Different segmentation techniques used

S. No.	Author name	Classification technique	Accuracy	Work findings
1	Chankong et al. [6]	Patch-based Fuzzy C-means clustering is used for segmentation, feature extraction (six nucleus-based features used), and classification done using 5 different classifiers (Bayesian, LDA, KNN, ANN, and SVM)	0.85–0.92	Single-cell level implementation and classification achieved with a moderate range of accuracy. But this work was not implemented on multiple cells
2	Lu et al. [8]	(a) Segmentation of subcellular components combining superpixel representation with Voronoi diagrams. (b) a variational approach used to detect overlapping of cells. (c) joint optimization of multiple-level set functions	0.87–0.89	First of a kind of implementation which was able to segment multiple cells. But was not applicable in complex clusters (cells greater than 3)
3	Li et al. [3]	Used neural network which consists of 10 input nodes, one hidden layer of 4 nodes and 2 output nodes describing the final classification of the sample as either normal or abnormal	0.99	High accuracy, but not tested on larger dataset

### 1.3 Related Works

See (Table 2).

## 2 Methodology

The above diagram depicts the flow of the classification process of a pap smear image. A brief overview of these phases is discussed below (Fig. 2).

**Table 2** Comparison analysis of different techniques

S. No.	Authors	Technique used	Comparison analysis
1	Tsai et al. [2]	(a) A cytoplasm and nucleus contour detector used to divide the nucleus and cytoplasm of the cell from a smear image (b) A median filter used to remove noises, bi-group enhancer for brightening the object contours (c) Implementation of K-mean algorithm to identify the cytoplasm from the background and extract nucleus contour	Gave better results in segmenting pap smear images with no overlapping but is not possible in complex clusters
2	Plissiti et al. (2011) [4]	Watershed method-single nucleus cell image was over segmented	ANN classifier worked quite well than other classifiers like (Bayesian, LDA, KNN and SVM) in terms of accuracy. But it could not solve the problem of identifying exact nuclei boundary
3	Zhang et al. [8]	Deep neural network for cervical cells nucleus segmentation by effectively combining the characteristics of all layers	Showed superior segmentation results by using this proposed method
4	Kashyap et al. [14]	Multi-class SVM classifiers such as polynomial SVMs, quadratic SVMs, Gaussian RBF SVMs, and linear SVMs along with PCA	Results showed polynomial SVMs gave better results than any other classifiers. Limitation is this method did not solve the problem of overlapping cells. Also contrast enhancement technique can be applied for reducing unwanted background information

### 3 Image Acquisition

This process involves capturing an image from source with the help of hardware systems like cameras, sensors, etc.

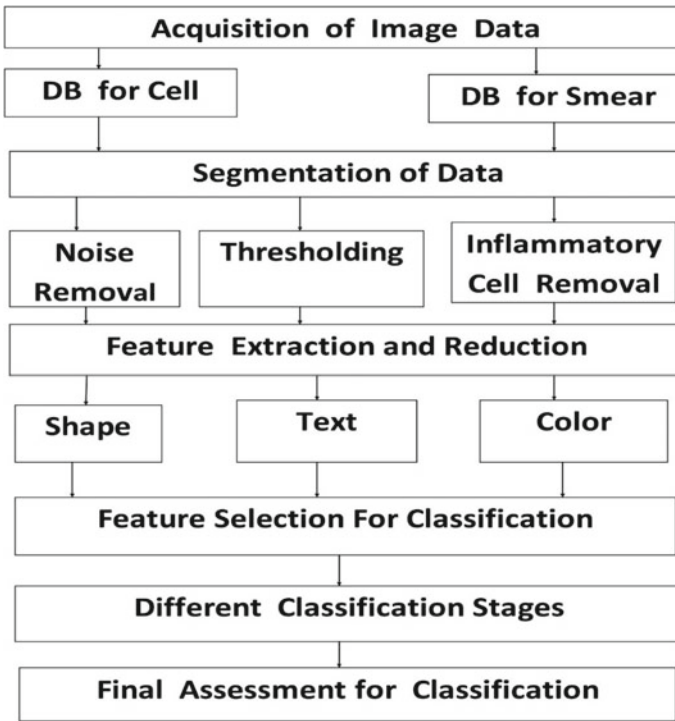


**Fig. 2** Classification methodology

### **3.1 Cell Level Database**

An expert marks the cervical cells, and then by cropping out the cells, single-cell image database is generated.

### **3.2 Smear Level Database**

For the above-mentioned works, conventional pap smear images were acquired from a healthcare lab and per slide, 10 best images were taken to create the smear level database.

### ***3.3 Existing Database***

The Herlev pap smear dataset containing 917 single-cell images belonging to separate distinct categories is available publicly.

## **4 Segmentation**

Segmentation is a process to segregate the region of interest from an image. So, it identifies the nuclei from all kinds of images acquired. Maximally Stable Extremal Region (MSER) technique has been used for detecting the nuclei from the image. Various factors like blurring effects, light change, scale change, region density, and region size MSER have accounted for high scores. But this technique alone cannot find the region of interest. The reason is poor quality of staining. Since in real life, one needs to gather information of more than 2000 images; hence in that case, this technique alone will be less efficient for segmentation. So, MSER is integrated with Discrete Wavelet Transform (DWT) to overcome this problem and can be used for better segmentation purpose.

### ***4.1 Preprocessing Filter***

The first filter which is used to an image is LL filter of DWT. This LL filter acts as a preprocessing filter, and it takes the approximation of the input image. HAAR wavelets are used for this because of poor staining quality of pap smear, which is a major problem while doing the segmentation task.

### ***4.2 Noise Removal Filter***

The second filter is the background removal filter which removes the noise and any RBC cells present. The noise is removed using the median filter whereas background is rejected using bit-plane slicing. By bit-plane slicing technique, the cluster gets identified which contains a number of cells. Then, the RBCs were segregated using K-means color segmentation process assuming that RBC can take only red color. Hence, removal of RBCs will increase the segmentation accuracy. Out of the several channels, intensity channel performs best in segmentation process hence is used for further processing.

### 4.3 Design of Component Tree

Component tree is built for MSER. For each node (one connected component), calculation of  $\Psi$  is done using the following formula:

$$\Psi(R_i^g) = \left( |R_i^{g-\Delta}| - |R_i^{g+\Delta}| \right) / R_i^g$$

$R_i^{g-\Delta}$  and  $R_i^{g+\Delta}$  are the extremal regions obtained by moving up and down in the component tree from region  $R_i^g$  until a region with  $g - \Delta$  and  $g + \Delta$  is found. Rig is a region which is got by thresholding at a gray value  $g$  and  $\Delta$  is a stability range parameter. Then, value of  $R_i^g$  is calculated having local minimum. This region is called maximally stable region.

### 4.4 Inflammatory Cells Removal

To achieve this, area, perimeter, and circulatory ratio (CR) are calculated using:

$CR = A/\text{new}_A$  where  $\text{new}_A = P^2/4\pi$ ,  $A$  = Nucleus area and  $P$  = Nucleus Perimeter.

It was found that the circularity ratio is approximately in range of  $CR \leq 0.71$ . According to this approach, objects inside this range were discarded. This technique increases the output largely, and this filtering technique comes as an inspiration from Malm et al. [13]. Hence, output after application of this filter contains only cervical cells.

## 5 Feature Set Design

### 5.1 Feature Extraction

To identify among several different classes, total of 121 features were extracted (having 5 shape descriptors, 50 textures, and 66 ripplet descriptors) from a Pap smear image. Shape features used for further analysis are perimeter, area, eccentricity, compactness, and circularity of the nucleus which compose the vector fshape as shown in below equation [12].

fshape = {Perimeter, Area, Eccentricity, Compactness, Circularity}.

Area (A)—Contains the number of pixels used to represent the object.

Perimeter (P)—Contains the number of pixels used to represent the boundary of the object.

Eccentricity (ECC)—It is the ratio of minor and major axes of the object.

Circularity =  $A/\text{new}_A$  where  $\text{new}_A = P^2/4\pi$ .

$$\text{Compactness} = (P2/2 * A).$$

The above features helped in studying the nucleus enlargement, nuclear membrane irregularity, and structural abnormality of the nucleus.

Texture features which were obtained using first-order statistics of histogram are Mean, Variance, Kurtosis, Skewness, Energy, and Entropy. Whereas the remaining 44 texture features were extracted using GLCM analysis using second order of statistics. Examples are Homogeneity, Correlation, Sum of Squares, Angular second moment, Sum Variance, Sum Average, Sum Entropy, etc.

## 6 Ripple Descriptors

These are used for quantifying both color as well as texture features. The color feature is used for checking excessive staining in cells, a condition named hyperchromasia and cytoplasmic changes. Since transforms like Fourier transform (FT) and wavelet transform have certain issues like discontinuities in edges and contours in images. Xu et al. proposed Ripple Transform (RT) which takes care of the above problem. The image prior to RT decomposition is transformed from RGB to YCbCr. RT decomposition over the intensity plane characterizes the texture whereas RT decomposition over the chromacity planes characterizes the color. Both texture and color features are extracted using the RT on each color plane with 4-level decomposition. This decomposition configuration produces  $11 (= 1 + 2 + 4 + 4)$  sub-bands for each image for each color plane. So, a total of  $33 (= 3 * 11)$  sub-bands we get for single image.

## 7 Identification Through Segmentation

### 7.1 Analysis of Input Image

Initially in the process of image segmentation, an input digital image is broken down into various subgroups which helps in further analysis of the image. In other words, segmentation process assigns labels to pixels. All the pixels which fall under same class have a common label. This entire process reduces the image processing time.

### 7.2 Wavelet Transform

The most widely used technique to identify objects in an image is the thresholding method. It is observed that the objects in the image have more intensity than the background (unwanted parts) in an image. The details of an image are retained using the image segmentation method based on wavelet transform. Wavelet analysis used

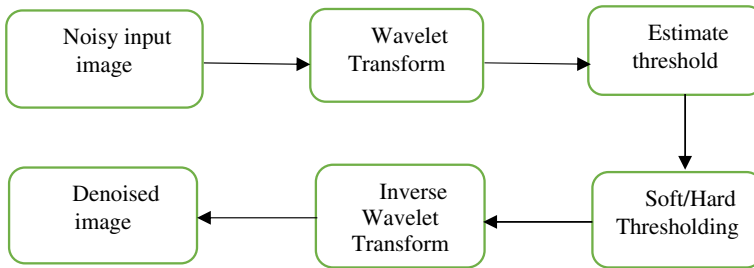


**Fig. 3** Block diagram of wavelet denoising process

in image analysis helps in dividing two discrete components such as details and approximations. A signal is passed through 2 filters, high pass and low pass filters. After that, the image is decomposed into high frequency (details) and low frequency components (approximation). After that, a simple log transformation is applied for better visualization. Again, we apply DWT once again on these partial components to get the final transformation. This wavelet transform is a widely used tool for compression and denoising. In this work, denoising of Gaussian noise present in an image is done after wavelet decomposition. So, it acts as a filter for removal of noise in the frequency domain (Fig. 3).

### 7.3 LL Filter

Low-low filter of DWT is applied in order to get approximate information of the input image. Hence, the input image gets decomposed into low frequency components (approximation). In this work, background removal filter helped in removing noises and RBC present. Median filter removed the noise, and background is rejected using bit-plane slicing. Using MSER, segmented output is fed for morphological operations like filling or opening of holes.

### 7.4 Morphological Operations

The term morphology means a set of image processing operations that process images based on shapes. Basic morphology operators are dilation, erosion, opening, and closing.

Dilation: Along the boundary of an object, pixels are added. So, the objects become more clearly visible and it fills the small holes in the object.

Erosion: It removes pixels from the boundary of an object. So, it removes islands and any other small objects thereby only substantive objects remain.

**Opening:** This operator erodes an image and then dilates that eroded image. It is useful for removing small objects and thin lines from an image while preserving shape and size of larger objects in the image.

**Closing:** This operator performs dilation first followed by erosion (reverse of opening). Because of the effect of this operator, it preserves background regions that have similar shape to the structuring element.

## 7.5 *Segmented Image Output*

In segmentation process, the digital image is partitioned into various subgroups (pixels) according to their features and properties. Hence, it helps in identifying the cancerous cells, thereby minimizing risk of human errors.

## 8 Classification

The accuracy for segmentation measures how close are the regions of interest obtained with comparison to the ground truth image. The images can be classified into classes using different classifiers like MLP, RF, and LSSVM. Performance of these classifiers is evaluated using metrics like accuracy, sensitivity, and specificity.

## 9 Conclusion

This paper shows the approach made on classification for cervical images using segmentation techniques. Such automated classification will help the pathologists immensely since there is always a risk of making human errors. In future, real-time medical image data can be compared with publicly available Herlev dataset for classification purpose. Also, another approach can be studying different deep learning techniques for classifying the pap smear images. Future enhancement can be done by detecting precisely overlapping of nuclei. Further research can be done for accurate classification of cervical images using cytoplasm feature extraction.

## References

1. Turashvili G (2022) Squamous cell carcinoma and variants. Pathologyoutlines.com. <https://www.pathologyoutlines.com/topic/cervixSCC.html>. Accessed 20 Aug 2022
2. Tsai MH, Chan YK, Lin ZZ, Yang Mao SF, Huang PC (2008) Nucleus and cytoplasm contour detector of cervical smear images. Pattern Recognit Lett 29(9):1441–1453

3. Li Z, Najarian K (2001) Automated classification of pap smear tests using neural networks. In: Neural networks, 2001 proceedings, IJCNN'01, international joint conference on, IEEE, Washington, DC, pp 2899–2901
4. Plissiti ME, Nikou C (2011) Combining shape, texture and intensity features for cell nuclei extraction in pap smear images. *Pattern Recognit Lett* 32(6):838–853
5. Martin E (2003) Pap-smear classification Master Thesis, Technical University of Denmark
6. Chankong T, Theera-Umpon N, Auephanwiriyakul S (2014) Automatic cervical cell segmentation and classification in pap smears. *Comput Meth Programs Biomed* 113(2):539–556
7. Zhang L, Sonka M, Lu L, Summers RM, Yao J (2017) Combining fully convolutional networks and graph-based approach for automated segmentation of cervical cell nuclei. In: 2017 IEEE 14th international symposium on biomedical imaging
8. Lu Z, Carneiro G, Bradley A, Ushizima D, Nosrati MS, Bianchi A, Carneiro C, Hamarneh G (2016) Evaluation of three algorithms for the segmentation of overlapping cervical cells. *IEEE J Biomed Health Inf*
9. Jantzen J, Norup J, Dounias G, Bjerregaard B (2005) Pap-smear benchmark data for pattern classification. *Nature Inspired Smart Inf Syst*:1–9
10. Marinakis Y, Dounias G, Jantzen J (2009) Pap smear diagnosis using a hybrid intelligent scheme focusing on genetic algorithm based feature selection and nearest neighbor classification. *Comput Biol Med* 39(1):69–78
11. Marinakis Y, Marinaki M, Dounias G (2008) Particle swarm optimization for pap-smear diagnosis. *Expert Syst Appl* 35(4):1645–1656
12. Bora K, Chowdhury M, Mahanta L, Kundu M, Das A (2017) Automated classification of Pap smear images to detect cervical dysplasia. *Comput Meth Programs Biomed* 138:31–47
13. Malm P, Balakrishnan BN, Sujathan VK, Kumar R, Bengtsson E (2013) Debris removal in pap-smear images. *Comput Meth Programs Biomed* 3(1):128–138
14. Kashyap D, Somani A, Sekhar J, Bhan A, Dutta MK (2016) Cervical cancer detection and classification using independent level sets and multi-SVMs. In: 39th International conference on telecommunications and signal processing

# Design of a Cost-Effective Remote Health Monitoring System Using IoT



**Subhadeep Paul, Madhusudan Maiti, Dibyendu Chowdhury,  
and Subhas Chandra Saha**

**Abstract** An IoT-based health monitoring system is developed by which a patient at a remote location can be monitored  $24 \times 7$  without any family member or health staff and updates the health data in real time using the Internet. The health monitoring system uses an Arduino board, a MAX30102 sensor, and a website. After attaching to a fingertip, the sensor senses the patient's body temperature and heart rate and sends that to the Arduino board for conversion to digital forms. Arduino board converts the health data to digital format and uploads the real time data to a database. The website uses an authentication and authorization process to verify whether the user is valid. After proper validation, it shows health data on the website according to the role of the logged user. One can monitor a patient's health data with this device from anywhere in the world, having an Internet connection.

**Keywords** IoT · Health monitoring · Remote access · Data security

## 1 Introduction

The Internet has become a part of our daily life as it is used almost everywhere to make our life smooth. The developments of mobile technology and communication network are the main reasons for this qualitative change. Now one can attend any function, ceremony, or meeting without being physically present in that place. This

---

S. Paul (✉) · S. Chandra Saha

Department of Electronics, Vidyasagar University, Midnapore, West Bengal 721102, India  
e-mail: [subhadeepaul191199@gmail.com](mailto:subhadeepaul191199@gmail.com)

M. Maiti

Department of Electronics and Communication Engineering, C. V. Raman Global University, Bhubaneswar, Odisha 752054, India

D. Chowdhury

Department of Electronics and Communication Engineering, Haldia Institute of Technology, Haldia, West Bengal 721657, India

approach saves time and helps us connect with our loved ones from distant locations. However, a good Internet connection is essential to perform such work.

The health condition of our family members is always a great matter of concern for us. Due to the recent advancement in mobile technology, we try to integrate medical facilities with the Internet-based system to monitor patients' health conditions seamlessly. The Internet of Things (IoT) helps us to create the environment easily. The IoT [1] is an interconnected network with physical devices, sensors, processing devices, and application software. An IoT-based health monitoring system can track a patient's medical data and conveys the information to doctors and/or family members. This way, a doctor analysing the incoming medical data understands the patient's condition and takes necessary action. Doctors do not have to visit a patient place when a patient needs a checkup, so the time for travelling can be used to monitor other patients. This could eventually increase the productivity of the current healthcare system. Also, at the same time, family members maintaining their normal duties can track the health status of their loved ones at a distant place without a health staff.

As in the COVID-19 pandemic, it has been observed how people suffered for not having a proper remote monitoring system because, in an epidemic like COVID-19, no family member was allowed to stay with a patient due to its highly infectious nature. In this kind of situation, a remote monitoring system can detect the health condition and possible threats to the patient's life. This information helps to save the patient's life. Doctors do not have to be in close contact with the infected person. So, the safety of healthcare workers will be increased, which was one of the significant drawbacks at the initial stage of COVID-19. Family members do not have to call the hospital when they need to know about the patient's health status; they can login to a mobile application and see the situation in real time. The COVID-19 pandemic helps us to understand the necessity of remote monitoring systems.

Paganelli et al. [2] designed an IoT-based early warning architecture using a wearable kit for health monitoring and a data analysis algorithm for prediction and decision making. It also consists of the machine learning algorithm, which sends an early alert for any emergency depending on previously trained data. Filho et al. [3] developed a remote healthcare platform to monitor ICU patients during the COVID-19 pandemic. The sensors attached to the patient's body provide information about ECG, blood pressure and glucose, heart rate, oxygen saturation, temperature, breathing rate, and capnography. The environment sensors provide information about environment temperature, location with latitude and longitude, and humidity. It helps to detect if any emergency condition for patients arises. A health monitoring system was created by Islam et al. [4] to monitor heart rate, body temperature, and environment in a hospital room: viz. humidity and gas concentrations of CO and CO<sub>2</sub>, and healthcare professionals who are concerned can check the health data instantaneously. Rahaman et al. [5] wrote a review of IoT devices used in healthcare and remote monitoring. This demonstrates the advantages of employing IoT devices for health monitoring and their potential. Using digital twin technology, Liu et al. [6] developed a cloud-based health monitoring system for older people. Karantonis et al. [7] presented a real time human movement and posture detection system for detecting functional ability

and activity levels. They used a waist-mounted 3-axis accelerometer sensor for this system and acquired a high level of accuracy. Thilakanathan et al. [8] developed a system where a patient connects sensors to his/her body and sends health data periodically to a web server (cloud-based storage) through a mobile application using a secure server. Tripathi et al. [9] made a system with wearable devices to detect patients' health conditions. Hossaina et al. [10] gave a brief review of some recently developed health monitoring systems. They concluded about how this IoT-based technology and interconnect device can improve the healthcare system. Banerjee et al. [11] created a heart rate detector using the photoplethysmography concept with an IR LED and photodiode as the fundamental sensors. Gregoski et al. [12] reported a system for monitoring heart rate employing mobile light and a camera. Oresko et al. [13] designed a cardiovascular disease (CVD) detection system. An interconnected mobile product was developed by Trivedi et al. [14] to monitor body temperature and heartbeat continuously.

In this paper, we report the development of a cost-effective, reliable, and continuous IoT-based health monitoring system consisting of an Arduino board, MAX30102 sensor, and a website to provide the best healthcare facilities to the people of rural areas. We have significantly improved our system in comparison with the preexisting technologies. While [13] can only display the health data in the measuring device and cannot send data to the cloud for remote health monitoring, our proposed device can send health data to a cloud-based database for remote access. [9, 12, 14] are not suitable for measuring health data continuously, whereas our device can be used in real time. Our developed system is not dependent on any particular device like a smartphone or smartwatch, so it is more cost-effective than [4, 8, 11, 12] and is more efficient for implementing in the rural area. Also, our website can be accessed through any device connected to the Internet. Our device is very compact, and unlike [3], this device can be used as a mobile health monitoring unit only with a proper Internet connection. Also, the device is simple to install and operate.

## 2 Methodology

The developed system consists of three modules: a sensing module, a processing module, and an interaction module. Figure 1 shows the functional flow diagram of the developed system and the interconnection between all three modules. The details description of these modules is described in later this section. Figure 2 shows the architectural flow diagram of the system.

The sensing module consists of sensors that collect health data from a patient and converts to digital form by processing the raw data. Then the digital data are transmitted to the processing module for further processing. The sensing module has two components: (i) MAX30102 sensor and (ii) Arduino UNO SMD R3. The MAX30102 senses the raw data and sends that to Arduino UNO which collects the data converts that to digital form and transmits that to a processing unit. The

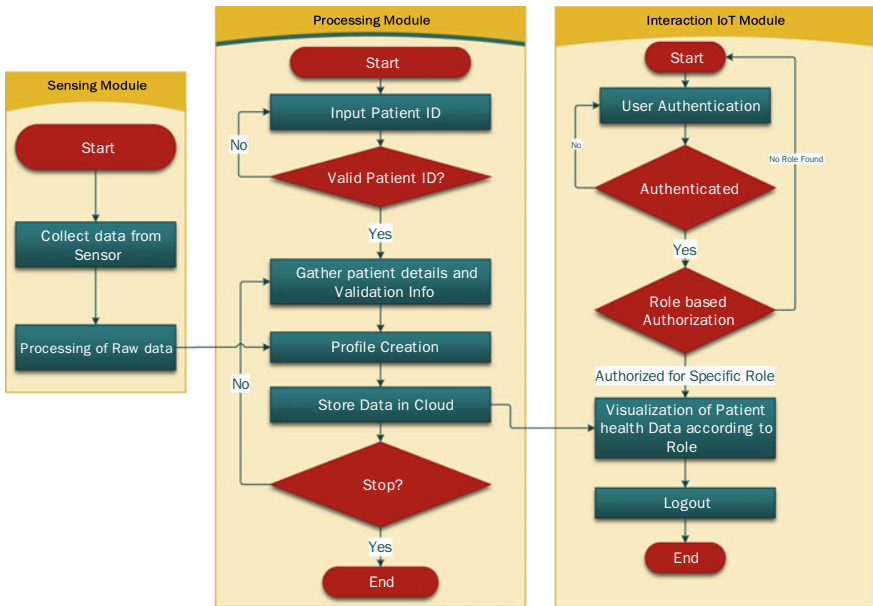


**Fig. 1** Functional flow diagram of the system

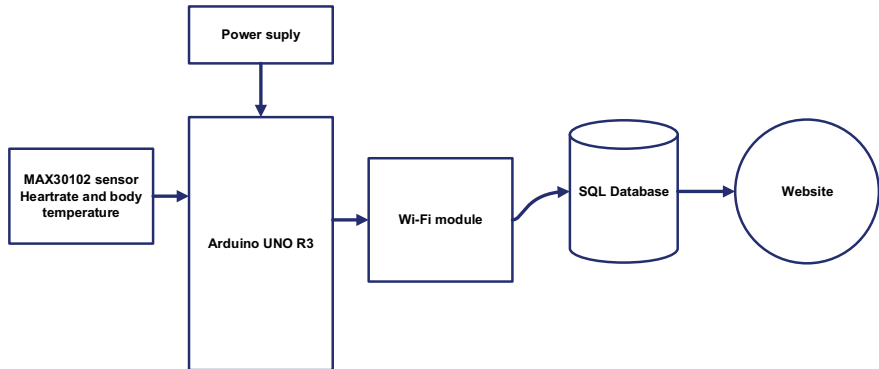


**Fig. 2** Architectural flow diagram of the system

circuit diagram for interfacing the MAX30102 sensor with Arduino is shown in Fig. 3.

The processing module gathers patient details and integrates that with the digital data transmitted from the sensing module for a particular patient. Then it stores the data in cloud-based storage and allows the interaction module to share with authenticated and authorized users.

The interaction module is an IoT-based software that authenticates the user identity and authorizes the user's specific role. After completing this process, it will show

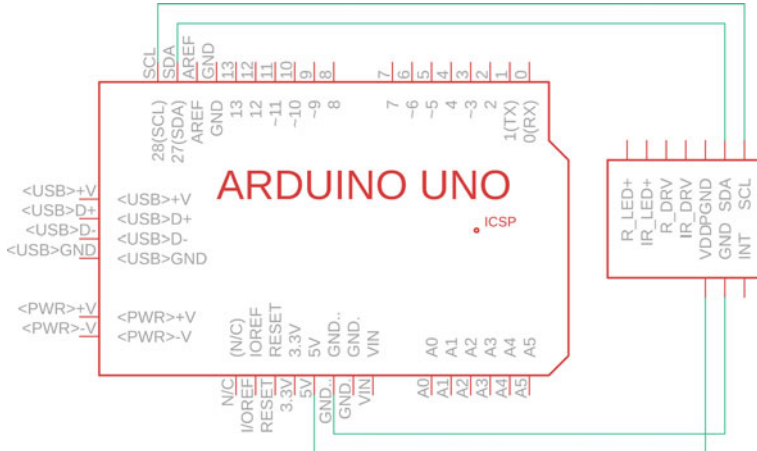


**Fig. 3** Circuit diagram for interfacing MAX30102 with Arduino UNO

the patient health data to the user. The authorization process will be the controller of the data one user can see, depending on his/her role.

In our present work, the sensing module is the hardware, and the processing and interaction module are the software. The processing module consists of a database and a backend server. The interaction module is a website and backend authentication process, that displays the health data using role-based authentication. It is designed for two types of roles for authentication—(i) Admin: has the privilege to view all patients data, update any parameter, and delete any patient details. (ii) User: can only view his/her patient details and health data.

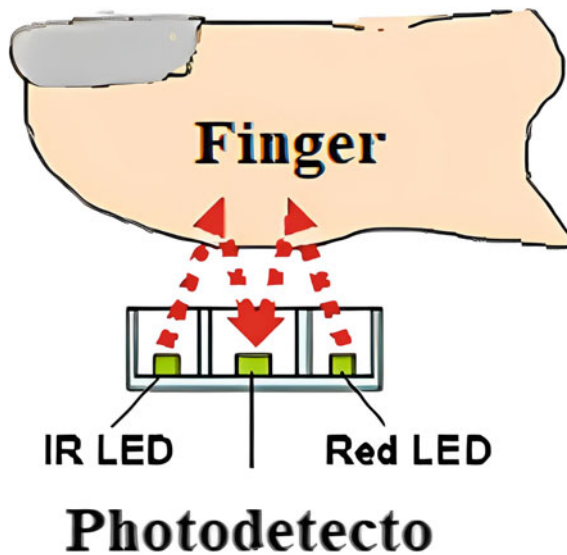
## 2.1 Heart Rate Measurement Using MAX30102

Figure 4 shows the setup to measure a patient's heart rate (HR). The MAX30102 sensor glows both the lights of IR and Red LEDs through the skin of a fingertip and measures the reflected light with a photodetector. The output waveforms of the photodetector are shown in Fig. 5. To determine HR, the enlarged output profile as detected with IR LED is shown in Fig. 6.

We first calculate the time difference ( $t$ ) in second of two consecutive beats in Fig. 6. Then, HR in beats per minute (BPM) is given by the Eq. 1

$$\text{BPM} = 60/t \quad (1)$$

As the time difference between two beats is very small and not always constant, the BPM value changes significantly for a slight variation in time difference. To



**Fig. 4** Setup with MAX30102 sensor for heart rate measurement

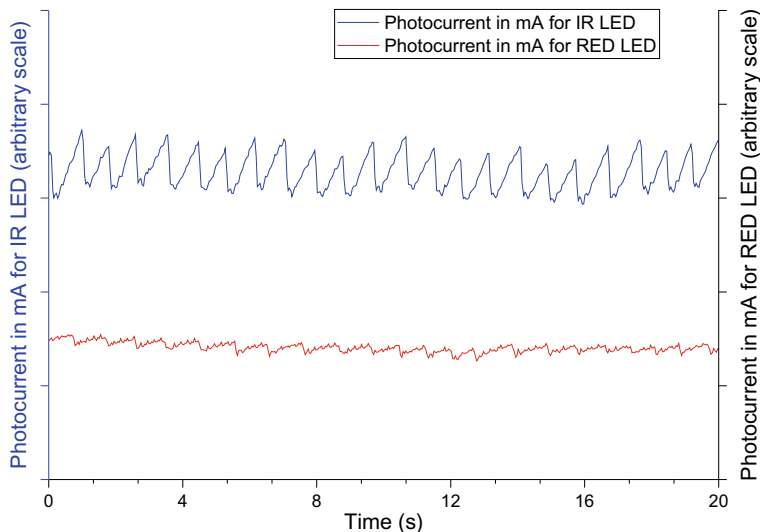


**Fig. 5** Output waveforms of the photodetector

overcome this problem, we take a few consecutive values of BPM and calculate their average. In this way, we get an average HR in BPM. So, every time we get an HR value is the average of the last few HR values. We can take different numbers of observed values for the standard in our requirement. For six consecutive BPM data, as shown in Fig. 6, the average BPM will be

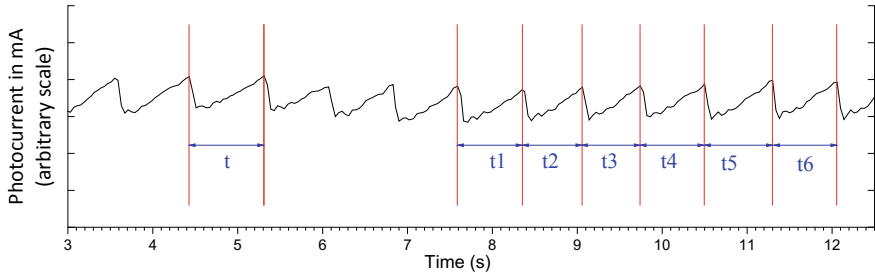


**Fig. 6** Enlarged output profile of IR LED

$$\text{Avg. BPM} = \frac{1}{6} \sum_{i=1}^6 \text{BPM}_i \quad (2)$$

where  $\text{BPM}_i = \frac{60}{t_i} \quad (i = 1 \text{ to } 6)$

## 2.2 Temperature Measurement Using MAX30102

For measuring body temperature, we used the on-chip temperature sensor of MAX30102, which stores the temperature data on the first in first out (FIFO) buffer.

## 3 Results and Discussion

The HR was determined using the developed system with six consecutive BPM data, and that was also measured manually. Figure 7 and Table 1 represent the results of the HR measurements of 30 patients. It is evident from Table 1 that the HR measured by the system is matched well with that obtained manually. Primarily the percentage error was noted as 0–4.5% taking four consecutive BPM data and that taken manually by an ordinary person. Considering six consecutive BPM for average HR and measuring the manual HR with professional health care personnel, the error decreases to 0–2.5% range. The reasons for improvement in accuracy on HR measurement are taking 6 BPM average and measuring HR with professional healthcare personnel.

Oxygen is delivered from the lungs to every cell of the body by the haemoglobin in the blood. When hemoglobin contains oxygen, it forms an unstable, reversible bond with oxygen, and it is called oxyhaemoglobin [Hb(O<sub>2</sub>)<sub>4</sub>]. Oxyhaemoglobin is bright red in colour. The form of hemoglobin without oxygen or oxygen unbounded form is called deoxyhaemoglobin which is purple in colour. Due to the colour difference, the oxyhaemoglobin in the arterial blood absorbs more IR light than that

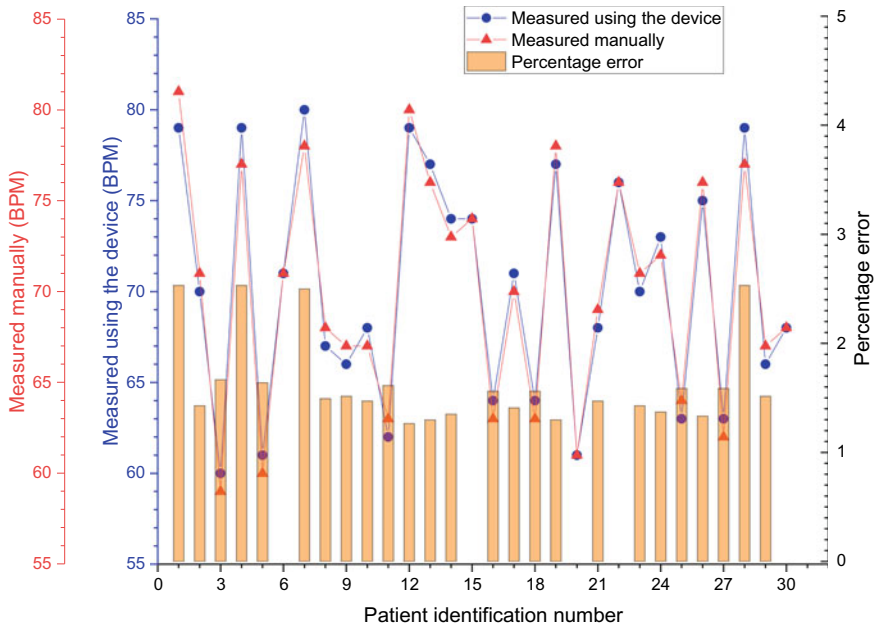


**Fig. 7** Graphical representation of heart rate measurements

by the deoxyhaemoglobin. Each time the heart beats, blood is pumped into the finger, altering the quantity of light that is reflected (Fig. 4) and resulting in a change in the waveform of the photodetector (Fig. 5). A slight shift in HR measurement done by the developed system and manual observation is due to the behaviour of the photodetector.

The body temperatures of 30 patients were measured with our system as well with a thermometer by a professional health care personnel, are displayed in Table 2 and Fig. 8. It is noted that the error in measuring body temperature lies 0–0.8%. The body temperature was measured with the developed system and by an ordinary person, and the maximum error was detected within 1%. Comparing Fig. 7 with Fig. 8, it may infer that the body temperature measurement by the device is more accurate than the HR measurement. It is primarily due to the better response of the on-chip temperature sensor than that of the photodetector.

The observed results are displayed on our developed website. The health data from the Arduino board are uploaded to the database using Wi-Fi, and that can be accessed through our developed website. The website has two types of login options: one is Admin login, and another is User login. When someone login through User login credentials, he/she will get access to only read his/her patient's health details. On the other hand, by logging through Admin login credentials, one can view all the patients health details and have access to create a new patient's profile and update or delete any patient details. Some snapshots of the developed website with functionalities

**Table 1** Results of heart rate measurements

Patient identification number	Measured using the device in BPM	Measured manually in BPM	Percentage error (%)
1	79	81	2.5
2	70	71	1.4
3	60	59	1.7
4	79	77	2.5
5	61	60	1.6
6	71	71	0.0
7	80	78	2.5
8	67	68	1.5
9	66	67	1.5
10	68	67	1.5
11	62	63	1.6
12	79	80	1.3
13	77	76	1.3
14	74	73	1.4
15	74	74	0.0
16	64	63	1.6
17	71	70	1.4
18	64	63	1.6
19	77	78	1.3
20	61	61	0.0
21	68	69	1.5
22	76	76	0.0
23	70	71	1.4
24	73	72	1.4
25	63	64	1.6
26	75	76	1.3
27	63	62	1.6
28	79	77	2.5
29	66	67	1.5
30	68	68	0.0

are shown in Fig. 9. Figure 9a shows the functionalities of the login page. Different functions of the Admin dashboard are described in Fig. 9b. In Fig. 9c, the patient details page from Admin panel is elaborated. Figure 9d displays the patient dashboard with the functionalities.

**Table 2** Body temperature measurement results

Patient identification number	Measured using the device in °F	Measured using a thermometer in °F	Percentage error (%)
1	97	96.7	0.31
2	99	98.4	0.61
3	97	97.2	0.21
4	99	99.7	0.71
5	98	98.3	0.31
6	100	100.7	0.70
7	98	98.5	0.51
8	100	99.6	0.40
9	102	102.1	0.10
10	98	97.3	0.71
11	102	102	0.00
12	101	100.8	0.20
13	99	99.1	0.10
14	102	102	0.00
15	98	98.7	0.71
16	99	98.3	0.71
17	98	97.4	0.61
18	101	101.3	0.30
19	98	98.1	0.10
20	99	98.9	0.10
21	100	100.7	0.70
22	98	98.2	0.20
23	102	102.1	0.10
24	99	98.9	0.10
25	98	98.7	0.71
26	99	99.7	0.71
27	100	99.2	0.80
28	98	98.5	0.51
29	98	98.7	0.71
30	101	100.4	0.59

#### 4 Future Work

Although the current device is reliable for measuring two important health parameters: heart rate and body temperature of a patient, sometimes more than these two health parameters are to be known. So, this work will be extended further to measure other health parameters namely SpO<sub>2</sub> (saturation of peripheral oxygen), electrocardiogram (ECG), and blood pressure and environmental data like humidity, room tem-

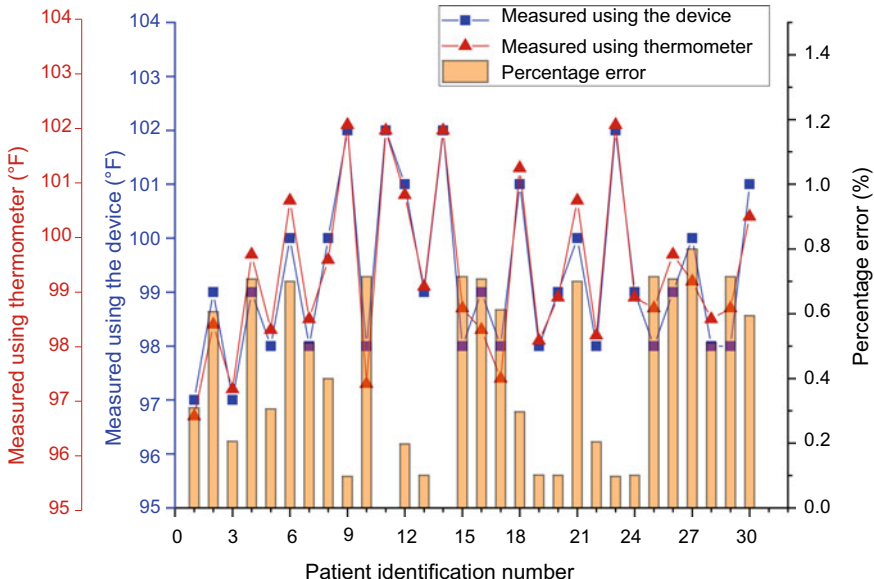


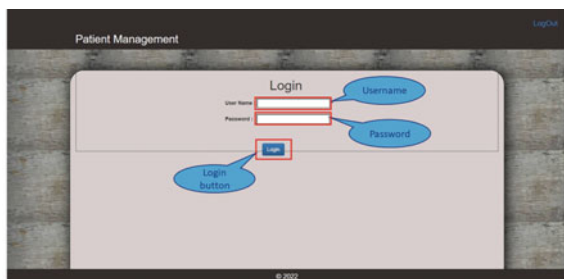
**Fig. 8** Graphical representation for body temperature measurement results

perature, PM<sub>2.5</sub> (particulate matter under 2.5 microns in size), PM<sub>10</sub> (particulate matter under 10 microns in size), CO<sub>2</sub> and CO levels. Also, we are planning to integrate an email notification to the patient and healthcare staff with the website upgradation.

## 5 Conclusion

The remote health monitoring system is reliable for remotely measuring heart rate and body temperature. It can be used for monitoring any patient. The sensor senses body temperature and heartbeat and uploads that to the database, which can be accessed wirelessly through the website. One can access data from anywhere in the world with an Internet connection. The authentication and authorization processes help to keep the data securely in the database. So there is no risk of leaking personal data or the patient's health data. Overall the system created a secure connection between the sensing device and the observer (patient party/doctor/administrator) by which an observer can track health data 24×7. By continuously monitoring health conditions, we can detect if any emergency medical situation is created for a patient. This helps us to take quick action on any medical emergency. The device is very cost-effective and made to support the rural people. Ease of setup and reusability are the main advantages of our device. There are future scopes to measure other health and environmental parameters for proper monitoring of a patient and for website upgradation.

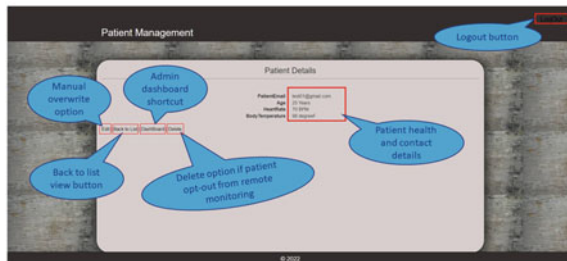
**Fig. 9** Different web pages of our developed website



(a) Login page of the website.



(b) Admin dashboard with all patient details.



(c) Admin panel with edit and delete options for any patient.



(d) Patient dashboard from the website.

## References

1. International telecommunications union—telecommunications sector: IUT-T, <https://www.itu.int/en/ITU-T/gs/iot/Pages/default.aspx>. Accessed 15 Nov 2022
2. Paganelli AI, Velmovitsky PE, Miranda P, Branco A, Alencar P, Cowan D, Endler M, Morita PP (2022) A conceptual IoT-based early-warning architecture for remote monitoring of COVID-19 patients in wards and at home. *Internet of Things.* 18:100399. <https://doi.org/10.1016/j.iot.2021.100399>
3. Filho I de MB, Aquino G, Malaquias RS, Girao G, Melo SRM (2021) An IoT-based healthcare platform for patients in ICU beds during the COVID-19 outbreak. *IEEE Access* 9:27262–27277. <https://doi.org/10.1109/access.2021.3058448>
4. Islam Md M, Rahaman A, Islam Md R (2020) Development of smart healthcare monitoring system in IoT environment. *SN Comput Sci* 1. <https://doi.org/10.1007/s42979-020-00195-y>
5. Rahaman A, Islam Md, Islam Md, Sadi M, Nooruddin S (2019) Developing IoT based smart health monitoring systems: a review. *Revue d' Intelligence Artificielle* 33:435–440. <https://doi.org/10.18280/ria.330605>
6. Liu Y, Zhang L, Yang Y, Zhou L, Ren L, Wang F, Liu R, Pang Z, Deen MJ (2019) A novel cloud-based framework for the elderly healthcare services using digital twin. *IEEE Access* 7:49088–49101. <https://doi.org/10.1109/access.2019.2909828>
7. Karantonis DM, Narayanan MR, Mathie M, Lovell NH, Celler BG (2006) Implementation of a real-time human movement classifier using a triaxial accelerometer for ambulatory monitoring. *IEEE Trans Inf Technol Biomed* 10:156–167. <https://doi.org/10.1109/titb.2005.856864>
8. Thilakanathan D, Chen S, Nepal S, Calvo R, Alem L (2014) A platform for secure monitoring and sharing of generic health data in the cloud. *Future Gener Comput Syst* 35:102–113. <https://doi.org/10.1016/j.future.2013.09.011>
9. Tripathi V, Shakeel F (2017) Monitoring health care system using internet of things—an immaculate pairing. In: 2017 International conference on next generation computing and information systems (ICNGCIS). <https://doi.org/10.1109/icngcis.2017.26>
10. Hossain MS, Muhammad G (2016) Cloud-assisted industrial internet of things (IIoT)—enabled framework for health monitoring. *Comput Netw* 101:192–202. <https://doi.org/10.1016/j.comnet.2016.01.009>
11. Banerjee S, Roy S (2016) Design of a photoplethysmography based pulse rate detector. *Int J Recent Trends Eng Res (IJRTER)* 02:302–306
12. Gregoski MJ, Mueller M, Vertegel A, Shaporev A, Jackson BB, Frenzel RM, Sprehn SM, Treiber FA (2012) Development and validation of a smartphone heart rate acquisition application for health promotion and wellness telehealth applications. *Int J Telemed Appl* 2012:1–7. <https://doi.org/10.1155/2012/696324>
13. Oresko JJ, Jin Z, Cheng J, Huang S, Sun Y, Duschl H, Cheng AC (2010) A wearable smartphone-based platform for real-time cardiovascular disease detection via electrocardiogram processing. *IEEE Trans Inf Technol Biomed* 14:734–740. <https://doi.org/10.1109/titb.2010.2047865>
14. Trivedi S, Cheeran AN (2017) Android based health parameter monitoring. In: 2017 International conference on intelligent computing and control systems (ICICCS). <https://doi.org/10.1109/iciccs.2017.8250646>

# Current Exploration in Microfluidics-Based Point-Of-Care Biosensor Applications: A Review



Pitam Chakrabarti, Sucheta Das, and Shamba Chatterjee

**Abstract** Biosensors are designed to amalgamate different point-of-care applications that in turn decipher physical, chemical, or biological actions into measurable signals and finally are resulting in qualitative and/or quantitative information about the target analytes. Scientists mimicked the natural capillary approach in the form of microchannels to improve the entirety of the concept in the area of biomedical instrumentations. This specific and sensitive approach is now popular as microfluidics and combines the principles of conventional subjects like biology, chemistry, physics along with advanced fluid dynamics, microelectronics as well as material science. Here, we have unveiled the developmental journey and modern advancements in microfluidics-based biosensors' arena.

**Keywords** Microfluidic biosensor · Point of care (POC) · Biomedical approach · Monitoring · Diagnostics

## 1 Introduction

Biosensors are useful devices that can identify a biological outcome through a transducing device by means of a signal proportional to the analyte concentration to quantify a sound response. Recently, they have opened up new prospects to serve for our benefit in homeland security, agro-food sector, medicine and biomedical as well as environmental monitoring sector in a high-throughput screening approach [1–6].

Microfluidics systems as biosensor analyze low amounts of fluids employing channels with magnitudes of tens to hundreds of micrometers [7]. Microfluidics or capillary approach is vastly implemented in case of point-of-care (POC)-based biosensor arena in the last decade. The sound fabrication of capillary applications

---

P. Chakrabarti · S. Das · S. Chatterjee (✉)

Department of Biotechnology, Haldia Institute of Technology, Haldia, West Bengal 721657, India  
e-mail: [shambac@gmail.com](mailto:shambac@gmail.com)

P. Chakrabarti

Regional Centre for Biotechnology, Faridabad, Haryana (NCR Delhi) 121001, India

© The Author(s), under exclusive license to Springer Nature Singapore Pte Ltd. 2023

139

D. K. Sarkar et al. (eds.), *Proceedings of the 4th International Conference*

*on Communication, Devices and Computing*, Lecture Notes in Electrical

Engineering 1046, [https://doi.org/10.1007/978-981-99-2710-4\\_12](https://doi.org/10.1007/978-981-99-2710-4_12)

is quite challenging following its low-volume usage made up with materials like glass, silicon, and diverse types of polymer (e.g., polystyrene, polycarbonate, cellulose acetate) [8]. The large surface-to-volume ratio allows handiness of microfluidic devices which is essential for on-site testing. The amalgamation of biosensors with microfluidic systems leads into a highly specific and sensitive compact mini-detection format in comparison to the existing repetitive laboratory techniques as well as it reduced the cost of reagent and energy consumption [9–11]. Overall, this integration creates a potent analytical tool toward the home-testing approach which in turn will help both developing and developed countries.

Here, we emphasized the major aspects of capillary design, simulation, and fabrication in relation to the flourishing area of microfluidics-based biosensors along with their advantages and disadvantages. Therefore, this will help the future researchers to implement the thoughts for the design and fabrication of POC-based biosensors for various biomedical applications.

## 2 Progress of Microfluidics

Microanalytical tools like gas-phase chromatography (GPC), high-pressure liquid chromatography (HPLC), as well as capillary electrophoresis (CE) have utilized the microfluidics approach during mid-1990s. The first “laboratory-on-a-chip” method was reported by Stephen Terry in the form of a miniaturized gas chromatograph (GC) with capillary fabrication via micromachining method [12]. Following this, soft lithography has paved the pathway for exploring different types of materials in the form of organic and biological molecules having dimensions initially varying from 500 nm upward [13]. Afterward, it has come down even below than 100 nm range and popularly known as nano-contact printing. “Soft lithography” is a way of replicating designs etched into silicon chips in extra biocompatible and flexible materials [14].

Furthermore, Andreas Manz invented microchip technology, viz., “Microchemical Total Analysis System” ( $\mu$ -TAS) that enabled us to have fast and precise sample separation with smaller transport times compared to traditional systems [15]. Then, polydimethylsiloxane (PDMS or dimethicone) was announced as material for microfluidics by Whitesides in 1998 [16]. From 2000 onward, the organ-on-chip tools gradually appeared in this scenario portraying different on-chip-based tissue replica. This can be portrayed simply as a single and perfused microfluidic chamber comprising one type of cultured cell that shows functions of one specific tissue type. In the last decade, organ on chip technology has prospered fast that is potentially substituting soft lithography as an advanced approach [17].

### 3 Assembly and Fabrication of Microfluidics Approach

Selection of sound microfluidics material mostly depends on robustness, diversity of fabrication materials, biological and chemical compatibility with the inferred reagents, surface fictionalization potential as well as thermal and pressure-related aspects. Besides polymer- and ceramics-based material, first-generation materials like silicon and glass are still popular instead of their expensive nature [18, 19]. Although silicon has benefits such as electrical conductivity, thermostability, and chemical compatibility, it has limitations when it comes to optical detection in the visible and ultraviolet spectrums. However, silicon-based technologies have an ample variety of biological implementations, including next-generation organ-on-chip devices for drug toxicity testing, medical diagnostics, and POC. Glass has various benefits, including being chemically inert, thermostable, stiff, and biologically compatible. It also allows for simple surface functionalization, has great optical qualities, and is less expensive than silicon. Despite its many benefits, glass has additionally exhibited chemically inert characteristics and microlevel fabrication challenges [18]. There are many different chemical production processes, but the most popular ones for developing microfluidics include wet and dry etching and electrochemical discharge machining [20].

When creating a compact microsystem, ceramic materials have the benefit of special surface chemistry, steadiness at elevated temperatures, and greater resistance to environmental corrosivity. However, they also exhibit porosity, brittleness, and dimensional stability [21].

Thermoplastics have been improved and used for mass producing high-quality goods since they were first used in industry in the 1930s. Following this, a large portion of microfluidics research geared toward practical applications has concentrated on building devices with hard polymers as their main constituents. In research labs, polymethyl methacrylate (PMMA) is frequently utilized because it is optically clear and can be manipulated with different fabrication techniques. However, the variability like channel roughness and deformation often make them inappropriate for large-scale commercial production. Alternatively, polydimethylsiloxane (PDMS) is tearing prone and chemically permeable and thus raises complexity in patterning as template [22]. Other popularly utilized polymers in device fabrication are fluoro-polymers, co-polymers, thiol-ene and cyclo-olefin polymers.

Nowadays, polysaccharides (e.g., alginates, dextran, and chitosan) and protein-based (e.g., gelatin) biodegradable polymers are of good choice to explore the manufacture of microdevices mostly employed for drug delivery, imaging, and sensing [23].

Polydimethylsiloxane (PDMS)-based xurography is extensively explored for the capillary fabrication, which applies considerable manual approaches and arrangement to achieve three-dimensional structures. This is quite inexpensive as well as accessible technique that is commonly used in the graphic arts' business [24].

In addition to CO<sub>2</sub> laser, UV laser is another popular tool for capillary manufacturing on various sheets of polymer. Miniaturized liquid microfluidic strips are

created using UV laser photoablation (photolithography) that generates microchannels on a variety of substrates, including polystyrene, polycarbonate, cellulose acetate, etc. These polymer substrate strips are well efficient in generating osmotic flow within the system and thus alleviate capillarity activity [25].

Separation techniques like injection molding is employed to manufacture economical electrophoretic chips which can be implied in a variety of DNA screening and sequencing as well as immunoassay-based testing methods [26].

Nanoimprint lithography (NIL) is a high-throughput, low-cost lithographic technique that uses mechanical pressure to press a prepared mold into a resist material. The resist can be further toughened by thermal, chemical, or optical methods like UV curing. Further, a combination of the above with regular UV lithography was used to develop a multichannel microfluidic device [27].

## 4 Simulation Approaches

Simulation can offer numerous insights into flow dynamics prior to developing a functional capillary. In this way, one can acquire description of variables through computational way without disturbing the physical system. A variety of parameters can be tested which is not even examined in real-time situations. Self-powered microfluidics is one such approach which successfully quantifies proteins in an embedded electrochemical biosensor format. Here, COMSOL Multiphysics 5.6 helps to portray computational analysis on fluids dynamics [28]. Moreover, a COMSOL multiphysics-based computational capillary model applied flow-induced shear stress to observe biomolecules secreted by cells [29].

Single-phase simulation studies have occasionally offered useful ways to comprehend dynamics, whereas multiphase models have occasionally helped to increase design precision. In one 3D-bioprinted vascular chip model, the modus operandi of circulating tumor cells was examined on the basis of both the finite element approach and the lattice Boltzmann method through the numerical simulation. This computational outcome had unveiled that those tumor cells are inclined to accumulate at the center of the blood vessel and the assessment is at par with the experimental outcome [30]. Furthermore, detailed computational studies on RBC mechanics-based sensitive microfluidic chip disclosed that it can differentiate heterogeneous cells even in presence of only a single sick cell [31].

Numerical optimization is a crucial step in the design process that assists researchers in improving and accelerating the development of microfluidics in order to solve a particular problem. Researcher from University of Nottingham confirmed that variation in inlet flow rates of blood and buffer efficiently improves separation of circulating tumor cells [32].

Recently, a microfluidics platform based on thermoplastic polyurethane (TPU) on a chip has been devised for cell cultivation under static and dynamic circumstances. An oxygenator made of such membrane was crucial for optimal oxygen flow pumping in on-chip cell growth. Here, COMSOL Multiphysics® was used for numerical

simulation to optimize the distribution of oxygen content inside the microchip [33]. So far, the COMSOL Multiphysics® software is the favored software for performing simulation studies in comparison with Ansys software®.

Thus, simulation studies support the advancement of microfluidics by offering a dais that can handle challenging investigations while saving time and money on research. Although scientists have started creating their own simulation software programs to get around some of the drawbacks of the ones that are already available. These studies speed up the entire process to combat various diseases in a quicker and more effective manner at the right moment.

## 5 Microfluidics Biosensor Devices' Application

Microfluidic system plays an important role as POC devices following its advantages similar to small amount of reagent and sample usage, compactness, user-friendly handling approach, and low budget in comparison to existing diagnostic methods. For example, materials such as PDMS, PMMA, and PC are cheaper and can be fabricated easily, and one can carry out a number of analysis simultaneously by coalescing different microchannels [34].

Lateral flow-based devices, which are the most fundamental and practical representation of capillary-based movement of a range of molecules in real-time situation, like conjugate molecules, capture antibodies and so forth are the most popular type of biosensor for various analyte detections. Microfluidics-based systems require small amount of reagents and samples in a cost-effective way. A capillary-like structure made of the fine threads or fibers of nitrocellulose membrane is sometimes employed in microfluidics to hold and transport items to the detecting zone (e.g., pregnancy test kit, COVID-19 rapid antigen test, etc.) [35]. Besides this, a minute, low-cost, sensitive optical biosensor made up of two standard single-mode fiber-based capillaries and functionalized with the ssDNA probe for label-free DNA molecules' detection is worth mentioning approach [36].

Recently, a multifaceted group of researchers from Dalian University of Technology devised a highly sensitive microcapillary-based surface plasmon resonance (SPR) biosensor that provides prospective real-time analysis detection with compact structure and low cost Fig. 1 [37].

Blood glucose levels in diabetes patients should be less than 3.9 mM, as any higher levels might cause a number of dangerous illnesses. Scientists from China have already developed an optofluidic biosensor which potentially detects glucose concentration at extremely low level with tiny sample volume and high stability [3]. The sensitivity of this system is significantly dependent on capillary boundary thickness and refractive index with possible implication in chemical and biomedical sensing sectors.

Automation and amalgamation of multiple processes have alleviated the implementation of microfluidic devices over lab-based lengthy applications.

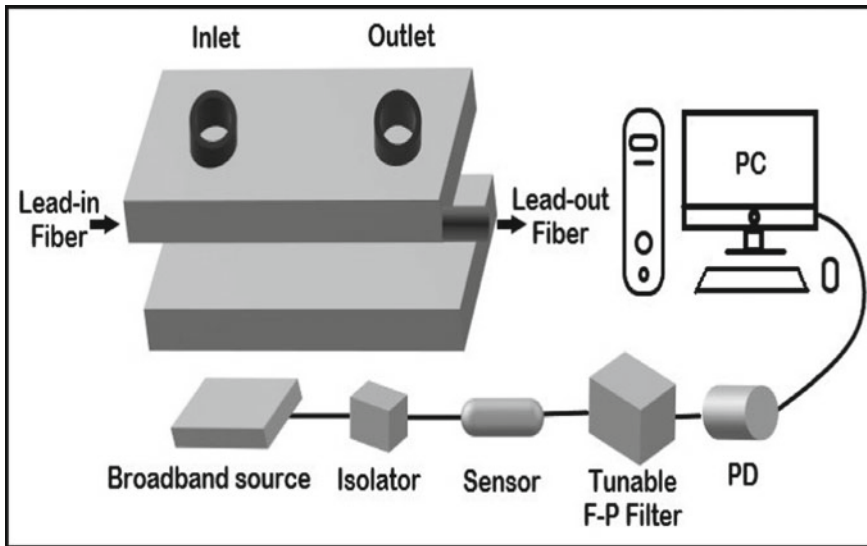


**Fig. 1** Schematic illustration of the microcapillary-based biosensor

In case of pre-stored chemical containing test strip-based microfluidic capillary flow systems, professional operators are not necessary as the sample usually flow inside by simple capillary forces (e.g., pregnancy kits) Fig. 2 [38]. Still, these platforms are not popular in complicated assays due to multiple steps' involvement. Continuous research is ongoing to minimize these limitations through multiplex practices [39, 40].

Microfluidics is also a promising technology in foodborne disease inspection arena. Following this, a speedy and sensitive smartphone imaging sensor came off for the successful detection of *Salmonella typhimurium* [41].

An optical biosensor is a microscopic platform that converts biological levels quantitatively into electrical signals with the aid of a calculating device. The sensor employs biological molecules to create a transuding platform that offers the preferred specificity to certain analyte. These are used in a variety of fields today, like clinical and diagnostic medicine, immunosensor device, monitoring and quality control of chemical food and drug processes as well as wearable body surface microfluidic system in sports [42–44].

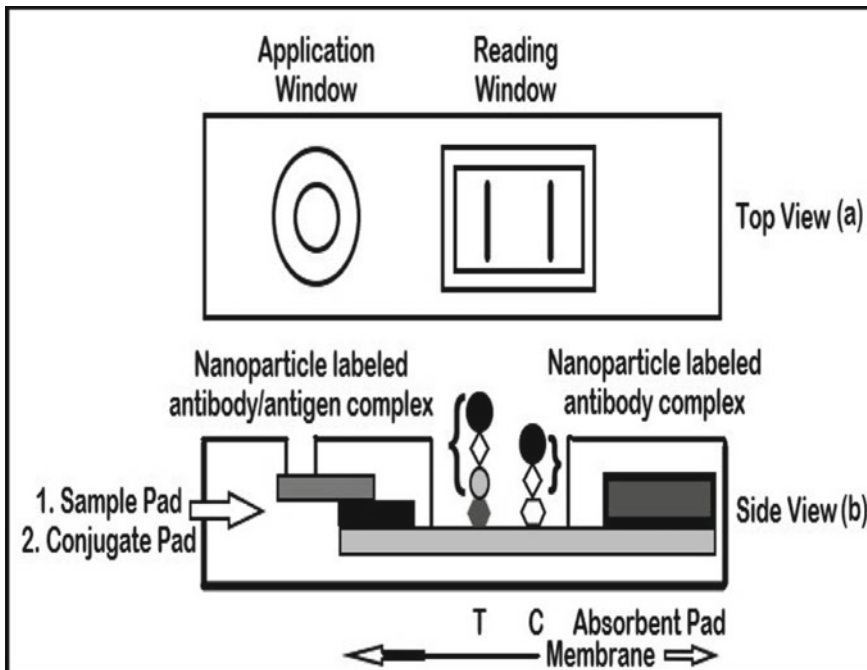


**Fig. 2** Top and side views of commercially available pregnancy kit. **a** Representative top view design of a test platform. The sample enters through the sample pad into the conjugate pad and subsequently drawn with the help of the membrane by the capillary action. **b** Representative side view design of a test platform. Two separate capturing antibodies are applied at the test line (T) and the control line (C). At (T), the antibody bind with the rehydrated nanoparticle-labeled antibody/antigen complex (positive outcome) while (C) attaches with the nanoparticle-labeled antibody complex (proof of experimental success)

## 6 Limitations, Challenges, and Future Scope in Fabrication of Microfluidics

Both academia and industries are engaged in microfluidics-based biosensor research for more than fifty years, but only a few of them have succeeded to fulfil global market demand. This lacuna remains due to problems in decoding academic research into real-time feasible prototypes for industry and clinical applications along with the non-availability of qualified researchers having specific educational background in biosensor technology. Despite already available commercial devices, there are some unrevealed questions that need to be unveiled for the advancement of miniaturized commercial biosensors, which can sense specific analytes of concern. One should consider factors like specificity, sensitivity, non-toxicity, low concentration detection, and cost-effectiveness to unravel essential criteria about biosensor technology with substantial limits.

The major challenge here is to coalesce different components like pumps, valves, and reservoirs in effectively designed microfluidic devices. Potential difficulties can arise from physical phenomena including surface tension, eluding vapor bubbles, and evaporation in designed microchannels. Besides this, capillary fabrication for any such system is fairly difficult due to sample channel blockage with tiny trapped particles or precipitates and absence of methods for monitoring fluid flow [45]. Interestingly, multilayer bonding holds two principal parameters, viz., pressure and temperature [46]. Furthermore, silicon and glass materials are becoming significant components in nanofluidics systems comprising patterned nanoscale features.

The global market size is expected to touch USD 58.8 billion by 2026. The demand is uprising as successful combination of microfluidics with POC diagnostic approach has accelerated technological progress. Growing cost-effectiveness of this technology is also of major concern. Certain factors like growth in pharmaceutical research, major investments by medical device sector industries in APAC region, rising influx of patients from international markets have portrayed the fast progress of microfluidics market.

## 7 Conclusions

Microfluidics-driven high precision POC technology has enriched medical arena with its nascent, cost-effective, user-friendly, and diverse outcomes in a portable fashion. Additionally, lightweight POC technology combined with smartphones can be a good choice for handheld inexpensive medical testing items as they have smooth manufacturing process and sensitivity.

Instead of the uprising demand being 22%, this technology is still reliant on end user and market appreciation. But, these tools on the other hand are holding its pace in making advanced POC-based devices, biomedical applications, drug screening, and forensic platforms.

Here, we depicted the gradual development of the major experimental outcomes and forthcoming aspects which in turn alleviates the pursuance of research work for both present and future researchers.

**Acknowledgements** The authors are grateful to the home institution for providing the space and resources to successfully carry out the work.

## References

1. Liu D, Wang J, Wu L, Huang Y, Zhang Y, Zhu M, Wang Y, Zhu Z, Yang C (2020) Trends in miniaturized biosensors for point-of-care testing. *Trends Anal Chem* 122:115701
2. Vigneshvar S, Sudhakumari CC, Senthilkumaran B, Prakash H (2016) Recent advances in biosensor technology for potential applications—an overview. *Front Bioeng Biotechnol* 4:11

3. Wan H, Chen J, Wan C, Zhou Q, Wang J, Zhang Z (2019) Optofluidic microcapillary biosensor for label-free, low glucose concentration detection. *Biomed Opt Express* 10:3929–3937
4. Padilla DA, Piñeres SH, Torres CO (2019) Sensitivity of an optical sensor based on capillary microresonator for the measurement the hydrostatic pressure in microfluidics. *J Phys Conf Series*:012073. IOP Publishing
5. Maduraiveeran G, Sasidharan M, Ganeshan V (2018) Electrochemical sensor and biosensor platforms based on advanced nanomaterials for biological and biomedical applications. *Biosens Bioelectron* 103:113–129
6. Naresh V, Lee N (2021) A review on biosensors and recent development of nanostructured materials-enabled biosensors. *Sensors* 21:1109
7. Shrimal P, Jadeja G, Patel S (2020) A review on novel methodologies for drug nanoparticle preparation: microfluidic approach. *Chem Eng Res Des* 153:728–756
8. Nielsen JB, Hanson RL, Almughamsi HM, Pang C, Fish TR, Woolley AT (2019) Microfluidics: innovations in materials and their fabrication and functionalization. *Anal chem* 92:150–168
9. Weibel DB, Whitesides GM (2006) Applications of microfluidics in chemical biology. *Curr Opin Chem Biol* 10:584–591
10. Hong J, Edel JB, deMello AJ (2009) Micro- and nanofluidic systems for high-throughput biological screening. *Drug Discov Today* 14:134–146
11. Choi S, Chae J (2009) A regenerative biosensing surface in microfluidics using electrochemical desorption of short-chain self-assembled monolayer. *Microfluid Nanofluid* 7:819–827
12. Garcia-Ramirez R, Hosseini S (2021) History of bio-microelectromechanical systems (BioMEMS), BioMEMS, pp 1–20. Springer
13. Qin D, Xia Y, Whitesides GM (2010) Soft lithography for micro- and nanoscale patterning. *Nat Protoc* 5:491–502
14. Li HW, Muir BVO, Fichet G, Huck WTS (2003) Nanocontact printing: a route to sub-50-nm-scale chemical and biological patterning. *Langmuir* 19:1963–1965
15. Manz A, Gruber N, Widmer HM (1990) Miniaturized total chemical analysis systems: a novel concept for chemical sensing. *Sens Actuator B Chem* 1:244–248
16. Duffy DC, McDonald JC, Schueller OJA, Whitesides GM (1998) Rapid prototyping of microfluidic systems in poly(dimethylsiloxane). *Anal Chem* 70:4974–4984
17. Pun S, Haney LC, Barrile R (2021) Modelling human physiology on-chip: historical perspectives and future directions. *Micromachines*. 12:1250
18. Shakeri A, Jarad NA, Leung A, Soleymani L, Didar TF (2019) Biofunctionalization of glass-and paper-based microfluidic devices: a review. *Adv Mater Interfac* 6:1900940
19. Hwang J, Cho YH, Park MS, Kim BH (2019) Microchannel fabrication on glass materials for microfluidic devices. *Int J Precis Eng Manuf* 20:479–495
20. Pandey CM, Augustine S, Kumar S, Kumar S, Nara S, Srivastava S, Malhotra BD (2018) Microfluidics based point-of-care diagnostics. *Biotechnol J* 13:1700047
21. Berenguel-Alonso M, Ortiz-Gómez I, Fernández B, Couceiro P, Alonso-Chamarro J, Capitán-Vallvey LF, Salinas-Castillo A, Puyol M (2019) An LTCC monolithic microreactor for the synthesis of carbon dots with photoluminescence imaging of the reaction progress. *Sens Actuators B Chem* 296:126613
22. Wu Z, Chen X, Wu Z, Zhang Q, Gao Q (2019) Experimental study of fabricating a four-layers Cantor fractal microfluidic chip by CO<sub>2</sub> laser system. *Microsys Tech* 25:1251–1256
23. Mandsberg NK, Christfort JF, Kamguyan K, Boisen A, Srivastava SK (2020) Orally ingestible medical devices for gut engineering. *Adv Drug Deliv Rev* 165:142–154
24. Phan THT, Kim S-J (2022) Super-hydrophobic microfluidic channels fabricated via xurography-based polydimethylsiloxane (PDMS) micromolding. *Chem Eng Sci* 258:117768
25. Scott SM, Ali Z (2021) Fabrication methods for microfluidic devices: an overview. *Micromachines*. 12:319
26. Yin B-F, Wan X-H, Yang M-Z, Qian C-C, Sohan A (2022) Wave-shaped microfluidic chip assisted point-of-care testing for accurate and rapid diagnosis of infections. *Military Med Res* 9:1–13

27. Isobe G, Kanno I, Kotera H, Yokokawa R (2012) Perfusionable multi-scale channels fabricated by integration of nanoimprint lithography (NIL) and UV lithography (UVL). *Microelectron Eng* 98:58–63
28. Haghayegh F, Salahandish R, Zare A, Khalghollah M, Sanati-Nezhad A (2022) Immuno-biosensor on a chip: a self-powered microfluidic-based electrochemical biosensing platform for point-of-care quantification of proteins. *Lab Chip* 22:108–120
29. Wong JF, Simmons CA (2019) Microfluidic assay for the on-chip electrochemical measurement of cell monolayer permeability. *Lab Chip* 19:1060–1070
30. Hynes W, Pepona M, Robertson C, Alvarado J, Dubbin K, Triplett M, Adorno J, Randles A, Moya M (2020) Examining metastatic behavior within 3D bioprinted vasculature for the validation of a 3D computational flow model. *Sci Adv* 6:eabb3308
31. Ye T, Shi H, Phan-Thien N, Lim CT, Li Y (2019) Numerical design of a microfluidic chip for probing mechanical properties of cells. *J Biomech* 84:103–112
32. Zhang X, Xu X, Ren Y, Yan Y, Wu A (2021) Numerical simulation of circulating tumor cell separation in a dielectrophoresis based YY shaped microfluidic device. *Separ Purif Technol* 255:117343
33. Ameri AR, Imanparast A, Passandideh-Fard M, Shaegh SAM (2022) A whole-thermoplastic microfluidic chip with integrated on-chip micropump, bioreactor and oxygenator for cell culture applications. *Anal Chim Acta* 1221:340093
34. Ranjan P, Sadique MA, Parihar A, Dhand C, Mishra A, Khan R (2022) Commercialization of microfluidic point-of-care diagnostic devices. Advanced microfluidics-based point-of-care diagnostics. CRC Press, pp 383–398
35. Huang L, Su E, Liu Y, He N, Deng Y, Jin L, Chen Z, Li S (2021) A microfluidic device for accurate detection of hs-cTnI. *Chin Chem Lett* 32:1555–1558
36. Adampoourezare M, Dehghan G, Hasanzadeh M, Feizi M-AH (2021) Application of lateral flow and microfluidic bio-assay and biosensing towards identification of DNA-methylation and cancer detection: recent progress and challenges in biomedicine. *Biomed Pharmacother* 141:111845
37. Chen S, Liu Y, Yu Q, Peng W (2020) Microcapillary-based integrated LSPR device for refractive index detection and biosensing. *J Lightwave Technol* 38:2485–2492
38. Hristov DR, Rodriguez-Quijada C, Gomez-Marquez J, Hamad-Schifferli K (2019) Designing paper-based immunoassays for biomedical applications. *Sensors* 19:554
39. Dai B, Yin C, Wu J, Li W, Zheng L, Lin F, Han X, Fu Y, Zhang D, Zhuang S (2021) A flux-adaptable pump-free microfluidics-based self-contained platform for multiplex cancer biomarker detection. *Lab Chip* 21:143–153
40. Bian S, Ye S, Yang S (2022) Application prospects for wearable body surface microfluidic system in sports. *Wearable Tech* 3:72–84
41. Zhang H, Xue L, Huang F, Wang S, Wang L, Liu N, Lin J (2019) A capillary biosensor for rapid detection of *Salmonella* using Fe-nanocluster amplification and smart phone imaging. *Biosens Bioelectron* 127:142–149
42. Leonardo S, Toldrà A, Campàs M (2021) Biosensors based on isothermal DNA amplification for bacterial detection in food safety and environmental monitoring. *Sensors* 21:602
43. Thompson CS, Traynor IM, Fodey TL, Barnes P, Faulkner DV, Crooks SR (2020) Screening method for the detection of residues of amphenicol antibiotics in bovine milk by optical biosensor. *Food Addit Contam* 37:1854–1864
44. McNeill L, Megson D, Linton PE, Norrey J, Bradley L, Sutcliffe OB, Shaw KJ (2021) Lab-on-a-chip approaches for the detection of controlled drugs, including new psychoactive substances: a systematic review. *Forensic Chem*:100370
45. Hassan S-U, Zhang X (2020) Design and fabrication of capillary-driven flow device for point-of-care diagnostics. *Biosensors* 10:39
46. Hammami S, Oseev A, Bargiel S, Zeggari R, Elie-Caille C, Leblois T (2022) Microfluidics for high pressure: integration on GaAs acoustic biosensors with a leakage-free PDMS based on bonding technology. *Micromachines* 13:755

# A Review on Memristor-Based Reactance-Less Relaxation Oscillator



Rajesh Dutta, Amiya Karmakar, and Sudakshina Kundu

**Abstract** Reactance-Less relaxation oscillators designed using a memristor, two comparators and an AND gate have already been simulated. In previous literature, the details of the AND circuit have been overlooked. This research finds that a simple AND circuit is not sufficient for the correct operation of the oscillator and confirms that a hysteresis circuit must be associated with the AND circuit to generate controllable oscillation. This work uses the LTspice simulator and compares the theoretically calculated time periods with the measured ones from the simulated graphs.

**Keywords** Memristor · Reactance-Less relaxation oscillator and R-M oscillator

## 1 Introduction

In the family of passive electronic elements, a new member called a memristor has been added [1]. Research is going on to implement the device in different domains of electronics. In the domain of analog electronics, different kinds of sinusoidal oscillators like Wien oscillators, Collpitts oscillators and RC phase shift oscillators are very popular. In [2], Wien oscillators have been designed using memristors. The use of memristors in places of resistors and inductors in RC phase shift and Collpitts oscillators is shown in [3]. Recently, a chaotic oscillator based on a memristor has been designed for the detection of weak signals [4]. Relaxation oscillators are nonlinear electronic oscillators that generate non-sinusoidal output waveforms. They include capacitors or inductors as energy-storing elements and charge and discharge continuously to produce oscillations. Memristors have a property to remember their last resistance. Though it does not possess any energy-storing property, its resistance-storing property can be used to design relaxation oscillators. In [5], resistor-memristor (R-M) relaxation oscillator circuit and memristor-resistor (M-R) relaxation oscilla-

---

R. Dutta (✉) · A. Karmakar · S. Kundu

Maulana Abul Kalam Azad University of Technology, Kolkata, West Bengal, India  
e-mail: [rajeshprl09@gmail.com](mailto:rajeshprl09@gmail.com)

tor circuit have been presented, and the simulation results are also shown. The first circuit uses two comparators, a resistor-memristor voltage divider and an AND gate. For the second circuit, a memristor-resistor voltage divider and a NAND gate are used instead. Both of these circuits' working principles are very similar.

In this paper, investigations with the R-M relaxation oscillator circuit using the LTspice simulator have been shown. It is found that this type of circuit cannot work in reality without specific properties associated with the AND gate which has not yet been discussed in the literature.

## 2 Overview of Memristor and the HP Model

A memristor is a passive element like resistor, capacitor and inductor. As the name suggests, it has the property of memorizing in terms of its resistance. A memristor's current-voltage relationship is described by the Ohm's law equation given by

$$V(t) = M(w, I)I(t) \quad (1)$$

where  $V(t)$  is the applied terminal voltage,  $I(t)$  is the current through the memristor, and  $M(w, I)$  is called the memristance of the device which depends upon a state variable  $w(t)$  and the input current  $I(t)$ . The resistance-changing property of the memristor is defined by

$$\frac{dw}{dt} = f(w, I) \quad (2)$$

The time rate of change of the resistive state of the device is a function of the memristor current and the state variable itself.

Research is going on to fabricate memristors with different materials. To name a few, titanium dioxide [6], tantalum oxide [7], zinc oxide [8] and graphene oxide [9] memristors have been fabricated. Out of the different models for simulating the behaviour of the memristors, the linear boundary drift model [6] of the memristor is the simplest and first ever. The model is related to the first laboratory-fabricated memristive device, the titanium dioxide ( $TiO_2$ ) memristor fabricated in Hewlett Packard (HP) Laboratory. The device has a  $TiO_2$  thin film inserted between two platinum electrodes. A part of the layer of the thin film contains mobile oxygen vacancies as the donors of electrons and thus has high conductivity; the other part is pure  $TiO_2$  having low conductivity. There is a boundary between these two types of layers. The oxygen vacancies are positively charged and can move from one side to another when voltage is applied between the electrodes. This movement of the boundary with the applied voltage changes the ratio of the width of the conductive and less conductive parts, and the overall resistance of the device changes accordingly. The following two equations describe the current-voltage relationship and the rate of change of the resistive state of the device.

$$V(t) = \left[ R_{\text{on}} \frac{W}{D} + R_{\text{off}} \left( 1 - \frac{W}{D} \right) \right] I(t) \quad (3)$$

and

$$\frac{dW}{dt} = \frac{\mu R_{\text{on}}}{D} I(t) \quad (4)$$

where  $W$  is the thickness of the conductive part of the  $\text{TiO}_2$  layer and  $D$  is the total thickness of the  $\text{TiO}_2$  layer.  $R_{\text{on}}$  and  $R_{\text{off}}$  are, respectively, the resistances of the low resistive and high resistive  $\text{TiO}_2$  layers when they have a thickness  $D$ . The mobility of the oxygen vacancies in the  $\text{TiO}_2$  layer is  $\mu$ . In terms of a state variable  $X$ , normalized between 0 and 1, the above two expressions can be rewritten as

$$V(t) = [R_{\text{on}}X + R_{\text{off}}(1 - X)]I(t) \quad (5)$$

and

$$\frac{dX}{dt} = K I(t) \quad (6)$$

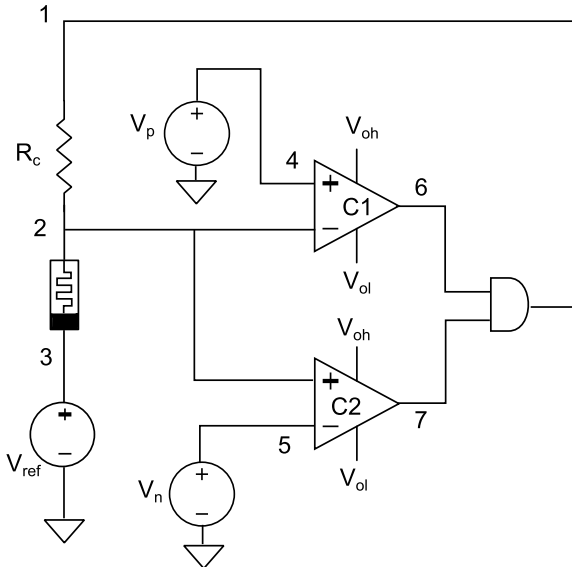
where  $X = \frac{W}{D}$  and  $K = \frac{\mu R_{\text{on}}}{D^2}$ . To ensure that the state variable  $X$  is limited between 0 and 1, the rate of change of  $X$  given by (6) should be brought down to zero near its limits. Multiplication of window functions like the Joglekar's window function [10] or Bielek's window function [11] to the right-hand side of (6) gradually reduces the rate of change of  $X$  towards 0 near its limits.

### 3 The Reactance-Less Relaxation Oscillator

An R-M reactance-less oscillator is shown in Fig. 1.

In this circuit, the voltage across the memristor becomes positive or negative when the voltage at node 1 is equal to the maximum supply voltage  $V_{\text{oh}}$  or the minimum supply voltage  $V_{\text{ol}}$ , respectively. A positive voltage across the memristor increases its resistance, and a negative voltage decreases its resistance. When the outputs of both comparators are at  $V_{\text{oh}}$ , their ANDed voltage at node 1 is also  $V_{\text{oh}}$ . This increases the resistance of the memristor, and therefore, the voltage at node 2 increases. When this voltage crosses the positive threshold voltage  $V_p$ , node 6 goes to the minimum supply voltage  $V_{\text{ol}}$ . Since node 7 already remains at  $V_{\text{oh}}$ , the AND operation on the voltages of nodes 6 and 7 produces a voltage  $V_{\text{ol}}$  at node 1. The memristor's resistance now decreases due to the negative voltage across it. The voltage of node 2 eventually

**Fig. 1** Reactance-Less relaxation oscillator redrawn after [5]



exceeds  $V_n$ , and the voltage at node 7 becomes  $V_{oh}$ . As the voltage at node 6 is already at  $V_{oh}$ , the AND operation now produces a voltage  $V_{oh}$  at node 1. This cycle keeps on repeating to generate the required oscillation. In [5], the following formulas were derived for the on-time duration ( $T_H$ ) and off-time duration ( $T_L$ ) of the oscillation, and the simulation results were also presented.

$$T_H = \frac{(R_{mp} - R_{mn})(R_{mp} + R_{mn} + 2R_c)}{2K'(V_{oh} - V_{ref})} \quad (7)$$

and

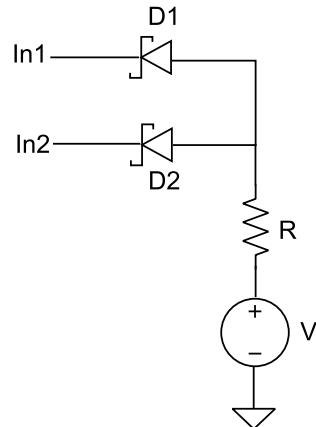
$$T_L = T_H \frac{(V_{oh} - V_{ref})}{(V_{ref} - V_{ol})} \quad (8)$$

where  $R_{mp}$  and  $R_{mn}$  are, respectively, the highest and lowest resistances the memristor can have during the oscillation and  $K'$  are given by  $K' = \mu R_{on}(R_{off} - R_{on})/D^2$ . In the derivation of the above formulas, the HP memristor model was used without any window function. In [12], the circuit was simulated with a more complicated memristor model shown in [13].

#### 4 Problem with the Relaxation Oscillator Circuit

The circuit in Fig. 1 was simulated in LTspice using a simple AND gate having the structure shown in Fig. 2. The circuit uses two Schottky diodes D1 and D2, one

**Fig. 2** AND gate with Schottky diodes



resistor R and a DC voltage source V. The oscillator should work fine with the simple AND gate circuit, but it does not in reality. An LTspice simulation of the circuit with this gate did not yield any controllable oscillation but an uncontrolled oscillation as shown in Fig. 3. In this simulation, two LT1720 comparators were used. The AND circuit used two 1N5817 Schottky diodes, a  $2\text{ k}\Omega$  resistor and a 5V DC voltage source. In reality, the operation of the circuit does not go step by step as described in the previous section. In the circuit of Fig. 1, if at any instant of time, the voltage of nodes 6 and 7 are equal to  $V_{oh}$ , then the ANDed voltage at node 1 is also  $V_{oh}$ . This makes the voltage at node 2 grow until it reaches the threshold voltage  $V_p$ . Now the output of comparator C1 should go to  $V_{ol}$ . As the voltage of node 6 starts to fall towards  $V_{ol}$ , the voltage at node 1 also starts to fall. The voltage at node 2 follows this and goes below the threshold voltage  $V_p$  again and moves the output of the C1 comparator towards  $V_{oh}$  again. In this way, a rapid oscillation happens in the circuit as shown in Fig. 3.

The inclusion of a non-inverting Schmitt trigger circuit with this diode AND gate as shown in the circuit diagram of Fig. 4 solves this problem.

The Schmitt trigger circuit produces a hysteresis. It holds the voltage of node 1 at  $V_{oh}$  until the AND gate output transits from  $V_{oh}$  to  $V_{ol}$ . Similarly, it holds the voltage of node 1 to  $V_{ol}$  until the AND gate output transits from  $V_{ol}$  to  $V_{oh}$ . In none of the previous papers, the circuit of the AND gate has been revealed. The LTspice simulations shown in the next section confirm that the AND gate must be associated with some kind of hysteresis circuit such as the Schmitt trigger for the successful operation of the circuit.

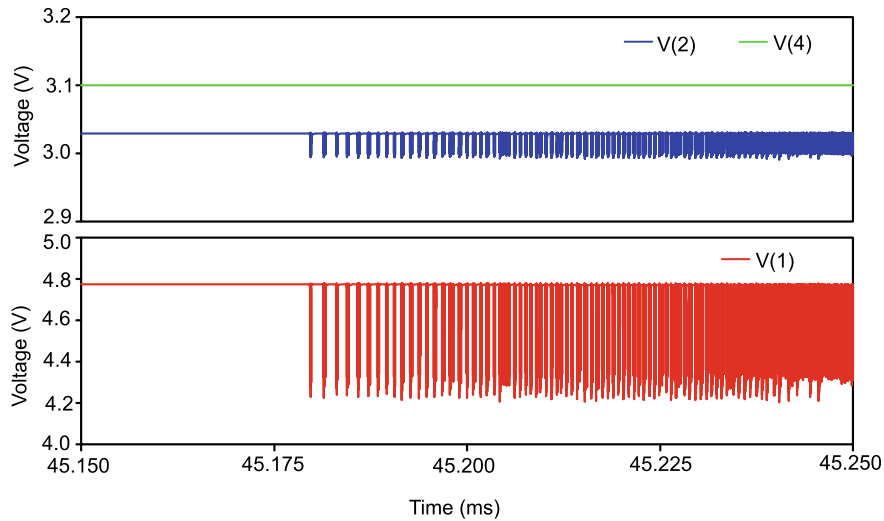


**Fig. 3** Voltages at nodes 1 and 2 oscillate back and forth rapidly as the voltage at node 2 approaches the threshold voltage present at node 4

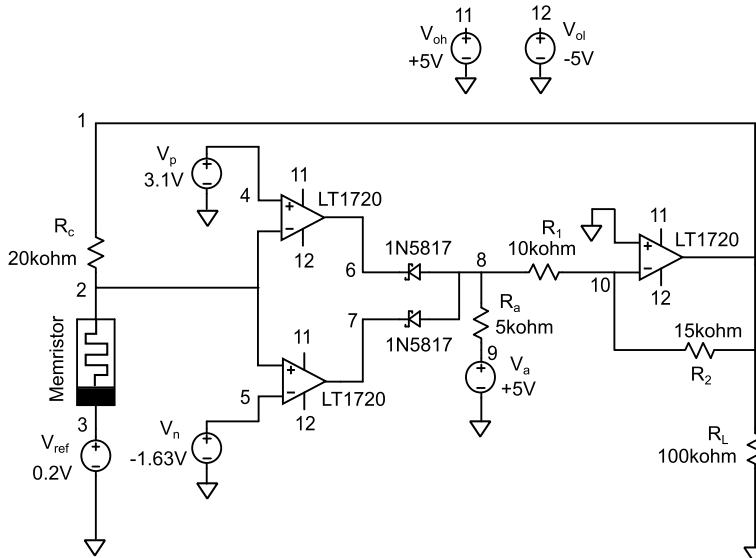


**Fig. 4** Reactance-Less relaxation oscillator with hysteresis associated to the AND gate

## 5 Simulations with LTspice

Figure 4 shows the circuit of the memristor relaxation oscillator with the Schmitt trigger circuit inserted after the AND gate. In the simulations of this circuit, the HP memristor model has been used and the formulas for the on-time duration ( $T_H$ ) and off-time duration ( $T_L$ ) are the same as given by (7) and (8). A comparison of the simulated results with the calculated results is given in Table 1.

The time durations  $T_H$  and  $T_L$  shown in the seventh and eighth column of Table 1 are the average of five measurements from different parts of the graphs in each case. The simulated graphs are shown in Figs. 5, 6 and 7. The parameters used for the simulations are mentioned in the respective captions.

The simulated values of  $T_H$  and  $T_L$  can deviate from the calculated values as the comparators used in these circuits have small amounts of leakage currents through their input pins, unlike an ideal comparator. When the resistances of the R-M voltage divider are small, the current through the memristor is large compared to the comparator leakage currents. For large values of these resistances, the problem becomes more prominent.

**Table 1** Comparison of  $T_H$  and  $T_L$ : calculated values and values measured from the simulated graphs

$R_c$ (k $\Omega$ )	$V_{ref}$ (V)	$V_p$ (V)	$V_n$ (V)	Calculated $T_H$ (ms)	Calculated $T_L$ (ms)	Simulated $T_H$ (ms)	Simulated $T_L$ (ms)
100	-0.5	1.77	-1.27	132.3	161.7	95.2	163.0
20	0.2	3.1	-1.63	17.0	15.7	16.6	16.1
10	1.0	3.25	-2.13	1.09	0.73	1.02	0.69

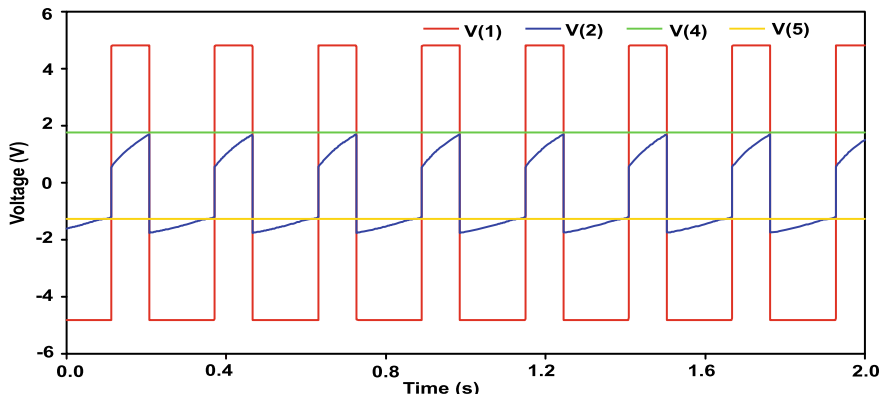


**Fig. 5** LTspice simulation done with the following parameters:  $R_{on} = 1\text{ k}\Omega$ ,  $R_{off} = 100\text{ k}\Omega$ ,  $R_{init} = 50\text{ k}\Omega$ ,  $D = 10\text{ nm}$ ,  $\mu_v = 10^{-14}\text{ m}^2\text{V}^{-1}\text{s}^{-1}$ ,  $R_c = 100\text{ k}\Omega$ ,  $V_{ref} = 0.5\text{ V}$ ,  $V_p = 1.77\text{ V}$ ,  $V_n = -1.27\text{ V}$

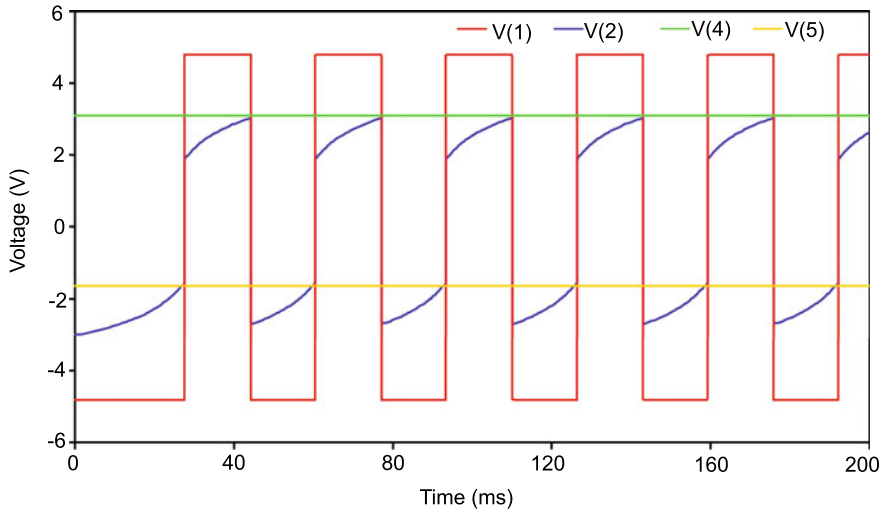


**Fig. 6** LTspice simulation done with the following parameters:  $R_{\text{on}} = 1 \text{ k}\Omega$ ,  $R_{\text{off}} = 100 \text{ k}\Omega$ ,  $R_{\text{init}} = 40 \text{ k}\Omega$ ,  $D = 10 \text{ nm}$ ,  $\mu_v = 10^{-14} \text{ m}^2 \text{V}^{-1} \text{s}^{-1}$ ,  $R_c = 20 \text{ k}\Omega$ ,  $V_{\text{ref}} = 0.2 \text{ V}$ ,  $V_p = 3.1 \text{ V}$ ,  $V_n = -1.63 \text{ V}$

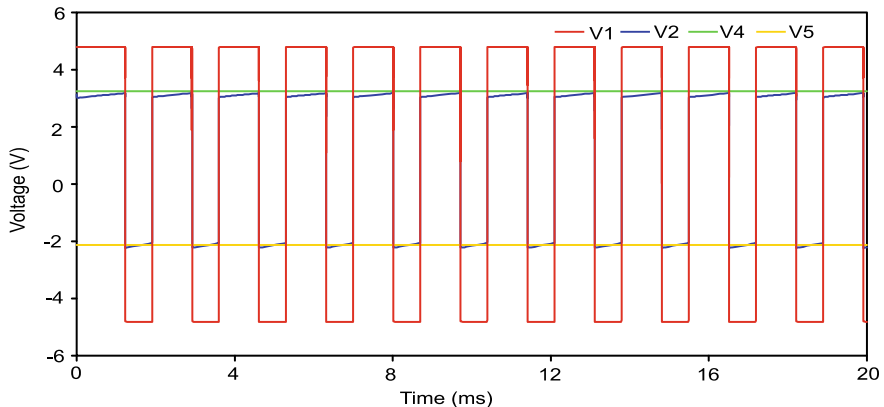


**Fig. 7** LTspice simulation done with the following parameters:  $R_{\text{on}} = 1 \text{ k}\Omega$ ,  $R_{\text{off}} = 100 \text{ k}\Omega$ ,  $R_{\text{init}} = 10.9 \text{ k}\Omega$ ,  $D = 10 \text{ nm}$ ,  $\mu_v = 10^{-14} \text{ m}^2 \text{V}^{-1} \text{s}^{-1}$ ,  $R_c = 10 \text{ k}\Omega$ ,  $V_{\text{ref}} = 1 \text{ V}$ ,  $V_p = 3.25 \text{ V}$ ,  $V_n = -2.13 \text{ V}$

## 6 Conclusion

The memristor may be used as an element to produce oscillations by its virtue of remembering resistance. It does not work like a capacitor in a relaxation oscillator circuit. The voltage across a capacitor depends upon the stored charge in it, and the charging and discharging time of the capacitor determines the time period of the

oscillation. The memristor on the other hand increases or decreases its resistance up to specific values bounded by the threshold voltages. When the output voltage changes, it is immediately fed back across the memristor, which again takes back the comparator to the previous state instantly. This generates an uncontrolled oscillation. The hysteresis circuit associated with the output stage of the oscillator prevents the immediate feedback process and allows the memristor to change its state in the desired range.

## References

1. Chua L (1971) Memristor-the missing circuit element. *IEEE Trans Circ Theory* 18(5):507–519
2. Talukdar A, Radwan AG, Salama KN (2011) Generalized model for memristor-based Wien family oscillators. *Microelectron J* 42(9):1032–1038
3. Anand A, Aggarwal B, Singh K (2019) Memristor based oscillator. In 2019 International conference on computing, power and communication technologies (GUCON). IEEE, pp 89–92
4. Dong K, Xu K, Zhou Y, Zuo C, Wang L, Zhang C, Hui Y (2022) A memristor-based chaotic oscillator for weak signal detection and its circuitry realization. *Nonlinear Dyn* 109(3):2129–2141
5. Fouda ME, Radwan AG (2014) Memristor-based voltage-controlled relaxation oscillators. *Int J Circ Theory Appl* 42(10):1092–1102
6. Strukov DB, Snider GS, Stewart DR, Williams RS (2008) The missing memristor found. *Nature* 453(7191):80–83
7. Yang Y, Sheridan P, Lu W (2012) Complementary resistive switching in tantalum oxide-based resistive memory devices. *Appl Phys Lett* 100(20):203112
8. Gul F, Efeoglu H (2017) Bipolar resistive switching and conduction mechanism of an Al/ZnO/Al-based memristor. *Superlattices Microstruct* 101:172–179
9. Romero FJ, Toral-Lopez A, Ohata A, Morales DP, Ruiz FG, Godoy A, Rodriguez N (2019) Laser-fabricated reduced graphene oxide memristors. *Nanomaterials* 9(6):897
10. Joglekar YN, Wolf SJ (2009) The elusive memristor: properties of basic electrical circuits. *Euro J Phys* 30(4):661
11. Bielek Z, Bielek D, Biolkov V (2009) Spice model of memristor with nonlinear dopant drift. *Radioengineering* 18(2)
12. El-Naggar AM, Fouda ME, Madian AH, Radwan AG (2016) Reactance-less RM relaxation oscillator using exponential memristor model. In 2016 28th International conference on microelectronics (ICM), pp 361–364
13. Yang JJ, Pickett MD, Li X, Ohlberg DA, Stewart DR, Williams RS (2008) Memristive switching mechanism for metal/oxide/metal nanodevices. *Nat Nanotechnol* 3(7):429–433

# Optimal Control and Voltage Sag Compensation in a PV/FC Integrated Microgrid Through Biography Based Optimization Technique



Gagan Kumar Sahoo, Subham Mohanty, and Subhashree Choudhury

**Abstract** Electrical power consumption has multiplied in recent decades as a result of the population explosion and rapid industrialization. The only viable option for generating green energy is to use renewable energy sources. The concept of Micro-Grid (MG) was thus established as a result of the deployment of small renewable producing units owing to the exhaustion of fossil fuel based sources of energy. However, due to the complex and abundance of nonlinear loads, complimentary power electronics devices connected to the MG and extensive integration of MG with conventional grid systems have led to problems with power quality. For the grid system to function healthily and effectively, these power quality issues must be resolved; otherwise, they risk causing equipment connected to the energy generation and distribution networks to break down. This research work aims to protect and survive the effects of voltage sag on photovoltaics (PV) and fuel cell (FC) based MG systems through a robust Biography Based Optimization (BBO) Technique. The proposed BBO technique dynamically tunes the Proportional Integral (PI) controller gains and responds efficiently in compensating voltage sag and eliminating harmonics. The efficacy of the suggested BBO technique is proven by comparing its characteristics with traditional Particle Swarm Optimization (PSO) and PI methods. A thorough review of the results obtained proves that the BBO technique surpasses the PI and PSO based controllers in eliminating distortions, compensating voltage sag, reducing THD, enhancing the control of active and reactive power, improving power factor, reducing voltage deviation, maintaining almost constant terminal voltage, DC link voltage, grid voltage and grid current more efficiently and robustly thus proving its real-time application in power grid networks.

---

G. K. Sahoo

Department of Electrical Engineering, ITER, Siksha ‘O’ Anusandhan Deemed To Be University, Bhubaneswar 751030, India

S. Mohanty · S. Choudhury (✉)

Department of Electrical and Electronics Engineering, ITER, Siksha ‘O’ Anusandhan Deemed To Be University, Bhubaneswar 751030, India

e-mail: [subhashreechoudhury@soa.ac.in](mailto:subhashreechoudhury@soa.ac.in)

**Keywords** PV · Fuel cell · Power quality · Sag · MicroGrid (MG) · Particle Swarm Optimization (PSO) · Biography Based Optimization (BBO) · Total Harmonic Distortion (THD) · Proportional Integral (PI)

## 1 Introduction

Coal and other fossil fuels are the main nonrenewable energy-based fuel sources used in the conventional power system. These resources are unreliable and are gradually becoming obsolete because they discharge harmful materials into the environment and are thus not environmentally friendly. As a result, the usage of Renewable sources of energy has rapidly risen in the last few decades [1]. Recently the concept of MicroGrid has been introduced by many researchers where renewable energy sources can be deployed to generate electrical energy with a less production capacity to supply local loads as well as to get tied up to the utility grid [2]. MG can be operated in both autonomous and grid-connected mode of operation. The development of the MG has made it possible for traditional grid systems to utilise several remote Distributed Energy Resources (DERs) [3]. MG utilizes many power electronic devices, FACTS devices and other equipment for interfacing with the grid [4]. Further, the growing population and rapid industrialisation have created more complicated and sensitive nonlinear loads. The above are the major reasons for creating disturbances in the power system network and are termed power quality issues. There can be numerous power quality problems such as frequency deviation, sag, notch, swell, poor power factor, harmonics, flicker, etc. For the power system network to function safely and stably, these power quality problems must be substantially eliminated [5]. These problems may lead to the malfunctioning and heating of sensitive and sophisticated equipment used in the generation, transmission, and distribution of energy.

To compensate for these power quality issues many authors have suggested numerous techniques for power quality enhancement and optimal control of MG systems. Authors in [6] have discussed power sharing and power quality improvement in Microgrids using the Artificial Intelligence technique. A thorough literature survey reveals that enhancement in power quality can also be brought about by adopting the use of active power filters [5]. A marine predator algorithm along with an adaptive dynamic voltage restorer has been proposed by researchers for effective operation control, power quality improvement and energy management for isolated microgrids [7]. The Salp Swarm Optimization Algorithm method has been suggested for dynamic response and power quality enhancement of an islanded MG in [8]. A control strategy based on hierarchical theory has been applied for efficient stability in the MG system [9]. Authors in [10] have investigated a Dynamic and boost converter has been Voltage Restorer system based on Dual P-Q Theory for mitigation of power quality issues in a distribution system. Various custom power devices such as D-STATCOM, UPQC, UPS, TVSS, and DVR have been incorporated into the MG system for the mitigation of power quality problems [11]. The impact of the swarm

intelligence control method in enhancing the quality of power of the AC micro-grid has been studied in [12]. An improved approach for robust control of dynamic voltage restorer and power quality enhancement using the grasshopper optimization algorithm has been verified by authors in [13]. The entire article has been divided into 6 sections. In Sect. 2 detailed mathematical modelling of all system components used for the study has been projected. Section 3 discusses the traditional and proposed controllers in depth. In Sect. 4, the Simulink model and the results found are conferred in detail. A thorough comparative study of values obtained from all system dynamics for conventional and proposed control methods has been elaborated. At last in Sect. 6 the inference drawn from the complete research work is deliberated.

## 2 Mathematical Modelling of Various System Components

### 2.1 Photovoltaic (PV)

Nowadays PV is considered to be one of the most vital renewable-based distributed energy resources that transforms solar energy into electrical energy using solar irradiance as a source of energy as its environmentally friendly, has no noise pollution, requires low maintenance costs and has zero fuel consumption [14]. It consists of several cells tied to form an array that works together to generate photoelectric current, which in turn traps solar radiation on their surfaces. In this research work, a single diode model-based PV cell is considered for the study. The PV panel serves as a source of current, generating a photoelectric current which is technically expressed as [15]:

$$I = I_L - I_0 \left[ \exp\left(\frac{qV_D}{nKT}\right) - 1 \right] - \frac{V}{R_p} \quad (1)$$

### 2.2 Fuel Cell (FC)

An FC is an electrochemical device that oxidises fuel to produce electrical energy. There are many types of FCs reported in the literature. However, among all the PEMFC is usually preferred over others because of the following advantages: (1) flexibility in input fuel, (2) fast startup, (3) lightweight, (4) compact design, (5) solidity of electrolyte and (6) low cost [16]. A basic equivalent model of an FC is considered in the MG system. The output voltage of FC and its basic equations can be mathematically represented as given below [17]:

$$U = V - V_1 - V_2 - V_3 \quad (2)$$

$$V = N \left[ V_0 + \frac{RT}{2F} \ln \left( \frac{\text{PH}_2(\text{PO}_2)^{0.5}}{\text{PH}_2\text{O}} \right) \right] \quad (3)$$

$$V_2 = i * R_C \quad (4)$$

$$V_1 = -A * \ln(i) \quad (5)$$

$$V_3 = i * R_0 \quad (6)$$

### 2.3 Boost Converter

A boost converter is a DC-DC power converter that increases the output voltage concerning its input side and operates on a Pulse Width Modulation (PWM) to bring control of the switching states of the switches [18]. It has a low to medium efficiency range. The basic model of a boost converter is demonstrated in [17] and the output voltage can be mathematically represented as:

$$V_0 = \left( \frac{1}{1 - T} \right) * V_S \quad (7)$$

## 3 Controllers

### 3.1 Proportional Integral (PI)

The PI controller is a traditional controller which is linear and easy to implement. It consists of the Proportional and Integral controllers having the gains parameters  $k_p$  and  $k_i$  respectively [19]. The improvement of rise time and the reduction in steady-state error are brought about by the controller's gains  $k_p$  and  $k_i$  respectively. The major demerit associated with the PI controller is that due to its linearity, it cannot respond robustly to any non-linearities in the electrical grid network, so the gain parameters need to be dynamically tuned by some other methods to respond efficiently. Mathematically the PI controller is presented as follows [19]:

$$X(t) = k_p e(t) + k_i \int e(t).dt \quad (8)$$

where ' $X(t)$ ' and ' $e(t)$ ' are the control variable and error signal respectively.

### 3.2 Particle Swarm Optimization (PSO)

Inspired by the group behaviour of social animals, swarm-based algorithms have become a prominent group of optimization tools [20]. Particle swarm optimization (PSO) defines the collection of candidate solutions to the optimization problem as a swarm of particles that may move around the parameter space while establishing paths that are influenced by their own and neighbours' best performances. PSO comprises of updating the position and velocity expression. Each particle's value is calculated using its most recent best value. The two fittest values that alter location and speed information are  $p_{\text{best}}$  (position best) and  $g_{\text{best}}$  (global best). The mathematical equations of PSO are given below [21].

$$vel_{\text{in}}^{t+1} = vel_{\text{in}}^t + k_1 r_1 (p_{\text{best}}^t - x_{\text{in}}^t) + k_2 r_2 (g_{\text{best}}^t - x_{\text{in}}^t) \quad (9)$$

$$x_{\text{in}}^{t+1} = x_{\text{in}}^t + v_{\text{in}}^{t+1} \quad (10)$$

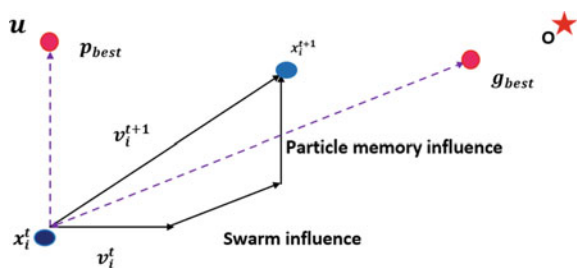
If  $n$  is the number of parameters to be optimised, then each potential solution, or "particle" in PSO represents a point in a  $n$ -dimensional space with  $m$  number of populations.  $x_{\text{in}}$  is the  $i$ th position of the particle with  $vel_{\text{in}}$  as the present velocity. The current iteration is designated a  $t$ .  $k_1$  and  $k_2$  are known as cognitive social factors. Two random numbers in between  $[0, 1]$  are selected and assigned to  $r_1$  and  $r_2$  respectively.

Figure 1 shows the position and velocity update of solutions for PSO, where 'U' indicates the entire search space of a function and 'O' is the theoretical optimum value which is to be found. The initial particle position, the initial velocity of the current individual member and the updated velocity of the next iteration are represented as  $x_i^t$ ,  $vel_{\text{in}}^t$  and  $vel_{\text{in}}^{t+1}$  respectively.

The particle memory influence and swarm influence are represented by two lines that are parallel to the  $x_i^t$  and tied to  $p_{\text{best}}$  and  $g_{\text{best}}$ . In this step, the particle  $i$  gets affected by  $v_i^t$ . In the next step,  $i$  reaches to  $x_i^{t+1}$  from previous  $x_{\text{in}}^t$  and velocity reaches to  $v_{\text{in}}^{t+1}$ . Similarly, the position of the particle in the next iteration will reach a new position and this process continues till the theoretical optimum solution or a nearer value is achieved.

The newly updated velocity formula is given below [21]:

**Fig. 1** Position and velocity update of solutions



$$vel_{\text{in}}^{t+1} = \omega vel_{\text{in}}^t + k_1 r_1 (p_{\text{best}}^t - x_{\text{in}}^t) + k_2 r_2 (g_{\text{best}}^t - x_{\text{in}}^t) \quad (11)$$

An inertia weight capability factor  $\omega$  is inserted between the local and global search to bring about equilibrium. The larger the value of  $\omega$ , the more will be the strength of global search and the more visible will be the local search capacity. Authors in [22, 23] have discussed the detailed steps for the algorithm and the flowchart of the PSO technique.

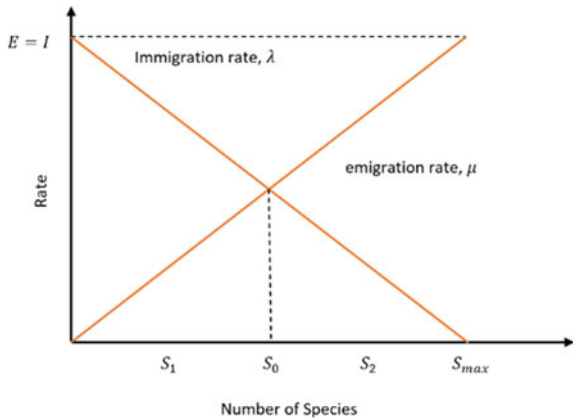
### 3.3 *Biography Based Optimization (BBO)*

#### 3.3.1 Concept of BBO

Most optimization issues involve restrictions. The final search space results that have complied with the stated limitations are where the answers to the problem are found. Heuristic algorithms can locate the estimated answers in certain situations; however, they occasionally have some restrictions. Among many optimization approaches reported in the literature, BBO is proved to be a promising tool that can handle complex optimization issues whereas other optimization techniques find it to be fairly challenging. The recently developed BBO algorithm replicates the mathematical model of biological species migration [24]. Simon and associates made the initial suggestion in 2008. Its central idea was derived from the biogeography theory, which focuses on investigating the geographic distribution of biological organisms. This algorithm is a great method for global optimization since it has the advantages of the use of fewer control parameters, minimum complexity, quick convergence and simple computation requirements. The BBO's initial applications include functional optimization and health evaluation of aircraft engines. After that, it was effectively used to resolve several challenging combinatorial optimization issues, including the scheduling of production, the diagnosis of heart disease, and the synthesis of array antennas. BBO has become a very powerful algorithm in evolutionary algorithms because of its marketable performance. The BBO evolutionary algorithm is predicated on the island biography equilibrium theory [25]. The scientific study of biological organisms' geographic distribution is known as biography. BBO is based on how species leave their islands and give rise to new species. BBO is likewise probabilistic; by estimating the pace of immigration and emigration to create a new population, it assesses the capacity for accepting the underprivileged.

The movement of species between islands in search of kinder habitats serves as its driving force. The process by which species travel from one environment to another, how new species emerge, and how old species become extinct are the three main aspects of biography that the BBO algorithm describes. From the standpoint of biography, regions with a high habitat appropriateness index are those that are best suited as homes for biological species (HSI). HSI is the same as "fitness" in other population-based optimization techniques. Each solution in an HSI is known as a "habitat" and is represented by an n-dimensional real vector. The traits of a person

**Fig. 2** Model of species-to-species migration [27]



define their habitability according to the suitability index criteria (SIVs). The initial production of the habitat vectors is random [26]. The desired solutions are seen to be habitats with low HSIs, whereas the perfect solutions are thought to be habitats with high HSIs. Solutions with high HSI and low HSI usually have aspects in common. The two fundamental actions, migration and mutation, of the BBO algorithm, can be explained as follows.

### Migration

High HSI habitats or islands have high emigration rates but low immigration rates. Thus, a habitat with a higher HSI would probably be more static. When a species has a high rate of emigration, it will typically relocate to the closest habitats, and vice versa. The species that migrate to another environment won't entirely vanish from its original location; it will still be visible in both areas at the same time. Figure 2 shows a schematic diagram of species-to-species migration. The following are the mathematical equations of biological geography's linear migration [27]:

$$\lambda_k = I_{\max} \left( 1 - \frac{k}{S_{\max}} \right) \quad (12)$$

$$\mu_k = E_{\max} \left( \frac{k}{S_{\max}} \right) \quad (13)$$

where,  $S_{\max}$  is the maximum species possible,  $I_{\max}$  denotes the highest rate of immigration,  $E_{\max}$  represents the highest rate of emigration,  $k$  is the  $k$ th individual's species,  $\lambda_k$  signifies the immigration rate of  $k$ th individual and  $\mu_k$  denotes the emigration rate of  $k$ th individual.

## Mutation

The mutation is a catastrophic occurrence in the habitat. The mutation rate is the likelihood of a mutation occurring in a particular ecosystem. The rate of mutation is affected by the number of species present in the ecosystem. When compared to habitats with low HSI values, high HSI habitats are more likely to have lower mutation rates. The old environment with low HSI values would be replaced by a new one brought about by the mutation. The low HSI solution would be more dominant in the absence of mutation, making it possible for them to become locked on the local optimum. The mutation rate can be mathematically defined as given below [27]:

$$m_k = m_{\max} \left( \frac{1 - P_k}{P_{\max}} \right) \quad (14)$$

where,  $m_k$ ,  $m_{\max}$ ,  $P_k$  and  $P_{\max}$  represents mutation rate, maximum mutation, Probability of the habitat's species diversity and the maximum probability that might be happened respectively.

## Steps for the BBO algorithm [28]

**Step 1. Initialization:** Define the number of species that can exist  $S_{\max}$ , there is room for all possible migration rates, including the maximum rates of  $E$  and  $I$ . Create various habitats at random, each of which corresponds to one of the problem's potential solutions.

**Step 2. Evaluation:** The number of species  $S$ , , immigration rate, and emigration rate should all be calculated for the habitat region, along with the habitat-specific index (HSI).

**Step 3. Emigration:** Use migration and emigration probabilistically to alter each habitat. Execute the emigration process following Eqs. (11) and (12).

**Step 4. Mutation:** Update the likelihood of each habitat having a certain species using formulae (13). Next, update each HSI and modify each habitat by its probability.

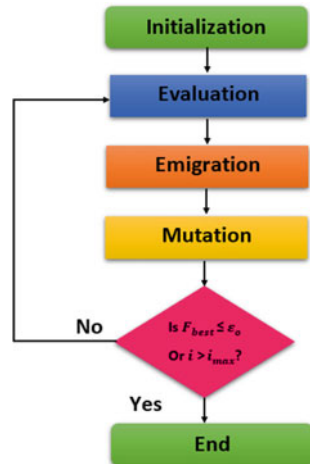
**Step 5.** Repeat until one of the stop criteria is met. Move on to **Step 2** for the subsequent iterations.

Figure 3. illustrates the flowchart of the BBO technique where  $F_{\text{best}}$ ,  $\varepsilon_0$ ,  $i$  and  $i_{\max}$  signifies the best fitness value, small pre-set value ( $10^{-8}$ ), iteration of the algorithm and maximum iteration possible respectively.

## 4 Simulink Model and Result Discussion

A grid-tied MG system consisting of PV, FC and boost converter has been simulated using MATLAB/Simulink software in this research work. The schematic block diagram illustration of the overall MG system considered for study has been depicted

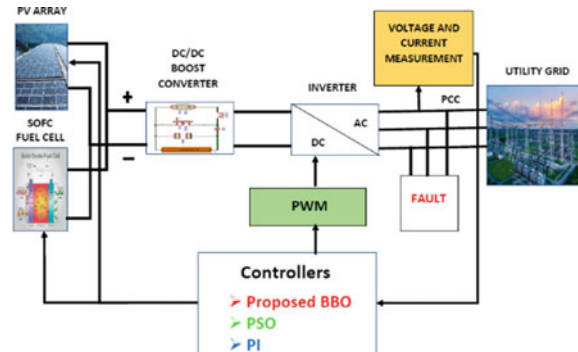
**Fig. 3** Flowchart of BBO technique



in Fig. 4. PV and FC are used as the source of generation units and the boost converter is used for enhancing the voltage level and is controlled by a PWM signal. To justify the efficacy of the proposed system, voltage sag is introduced by adding a three-phase fault (LLL-G) in the system between times 0.3–0.6 s. The Simulink model is run for 1 s and all the system characteristics such as terminal voltage, DC link voltage, voltage deviation, active power, reactive power, apparent power, THD, power factor, frequency, grid voltage and grid current have been found out. Further, a detailed comparison of the results obtained from the proposed BBO method is made with the traditional PI and PSO techniques both graphically as well as in tabulated form for easy understanding of the readers.

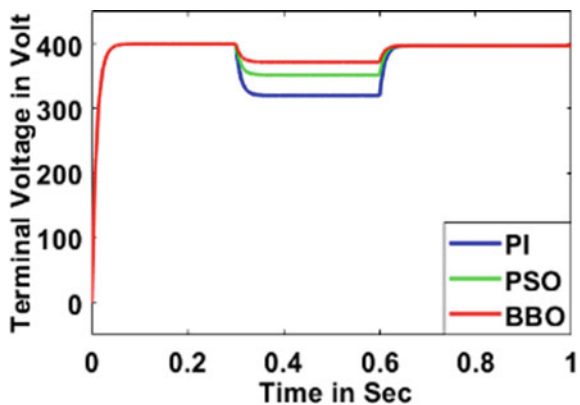
Figures 5, 6 and 7 represent the terminal voltage, DC link voltage and voltage deviation for the various controllers. From the results, it can be observed that the proposed BBO technique effectively maintains the terminal voltage and DC link voltage with minimum voltage deviation when the system is led to a voltage sag in comparison to PI and PSO methods. The active power, reactive power and apparent power are depicted

**Fig. 4** Overall MG system modelling considered for the study

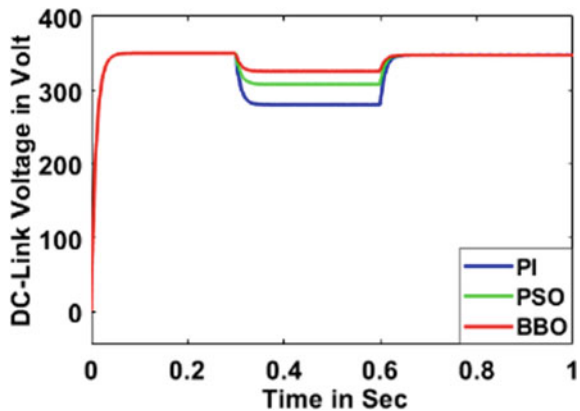


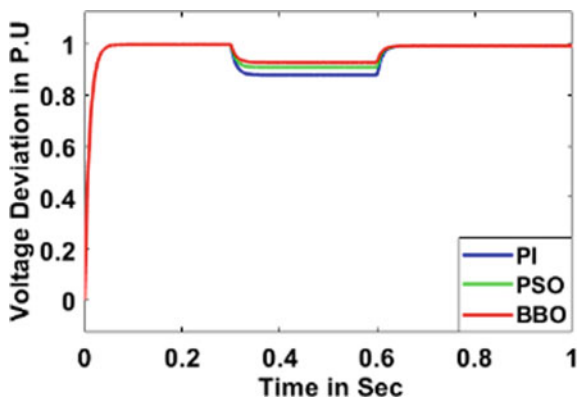
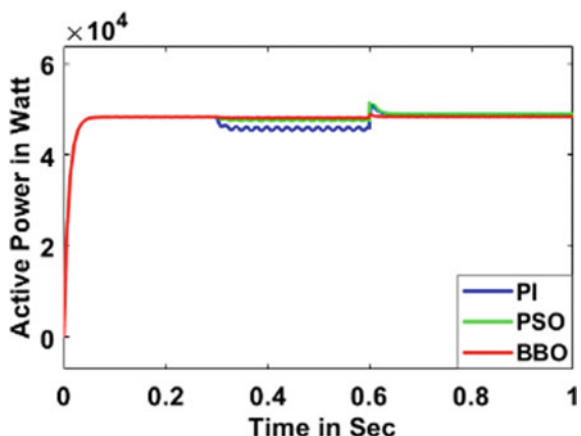
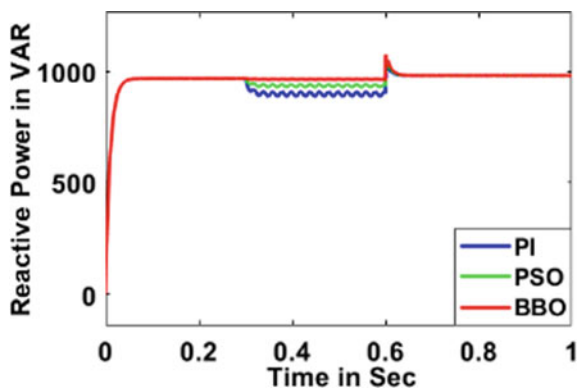
in Figs. 8, 9 and 10 respectively which show that even on the occurrence of the fault, the PI controller tuned by the BBO technique has fewer harmonics, minimum oscillations and better stability as compared to other controllers. Figures 11, 12 and 13 illustrates the THD, power factor and frequency of the MG system. From the simulated characteristics, it can be inferred that the THD is minimum, the power factor is better and frequency is maintained respectively for the suggested BBO-tuned PI controller. The grid voltage for BBO, PSO and PI methods are demonstrated in Figs. 14, 15 and 16 respectively. Similarly, Figs. 17, 18 and 19 manifest the grid current for BBO, PSO and PI control techniques. From the figures obtained, it can be noticed that the BBO-tuned PI controller compensates voltage sag efficaciously and almost maintains the grid voltage and the grid current constant.

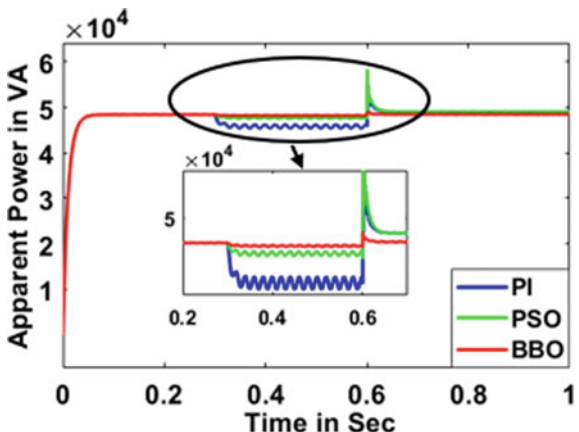
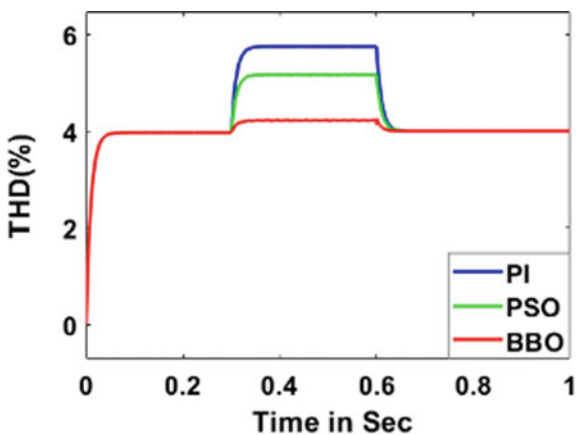
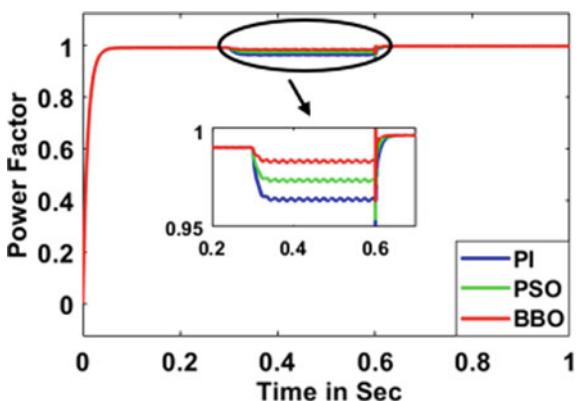
**Fig. 5** Terminal voltage



**Fig. 6** DC link voltage



**Fig. 7** Voltage deviation**Fig. 8** Active power**Fig. 9** Reactive power

**Fig. 10** Apparent power**Fig. 11** THD**Fig. 12** Power factor

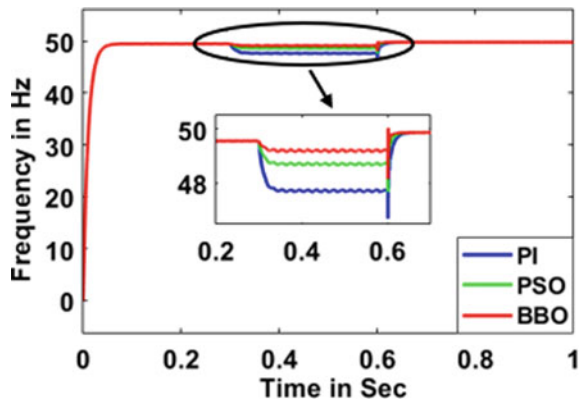


Fig. 13 Frequency

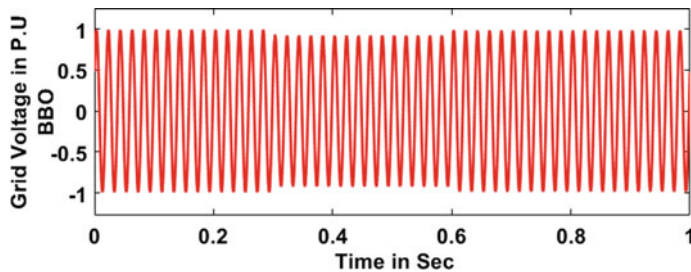


Fig. 14 Grid voltage (BBO)

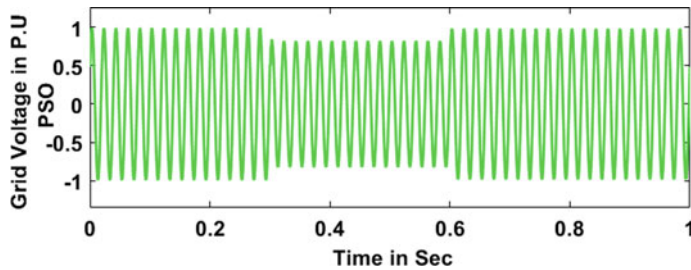


Fig. 15 Grid voltage (PSO)

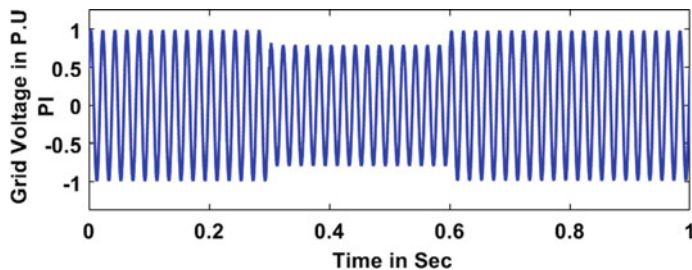


Fig. 16 Grid voltage (PI)

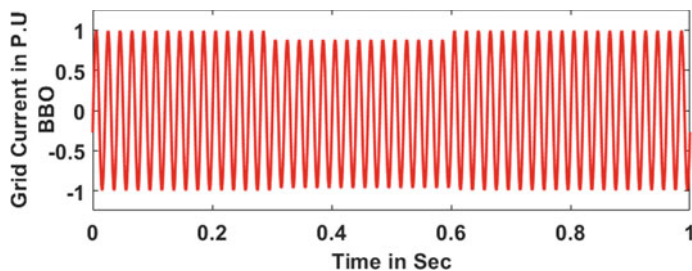


Fig. 17 Grid current (BBO)

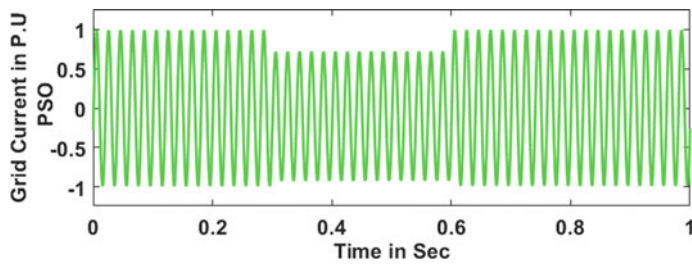


Fig. 18 Grid current (PSO)

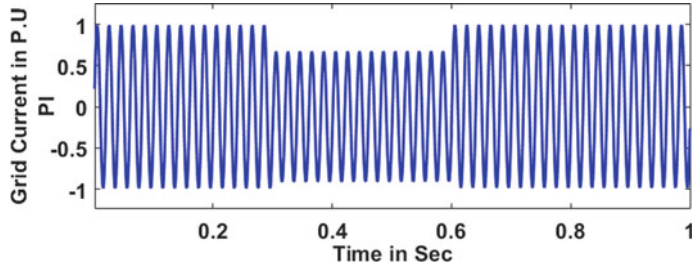


Fig. 19 Grid current (PI)

## 5 Analytical Comparision Among BBO, PSO and PI Control Methods

A comprehensive contrast of values found for different MG system parameters using proposed BBO, PSO and PI controller techniques have been summarized in Table 1 for easy study understanding of the readers.

**Table 1** Comparative study of all system parameters for proposed BBO, PSO and PI methods

System parameters	Type of controllers					
	PI		PSO		BBO	
PI controller gains	$K_p$	$K_i$	$K_p$	$K_i$	$K_p$	$K_i$
	0.087	0.0032	0.323	0.0073	0.618	0.0091
Terminal voltage (V)	325		356		386	
DC link voltage (V)	329		343		348	
Voltage deviation (P.U)	0.88		0.91		0.93	
Active power (W)	43,260		47,350		49,500	
Reactive power (Var)	950		988		997	
Apparent power (VA)	43,110		47,250		48,050	
THD (%)	5.98		5.17		4.10	
Power factor	0.965		0.975		0.985	
Frequency (Hz)	45.47		48.2		49.1	
Grid Voltage (P.U)	0.77		0.86		0.94	
Grid Current (P.U)	0.67		0.80		0.89	

## 6 Conclusion

The voltage sag enhancement of a grid-tied MicroGrid system comprising of PV and fuel cell has been discussed in this research paper. A BBO method has been proposed for efficient voltage sag compensation and harmonics elimination. The system is made using the MATLAB/Simulink software and various system characteristics such as terminal voltage, DC link voltage, voltage deviation, active power, reactive power, apparent power, THD, power factor, frequency, grid voltage and grid current have been obtained. The efficacy of the suggested BBO technique is verified by introducing a voltage sag (three-phase fault) for some duration. The simulation results of the traditional PI, PSO and proposed BBO technique are compared and contrasted both schematically as well as in tabulated form. A thorough study of the results found out indicates the superiority of the suggested BBO technique in potentially eliminating the harmonics, compensating the active and reactive power, lowering THD, improving power factor, maintaining terminal voltage, DC link voltage and frequency of the system constant on the occurrence of the fault. The overall system stability and reliability have been enhanced by the proposed BBO technique thus proving its application in real-time.

## References

1. Olabi AG, Abdelkareem MA (2022) Renewable energy and climate change. Renew Sustain Energy Rev 158:112111

2. Choudhury S (2020) A comprehensive review on issues, investigations, control and protection trends, technical challenges and future directions for Microgrid technology. *Int Trans Electr Energy Syst* 30(9):e12446
3. Choudhury S (2022) Review of energy storage system technologies integration to microgrid: types, control strategies, issues, and future prospects. *J Energy Storage* 48:103966
4. Elmetwally AH, Elde souky AA, Sallam AA (2020) An adaptive D-FACTS for power quality enhancement in an isolated microgrid. *IEEE Access* 8:57923–57942
5. Li D et al (2021) A comprehensive review of improving power quality using active power filters. *Electr Power Syst Res* 199:107389
6. Nair DR, Nair MG, Thakur T (2022) A smart microgrid system with artificial intelligence for power-sharing and power quality improvement. *Energies* 15(15):5409
7. Barik PK, Shankar G, Sahoo PK (2022) Investigations on split-source inverter based shunt active power filter integrated microgrid system for improvement of power quality issues. *J Electr Eng Technol* 1–23
8. Juman TA et al (2019) Salp swarm optimization algorithm-based controller for dynamic response and power quality enhancement of an islanded microgrid. *Processes* 7(11):840
9. Feng W et al (2016) Active power quality improvement strategy for grid-connected microgrid based on hierarchical control. *IEEE Trans Smart Grid* 9(4):3486–3495
10. Pradhan M, Mishra MK (2018) Dual \$ P \\$\\$ Q \\$ theory based energy-optimized dynamic voltage restorer for power quality improvement in a distribution system. *IEEE Trans Industr Electron* 66(4):2946–2955
11. Hossain E et al (2018) Analysis and mitigation of power quality issues in distributed generation systems using custom power devices. *IEEE Access* 6:16816–16833
12. Juman TA et al (2020) Swarm intelligence-based optimization techniques for dynamic response and power quality enhancement of AC microgrids: a comprehensive review. *IEEE Access* 8:75986–76001
13. Omar AI et al (2019) An improved approach for robust control of dynamic voltage restorer and power quality enhancement using grasshopper optimization algorithm. *ISA Trans* 95:110–129.
14. Choudhury S, Rout PK (2015) Adaptive fuzzy logic based MPPT control for PV system under partial shading condition. *Int J Renew Energy Res* 5(4):1252–1263
15. Choudhury S et al (2020) A novel control approach based on hybrid fuzzy logic and seeker optimization for optimal energy management between micro-sources and supercapacitor in an islanded microgrid. *J King Saud Univ-Eng Sci* 32(1):27–41
16. Choudhury S et al (2020) Improvement of performance and quality of power in grid tied SOFC through crow search optimization technique. In: 2020 5th International conference on communication and electronics systems (ICCES). IEEE
17. Choudhury S et al (2021) harmonic profile enhancement of grid connected fuel cell through cascaded h-bridge multi-level inverter and improved squirrel search optimization technique. *Energies* 14(23):7947
18. Choudhury S, Sahu S (2021) Robust State vector controller design for energy management scheme of a hybrid power system based on more-electric aircraft. In: 2021 International conference in advances in power, signal, and information technology (APSIT). IEEE
19. Mohanty M et al (2020) Application of salp swarm optimization for pi controller to mitigate transients in a three-phase soft starter-based induction motor. In: Advances in electrical control and signal systems. Springer, Singapore, pp 619–631
20. Jain M et al (2022) An overview of variants and advancements of PSO algorithm. *Appl Sci* 12(17):8392
21. Acharya DP et al (2020) Power quality improvement in a fuel-cell based micro-grid with shunt active power filter. *Int J Renew Energy Res (IJRER)* 10(3):1071–1082
22. Marini F, Walczak B (2015) Particle swarm optimization (PSO). A tutorial. *Chemom Intell Lab Syst* 149:153–165
23. Amponsah AA et al (2021) An enhanced class topper algorithm based on particle swarm optimizer for global optimization. *Appl Intell* 51(2):1022–1040

24. Li W, Wang G-G (2022) Elephant herding optimization using dynamic topology and biogeography-based optimization based on learning for numerical optimization. Eng Comput 38(2):1585–1613
25. Guo W et al (2017) A survey of biogeography-based optimization. Neural Comput Appl 28(8):1909–1926
26. Daneshyar SA, Charkari NM (2022) Biogeography based optimization method for robust visual object tracking. Appl Soft Comput 108802
27. Ma H et al (2017) Biogeography-based optimization: a 10-year review. IEEE Trans Emerging Top Comput Intell 1(5):391–407
28. Zhao F et al (2019) A two-stage differential biogeography-based optimization algorithm and its performance analysis. Expert Syst Appl 115:329–345

# Performance Comparisons of MPEDE-Based Integer and Fractional-Order PID Controllers for a Cruise Control System



**Mou Das Mahapatra, Shibendu Mahata, Ritu Rani De, Rajani Kanta Mudi,  
and Chanchal Dey**

**Abstract** An effective technique for the optimal design of fractional-order proportional-integral-derivative (FOPID) controller in a cruise control application is presented. The minimization of step response error is formulated as an objective function. Such a proposal avoids evaluating the transient and steady-state response parameters at run-time of the optimizer. The optimization is carried out using a multi-population ensemble differential evolution (MPEDE) method. Comparisons with a classical PID controller also designed using MPEDE demonstrate the faster response time for the FOPIP controlled system. The superiority of the proposed fractional controller over those of the recently reported models is demonstrated using various performance metrics.

**Keywords** Cruise control system · Fractional-order controller · Multi-population ensemble differential evolution · Optimization · PID controller

---

M. D. Mahapatra (✉) · S. Mahata · R. R. De

Department of Electrical Engineering, Dr. B. C. Roy Engineering College, Durgapur, India

e-mail: [mou.dasmahapatra@bcrec.ac.in](mailto:mou.dasmahapatra@bcrec.ac.in)

S. Mahata

e-mail: [shibendu.mahata@bcrec.ac.in](mailto:shibendu.mahata@bcrec.ac.in)

R. R. De

e-mail: [riturani.de@bcrec.ac.in](mailto:riturani.de@bcrec.ac.in)

R. K. Mudi

Department of Instrumentation and Electronics Engineering, Jadavpur University, Kolkata, India

C. Dey

Department of Applied Physics, University of Calcutta, Kolkata, India

e-mail: [cdaphy@caluniv.ac.in](mailto:cdaphy@caluniv.ac.in)

## 1 Introduction

The traffic situation is worsening day-by-day due to ever-increasing number of vehicles. High traffic results in increased fuel consumption, air pollution, and probability of occurrence of accidents. Automobile manufacturers are interested in exploring numerous strategies to develop self-driven vehicles that optimize the usage of highways and provide traffic information. The cruise control system (CCS) emerged in the 1950s as an automatic vehicle longitudinal control system that facilitates hands-off and feet-off driving system along with an ability to keep track of the preceding automobile [1]. With the help of CCS, a vehicle moves at a desired reference speed when the lane is traffic free but maintains a safe distance from the preceding vehicle if they are close, by controlling the vehicle's speed. CCS has a positive impact on environment, crowd control, fuel consumption, and passenger safety.

Continuous refinements and modifications have been done over the years to upgrade the CCS for achieving better performances [2]. Many researchers have introduced efficient control methods for the CCS, which include the conventional proportional-integral-derivative (PID) controller [3], linear quadratic regulator controller [4], sliding mode controller [5], fuzzy logic controller [6], neural network [7], model predictive control [8], etc. Introducing the PID controller into CCS to reduce string instabilities is of great practical significance. Conventional PID parameters are tuned by the Ziegler-Nichols technique, root-locus method [9], etc. Tuning of PID controller for cruise control application using metaheuristics such as battle royale optimization [10], hybridization of atom search optimization and Nelder-Mead simplex method [11], genetic algorithm, memetic algorithm, and mesh adaptive direct search method [12] has been reported. Ant lion optimization and an improved arithmetic optimizer have been applied to design the PID controller for Bode's ideal transfer function-based CCS [13, 14]. A well-tuned optimized robust CCS that efficiently takes care of load disturbance rejection for an electric vehicle was reported in [15].

The applicability of fractional-order controllers for performance enhancement of CCS has been explored in recent years. Recall that a fractional-order PID (FOPID) controller is modeled as per (1) [16].

$$G_C(s) = \frac{U(s)}{E(s)} = k_p + \frac{k_i}{s^\lambda} + k_d s^\mu \quad (1)$$

where  $k_p$ ,  $k_i$ , and  $k_d$  are the well-known gain terms;  $\lambda$  and  $\mu$  are the fractional integral and differentiator orders, respectively;  $E(s)$  is an error signal fed to controller;  $U(s)$  is the output of FOPID controller;  $\lambda$  and  $\mu$  are non-integer values that lie between 0 and 2. A FOPID controller-based feedback system may attain better time-domain response and disturbance rejection. On proper tuning of these controllers, sensitivity, robustness, and noise filtration are also expected to improve [17]. A hybrid fractional controller was designed in [18] to demonstrate the effectiveness of an adaptive low-speed control strategy. An optimal FOPID controller for an automobile CCS was

also developed using pole placement technique along with the optimization being carried out using MATLAB's fmincon solver [19]. The Harris Hawks optimization (HHO) algorithm helped in designing an improved FOPID controller [20].

In this paper, an evolutionary approach using a multi-population ensemble differential evolution (MPEDE) is presented to design the FOPID controller that enhances the time-domain performance of the CCS. Unlike [20] where the objective function comprised of various parameters such as the maximum overshoot ( $M_p$ ), rise time ( $t_r$ ), settling time ( $t_s$ ), and steady-state error ( $e_{ss}$ ), the proposed fitness function is based on reduction of closed-loop step-response error. It is demonstrated that iterative minimization of the proposed objective function using MPEDE significantly improves both the transient and steady-state behaviors of CCS as compared to the techniques reported in the recent literature. An integer-order PID (IOPID) controller is also designed using MPEDE to demonstrate the benefits of the fractional controller for solving the CCS design problem.

## 2 Vehicle Cruise Control System

Cruise control is a speed regulating system that adjusts the cruise speed based on driver's command given as a reference input. Newton's second law is applied to model the vehicle's nonlinear motion. The total longitudinal force  $F$  applied on a vehicle is expressed in terms of acceleration as per (2).

$$\sum F = Ma = M\dot{v} \quad (2)$$

where  $M$  represents the mass of vehicle with passenger,  $a$  is the vehicle's acceleration, and  $v$  is its velocity.

The engine force or drive force ( $F_d$ ) is yielded by the burning of fuel injected in the vehicle. The total force acting on the vehicle is the algebraic summation of drive force ( $F_d$ ), the aerodynamic drag force ( $F_a$ ), and the gravitational force ( $F_g$ ). The force balance equation may be represented as per (3) [19].

$$F_d - F_a - F_g = M\dot{v} \quad (3)$$

The dynamical model of a vehicle cruise control is shown in Fig. 1 [21], where  $C_a$ ,  $v_w$ ,  $\theta$ , and  $g$  are, respectively, the aerodynamic drag coefficient, wind gust speed, slope angle of the road, and gravitational constant. Adjusting the actuator movement on the pedal allows the vehicle to run at a desired constant speed. To derive the system's model, design parameters are used from [20]. The linear model of the CCS ignores the disturbance terms. Thus, considering no wind gust speed and slope angle of the road, the linear plant dynamics may be represented by (4) and (5).

$$\dot{v} = \frac{1}{M}(F_d - C_a v^2) \quad (4)$$

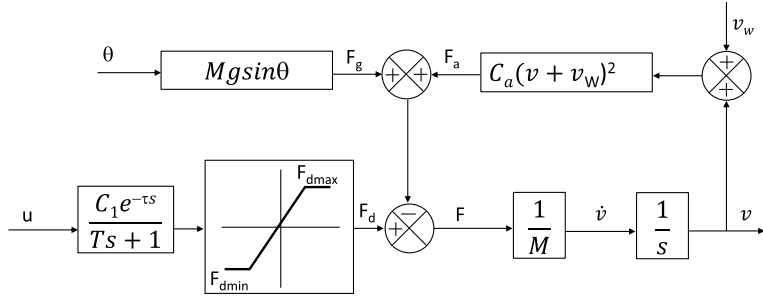


**Fig. 1** Model of CCS [21]

$$\dot{F}_d = \frac{1}{T} [C_1 u(t - \tau) - F_d] \quad (5)$$

Based on the set-points in (4)–(5), it follows that

$$\delta \dot{v} = \frac{1}{M} (-2C_a v \delta v + \delta F_d) \quad (6)$$

$$\delta \dot{F}_d = \frac{1}{T} [C_1 \delta u(t - \tau) - \delta F_d] \quad (7)$$

Taking Laplace transform of (6) and (7) and considering all initial conditions as zero, (8) and (9) may be obtained.

$$s \Delta V(s) = \frac{1}{M} [-2C_a v \Delta V(s) + \Delta F_d(s)] \quad (8)$$

$$s \Delta F_d(s) = \frac{1}{T} [C_1 \Delta U(s) e^{-\tau s} - \Delta F_d(s)] \quad (9)$$

Eliminating  $\Delta F_d(s)$ , the linearized CCS plant transfer function may be approximated as per (10).

$$\frac{\Delta V(s)}{\Delta U(s)} = \frac{C_1 / (MT\tau)}{(s + 2C_a v/M)(s + 1/T)(s + 1/\tau)} \quad (10)$$

Substituting the system parameter values reported in [20] in (10) and assuming a nominal speed of 30 kmph, the plant model is obtained as per (11).

$$G_P(s) = \frac{2.4767}{(s + 0.0476)(s + 1)(s + 5)} \quad (11)$$

### 3 Proposed Method

#### 3.1 Objective Function Formulation

An optimal procedure that efficiently reduces the step response error of the closed-loop CCS is proposed here. The controller (both classical and fractional) parameters are optimally achieved by minimizing the objective function given in (12).

$$f = \sum_{t=t_i}^{t_f} |c(t) - v(t, X)| \quad (12)$$

where  $c(t)$  denotes the unit step input;  $v(t)$  is the system output;  $t_i$  and  $t_f$  denote the initial and final time instants within which the error minimization is carried out. The decision variables are denoted in the form of  $X = [k_p \ k_i \ k_d]$  or  $X = [k_p \ k_i \ k_d \ \lambda \ \mu]$  for the IOPID and FOPID controllers, respectively. The problem dimension is 3 and 5, respectively, for designing the traditional and fractional controllers. Unlike [20], the proposed objective function does not require evaluating  $M_P$ ,  $e_{ss}$ ,  $t_r$ , and  $t_s$ . For this work,  $t_i$  and  $t_f$  are set as 0 s (s) and 10 s, respectively, with 1001 linearly spaced sample points in the interval  $[t_i, t_f]$ .

#### 3.2 Algorithm Employed

Metaheuristics have demonstrated promising performances in solving fractional-order controller-related problems [22–24]. Differential evolution (DE) is a metaheuristic global-search optimizer that has attracted immense attention in the evolutionary computing community due to its efficiency in solving diverse real-world problems. Research results in recent years have revealed that incorporation of ensemble strategies at both the algorithmic and parameter levels in the DE may further improve its problem solving capability [25].

In this paper, the MPEDE algorithm [26] is applied for designing the proposed controllers to solve the cruise control problem. Ensemble features are integrated at the parameter level in MPEDE, wherein both the population and the mutation strategies are ensembled. Three different mutation techniques are employed in MPEDE. This algorithm also divides the entire population into four parts (three indicator and single reward sub-population). Each indicator sub-population is associated with a mutation process. Over a certain number of generations, the best performing strategy is determined, which receives the reward sub-population for the next sequence of generations. In addition, adaptive mechanisms for the parameter strategies are also introduced in MPEDE. This work used the same values of control parameters for MPEDE as reported in [26]. The termination condition of the optimization rou-

tine was set as 30,000 and 50,000 function evaluations for the IOPID and FOPID controller design, respectively. The best values of controller parameters are obtained after performing 25 independent algorithmic trial runs.

## 4 Simulation Results

All the simulations in this paper are carried out in MATLAB (R2014a). The boundary limits of the design parameters  $k_p$ ,  $k_i$ , and  $k_d$  for both the proposed controllers which are set as 0 and 10, respectively. For the two additional parameters ( $\lambda$ ,  $\mu$ ) of the fractional controller, the limits lie between 0 and 2. Time-domain performance accuracy for the proposed system is quantified using well-known integral error metrics (IAE, ISE, ITAE) [27]; the frequency-domain performance measures include the gain margin (GM), phase margin (PM), gain crossover frequency ( $\omega_{cg}$ ), and phase crossover frequency ( $\omega_{cp}$ ).

### 4.1 Performance Comparisons Between the Proposed IOPID and FOPID Controllers

The transfer functions of the MPEDE-based proposed IOPID and FOPID controllers are given by (13) and (14), respectively.

$$G_C(s) = 3.7981 + \frac{0.1728}{s} + 3.7176s \quad (13)$$

$$G_C(s) = 5.4708 + \frac{0.7995}{s^{0.5561}} + 6.0001s^{1.0770} \quad (14)$$

The IAE, ISE, and ITAE indices yielded by the proposed PID controlled CCS are 0.5621, 0.3732, and 0.7848, respectively, whereas the proposed FOPID-based control system attains 0.4168, 0.2520, and 0.2964, respectively. Thus, smaller time response errors are achieved using FOPID system. The time responses for both the proposed controllers based system are compared in Fig. 2. The speed of response of the FOPID controlled system is faster as compared to its classical counterpart ( $t_r = 1.012$  s vs. 1.602 s).

Comparisons about GM, PM,  $\omega_{cg}$ , and  $\omega_{cp}$  reveal that the IOPID-based system yields  $7.8430 \times 10^9$ ,  $71.5706^\circ$ ,  $2.6873 \times 10^5$  radians per second (rad/s), and 1.7291 rad/s, respectively. The FOPID controller-based system attains GM =  $\infty$ , PM =  $71.3595^\circ$ ,  $\omega_{cg} = \infty$  rad/s, and  $\omega_{cp} = 2.6371$  rad/s. Since higher the GM and PM, better the margin of stability, therefore, the fractional controller system achieves superior GM and similar PM characteristics compared to the IOPID controller system.

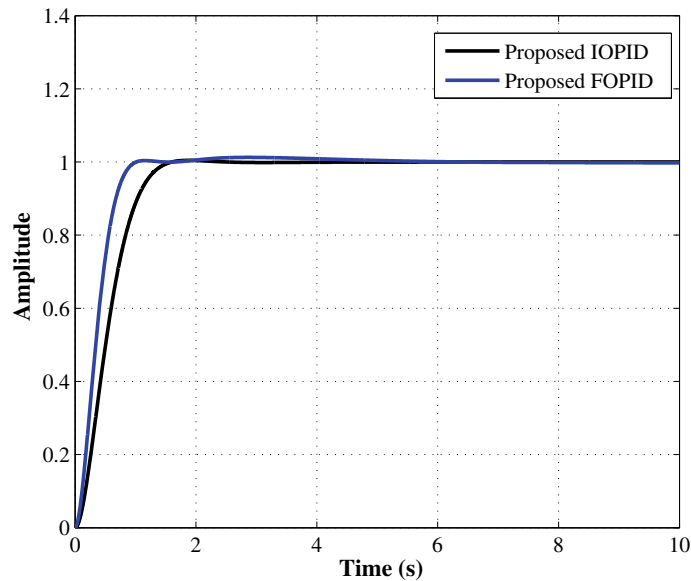


**Fig. 2** CCS step response comparison plots employing the proposed IOPID and FOPID ( $PI^{\lambda}D^{\mu}$ ) controllers

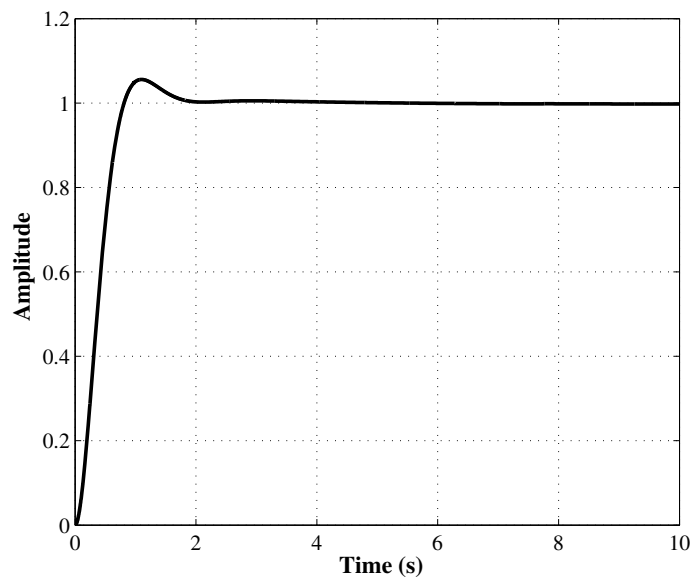


**Fig. 3** CCS step response exhibiting an overshoot for the  $PI^{\lambda}D$  controller

Note that the value of  $\mu$  for the FOPI controller defined in (14) is 1.0770, which is close to 1. Therefore, it may be worth investigating the performance of the fractional controller when  $\mu$  is fixed as 1; thus, leading to a  $PI^\lambda D$  controller instead of the  $PI^\lambda D^\mu$  controller shown in (14). The step response of the  $PI^\lambda D$  controller-based closed-loop system is shown in Fig. 3. The system response now exhibits a substantial overshoot ( $M_P = 5.6\%$ ), which was not obtained using the  $PI^\lambda D^\mu$  controller. This behavior substantiates the necessity of employing the fractional derivative term ( $\mu = 1.0770$ ) instead of the integer value ( $\mu = 1$ ).

## 4.2 Comparison with the Literature

Two recently reported FOPI controllers designed for the CCS are considered for comparison purposes. The transfer function of the FOPI controller published in [19], which is based on a dominant pole placement method followed by optimization using the fmincon solver, is given by (15).

$$G_C(s) = 3.4187 + \frac{0.2339}{s^{0.9968}} + 3.7912s^{0.9973} \quad (15)$$

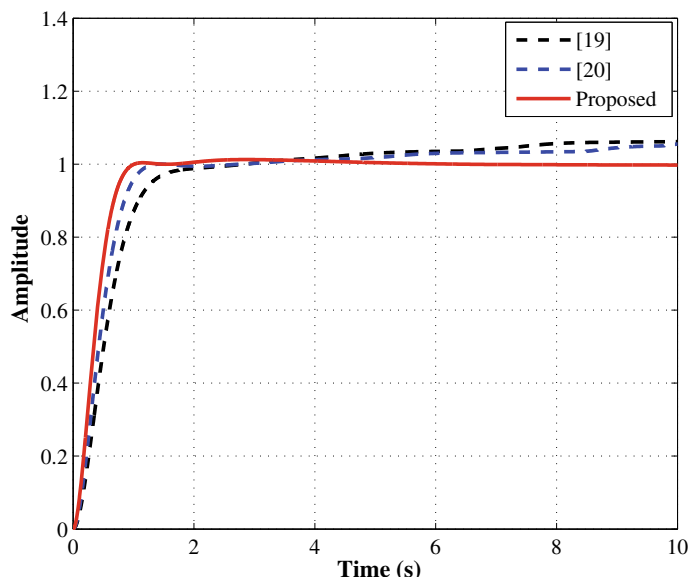


**Fig. 4** CCS step response comparison plots based on the proposed and reported FOPI controllers

**Table 1** Performance comparisons of the proposed FOPID-based CCS with the recently published literature

Reference	IAE	ISE	ITAE	GM	PM (°)	$\omega_{cg}$ (rad/s)	$\omega_{cp}$ (rad/s)
[19]	0.6539	0.3768	1.3380	$1.58 \times 10^5$	74.5304	$1.21 \times 10^3$	1.7061
[20]	0.4818	0.3135	0.7100	$\infty$	71.1784	$\infty$	2.1065
Proposed	0.4168	0.2520	0.2964	$\infty$	71.3595	$\infty$	2.6371

The HHO algorithm-based fractional controller reported in [20] is defined by (16).

$$G_C(s) = 4.4816 + \frac{0.2261}{s^{0.9523}} + 4.6939s^{1.0217} \quad (16)$$

The step response plot of the designed FOPID controlled CCS is compared with the reported ones in Fig. 4. The response time of the model published in [19] is larger compared to the other two. Although the rise time for systems based on the proposed and HHO-based [20] controllers is comparable, the deviation in step response between 4 s and 10 s for both [19, 20] may be observed. Hence, the proposed fractional controller helps to achieve the steady-state much faster than the reported literature. The lower error in the time-domain characteristic of the proposed system compared to [19, 20] may be confirmed from the IAE, ISE, and ITSE metrics shown in Table 1. The proposed system's frequency response performances are comparable with [20]. This is expected since the present study did not include frequency-domain performance specifications in the objective function.

## 5 Conclusions

Design of an optimal FOPID controller for a linearized cruise control system is presented in this paper. The system step response error minimization is carried out using a state-of-the-art variant of differential evolution technique. For comparison purposes, a PID controller is also designed using the MPEDE algorithm. Results reveal superior response time of the proposed FOPID controller over the IOPID controller ( $t_r = 1.012$  s vs. 1.602 s). Comparisons with the recently reported literature highlight significantly lower IAE, ISE, and ITAE along with faster settling to the steady-state value for the proposed FOPID controller system.

## References

1. He Y, Ciuffo B, Zhou Q, Makridis M, Mattas K, Li J, Xu H (2019) Adaptive cruise control strategies implemented on experimental vehicles: a review. IFAC-PapersOnLine 52(5):21–27
2. Yu L, Wang R (2022) Researches on adaptive cruise control system: a state of the art review. Proc Inst Mech Eng Part D: J Autom Eng 236(2–3):211–240
3. Chaturvedi S, Kumar N (2021) Design and implementation of an optimized PID controller for the adaptive cruise control system. IETE J Res 23:1–8
4. Al-Gabalawy M, Hosny NS, Aborisha AHS (2021) Model predictive control for a basic adaptive cruise control. Int J Dynam Control 9:1132–1143
5. Ganji B, Kouzani AZ, Khoo SY, Shams-Zahraei M (2014) Adaptive cruise control of a HEV using sliding mode control. Expert Syst Appl 41(2):607–615
6. Prabhakar G, Selvaperumal S, Nedumal Pugazhenthi P (2019) Fuzzy PD plus I control-based adaptive cruise control system in simulation and real-time environment. IETE J Res 65(1):69–79
7. Tran HD, Yang X, Manzanas Lopez D, Musau P, Nguyen LV, Xiang W, Bak S, Johnson TT (2020) NNV: the neural network verification tool for deep neural networks and learning-enabled cyber-physical systems. In: Proceedings of 2020 international conference on computer aided verific. Springer, pp 3–17
8. Nie Z, Farzaneh H (2020) Adaptive cruise control for eco-driving based on model predictive control algorithm. Appl Sci 10(15):5271
9. Prasad MM, Inayathullah MA (2021) Root locus approach in design of PID controller for cruise control application. J Phy Conf Ser 2115(1):012023
10. Şahin AK, Akgul T, Cakir O (2021) Battle royale optimization based PID controller design for vehicle cruise control system. In: Proceedings of 5th international conference on advances in natural and applied science, pp 181–191
11. Izci D, Ekinci S (2022) A novel hybrid ASO-NM algorithm and its application to automobile cruise control system. In: Proceedings of 2nd international conference on artificial intelligence advances applications. Springer, pp 333–343
12. Naranjo JE, Serradilla F, Nashashibi F (2020) Speed control optimization for autonomous vehicles with metaheuristics. Electronics 9(4):551
13. Pradhan R, Majhi SK, Pradhan JK, Pati BB (2018) Antlion optimizer tuned PID controller based on Bode ideal transfer function for automobile cruise control system. J Industr Info Integr 1(9):45–52
14. Izci D, Ekinci S, Kayri M, Eker E (2022) A novel improved arithmetic optimization algorithm for optimal design of PID controlled and Bode's ideal transfer function based automobile cruise control system. Evolving Syst 13(3):453–468
15. Diba F, Arora A, Esmailzadeh E (2014) Optimized robust cruise control system for an electric vehicle. Syst Sci Control Eng Open Access J 2(1):175–182
16. Podlubny I (1999) Fractional-order systems and  $P I^\lambda D^\mu$ -controllers. IEEE Trans Autom Control 44:208–214
17. Teplyakov A, Alagoz BB, Yeroglu C, Gonzalez E, Hosseini SH, Petlenkov E (2018) FOPID controllers and their industrial applications: A survey of recent results. IFAC-PapersOnLine 51(4):25–30
18. Hosseini SH, Tejado I, Milanés V, Villagrá J, Vinagre BM (2014) Experimental application of hybrid fractional-order adaptive cruise control at low speed. IEEE Trans Control Syst Technol 22(6):2329–2336
19. Pradhan R, Pati BB (2018) Optimal FOPID controller for an automobile cruise control system. In: Proceedings of 2018 IEEE international conference on recent innovations in electrical electronics and communication engineering (ICRIEECE), pp 1436–1440
20. Izci D, Ekinci S (2021) An efficient FOPID controller design for vehicle cruise control system using HHO algorithm. In: Proceedings of 2021 3rd IEEE international congress on human-computer interaction, optimization robotic applications (HORA), pp 1–5

21. Lewis PH, Houghton Y (1997) Basic control systems engineering. Prentice Hall. Upper Saddle River, NJ, US, United States
22. Mahata S, Saha SK, Kar R, Mandal D (2017) Optimal and accurate design of fractional order digital differentiator—an evolutionary approach. *IET Signal Process* 11(2):181–196
23. Mahata S, Saha SK, Kar R, Mandal D (2018) Optimal design of wideband fractional order digital integrators using symbiotic organisms search algorithm. *IET Circuits Devices Syst* 12(4):362–373
24. Mahata S, Saha SK, Kar R, Mandal D (2019) A metaheuristic optimization approach to discretize the fractional order laplacian operator without employing a discretization operator. *Swarm Evol Comput* 44:534–545
25. Pant M, Zaheer H, Garcia-Hernandez L, Abraham A (2020) Differential evolution: a review of more than two decades of research. *Eng Appl Artif Intel* 90:103479
26. Wu G, Mallipeddi R, Suganthan PN, Wang R, Chen H (2016) Differential evolution with multi-population based ensemble of mutation strategies. *Inf Sci* 329:329–345
27. Mahata S, Herencsar N, Alagoz BB, Yeroglu C (2021) A robust frequency-domain-based order reduction scheme for linear time-invariant systems. *IEEE Access* 9:165773–165785

# Novel CMOS 1-Digit BCD-Adder Correction Circuit



Shatabhisa Goswami, Ananya Mandal, Aishikée Mishra, Joyoshri Goswami, and Aloke Saha

**Abstract** BCD (Binary Coded Decimal)-adder finds wide applications in favor of state-of-the-art decimal arithmetic in order to interface with binary computation. Conventionally, RCA (Ripple Carry Adder) is the building block used to generate the corrected base-10 output after two 1-digit BCD addition. The present study unfolds a novel correction strategy for speed-power efficient BCD addition. Proposed idea eliminates the complex full-adder logic cell and optimizes critical path carry propagation delay to achieve overall PDP (Power-Delay-Product) decrease with respect to conventional strategy. Proposed BCD-correction circuit is designed on 32 nm CMOS technology using BSIM4 device model and 0.9 V supply voltage at 27 °C temperature. Proposed circuit is validated and evaluated through extensive T-Spice simulations by applying all possible custom test patterns. The evaluated speed-power response is then compared with its conventional counterpart in identical operating condition and 100 MHz input to benchmark.

**Keywords** Binary Coded Decimal (BCD)-Adder · Number system · Pass Transistor Logic (PTL) · Power-Delay-Product (PDP) · 2:1 Multiplexer

## 1 Introduction

Binary is the well-suited and worldwide recognized radix-system to implement digital circuit/system mainly because of inherent stable ON-OFF conditions of physical semiconductor devices [1, 2]. However, decimal (base-10) is the conventional number system for commercial (i.e., banking, Internet-based, etc.) use [1] and hence, developing efficient decimal computing system is at the center of attraction for research in recent time [3, 4]. Binary Coded Decimal (BCD) [3–12] is applied to provide human interface between base-2 (binary) and base-10 (decimal)

---

S. Goswami · A. Mandal · A. Mishra · J. Goswami · A. Saha (✉)

Department of Electronics and Communication Engineering, Dr. B. C. Roy Engineering College, Durgapur, India

e-mail: [saha81@gmail.com](mailto:saha81@gmail.com)

number system. Conventionally, Ripple Carry Adder (RCA) is applied to generate the corrected BCD output after two 1-digit BCD addition. Circuit complexity along with long critical path delay is the matter of concern for conventional correction circuit structure.

The present study reveals a novel circuit strategy to generate the corrected BCD output with improved speed-power efficiency as compared to its conventional counterpart. In proposed idea, a fixed value “0110” (i.e., “6”) is added to the 4-bit binary input if the input is more than “1001” (i.e., “9”). Otherwise, the same input will pass to the output without any modification. PTL (Pass Transistor Logic)-based 2:1 multiplexer is exploited at the output end to pass the correct result to the output. A control bit is generated as per 4-bit input value by applying conventional idea for connecting proper input to the output through 2:1 multiplexer. Proposed circuit is optimized by considering fixed value (“0110”) addition with the input if the control-bit value is “1” (4-bit input is more than “1001”). The complete circuit is designed using E-MOS device on 32 nm standard CMOS technology using BSIM4 device model with 0.9 V rail-to-rail supply at 27 °C. The T-Spice transient response, considering every possible test combination, validates the functionality proposed circuit. Evaluation with respect to speed-power response as compared to its conventional counterpart revealed the novelty of proposed design.

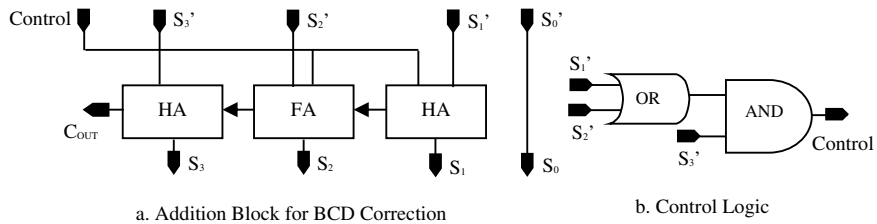
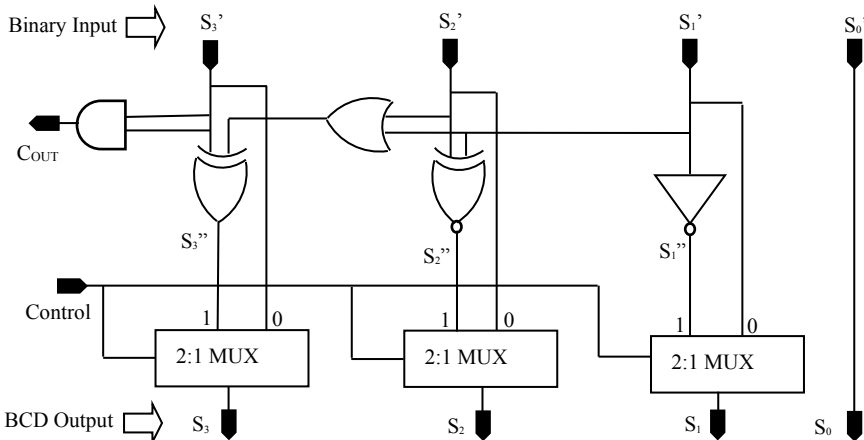
Further parts of the manuscript are organized as: Proposed idea to generate the corrected BCD result is discussed in Sect. 2. Section 3 presents the front-end circuit design along with T-Spice simulation outcome of proposed circuit. Finally, the paper is concluded in Sect. 4.

## 2 Proposed Correction Strategy for BCD-Addition

The conventional correction circuitry for two single-digits BCD-Addition are presented in Fig. 1. The RCA-based addition block and the control-logic for the process is presented in Fig. 1a and in Fig. 1b correspondingly. The 4-bit binary input to the circuit is denoted by  $(S_3' S_2' S_1' S_0')_2$  in Fig. 1a, whereas  $(C_{\text{OUT}} S_3 S_2 S_1 S_0)_{\text{BCD}}$  indicates the corresponding BCD output. The conventional circuit shown in Fig. 1 suffers from long channel critical path delay as well as high power dissipation along with large circuit complexity.

Proposed speed-power efficient correction circuit for BCD-Addition is explained below with the respective logic diagram depicted in Fig. 2.

- Consider 4-bit binary input to the proposed correction circuit (Fig. 2) is  $(S_3' S_2' S_1' S_0')_2$  and  $(C_{\text{OUT}} S_3 S_2 S_1 S_0)_{\text{BCD}}$  is the corresponding BCD output. Here,  $S_3'$  and  $S_0'$  denote the MSB and LSB of the input whereas  $C_{\text{OUT}}$ ,  $S_3$ , and  $S_0$  indicate Carry-out, MSB, and LSB of the BCD output.
- If the 4-bit input is more than “9 (i.e., 1001)”, a fixed value of “6 (i.e., 0110)” will be added with the input in order to generate the corrected BCD result and the corresponding control bit is “1”. Otherwise, the output will follow the input

**Fig. 1** Conventional correction circuit for BCD addition**Fig. 2** Proposed BCD-Adder correction circuit

directly without any modification with control bit value “0”. Control-bit for the circuit is generated as per conventional strategy presented in Fig. 1b. In proposed scheme, PTL-based 2:1 MUX is used at the output end to select and pass the correct result to the output based on control-bit input.

- Consider the output after fixed value (i.e., 0110) addition with the input  $(S_3', S_2', S_1', S_0')_2$  is  $(S_3'', S_2'', S_1'', S_0'')_2$ , and the result will be connected to the output if the corresponding control bit is “1”. Otherwise, no modification to the input will take place and the original input will pass to the output through 2:1 MUX (i.e., control bit is “0”).
- Proposed hardware optimization strategy for fixed value (i.e., 0110) addition can be explained through optimized I/O relation presented in Table 1 and in Table 2 for  $S_1''$  and  $S_2''$ , respectively. Here,  $S_0$  output is always same as  $S_0'$  input as shown in Fig. 2.
- As from Table 1, the bulky half-adder of Fig. 1a can be replaced by simple inverter to generate  $S_1''$  output after fixed value (i.e., “1”) addition with input bit  $S_1'$  and the corresponding carry1 output will simply follow  $S_1'$  input.

**Table 1** Optimized I/O relation for  $S_1''$ 

I/P $S_1'$	Fixed I/P		SUM $S_1''$	Carry1
0	1		1	0
1	1		0	1

**Table 2** Optimized I/O relation for  $S_2''$ 

I/P $S_2'$	Carry I/P	Fixed I/P	SUM $S_2''$	Carry2
0	0	1	1	0
0	1	1	0	1
1	0	1	0	1
1	1	1	1	1

- Again, as per optimized I/O relation presented in Table 2 for  $S_2''$ , the Full-adder of Fig. 1a can be replaced by simple NOR and OR-gate to generate  $S_2''$  and Carry2, respectively. The MSB output  $S_3''$  and the carry output  $C_{\text{OUT}}$  can be generated by adding input  $S_3'$  with Carry2 from previous stage using half-adder as shown in Fig. 2.

The front-end schematic along with result analysis and comparative study with its conventional counterpart is presented in Sect. 3.

### 3 The Circuit Performance and Benchmarking

The proposed BCD-correction circuit is designed using BSIM4 parameter model on 32-nm CMOS technology with 0.9 V supply voltage at 27 °C temperature. Custom input with all possible test pattern has been applied to validate the proposed BCD-encoder through extensive T-Spice simulations. The transient response of proposed BCD-correction circuit with 100 MHz test input is presented in Fig. 3 and the respective circuit schematic is shown in Fig. 4.

The power-delay report of designed circuit is compared with its usual counterpart (shown in Fig. 1), and the comparative outcome is shown in Table 3. In order to have fair comparison, both the structures (proposed and conventional) are designed and compared in identical operating conditions (as mentioned in Table 3) considering same sets of 100 MHz test input at 27 °C temperature.

As per comparative study explored in Table 3, the proposed circuit can be suitable for 38.09% average power, 31.25% delay, and 57.44% Power-Delay-Product (PDP) reduction as compared to its conventional counterpart when compared to aforementioned operating condition. As per investigation, the proposed scheme can be an effective choice in order to generate the corrected BCD output for high-speed low-power BCD arithmetic.

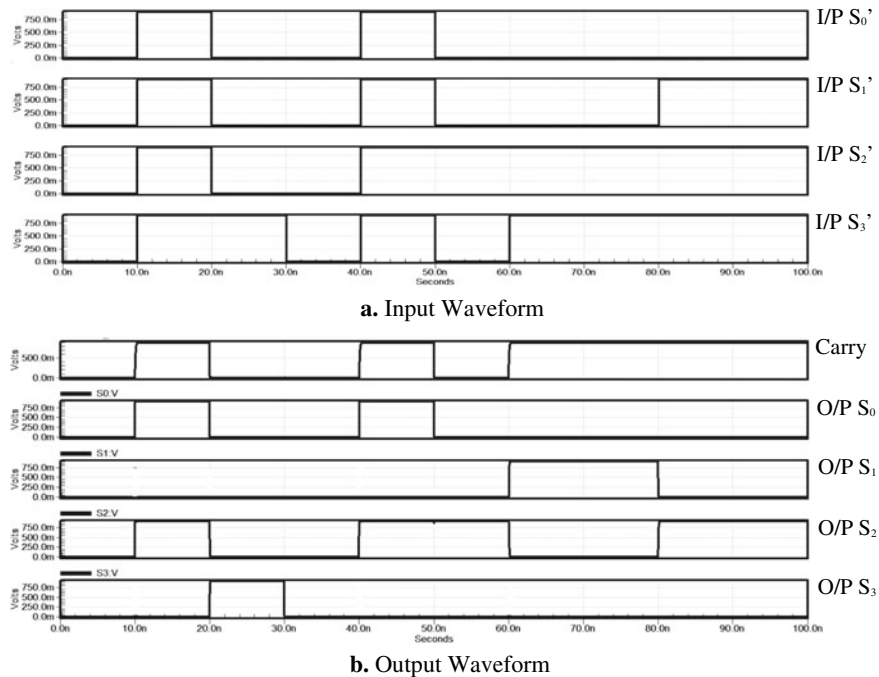


**Fig. 3** Transient response of proposed BCD-Adder correction circuit

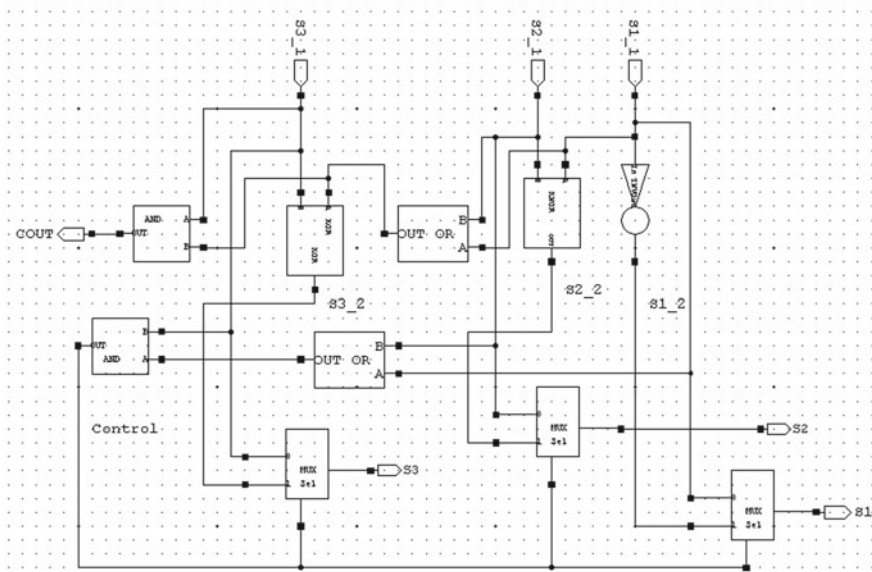


**Fig. 4** Front-end schematic of proposed BCD-Adder correction circuit

**Table 3** Speed-power comparative study with conventional counterpart

Device model: BSIM4				
Tech. 32 nm Standard CMOS				
Supply: 0.9 V				
Temperature: 27 °C				
BCD-correction Circuit	Avg. Power@ 100 MHz ( $\mu\text{W}$ )	Delay (ps)	PDP (J) @ 100 MHz	Norm. (PDP)
Conventional (Fig. 1)	3.57	68.63	$245.01 \times 10^{-18}$	1
Proposed (Fig. 2)	2.21	47.18	$104.27 \times 10^{-18}$	0.43

## 4 Conclusion

A novel circuit strategy to generate the corrected BCD output is explored in this work. Proposed circuit is optimized by adding fixed value “6” (i.e., 0110) with the input if the input value is more than “9” (i.e., 1001). If the input is not more than “9” (i.e., 1001) the output will be connected to the input without any modification. A PTL (Pass Transistor Logic) based 2:1 Multiplexer is applied at the output to pass the correct result to the output. The full circuit is designed using BSIM4 device model on 32-nm Standard CMOS technology with 0.9 V supply at 27 °C nominal temperature. The speed-power response of the designed circuit is evaluated through extensive T-Spice simulations by applying all possible custom test patterns and compared with its conventional counterpart. As per study, the proposed idea can be considered to achieve speed-power efficiency in BCD-arithmetic operation.

## References

1. Saha A, Singh RK, Pal D (2022) Pair-Wise Urdhava-Tiryagbhya (UT) vedic ternary multiplier. *Microelectron J* 119:105318
2. Saha A, Singh ND, Pal D (2021) Efficient ternary comparator on CMOS technology. *Microelectron J* 109:105005
3. Chu Z, Li Z, Xia Y, Wang L, Liu W (2021) BCD Adder designs based on three-input XOR and majority gates. *IEEE Trans Circuits Syst II Express Briefs* 68(6):1942–1946
4. Hossain N, Hossain N, Sworna ZT, Haque MU (2019) A fast and compact binary to BCD converter circuit. In: 2019 IEEE international WIE conference on electrical and computer engineering (WIECON-ECE), 2019, pp 1–4
5. Anumula SK, Xiong X (2019) Design and simulation of 4-bit QCA BCD full-adder. In: 2019 IEEE long island systems, applications and technology conference (LISAT), 2019, pp 1–6
6. Ragunath G, Sugandh V, Sakthivel R (2019) Delay optimized binary to BCD converter for multi-operand parallel decimal adder. In: 2019 International conference on vision towards emerging trends in communication and networking (ViTECoN), 2019, pp 1–5
7. Sengupta D, Sultana M, Chaudhuri A (2017) Proposal for fast BCD addition. In: 2017 Third international conference on research in computational intelligence and communication networks (ICRCICN), 2017, pp 343–348

8. Sworna ZT, Haque M, Tara N, Md H, Babu H, Biswas AK (2016) Low-power and area efficient binary coded decimal adder design using a look up tablebased field programmable gate array. *IET Circuits Devices Syst* 10(3):163–172
9. Saida G, Meena S (2016) Implementation of low power BCD adder using gate diffusion input cell. In: 2016 International conference on communication and signal processing (ICCSP), 2016, pp 1352–1355
10. Mishra S, Verma G (2013) Low power and area efficient implementation of BCD adder on FPGA. In: 2013 International conference on signal processing and communication (ICSC), 2013, pp 461–465
11. Sundaresan C, Chaitanya CVS, Venkateswaran PR, Bhat S, Kumar JM (2011) Modified reduced delay BCD adder. In: 2011 4th International conference on biomedical engineering and informatics (BMEI), 2011, pp 2148–2151
12. Holten CV (1980) The conversion of BCD coded words into binary numbers. *Microelectron J* 11(2):29–34

# Digital Image Tampering Detection Using Deep Learning: A Survey



Sunen Chakraborty, Paramita Dey, and Kingshuk Chatterjee

**Abstract** Digital images can be considered as a source of information in various cases. But digital images have been tampered using various image editing software like Adobe Photoshop, GNU Image Manipulation Program (GIMP), etc. Many techniques are employed to tamper an image like copy-move, splicing, removal, etc. Traditional methods that use handcrafted features and laid the foundation of tampering detection are not that efficient. Deep learning proves to be an effective method to detect changes in an image. These methods have greater accuracy than traditional methods because they can extract complex features from an image at a faster rate. They are also automatic which saves time and effort. In this paper, we present a detailed survey of deep learning-based techniques for image tampering detection.

**Keywords** Image tampering · Image forgery detection · Deep learning · Convolutional neural network

## 1 Introduction

Today, we live in a world where digital images are abundant. We can have access to millions of images in a moment. Previously, almost every image was considered an authentic source of information. But with the rapid growth of technology that authenticity is not just the same as it was used to be. Now, there are technologies that can tamper with an image in innumerable ways for malicious purposes. Most of the time the tampering is done with such finesse that it can deceive human eyes. To

---

S. Chakraborty (✉)  
Haldia Institute of Technology, Haldia 721657, India  
e-mail: [sunenblaze16@gmail.com](mailto:sunenblaze16@gmail.com)

P. Dey (✉) · K. Chatterjee  
Government College of Engineering and Ceramic Technology, Kolkata 700010, India  
e-mail: [dey.paramita77@gmail.com](mailto:dey.paramita77@gmail.com)

restore trust in digital images, many technologies emerged in recent years. That is how the term digital forensics came into the light.

There are techniques to detect tampered digital images. Researchers have classified this into two categories: (i) Active and (ii) Passive. In Active techniques when an image is created, some additional information like a signature or a watermark is embedded which helps with authentication. The disadvantage of active technique is that a watermark or signature must be embedded at the time of recording, which would restrict this approach to specific hardware or software equipped for the task. But Passive techniques operate without the presence or knowledge of any watermark or signature. These strategies work on the supposition that albeit digital tampering may leave no visual hints of altering, they may change the hidden statistics of a picture. Passive image forgeries are very hard to identify by human eyes. Therefore, it becomes very essential to detect these kinds of forgeries, and also it will be useful for digital image forensics. Passive techniques are difficult to perform, but they present many opportunities. The techniques are shown in Fig. 1.

There are millions of real and tampered images available on the Internet. But to check every image in a one-by-one manner using a particular technique will take countless hours. Here, deep learning has a solution for us. Convolutional Neural Networks (CNN) and their variants can extract complex features from multiple images at a time. We will be discussing some of the state-of-the-art techniques which employ deep learning in this literature survey.

In this paper, we will mainly focus on forgery-dependent Passive image tampering (e.g., Copy-Move and Image Splicing) because forgery-independent tampering (e.g., Image Retouching) is considered to be comparatively less harmful. In Sect. 2 of this paper, we will discuss the passive forgery (Copy-Move and Image Splicing) and their respective detection. In Sect. 3, we will talk about tampering detection using deep

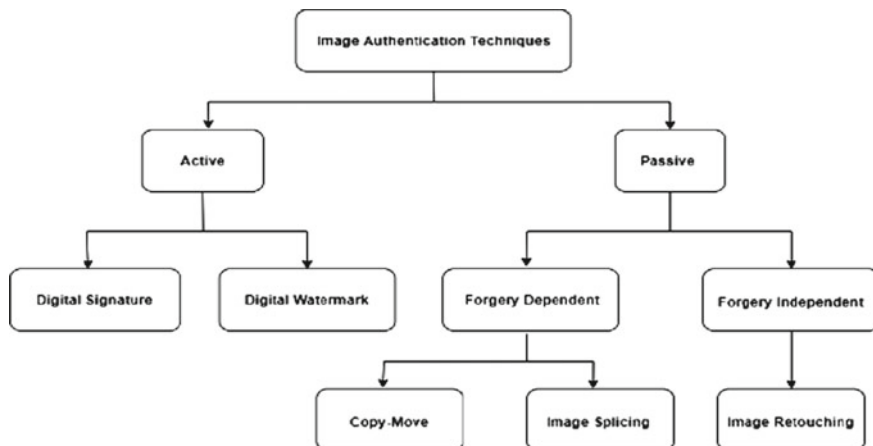


**Fig. 1** Classification of image tampering detection approaches



**Fig. 2** Copy-move forgery

learning. Sect. 4 will consist of analysis and discussions. In Sect. 5, we will discuss our future prospect in this field. Finally, Sect. 6 presents the conclusion.

## 2 Passive Tampering and Detection

### 2.1 *Copy-Move Tampering Detection*

Copy-move forgery is one of the most popular and commonly used forgery techniques that employ image processing tools (e.g., Photoshop and Corel DRAW). In copy-move forgery, a part of the image is copied and pasted into another part of the same image. Its main purpose is to conceal certain objects or to duplicate certain elements of an image. One example of copy-move forgery is shown in Fig. 2.

Here, in the second image some features are copied to add additional elements, whereas in the third image some features are copied to conceal original elements. The traditional techniques to detect copy-move forgery are (i) Block-based where an image is divided into square blocks of a certain length, and then, features are extracted using any proposed algorithms like DCT [1], PCA [2], DWT [3], and SVD [4]. (ii) Keypoint-based, here high entropy regions of an image are first identified and selected, then features are extracted using algorithms like SIFT [5, 6] and SURF [7, 8].

After extracting features in either way, if similar features are found in two different regions then the image has been tampered. Basic steps for copy-move forgery detection are shown in Fig. 3.

### 2.2 *Image Splicing Detection*

Image splicing is another form of digital image tampering where fragments from two or more images are merged to create a finished image. An example of Image splicing is shown in Fig. 4. Detection of Image splicing is harder than the copy-move approach due to the absence of the same features in multiple regions. In the hands of an expert

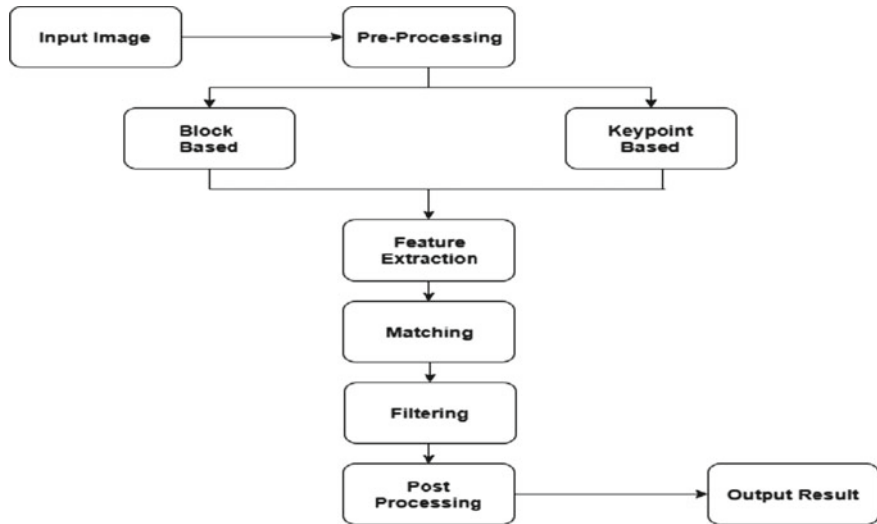


**Fig. 3** Basic steps for copy-move forgery detection



**Fig. 4** Image splicing

signs of splicing will be untraceable. There are still traces of tampering that can be detected. When an object is spliced from one image into another, sometimes it gives rise to sharp edges around that object and disrupts the edges that were originally there, this leads to edge inconsistency [42]. Another way is that different camera manufacturers configure their devices differently, if splicing is done using images from dissimilar camera models then there will be a difference in lighting effects [43, 44].

### 3 Deep Learning Detection

Most of the techniques which are discussed in the previous sections are traditional approaches. They work only to detect a particular kind of tampering. Also, those techniques are only applied to a handful of images. But, what if there is a dataset that consists of a large number of images, all of which are tampered in multiple

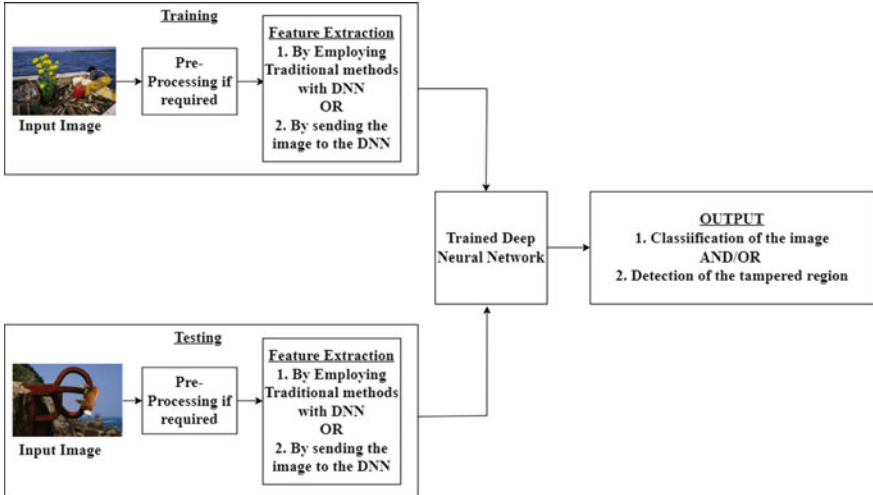


**Fig. 5** Basic workflow for image tampering detection using deep neural networks

ways. Then, those techniques will not be efficient and time-consuming. Thanks to the emergence of deep learning these problems can be tackled. Deep learning gained popularity when it comes to working with image data. Deep learning models like convolutional neural networks (CNN) or deep neural networks (DNN) can extract complex features from multiple images at a faster rate. The whole process is automatic which saves time and energy.

After studying several of research paper regarding image tampering detection that utilizes deep learning models, we found that the researchers have separated the entire procedure into two different stages. First stage is training stage where the model learns the features of the tampering and the second stage is testing how well the model can classify whether an image is tampered or not. Figure 5 depicts a general estimation of this process.

But, training a convolutional neural network is harder, and it requires additional hardware requirements like GPU or TPU and more RAM. Also, training requires a huge amount of data else the neural network risks overfitting. Another problem is that if tampered images are feed into CNN directly, then it will extract features from images rather than extracting features of tampering.

This problem is noticed by Chen et al. [9] which is why he introduced a filter layer in his network, which helps to detect median filtering done on an image to hide the evidence of any tampering. Similarly, Yu et al. [10] also used a filter layer that employed several high-pass filters to detect median filtering. Bayar et al. [11] introduced an additional layer to their model to eliminate the necessity of pre-processing. It works on the concept that tampering changes the association between pixels of a specific region. Hence, the new layer can discover those features while ignoring the additional contents of the images. Zhang et al. [12] divide images into patches, and then, deep learning Stacked Autoencoder (SAE) is used for feature learning of

individual patch, after that contextual information was incorporated into individual patch to detect tampered regions. To detect tampering, Rao et al. [13] initialized the first layer of CNN with filters that capture objects generated during the tampering. The CNN is used to draw out features from the images patch-wise, and then, features are combined using a fusion method to obtain the final features for classification. Rota et al. [14] divided images into patches for the classification that can be used to train large neural networks that can also identify those patches which contain the edges around the altered regions. This method can be implemented further to localize the manipulated regions.

Previously, we discussed that tampering images from dissimilar camera models leads to a difference in lighting effects. Bondi et al. [15] came up with an approach to detect splicing in images from multiple camera models, where the features are extracted patch-wise using a CNN and then analyzed using a clustering method to classify the images and detect regions from another camera model. Ouyang et al. [16] proposed a method that utilizes neural network previously trained on substantial databases and then tune the model correspondingly for small training samples to detect copy-move tampering. Salloum et al. [17] preferred a fully convolutional network to detect splicing. They also demonstrate that it is better to use a multi-task FCN over a single-task FCN because of the rough localization generated by the single-task FCN in some instances. The network has dual output branches. One branch is utilized to get the surface label, and the other one is to localize and detect the border of the tampered region.

Wu et al. [18] proposed a DNN for identifying and localization of spliced images. It takes two images, where one of them is a tampered image and the other one is likely to be a contributor image. Then, it detects the likelihood of whether the contributor image was used on the tampered image. After that, the network produces splicing masks for each image. Wu et al. [19] designed a DNN to spot copy-move tampering called BusterNet. Here, one branch is used to identify altered regions, and then, it creates a mask of those regions. Another branch identifies those regions which are applied on the altered region creating a copy-move mask. Then, a module merges masks from both the branches for final results. Wu et al. [20] proposed another DNN for copy-move tampering. First, a CNN is utilized to obtain features from an image. Then, resemblances between pixels of any two features are evaluated. After that, a network is used to find equivalent feature pairs based on the resemblance results. At last, another network is used to generate a tampering mask based on the information from the previous network. Wu et al. [21] designed a fully convolutional network for identifying various kinds of tampering called ManTra-Net. This technique is based on the earlier approaches proposed by Wu et al. [18–20]. The network comprises two sub-networks. The first network is used to produce a depiction of unified features. The second one uses the output generated from the earlier sub-network to extract unusual features for localizing tampered regions.

To detect copy-move tampering, Liu et al. [22] used a convolutional kernel network (CKN) instead of a CNN. This is because a CNN is used only for depicting features or for some classification task, but CKN computes how to estimate the kernel feature map on training data. First, the image is divided into multiple parts,

and then, keypoints are detected. Then, the images are fed into the CKN patch-wise for extracting features and to detect similar keypoint pairs. A second phase is conducted to remove regions that might be classified as tampered after the first phase. Amerini et al. [23] proposed a method when the forger used single or double JPEG compression to cover up the tampering. First, they used a CNN that divides an image into RGB color patches, and then, they used another CNN to evaluate a histogram from the coefficients of discrete cosine transform of an individual patch. At last, a CNN combines the information of the two previous CNNs that can classify between uncompressed, single, or double JPEG compressed images and can also localize the tampered regions.

Zhang et al. [24] used sliding window detection on forged images to generate patches which are then fed into a shallow CNN to detect and localize tampered edges. They used a shallow network to prevent it from learning complex features. Though the technique was efficient, it was time-consuming. Hence, they proposed fast shallow CNN which accepts the complete image as input instead of patches, and then feature are extracted. It performs well to detect edges of the tampered areas in low-resolution images. Huang et al. [25] detects various post-processing done to hide the traces of tampering. First, a proposed steganalysis means is used to get the features from the images. Then, a CNN is used to scan the features using a sliding window approach, a fusion technique is used to obtain the final features. At last, classification of different operations is done. Zhou et al. [26] proposed a faster region-based CNN consisting of two branches. In its first branch, color images are fed directly for obtaining the features and classifying the tampering style. In the second branch suggested filters are used to detect noise alterations in case the forger performs post-processing. Finally, a method is employed to fuse the output of both the branches to localize altered regions as well as classify tampering style.

Shi et al. [27] proposed a CNN to detect and localize altered regions. In the first CNN, the image patches are passed through a filter layer to learn the signs of tampering. Then, convolutional layers are used to extract features and find out the relationship between them. In the second CNN, a wavelet transform is applied to the image patches to extract features. Then, their outputs are merged to label the patch as real or fake and also to generate a detection map. Thakur et al. [28] proposed a method to detect copy-move and splicing. First, the images are resized and transformed into greyscale. Then, traces of median filtering and image blurring are detected using suitable methods which are common post-processing employed to hide the tampering. Lastly, a CNN is used to classify the images. Cao et al. [29] suggested a strategy to spot resampling in recompressed pictures using the JPEG format. At first, filters are used to obtain noise residuals while ignoring extra details. Then, two channels are used to extract features from the noise, one channel does it in a horizontal manner and another one in a vertical manner. One extra channel is added to merge the features obtained by both the channels, whose output is integrated back to the previous channels. Finally, classification is done from final features by both channels.

Wang et al. [30] used a Mask R-CNN. At first, features are obtained, which are used to generate feature maps. Then those maps are employed to obtain crude segments of

the altered area. To further refine the masks created after segmentation, a Sobel filter is used. Saleem et al. [31] used a new approach to detect tampering. They separate the process into two different modules. One module comprises a CNN based on the Inception module which is utilized to classify whether the image is tampered or not. After an image is classified as tampered, it is passed to the other module that uses a mask R-CNN to spot tampered region. Bi et al. [32] utilized an improved version of U-Net over CNN to detect spliced regions. First, a procedure handles the gradient degradation issue faced by deep CNNs which leads to a decrease in accuracy by remembering details of the captured features. Then another procedure reinforces details of those features to form the distinction between real or tampered regions. Xiao et al. [33] proposed a network to detect splicing which uses two CNN. First, CNN is employed to roughly detect suspected forge regions. Then, another CNN is used to filter out the false regions detected by the previous CNN. After which, a suggested method of adaptive clustering is used to finally spot the altered areas.

Yao et al. [34] proposed a method to detect and localize splicing. At first, a filter is applied to get the residuals from a single image which is then divided into patches. Then, features are obtained in a two-step approach. First, a CNN is used to get features from each patch. Then, a suggested module is used to prevent uncertain results generated by the CNN when encountering a patch with few textures. At last, a proposed method is employed which combines the output of the CNN and the module along with some other details to obtain the detection map. Yang et al. [35] used an R-CNN, which cannot only localize the tampered region but can also classify the tampering techniques. First, features from traces of tampering are extracted. Then, a rough detection of the tampering technique and the tampered region is done. At last, refining is done on pixel level to obtain the final mask of the manipulated region.

Goel et al. [36] applied a dual branch CNN to distinguish between images that have undergone copy-move tampering. They kept the filter size non-identical in both the branches. This is done so that each branch of the CNN can extract features of distinct spatial scale from the images which can be used for classification. Walia et al. [37] merged the features from a traditional technique and a pre-trained CNN. In the first branch, images are divided into smaller segments and then Markov features are generated by applying discrete cosine transform over quaternion field. In the second branch, maps are produced using the local binary patterns from the images and were inserted into a ResNet-18 network for feature extraction. At last, features from both the branches are combined and fed into a shallow neural network for the classification. Ding et al. [38] proposed a UNET with dual branch to detect splicing. High-pass filters are applied on an image to create another image with edge information. First branch accepts the tampered image and the second branch accepts the image with edge information. Both branches used encoder networks to extract features from the two different images. Then, features from both the branches are fused and sent to a decoder network to generate a rough tampering map. That map is again processed to generate a more refined tampering map.

Biach et al. [39] created a U-Net made out of an encoder and a decoder network which is called as Fals-Unet. The encoder obtains significant features through a sequence of operations which are required to differentiate between authentic and

tampered regions. The decoder determines the authenticity of the pixels individually from the maps generated by the encoder in order to produce the binary mask at the end. Chakraborty et al. [40] used error level analysis (ELA) where a tampered image undergoes compression, then difference between the compressed image and the uncompressed tampered image is used to extract the final tampering features. After this, the ELA image is sent to a CNN for final classification. Jaiswal et al. [41] utilized multiple layers of encoder-decoder network to detect copy-move tampering. An image is resized multiple times, and each resized image is fed to an encoder network. This way the network can learn the tampering features even if the image is resized several times. Features extracted from the encoders are minuscule. Hence, the features are then passed through multiple levels of decoders until the size of the features are big enough. Lastly, a classifier detects whether a pixel is forged or not and generates the final map. Their network performs well even if the image has undergone other post-processing operations.

A comparative analysis of the various deep learning tampering detection approaches is presented in Table 1. Here, ‘–’ sign shows that the data is too detailed and cannot be put in a concise manner.

## 4 Analysis and Discussions

After analysis of different research papers that use deep learning-based tampering detection, we found that:

- A. Deep Learning Method has greater performance than traditional handcrafted approach.
- B. CNN and other deep neural networks are capable of automatically extracting features from an image.
- C. Although CNNs can learn features from images, automatically they are unable to deal with the task of tampering detection in their basic form.
- D. Hence, some researchers use additional filters or additional layers along with CNN to extract the hidden features in an image, while others used variants of CNN or some other deep neural network.
- E. Deep Learning methods can not only classify whether an image is real or tampered but can also do much more than that like detection of tampering regions and type.
- F. Though deep learning excels at tampering detection, many of these techniques performed differently for different datasets because there is not a single large dataset that can be used to detect all kinds of tampering.

**Table 1** Comparative analysis of various deep learning tampering detection approach

Paper and Year	Tampering detection	Deep learning model	Architecture	Dataset used	Performance
Chen et al. [9]	Median filtering, cut-and-paste	CNN	1 Filter layer, 5 convolutional layers, 3 fully connected layers (last layer is a 2-way softmax)	BOSSbase, UCID, BOSS RAW, dresden image, NRCS photo gallery	Accuracy—85.14%
Zhang et al. [12]	Copy-move, splicing	SAE (stacked auto-encoder)	3 Hidden Layer and an MLP Layer for fine tuning	CASIA v1.0, CASIA v2.0	Accuracy—91.09% (overall), 87.51% (JPEG Images), 81.91% (TIFF Images)
Rao et al. [13]	Copy-move, splicing	CNN	8 convolutional layers, 2 pooling layers, and a fully connected layer with a 2-way softmax classifier	CASIA v1.0, CASIA v2.0, Columbia gray DVMM	Accuracy—98.04% (CASIA v1.0), 97.83% (CASIA v2.0), 96.38% (DVMM)
Bayar et al. [11]	Median filtering, resampling, gaussian blurring, additive white gaussian noise (AWGN)	CNN	1 new proposed convolutional layer, 2 convolutional layers, 2 max-pooling layers, and 3 fully connected layers	Image datasets collected from 12 different camera models	Accuracy—99.10%

(continued)

**Table 1** (continued)

Paper and Year	Tampering detection	Deep learning model	Architecture	Dataset used	Performance
Rota et al. [14]	Splicing	CNN	2 Convolutional blocks (Each with 2 convolutional layers and 1 pooling layer) and two fully connected layers	CASIA v2.0	Accuracy—97.44%
Bondi et al. [15]	Splicing	CNN	4 convolutional layers, 3 max-pooling layers, 2 fully connected layers, 1 ReLU layer, 1 softmax layer	Dresden image database	Accuracy—91% (Images from camera model in the dataset), 81% (Images from camera model not in the dataset)
Ouyang et al. [16]	Copy-move	CNN	5 convolutional layers, 3 fully connected layers	UCID, OXFORD flower, CMFD image database	Test Error %—2.32 (OXFORD), 2.43 (UCID), 3.56(UCID + OXFORD), 42 (CMFD)
Salloum et al. [17]	Splicing	Fully Convolutional Network (Edge-Enhanced Multi-task FCN-MFCN)	—	CASIA v1.0, CASIA v2.0, Columbia Uncompressed, Carvalho, DARPA/NIST Nimble Challenge 2016 SCI datasets	Average F1 Score—0.5410 (CASIA v1.0), 0.6117 (Columbia), 0.5707 (Nimble 2016 SCI), 0.4795 (Carvalho)
Wu et al. [18]	Splicing	Deep CNN—deep matching and validation network (DMVN)	—	SUN2012 object detection Dataset, MS COCO, CASIA, NIST- Nimble 2017	—

(continued)

**Table 1** (continued)

Paper and Year	Tampering detection	Deep learning model	Architecture	Dataset used	Performance
Liu et al. [22]	Copy-move	CKN (Convolutional Kernel Network)	–	RomePatches dataset, MICC-F220, MICC-F2000, CoMoFoD	Average F1 Measure—0.6318
Amerini et al. [23]	Double JPEG compression, splicing	CNN (Multi-domain CNN)	–	UCID dataset	Accuracy—95%
Zhang et al. [24]	Detection of tampered region boundaries	CNN (Fast SCNN- Fast Shallow CNN)	2 convolutional layers, 2 fully connected layers	CASIA v2.0	Accuracy—85.35% (JPEG Images), 82.93% (TIFF Images)
Huang et al. [25]	Gamma correction, histogram equalization, mean filtering, gaussian filtering, JPEG lossy compression, low-pass filtering, high-pass filtering	CNN	2 convolutional layers, 2 pooling Layers, 1 fully connected layer followed by 1 Softmax classifier	Boss base v1.0	Accuracy—97.25% (average)
Zhou et al. [26]	Copy-move, splicing, removal	Two Stream Faster R-CNN (Region-based CNN)	–	MS COCO, NIST Nimble 2016 (NIST16), CASIA v1.0, CASIA v2.0, COVER, Columbia dataset	$F_1$ Score—0.722(NIST16), 0.697(Columbia), 0.437(COVER), 0.408(CASIA)
Shi et al. [27]	Splicing	Dual-Domain-CNN(D-CNNs) [spatial-domain CNN-SCNN, frequency-domain CNN-FCNN]	–	CASIA v2.0, Columbia Uncompressed, Carvalho	Highest F1 Score—0.62 (CASIA v2.0) Average F1 Score—0.69 (Columbia), 0.58 (Carvalho)

(continued)

**Table 1** (continued)

Paper and Year	Tampering detection	Deep learning model	Architecture	Dataset used	Performance
Wu et al. [19]	Copy-move	Deep Neural Network (DNN) BusterNet	–	MIT SUN2012, MS COCO, IEEE IFS-TC first image forensics challenge dataset, weild web tampered image dataset, CASIA v2.0, CoMoFoD	–
Wu et al. [20]	Copy-move	Deep Neural Network (DNN)	–	SUN2012 object detection, MS COCO, CASIA v2.0	F-Score—83.52% (Image-level on Synthetic dataset), 74.43% (Pixel-level on Synthetic dataset), 75.72% (CASIA v2.0)
Thakur et al. [28]	Copy-move, splicing	CNN	6 convolutional layers, 5 max-pooling layers, 2 fully connected layers, 1 softmax layer	CoMoFoD, BOSSBase	Validation Accuracy—95.97% (CoMoFoD), 94.26% (BOSSBase)
Yu et al. [10]	Median Filtering, splicing	CNN	1 Filter Layer, 4 convolutional layers, 2 fully connected layers, 2-way softmax layer	BOSSbase 1.01, UCID, Dresden Image Database, NRCS Photo Gallery database	Accuracy—92.31%
Cao et al. [29]	Resampling, splicing	CNN (Dual-Stream CNN)	–	ALASKA steganography challenge dataset, Dersm database	Accuracy—97.37%

(continued)

**Table 1** (continued)

Paper and Year	Tampering detection	Deep learning model	Architecture	Dataset used	Performance
Wang et al. [30]	Copy-move, splicing	Mask Regional CNN (Mask R-CNN)	–	MS COCO, Cover, Columbia	Average—F1 Score-0.936 (Cover), 0.978 (Columbia)
Saleem et al. [31]	Splicing	Mask Region-based CNN	–	CASIA v1.0, CASIA v2.0	Accuracy—98.76% (CASIA v1.0), 97.92% (CASIA v2.0)
Bi et al. [32]	Splicing	U-Net (Ringed Residual U-Net: RRU-Net)	–	CASIA v2.0, COLUMB	Accuracy—76%
Wu et al. [21]	Copy-move, splicing, removal, enhancement	Fully Convolutional Network (ManTra-Net)	–	Dresden Image Database, Kaggle Camera Model Identification (KCMi) Dataset, Photoshop-battle dataset, NIST 2016, CASIA, COVERAGE, Columbia dataset, synthetic dataset made from datasets by Wu et al. [18, 19]	AUC Score—79.5% (NIST), 82.4% (Columbia), 81.9% (COVERAGE), 81.7% (CASIA)

(continued)

**Table 1** (continued)

Paper and Year	Tampering detection	Deep learning model	Architecture	Dataset used	Performance
Xiao et al. [33]	Splicing	CNN (C2RNet)	Coarse CNN(C-CNN)—13 convolutional layers, 5 max-pooling layers, 2 fully connected layers Refined CNN(R-CNN)—16 convolutional layers, 5 max-pooling layers, 3 fully connected layers	CASIA v2.0, COLUMB, IEEE Forensics	Average F-Measure—0.6758 (CASIA), 0.695 (COLUMB), 0.492 (Forensics)
Yao et al. [34]	Splicing	CNN	13 convolutional layers, 3 fully connected layers, 1 softmax layer	Dresden database	Accuracy—92.2% (Average), 94.9% (Best)
Yang et al. [35]	Copy-move, splicing, removal	R-CNN (Constrained R-CNN)	—	COCO, NIST16, CASIA, COVERAGE, Columbia	$F_1$ Score—0.927 (NIST16), 0.757 (COVER), 0.790 (Columbia), 0.475 (CASIA)

(continued)

**Table 1** (continued)

Paper and Year	Tampering detection	Deep learning model	Architecture	Dataset used	Performance
Goel et al. [36]	Copy-move	Dual-branch CNN	1st Branch—3 Conv. layers, 3 Max Pool layers, 1 Zero-padding layer, 2 <sup>nd</sup> Branch - 3 Conv. layers, 3 Max Pool Layers 1 Concat Layer, 1 Global-max Pool layer, 2 Fully Connected layers, 1 Sigmoid Classifier	MICC-F2000	Accuracy—96% Precision-0.89 Recall-1 $F_1$ Score 0.94
Walia et al. [37]	Copy-move, splicing	CNN in combination with handcrafted technique	–	CASIA v1.0, CASIA v2.0	Accuracy—97.94% (CASIA v1.0) 99.31% (CASIA v2.0)
Ding et al. [38]	Splicing	Dual channel u-net (DCU-Net)	–	CASIA v2.0, Columbia Uncompressed	Accuracy—97.93% (CASIA v2.0), 97.27% (Columbia Uncompressed)
Biach et al. [39]	Copy-move, splicing, removal	U-Net (Fals-Unet)	–	NIST 2016, CoMoFoD, COVERAGE, CASIA v1.0, CASIA v2.0	$F_1$ —Score—63.89% (NIST 2016), 81.56% (CoMoFoD), 79.52% (COVERAGE), 73.62% (CASIA v1.0), 69.53% (CASIA v2.0)
Chakraborty et al. [40]	Copy-move, splicing	CNN	2 Conv. Layers, 2 max pool layers, 1 fully connected layer, 1 two-way softmax classifier	CASIA v2.0	Accuracy—96.18%

(continued)

**Table 1** (continued)

Paper and Year	Tampering detection	Deep learning model	Architecture	Dataset used	Performance
Jaiswal et al. [41]	Copy-move	CNN	—	CoMoFoD, CMFD	Accuracy—98.78% (CMFD), 98.39% (CoMoFoD)

## 5 Future Works

We have already mentioned few challenges regarding image tampering detection involving deep neural networks. In our future researches, we will try to address these challenges. Our primary objective will include creation of a dataset that will contain images tampered in multiple ways, which we will be made available to everyone.

Next objective will be to create a deep neural network which will be lightweight yet powerful enough to detect various kinds of tampering.

## 6 Conclusion

In this paper, we have discussed various image tampering detection techniques using deep learning. Image tampering detection is a basic need of this digital age. We have briefly explained traditional handcrafted techniques to detect tampering. But in case of deep neural networks, the performance difference is substantial. We have also presented a comparative analysis of various deep learning methods, their detection type, DNN type used, the architecture of proposed DNN, dataset used, and performance of the network.

Many of these techniques discussed in this paper are used to detect one or more than one kind of tampering. Some of these methods can (a) classify whether an image is original or tampered, (b) detect and localize the tampered regions, (c) determine what kind of tampering was performed, (d) determine what kind of post-processing operations are performed to hide traces of tampering, and (e) perform more than one operations stated above. Even though deep learning approaches are better than traditional handcrafted techniques, they have a long way to go. There is still a need for generalized algorithms that can detect all kinds of tampering. At last, we conclude that traditional methods that laid the foundation of tampering detection are not that efficient. Whereas, the deep learning-based approaches are the new ways that can detect tampering from multiple images at a faster rate. The whole process is automatic which saves time and energy.

## References

1. Fridrich J, Soukal BD, Lukáš AJ (2003) Detection of copy-move forgery in digital images. In: Proceedings of digital forensic research workshop
2. Popescu AC, Farid H (2004) Exposing digital forgeries by detecting duplicated image regions. TR2004-515, Technical Report, Dartmouth College
3. Myrna AN, Venkateshmurthy MG, Patil CG (2007) Detection of region duplication forgery in digital images using wavelets and log-polar mapping. In: International conference on computational intelligence and multimedia applications, vol 3. IEEE

4. Li G, Wu Q, Tu D, Sun S (2007) A sorted neighborhood approach for detecting duplicated regions in image forgeries based on DWT and SVD. In: IEEE international conference multimedia and expo, Beijing, China, 2007, pp 1750–1753
5. Lowe DG (2004) Distinctive image features from scale-invariant keypoints. *Int J Comput Vis* 60(2):91–110
6. Huang H, Guo W, Zhang Y (2008) Detection of copy-move forgery in digital images using sift algorithm. In: 2008 IEEE Pacific-Asia workshop on computational intelligence and industrial application, vol 2. IEEE, pp 272–276
7. Bay H, Ess A, Tuytelaars T, Van Gool L (2008) Speeded-up robust features (SURF). *Comput Vis Image Underst* 110(3):346–359
8. Bo X, Junwen W, Guangjie L, Yuewei D (2010) Image copy move forgery detection based on surf. In: 2010 international conference on multimedia information networking and security. IEEE, pp 889–892
9. Chen J, Kang X, Liu Y, Wang ZJ (2015) Median filtering forensics based on convolutional neural networks. *IEEE Signal Process Lett* 22(11):1849–1853
10. Yu L, Zhang Y, Han H, Zhang L, Wu F (2019) Robust median filtering forensics by CNN-based multiple residuals learning. *IEEE Access* 7:120594–120602
11. Bayar B, Stamm MC (2016) A deep learning approach to universal image manipulation detection using a new convolutional layer. In: Proceedings of the 4th ACM workshop on information hiding and multimedia security (IH&MMSec '16), pp 5–10
12. Zhang Y, Goh J, Win LL, Thing VL (2016) Image region forgery detection: a deep learning approach. In: SG-CRC, pp 1–11
13. Rao Y, Ni J (2016) A deep learning approach to detection of splicing and copy-move forgeries in images. In: 2016 IEEE international workshop on information forensics and security (WIFS) (2016), pp 1–6
14. Rota P, Sangineto E, Conotter V, Pramerdorfer C (2016) Bad teacher or unruly student: Can deep learning say something in image forensics analysis? In: 2016 23rd International conference on pattern recognition (ICPR). IEEE, pp 2503–2508
15. Bondi L, Lameri S, Güera D, Bestagini P, Delp EJ, Tubaro S (2017) Tampering detection and localization through clustering of camera-based CNN features. In: 2017 IEEE conference on computer vision and pattern recognition workshops (CVPRW), Honolulu, HI, pp 1855–1864
16. Ouyang J, Liu Y, Liao M (2017) Copy-move forgery detection based on deep learning. In: 2017 10th international congress on image and signal processing, biomedical engineering and informatics (CISP-BMEI), pp 1–5
17. Salloum R, Ren Y, Kuo CCY (2018) Image splicing localization using a multi-task fully convolutional network (MFCN). *J Visual Commun Image Representation* 51:201–209
18. Wu Y, Abd-Almageed W, Natarajan P (2017) Deep matching and validation network: an end-to-end solution to constrained image splicing localization and detection. In: MM '17: Proceedings of the 25th ACM international conference on multimedia, 2017, pp 1480–1502
19. Wu Y, Abd-Almageed W, Natarajan P (2018) Busternet: detecting copy-move image forgery with source/target localization. In: Proceedings of the European conference on computer vision (ECCV), pp 168–184
20. Wu Y, Abd-Almageed W, Natarajan P (2018) Image copy-move forgery detection via an end-to-end deep neural network. In: 2018 IEEE winter conference on applications of computer vision (WACV) 2018, pp 1907–1915
21. Wu Y, AbdAlmageed W, Natarajan P (2019) ManTra-Net: manipulation tracing network for detection and localization of image forgeries with anomalous features. In: Proceedings of the IEEE conference on computer vision and pattern recognition, pp 9543–9552
22. Liu Y, Guan Q, Zhao X (2018) Copy-move forgery detection based on convolutional kernel network. *Multimedia Tools Appl* 77:18269–18293
23. Amerini I, Uricchio T, Ballan L, Caldelli R (2017) Localization of jpeg double compression through multi-domain convolutional neural networks. In: 2017 IEEE conference on computer vision and pattern recognition workshops (CVPRW), pp 1865–1871

24. Zhang Z, Zhang Y, Zhou Z, Luo J (2018) Boundary-based image forgery detection by fast shallow CNN. In: 2018 24th international conference on pattern recognition (ICPR), Beijing, 2018, pp 2658–2663
25. Huang T, Yuan X (2018) Detection and classification of various image operations using deep learning technology. In: 2018 International conference on machine learning and cybernetics (ICMLC), vol 1. IEEE, pp 50–55
26. Zhou P, Han X, Morariu VI, Davis LS (2018) Learning rich features for image manipulation detection. In: 2018 IEEE/CVF conference on computer vision and pattern recognition, Salt Lake City, UT, 2018, pp 1053–1061
27. Shi Z, Shen X, Kang H, Lv Y (2018) Image manipulation detection and localization based on the dual-domain convolutional neural networks. *IEEE Access* 6:76437–76453
28. Thakur R, Rohilla R (2019) Copy-Move forgery detection using residuals and convolutional neural network framework: a novel approach. In: 2019 2nd International conference on power energy, environment and intelligent control (PEEIC), Greater Noida, India, 2019, pp 561–564
29. Cao G, Zhou A, Huang X, Song G, Yang L, Zhu Y (2019) Resampling detection of recompressed images via dual-stream convolutional neural network. arXiv preprint [arXiv:1901.04637](https://arxiv.org/abs/1901.04637)
30. Wang X, Wang H, Niu S, Zhang J (2019) Detection and localization of image forgeries using improved mask regional convolutional neural network. *Math Biosci Eng*
31. Saleem S, Dilawari A (2019) Multimedia forensic: an approach for splicing detection based on deep visual features. In: 2019 International conference on robotics and automation in industry (ICRAI) 2019 Oct 21. IEEE, pp 1–6
32. Bi X, Wei Y, Xiao B, Li W (2019) RRU-Net: the ringed residual U-Net for image splicing forgery detection. In: 2019 IEEE/CVF conference on computer vision and pattern recognition workshops (CVPRW), pp 30–39
33. Xiao B, Wei Y, Bi X, Li W, Ma J (2020) Image splicing forgery detection combining coarse to refined convolutional neural network and adaptive clustering. *Inf Sci* 511:172–191
34. Yao H, Xu M, Qiao T, Wu Y, Zheng N (2020) Image forgery detection and localization via a reliability fusion map. *Sensors* 20(22):6668
35. Yang C, Li H, Lin F, Jiang B, Zhao H (2020) Constrained R-CNN: a general image manipulation detection model. In: 2020 IEEE international conference on multimedia and expo (ICME), London, United Kingdom, pp 1–6
36. Goel N, Kaur S, Bala R (2021) Dual branch convolutional neural network for copy move forgery detection. *IET Image Proc* 15(3):656–665
37. Walia S, Kumar K, Kumar M, Gao XZ (2021) Fusion of handcrafted and deep features for forgery detection in digital images. *IEEE Access* 9(12):99742–99755
38. Ding H, Chen L, Tao Q, Fu Z, Dong L, Cui X (2021) DCU-Net: a dual-channel U-shaped network for image splicing forgery detection. *Neural Comput Appl* 12:1–7
39. El Biach FZ, Iala I, Laanaya H, Minaoui K (2022) Encoder-decoder based convolutional neural networks for image forgery detection. *Multimedia Tools Appl* 81(16):22611–22628
40. Chakraborty S, Chatterjee K, Dey P (2022) Discovering tampered image in social media using ELA and deep learning. *SN Comput Sci* 3(5):1–8
41. Jaiswal AK, Srivastava R (2022) Detection of copy-move forgery in digital image using multi-scale, multi-stage deep learning model. *Neural Process Lett* 54(1):75–100
42. Fang Z, Wang S, Zhang X (2010) Image splicing detection using color edge inconsistency. In: International conference on multimedia information networking and security
43. Ng T-T, Chang S-F (2004) A model for image splicing. In: Proceedings of IEEE international conference image processing, Singapore, vol 2, pp 1169–1172
44. Johnson MK, Farid H (2005) Exposing digital forgeries by detecting inconsistencies in lighting. In: Proceedings of the 7th workshop on multimedia and security. ACM, pp 1–10

# Nanorod Shaped TiO<sub>2</sub> Photoanode and Mixed Halide Absorber-Based Perovskite Solar Cell Device Fabrication



Anitesh Anand, Niranjan Polai, Madhu Paswan, Manas Mishra, Chanchal Kumar De, and Debasis De

**Abstract** This paper is mainly focused toward the fabrication of halide-based perovskite solar cells (PSCs) devices and nanorod shaped TiO<sub>2</sub> electron transport layer (ETL). The synthesis of nanorod shaped photoanode is carried out using very simple hydrothermal process, and PSCs are fabricated using spin coating. The effects of individual and mixed halides are compared and characterization of each type of PSC carried out. Regarding the ETL, the scanning electron microscopy (SEM) analysis confirms the nanorod shaped structure of TiO<sub>2</sub>, and XRD is used to confirm the rutile phase and the crystallite size of 27.542 nm. For the PSC device, composition of different halides is studied, and absorbance and electrical characterizations are carried out. Electrical characteristics are measured under AM 1.5G illuminations. The  $V_{oc}$ ,  $I_{sc}$ , fill factor (FF), and cell power conversion efficiency ( $\eta$ ) of the MAPbI<sub>2</sub>Cl PSC are calculated to be 2.9 V, 1.67 mA and 1.44 mW, and 2.89%, respectively.

**Keywords** Perovskite solar cells · Nanorod shaped TiO<sub>2</sub> · ETL · Spin coating · Hydrothermal process

## 1 Introduction

Perovskite solar cells based on metal halides (PSCs) have significantly gained attention as emerging photovoltaics since the time the first such PSC was reported. The increasing research in this field is mainly because of the possibility of fabrication of PSCs using low-cost materials without using high-energy consuming processes. A PSC having a power conversion efficiency (PCE) equal to 17.8% was reported

---

A. Anand · N. Polai · M. Paswan · M. Mishra · D. De (✉)  
Energy Institute, Bengaluru (Centre of Rajiv Gandhi Institute of Petroleum Technology),  
Bengaluru 562157, India  
e-mail: [debasisd@rgipt.ac.in](mailto:debasisd@rgipt.ac.in)

C. K. De  
Department of Electronics and Communication Engineering, Haldia Institute of Technology,  
Haldia, West Bengal, India

by using materials of low cost, without using any vacuum step procedure and only maximum process temperature of 200 °C [1]. Stability was another limiting factor in PSCs, [2] reported a PSC of laboratorial size which could operate for 1 entire year under the illumination of 1 sun and 55 °C, without any loss of efficiency. According to National Renewable Energy Laboratory, a perovskite module which was fabricated by Panasonic achieved a PCE of 17.9% for 802 cm<sup>2</sup> illuminated area [3]. Another challenge as faced by researchers is the use of lead, which is toxic in nature. But the efficiency of a perovskite is very much affected by lead. So, to tackle this issue, prevention of lead leakage from PSCs can be a solution. To tackle this lead, absorbing films were used by [4] which helped in retaining the structure and easy collection of lead.

The progress in PCE trend of perovskites is the most obvious factor in calling it the emerging photovoltaics and comparing it already commercialized silicon-based solar cells. Weber first studied the organic–inorganic perovskites in 1978, but its application as a photovoltaic absorber was not studied in depth [5]. A PCE of 2.19% by using a methylammonium lead bromide (MAPbBr<sub>3</sub>) and lithium halide/halogen utilized as redox couple along with FTO glass coated with Pt as a counter electrode was reported in 2006 [6]. And the PCE was able to increase up to 3.8% in 2009, by replacement of bromine by iodine [7]. In 2011, a PCE of 6.5% was achieved using thin nanoporous TiO<sub>2</sub> films by optimization of the concentration of perovskite coating solution, the conditions post-annealing and conducting surface modification of TiO<sub>2</sub> with Pb(NO<sub>3</sub>)<sub>2</sub> [8]. Further, a PCE of 9.7% was reported in 2012 using spiro-MeOTAD (2,2',7,7'-tetrakis(N,N-di-p-methoxyphenylamine)-9,9'-spirobifluorene) as hole conductor and nanoparticles of methyl ammonium lead iodide (MAPbI<sub>3</sub>) [9].

In 2012, the structured films having nanoparticles of alumina were solution coated with the layer of lead halide perovskite to reach an efficiency of 10.9% [10]. Later, a certified efficiency of 14.1% in 2013 using TiO<sub>2</sub> and 2 step iodine deposition method was also reported [11].

Also in 2013, it was showed that nano-structuring was not necessary to achieve high PCE, and a planar heterojunction solar cell was able to achieve a solar to electrical conversion efficiency of 15.4% [12]. This was mentioned to happen because of the ambipolar transport ability of the perovskite. In the year 2014, the antisolvent crystallization method was introduced for PSCs, and this approach was used to fabricate a PSC completely by solution processing and reaching a certified efficiency of 16.2% [13]. In this work, the deposition of perovskite by utilizing a mixture containing γ-butyrolactone (GBL), dimethyl sulphoxide (DMSO), further using toluene dripping while spinning, formed layers which were extremely dense and uniform. In 2014, an efficiency of 19.3% was reported by yttrium doping the electron extraction layer [14]. This improved the electron transport through the scaffold and modified the work function of ITO electrode; thus, the overall PCE was improved. In 2015, 20.1% efficiency was reported in which the use of formamidinium lead iodide (FAPbI<sub>3</sub>) perovskite films, without any residual lead iodide (PbI<sub>2</sub>), was mentioned [15]. Again in 2017, the same research group further enhanced the efficiency to 22.1%, in which into the organic cation solution additional iodide ions were introduced, which decreased deep level defects [16].

In 2018, defect healed grain boundaries were demonstrated by matching a precursor additive of Pb(SCN)<sub>2</sub> with appropriate ratio of FAX where X:Br and I [17]. This produced large sized grains with grain boundaries that were defect healed. Due to this, the wide band gap FA<sub>0.17</sub>Cs<sub>0.83</sub>PbI<sub>3-x</sub>Br<sub>x</sub> was photostable both at the room temperature and at 85 °C. The solar cells exhibited an output power efficiency of 18.6%. National Renewable Energy Laboratory mentioned the following certified efficiencies from 2018 to 2021.[18] In 2018, the PCE of 23.3% was achieved by Chinese Academy of Sciences, which was again surpassed and reached 23.7% by the same team. In 2019, Korean Research Institute of Chemical Technology and Massachusetts Institute of Technology achieved a PCE equal to 25.2%. Then again in 2021, the Ulsan National Institute of Science and Technology situated in South Korea achieved an efficiency of 25.5%.

In this paper, TiO<sub>2</sub> has been used as photoanode due to its n type nature, moderate bandgap of about 3.2 eV, nontoxic nature, high chemical stability, and anti-corrosive nature. TiO<sub>2</sub> nanorods as ETL were deposited on conducting glass substrate using hydrothermal process, and the synthesis of halide-based PSC device in open atmosphere without the use of glovebox was attempted.

## 2 Experimental Setup

### 2.1 Synthesis of Electron Transport Layer (ETL)

Fluorine doped tin oxide (FTO) glass substrates which are used for the fabrication of PSCs are basically rectangular shaped glasses having nominal uniform thickness and transparency ~ 80%. The very first step of the synthesis process performed was proper cleaning of the FTO substrate. Hydrothermal process was chosen for fabrication of nanorod shaped titanium dioxide (TiO<sub>2</sub>)-based ETL.

First FTO was cleaned in an ultrasonic bath for 10 min at 30 °C. Then again, it was cleaned one by one using ethanol and acetone by the same process for 10 min each. Parallelly, a solution of TiO<sub>2</sub> was prepared. To prepare the required solution, 8 ml HCL was added in 8 ml DI water and then subjected to constant stirring at 450 rpm. Then, dropwise 0.3 ml of titanium isopropoxide was added into this solution subjected to constant stirring. Then, this solution was placed in an autoclave, and the FTO was dipped at obtuse angles inside the autoclave. Then, the autoclave was placed in an hot air oven at 130 °C for 16 h. Then after that it was again heated in a muffle furnace at 500 °C for 1 h (Fig. 1).

### 2.2 Preparation of MAPbI<sub>3</sub> PSC

Two types of MAPbX<sub>3</sub> perovskite solutions were prepared with X<sub>3</sub> as I<sub>3</sub> and I<sub>2</sub>Cl.

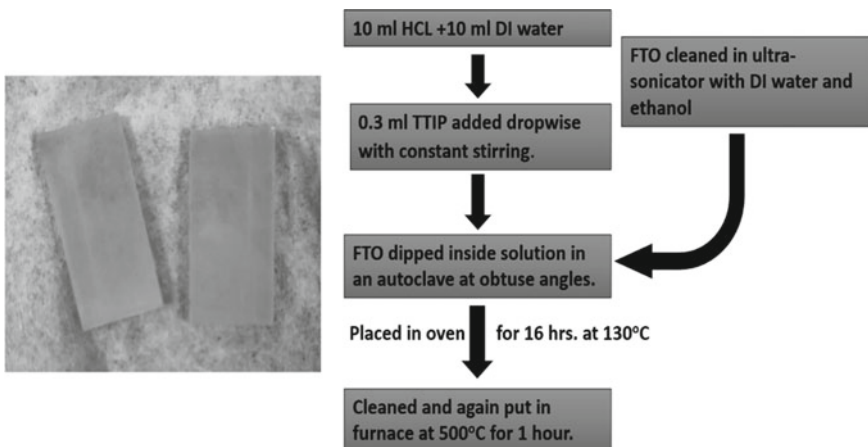


**Fig. 1** Flowchart for deposition of  $\text{TiO}_2$  nanorods as photoanode on FTO for the fabrication of PSC

For preparation of  $\text{MAPbI}_3$ , first 0.147 M of  $\text{PbI}_2$  solution was obtained by dissolving 0.4610 g  $\text{PbI}_2$  in a mixed solvent that contained 4.8 mL dimethylformamide(DMF), 1.2 mL DMSO, and 0.8 mL acetic acid. The  $\text{PbI}_2$  solution was heated while stirred at 70 °C for 3–4 h. After 2 h, 1 mL DMF and 0.25 mL DMSO were taken separately then stirred for 25 min. Then,  $23.4 \text{ mg mL}^{-1}$  solution or 0.147 M of MAI was produced by dissolving 0.227 g MAI in 8.45 ml IPA (99.8%) and adding it to the above separate mixture and stirred for 15 min at 700 rpm. FTO substrate with titanium nanoparticles (TNP) was preheated at 150 °C on a hot plate for about of 90 s. Thereafter, 68 $\mu\text{L}$   $\text{PbI}_2$  solution was added dropwise on TNPs, followed by spin coating at 3000 rpm for 30 s. After this, 100  $\mu\text{l}$  MAI solution was dropped on the  $\text{PbI}_2$  precursor (standing for 30 s), followed again by spin coating at 5000 rpm for 10 s. After this, the film was heated at 40°C for 5 min.

For hole transport layer (HTL), the Poly(3,4-ethylenedioxythiophene)-poly(styrenesulfonate) (PEDOT: PSS) solution was diluted in isopropyl alcohol (IPA). 1 ml PEDOT: PSS and 3 ml IPA were taken (1:3 ratio). This solution was filtered, dropped 100  $\mu\text{l}$  on the substrate, and spin coated at a frequency of 1000 rpm for 20 s and again at 4000 rpm for 40 s. At the end, it was dried at 120 °C for 5 min to prepare PEDOT: PSS layer. For counter electrode (CE), Ag paste was applied, and the fabrication of the required PSC was completed (Fig. 2).

### 2.3 Preparation of $\text{MAPbI}_2\text{Cl}$ PSC

For preparation of  $\text{MAPbI}_2\text{Cl}$ , 0.04 M  $\text{PbI}_2$  solution was obtained by dissolving 0.653 g  $\text{PbI}_2$  into a solvent consisting of 30 mL DMSO and 0.8 mL acetic acid. The  $\text{PbI}_2$  solution was heated while stirred continuously at 70 °C for 3–4 h. Thereafter, a

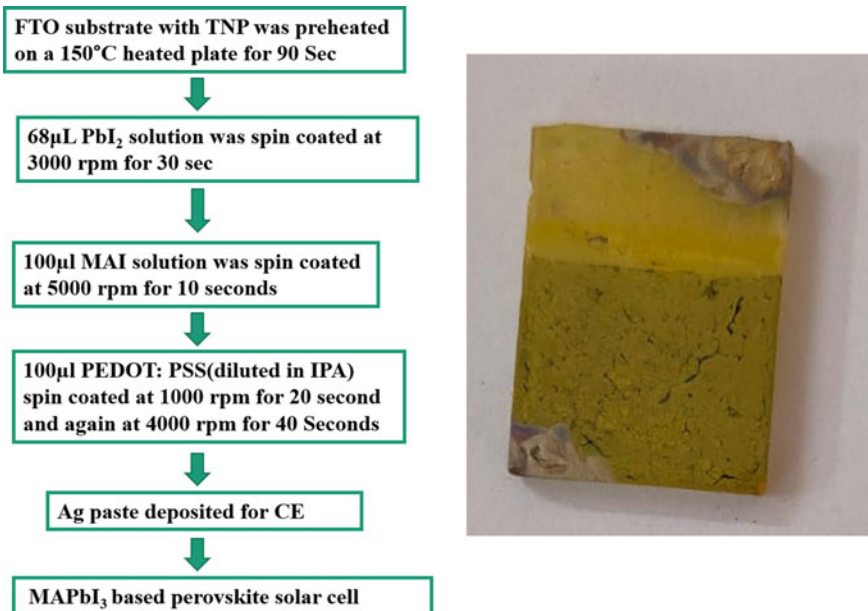


**Fig. 2** Flowchart for synthesis of MAPbI<sub>3</sub> type PSC by the use of spin coating process in the ambient atmosphere

0.04 M MACl solution was prepared by adding 0.081 g of MACl in the same solvent. Then, both the solutions were mixed, stirred, and heated for 30 min at 80–100 °C.

100 µl of the prepared solution was then spin coated on top of the ETL layer at 2000 rpm for 30 seconds and heated for 10 min each in 2 times. For HTL, copper thiocyanate (CuSCN) was diluted in ammonia solution. 1.2163 g of CuSCN and 10 ml ammonia solution was taken. This solution was filtered and dropped 100 µl on the substrate, and spin coating at 3000 rpm for 30 s was performed. Finally, it was dried at 120 °C for 5 min to prepare CuSCN layer. Then for counter electrode (CE), Ag paste was applied, and the fabrication of the required PSC was completed (Fig. 3).

### 3 Results and Discussion

For examining the crystal structure of TiO<sub>2</sub>, X-ray diffraction (XRD) is used. The diffraction pattern of TiO<sub>2</sub> is shown in Fig. 4. The crystal structures and purity of phase of the as samples were performed by using the powder X-ray diffractometer (XRD) (Rigaku Ultima-IV) which ranged from 20 to 70° in 2-theta with 0.02 steps/sec using Cu-Ka as source of radiation ( $\lambda = 0.15406$  nm) at room temperature. The diffracted peaks are matching with standard rutile phase of TiO<sub>2</sub> and are comparable

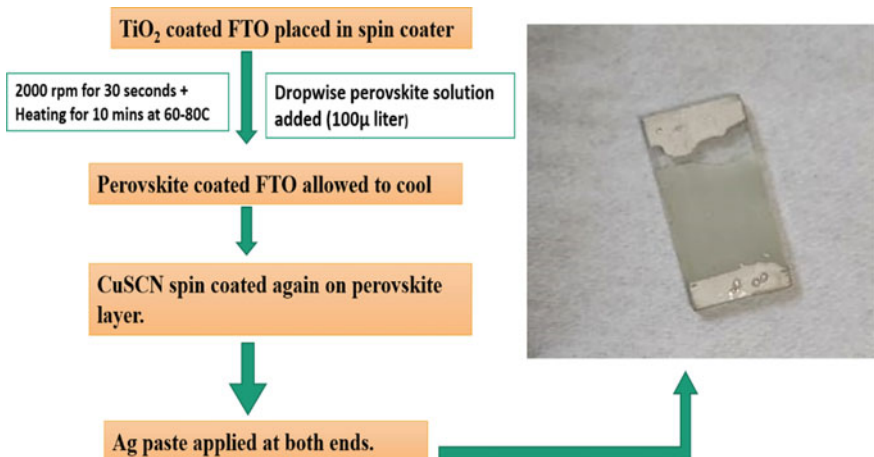


**Fig. 3** Flowchart for the fabrication of MAPbI<sub>2</sub>Cl PSC using spin coating method in ambient atmosphere

with the JCPDS card number 21-1276. The extra small peaks are due to the presence of FTO. Utilizing the results obtained from the most intense peak the crystallite size was calculated by using the values of full width half maxima (FWHM( $\beta$ )),  $k$ ,  $\lambda$ , and  $\theta$ .

$$D = k\lambda/\beta \cos\theta \quad (1)$$

Here,  $k = 0.94$ ,  $\lambda = 0.15406$ ,  $\beta = 0.00553$ ,  $\cos\theta = 0.950785$ , and  $D$  was calculated to be 27.542 nm.

The morphology and surface chemical composition of the samples were analyzed by use of scanning electron microscopy (SEM) SU1510 and by energy dispersive X-ray spectroscopy (EDX), respectively. From the SEM image in Fig. 5, it can be seen that there is presence of the nanorod structure of the TiO<sub>2</sub> ETL. The average diameter of the nanorods was about 200 nm.

Energy dispersive X-ray (EDX) spectroscopy is used to identify those elements which are present in the prepared sample. The obtained EDX spectra shown in Fig. 6 depict that separate maxima of titanium and oxygen were detected, thus confirming that no other impurity elements are present in the prepared sample.

The light absorbance properties of the most efficient cell, MAPbI<sub>2</sub>Cl PSC, were characterized using UV-Vis spectroscopy. The UV-Vis spectra of the prepared samples were conducted by the Perkin-Elmer spectrometer. This result showed that the fabricated MAPbI<sub>2</sub>Cl cell showed good absorbance in the visible range from 380 to 700 nm wavelength of incident light. The absorbance maximum was found at 390 nm (Fig. 7).

Using the Tauc's relation shown in Eq. (2), the bandgap energy can be derived from the UV Visible spectrum. The Tauc's plot depicts the light energy ( $h\nu$ ) on the

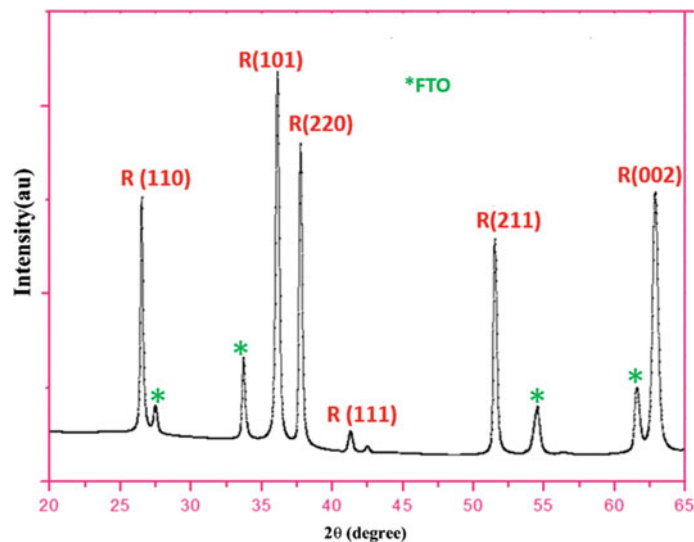


**Fig. 4** XRD pattern of the deposited TiO<sub>2</sub> ETL on FTO using hydrothermal process

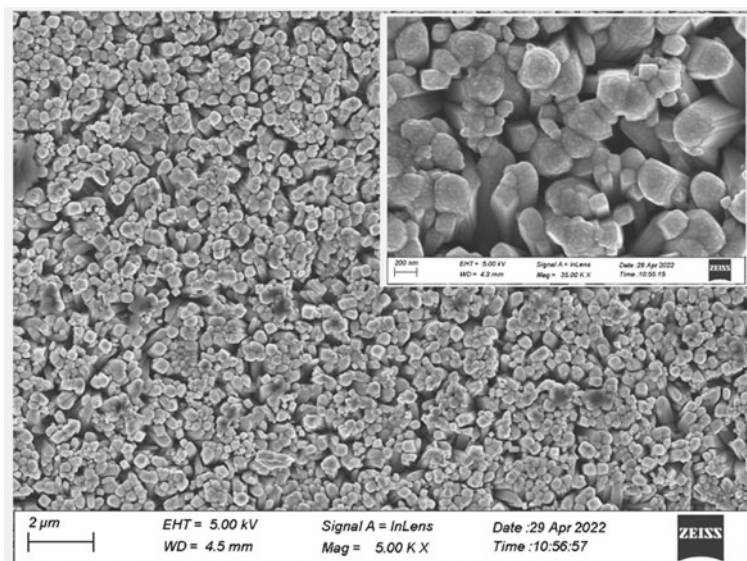


**Fig. 5** SEM image of the fabricated TiO<sub>2</sub> along with enlarged image in the inset

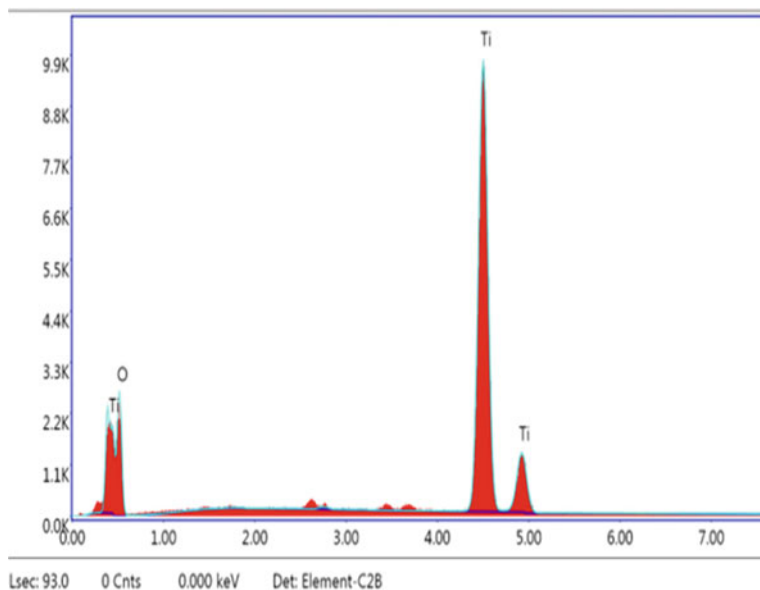


**Fig. 6** EDX spectrum of nanorod shaped  $\text{TiO}_2$  photoanode deposited on FTO

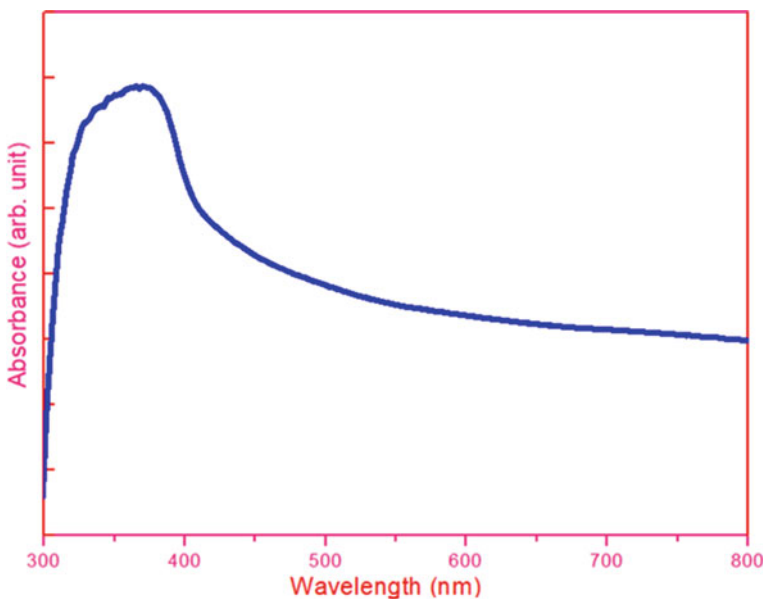


**Fig. 7** Absorbance spectra obtained using UV Visible spectroscopy of the  $\text{MAPbI}_2\text{Cl}$  PSC

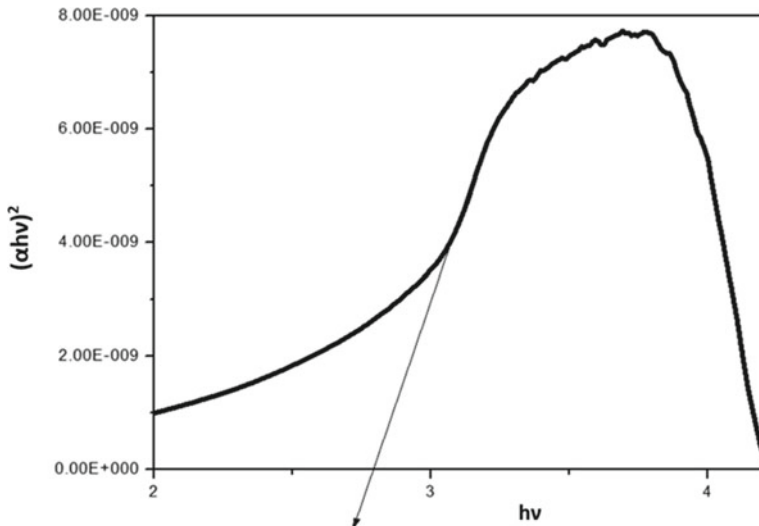


**Fig. 8** Tauc's plot made by using data from UV Visible spectroscopy to determine the bandgap of the MAPbI<sub>2</sub>Cl PSC

abscissa and on the ordinate the quantity  $(\alpha h v)^2$ . By performing the extrapolation of the linear region to reach zero absorbance, the bandgap of the sample can be determined.

$$(\alpha h v)^2 = \beta(h v - E_g) \quad (2)$$

In the above equation, “ $\alpha$ ” is the absorbance, “ $h$ ” is the planck’s constant, “ $v$ ” is the frequency, “ $\beta$ ” is a constant, and “ $E_g$ ” is the bandgap. From Tauc's plot, the band gap was calculated, and it was obtained as 2.7 eV (Fig. 8).

The I-V characteristics were determined using a solar simulator with input intensity 100 mW/cm<sup>2</sup>. The  $I$  vs  $V$  and  $P$  vs  $V$  curve for both cells were plotted from obtained results, and  $V_{oc}$ ,  $I_{sc}$ ,  $FF$ , and  $\eta$  were calculated.  $I_{sc}$  is the short circuit current obtained when voltage is zero after both the terminals are shorted.  $V_{oc}$  is the open circuit voltage at zero current value. Fill factor ( $FF$ ) is the ratio of maximum obtained power ( $P_{max}$ ) to the maximum ideal power that is the product of  $V_{oc}$  and  $I_{sc}$ .

$$FF = \frac{P_{max}}{I_{SC} \times V_{OC}} \quad (3)$$

$$\eta = \frac{V_{OC} \times I_{SC} \times FF}{P_{in}} \quad (4)$$

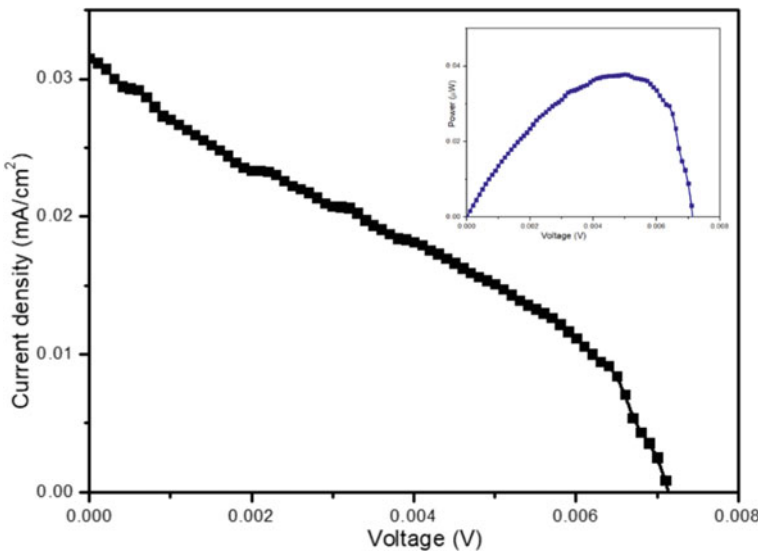


**Fig. 9**  $I$ - $V$  and  $P$ - $V$  characteristics curve of the fabricated  $\text{MAPbI}_3$  PSC based on nanorod shaped  $\text{TiO}_2$  anode

The  $V_{\text{oc}}$ ,  $I_{\text{sc}}$ ,  $P_{\text{max}}$ , and  $FF$  values were found to be 0.0072 V, 0.0157 mA, 37.863 nW, and 33.37%, respectively, for the  $\text{MAPbI}_3$  cell depicted in Fig. 9. The efficiency of the cell ( $\eta$ ) was 0.0000757%.

Similarly, the values of  $V_{\text{oc}}$ ,  $I_{\text{sc}}$ ,  $P_{\text{max}}$ , and  $FF$  for the  $\text{MAPbI}_2\text{Cl}$  cell (Fig. 10) were 2.9 V, 1.67 mA, 1.44 mW, and 29.73%, respectively. The efficiency of this cell ( $\eta$ ) was much higher than the  $\text{MAPbI}_3$  and was found to be 2.89%.

It is seen that the efficiency of the fabricated cells cannot be called a breakthrough. In this paper, no glovebox or controlled atmosphere was used during fabrication the PSC devices to prevent them from degradation. The low efficiency might be considered to be an influence of degradation in ambient atmosphere and humidity. However, under the same conditions, the efficiency of the  $\text{MAPbI}_2\text{Cl}$  was much higher than  $\text{MAPbI}_3$ . This gap in efficiency might be due to the exposure of the  $\text{MAPbI}_3$  cell to ambient atmosphere for 1 week more than the other. Thus, it can be inferred that the PSC device undergoes degradation very rapidly in ambient conditions.

## 4 Conclusions

XRD results confirmed the presence of rutile phase  $\text{TiO}_2$ , the crystallite size ( $D$ ) = 27.54 nm. SEM images illustrated the nanorods structure of  $\text{TiO}_2$ , and average diameter of nanorods is 200 nm. EDX results verified that Ti and O were present in the ETL with no impurity. Single halide and mixed halide perovskites were successfully

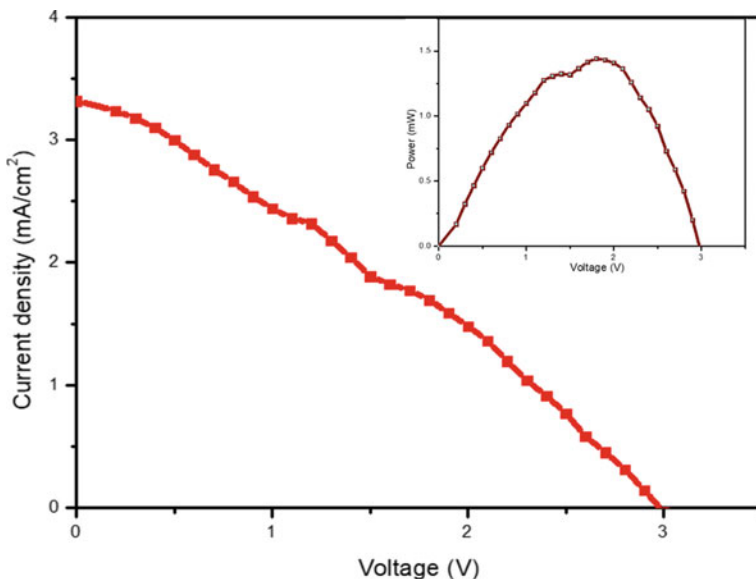


**Fig. 10**  $I$ - $V$  and  $P$ - $V$  characteristics curve of the fabricated MAPbI<sub>2</sub>Cl PSC based on nanorod shaped TiO<sub>2</sub> anode

fabricated, and results compared. The efficiency of the best cell was 2.89%. The  $V_{oc}$ ,  $I_{sc}$ , and  $P_{max}$  values were found to be 2.9 V, 1.67 mA, and 1.44 mW for this cell. The MAPbI<sub>2</sub>Cl PSC has smooth and good absorbance in visible region with absorbance maxima at 390 nm, and the bandgap was calculated using Tauc's plot to be 2.7 eV. The less efficiency and slightly larger bandgap were due to the degradation of the PSC device in ambient atmosphere.

## References

1. Ye H et al (2019) 17.78% efficient low-temperature carbon-based planar perovskite solar cells using Zn-doped SnO<sub>2</sub> electron transport layer. *Appl Surf Sci* 478:417–425. <https://doi.org/10.1016/J.APSUSC.2019.01.237>
2. Grancini G et al (2017) One-Year stable perovskite solar cells by 2D/3D interface engineering. *Nat Commun* 8. <https://doi.org/10.1038/ncomms15684>
3. NREL champion module efficiency chart
4. Li X, Zhang F, He H, Berry JJ, Zhu K, Xu T (2020) On-device lead sequestration for perovskite solar cells. *Nature* 578(7796):555–558. <https://doi.org/10.1038/s41586-020-2001-x>
5. Weber D (1978) CH<sub>3</sub>NH<sub>3</sub>PbX<sub>3</sub>, ein Pb(II)-system mit kubischer Perowskitstruktur/CH<sub>3</sub>NH<sub>3</sub>PbX<sub>3</sub>, a Pb(II)-system with cubic perovskite structure 33(12):1443–1445. <https://doi.org/10.1515/znb-1978-1214>
6. Kojima A, Teshima K, Miyasaka T, Shirai Y, Society E, de Electroquimica SM (2006) Novel photoelectrochemical cell with mesoscopic electrodes sensitized by lead-halide compounds

- (2). In: Joint international meeting, the electrochemical society, p 397. (Online). Available: <https://www.tib.eu/de/suchen/id/BLCP%3ACN063207352>
- 7. Kojima A, Teshima K, Shirai Y, Miyasaka T (2009) Organometal halide perovskites as visible-light sensitizers for photovoltaic cells. *J Am Chem Soc* 131(17):6050–6051. <https://doi.org/10.1021/ja809598r>
  - 8. Im J-H, Lee C-R, Lee J-W, Park S-W, Park N-G (2011) 6.5% Efficient perovskite quantum-dot-sensitized solar cell. *Nanoscale* 3(10):4088–4093. <https://doi.org/10.1039/C1NR10867K>
  - 9. Kim HS et al (2012) Lead iodide perovskite sensitized all-solid-state submicron thin film mesoscopic solar cell with efficiency exceeding 9%. *Sci Rep* 2. <https://doi.org/10.1038/sre00591>
  - 10. Lee MM, Teuscher J, Miyasaka T, Murakami TN, Snaith HJ (2012) Efficient hybrid solar cells based on meso-superstructured organometal halide perovskites. *Science* 338(6107):643–647. <https://doi.org/10.1126/science.1228604>
  - 11. Burschka J et al (2013) Sequential deposition as a route to high-performance perovskite-sensitized solar cells. *Nature* 499(7458):316–319. <https://doi.org/10.1038/nature12340>
  - 12. Liu M, Johnston MB, Snaith HJ (2013) Efficient planar heterojunction perovskite solar cells by vapour deposition. *Nature* 501(7467):395–398. <https://doi.org/10.1038/nature12509>
  - 13. Jeon NJ, Noh JH, Kim YC, Yang WS, Ryu S, Seok SI (2014) Solvent engineering for high-performance inorganic–organic hybrid perovskite solar cells. *Nat Mater* 13(9):897–903. <https://doi.org/10.1038/nmat4014>
  - 14. Zhou H et al (2014) Interface engineering of highly efficient perovskite solar cells. *Science* 345(6196):542–546. <https://doi.org/10.1126/science.1254050>
  - 15. Yang WS et al (2015) High-performance photovoltaic perovskite layers fabricated through intramolecular exchange. *Science* 348(6240):1234–1237. <https://doi.org/10.1126/science.aaa9272>
  - 16. Yang WS et al (2017) Iodide management in formamidinium-lead-halide-based perovskite layers for efficient solar cells. *Science* 356(6345):1376–1379. <https://doi.org/10.1126/science.aan2301>
  - 17. Zhou Y et al (2018) Composition-Tuned wide bandgap perovskites: from grain engineering to stability and performance improvement. *Adv Funct Mater* 28(35):1803130. <https://doi.org/10.1002/adfm.201803130>
  - 18. NREL, Best Research cell efficiency chart. <https://www.nrel.gov/pv/cell-efficiency.html>

# GA-Based IMC Fractional PI Controller Design for Dissolved Oxygen Control with a Non-integer Order Biological Wastewater Treatment Plant



Indranil Dey, Sridhar Pilli, and Seshagiri Rao Ambati

**Abstract** Wastewater treatment plants (WWTPs) are nonlinear dynamic processes which require optimization in order to be consistent with strict environmental water regulations. In this study, a seven reactor arrangement activated sludge process is used to permit simultaneous elimination of phosphorus besides nitrogen. The most challenging and energy-consuming stage of a WWTP is the activated sludge process (ASP) and its aeration process. Two different IMC-based fractional filter with relevant PI and FPI controllers coupled with the corresponding integer order and fractional order models are designed to control the levels of dissolved oxygen (DO) in aerobic reactors. The IMC fractional P-I controller was built with the maximum sensitivity in relation to gain margin (GM) and phase margin (PM) of the process as a restriction. A constrained Genetic Algorithm (GA) is used to optimize the fractional filter parameter using criteria like GM, PM, Gain crossover frequency ( $W_{gc}$ ), Phase crossover frequency ( $W_{pc}$ ), and Maximum Sensitivity ( $M_S$ ). For set point tracking and disturbance rejection, the performance of the suggested approach is evaluated in terms of Integral Absolute Error (IAE) and Integral Square Error (ISE).

**Keywords** Activated sludge process · Non-integer order model · ASM3-bioP · DO control · IMC-FPI · GA

---

I. Dey (✉) · S. R. Ambati

Department of Chemical Engineering, National Institute of Technology, Warangal,  
Telangana 506004, India

e-mail: [indracool.1990@gmail.com](mailto:indracool.1990@gmail.com)

S. Pilli

Department of Civil Engineering, National Institute of Technology, Warangal, Telangana 506004,  
India

S. R. Ambati

Department of Chemical Engineering, Indian Institute of Petroleum & Energy (IIPE),  
Visakhapatnam, Andhra Pradesh 530003, India

## 1 Introduction

Water is essential for all kinds of life to sustain. The steadily increasing demand for water resources, which is essential to both civil activity and industrial production, has aided modern mankind's rapid evolution. Water quality crises may occur at the start of the twenty-first century as a result of ineffective water use habits and wastewater (WW) management techniques. Obtaining the desired water treatment is critical for living a healthy lifestyle. More than 60% of the world's water is introduced into the atmosphere untreated. However, protection of the environment has now become extremely relevant in recent decades, with sewage treatment plants having rigid effluent discharge limits for pollutant substances such as organic matter, priority substances, and other contaminants for WWTP. Mechanical, chemical, and biological functions are all explored in a typical WWTP. The biological stage is in charge of reducing bio pollutants such as nitrogen (N) phosphorus (P) along with carbon (C) in the effluents to a tolerable range. The utmost widely accepted technique for removing biological compounds is the activated sludge process, which engages a complex microbial growth already present in bioreactors. This stage of the WWTP involves the most complex, and it is susceptible to a number of disturbances like changes in inlet flow and a huge range in time constants of the process brought on by bio-mechanisms. A task group of the International Water Association (IWAQ) suggested multiple activated sludge models (ASM), which include ASM1, ASM2 as C and N removal model and ASM2d and ASM3bioP as C, N, and P removal model [1].

Control engineers play a significant role in wastewater treatment facilities. Effective plant operation increases plant lifespan, lowers unit product costs, and limits the amount of nutrients in the effluent. Matter of fact, sophisticated control techniques have elevated the interest of many researchers, as the advancement of automation and instrumentation inside a WWTP technique minimizes the most difficulty and uncertainty of the controlling aim in a running complex and difficult plant function. The amount of dissolved oxygen (DO) that the diffusers deliver to the aeration basin is a key sign of how effectively the secondary biological treatment is working. It is inextricably linked to the operation of the microbial consortium. Controlling and maintaining a close watch on the dissolved oxygen (DO) is an easy way to manage and supervise the treatment procedure. For WWTP researchers, adjusting the DO set point is a key challenge. In the literature, a variety of control strategies have been developed to operate a WWTP as efficiently as possible under subject to load variation. A framework for contrasting various control strategies has emerged, called the benchmark simulation model (BSM1) [2].

Research on fractional calculus and its approach in the field of control theory has significantly increased over the last couple of years [3, 4]. Contrarily, advances in the study of fractional order calculus have made it possible for scientists to exhibit that real-time complex process exert fractional order dynamic nature. Systems with fractional order can be represented with fewer terms while still having complex system dynamics. A generalized version of the conventional PID controller along

with two additional Integrating ( $\lambda$ ) plus differentiating ( $\mu$ ) order parameters creates the fractional order PID ( $P^{1-\lambda}D^\mu$ ) controller. Further parameter tuning improves the closed-loop response's solidity [5, 6]. After that, Integral Square Error (ISE) along with Integral Absolute Error (IAE) is minimized to achieve each system's desirable fractional order controller. Recently one study has presented a fractional order internal model control (FOIMC) for controlling nonlinear conical tank systems [7]. PSO and WOA algorithms are used to tune the FOIMC controller parameters. It uses less control energy and is more resistant to changes in gain than the other controller. Literature explicates fractional calculus and its adaptation in system identification for modelling aspects of the linear system in a fractional form [8].

There are few articles in the WWTP field for fractional control-based applications. In the sludge treatment process, a fractional order PI controller implemented [9]. Some study suggested a reliable non-integer order feedback controller for urban systems [10]. The ASM3bioP model, which includes a secondary clarifier and a connective with seven reactors, is the foundation of the current study. According to a recent study, Indranil et al. has developed a fractional model and tuned a fractional controller using an optimization technique [11]. The study of control approach design in the ASM3bioP model does not include a fractional controller design based on an IMC technique. In the proposed investigation, an IMC-based fractional filter is created using constrained GA to eliminate both the ISE and IAE criterions. Additionally, a fractional model for the aeration process of the ASM3bioP model was formed. The novel aspect of this work is the development of a systematic procedure for generating a fractional order models and then designing fractional order controllers and analysing the fractional order controllers' performance. In addition, a GA-based fractional filter was designed for DO control in the closed-loop.

## 2 Material and Methods

### 2.1 Process Description: *ASM3bioP Model in WWTP Layout*

ASM1, ASM2, and ASM3 are some models that only remove carbon and nitrogen. But unlike the earlier models, ASM3bioP also eliminates phosphorus. Improved biological phosphorus exclusion can be forecast by incorporating customized ASM2d processes into the ASM3 model (i.e. ASM3bioP) without the fermentation of easily degradable substrates. The double exponential settling velocity Takács model for the secondary settler follows the seven reactor systems that make up ASM3bioP's biological processes. The 17 state variables in ASM3bioP in the absence fermentation and decay, which would remove both N and P [12]. The production of PAOs, or poly-accumulating organisms, which are essential for the removal of P, takes place in the anaerobic reactor.

The framework for a WWTP is shown in Fig. 1, and it consists of seven biological reactors connected in succession by a secondary settling tank. ASM3bioP at 15 °C

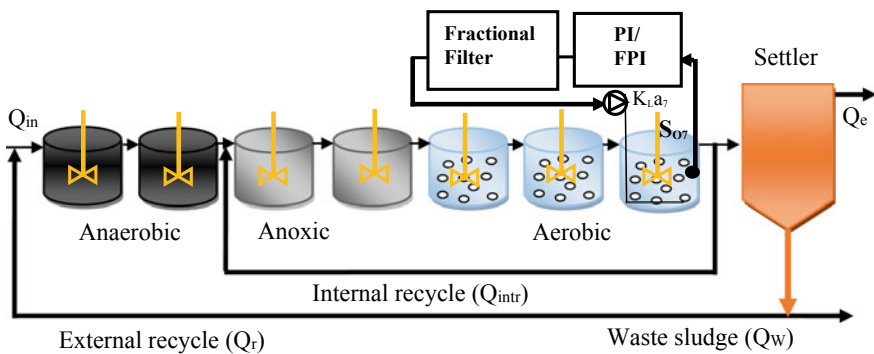


**Fig. 1** BSM-1P plant framework with IMC-based PI and FPI control approach for DO control

also includes the variation of kinetic parameters, oxygen saturation level, and  $K_{La}$  (mass transfer coefficient). The state variables, and including their symbols and units, are shown in Table 1.

**Table 1** Symbols of state variables and their and units

No.	Symbol	Compound	Units	Average influent
1	$S_O$	Dissolved oxygen	$g(COD)m^{-3}$	0
2	$IS_S$	Readily biodegradable organic substrate		90.34
3	$S_I$	Inert soluble organic		30
4	$S_{NH}$	Ammonia + nitrogen	$g(N)m^{-3}$	39.40
5	$S_{NO}$	Nitrate and nitrite		0
6	$S_N$	Dinitrogen		0
7	$iSPO$	Primarily orthophosphates		8.86
8	$S_{HCO}$	Alkalinity	$mol(HCO_3)m^{-3}$	7
9	$X_I$	Inert particulate	$g(COD)m^{-3}$	51.20
10	$X_S$	Slowly biodegradable substrates		202.34
11	$X_H$	Heterotrophic organisms		28.17
12	$X_{STO}$	Cell internal storage		0
13	$X_{PAO}$	Phosphate accumulating organisms		0
14	$X_{PP}$	Polyphosphate	$g(P)m^{-3}$	0
15	$X_{PHA}$	Primarily polyhydroxy alkanoates		0
16	$X_A$	Nitrifying organisms	$g(COD)m^{-3}$	0
17	$X_{TSS}$	Total suspended solids	$g(SS)m^{-3}$	215.51

## 2.2 Influent Data

ASM2d wastewater data were modified to change the values and composition of the influent data [13]. ASM3bioP integrates  $S_A$  (fermentation products) and  $S_F$  (readily biodegradable substrate) as  $S_S$  (biodegradable substrate), and there is no metal precipitation reaction, which is the primary difference [11].

## 3 Process Identification

Finding the appropriate process model is essential before attempting to implement a control scheme for any type of process. Transfer Functions (TF), which have been created by applying fundamental physics and bio-chemical engineering fundamentals to very well systems (such as Newton's law, material balance, heat transfer, and fluid mechanics), explain the processes in our control system. In actuality, many of the industrial processes that need to be managed are far too complicated to be explained using basic principles. A reader can go through the content to understand equations and modelling methodology involved in ASM3-bioP model process identification [12]. In this work as discussed earlier, from simulation study non-integer order model with time delay of WWTP are identified and hence GA-based IMC fractional filter cascaded with fractional controller are implemented on it. An integer model from Indranil et al. is taken to design PI controller with fractional filter using IMC technique.

### 3.1 Fractional Order Model Identification

Fractional order calculus involves arbitrary order differential and integral equations and is a generalization of integer order calculus. Fractional calculus theory can solve any derivative or integral of any order, as well as continuous versions of the fractional calculus operator which is defined as follows [12] in Eq. (1)

$$a\mathcal{D}_t^p = \begin{cases} \frac{d^p}{dt^p} & \text{Re}(p) > 0 \\ 1 & \text{Re}(p) = 0 \\ \int_a^t (dt)^{-p} & \text{Re}(p) < 0 \end{cases} \quad (1)$$

where 'a' and 't' are the calculus top and bottom level bounds, respectively, and is an arbitrary complex. Fractional order calculus theory has developed many different definitions of fractional calculus, including the GL, RL, and Caputo definitions [14].

Based on the time domain approach, a non-integer order time delay transfer function model is found using the MATLAB FOMCON toolbox [15]. We can choose the kind of system simulation we want to use using the Simulation parameters window. The input and output data is generated by giving the random input to the model of ASM3-bioP model at steady state with plant influent and relating all state variable.

Steps to identify a good fitted identified model

- A ‘fidata’ structure must be chosen first and foremost.
- Select ‘Time domain Identification’, where you can choose frequency domain too.
- Choose the ‘simulation parameter methods’ in Grunwald–Letnikov method or Oustaloup filter or Refined Oustaloup filter. (You need to select ‘w’ range and order for the last two options). We select the Oustaloup filter.
- In the ‘Identification and options’ section chosen ‘fidata’ name will show and the preferred algorithm is ‘Trust-Region-Reflective’.
- There is a symbolic form of identified model in terms of the fractional pole and zero polynomials. A first-guess model is created. In order to create polynomials autonomously, a commensurate-order  $q$  that has the property that  $0.01 \leq q < 2$ —the order of the polynomial—can be defined.
- A plot that displays a good fitting result and shows the identified system’s stable behaviour should be displayed at the conclusion of the identification process. As long as the outcomes are pleasing, the model is saved for use in creating a controller.

Finally a process model is found in form of non-integer order with time delay

$$G_P = \frac{K}{TS^\beta + 1} e^{-T_d S}$$

## 4 Controller Implementation

Making an effective control scheme requires careful consideration when choosing a control structure. Controlling the rates of nitrification and denitrification is praised as the fundamental strategy. The necessary nitrification in the oxic reactors is ensured by changing the air flow rate, which controls the DO. In this study,  $S_{O7}$  are regulated by adjusting  $K_{La7}$  in the seventh reactor (aerobic) using an IMC-based fractional filter cascaded with FPI controllers (in Fig. 1) and the result is compared with a implemented IMC-based integer order PI with fractional filter.

The aeration tank uses between 40 and 50% of the energy used in a WWTP [16]. As a conclusion, energy usage and relevant expenses can be reduced by employing an effective controller to conduct efficient aeration.

## 4.1 IMC Fractional Filter Design Using Multi Objective GA

IMC is a sophisticated model-based design methodology that Morari and colleagues designed. Figure 2 depicts the IMC scheme and feedback control loop with internal blocks, with  $G$ ,  $G$ , and  $G_c^*$  standing for the process, the internal model of the process, and the IMC controller, respectively. Let  $(Y_{sp})$  be the set point,  $(Y)$  be the controlled variable as output, and  $D$  be the disturbance. The controller design utilizing the IMC technique is as follows.

The form of Eqs. (2)–(5) represent the steps involved in creating an IMC-PID controller. For classical feedback controller, output response is given in Eq. (2)

$$Y = \frac{G_C G}{1 + G_C G} Y_{SP} + \frac{1}{1 + G_C G} D \quad (2)$$

Step 1: Factor process method of the model is followed in the Eq. (3)

$$G_P = G_+ G_- \quad (3)$$

Step 2: Derive IMC transfer function from the IMC structures is follows in the Eq. (4)

$$Y = \frac{G_C^* G}{1 + G_C^*(G - G_P)} Y_{SP} + \frac{1 - G_C^* G_P}{1 + G_C^*(G - G_P)} D \quad (4)$$

$$G_C = \frac{G_C^*}{1 - G_C^* G_P} G_C^* = \frac{1}{G_-} f$$

where  $f$  is filter function for the physical reliability of the system  $f = \frac{1}{(TS^\alpha + 1)^r}$

$T$  = time constant  $r$  = positive integer.

Step 3: Derive controller of the model from the IMC method is in the Eq. (5)

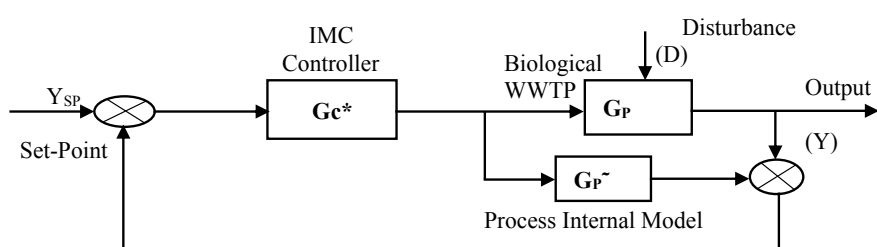


**Fig. 2** Feedback control strategy with IMC approach

$$G_C = \frac{G_C^*}{1 - G_C^* G_P} \quad (5)$$

## 4.2 Fractional Filter with Integer PID Controller (FF-IOPID)

General integer order controller equation of the time domain form represented in the Eq. (6)

$$u(t) = K_P e(t) + K_d \text{De}(t) + K_i \int e(t) \quad (6)$$

Here  $e(t)$  is error signal, and  $K_P$ ,  $K_d$ , and  $K_i$  are the proportional, integral, and derivative gains. By applying Laplace transform to the controller with zero initial conditions Eq. (6) is transformed in Eq. (7)

$$G_C(s) = K_P + \frac{K_i}{s} + K_d s \quad (7)$$

Integer order system with fractional filter represented in Eq. (8)

$$C_{IF}(s) = \frac{1}{(\lambda s^{\alpha-1} + T_d)} \frac{T}{K} \left( 1 + \frac{1}{Ts} \right) \quad (8)$$

Fractional filter term represented in Eq. (9)

$$H(s) = \frac{1}{(\lambda s^{\alpha-1} + T_d)} \quad (9)$$

PID controller gain values from the IMC method is  $.K_p = \frac{T}{K}$ ,  $K_i = \frac{1}{T_i}$ ,  $K_d = 0$

## 4.3 Fractional Filter Cascaded with Fractional Order PID Controller (FF-FOPID)

General time domain form of fractional order controller equation is in the form of Eq. (10)

$$u(t) = K_P e(t) + K_i \mathcal{D}^{-\eta} e(t) + K_d \mathcal{D}^{\gamma} e(t) \quad (10)$$

Here  $e(t)$  is error signal, and  $K_P$ ,  $K_i$ , and  $K_d$  are the proportional, integral, and derivative gains.  $\eta$ ,  $\Upsilon$  is the fractional derivate and integral coefficients. By applying Laplace transform to the controller with zero initial conditions, Eq. (10) is transformed into Eq. (11)

$$G_C(s) = K_P + \frac{K_i}{s^\eta} + K_d s^\Upsilon \quad (11)$$

Fractional order system with fractional filter  $C_{FF}(s)$  from the IMC procedure is follows in Eq. (12)

$$C_{FF}(s) = \frac{1}{(\lambda s^{\alpha-\beta} + T_d s^{1-\beta})} \frac{T}{K} \left( 1 + \frac{1}{T s^\beta} \right) \quad (12)$$

Fractional filter term  $V(s)$  represented in Eq. (13)

$$V(s) = \frac{1}{(\lambda s^{\alpha-\beta} + T_d s^{1-\beta})} \quad (13)$$

Fractional PID controller values from the IMC method is  $K_P = \frac{T}{K}$ ,  $K_i = \frac{1}{T_i}$ ,  $K_d = 0$ ,  $\eta = \beta$

#### 4.4 Constrained GA Optimization-Based Tuning Based on $M_S$

Genetic algorithms are a type of evolutionary algorithm that employs processes like inheritance, mutation, selection, and crossover that are inspired by evolutionary biology (also called recombination). Utilizing genetic algorithms, which are realized as simulation software, a population of abstract concepts (called chromosomes or the genotype) of potential solutions (called people or phenotypes) to an optimization process develops towards better solutions. Flow chart of the constrained genetic algorithm is shown below in Fig. 3.

The maximum sensitivity in relationship to gain margin and phase margin was used as a restriction when constructing the IMC fractional P-I-D controller of the first order plus time delay model [17]. The filter parameters ( $\lambda$ ,  $\alpha$ ) are fine-tuned using a constrained genetic algorithm using criteria as Gain Margin (GM), Phase Margin (PM), Gain crossover frequency ( $W_{gc}$ ), Phase crossover frequency ( $W_{pc}$ ), and Maximum Sensitivity ( $M_S$ ).

The closed-loop model is following in Eq. (14)–(15)

$$L(s) = G_P(s)c(s) \quad (14)$$

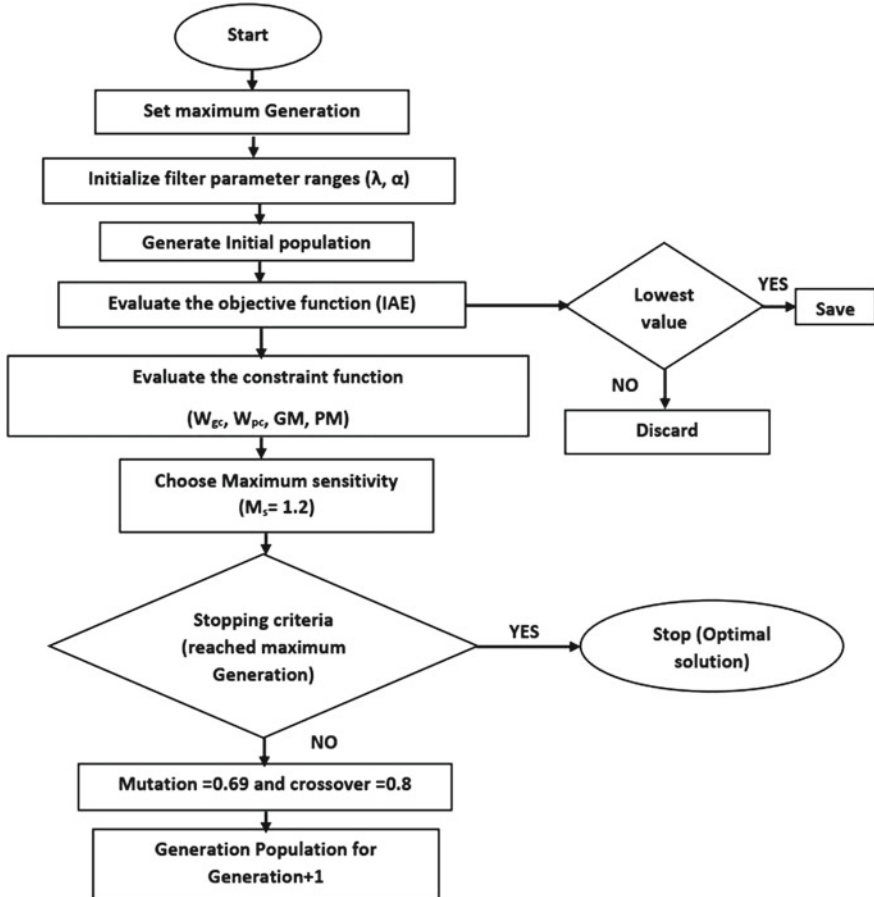


**Fig. 3** Flowchart of constrained GA optimization

$$L(s) = \frac{1 - T_d s}{(\lambda s^\alpha + T_d s)} \quad (15)$$

Put  $s = jw$  in Eq. (14) and it transferred to Eq. (16)

$$L(jw) = \frac{1 - T_d j w}{(\lambda(jw)^\alpha + T_d j w)} \quad (16)$$

From the complex numbers,  $j = \cos\left(\frac{\pi}{2}\right) + j\sin\left(\frac{\pi}{2}\right)$ . From De Moivre's Theorem it is simple to find the power and roots of complex numbers. Then the process model is follows Eq. (17)

$$L(jw) = \frac{1 - T_d j w}{[\lambda(w)^\alpha \cos(\alpha \frac{\pi}{2}) + j(T_d w + \lambda(w)^\alpha \sin(\alpha \frac{\pi}{2}))]} \quad (17)$$

Gain Margin (GM), Phase Margin (PM), Gain crossover frequency ( $W_{gc}$ ), Phase crossover frequency ( $W_{pc}$ ) are calculated for closed-loop model  $L(S)$  to run the GA algorithm in a pre-established equation form.

**Maximum Sensitivity ( $M_S$ ):** The sensitivity function's greatest value across the frequency range and it follows in Eq. (18)

$$M_S|_{\max(0 < \omega < \infty)} = \frac{C(s)G(s)}{1 + C(s)G(s)} \quad (18)$$

The relationship between maximum sensitivity and gain margin and phase margin of the process models are in Eq. (19–20).

$$GM \geq \frac{M_S}{M_S - 1} \quad (19)$$

$$PM \geq 2\sin^{-1}\left(\frac{1}{2M_S}\right) \quad (20)$$

## 4.5 Performance Indices

Integral of squared error (ISE), integral of absolute error (IAE) are used to measure the controller's performance. These are represented in the follow Eq. (21)–(22)

$$ISE = \int_0^{\infty} e^2(t) dt \quad (21)$$

$$IAE = \int_0^{\infty} |e(t)| dt \quad (22)$$

## 5 Results and Discussion

The identified integer and non-integer order transfer function models for DO control are shown below. The controller structure with cascaded filter, where the filter parameter ( $\lambda$ ,  $\alpha$ ) are tuned through GA by minimizing ISE of closed-loop response by selecting  $M_S = 1.2$ . The controllers from the IMC structure are in two forms for

integer order and non-integer model as  $C_{IF}(S)$  and  $C_{FF}(S)$  are designed. Table 2 displays the IMC controller with GA-tuned parameters for the non-integer order plant transfer function.

In the case of this fractional order filter with Integer order PI controller (FF-IOP) response is slower than fractional order filter with fractional order PI (FF-FOPI) and both ISE and IAE are minimized in FF-FOPI scheme (Table 3).

### 5.1 Controller Response with Disturbance to Process Model

The below MATLAB produced Fig. 4 illustrates the DO set point of 2 mgO<sub>2</sub>/L (red colour line) is tracked by both the control strategy applied to the aeration control system. The controller response was also tested with a step disturbance at 5 s. Performance of the controllers in both servo and regulatory cases is satisfactory. The controller performance is evaluated based on IAE and ISE.

## 6 Conclusion

A non-integer order system of biological WWTP is identified from ASM3bioP model using FOMCON toolbox. An IMC-based controller tuning is intended for both Integer and fractional order controllers. A fractional filter is cascaded with the controller, and the filter originates from IMC method. GA is used to optimize IAE of closed-loop response to get the filter parameter ( $\lambda, \alpha$ ). The optimized controller is implemented on the aeration system (DO control) in MATLAB Simulink and a closed-loop response is generated. Closed-loop response shows the better desired set point tracking and same time controller performance (ISE, IAE) is also minimized in the FF-FOPI control strategy. Apart from DO control, as a future study, we can implement this control scheme for nitrate control (NO) and furthermore it can be used for ASM3-bioP simulation models in the BSM1 framework with real influent data with a continuous load variation.

**Table 2** Process model and designed controller by IMC method

Transfer function	Identified model	Fractional filter parameters	IMC-based controller (according to Eqs. 8, 12)
Integer order [11] $\frac{K}{TS+1} e^{-T_d S}$	$\frac{0.013824}{0.0015778*5+1} e^{-0.006021*s}$	$\lambda = 0.4564$ $\alpha = 0.8758$	$C_{IF}(s) = \frac{1}{(0.4564e^{0.8758s}-1+0.006021)} [0.11413(1 + \frac{1}{0.0015778 s^{\frac{1}{5}}})]$
Non-integer order $\frac{K}{TS^\beta+1} e^{-T_d s}$	$\frac{0.007985}{0.00057858*s^{\frac{1}{1.1}}+1} e^{-0.00594s}$	$\lambda = 0.0015$ $\alpha = 1.7485$ $\beta = 1.1$	$C_{FF}(s) = \frac{1}{(0.0015s^{1.7485}-1+0.0059s^{1-1.1})}$ $[0.07245\left(1 + \frac{1}{0.00057858 s^{\frac{1}{1.1}}}\right)]$

**Table 3** Controller performance index

Controller	IAE	ISE
FF-IOPI	1.384	1.175
FF-FOPI	0.5632	0.4184

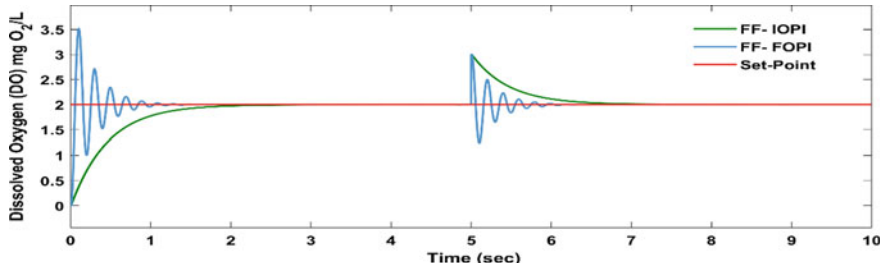


**Fig. 4** DO tracking by IMC-based FF-IOPI and FF-FOPI controller

## References

1. Henze M, Gujer W, Mino T, van Loosdrecht MC (2000) Activated sludge models ASM1, ASM2, ASM2d and ASM3. IWA scientific and technical report no. 9. IWA Publishing, London
2. Copp J (2002) The COST simulation benchmark: description and simulator manual. Office for Official Pub of the EurComm, Luxembourg
3. Magin RL (2004) Fractional calculus in bioengineering crit. Rev Biomed Eng 321–4:1–390
4. Podlubny I (2008) Geometric and physical interpretation of fractional integration and fractional differentiation, pp 1–18
5. Muresan CI, Folea S, Mois G, Dulf EH (2013) Development and implementation of an FPGA based fractional order controller for a DC motor. Else J Mecha 23(7):798–804
6. Luo Y, Chen YQ, Wang CY, Pi YG (2010) Tuning fractional order proportional integral controllers for fractional order systems. J Pro Cont 20:823–831
7. Vavilala SK, Thirumavalavan V, Chandrasekaran K (2020) Level control of a conical tank using the fractional order controller. Comp Electr Eng 87:106690
8. Das S (2008) Functional fractional calculus for system identification and controls. Springer, Berlin
9. Harja G, Vlad G (2015) Fractional order PI control strategy on an activated sludge wastewater treatment process. In: 19th international conference on system, theory, control and computing. ICSTCC 2015—Joint Conference SINTES 19, SACCS 15, SIMSIS 19, pp 577–582
10. Barbu M, Ceanga E (2015) Fractional order controllers for urban wastewater treatment systems. In: 23rd Mediterranean conference on control and automation (MED)—conference proceedings, pp 1174–1179
11. Dey I, Sheik AG, Ambati SR (2022) Fractional-order models identification and control within a supervisory control framework for efficient nutrients removal in biological wastewater treatment plants. Environ Sci Pollut Res 30:16642
12. Solon K (2015) Activated sludge model no. 3 with bioP module (ASMBioP) implemented within the benchmark simulation model no 1. Technical Report
13. Gerenaey KV, Jørgensen SB (2004) Benchmarking combined biological phosphorus and nitrogen removal wastewater treatment processes. Control Eng Pract 12(3):357–373
14. Teplyakov A (2017) FOMCON: fractional-order modeling and control toolbox. In: Fractional-order modeling and control of dynamic systems. Springer, Berline, pp 107–129

15. Tepljakov A, Petlenkov E, Belikov J (2011) FOMCOM: a MATLAB toolbox for fractional-order system identification and control. *Int J Microelectron Comput Sci* 2(2):51–62
16. Henderson M (2001–2002) Energy reduction methods in the aeration process at perth waste water treatment plant. University of Strathclyde, Renewable Energy Systems and the Environment MSc Individual Theses
17. Maamar B, Rachid M (2014) IMC-PID-fractional-order-filter controllers design for integer order systems. *ISA Trans* 53(5):1620–1628

# A Comprehensive Study for Maximum Power Point Tracking Methodologies for Wind Power Systems



Ahmed G. Abo-Khalil, Ramesh C. Bansal, and Nsilulu T. Mbungu

**Abstract** Wind turbines have the fundamental characteristic of directly converting wind energy into electricity; however, the conversion efficiency largely depends on atmospheric conditions such as wind speed. Therefore, it is essential to consider the wind power operation to control at the maximum power point to extract the optimum power. Several techniques have been established to determine the effectiveness at which the energy from wind power is the maximum for each parameter that could affect the system efficiency. An experimental comparison between the perturbation and observation control and support vector regression methods is implemented for a permanent magnet synchronous generator topology. This structure assesses the performance of the traditional and the intelligent-based methods. This paper compares different maximum power point tracking methods in wind energy conversion systems. The selected methods have already been implemented in the literature and industry. However, the novelty of this paper is that it concentrates on the main characteristics and six critical factors of the methods to have a thorough investigation, unlike in any previous study. The advantages, disadvantages, classification, and comparisons make it possible to define the best tracking technique for maximum power.

---

A. G. Abo-Khalil (✉)

Sustainable and Renewable Energy Engineering Department, College of Engineering, University of Sharjah, Sharjah, UAE

e-mail: [aabokhalil@sharjah.ac.ae](mailto:aabokhalil@sharjah.ac.ae)

Department of Electrical Engineering, College of Engineering, Assuit University, Assuit 71515, Egypt

R. C. Bansal · N. T. Mbungu

Department of Electrical Engineering, University of Sharjah, Sharjah, United Arab Emirates

R. C. Bansal

Department of Electrical, Electronic and Computer Engineering, University of Pretoria, Pretoria, South Africa

N. T. Mbungu

Department of Electrical Engineering, Tshwane University of Technology, Pretoria, South Africa

**Keywords** Intelligent control · MPPT · Optimal control · Synchronous generator · Renewable energy · Wind speed

## 1 Introduction

Due to the rise of oil in the twentieth century as an abundant and cheap energy possibility, energy extraction from the wind suffered a lag in its development. However, in the 1980s, wind energy began to be considered again as an energy alternative, given the volatility of oil prices and, on the other hand, the progress made in the development of technology in the area of electronics and computing, allowing to produce electrical energy efficiently and reliably [1]. Furthermore, climate change has also seriously affected hydroelectric generation in recent years, making places with geographical advantages where large plants have been built susceptible to highly variable climatic conditions.

This is how a resurgence of technological development in the wind industry is presented, added to the tremendous global concern for the care of the environment and the search for independent energy sources [2]. In the middle of 2013, the electricity generation from wind worldwide reached 296 GW, about 3.5% of the demand for global electric power [3]. In 2018, wind energy capacity went from just 1.29 GW in 1995 to approximately 528 GW at the end of 2018 [4]. By 2025, wind energy will supply about 12% of global energy demand [5]. Thus, there is a need for permanent innovation in control systems, the design, and implementation of projects in the wind industry.

Unlike conventional sources, such as natural gas and oil, wind energy does not emit greenhouse gases. Furthermore, it does not present the supply problems typical of other sources, such as price variations or depletion of deposits, because its fuel is free, and its deposits are inexhaustible. These characteristics make wind energy one of the most suitable sources to meet the energy needs of modern society, given the severe environmental crisis humanity faces and the constant search for savings and greater energy security.

Wind turbines are classified according to their power scale: small-wind turbines in the range of 0.025–10 kW, medium-scale wind turbines between 10 and 100 kW, and large-wind turbines with over 100 kW [6]. Wind turbines are also classified according to the swept area of their blades. For instance, the International Electrotechnical Commission (IEC) has defined small-scale ones with a maximum swept area of 200 m<sup>2</sup> [7]. Different criteria are presented for the classification of wind turbines: According to the arrangement of the rotation axis, the number of blades, the turbine rotor speed, control and regulation, type of generator used, location, type of wind, etc., interconnection to the network and according to its nominal power. In addition, wind power is classified as the second potential renewable energy resource after solar power [8]. A comparison between the various types of wind turbines according to criteria such as volume and weight, cost and efficiency, system reliability, and failure presentation according to capacity is presented in [9]. However, most research on

extracting electrical energy from the wind has been dedicated to medium- and large-scale wind turbines, where direct connection to the electrical network is sought [10]. For this, they must comply with energy quality standards compatible with the network to which they are connected [11].

Small-scale wind turbines, generally used in places isolated from the electrical grid [12], are increasingly used in metropolitan areas and different applications, such as telecommunications, electro-water pumping, and remote military bases. In addition, this type of system has also been implemented where the energy demand is not high or where they can be combined with photovoltaic devices to supply specific energy needs [13]. These new applications have aroused the interest of researchers in seeking ways to offer greater efficiency in the generation of electrical power in this type of wind turbine since the information on technical characteristics and performance data are minimal for small-scale wind turbines [14], since the manufacturers of these only supply basic parameters, giving rise to uncertainties about the evaluation of the performance of this type of wind turbines [13].

Wind power is classified into two types in the system speed function: variable speed and fixed speed. Besides, the wind turbines are primarily squirrel-cage induction machines in the fixed-speed system, constituting the induction generators directly tied to the electric network [14]. Thus, the latter types possess the simplicity of operation and maintenance and have excellent mechanical strength and a relatively low cost. The speed is kept practically constant in the normal operating range due to a direct connection to the grid. Wind turbines that work at a fixed-speed benefit from a relatively low cost and good robustness. Nevertheless, the main disadvantages are limited aerodynamic efficiency, a constant need for gearbox maintenance, and the installation of capacitor banks to compensate for reactive power [15].

Variable-speed systems have higher quality, efficiency, and performance than fixed-speed systems; however, they generally have a higher degree of complexity and cost associated with their implementation because their operation requires power converters. For instance, the doubly fed induction generator (DFIG) and permanent magnet synchronous generator (PMSG) are the main variable-speed structures, usually tied to the power network through converters [16]. The PMSG is currently extensively used because of its direct coupling to the wind turbine, which is feasible without speed multipliers. The generator was designed with many poles and directly linked to the turbine. With no brushes and gear systems in the coupling, its efficiency increases because of the rotational losses due to friction. One of the primary disadvantages of the PMSG is that the converter tied to the generator, which is connected to the grid, needs to be sized for the generator's rated power, i.e., the generator's full power [17].

One option to reduce the power converter's power is to use the DFIG. The DFIG rotor usually is tied to the wind power through a hardware device and electrically coupled to the wind turbine network with the help of an energy converter in a back-to-back configuration, which allows the bi-directional flow of power in the rotor, as a function of the generator speed [18]. In addition, the stator is tied immediately to the power grid. Thus, the great advantage obtained with the DFIG is that the power

in the rotor circuit is limited to approximately 30% of the nominal power [19, 20], reducing the dimensioning of the converter and, consequently, its cost.

In small- and medium-power wind energy conversion systems (WECSs), the optimum operating point depends directly on the current environmental conditions in a variable-speed technique. For this reason, in some cases, the wind speed is measured to approximate the end of the operation. Nevertheless, for several purposes, the optimal point is achieved through closed-loop techniques depending on the structure model and its output power, entitled maximum power point tracking algorithms (MPPT) [21–24]. Several MPPT techniques for variable-speed wind turbines have been developed [25–30]. Various control schemes with greater or lesser complexity and increased economic cost have been proposed in several studies; however, all systems that contain power converters are designed to increase the power extracted throughout the full wind speed scale. In principle, the MPPT techniques explore the relationship between the power available in the wind and the mechanical power extracted from the wind turbine by studying variables influencing energy generation, such as torque, the speed ratio of the blade ( $\lambda$ ) (also known as tip speed ratio (TSR)), and the power coefficient ( $C_p$ ).

This study evaluates the performance of two selected MPPT algorithms. First, a comparison is made between the artificial intelligence (AI)-based SVR method and a traditional MPPT algorithm—the P&O control method. The performance comparisons of the techniques were performed by considering that the wind turbine operates in a standard test condition and an abruptly varying wind speed [31–35]. Therefore, MPPT strategies may be divided into four categories, as summarized in Table 1. This way, a detailed description of some selected MPPT algorithms is provided in the following sections. Moreover, the study compares the main MPPT methods currently used in wind power systems. These methods have been compared based on parameters such as necessary sensors, knowledge of turbine characteristics, cost, complexity, convergence speed, previous training, and efficiency. Such categorization and comparison can be used when selecting the optimum MPPT method for different wind power topologies and sizes.

## 2 Fundamentals of Wind Generation

Wind power transforms the kinetic energy of the wind into mechanical energy. As air flows through the blades, a pressure difference is created between the top and bottom sides of the blades, causing them to rotate—modern aerodynamic blades with carefully developed profiles.

The generated mechanical energy depends on the wind speed, physical parameters, and angular speed of the turbine can be represented by the [36]:

$$P_t = \frac{1}{2} \rho \pi R^2 v^3 C_P(\beta, \lambda) \quad (1)$$

**Table 1** MPPT techniques-based classification

Category	Methods
Strategy based on the power profile of the turbine	Perturbation and observation (P&O) Power signal feedback control (PSF)
Strategy based on optimal speed control ratio	Optimal tip speed ratio
Strategy based on optimal torque control	Optimal torque control
Strategy based on intelligent prediction	Artificial neural network (ANN) Fuzzy logic control (FLC) Support vector regression (SVR)

with  $P_t$  is the mechanical energy generated,  $v$  is wind speed,  $C_p$  is the power coefficient,  $\rho$  is the air density, and  $R$  is the length of the turbine blades.  $C_p$  is related to the tip speed ratio and the blade pitch angle. Thus, the power coefficient is characteristic of each turbine, and the following equation [37, 38] can be given as:

$$C_p(\beta, \lambda) = C_1 \left[ \frac{C_2}{\lambda_1} - C_3\beta - C_4 \right] e^{\frac{-C_5}{\lambda_1}} + C_6\lambda \quad (2)$$

$$\frac{1}{\lambda_1} = \frac{1}{\lambda - 0.089\beta} - \frac{0.035}{\beta^3 + 1} \quad (3)$$

where  $\beta$  is the inclination angle of the blades, coefficients  $C_1$  to  $C_6$  are constants (and determined empirically), and  $\lambda$  is the tip speed ratio, which is formulated as follows:

$$\lambda = \frac{\omega_r R}{v} \quad (4)$$

with  $\omega_r$  is the rotor angular speed.

The  $C_p$  graph as a function of the tip speed ratio for different blade inclination angles for a given turbine is shown in Fig. 1a. From the behavior of the power coefficient defined in (2) and presented in Fig. 4, it can be seen that the wind turbine's mechanical power can be controlled through the turbine speed or  $\beta$ . Usually, the turbine's power control is carried out by holding the rotational speed. However, for this to be possible, it is necessary that the generation system can operate with variable speed [39]. Furthermore, suppose the wind turbine operates with variable speed. In that case, it is possible to continuously adjust the turbine speed to guarantee maximum aerodynamic efficiency, that is, to ensure that the value of the power coefficient is maximum regardless of the wind speed [40].

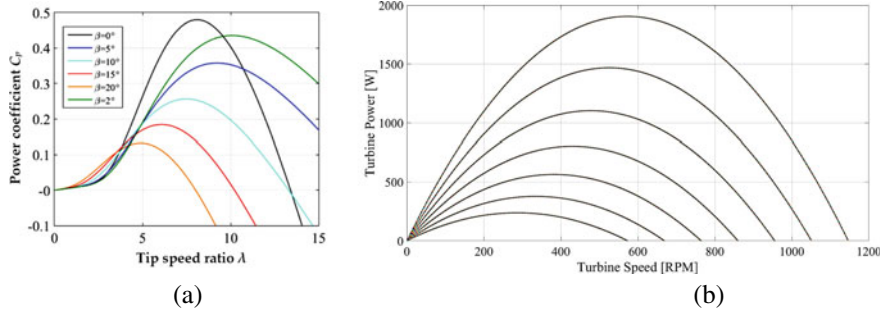


**Fig. 1** **a** Power coefficient characteristics at different tip speed ratios and the pitch blade angles, **b** power generated through the wind turbine versus rotor speed

Figure 1b illustrates the wind turbine characteristics of the generated power as a function of the rotor speed for different wind speeds. Figure 5 shows that, for different wind speeds, maximum power is reached at a specific rotational speed; therefore, the generator speed must be adjusted at the optimum speed. The line that unites all the maximum power points (MPP) (ideal line) gives us the MPP information for all wind speeds.

Applying Eqs. (1) and (4), the mechanical output considering the wind speed and the rotational speed of the rotor is as follows:

$$P_t = \frac{1}{2} \rho \pi R^2 C_P(\beta, \lambda) \frac{R^3}{\lambda^3} \omega_r^3 \quad (5)$$

In the transition region where the turbine power is less than the rated power, the pitch angle  $\beta = 0$ . When the tip speed ratio  $\lambda$  is the optimum value, the value of  $C_p$  becomes maximal so that the maximum output can be expressed as Eq. (6):

$$P_{\max} = \frac{1}{2} \rho \pi R^2 C_{P \max}(\beta, \lambda) \frac{R^3}{\lambda_{\text{opt}}^3} \omega_r^3 \quad (6)$$

In Eq. (6), the remainder except  $\omega_r$  can be expressed as a constant, so the maximum power can also be formulated as

$$P_{\max} = K_{\text{opt}} \omega_r^3 \quad (7)$$

The reference torque for maximum output can also be described as follows:

$$T_{\text{ref}} = K_{\text{opt}} \omega_r^2 \quad (8)$$

Thus, it is essential to adjust the rotation speed of the turbine to guarantee maximum power extraction at every instant of operation. In addition, tracking the

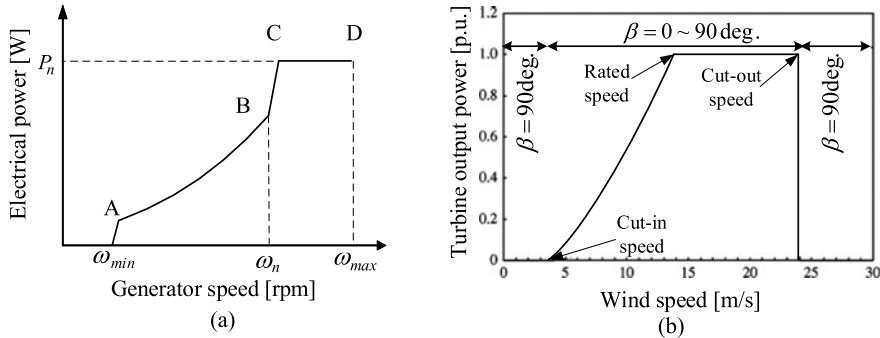


**Fig. 2** Wind turbine characteristics

MPP may require knowledge of different parameters, measurement of different quantities, or systematic calculations to adjust the operating machine quantities, thus ensuring convergence to the point of maximum power extraction [41].

Suppose the MPP search requires power control. In that case, it is essential to measure the rotation speed and the generator output power and know the turbine power characteristic curve. If speed control is used, prior knowledge of the optimum relative speed  $\lambda$ , wind speed measurement, and generator rotation speed is necessary.

Power converters make it possible to manage the rotation speed of wind power by varying the generator current, which varies the load torque and, consequently, the speed. It is then possible, through tracking algorithms, to reach the point of maximum electrical power generated.

While the turbine operates within the speed limits, it is controlled to remain above the maximum power point, represented by the curve in Fig. 2a. However, when the available power in the wind is greater than the rated power of the wind turbine, the pitch angle of the turbine blades is changed to reduce the efficiency of the turbine. Consequently, the power absorbed by the turbine is reduced, keeping the unit operating within the speed and power limits.

Manufacturers describe three parameters in the function of wind speed to determine wind turbine operation. These are: (1) cut-in wind speed, from which the turbine is unlocked and begins to accelerate, usually between 3 and 5 m/s; (2) rated wind speed, from which the power absorbed by the turbine corresponds to the nominal value of the wind unit, generally between 11 and 14 m/s; and (3) cut-out wind speed, which determines the maximum wind speed for the safe operation of the wind farm, normally 25 m/s [39].

However, control systems dedicated to high wind speeds have been developed. With these systems, the use of available energy is gradually reduced when the wind speed exceeds a pre-established limit. In the case of these new control systems, mechanical blocking of the wind turbine occurs if the wind speed exceeds, for example, the limit of 34 m/s, and remains above this value for several minutes.

Figure 2b shows the typical operating regions or zones of a wind turbine; as a function of wind speed. The figure shows the turbine speed, the blade angle, and the

power extracted from the generator stator, considering the MPPT control. In Zone 1, the wind turbine accelerates until the minimum speed ( $\omega_{\min}$ ) is reached while the stator power is zero. In Zone 2, the turbine speed is not altered, maintained at  $wt$  min, as variations in this operating zone do not result in significant variations in the power extracted by the turbine. Upon entering Zone 3 of operation, the turbine speed is controlled by the MPPT control to manage the wind farm at MPP. In Zone 4, the turbine speed reaches the maximum speed limit ( $\omega_{\max}$ ). In Zone 5, the turbine reaches its rated power, and the blade angle control maintains the power at the rated value while the wind speed varies. When exceeding the maximum wind speed of 25 m/s, the blade angle is kept at the maximum value, and the mechanical brake is activated, blocking the wind turbine [36, 39].

There are two ways to operate the loaded wind unit using the speed control, operating the turbine in the over-speed region or the under-speed region [36]. The under-speed area is delimited by the minimum operating speed ( $\omega_{\min}$ ) and the speed corresponding to the MPP, which depends on the wind speed. The MPP speed and the maximum operating speed of the turbine bound the over-speed region ( $\omega_{\max}$ ). The operational and stability limits of the wind farm in the two functional regions are directly linked to the aforementioned speed limits. If the turbine speed becomes less than ( $\omega_{\min}$ ), the wind unit operates in Zone 1, described above and shown in Fig. 6b. In this case, the active power delivered by the wind unit to the grid becomes null. Suppose the turbine speed exceeds the upper limit ( $\omega_{\max}$ ). In that case, the entire mechanical parts of the unit may suffer from mechanical wear and over-temperature, which may even result in the collapse of the wind unit. The following sections discuss several MPPT methods.

### 3 Mathematical Model of the PMSG

In the PMSG, permanent magnets are used to produce the magnetic flux in the rotor; therefore, it does not have an excitation winding. For this reason, the permanent magnet machine has a high power density, reduced size, and weight compared to the machine with excitation winding and reduces thermal dissipation due to the absence of rotor windings [42–47].

The dynamic model of PMSG in the dq coordinates can be represented by Eqs. (9) and (10):

$$v_{ds} = R_s i_{ds} + L_{ds} \frac{di_{ds}}{dt} - \omega_e \lambda_{qs} \quad (9)$$

$$v_{qs} = R_s i_{qs} + L_{qs} \frac{di_{qs}}{dt} - \omega_e \lambda_{ds} \quad (10)$$

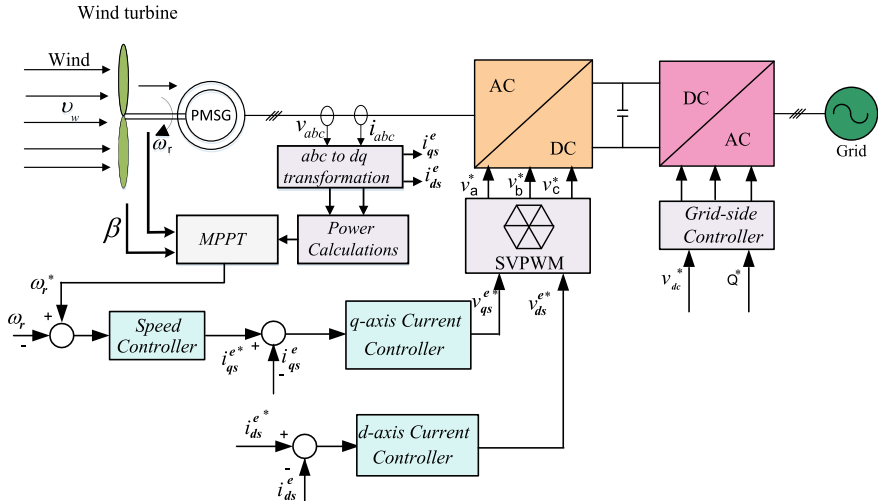
where  $v_{ds}$  and  $v_{qs}$  are the stator voltage components,  $R_s$  is the stator resistance,  $L_{ds}$  and  $L_{qs}$  are the stator inductance components,  $i_{ds}$  and  $i_{qs}$  are the current components

of the stator,  $\omega_e$  is the generator speed, and the flux component are presented by  $\lambda_{ds}$  and  $\lambda_{qs}$ .

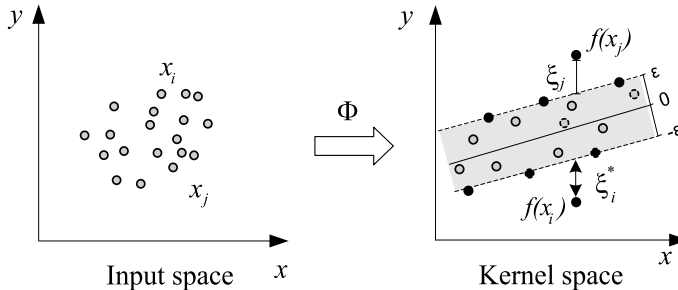
The generator electromagnetic torque is formulated by [45, 48]

$$T_e = 1.5N_p[\lambda_m + (L_{ds} - L_{qs})i_{ds}]i_{qs} \quad (11)$$

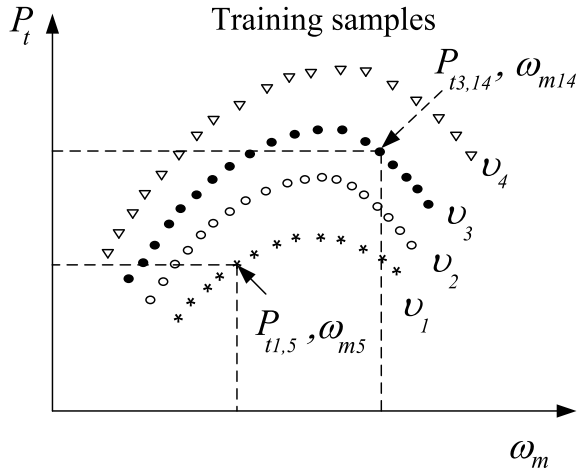
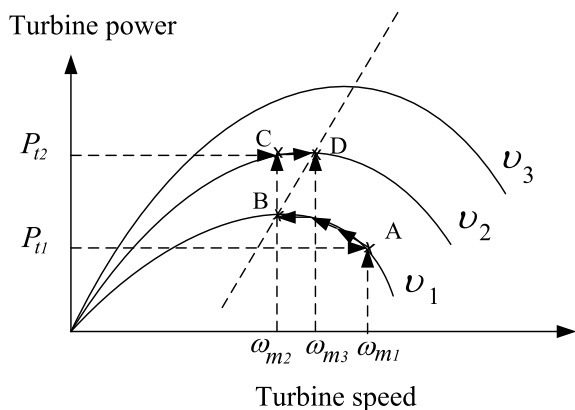
where  $T_e$  and  $N_p$  are the electromagnetic torque and the number of pole pairs. The generator control is performed by the quadrature axis,  $i_{ds} = 0$ , and the generator speed is controlled by the MPP. The PMSG overall control system is shown in Fig. 3 [49].



**Fig. 3** PMSG control scheme in wind power generation systems



**Fig. 4** Feature map from input to higher-dimensional feature space

**Fig. 5** Training samples**Fig. 6** Wind speed estimation for MPPT

#### 4 MPPT Algorithms

Usually, when the wind speed is less than the rated wind speed, variable-speed wind units are controlled to maximize the use of wind energy. This objective is achieved using the MPPT control, which contains the speed of the turbine. Thus, the wind turbine operates with the power coefficient maximum value ( $C_p$ ), as mentioned in Sect. 2.

## 4.1 Perturbation and Observation Method

In the P&O approach, the intention is to cause a slight disturbance of a determined control variable and then study its effect, observing the change in the turbine-extracted power [50]. Thus, the turbine speed is disturbed in a specific direction, and the generated power is kept. If the turbine power increases, the disturbance remains in an equal direction; otherwise, the direction must be overturned. The process continues, and the speed will oscillate around the maximum power point [37]. The P&O method has a stopping criterion. It is verified when the slope of the curve is zero when the power derivative concerning the control variable approaches zero.

As well as being one of the simplest MPPT algorithms, the P&O approach presents excellent performance and is easy to implement in low-cost systems [51]. Moreover, there is no requirement for a prior understanding of the wind power's static properties or the turbine parameters, which is the main advantage, as it can be implemented in different types of turbines without reducing efficiency. It is also a simple method and does not require mechanical sensors, which causes a reduction in costs and increases reliability and robustness [52, 53].

However, the disadvantage of this method is noticeable when the turbine is subject to rapid variations in wind, which can cause a failure in the algorithm because of the turbine's high response time when subjected to the speed command. Another possible source of error is the absence of particularity between the cause of the power variation at the output, which can be influenced by a disturbance arising from the algorithm or a rapid variation in wind speed.

## 4.2 Support Vector Regression

The use of support-based vector algorithms was proposed by Vapnik [54]. As a result, support vector machines (SVMs) have been developed to solve pattern recognition problems. The main idea of SVM, when used for classification, is to build a hyperplane as a decision plane that maximizes the margin of separation between different classes. Support vectors include a small subset of training data obtained by the SVM approach, representing the decision surface [55].

Subsequently, Vapnik and Kaufman [56] expanded the use of support vectors to regression problems and became known as support vector regression (SVR). In addition, Vapnik introduced the “insensitive loss function” and the tube concept to maintain the characteristics of the method in the context of function approximation (Fig. 4). These new elements made it possible to apply vectors to support the regression problem, thus allowing SVR development.

Consider a training dataset  $D = (x_1, y_1), \dots, (x_N, y_N)$  formed by  $N$  pairs of inputs  $x_n \in R^d$  and corresponding outputs  $y_n \in R^d$ , for  $n = 1, \dots, N$ . In a regression problem, the objective is to find a function  $f(\cdot)$ ; this presents outputs closer to the  $y_n$  value for

each  $x_n$  value. For linear regression,  $f(\cdot)$  has the following form [57]:

$$f(x_n) = (w^T x_n) + b \quad (12)$$

where  $w \in R^d$  is a vector of parameters, and  $b \in R$  is the bias. The parameters  $w$  and  $b$ , from Eq. (12), with less complexity and greater generalization, are found by minimizing the Euclidean standard  $\|w\|^2$ :

$$R_{\text{reg}}(f) = \frac{1}{2} \|w\|^2 + C \sum_{i=1}^n \Gamma(f(x_i) - y_i) \quad (13)$$

subject to

$$\begin{cases} y_n - w^T x_n - b \leq \varepsilon + \xi_i \\ w^T x_n - b - y_i \leq \varepsilon + \xi_i \\ i = 1, 2, \dots, n \quad \xi_i, \xi_i^* \geq 0 \end{cases} \quad (14)$$

The parametric formulation in Eq. (13) with the inequality limitations in Eq. (14) is an optimization challenge in the primary weight space, also known as a problem in primal form because it is specified in the input space  $R^d$  of the original vector for the given data  $x_n$  and the weight vector  $w$ . Solving such a simple problem is accomplished by constructing a Lagrangian function of Eqs. (13) and (14), transforming the initial problem into a dual one. The problem is now solved in the  $2N$  space using the variables  $\alpha_n$  and  $\alpha_n^*$  instead of  $w$  in the primary space. The dual solution of Eq. (12) is given by [58]:

$$f(x) = \sum_{i=1}^n (\alpha_i - \alpha_i^*) K(x_i, x) + b \quad (15)$$

where  $\alpha_i$  and  $\alpha_i^*$  are Lagrange multipliers, and  $K(x_i, x_j) = \Phi(x_i)^T \Phi(x_j)$  is the kernel function. The radial base function is used as a kernel function [59]:

$$K(x_i, x) = \exp \left\{ -\frac{|x_i - x|^2}{\sigma^2} \right\}. \quad (16)$$

The training process and estimation process are shown in Fig. 5.

For a certain measured wind speed  $v_1$ , the reference generator speed can be obtained from the power-speed characteristics data and the decision function and wind speed  $v_1$ . The rotor speed reference  $\omega_r^*$  is then moved from point A to the maximum power point at point B in Fig. 6. For any change in the wind speed, the generator speed and power are used the same way to estimate the new wind speed.

## 5 Experimental Results

The experimental prototype of the PMSG wind power structure is built in the function of the PMSG experimental setup. Thus, the wind system consists of an MG set where the motor is used as a wind simulator, and the PMSG is tied to the power grid over a back-to-back converter. Thus, the back-to-back power converter used IGBT modules (SKM100GB12T4-Semikron). The PPL and MPPT schemes and the controllers were shipped on the DSP board TMS320C33. The magnitude of the generator and grid side voltage and current measurements were sensed and conditioned by Hall effect transducers.

The operation of the SVR MPPT technique is examined in various wind speed conditions. Figure 7a shows the wind speed variation from 8 to 11.5 m/s, and Fig. 7b shows the generator-speed changes when the wind speed increases to track the maximum power. In Fig. 7c, the power follows the speed variation from 1050 to 22,875 W, which is the maximum power at 11.5 m/s. The MPPT convergence speed and accuracy are good, with minimum high- and low-frequency ripples.

To compare the performance of the SVR MPPT with the P&O technique, wind speed, generator speed, and power are measured, as shown in Fig. 8. The MPPT controller takes longer to reach the steady state and the maximum power speed. The generator power follows the changes in the generator speed with slow transient and high oscillations of the generator power in the steady-state condition. Figures 7 and 8 found that the SVR method is faster and has low oscillations around the MPP.

By analyzing the different methods in the literature, it is concluded that the power signal feedback control (PFSC) and P&O methods obtain greater precision; they present better convergence than the TSR method. Comparing the P&O and PSFC methods found that the P&O technique is the most suitable for systems with

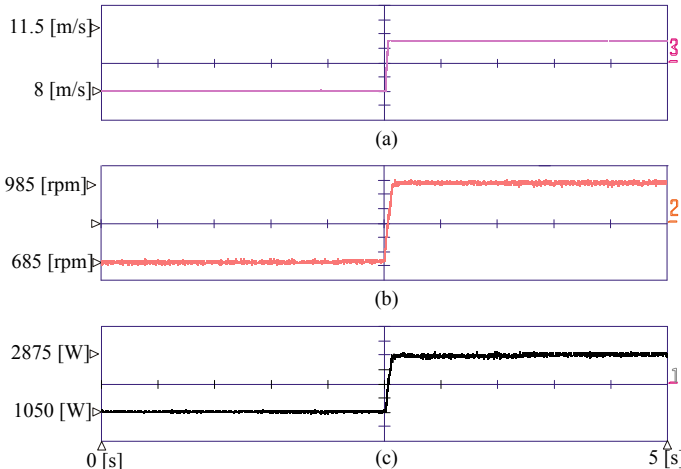


**Fig. 7** SVR MPPT: **a** Wind speed, **b** generator speed, **c** turbine power

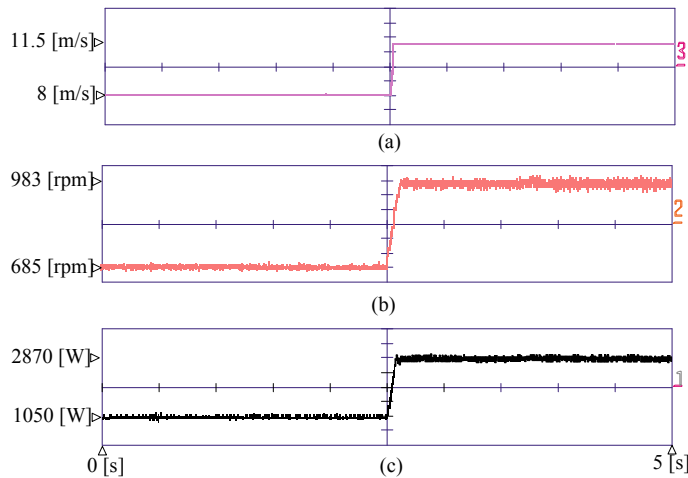


**Fig. 8** P&O MPPT: **a** Wind speed, **b** generator speed, **c** turbine power

low-inertia wind turbines. The PSFC method is recommended for large generators because of its precision and rapid dynamic response. The simulation results show the successful tracking of maximum power extraction for different wind speeds. Table 2 summarizes the features of the selected MPPT methods based on the study of these methods in the literature. Implementing intelligent technology can effectively benefit these techniques in coordinating demand management with various renewable resources [60].

**Table 2** Comparison of MPPT methods

Method	Complexity	Convergence speed	Prior knowledge/training	Memory required	Wind speed measurement	Perform under varying wind
Tip-speed ratio	Simple	Fast	No	No	Yes	Moderate
P&O	Simple	Depends	No	No	No	Moderate
PSFC	Simple	Fast	Yes	No	Yes	Moderate
Torque optimal control	Simple	Fast	No	No	Yes	Moderate
Fuzzy logic	High	Fast	Yes	High	Depends	High
ANN	High	Fast	Yes	High	Depends	High
SVR	High	Fast	Yes	High	No	High

## 6 Conclusions

This work experimentally evaluated the performance of the P&O and SVR techniques using the generator-speed control methodology to achieve these results. These experiments indicated a slight generation advantage over the P&O scheme for SVR techniques. In addition, the SVR method can effectively converge to the MPP track even when the wind speed varies continuously or abruptly. Finally, by comparing SVR with the P&O strategy, it was demonstrated that the SVR technique has lower fluctuations and shorter convergence time across the MPP.

The MPPT control of a WECS aims to convert the MPP from wind power into electricity. Representative MPPT controller of such a wind energy system includes power signal feed (PSF), OTC, TSR control, and P&O search method. The TSR control method maintains the wind speed and each measured speed at the optimal primary speed ratio, and the MPPT algorithm is performed through the speed controller. PSF and OTC do not require an anemometer, but simulation through offline experiments must obtain parameter K in advance. In addition, HCS does not require wind speed measurement and the parameter K value in advance. Still, it has a disadvantage in that the MPPT control speed and accuracy vary depending on the dimension of the changing step. Several studies have been conducted on MPPT techniques of mixed form to solve this problem, which complements the disadvantages of control techniques. Future research will develop an intelligent control technique to handle the MPP of wind turbines interacting with several distributed power generations for an optimal demand-supply.

## References

1. Praveen RP, Keloth V, Abo-Khalil AG, Alghamdi AS, Eltamaly AM, Tlili I (2020) An insight to the energy policy of GCC countries to meet renewable energy targets of 2030. Energy Policy 147
2. Madiba T, Bansal RC, Mbungu NT, Bettayeb M, Naidoo RM, Siti MW (2021) Under-frequency load shedding of microgrid systems: a review. Int J Model Simulat 42(4):653–679
3. International Energy Agency, IEA (2018) World energy outlook. Available online: <http://www.iea.org/>
4. Zu Y, Cheng M (2014) The state of the art of wind energy conversion systems and technologies: a review. Energy Convers Manage 88:332–347
5. Abo-Khalil AG (2013) Impacts of wind farms on power system stability. In: Wind farm. ISBN 980-953-307-562-9
6. Ali MH (2012) Wind energy conversion systems. In: Wind energy systems solutions for power quality and stabilization, Boca Raton, CRC Press Taylor & Francis Group, pp 17–35
7. Eltamaly A, Abdulaziz A, Abo-khalil AG (2021) Control and operation of grid-connected wind energy systems. In: Green energy and technology. Springer, Berlin
8. Hamid AK, Mbungu NT, Elnady A, Bansal RC, Ismail AA, AlShabi MA (2022) A systematic review of grid-connected photovoltaic and photovoltaic/thermal systems: benefits, challenges and mitigation. Energy Environ 0958305X221117617.5
9. Bhardwaj U, Teixeira AP, Soares CG (2019) Reliability prediction of an offshore wind turbine gearbox. Renew Energy 141:693–706

10. Inthamoussou FA, De Battista H, Mantz RJ (2016) LPV-based active power control of wind turbines covering the complete wind speed range. *Renew Energy* 99:996–1007
11. Sayed K, Abo-Khalil AG, Eltamaly AM (2021) Wind power plants control systems based on SCADA system. In: Energy and technology. Springer, Berlin
12. Fathabadi H (2016) Maximum mechanical power extraction from wind turbines using novel proposed high accuracy single-sensor-based maximum power point tracking technique. *Energy* 113:1219–1230
13. Wu YK, Yang Y-H, Lin H-J, Yang S-Y (2014) Modelling and control of a small wind turbine by using PSIM. In: 2014 CACS international automatic control conference (CACS 2014), pp 91–96. <https://doi.org/10.1109/CACS.2014.7097168>
14. Drumheller DP, D'Antonio GC, Chapman BA, Allison CP, Pierrickos O (2015) Design of a micro-wind turbine for implementation in low wind speed environments. In: Systems and information engineering design symposium, pp 125–130. <https://doi.org/10.1109/SIEDS.2015.7116959>
15. Thongam JS, Bouchard P, Ezzaidi H, Ouhrouche M (2009) Wind speed sensorless maximum power point tracking control of variable speed wind energy conversion systems. In: Proceedings of the IEEE international electric machines and drives conference IEMDC 2009, 3–6 May 2009, Florida, USA
16. Eltamaly AM, Al-Saud MS, Sayed K, Abo-Khalil AG (2020) Sensorless active and reactive control for DFIG wind turbines using opposition-based learning technique. *Sustainability* 12(9):3583
17. Matsui M, Xu D, Kang L, Yang Z (2004) Limit cycle based simple MPPT control scheme for a small sized wind turbine generator system. In: Proceedings of 4th international power electronics and motion control conference, Xi'an, 14–16 Aug 2004, vol 3, pp 1746–1750
18. Higuchi Y, Yamamura N, Ishida M (2000) An improvement of performance for small-scaled wind power generating system with permanent magnet type synchronous generator. In: Proceedings of IECON
19. Eltamaly A, Mohamed MA, Abo-khalil AG (2021) Maximum power point tracking strategies of grid-connected wind energy conversion systems. In: Energy and technology. Springer, Berlin
20. Bansal RC, Bhatti TS, Kothari DP (2002) On some of the design aspects of wind energy conversion systems. *Energy Convers Manage* 43(16):2175–2187
21. Pan T, Ji Z, Jiang Z (2008) Maximum power point tracking of wind energy conversion systems based on sliding mode extremum seeking control. In: Proceedings of the IEEE energy 2030, Atlanta, GA, USA, 17–18 Nov 2008, pp 1–5
22. Abo-Khalil AG (2015) Control system of DFIG for wind power generation systems. LAP LAMBERT Academic Publishing. ISBN-10: 3659649813, ISBN-13: 978-3659649813
23. Hui J, Bakhshai A (2008) A new adaptive control algorithm for maximum power point tracking for wind energy conversion systems. In: Proceedings of IEEE PESC 2008, Rhodes, 15–19 June 2008, pp 4003–4007
24. Abo-Khalil AG, Alharbi W, Al-Qawasmi A, Alabd M, Alarifi I (2021) Modeling and control of unbalanced and distorted grid voltage of grid-connected DFIG wind turbine. *Int Trans Electr Energy Syst*
25. Hui J, Bakhshai A (2008) Adaptive algorithm for fast maximum power point tracking in wind energy systems. In: Proceedings of IEEE IECON 2008, Orlando, USA, pp 2119–2124
26. Gidwani L, Tiwari H, Bansal RC (2013) Improving power quality of wind energy conversion system with unconventional power electronic interface. *Int J Electr Power Energy Syst* 44(1):445–453
27. Abo-Khalil AG (2012) Synchronization of DFIG output voltage to utility grid in wind power system. *J Renew Energy* 44:193–198
28. Muller S, Deicke M, De Doncker RW (2002) Doubly fed induction generator systems for wind turbines. *IEEE Ind Appl Mag* 26–33
29. Abo-Khalil AG, Alghamdi AS, Eltamaly AM, Al-Saud MS, Praveen PR, Sayed K (2019) Design of state feedback current controller for fast synchronization of DFIG in wind power generation systems. *Energies* 12(12):2427

30. Eltamaly AM, Al-Saud MS, Abo-Khalil AG (2020) Dynamic control of a DFIG wind power generation system to mitigate unbalanced grid voltage. *IEEE Access* 8:39091–39103
31. Chalikosa B, Bansal RC, Mbungu NT, Naidoo R (2022) Performance analysis of wake models on the energy production of large offshore wind farms. *Int J Model Simulat* 1–12
32. Ellabban OA-RHF (2014) Renewable energy resources: Current status, future prospects and their enabling technology. *Renew Sustain Energy Rev* 39:748–764
33. Abo-Khalil AG, Al-Qawasmi A-R, Eltamaly AM, Yu BG (2020) Condition monitoring of DC-link electrolytic capacitors in PWM power converters using OBL method. *Sustainability* 12(9):3719
34. Gao R, Gao Z (2016) Pitch control for wind turbine systems using optimization, estimation. *Renewab Energy* 501–515
35. Abo-Khalil AG, Alyami S, Awan AB, Alhejji A (2019) Real-time reliability monitoring of DC-link capacitors in back-to-back converters. *Energies* 12(12):2396
36. Bansal RC, Zobaa AF (eds) (2022) Handbook of renewable energy systems. World Scientific Publisher, UK
37. Abo-Khalil AG, Alghamdi A, Tlili I, Eltamaly A (2019) A current controller design for DFIG-based wind turbines using state feedback control. *IET Renew Power Gener* 13(11):1938–1949
38. Abokhalil AG (2019) Grid connection control of DFIG for variable speed wind turbines under turbulent conditions. *Int J Renew Energy Res (IJRER)* 9(3):1260–1271
39. Minz J et al (2020) Regional wind energy potentials are defined by the kinetic energy budget of the atmospheric boundary layer. AGU fall meeting abstracts.
40. Polinder H et al (2013) Trends in wind turbine generator systems. *IEEE J Emerg Select Top Power Electron* 1(3):174–185
41. Kim HK, Abo-Khalil A, Lee DC, Seok JK (2003) CVCF control of stand-alone wind power system. In: Proceedings of Korean Institute of power electronics conference, pp 379–382
42. Biswas D, Sahoo SS, Tripathi PM, Chatterjee K (2018) Maximum power point tracking for wind energy system by adaptive neural-network based fuzzy inference system. In: 2018 4th international conference on recent advances in information technology (RAIT), Dhanbad, pp 1–6
43. Abo-Khalil AG, Lee DC (2007) SVR-based wind speed estimation for power control of wind energy generation system. In: Proceedings of power conversion conference, Nagoya, Japan
44. Abo-Khalil AG, Lee DC (2008) Maximum power point tracking based on sensorless wind speed using support vector regression. *IEEE Trans Indus Electron* 55(3)
45. Abo-Khalil AG, Eltamaly AM, Praveen PR, Alghamdi AS, Tlili I (2020) A sensorless wind speed and rotor position control of PMSG in wind power generation systems. *Sustainability* 12(20):8481
46. Geng H, Liu L, Li R (2018) Synchronization and reactive current support of PMSG based wind farm during severe grid fault. *IEEE Trans Sustain Energy* 9:1596–1604
47. Abo-Khalil AG, Alghamdi AS (2021) MPPT of permanent magnet synchronous generator in tidal energy systems using support vector regression. *Sustainability* 13(4)
48. Weiliang L, Lei C, Jing O, Shukang C (2011) Simulation of PMSG wind turbine system with sensor-less control technology based on model reference adaptive system. *Electr Mach Syst (ICEMS)* 1–3
49. Abo-KhalilAG et al (2016) A low-cost PMSG topology and control strategy for small-scale wind power generation systems. *Int J Eng Sci Res Technol IJESRT* 585–592
50. Errami YOMMM (2012) Control of grid connected PMSG based variable speed wind energy conversion system. *Int Rev Model Simulat* 5(2):655–664
51. Koutroulis E, Kalaitzakis K (2006) Design of a maximum power tracking system for wind-energy-conversion applications. *IEEE Trans Industr Electron* 53(2):486–494
52. Wai RJ, Lin CY, Chang YR (2007) Novel maximum-power extraction algorithm for PMSG wind generation system. *IET Electr Power Appl* 1(2):275–283
53. Abdullah MA, Yatim AHM, Tan CW, Saidur R (2012) A review of maximum power point tracking algorithms for wind energy systems. *Renew Sustain Energy Rev* 16(5):3220–3227

54. Vapnik VN, Chervonenkis AY (1963) On a class of perceptrons. *Autom Remote Control* 25(1):103–109, 1964. In Russian: В. Н. Вапник, А. Я. Червоненкис. Об одном классе персептронов. Автоматика и телемеханика 25(1):112–120, 1964; with English summary entitled “On a perceptron class”. The original article submitted on 21 February 1963
55. Wang Q, Chang L (2004) An intelligent maximum power extraction algorithm for inverter-based variable speed wind turbine systems. *IEEE Trans Power Electron* 19(5):1242–1249
56. Vapnik V, Golowich SE, Smola AJ (1997) Support vector method for function approximation, regression estimation and signal. In: Mozer MC, Jordan M, Petsche T (eds) *Advances in neural information processing systems*, vol 9, MIT Press, Cambridge, pp 281–287
57. Li H, Shi KL, McLaren PG (2005) Neural-network-based sensorless maximum wind energy capture with compensated power coefficient. *IEEE Trans Ind Appl* 41(6):1548–1556
58. Thongam JS, Bouchard P, Ezzaïdi H, Ouhrouche M (2009) ANN-based maximum power point tracking control of variable speed wind energy conversion systems. In: *Proceedings of the 18th IEEE international conference on control applications 2009*, 8–10 July 2009, Saint Petersburg, Russia
59. Karthi K, Radhakrishnan R, Baskaran JM, Titus LS (2018) A review of maximum power point tracking controls and wind electric generators. In: *2018 international conference on inventive research in computing applications (ICIRCA)*, pp 1122–1126
60. Azaroual M et al (2022) Toward an intelligent community microgrid energy management system based on optimal control schemes. *Int J Energy Res* 46(15):2134–2156
61. Abo-Khalil AG (2015) Control system of DFIG for wind power generation systems. LAP LAMBERT Academic Publishing. ISBN-10:3659649813, ISBN-13:978-3659649813

# Deep Learning Approach to Recognize Yoga Posture for the Ailment of the Low Back Pain



Katta Uday Kiran, Manvendra Singh, Md. Sarfaraj Alam Ansari, and Mahesh Chandra Govil

**Abstract** In today's fast-paced life, lower back pain (LBP) has become a common problem affecting the lives of millions of people across the globe. In this disease, the person not only experiences pain but also becomes a major cause of disability and affects the person's quality of life. There are various LBP treatment options available, but none are adequate. Therefore, the doctor recommends yoga exercise as an initial line of treatment for LBP. The accuracy of the yoga exercise is very important for the patient's quick recovery. Still, it is very challenging for the patient to go to the professionals to keep track of yoga exercises. In this paper, we propose deep learning (DL)-based approach to check the accuracy of yoga performed by a patient. The convolutional neural network (CNN) and artificial neural network (ANN) system model measure the body keypoint angles and distances to get accuracy on selected yoga poses. The proposed model has successfully recognized the yoga poses based on the accuracy of that particular yoga. We have also created our dataset to train our model, giving the test accuracy of 91.61% and 99.24% for ANN and CNN-based models, respectively.

**Keywords** Yoga posture detection · Low back pain · Convolutional neural network (CNN) · Artificial neural network (ANN) · Deep learning

---

K. Uday Kiran · M. Singh · Md. Sarfaraj Alam Ansari (✉) · M. Chandra Govil  
National Institute of Technology Sikkim, Ravangla 737139, India  
e-mail: [sarfaraj@nitsikkim.ac.in](mailto:sarfaraj@nitsikkim.ac.in)

K. Uday Kiran  
e-mail: [b190019@nitsikkim.ac.in](mailto:b190019@nitsikkim.ac.in)

M. Singh  
e-mail: [phcs220017@nitsikkim.ac.in](mailto:phcs220017@nitsikkim.ac.in)

## 1 Introduction

Low back pain (LBP) is one of the diseases that affect people from all sections. The prevalence of LBP is increasing day by day, and 84% of the population are suffering from low back pain at least once in their life [1]. The main symptoms of low back pain are the persons having improper structure of the backbone, heavy lifts, and some accidental jerks leading to low back pain. Due to LBP, people cannot do their jobs or work properly [2]. The treatment for such kind of low back pain includes some exercises and some inoculations, and in bad cases, this leads to operations to the backbone. The most common reason for disability in the world and a major factor in active population absence from work is low back pain (LBP), and preventing this recurring illness is essential. Yoga exercises for LBP rehabilitation performed at home will be useful for reducing back pain. To perform yoga accurately, trainer is necessary to guide the patients, but it is challenging for the person to go to the professionals to keep track of yoga exercises. Artificial intelligence and machine learning (AI/ML)-based model are capable of monitoring yoga exercises that can accurately track the person's yoga exercises without the trainee [3].

Our goal is to look for and examine research that applies AI/ML and deep learning approaches for BP recovery. To gain knowledge of the outcomes assessed, the clinical environment (face-to-face or remote rehabilitation) where interventions were carried out, low back pain care, and capability play a crucial part in keeping your body in good shape and preventing lower back problems. Yoga exercise therapy is more effective when the spine is held upright. To ensure efficient muscle reflexes, such solutions require the body position and moment of our body. This can also control the lower back [4]. However, LBP patients are often impacted by this because of their weakened capacity for playing games and doing exercises, which is connected to a decrease in postural capability. To expand the system in people with pain in the low back and maximize their performance in the practice [5]. This problem should be resolved by an efficient AI-based system that could give accuracy in monitoring the work of exercise. We have created a deep learning system to read the problems in real-time. The primary contributions of this paper condense as follows:

1. This paper proposes an efficient system model with convolutional neural network (CNN) and artificial neural network (ANN), namely *YPPD\_FS\_ANN* and *YPPD\_FS\_CNN* for monitoring yoga exercises.
2. Yoga pose posture detection (YPPD) dataset has been developed by generating keypoints of the human body using OpenCV and mediapipe for training the classifier.
3. The proposed models provide better accuracy compared to other proposed models and outperform the other state of the arts.

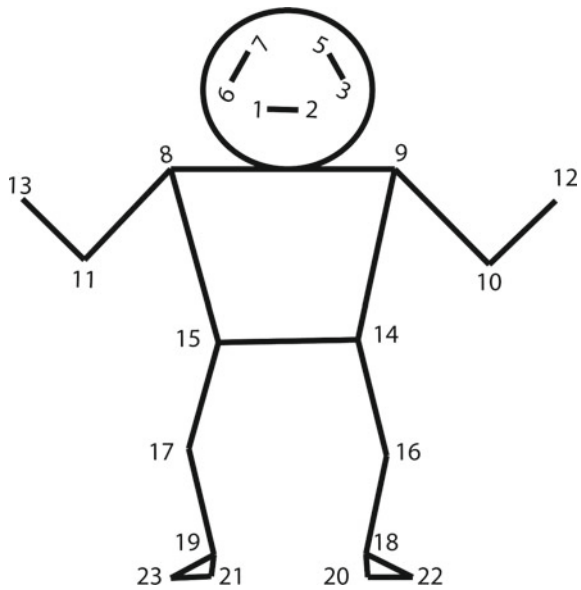
The rest of the papers are organized as follows: Sect. 1 presents the related survey works. In Sect. 2, we have discussed the methodology of our work. In Sect. 3, we analyzed the obtained results. Section 4 discusses the comparative study with the other works, and Sect. 5 concludes with the future direction of the proposed work.

## 2 Related Works

Systems for estimating posture have been widely utilized in different fields. The previous work has included a wearable device and developed a posture control device for LBP therapy, a real-time gaming platform to promote orthopedic rehabilitation [6], smart healthcare [7], real-time dynamics analysis for patient monitoring, sports, and wearable sensors for the lumbar region (among many other applications) [8]. The research from these articles is used in context. This study aims to eliminate LBP and provide healthcare solutions. Deep learning methods like CNN and ANN are extensively used in the research field of monitoring posture classification [9]. Another author, Gonzalez-Ortega et al., proposed a model based on cognitive exercise rehabilitation monitoring with an accuracy of 96.28%. The method is designed to test and evaluate left-right and body scheme dysfunctions. The research needs to address these problems in other computer vision-based systems specifically. Utilizing the depth data supplied by the Kinect device, monitoring is accomplished by the tracking of human body joints (the head and hands) and the recognition of faces and facial features (the eyes, nose, and ears) [10]. Avishkar Seth et al. developed a model with less than 90% accuracy for estimating a real-time 3D posture for lower back discomfort. The technique is created for the real 3D pose estimate for back pain for people undergoing physical retraining activities to enhance these treatments' efficacy [11].

Sellmann et al. [12] proposed a model using compensatory movements during autonomously performed exercises to prevent low back pain. It has a maximum accuracy of 98.3%. This research demonstrates that monitoring rehabilitation and preventative workouts with only one sensor is feasible for two test activities. Ordonez et al. [13] proposed a model using LSTM recurrent neural networks for multimodal wearable activity recognition with an accuracy of 95.8%. This research illustrated the benefits of a deep architecture that combines LSTM and convolutional layers to recognize activities from wearable sensors. Duc Ngoc Tran et al. proposed a model using activities recognition in android smartphones using a support vector machine with an accuracy of 89.59%, and this research has created a comprehensive algorithm to identify human involvement in this publication. The finished system includes tools for gathering data, extracting its characteristics, processing it, training, and identifying human activity [14].

Alshurafa et al. proposed a model using remote health monitoring systems to enhance user adherence with an accuracy of 95.3%. This research demonstrates the strong association between participant adherence and battery life in a remote health monitoring system that uses a smartphone as an information gateway [15]. Zhao et al. proposed a model using LSTM for human activity recognition using wearable sensors with an accuracy of 93.6%. This research significance of HAR research is examined, and a summary of recently developed techniques in the field is given [16]. Kalantarian et al. proposed a model using low-power wearable health monitoring systems with an accuracy of 90%. This research presents a novel method for selective compute offloading based on user-defined accuracy restrictions. Making the proper offloading selection reduces power by 0.2 mW with a baseline classifier execution cost and feature extraction cost, according to our calculations [17].

**Fig. 1** Body keypoints

### 3 Methodology

In this section, we have discussed the dataset used for classifying our works and the proposed model workflow.

#### 3.1 Dataset

In this section, we are describing our dataset, named yoga pose posture detection(YPPD), which is used in this work. Our dataset is based on LBP rehabilitation yoga exercises which make it special. The existing datasets are not challenging in term of object occlusion also not made specifically for LBP rehabilitation. In our dataset, seventeen main features are created as keypoints of human body joints, which are Nose\_angle, left\_elbow\_angle, right\_elbow\_angle, right\_shoulder\_distance, left\_shoulder\_distance, left\_wrist,right\_wrist, left\_hip, right\_hip, left\_knee,right\_knee, left\_ankle,right\_ankle, left\_ear,right\_ear, left\_heel, right\_heel,right\_arm\_angle,right\_arm\_distance, left\_arm\_angle, left\_arm\_distance, right\_arm, left\_arm. The Fig. 1 depicted all the keypoints mentioned above.

In figure Fig. 1, the numbers indicate the various keypoints. In this case, the number 6 represents the right ear. When figuring up angles and distances, the number 7 is used. It cannot be used to create any feature. Three number point represents the left ear, two number point for the mouth, also we take the eight number point for the right shoulder, nine number point act for the left shoulder, eleven and ten number points for the right and left elbows, thirteen and twelve number points represent left and right

**Table 1** Sample dataset

Nose_angle	Left_wrist	Right_wrist	Left_hip	Right_hip	Left_knee	Right_knee	Left_ankle	Right_ankle
180.934	56.6123	50.2496	339.418	339.418	355.304	199.366	128.506	37.2156
186.341	57.2012	61.4032	339.536	339.536	388.046	178.614	112.522	38.4737
161.565	39.0511	50.0392	316.056	316.056	260.443	126.503	73.6925	32.8934
225.121	38.4712	43.0113	288.626	288.626	253.505	125.716	71.8559	24.3513
135.121	35.1716	44.0115	286.632	286.632	253.789	117.927	71.2048	27.2022
153.434	29.8325	46.0112	282.492	282.492	271.661	131.343	72.7477	29.1541
206.565	31.3846	46.1213	281.711	281.715	273.383	132.179	75.2446	30.4137
90.1523	34.0147	47.2654	281.226	281.227	214.189	100.631	53.5426	29.8327

wrists, fifteen and fourteen number points speak for left and right hips, seventeen and sixteen number points for both knees, nineteen and eighteen number points stand for both right and left ankle, at last, we have taken twenty-one and twenty-two number points for representing left and right knees.

By using the mediapipe framework, we have extracted those above-mentioned body keypoints. A sample of the YPPD dataset is given below as a Table 1 for ready reference. In Table 1, we have shown only eight features out of seventeen to understand the format of the dataset.

### 3.2 Proposed Framework

First, we collected exercise videos related to the back pain problem from social media like YouTube to perform our method. We have taken the different yoga poses videos to train our deep learning models CNN and ANN. After collecting the videos, we detect the objects using OpenCV (an open-source computer vision library) [19] and extract the seventeen main features. Following that object, the mediapipe framework extracts the body's keypoints.

### 3.3 Role of Angle Between Keypoints

The proposed dataset presenting the results for different incidence angles would provide a more comprehensive evaluation of the models' performance and give a better understanding of their robustness in other conditions. We are creating a recognition system for yoga poses related to back pain by calculating the angles between three points in each frame of different yoga videos. The points used for each pose vary, such as the left and right elbow and shoulder and the left and right pinky for the cobra pose. The angles are calculated based on the corresponding coordinates to identify each yoga pose accurately [20].

**Algorithm 1:** Accuracy Prediction of YPPD using the Proposed Model

---

**Input:** video as input  
**Output:** Prediction

```

1 l ← Conversion of input video into 2D array
2 ll ← Features extraction from l (ll is a list)
3 m ← models for training
4 for i = 1 to n do
5   |           ▷ n is the number of DL models, here we have used CNN & ANN so n=2
6   |   mi ← model(ll)
7   |           ▷ mi will save all models after training with DL techniques
8 end
9 t ← An integer initialized with 0
10 A ← A variable for storing prediction score
11 tt ← Variable for storing the name of the Yoga posture
12 ln ← is the new list of a new video for testing the models capacity in basis of accuracy
13 for i = 1 to n do
14   |   A=model_predict(mi,ln)
15   |   if A lessthan t then
16   |     |   t=A
17   |     |   tt
18   |   end
19 end
20 return(tt)
```

---

### 3.4 Role of Distance Between Keypoints

We determine the exact yoga pose by measuring the distance between three keypoints in each step. This is necessary because the distance changes as the pose changes. For example, the cobra pose is determined by calculating the distance between the left and right elbow, shoulder, and pinky. These points serve as key indicators to predict the correct posture. Once we have obtained the angles and distances, we label the features and save them in a CSV file. This data is then used to train a model and evaluate its performance using various metrics [21]. The architecture of the yoga posture detection model is depicted in the accompanying. In the algorithm 1, we have shown the working logic of our proposed system of yoga posture recognition in a details manner in Fig. 2.

### 3.5 Classification Techniques

Convolutional neural network(CNN) is a deep learning model used for image recognition and classification, finding patterns in images to recognize the object. It has three layers: convolutional layers, pooling layers, and fully connected layers.

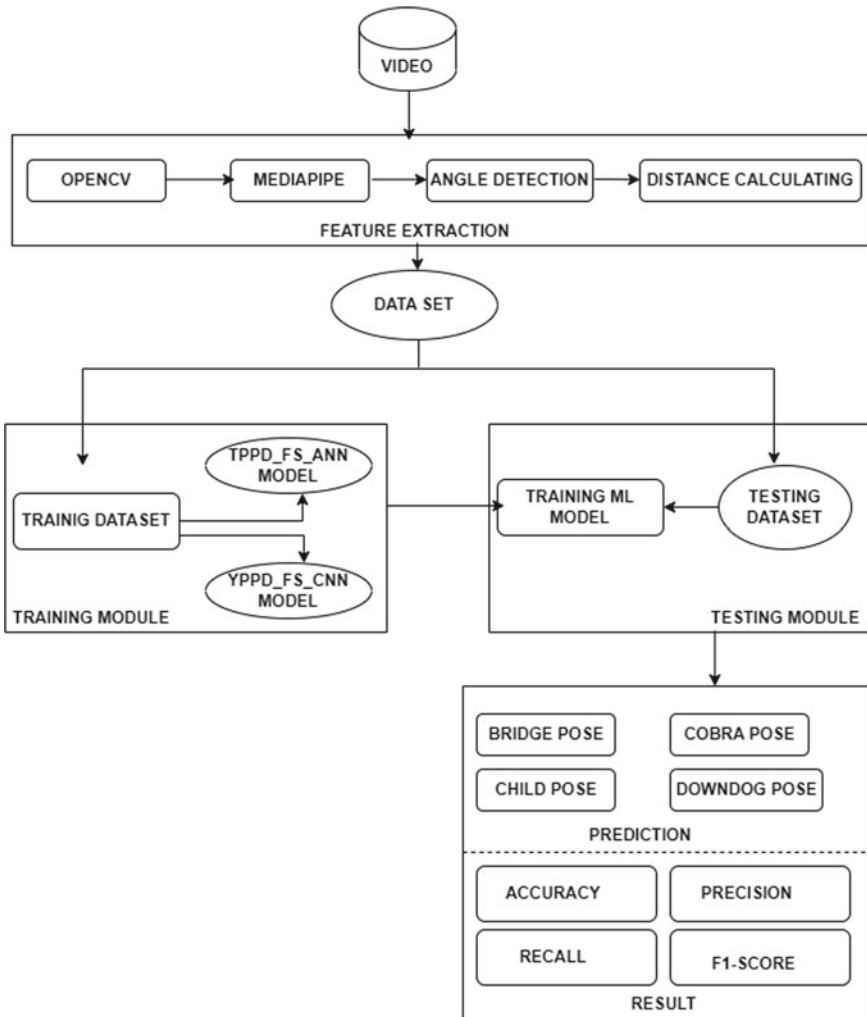


**Fig. 2** Flow diagram of proposed model

An artificial neural network(ANN) is a computational network with nodes linked to each in various layers of the network, which makes the computer able to think in a human manner. It consists of a large number of artificial neurons arranged in a sequence of layers. ANN has three layers: an input layer, a hidden layer, and an output layer. In the Fig. 3a, b, the details of the custom build deep learning models (*YPPD\_FS\_ANN* and *YPPD\_FS\_CNN*) are shown.

Layer (type)	Output Shape	Layer (type)	Output Shape
conv1d (Conv1D)	(None, 12, 128)	dense (Dense)	(None, 32)
conv1d_1 (Conv1D)	(None, 6, 32)	dropout (Dropout)	(None, 32)
max_pooling1d (MaxPooling1D)	(None, 3, 32)	dense_1 (Dense)	(None, 64)
)		dropout_1 (Dropout)	(None, 64)
flatten (Flatten)	(None, 96)	dense_2 (Dense)	(None, 128)
dense (Dense)	(None, 64)	dropout_2 (Dropout)	(None, 128)
dropout (Dropout)	(None, 64)	dense_3 (Dense)	(None, 128)
dense_1 (Dense)	(None, 128)	dropout_3 (Dropout)	(None, 128)
dropout_1 (Dropout)	(None, 128)	dense_4 (Dense)	(None, 128)
dense_2 (Dense)	(None, 128)	dropout_4 (Dropout)	(None, 128)
dropout_2 (Dropout)	(None, 128)	dense_5 (Dense)	(None, 512)
dense_3 (Dense)	(None, 128)	dropout_5 (Dropout)	(None, 512)
dropout_3 (Dropout)	(None, 128)	dense_6 (Dense)	(None, 128)
dense_4 (Dense)	(None, 256)	dense_7 (Dense)	(None, 64)
dense_5 (Dense)	(None, 256)	dense_8 (Dense)	(None, 4)
dense_6 (Dense)	(None, 128)		
dropout_4 (Dropout)	(None, 128)		
dense_7 (Dense)	(None, 128)		
dropout_5 (Dropout)	(None, 128)		
dense_8 (Dense)	(None, 64)		
dropout_6 (Dropout)	(None, 64)		
dense_9 (Dense)	(None, 128)		
dropout_7 (Dropout)	(None, 128)		
dense_10 (Dense)	(None, 5)		

(a) CNN

(b) ANN

**Fig. 3** Hyperparameters used for the CNN and ANN

## 4 Experimental Results

In this section, we have presented the details of the experimental environment. The performance of the models is also analyzed in this section.

### 4.1 Experimental Environment

For our work, we have used a system with a decent configuration. In our system, the memory is 16 GB, and the processor is i7-10750H CPU @ 2.60GHz 2.59 GHz; for the operating system, we have chosen Windows 11 64 bit; for project, we have used the sklearn, OpenCV, and MediaPipe libraries.

**Table 2** Results analysis of DL models

DL model	Precision (%)	Recall (%)	F1-score (%)	Accuracy (%)
ANN	92.05	90.31	91.00	91.61
CNN	99.03	99.27	99.15	99.24

In this section, we evaluate our model's performance with the help of recall, precision, F1-score, and accuracy. In recall, it measures how the model identifies the true positives. Our scenario identifies how the persons are doing yoga exercises correctly. Precision correspondence between true positives and all positives and measures the persons doing a yoga pose correctly identifies out of all persons doing the yoga exercise. F1-score takes the average of precision and recall, which is the harmonic mean of recall and precision. Accuracy is used for classification models and measures how the model predicts the correct predictions with the total predictions [22, 23].

## 4.2 Result Analysis

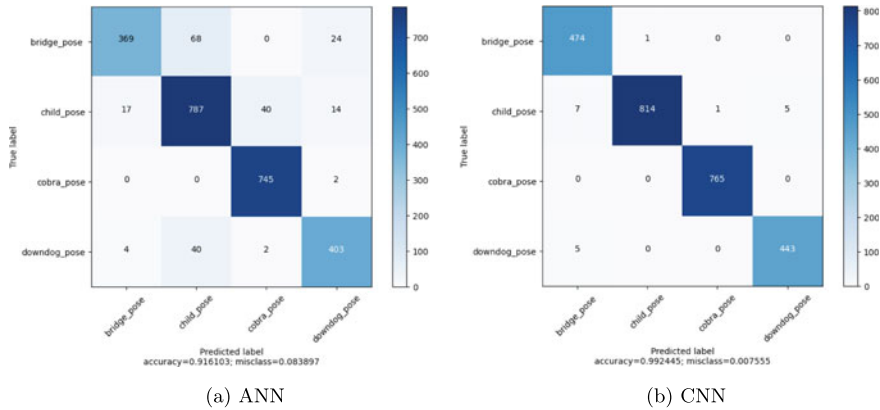
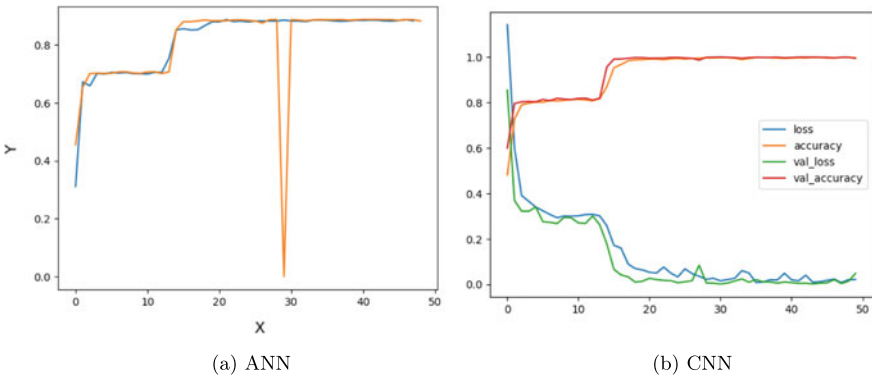
In this section, we have shown the benchmark results of the experiments. By the parameters mentioned above, we analyze the performance of the models that fit our model in the yoga recognition task.

**Confusion Matrix** The confusion matrix tells about the performance of the classification models by giving the testing dataset, and it has four cases: true positive, true negative, false positive, and false negative. Using this case, it evaluates the model and tells how it works on the dataset. In the Table 2, we have shown the performance of both models used in work. Figure 4 presents the confusion matrix of both DL models.

**Training and Validation Accuracy** Visual representations of the performance of convolutional neural network (CNN) and artificial neural network (ANN) models are shown in Fig. 5. The accuracy and validation loss graphs can provide insights into the model's ability to generalize to new data and prevent overfitting. The graph showing a higher accuracy for the CNN model indicates that it makes better predictions than the ANN model. And here, the x-axis is training accuracy. The y-axis is validation accuracy. At the same time, the validation loss can indicate the model's robustness and ability to generalize to new data.

## 4.3 Comparison with Other State of the Arts

We compared our model with other works which are related to exercise monitoring. Our model uses our dataset that predicts the best accuracy compared to the other models discussed in [18]. They have used the coco dataset for vision-based human posture classification using CNN with an accuracy of 97.5%. In [19], author uses the

**Fig. 4** Confusion matrix**Fig. 5** Training and validation accuracy graph**Table 3** Comparative study

References	Year	Dataset	Accuracy (%)
[18]	2021	COCO	97.5
[19]	2020	UCI_HAR, WISDM, OPPURTUNITY	95.8
[20]	2022	Yoga Posture Dataset(Kaggle)	92.99
Proposed work	2022	YPPD	99.24

UCI\_HAR, WISDM, OPPURTUNITY datasets for yoga pose detection and classification. They also used a deep learning model and achieved an accuracy of 95.8%. Wang et al. [20] have used the yoga posture dataset from Kaggle for multiclassification yoga pose based on deep learning with an accuracy of 92.99%. Therefore, our proposed model gives better accuracy as compared to the above-reported similar model (Table 3).

## 5 Conclusion and Future Work

In recent times, human posture assessments have been widely used to classify and recognize yoga poses correctly for getting the accuracy of the assessments. This paper proposes an efficient yoga posture recognition system model based on deep learning techniques like CNN and ANN. The yoga video is passed into the model in our model, and features will be extracted for the classification task. Then, the model predicts the yoga posture of the person and gives feedback to the patient, which helps to do the yoga in a precise way. Our result reveals that the CNN model has better prediction accuracy than ANN in our dataset. Based on the overall performance, the proposed model got outperformed accuracy. In future, we will use a hybrid classifier to get better accuracy in the yoga posture detection task.

## References

1. Freburger JK, Holmes GM, Agans RP, Jackman AM, Darter JD, Wallace AS, Carey TS (2009) The rising prevalence of chronic low back pain. *Arch Internal Med* 169(3):251–258
2. Koes BW, Van Tulder M, Thomas S (2006) Diagnosis and treatment of low back pain. *Bmj* 332(7555):1430–1434
3. Ferreira PH, Ferreira ML, Maher CG, Refshauge KM, Latimer J, Adams RD (2013) The therapeutic alliance between clinicians and patients predicts outcomes in chronic low back pain. *Phys Ther* 93(4):470–478
4. Monfort-Pañego M, Miñana-Signes V (2020) Psychometric study and content validity of a questionnaire to assess back-health-related postural habits in daily activities. *Measur Phys Educ Exerc Sci* 24(3):218–227
5. Costa C, Tacconi D, Tomasi R, Calva F, Terreri V (2013) RIABLO: a game system for supporting orthopaedic rehabilitation. In: Proceedings of the biannual conference of the Italian chapter of SIGCHI, pp 1–7
6. Singh M, Sharma A (2022) Assessment and rehabilitation of low back pain (LBP) using artificial intelligence and machine learning-a review. In: Artificial intelligence trends in systems: proceedings of 11th computer science on-line conference 2022, vol 2. Springer International Publishing, Cham, pp 449–461
7. González-Ortega D, Díaz-Pernas FJ, Martínez-Zarzuela M, Antón-Rodríguez M (2014) A Kinect-based system for cognitive rehabilitation exercises monitoring. *Comput Methods Prog Biomed* 113(2):620–631
8. Anwary AR, Cetinkaya D, Vassallo M, Bouchachia H (2021) Smart-cover: a real-time sitting posture monitoring system. *Sens Actuators A: Phys* 317:112451
9. Zhang Y, Haghghi PD, Burstein F, Yap LW, Cheng W, Yao L, Cicuttini F (2020) Electronic skin wearable sensors for detecting lumbar-pelvic movements. *Sensors* 20(5):1510
10. Zhang Y, Haghghi PD, Burstein F, Yao L, Cicuttini F (2021) On-device lumbar-pelvic movement detection using dual-IMU: a DNN-based approach. *IEEE Access* 9:62241–62254
11. Seth A, James A, Mukhopadhyay S (2021) Wearable sensing system to perform realtime 3D posture estimation for lower back healthcare. In: 2021 IEEE international symposium on robotic and sensors environments (ROSE). IEEE, pp 1–7
12. Sellmann A, Wagner D, Holtz L, Eschweiler J, Diers C, Williams S, Disselhorst-Klug C (2021) Detection of typical compensatory movements during autonomously performed exercises preventing low back pain (LBP). *Sensors* 22(1):111
13. Ordóñez FJ, Roggen D (2016) Deep convolutional and lstm recurrent neural networks for multimodal wearable activity recognition. *Sensors* 16(1):115

14. Tran DN, Phan DD (2016) Human activities recognition in android smartphone using support vector machine. In: 2016 7th international conference on intelligent systems, modelling and simulation (ISMS). IEEE, pp 64–68
15. Alshurafa N, Eastwood J, Nyamathi S, Xu W, Liu JJ, Sarrafzadeh M (2014) Battery optimization in smartphones for remote health monitoring systems to enhance user adherence. In: Proceedings of the 7th international conference on pervasive technologies related to assistive environments, pp 1–4
16. Zhao Y, Yang R, Chevalier G, Xu X, Zhang Z (2018) Deep residual bidir-LSTM for human activity recognition using wearable sensors. *Math Probl Eng*
17. Kalantarian H, Sideris C, Mortazavi B, Alshurafa N, Sarrafzadeh M (2016) Dynamic computation offloading for low-power wearable health monitoring systems. *IEEE Trans Biomed Eng* 64(3):621–628
18. Hasib R, Khan KN, Yu M, Khan MS (2021) Vision-based human posture classification and fall detection using convolutional neural network. In: 2021 International conference on artificial intelligence (ICAI). IEEE, pp 74–79
19. Kumar D, Sinha A (2020) Yoga pose detection and classification using deep learning. LAP LAMBERT Academic Publishing
20. Wang X (2022) Multi-classification for yoga pose based on deep learning. In: CIBDA 2022; 3rd international conference on computer information and big data applications. VDE, pp 1–4
21. Cao Z, Simon T, Wei SE, Sheikh Y (2017) Realtime multi-person 2d pose estimation using part affinity fields. In: Proceedings of the IEEE conference on computer vision and pattern recognition, pp 7291–7299
22. Ansari MSA, Pal K, Govil P, Govil MC, Awasthi LK (2022) A statistical analysis of SAMPARK dataset for peer-to-peer traffic and selfish-peer identification. *Multimedia Tools Appl* 1–29
23. Ansari M, Alam S, Pal K, Govil MC, Govil P, Srivastava A (2021) Ensemble machine learning for P2P traffic identification. *Int J Comput Digital Syst*

# Multicrops Disease Identification and Classification System Using Deep MobileNetV2 CNN Architecture



R. Ramya, N. Deepikasri, T. Madhubala, and A. Manikandan

**Abstract** A significant proportion of the Indian economy depends on agricultural productivity. Many plants perish due to such illnesses and a lack of knowledge about the conditions, symptoms, and remedies. The most significant application of artificial intelligence (AI) is agriculture nowadays. A creative strategy is used to adopt technology in agriculture. It is important to control damaged leaves, while crops are still growing. In this paper, a plant disease detection system using deep CNN algorithms is presented that quickly recognizes the indications and symptoms shown on the plant's leaves and stems and promotes the growth of a farm with wholesome vegetation. A deep learning-based model used to extract information from photos identified the ill and healthy leaves. This project presents a review of current plant disease detection methods. The accuracy of image classification has been greatly improved by the most current development in deep learning-based convolutional neural networks (CNNs). This thesis relies on a pre-trained deep learning-based technique for detecting plant illnesses and is motivated by CNN's success in image categorization. This work's two contributing factors are large-scale architectures with the highest level of sophistication, including ResNet and MobileNet. The MobileNetV2 CNN model suggested was trained and tested using data from the Kaggle Website. Here, a CNN-based approach to identify plant diseases is proposed. The suggested model is more accurate than earlier CNN-based models, with a 99% accuracy rate. The proposed study explicitly advocates for raising agricultural food output.

**Keywords** Deep learning · CNN · MobileNetV2 · Accuracy · Diseases · Classification

---

R. Ramya (✉) · N. Deepikasri · T. Madhubala · A. Manikandan

Department of Electronics and Communication Engineering, K.S. Rangasamy College of Technology, Namakkal, Tamil Nadu, India

e-mail: [srvece@gmail.com](mailto:srvece@gmail.com)

## 1 Introduction

As of April 2020, roughly, 1.38 billion people were living in India. There are around 95.8 million farmers in India, according to estimates. It must be noted that 18% of India's GDP is produced in the agricultural sector. Therefore, it is reasonable to expect that modernizing agriculture would benefit the country. It would also create a lot of employment and expansion chances in the agricultural industries, in addition to improving conditions for farmers. Pesticides, fungicides, and herbicides research and development have progressed very well in India. But every year, because of natural causes, crops are prone to various known diseases, and tons of produced crops are lost. This can be handled with the prompt discovery of plant diseases at the appropriate time. Moreover, it will help the nation's farmers get through their challenging economic environment [1]. Life, today, is better because of technology. Almost anything is available now through the Internet. Using a standard camera, one can quickly click photos of affected parts and upload them to the system, which detects the particular disease and offers the precise remedy, along with a pesticide if necessary. Various fungal and bacterial diseases infect most plants. With the exponential increase in population, climatic conditions also cause plant diseases [2]. To find the ailment, the leaves must be closely observed; many researchers report several techniques for plant disease detection and monitoring [3]. The proposed system consists of two parts. One is the extraction of disease features, and the other is the classification of the same. A healthy plant with no disease, rust, scab, downy, or mildew is the five classes considered in this work. With these variations of grape leaf diseased images, the proposed system's classification performance is examined in terms of accuracy, and a desirable score of 90% is obtained for the same. Image data collection, pre-processing, segmentation, analysis, image definition, and real-world identification and classification are among the steps required. Image processing, also known as machine learning, is a growing field plagued by problems, particularly in developing artificial and intelligent systems that digitize information and data using images [4]. Machine learning is the recognition of incorporation into industry, automation, and architecture. New advances in computing have automated image processing and deep learning.

## 2 Related Works

Various methods and approaches are available to classify diseases and weeds. A significant area of machine learning is deep learning (DL). It is developed using an artificial neural network (ANN) and has several hidden layers. A class of deep and feed-forward ANNs called convolutional neural networks (CNNs) was developed. The learning dataset is represented using a variety of convolutions at different levels of the network, starting with more general representations at the initial primary layers and progressing to more specialized ones at the deeper layers. The pooling layers

lower the dimensionality of the input images after the convolutional layers have extracted features from them [5]. Plant disease detection uses CNN designs like LeNet, AlexNet, GoogleNet, and VGG19. The research projects' data came from two sources: (1) Plantvillage and (2) their dataset (manually by visiting various places). It has been noted that AlexNet is employed more frequently than alternative topologies. These datasets were subsequently divided into various classes that included healthy and sick picture samples. After that, training and testing sub-datasets were created from these samples [6]. The first stage in developing an image database for a disease recognition model is to collect images. The second stage is building a deep learning framework to train CNN. Its two main strengths are this model's simplicity and capacity to discriminate between healthy and unhealthy leaves using CNN [7]. CNN's first and central layer is called the convolution layer. A grayscale image with a 128 by 128 by one array of pixel values serves as the model's input. With a kernel size of  $3 \times 3$ , the first convolution layer employs 32 filters. It comprises a group of expandable learnable filters or kernels with a restricted receptive field that can be extended to the full depth [8]. MATLAB is used to carry out the procedure. While working with an interface in an Arduino microcontroller, an image could be retrieved using the image acquisition toolbox in MATLAB. It could be obtained live from a camera connected to a computer. The user provides the input image, which is then taken through image processing, including extracting the RGB color map for background separation. Following image segmentation, the segmented image is used to run the SVM algorithm and determine the mean [9]. This paper proposes an effective deep CNN-based smart mobile application model to detect illnesses in tomato leaves. The concept that MobileNet inspired was used to create such an application. CNN model can identify the ten most prevalent varieties of tomato leaf disease and build a program using the datasets of tomato leaves as training. The clever mobile system uses 7176 photos of tomato leaves to diagnose tomato disease [10].

### 3 Methodology

#### Deep CNN

A machine learning method called deep learning is used to create artificial intelligence (AI) systems. It is based on the concept of artificial neural networks (ANNs), which use several layers of neurons to process enormous amounts of data to do complicated analyzes. Many different types of deep neural networks exist (DNN). The most popular deep convolutional neural network (CNN or DCNN) is used for recognizing pattern in images [11]. A model of CNN's architecture is shown in Fig. 1. Conventional artificial neural networks gave rise to DCNNs, and two crucial aspects of deep CNN are (a) several layers and (b) supervised and unsupervised learning in nonlinear processing. Nonlinear processing employs numerous layers, each receiving an input value that is the result of the layer before it. The mapping function from input to output must be used in supervised learning, where we only have the input.

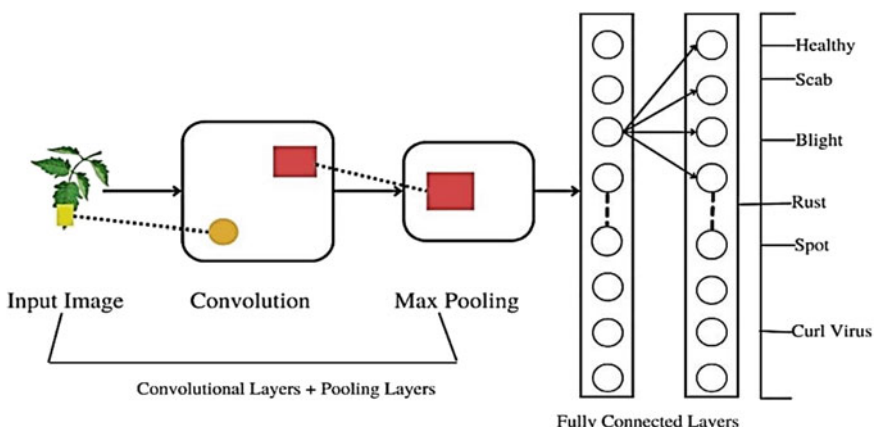


**Fig. 1** CNN architecture model

Additionally, unsupervised learning creates clusters based on similar behavior, even if there are only inputs and no corresponding outputs.

Various steps are involved to identify plant diseases. The system architecture for this work deep learning-based plant infection detection and classification system is shown in Fig. 2.

**Image acquisition:** Use the camera to acquire a high-quality image of a tomato plant leaf, which is then added to a database for use in subsequent operations.

**Pre-processing:** To reduce image noise, leaf images are added during pre-processing. In the pre-processing stage, the image is improved by background removal using image clipping, image smoothing with a smoothing filter, and contrast boosting using image enhancement.

**Segmentation:** Using the k-means clustering approach, image segmentation involves dividing an image into several segments with the same features or a degree of similarity.

**Feature Extraction:** In feature extraction, the highlights are eliminated. Selecting the entire arrangement of pixels allows one to choose only the necessary and sufficient to represent the whole segment. Instead of defining the ReLU activation function to be 0 for negative input values, it is represented as a very small linear component of  $x$ . The leaky ReLU function has increased the ReLU activation function. The ReLU activation function's gradient is zero for any input values below zero.

The feature extraction process involves applying the k-means clustering approach to extract the similarity values for energy, entropy, standard deviation, color enhancement, etc.

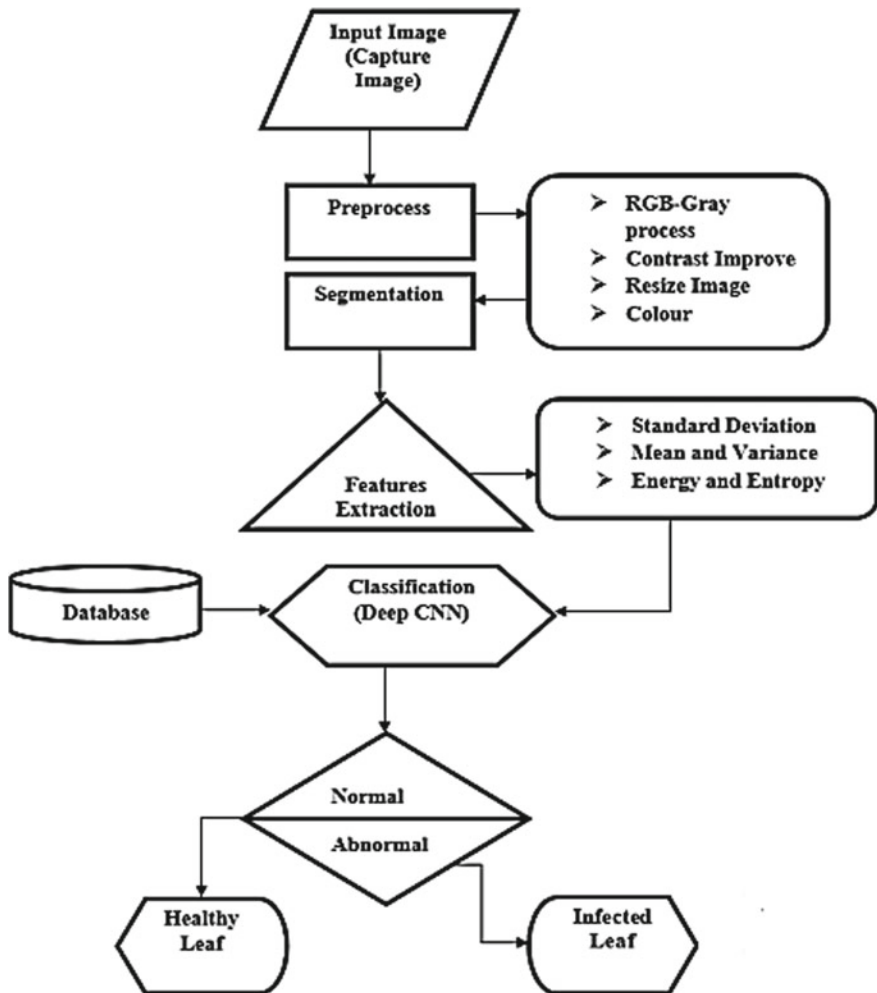


**Fig. 2** Overall process for disease detection and classification

### MobileNetV2

To function well on mobile devices, MobileNetV2 is a convolutional neural network design. It is founded on an inverted residual structure, with the bottleneck layers acting as the residual connections. Lightweight depthwise convolutions are used in the intermediate expansion layer to filter features and add non-linearity [12]. It initially consists of a complete convolution layer with 32 filters which is the first layer in the MobileNetV2 design, followed by 19 other bottleneck levels. The MobileNetV2 model architecture is as shown in Fig. 3. There are two different kinds of blocks in MobileNetV2. Remaining block one has a stride of one. Another is a

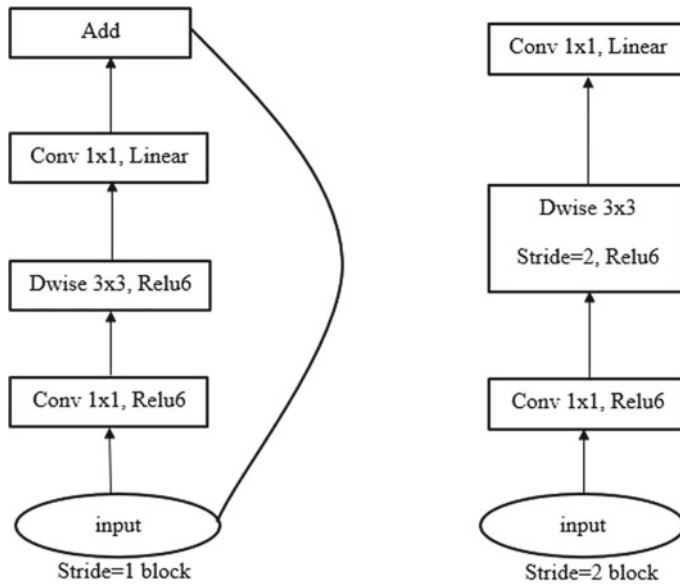


**Fig. 3** Block of MobileNetV2 model

block for shrinking with a stride of two. For both varieties of blocks, there are three levels:

- 1  $\times$  1 convolution with ReLU6 makes up the first layer.
- The depthwise convolution is the second layer.
- The third layer is an 1  $\times$  1 convolution once more, but this time, there is no non-linearity.

Deep networks are said to only have the power of a linear classifier on the non-zero volume portion of the output domain if ReLU is applied once more.

MobileNetV2 has been used for autonomous feature extraction across several datasets. Multiple factors led to the selection of the MobileNetV2 architecture. First off, utilizing a smaller, more expressive network, such as the MobileNetV2, minimized the effect of overfitting caused by the relatively limited dataset used to train a network on visual recognition. The MobileNetV2 design lowers error costs while enhancing memory efficiency and execution speed. Although minimal memory use is a desirable trait in the setting of an ensemble of networks, testing and parameter changing are made much simpler by the fast execution speed. The classification of plant leaf diseases performs better when ensemble MobileNetV2 is used. The model might be implemented with fewer parameters and reduced file size and perform equally well. In order to reduce redundancy, the model changed the previous model by adding dense layer with fully connected layers after the global average pooling layer with output 1024 and N-class variables, accordingly. This modification is shown in Fig. 4.

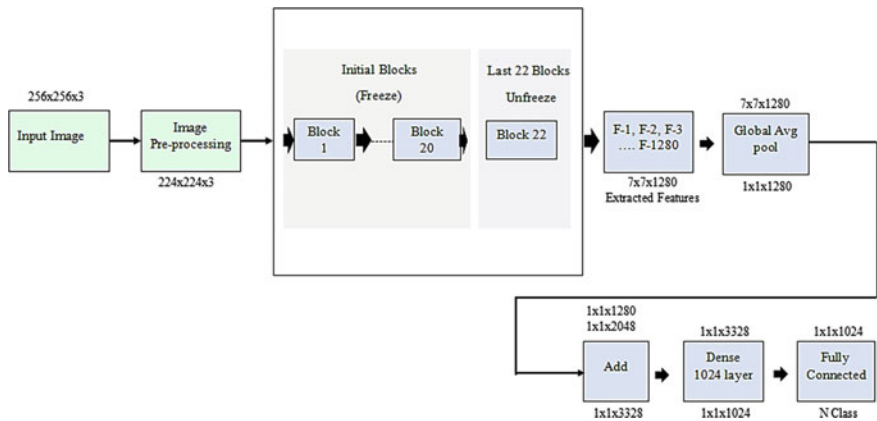


**Fig. 4** Architecture of proposed MobileNet model

A MobileNet layer is formed of pooling layers and convolutional layers of varying sizes (such as 3 3 and  $n \times n$  layers), with all outputs combined and propagating to the input of the subsequent layer instead of the block's typical convolution. In comparison with regular convolution, depthwise separable convolution requires low parameters. The number of layers and parameter sizes for this CNN model is displayed in Table 1.

## 4 Results and Discussion

MATLAB is currently a competitive tool in artificial intelligence, machine learning, data analytics, and others. The leaves with the disease and the healthy leaves are given to the processing unit as samples. The input leaf image is first loaded, after which pre-processing, segmentation, and feature identification are applied to the image. To diagnose diseases, various CNN classifications are used.

### 4.1 Dataset-Training Process

A convolutional neural network (CNN) is an effective deep learning method; numerous varied image collections are used to train CNNs. This proposed CNN model can learn rich feature representations for various images from these sizable databases.

Figure 5 shows the dataset, which is given as input. The image dataset includes the plant varieties such as tomato, grape, squash, potato, apple, blueberry, and cherry. The developed models are trained and tested on public datasets to create a successful

**Table 1** Model's relevant parameters using standard convolution

Layer/stride	Filter size	Input size
Conv/s2	3 * 3 * 3 * 32	224 * 224 * 3
Conv dw/s1	3 * 3 * 32 dw	112 * 112 * 32
Conv/s1	1 * 1 * 32 * 64	112 * 112 * 32
Conv dw/s2	3 * 3 * 64 dw	112 * 112 * 64
Conv/s1	1 * 1 * 64 * 128	56 * 56 * 64
Conv dw/s1	3 * 3 * 128 dw	56 * 56 * 128
Conv/s1	1 * 1 * 128 * 128	56 * 56 * 128
Conv dw/s2	3 * 3 * 128 dw	56 * 56 * 128
Conv/s1	1 * 1 * 128 * 256	28 * 28 * 128
Conv dw/s1	3 * 3 * 256 dw	28 * 28 * 256
Conv/s1	1 * 1 * 256 * 256	28 * 28 * 256
Conv dw/s2	3 * 3 * 256 dw	28 * 28 * 256
Conv/s1	1 * 1 * 256 * 512	14 * 14 * 256
5 * Conv/s1	3 * 3 * 512 dw	14 * 14 * 512
Conv/s1	1 * 1 * 512 * 512	14 * 14 * 512
Conv dw/s2	3 * 3 * 512 dw	14 * 14 * 512
Conv/s1	1 * 1 * 512 * 1024	7 * 7 * 512
Conv dw/s2	3 * 3 * 1024 dw	7 * 7 * 1024
Conv/s1	1 * 1 * 1024 * 1024	7 * 7 * 1024
Avg Pool/s1	Pool 7 * 7	7 * 7 * 1024
FC/s1	1024 * 1000	1 * 1 * 1024
Softmax/s1	Classifier	1 * 1 * 1000

method for identifying plant diseases. All of the images were gathered from a variety of healthy and disease leaves. Plant diseases can be identified in plantation leaf images and agricultural fields using CNN models. Tables 2 and 3 are the representation of the data distribution of training and validation process images.

## 4.2 Performance and Analysis

Precision, recall, F1-score, and accuracy are a few common evaluation variables that are utilized to assess the categorization abilities of our work in classifying the various plant leaf disease types. We calculated the accuracy using the equation below

$$\text{Precision} = \frac{\text{Tp}}{\text{Tp} + \text{Fp}} \quad (1)$$

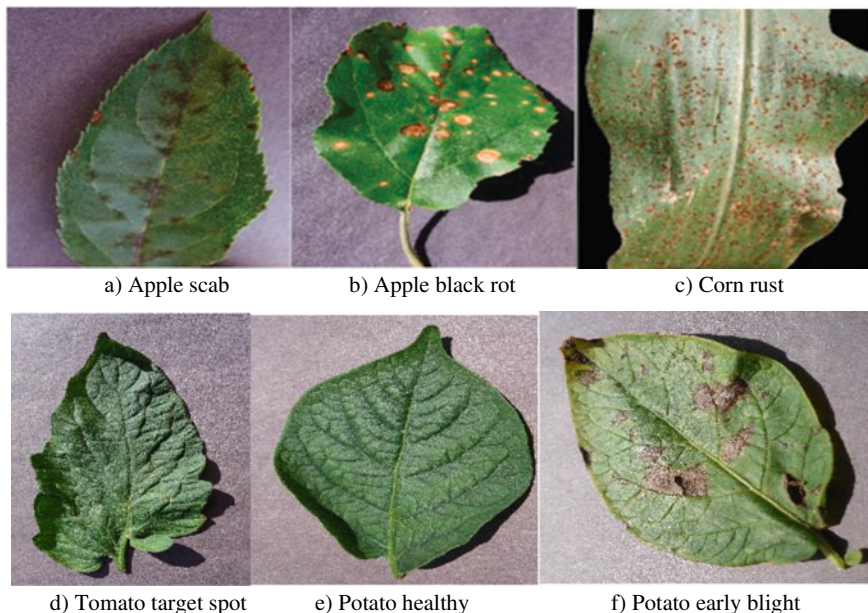


**Fig. 5** Sample leaf disease and healthy images on dataset

**Table 2** Training and validation images

Names of the diseases	Number of input images	
	Training	Validation
Apple scab	956	400
Apple Black_rot	1124	577
Apple Cedar_apple_rust	1260	540
Apple healthy	1200	402
Corn_(maize)_Cercospora_leaf_spot	980	390
Corn_(maize) Common_rust_	1120	477
Corn_(maize) healthy	850	265
Potato_Early_blight	824	256
Potato_healthy	939	345
Tomato_Bacterial_spot	702	225
Tomato_Early_blight	940	280
Tomato healthy	896	240

**Table 3** Few various diseases categorize on dataset in each class

Classes	Name of the diseases
0	Apple scab
1	Apple Black_rot
2	Apple Cedar_apple_rust
3	Apple healthy
4	Corn_(maize)_Cercospora_leaf_spot
5	Corn_(maize) Common_rust_
6	Corn_(maize) healthy
7	Potato_Early_blight
8	Potato_healthy
9	Tomato_Bacterial_spot
10	Tomato_Early_blight
11	Tomato healthy

$$\text{Recall} = \frac{\text{Tp}}{\text{Tp} + \text{Fn}} \quad (2)$$

$$\text{Accuracy} = \frac{\text{Tp} + \text{Tn}}{\text{Tp} + \text{Fn} + \text{Fp} + \text{Tn}} \quad (3)$$

where TP is truly positive, TN is true negative; similarly, FP and FN are false positive and negative in the confusion matrix process.

Table 3 displays several diseases in plants for each class of labels.

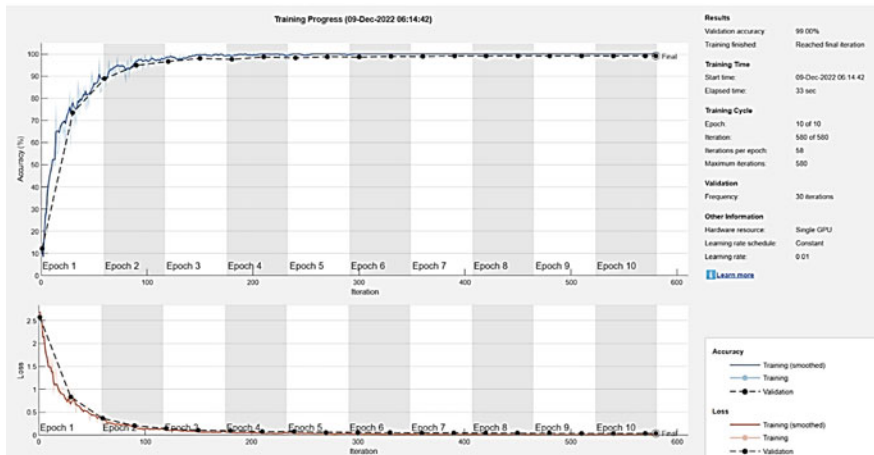
Figure 6 displays an example of the training and validation progress accuracy, along with the cross-entropy loss during training for the CNN model utilizing a data split.

A measure of the level of accurate predictions is precision. Among all of those expected to acquire the disease, recall provides information about the model's ability to identify true positives, and others are afflicted with the illness. Figure 7 shows the confusion matrix for recall and precision of some sample classes.

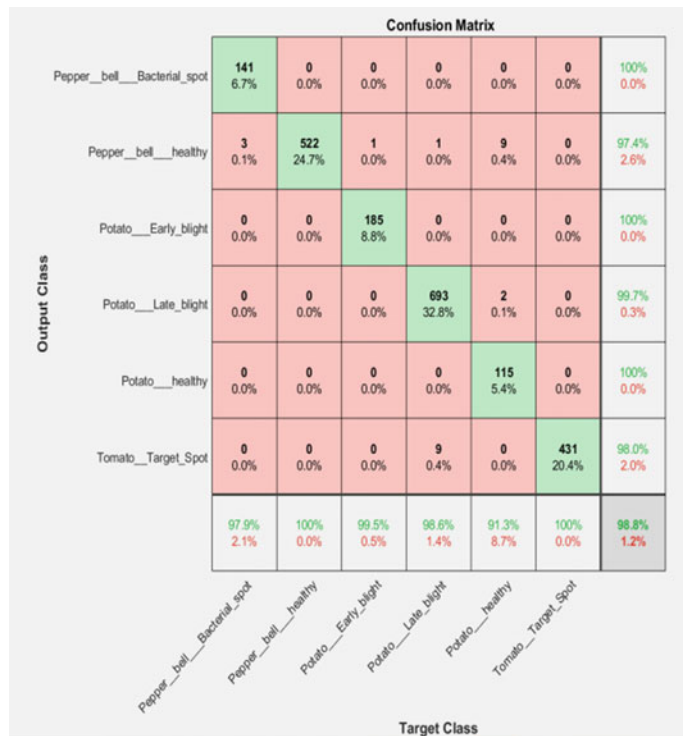
Figure 8 shows the network architecture in its complete using analyzed network along with an interactive visualization of the network layers. The ReLU activation function applied after every convolutional layer.

Figure 9 displays the overall precision and recall values for each class of the MobilenetV2 model.

The use of deep learning in agriculture is becoming more prominent in the literature. A comparison of the most recent discoveries in the classification of various leaf diseases is shown in Table 4.

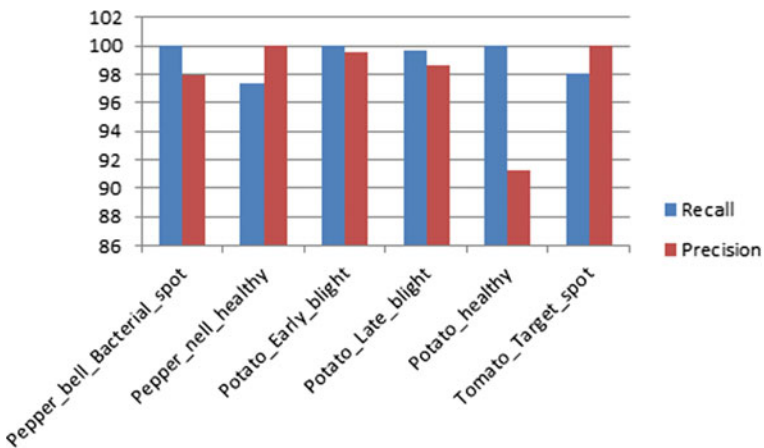


**Fig. 6** Sample training/validation progress the accuracy versus losses outputs



**Fig. 7** Confusion matrix for few samples classes

ANALYSIS RESULT				
	Name	Type	Activations	Learnables
1	imageinput 256×256×3 images with 'zeroce...	Image Input	256×256×3	-
2	conv_1 8 7×7×3 convolutions with stride...	Convolution	256×256×8	Weights 7×7×3×8 Bias 1×1×8
3	batchnorm_1 Batch normalization with 8 chan...	Batch Normalization	256×256×8	Offset 1×1×8 Scale 1×1×8
4	relu_1 ReLU	ReLU	256×256×8	-
5	maxpool_1 5×5 max pooling with stride [2 2]...	Max Pooling	126×126×8	-
6	conv_2 16 7×7×8 convolutions with strid...	Convolution	126×126×16	Weights 7×7×8×16 Bias 1×1×16
7	batchnorm_2 Batch normalization with 16 cha...	Batch Normalization	126×126×16	Offset 1×1×16 Scale 1×1×16
8	relu_2 ReLU	ReLU	126×126×16	-
9	maxpool_2 2×2 max pooling with stride [2 2]...	Max Pooling	63×63×16	-
10	conv_3 32 7×7×16 convolutions with stri...	Convolution	63×63×32	Weights 7×7×16×32 Bias 1×1×32

**Fig. 8** Analysis of convolution layers with activations parameters**Fig. 9** Recall and precision for various disease classes**Table 4** Comparison to the latest results in classification

Authors	Performance level in %
Chakraborty et al. [7]	Accuracy 96%, recall and precision 96%
Li et al. [1]	Accuracy 95.33% (custom CNN)
This work CNN model	(> 97%) for all measures parameters

## 5 Conclusion

Due to its enormous potential, deep learning is becoming more and more popular as data quality and volume increase system. The problem of identifying apple, potato, tomato, and corn leaf diseases was addressed using deep convolutional neural networks. High categorization accuracy may be achieved with little effort required of the specialists, and farmers would benefit significantly. The plant diseases were found utilizing MATLAB's image processing methods. The process includes adding an image, processing it beforehand, segmenting it, extracting its features, and classifying it. The suggested CNN model detects several plant diseases with an average accuracy of 99%. The creation of an automatic detection system utilizing image processing makes it possible to assist users in early disease detection and provide helpful information for its management. By using continuous learning techniques to modify the application during deployment, future work will concentrate on enhancing the system.

## References

1. Liu J, Wang X (2021) Plant diseases and pests detection based on deep learning: a review. *Plant Method*
2. Shoib M, Hussain T (2022) Deep learning-based segmentation and classification of leaf images for detection of tomato plant disease. *Front Plant Sci* 13
3. Mahmudul Hassan Sk, Maji AK (2021) Identification of plant-leaf diseases using CNN and transfer-learning approach. *Electronics* 10(12):1388
4. Akbar M, Ullah M, Shah B (2022) An effective deep learning approach for the classification of Bacteriosis in peach leaves. *Front Plant Sci*
5. Kamilaris A, Prenafeta-Boldú FX (2018) Deep learning in agriculture: a survey, computers, and electronics in agriculture
6. Arya S, Singh R (2019) An analysis of deep learning techniques for plant leaf disease detection. *Int J Comput Sci Inform Secur*
7. Tarikul Islam Md., Shamsuzzaman Md. (2022) Transfer learning based approach to crops leaf disease detection: a diversion changer in agriculture. *Int J Eng Res Technol (IJERT)*
8. Udawant P, Srinath P (2019) Diseased portion classification & recognition of cotton plants using convolution neural networks. *Int J Eng Adv Technol* 8(6):3492–3496
9. Gajendran P, Harish A, Kavinprasad S (2022) IoT-based disease and quality identification of tomato leaf using Image Processing. *Int Res J Modern Eng Technol Sci*
10. Elhassouny A, Smarandache F (2019) Smart mobile application to recognize tomato leaf diseases using convolutional neural networks. *IEEE/ICCSRE2019*, Agadir Morocco
11. Pandey A, Jain K (2022) A robust deep attention dense convolutional neural network for plant leaf disease identification and classification from smart phone captured real world image. *Int J Comput Ecol Ecolog Data Sci* 70:101725
12. Ashwinkumar S, Rajagopal S, Manimaran V, Jegajothi B (2022) Automated plant leaf disease detection and classification using optimal MobileNet based convolutional neural network. *Mater Today Proc*

# Machine Learning and Deep Learning-Based Smart City Infrastructure to Connect Intelligent Domain Using Internet of Things



Shiplu Das, Srinjoy Sarkar, Subhadip Dutta, Sohini Ghosh, Sudipto Dhar, Buddhadeb Pradhan, and Sudipta Sahana

**Abstract** Recycling and landfilling are steps in waste management that destroy trash. The Internet of Things (IoT) and the different machine learning and deep learning approaches presented in the article work together to provide an agile solution for real-time data monitoring and categorization. This study seeks to close the gap between ML and DL algorithms in innovative waste management in smart cities. The traditional trash management system may be replaced with intelligent sensors incorporated into the system to perform real-time monitoring and improve waste management thanks to the advent of the Internet of Things (IoT) and artificial intelligence (AI). ML algorithms, including logistic regression, support vector machine, random forest, and DL algorithms like Yolov3 and CNN, were mentioned in this work. Six object classes have been trained into the Yolov3 network (namely: cardboard, glass, metal, paper, plastic, and organic waste). The convolutional neural network (CNN) model, a popular deep learning approach, provides a better technique to separate biological from non-biological waste. Real-time trash monitoring will enable this intelligent system to be adjusted to domestic activities.

**Keywords** Internet of things (IoT) · Smart waste management system · Convolutional neural network · Yolov3 algorithm

---

S. Das · S. Sarkar · S. Dutta · S. Ghosh

Department of CSE, Brainware University, Barasat, West Bengal, India

S. Dhar · B. Pradhan (✉) · S. Sahana

Department of CSE, University of Engineering and Management, Kolkata, West Bengal, India

e-mail: [buddhadebpradhan@gmail.com](mailto:buddhadebpradhan@gmail.com)

## 1 Introduction

Population growth in India has resulted in a massive increase in pollution. India is again heading into a terrifying period of decay, a time when the notorious quality of a notorious country is even turning into tons of toxins. Pollution has reached its peak with the modernization and mobility of our lives. Provides travel to general temperature changes and human suffering. Eliminating or reducing waste and maintaining cleanliness requires an intelligent waste management architecture. The Internet of Things (IoT) is now an early technology that will transform the globe into smart cities. The mechanization is being used to build metropolises more intelligent by implementing multiple broadcast procedures, so this method has been implemented for active goods supervision and creative efficiency improvements in city extents. The expeditious growth of smart metropolises along with inventive corporations leads to a gradual rise in garbage and debris. Waste can be split into material waste, toxic waste, and inception-connected waste. Having a clean city is a routine job, but it takes plenty trained workers and efficiency. This IoT using machine intelligence and deep learning algorithms, determines active results in waste administration orders for evolving smart cities. The following machine intelligence and deep learning approach mainly used in garbage control systems are linear regression, logistic regression, support vector machines, decision trees, convolutional neural network, and YOLOv3 algorithm. These algorithms are used for intelligent city waste accumulation and prognosis with aspects such as quick decision-making and effective services; IoT instruments are fast growing in industries and metropolises. The IoT format can be redistributed in 3 tiers—These are the device, access, and platform layers. The layers are attained through ingestion, edge data processing, and cloud depository processes. The classifications of garbage and the debris volume, smoke level, and metal level can be observed continuously using IoT-planted dustbins. Also, segregate the various types of possessions like cardboard, paper, plastic, and metal from the garbage in the metropolitan. Then, our suggested procedure maybe tested by machine learning and deep learning categorization methods such as linear regression, logistic regression, support vector machine, convolutional neural network, and YOLOv3 algorithm. The projected method is examined accompanying ML and DL classification methods with respect to accuracy and time evaluation. The paper uses various types of ML and DL algorithms to create a smart waste monitoring arrangement for a smart city utilizing IoT. At first, the waste is isolated into six classifications: cardboard, paper, and metal. Then DL algorithms isolate the waste into six types, and ML algorithms train the motors to separate them in their particular garbage boxes. This paper tests the suggested algorithms' range of capabilities and decides that the YOLOv3 algorithm is highest in rank-fit algorithm subsequently comparing them. Because it has an accuracy of 94.99% accompanying a compilation time of 0.2 ms, the random forest classifier has an accuracy of 99.1% but the compilation time is more than YOLOv3, that is 0.4 ms. As a result, the YOLOv3 algorithm adds a more exact result for classification waste into six types, and the algorithm is part of deep learning (Fig. 1).

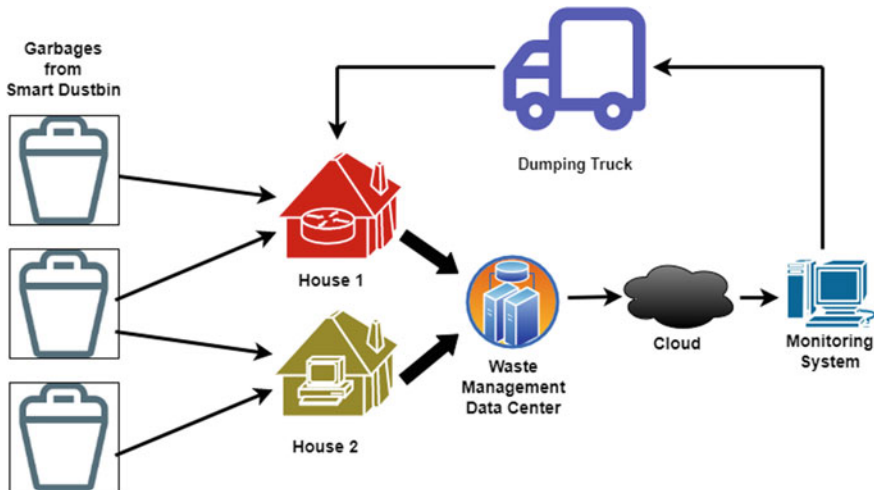


**Fig. 1** Smart waste management system

## 2 Literature Review

IoT with machine learning-based waste management systems will primarily focus on waste distribution, making the environment healthier. One of the real obstacles in many urban communities is strong waste management, and viable management of incoming heavy waste is becoming a fundamental part of a shining city. With the rapid development of smart cities and the population, more waste is generated daily by traditional methods, so waste decomposition requires more workforce and time. And ruin the environment, social life, and atmosphere. The Internet of Things (IoT) constantly evolves, offering unique solutions to people's everyday problems. A review of garbage administrating systems depending on the IoT was discussed. Monica etc. Equipped with a GSM module, he proposed an intelligent dustbin system that collects garbage with an Arduino UNO board. However, it has limitations such as difficult maintenance and time-consuming collection [1]. In India, Siam et al. proposed a smart trash can in Pune using an IoT prototype. Analyze IoT-based waste management, including nearest neighbor search, state progress, inheritance computation, and swarm amplification strategies. Pardini et al. suggest a waste administration structure that collects debris information from different organizations—Existing work focuses only on data accumulation. Hannan et al. paper has suggested a garbage waste administration method that uses line-following robots to accumulate waste, but it is not planned to optimize waste. In contrast, growing use trends have attained levels in quantity and harmful content that expose human health and the atmosphere. Chemical, production, physical, and consumption traits are studied to categorize waste [2]. Recycling is a feasible answer, but accurately classifying waste maybe troublesome. Efficient waste administration has a serious influence people's quality of existence. Waste disposal is connected to negative environmental impacts and, consecutively,

to human health. Therefore, there is a need for suitable waste administration method preparation for the improvement of people who wish to live in a healthy environment [2]. Hulyalkar et al. [3] proposes a smart bin design based on ML, image processing, and Internet of Things. This system's CNN allows it to recognize and classify garbage into many categories, including metal, glass, paper, and plastic. 400–500 photos with four distinct categories are employed to train the model. Keras is applied to implement the CNN in TensorFlow. There are eight tiers in the network. Fifty epochs are employed, with a train/validation separation of 350–400/50–100 per category. The Raspberry Pi micro-image controller's processing software allows the system to categorize and identify garbage with an accuracy of about 84%. In [4], a smart recycling container is suggested. Pretrained ResNet-34, a CNN with 34 pre-trained tiers, is used by the model together accompanying the Raspberry Pi 3 and Xilinx PYNQ-Z1 FPGA board to conduct trash categorization. A sensor node sends the data gathered from the bin to the gateway through a LoRa communication network. The system achieved a detection accuracy of 92.1% with an average processing time of 1.82 s. After garbage categorization, the system does not, however, engage in any waste segregation. Adedeji and Wang [5] suggests an intelligent trash sorting system. It employs a Support Vector Machine (SVM) and a 50-layer ResNet-50 model, which functions as an extractor, to categorize garbage into distinct types, including glass, metal, paper, and plastic. Features are deleted from the network, and the top classification layer of the model is removed. Multi-class SVM is then used to classify the retrieved feature [6, 7]. The accuracy of the suggested method is 87%. ResNet-50, however, needs more processing power than is appropriate for mobile platform applications. The proposed approach provided a detailed strategy for optimizing the ResNet-50 model for garbage monitoring by providing a set of given specifications for the SVM enhancement. In [8], a smart waste separator is suggested. The Hu's Invariant Moments [8] and the k-Nearest Neighbor algorithm are used by the system to identify rubbish using Euclidean distance. Using the k-NN method with  $k = 3$ , the suggested system can attain an efficiency of 98.33%. The suggested system can accurately identify various forms of garbage. Still, because it bases its waste detection on the shape of the waste, it cannot recognize the deformed waste that has been disposed of. Bharadwaj et al. [9] makes a case for an IoT-based solid waste management system. This system uses a load cell, an IR sensor, a passive infrared sensor, a PIR sensor, a DHT22 temperature sensor, an MQ-135 gas sensor, and an IR sensor to measure temperature and humidity, as well as the amount of rubbish, the presence of users, and the weight of the waste. Data are transferred to a gateway using LoRa connectivity, and the gateway then sends the data to the cloud for cloud monitoring. With each trash bin having its own set of sensors, the system utilizes five garbage bins to manage five distinct sorts of waste, which raises the system's overall cost. Deep neural network garbage sorting research is conducted in [10]. Deep convolutional neural network architectures are employed for training and testing, including ResNet, MobileNet, Inception-v4, DenseNet, and Xception. The training dataset comprises 2527 waste photos, including paper, glass, plastic, metal, cardboard, and rubbish. Adam [11] and Adadelta [12] employ various optimization techniques.

### 3 Proposed Methodology

For IoT-based trash management, machine learning (ML) offers efficient solutions, including regression, classification, clustering, and correlation rules perception. This is due to three key factors: First, because IoT apps use linked devices across the board, massive amounts of data are gathered daily. Additionally, they could have pre-programmed activities based on an exciting response from the data collected or specified circumstances. Second, computers are capable of picking up new skills. Examples include categorization, clustering, making predictions, and pattern recognition. These systems are also trained to utilize a variety of statistical models and algorithms to analyze sample data. Thirdly, the sample data often has quantifiable properties (referred to as features), and many ML algorithms try to detect connections between the parts and specific output values (called labels). The knowledge gained via training is then applied to find patterns or make choices based on new data. IoT-based waste management models are crucial in raising living standards and expanding human welfare by boosting energy efficiency, enhancing governance, and cutting costs. The ML classifier algorithm can categorize the garbage according to its properties. There are three main categories in which to place ML algorithms. Unsupervised learning, supervised learning, and reinforcement learning are these. To create a compelling smart city, supervised learning algorithms are mainly employed for garbage collection and management. To address the classification and regression challenges and because it produces superior results. The supervised learning is broken down into the random forest procedure, logistic regression, decision tree, support vector machine, and linear regression. The agency's most widely utilized classification technique is logistic regression. Logistic regression is more accurate than straightforward algorithms like decision trees and Naive Bayes categorisation [13]. Additionally, logistic regression's training time is less compared to other categorization algorithms like support vector machines and neural networks [14]. Choosing a hypothesis function that produces a constant value is the goal of a multiple regression model. This study now introduces a different group of supervised learning technique called classification, where the goal is to obtain a specific yield. A quantitative approach for presenting a binomial result is logistic regression. The input, like before, may include one or perhaps more attributes (or variables). The result of a bivariate analysis may be a 0 or 1, performing binary classification of the positive class from the negative samples. The classification is carried out in accordance with the probability level, which is displayed by a logistic curve in regression models. The hypothesis function for a logistic regression is given by Eq. (1).

$$h(x) = S(w_0 + w_1x_1 + w_2x_2 + \dots + w_nx_n) \quad (1)$$

where  $S()$  is a Sigmoid function given by Eq. (2).

$$S(p) = \frac{1}{1 + e^{-p}} \quad (2)$$

The sigmoid function results to a value amidst 0 and 1. All values beneath 0.5 relate to the negative samples, and numbers exceeding or similar to 0.5 relate to the positive samples. The utilization of LR is seen in miscellaneous fields, inclusive of gauging Trauma care, patient asperity evaluation, deciding the risk of ischemic heart disease, early detection and recognition of Glaucoma in optic thermographs. The test image was separated into two groups: biodegradable and non-biodegradable. The paper suggests the logistic regression (LR) machine learning approach for classification. The machine's algorithm determines which trash is biodegradable and which is not, notifies the controller, and the controller turns on the appropriate relay. The hardware consists of two relays, one for degradable materials and the other for non-degradable. An ultrasonic sensor determines the level of the trashcan, and a buzzer will sound if the dustbin is full. The hyperplane of SVM is a name for this optimal boundary. The number of features decides the hyperplane's length. The hyperplane is essentially flattery if there are just two input traits. Linear Kernel can be attained from the dot product between any two remarks. Each input pair's multiplication produces the product between two vectors,  $\alpha$  &  $\alpha_i$ , which is the total of all input multiplications. The symbol for it is Eq. (3).

$$K(\alpha, \alpha_i) = \text{sum}(\alpha \cdot \alpha_i). \quad (3)$$

A curved or nonlinear input space can be distinguished using a polynomial kernel, an imperfect variant of a linear kernel. The symbol for it is Eq. (4).

$$K(\alpha, \alpha_i) = 1 + \text{sum}(\alpha \cdot \alpha_i)^d; \quad (4)$$

where  $d$  denotes the polynomial's degree. The RBF kernel maps the input area in an undefined dimension and is mostly utilized in SVM classification. The symbol for it is Eq. (5).

$$K(\alpha, \alpha_i) = \exp(-\gamma * \text{sum}(\alpha - \alpha_i^2)) \quad (5)$$

where  $\gamma$  ranges from 0 to 1. We need to manually specify it in the learning algorithm. Paper can implement SVM for nonlinearly separable data using the RBF Kernel. Support vector machine (SVM) was employed by the authors of [15] to categories the item that was discovered in the collected frame. They had trained the classifier utilizing the linear kernel type of SVM and the C-SVC type parameter for identifying a multiclass object ( $n \geq 2$ ). For the classifier's training, they had produced an image dataset including pictures of non-waste, non-organic trash, and garbage objects. Using the percentage of classification accuracy dataset, they evaluated the classifier's performance. With the help of the IoT and the YOLOv3 deep learning algorithm, different types of waste can be detected in a considerable amount of waste. This will see the scraps that are recycled and those that are not, like paper, metal, cardboard, plastic, glass, and organic waste. After scanning the waste, this algorithm will take the images and separate the items mentioned above. This algorithm's operation is described in detail below. You Only Look Once (YOLO) is a

popular cutting-edge deep learning approach that allows for simultaneous object identification and categorization. The YOLOv3 form takes an input picture and runs it through an interconnected system (akin to CNN) to receive a vector of bounding boxes and class forecasts. YOLOv3 extracts a sole image that is formerly scaled to  $416 \times 416$  and augmented into the YOLOv3 interconnected system. The YOLOv3 interconnected system design is used in the darknet-53 frame. The YOLOv3 neural network is given an image and outputs a vector. The following limits are embedded in the output vector: Probability of disclosure (Pc): The odds that each restricting box subsists of a detected element. Image restricting box characteristics: breadth (Bw), height (Bh), and Cartesian locale (x and y) of the box inside the image (Bx, By). Class probabilities (C1, C2, C3, C4, C5, C6): the chance that each element inside its restricting box belongs to a certain class. In YOLOv3, logistic regression envisions an object's score for each restricting box. The element has a score of 1 if the earlier coinciding of the restricting box is the largest among all additional restricting-box priors regarding the ground reality object. Different restricting box priors are excluded from forecasting, even though their coinciding is more significant than the threshold. Only one restricting box is assigned for each ground reality object in YOLOv3.

Precision is defined as the ratio of the number of accurately detected items to the total number of detected objects. Precision may be calculated mathematically using Eq. (6).

$$\text{Precision} = \frac{S_{AB}}{S_{AB} + S_{AC}} \quad (6)$$

Recall is calculated as a fraction of the number of accurately discovered elements to the total number of ground reality objects Eq. (7).

$$\text{Recall} = \frac{S_{AB}}{S_{AB} + S_{CB}} \quad (7)$$

where  $S_{AB}$  = Estimate of True Positives, that is, number of objects discovered precisely;  $S_{AC}$  = Estimate of False Positives, that is, number of discovered objects that did not pertain to the ground reality objects.  $S_{CB}$  = Estimate of False Negatives, that is, number of ground reality objects that could not be identified. IoU is an eminent decision measure in object recognition tasks, and it is mathematically articulated by Eq. (8).

$$\text{IoU} = \frac{P \cap Q}{P \cup Q} = \frac{\text{Area of intersection}}{\text{Area of Union}} \quad (8)$$

Here,  $P$  and  $Q$  represent the bounding boxes of prediction and ground truth, respectively. After identifying the precision and recall values, a precision-recall curve for a given threshold value of IoU may be constructed. The average precision (AP) is defined as the area under the precision-recall curve, which may be written as Eq. (9).

$$AP = \int_0^1 p(r)dr \quad (9)$$

This is the average preciseness of all classes outlined in the test model and is depicted by Eq. (10) for  $N$  categories.

$$mAP = \frac{\sum_{i=1}^N AP_i}{N} \quad (10)$$

The suggested approach will function based on the preceding mathematical equations and has higher accuracy than other deep learning techniques. Convolutional neural networks support real-time data monitoring by IoT. Sorting waste into the correct category helps identify reusable waste. This paper identifies recyclable waste and uses it without dismantling it. In image categorization, DL algorithms are achieving exceptional results. This document monitors waste to recognize recyclable waste and includes DL to categorize waste to minimize the misuse of recyclable elements. This article divides garbage into two broad groups named absorbable and non-absorbable. Due to the need for more adequate data for waste categorization, a carefully tuned waste categorization model was used here. Waste categorization utilizing DL science helps recognize waste classifications from images. A CNN is an intricate feed forwarding system. One is able to resolve a variety of formerly inscrutable problems. CNN works by deriving attributes from pictures. CNNs are established for image categorization in view of their great preciseness.

## 4 Result Analysis and Comparison of Various ML Algorithms and DL Algorithms

The smart waste administration method provides exact waste accumulation and prediction in comparison to additional classifier algorithm. It accumulates the data for every month and analyses it accompanying other classifying techniques. It includes waste depended on attributes like garbage, organics, and reusing waste. The suggested work with random forest relies on good preciseness in comparison to additional classifier algorithms, containing linear regression, logistics regression, SVM, and decision tree method. The following section discusses the efficiency inspection of miscellaneous categorization techniques. Additional Machine Learning Algorithms that were proposed in added research documents is proved in Table 1.

The enhanced RF with the widespread features obtained great categorization performance: 99.1% accuracy, 98.2% recall, and 0.974 MCC score. Exploratory results revealed that their detection system was appropriate for detecting garbage accompanying a categorization accuracy of 82.7% for fivefold cross-validation output. It could reach 73.49% accuracy for the confusion matrix confirmation test.

**Table 1** Different ML algorithms implemented in smart waste monitoring system

Algorithm used	Accuracy	Computation time (in ms)
Linear regression	73.12	2.5
Logistic regression	78.38	1.4
SVM	89.43	0.6
Decision tree	85.27	0.7
RF classifier	99.1	0.4

The exploratory results show that our method is hopeful in detecting and classifying garbage objects. There are two connected components to this section. First, we'll show how object discovery, accuracy rank, and comparisons between different CNN versions affect the results. This study uses a single, modified CNN network layout with 34 distinct levels. The accuracy of classification is divided into training, valid, and test data at each level of the network in a variety of ways. Eighty percent of the data were used for training, ten percent for validation, and ten percent for testing. 25% validation data, 25% testing data, and 50% training data. We've created a debris dataset with examples of glass, paper, cardboard, plastic, metal, and trash. This dataset has also been used to create models to find inedible trash (Table 2).

It maybe visualized in Table 1 that the prepared model accompanying 34 epochs results in outstanding precision. The more data has been provided, the more definite the result is. We have traced out the in general accuracy of 95.3125% accompanying 34 epochs is a adequate result for specific an inadequate dataset. This accuracy maybe even greater if the dataset is larger. The obstacle herewith prepared model, we have encountered up until now, is the range of distinctness of miscellaneous objects is immense (Table 3).

Sometimes an individual finds it challenging to classify certain phenomena. When the model separates the garbage, it may be better educated and promise greater accuracy. We used pre-prepared fastai models AlexNet, VGG16, ResNet34, and ResNet50 together with two different train-test-validation data splits. With 80%–10%–10% data separation, AlexNet most likely produced a minimum error rate of 0.17188% while operating at 34 epochs in 1584 s. In terms of output, VGG16 has outperformed AlexNet by a small margin (0.05859% error rate with constant data separation). 34 epochs totaling 2193 s were recorded by VGG16. Additionally, we used the pre-prepared ResNet50 as a more current iteration of the CNN design and increased the error rate to 0.0586% along with an 80%–10%–10% data split and 34 epochs. The design uses 34 epochs and 2093s to run. ResNet34, one of the four

**Table 2** Table of 34-layer network (image resolution  $224 \times 224$  pixels)

Training–testing—validation	20 epochs error rate %	27 epochs error rate %	34 epochs error rate %
50%–25%–25%	0.06984	0.07619	0.06349
80%–10%–10%	0.04365	0.05158	0.03968

**Table 3** shows the corresponding comparison among different CNN models and presents why ResNet34 is preferable for this research

CNN Model	Number of divisions	Training–testing-validation	20 epochs error rate%	Time(s)	27 epochs error rate%	Time(s)	34 epochs error rate%	Time(s)
Resnet34	1	50%–25%–25%	0.0698	637	0.07619	968	0.0634	1172
Vgg16	1	80%–10%–10%	0.07422	1320	0.0781	1766	0.0585	2193
AlexNet	1	80%–10%–10%	0.2187	967	0.02109	1316	0.1718	1584
ResNet	1	80%–10%–10%	0.0421	1237	0.0507	1558	0.0586	2093

**Table 4** Six classes with different accuracy

Class	Number of test images	Accuracy (%)
Cardboard	41	100
Glass	52	94.231
Metal	42	95.238
Paper	63	93.651
Plastic	45	95.556
Trash	13	92.308

models, has produced a remarkably excellent outcome. ResNet34 has provided an error rate of only 0.039683% with an 80%–10%–10% data split and 34 epochs. Additionally, we have promised an observation to go along with the ResNet34 data split of 50%–25%–25%, which yields a solid but not exceptional result.

Also, VGG16 uses 16 convolutional tiers, compared to AlexNet's use of just five. ResNet34 employs 34 convolutional levels, whereas CNN uses more complex design. It generates the CNN model's deeper tier and provides superior results. Although ResNet50 has 50 convolutional layers, we have determined that the design takes longer and is only slightly more accurate than ResNet34. The six categories of litter that we classify in our work are cardboard, glass, metal, plastic, paper, and rubbish. As seen in Table 4, we have also given these six groups varying degrees of definiteness. According to the experiment, cardboard precision comes out on top. Since cardboard images are less illusory than those made of plastic or glass. Different categories' level of accuracy is too tolerable. Furthermore, it indicates for the YOLOv3 algorithm that the intelligent stationed clever garbage administration approach defines correct trash disclosure and group distinguished in conjunction with another algorithm. It gathers trash made of its components, such as metal, bottles, paper, and cardboard. The YOLOv3 projected work achieves a remarkable accuracy that is superior to other algorithms like CNN. The YOLOv3 efficiency interpretation achieved very high classification success rates of 94.99% map, 0.87% recall, and 67.42% IoU.

## 5 Conclusion

Powered by ML and DL, IoT is the arising technology to improve the globe to bright metropolises. With the accelerated advancement of these smart metropolises and corporations, garbage era is likewise expanding. Throwing away additional stuff is a large challenge in IoT. Even though a consistent and usual duty in metropolises, garbage grinder is work force demanding and weakens nature, communal features, and adept development. Relevant publications discuss many methods of waste management systems for disposing of unwanted items. This paper has several advantages over existing systems. Whereas existing systems only monitor waste and separate it into metallic and non-metallic waste, wet and dry waste, this paper monitors

waste and divides it into metal-degradable trash. And non-degradable waste. We split each type of garbage to make it easier to separate them. Furthermore, garbage analyses are directed straight to the cloud directory in real-time. In this way, the smart garbage separation administration method assistances garbage disposer by segregating garbage by class and preparing a green offering to humankind and the surroundings. The suggested article is detached into two main concerns. One is machine learning algorithms for garbage administration arrangements, in addition to deep learning algorithms. This article demonstrates a data computing procedure for a suggested CNN model that boosts this YOLOv3 garbage separation algorithm as a means to improve the structure of smart city garbage separation and administration. An interconnected system was prepared to identify six garbage grades on self-generated dataset of 6,437 figures of city debris. The acquired test and probe outcomes illustrate the effectiveness of the projected work in segregating the garbage into two classifications, environmental and non-environmental debris. The forthcoming real-time discovery of garbage was accomplished within paper. The determinable analogy of the outcomes achieved by YOLOv3 and CNN and ml algorithm affirm the effectiveness of YOLOv3 in debris separation. Additionally, the upgraded forecasting feasibility by YOLOv3 shows its efficiency over all these suggested algorithms.

## References

1. Uganya G, Rajalakshmi D, Teekaraman Y, Kuppusamy R, Radhakrishnan A (2022) A novel strategy for waste prediction using machine learning algorithm with IoT based intelligent waste management system. *Wirel Commun Mobile Comput*
2. Cheema SM, Hannan A, Pires IM (2022) Smart waste management and classification systems using cutting edge approach. *Sustainability* 14(16):10226
3. Hulyalkar KSS, Deshpande R, Makode K (2018) Implementation of Smartbin using convolutional neural networks. *Int Res J Eng Technol* 5(4):1–7
4. Ziouzios D, Dasygenis M (2019) A smart recycling bin for waste classification. In: Proceedings of Panhellenic Conference on Electronics & Telecommunications (PACET), November 2019, pp 1–4
5. Adedeji O, Wang Z (2019) Intelligent waste classification system using deep learning convolutional neural network. *Procedia Manuf* 35:607–612
6. Tang Y (2013) Deep learning using linear support vector machines. In: Proc. Int. Conf. Mach. Learn. Chal-lenges Represent. Learn. Workshop, Atlanta, GA, USA, 2013, pp. 1–6.
7. Tian DP (2013) A review on image feature extraction and representation techniques. *Int J Multimed Ubiquitous Eng* 8(4):385–395
8. Torres-García A, Rodea-Aragón O, Longoria-Gandara O, SánchezGarcía F, González-Jiménez LE (2015) Intelligent waste separator. *Computación y Sistemas* 19(3):487–500
9. Bharadwaj AS, Rego R, Chowdhury A (2016) IoT based solid waste management system: a conceptual approach with an architectural solution as a smart city application. In: Proceedings of IEEE Annual India Conference (INDICON), December 2016, pp 1–6
10. Bircanoglu C, Atay M, Beser F, Genc O, Kizrak MA (2018) RecycleNet: intelligent waste sorting using deep neural networks. In: Proceedings of innovations in intelligent systems and applications (INISTA), pp 1–7
11. Kingma DP, Adam JB (2014) Adam: a method for stochastic optimization [Online]. Available: <https://arxiv.org/abs/1412.6980>

12. Zeiler MD (2012) ADADELTA: an adaptive learning rate method [Online]. Available: <http://arxiv.org/abs/1212.5701>
13. Kang K, Gao F, Feng J (2018) A new multi-layer classification method based on logistic regression. In: 13th international conference on computer science and education, ICCSE 2018, pp 52–55
14. Salazar DA, Salazar JC, Velez JI (2012) Comparison between SVM and logistic regression: which one is better to discriminate? Rev Colomb Estad 35(2):223–237
15. I. Salimi BS, Dewantara B, Wibowo IK (2018) Visual-based trash detection and classification system for smart trash bin robot. In: 2018 international electronics symposium on knowledge creation and intelligent computing (IES-KCIC), pp 378–383

# Experimental Investigation on Spectrum Sensing Testbed Using GNU Radio and SDR



**Manas Pandey, Anjali Chauhan, Dibyendu Chowdhury,  
and Sudhendu DasMahapatra**

**Abstract** Spectrum sensing is one of the major annexes in modern communication systems. It is the basis of a cognitive radio system. Implementation of an efficient spectrum sensing machine involves many challenges, such as processing delay, false alarms, misdetection, detection of weak signals in a noisy environment. The present work reports a physical experimental setup on spectrum sensing. Energy detection-based spectrum sensing machine is implemented with a software-defined radio and an open-source software toolkit GNU Radio. The design of the device is thoroughly deliberated. The result proves the proficiency of the device. The scope of this work is to implement the backbone of a spectrum sensing test bench that can be further utilized for executing and testing new emerging studies.

**Keywords** Spectrum sensing testbed · GNU radio · Software-defined radio · Cognitive radio

## 1 Introduction

The frequency bands of the wireless communication spectrum are not being profitably utilized, primarily because of the predominant inflexible frequency distribution strategy. In that methodology, different frequency bands are relegated to various clients and specialist co-ops, and licenses are expected to work inside those bands. According to the specialized perspective, this approach causes the plan and execution of a communication framework simpler. The developing interest in wireless applications has placed a ton of requirements on the use of accessible radio spectrum, which is a restricted and valuable asset. Cognitive radio (CR) [1] is a promising innovation, which gives an original method for further developing the use effectiveness of

---

M. Pandey · A. Chauhan · S. DasMahapatra (✉)  
Manipal University Jaipur, Jaipur, Rajasthan, India  
e-mail: [suddm.kgp@gmail.com](mailto:suddm.kgp@gmail.com)

D. Chowdhury  
Haldia Institute of Technology, Haldia, West Bengal, India

accessible electromagnetic spectrum. Spectrum detecting assists with distinguishing the spectrum openings (underutilized bands of the spectrum) giving high unearthly goal ability.

CR clients are unlicensed [2] who find unused authorized spectrum progressively for their own utilization without making any obstruction authorized users. Some of the current strategies utilized in CR incorporate spectrum detection, spectrum data set and pilot channel. These procedures either overwhelmingly require a high computational ability to distinguish unused spectrums or neglect to benefit from spectrum space made progressively.

Energy detection (ED) [3] is one of the vastly recognized spectrum sensing techniques. This is a non-reasonable detection technique that distinguishes the essential sign in view of the detected energy. The energy of the received signal is compared with the threshold value to detect the presence of the transmitting signal at that moment and location.

The reported research is based on the design and testing of a practical spectrum sensing module and verifying results. The module can be used as a test bench for further developments in this emerging area.

## 2 Literature Survey

Spectrum detecting, spectrum choice, spectrum sharing and spectrum portability are four significant elements of cognitive radio frameworks [4]. The cognitive radio-based Internet of Things (IoT) framework is a viable move toward a universe of shrewd innovation. Effective spectrum detecting and sharing are the vitally practical parts of the CR-based IoT [5]. CR innovation can possibly address the deficiency of accessible radio spectrum by empowering dynamic spectrum access. Authors of the paper [6] feature the productivity and limits of both narrowband and wideband spectrum sensing strategies as well as the difficulties engaged with their execution. The CR is a compelling method for improving the utilization of spectrum assets. The paper [7] reported the cooperative spectrum sensing algorithm based on face compensation in a cognitive radio cloud network, zeroed in on the spectrum sensing in cognitive radio cloud networks. The authors proposed a cooperative spectrum sensing algorithm based on stage compensation to further develop the spectrum sensing execution. The throughput for the cooperative spectrum sensing scheme is determined using a Game-theoretic model in [8]. In the paper [9], three explicit machine learning strategies (neural organizations, assumption expansion and k-implies) are applied to a multiband spectrum detecting procedure for cognitive radios. The CR assumes a key part in distinguishing free transfer speeds in the Radio Frequency (RF) spectrum. The CR4S calculation pointed toward further developing CR spectrum detection by using procedures, for example, Real-esteemed FFT, Sparse Fast Fourier Transform and Cooperative Spectrum Detecting. It has been supported by recreation to above 95% identification execution [10]. Similarly, the paper [11] fostered a two-step compressive spectrum detecting calculation for wideband cognitive radios. The

sub-Nyquist wideband spectrum-detecting plan can accomplish great recognition execution as well as decrease the calculation and execution intricacy [12]. The CR innovation is certainly standing out enough to be noticed to take out the issue of spectrum shortage. This innovation depends on software defined radio (SDR) [13] and a few coordinated perceptive works, for example, spectrum detection. The paper [14] presents trial consequences of the equipment execution of the Goodness of Fit (GoF) based detecting for CR. Secondary Users (SU)/ CRs may employ Artificial Intelligence (AI) to detect the primary user's (PU) band [15].

### 3 Objective and Methodology

The work represents the experimental setup of an efficient spectrum sensing scheme for the new-generation communication system. Amitec-made software defined radios (SDRs) are used for practical implementation of the PUs and sensing SU. The device is driven by an open-source software JNU Radio. At the SU end, the received signal is transformed into the frequency domain. Therefore, its power spectrum is compared with a predetermined threshold to implement energy detection (ED).

The objectives of the present work are represented as follows:

- To implement a prototype model of transmitting PU and sensing SU using GNU Radio.
- To physically implement the spectrum sensing model using SDR.
- To verify the experimental result and determine the efficiency of the system.

A fundamental architecture of a CR network is considered the system model for experimentation. Some licensed PUs are assumed to transmit signals at different frequencies of the licensed band. A SU, which intends to opportunistically use the licensed spectrum, is sensing the band for vacant spectrum. Both, the PUs and SU are implemented using GNU Radio.

GNU Radio is an open-source toolkit that supports users to implement SDRs using signal-processing blocks. It is used with Amitec-made SDR, which is a readily available low-cost RF hardware.

### 4 Experimentation Setup

Multiple PUs are implemented in the same block of the toolkit (Fig. 1). For experimentation, four signal sources are used as the PU. Their transmitted signals are added and transmitted through SDR.

The SU block is designed with an inbuilt energy detection spectrum sensing mechanism (Fig. 2). The SU senses the environment for available spectrum using an SDR. A particular licensed band is scanned and the power spectrum is estimated using FFT. Therefore, the received power spectrum is compared with a predetermined

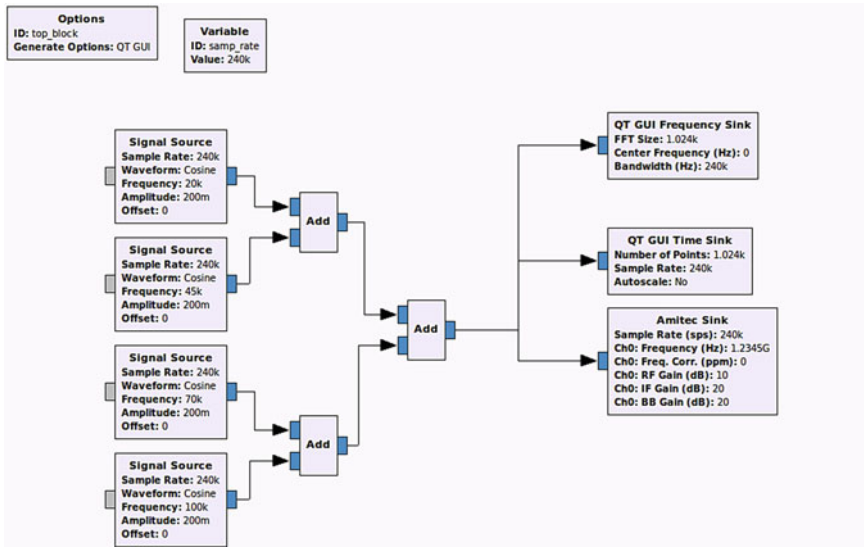


**Fig. 1** Primary users' flow-graph at GNU radio

threshold. The result is shown via File Sink in a GNU Radio. Python codes are used to customize the design blocks at GNU Radio.

The experimental setup includes two Amitec-made SDRs and two computers with GNU Radio and the driver of SDR installed in it. The SDRs are the transceiver with one transmitter and one receiver channel with 0.3–3.8 GHz bandwidth. Baseband bandwidth is up to 15 MHz and ADC, and the DAC sampling rate is 40 MS, 12 bits.

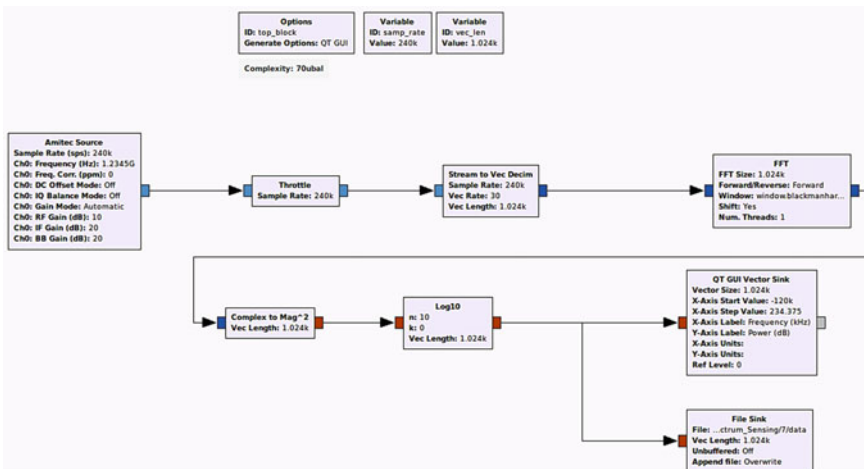


**Fig. 2** Secondary users' flow-graph at GNU radio



**Fig. 3** Experimental arrangement during operation

The device output amplitude is 250 mV p/p differential with a receive gain of 50 dB. The experimental arrangement is shown in Fig. 3.

## 5 Result Analysis

For ease of execution, we took four channels with carrier frequencies 20, 45, 70 and 100 kHz these signals are added and transmitted through the same SDR. The other SDR scans the frequency band. The received stream is first converted into vector data to the compute power spectrum of the signal. FFT block is used to transform the time domain to the frequency domain. The square of the magnitude of FFT, which represents the power spectrum, is taken to compare with the threshold. If the signal power is more than the threshold for a particular channel, then the sensing CR will consider that the PU occupies the channel at that moment. We tested our system for the variety of PU frequencies and the system detects the PU-occupied spectrum almost perfectly and with an insignificant delay. For the mentioned channel frequencies, the result at the file sink is shown in Fig. 4.

The result shows the initial and final frequencies of the occupied bands. Some of the frequencies are wrongly detected as busy, which indicates false alarm possibilities. The probability of false alarm may be reduced by choosing the proper threshold for the energy detection segment.

```
amitec@amitec-master:~/Documents/Spectrum_Sensing/7$ python read_v4.py
          Frequencies :
Initial Range, Final Range :
-1.0, -120042.0
-468.0, 468.0
20358.0, 21060.0
45396.0, 45864.0
70434.0, 70902.0
100386.0, 100854.0
amitec@amitec-master:~/Documents/Spectrum_Sensing/7$
```

**Fig. 4** Detected occupied PU frequencies

## 6 Conclusion

The present work reports an experimental spectrum sensing arrangement and its result. An open-source software toolkit, GNU Radio and Amitec-made software-defined radio are used to implement the setup. The results show that the system can competently detect busy channels. Therefore, it can be utilized by researchers as a prototype spectrum sensing device. Further, new algorithms of similar research are easily implementable by modifying flow-graph. The system can be further improved with the addition of noise cancelation and delay mitigation mechanisms.

## References

1. Mitola J (2000) Cognitive radio: an integrated agent architecture for software defined radio. KTH, Stockholm, Sweden
2. DasMahapatra S, Gandhi I, Nair K, Sharan SN (2020) Sensing schedule optimization to minimize interference with primary users in cognitive radio network. *Indonesian J Electr Eng Comput Sci* 17(3):1399–1404
3. DasMahapatra S, Sharan SN (2018) Effect of sensing duration optimization in cooperative spectrum sensing game. In: 7th international conference on reliability, Infocom technologies and optimization (trends and future directions) (ICRITO). IEEE
4. Xing X, Jing T, Cheng W, Huo Y, Cheng X (2013) Spectrum prediction in cognitive radio networks. *IEEE* 20(2):90–96
5. Awin F, Alginahi Y, Abdel-Raheem E, Tepe K (2019) Technical issues on cognitive radio-based internet of things systems: a survey. *IEEE* 7:97887–97908
6. Arjoune Y, Naima K (2019) A comprehensive survey on spectrum sensing in cognitive radio networks: recent advances, new challenges, and future research directions. *Sensors* 8(11):1–32
7. Wang L, Wu X, Zhang S, Zhang G, Bao Z (2018) Cooperative spectrum sensing algorithm based on phase compensation in cognitive cloud networks. In: ICUFN
8. DasMahapatra S, Sharan SN (2018) A general framework for multiuser de-centralized cooperative spectrum sensing game. *AEU—Int J Electr Commun* 92:74–81
9. Tenorio M, Guerrero AP, Gonzalez RA, Boque SR (2019) Machine learning techniques applied to multiband spectrum sensing in cognitive radios. *SENSORS*, pp 1–22
10. Mohammad K, Mohammadi K (2020) Cooperative wideband spectrum sensing in cognitive radio based on sparse real-valued fast Fourier transform. *IET* 14(8):1340–1348
11. Wang Y, Tian Z, Feng C (2012) Sparsity order estimation and its application in compressive spectrum sensing for cognitive radios. *IEEE* 11(6):2116–2125
12. Ma Y, Gao Y, Liang YC, Cui S (2016) Reliable and efficient sub-Nyquist Wideband spectrum sensing in cooperative cognitive radio networks. *IEEE* 34(10):2750–2762
13. Mitola J, Maguire GQ (1999) Cognitive radio: making software radios more personal. *IEEE* 6(4):13–18
14. Diamal T, Azzaz MS, Sadoudi S (2020) Analysis study and SDR implementation of GoF-based spectrum sensing for cognitive radio. *IET* 14(5):857–864
15. DasMahapatra S, Patnaik S, Sharan SN, Gupta M (2019) Performance analysis of prediction based spectrum sensing for cognitive radio networks. In: 2019 2nd international conference on intelligent communication and computational techniques (ICCT)

# Harris Hawks Optimization-Based Multilevel Thresholding Segmentation of Magnetic Resonance Brain Images



Elisabeth Thomas and S. N. Kumar

**Abstract** The segmentation role is inevitable in computer vision and image processing for delineating the specific region of interest. In the healthcare sector, the segmentation role is vital in the diagnosis and prediction of diseases. This research work proposes Harris Hawks optimization-based multilevel thresholding segmentation approach for the MR brain images. Multilevel thresholding is an improved version classical thresholding algorithm, and the optimization algorithm chooses the optimum threshold values for the segmentation. The segmentation model was tested on Alzheimer's MR brain images and validated in terms of performance computer-aided threshold level of 5 which was found to generate satisfactory results in terms of performance metrics.

**Keywords** Alzheimer's disease · Harris Hawks optimization · PSNR · SSIM · FSIM

## 1 Introduction

Segmentation is the computer-aided algorithm approach in image processing for the extraction of desired objects in an image. In medical image processing, the region of interest can be an anatomical organ, tissue, tumour region, or cyst. Magnetic resonance imaging (MRI) gains much prominence in healthcare sector for the detection and treatment of neuro disorders. Alzheimer's disease is a neurological disorder in which the brain regions shrink (atrophy) and eventually the brain cell die. The 3D anatomical representation of the brain volume from 2D slices for the detection of atrophy was proposed in [1]. The denoising followed by a region of construction

---

E. Thomas  
Lincoln University College, 15050 Kota Bharu, Malaysia  
e-mail: [ethomas@lincoln.edu.my](mailto:ethomas@lincoln.edu.my)

S. N. Kumar (✉)  
Department of EEE, Amal Jyothi College of Engineering, Kottayam, Kerala 686518, India  
e-mail: [appu123kumar@gmail.com](mailto:appu123kumar@gmail.com)

and 3D modelling by the utilization of software slice-o-Matic was carried out in this work, and the residual volume estimation aids in the detection of atrophy.

The classical thresholding techniques along with the bimodal and multimodal strategies were proposed in [2] for Alzheimer's disease detection. The bimodal and multimodal algorithms rely on the variance of classes and gamma distribution. An improved multi-atlas segmentation model was proposed in [3] for the extraction of hippocampus from MR images of the brain. The hippocampus is the part of the brain that is likely to be first affected by Alzheimer's disease. In [4], the various imaging modalities, segmentation approaches, and machine learning models for the detection of Alzheimer's disease were discussed. The classical and advanced segmentation approaches along with the widely used machine learning architectures are discussed in this work. The adaptive thresholding was found to be efficient for many images, and the SVM was found to generate proficient classification results. The thresholding along with the other segmentation approaches was evaluated in [5]. The support vector machine based on polynomial kernel was found to be proficient in the proficient classification of white matter, grey matter, and cerebrospinal fluid. The independent component analysis along with the band expansion process was found to be proficient in the detection of atrophy.

A hybrid entropy thresholding approach was proposed in [6] for Alzheimer's disease (AD) detection and validated on benchmark data sets, and results were found to be proficient when compared with the classical approaches. The deep learning model was put forward in [7] for the region of interest (ROI) extraction of brain regions in AD magnetic resonance images. The arithmetic optimization algorithm was utilized in [8] for the tuning of parameters in VGG16 deep learning architecture for the detection of atrophy in MR images. A hybrid segmentation model comprising of clustering based on grey wolf optimization was employed in [9] for the detection of AD. The probabilistic cluster along with the 3D wavelet was utilized for the efficient region of interest (ROI) extraction on MR brain images [10]. The enhanced fuzzy elephant herding optimization (EFEHO) was utilized in Otsu thresholding for the region of interest (ROI) extraction on MR brain images, and deep learning was employed for the diagnosis of AD [11]. A detailed review on the automatic detection of AD was proposed in [12], and various artificial intelligence models for the initial detection of AD were also proposed in [13]. The deep learning AlexNet architecture was proposed in [14] for the primary detection of AD, and various CNN architectures were proposed in [15] for the detection of AD. Section 2 focusses on the medical image segmentation using multilevel thresholding coupled with HHO algorithm, Sect. 3 describes the results, and conclusion is put forward in Sect. 4.

## 2 Medical Image Segmentation Using Multilevel Thresholding Based on HHO Algorithm

This research work employs multilevel thresholding based on optimization algorithm for the region of interest (ROI) extraction on medical images. Classical thresholding is a simple region of interest extraction algorithm that works on the principle of threshold value chosen by the user. In the case of images with complex objects, the single threshold value is not sufficient, and multiple threshold values are required. Estimation of multiple threshold values by the user is a tedious task, and hence, optimization algorithms are combined with the thresholding approach to choose the optimum threshold values. The Harris Hawks optimization was utilized in the multilevel thresholding approach for the optimum selection of threshold values.

### 2.1 Minimum Cross-Entropy Thresholding Method

Minimum cross-entropy thresholding is a technique used in image processing and computer vision to segment an image based on the minimum cross entropy between the image and its thresholded version. In this technique, a threshold is chosen such that it minimizes the cross entropy between the original image and the thresholded image. This threshold is used to segment the image into foreground and background regions, with pixels above the threshold considered as part of the foreground and pixels below the threshold considered as part of the background. This method is particularly useful for images with low contrast or a high degree of noise.

The information theoretical distance with respect to two probability density distributions  $T = \{p_1, p_2, \dots, p_N\}$  and  $U = \{q_1, q_2, \dots, q_N\}$  is measured by the cross entropy, which is defined by Eq. (1):

$$D(T, U) = \sum_{i=1}^N p_i \log \frac{p_i}{q_i} \quad (1)$$

Let  $P$  represents the input medical image and  $h(p)$ ,  $p = 1, 2, \dots, R$  represents the appropriate histogram, where  $R$  is the count of grey levels.

$$P_{\text{threshold}(x,y)} = \begin{cases} \mu(1, \text{threshold}), & \text{if } P(x, y) < \text{threshold} \\ \mu(\text{threshold}, R + 1), & \text{if } P(x, y) \geq \text{threshold} \end{cases} \quad (2)$$

$$\text{where } \mu(x, y) = \sum_{p=x}^{y-1} i h(i) / \sum_{p=x}^{y-1} h(i)$$

The objective function relies on the entropy value, and the cross entropy is represented as follows:

$$f_{\text{cross}(\text{threshold})} = \sum_{p=1}^{\text{threshold}-1} I h(p) \log \left( \frac{I}{\mu(1, \text{threshold})} \right) + \sum_{p=\text{threshold}}^R p h(p) \log \left( \frac{i}{\mu(\text{threshold}, R+1)} \right) \quad (3)$$

In classical thresholding, a single threshold value is used, and bi-level thresholding takes place. For the images with complex objects, single threshold value is not sufficient. Equation 3 was re-written as follows:

$$f_{\text{cross}(\text{threshold})} = \sum_{p=1}^R p h(p) \log(i) - \sum_{p=1}^{\text{threshold}-1} p h(p) \log(\mu(1, \text{threshold})) - \sum_{p=\text{threshold}}^R p h(ip) \log(\mu(\text{threshold}, R+1)) \quad (4)$$

The multilevel approach is based on the vector threshold = [threshold<sub>1</sub>, threshold<sub>2</sub>, threshold<sub>nt</sub>], which contains various threshold values, by:

$$f_{\text{cross}(\text{threshold})} = \sum_{p=1}^R p h(p) \log(p) - \sum_{p=1}^{nt} H_p \quad (5)$$

and nt denotes the entire number of thresholds and H<sub>p</sub> and H<sub>k</sub> are defined as follows:

$$H_p = \sum_{p=1}^{\text{threshold}_{p-1}} p h(p) \log(\mu(1, \text{threshold}_p))$$

$$H_k = \sum_{i=\text{threshold}_{k-1}}^{\text{threshold}_{k-1}} p h(p) \log(\mu(\text{threshold}_{k-1}, \text{threshold}_k)), \quad 1 < k < n$$

$$H_{nt} = \sum_{p=\text{threshold}_{nt}}^R p h(p) \log(\mu(\text{threshold}_{nt}, R+1))$$

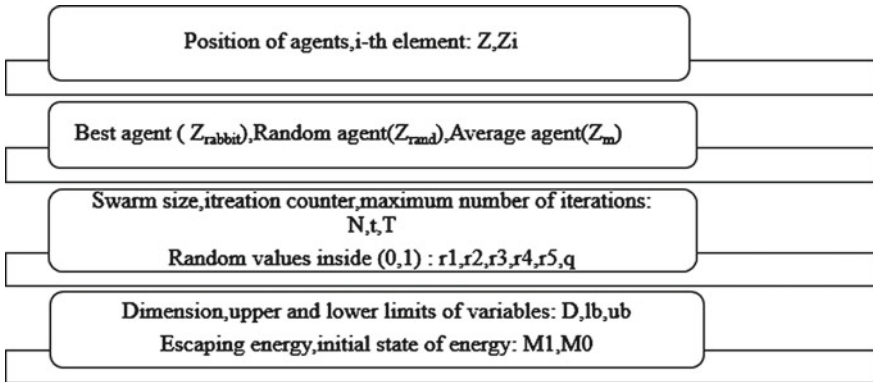


**Fig. 1** Parameters of the optimization model

## 2.2 *Harris Hawks Optimization-Based Multilevel Thresholding for the Selection of Optimum Threshold Values*

Harris Hawks are amongst the most intelligent birds found in the wild. These birds realize by what method to lead a group and work together logically to discover a specific rabbit [16]. In [17], the authors observe various attacking and evading behaviours. The Harris Hawks optimization (HHO) [18] is a technique for mathematically modelling these communications in order to solve optimization problems. HHO, with a sequence of hawks that represent possible solutions, and the best-obtained answer are referred to as a rabbit. This approach consists of two exploration stages and four exploitation stages. It employs hard and soft sieges in the exploitation process that will further focus on the proximity of acquired answers. The complete phases of HHO are depicted in Fig. 1.

**Exploration stage.** In HHO, there are two methods for carrying out the exploratory stages:

$$Z(t+1) = \begin{cases} Z_{\text{rand}(t)-r_1} | Z_{\text{rand}(t)-2r_2} Z(t) | & q \geq 0.5 \\ Z_{\text{rabbit}} - Z_{m(t)-r_3(lb+r_4(ub-lb))} & q < 0.5 \end{cases} \quad (6)$$

$Z_m$  is the mean position of hawks and is calculated as follows:

$$Z_m(t) = \frac{1}{N} \sum_{p=1}^N Z_p(t) \quad (7)$$

The transition from exploration to exploitation, represented using the parameter  $M_1$ .

$$M_1 = 2M_0 \left(1 - \frac{t}{T}\right) \quad (8)$$

where  $M_0$  is a random value inside  $(-1, 1)$ .

**Exploitation stages.** The following are the features of this stage.

**Soft Besiege.** The following rules model this behaviour:

$$\begin{aligned} Z(t+1) &= \Delta Z(t) - M_1/J Z_{\text{rabbit}} \\ \Delta Z(t) &= Z_{\text{rabbit}}(t) - Z(t) \end{aligned} \quad (9)$$

where  $J = 2(1 - r5)$  is the jump strength of the rabbit.

**Hard Besiege.** Equation (10) defines this operator:

$$Z(t+1) = Z_{\text{rabbit}}(t) - M_1 |\Delta Z(t)| \quad (10)$$

**Soft Besiege Having the Progressive Rapid Dives (PRD).** It is assumed that during the gentle besiege stage, agents can choose on their following move based on the condition given in Eq. 11:

$$U = Z_{\text{rabbit}}(t) - M_1 |J Z_{\text{rabbit}}(t) - Z(t)| \quad (11)$$

The Levy Flight (LF) movements are used in this stage of the HHO by following the rule:

$$R = U + S \times RF(D) \quad (12)$$

where  $S$  is a vector of dimension  $1*D$  and  $RF$  is the levy flight function, which is calculated using Eq. 13:

$$LF(x) = \frac{ux\sigma}{|v|^{\frac{1}{\beta}}}, \sigma = \left(r(1+\beta) * \sin\left(\frac{\pi\beta}{2}\right) / \frac{r(1+\beta)}{2} * \beta * 2\left(\frac{\beta-1}{2}\right)\right) \frac{1}{\beta} \quad (13)$$

where  $u$  and  $v$  are randomly defined LF values and  $\beta$  is 1.5 As a result, Eq. (14) is applied in this stage.

$$Z(t+1) = \begin{cases} U & \text{if } F(U) < F(Z(t)) \\ R & \text{if } F(R) < F(Z(t)) \end{cases} \quad (14)$$

**Hard Besiege Having the PRD Values.** The following rule represents this HHO operator:

$$Z(t+1) = \begin{cases} U' & \text{if } F(U') < F(Z(t)) \\ R' & \text{if } F(R') < F(Z(t)) \end{cases} \quad (15)$$

where  $U'$  and  $R'$  are computed as follows:

$$U' = Z_{\text{rabbit}}(t) - M1|JZ_{\text{rabbit}}(t) - Z_m(t)|$$

$$R' = U' + S * RF(D)$$

where  $Z_m(t)$  is obtained using Eq. (7).

The number of threshold is a user defined value, and it ranges from 2 to 5. The fitness value is estimated, and best solution is noted for each case. In the HHO algorithm, each bird is initialized with a random position and velocity, and they fly in search of the prey. The position of the bird is updated based on its velocity and its distance from the prey. The velocity of the bird is updated based on the information received from the other birds in the population. Birds exchange information with each other by communicating their position and velocity, and this exchange of information allows them to cooperate and improve their hunting success. One of the key features of Harris Hawks optimization is the ability of the birds to collaborate and share information. This feature allows the algorithm to explore the search space more efficiently and improve the chances of finding the optimal solution. Another important feature of the algorithm is its ability to adapt to the characteristics of the problem, as the algorithm can be fine-tuned by adjusting the parameters such as the number of birds, the communication range, and the update rate.

### 3 Results and Discussion

The algorithms are developed in MATLAB 2020 and executed on the system with the following specifications; Intel i5 processor, 8 GB RAM. The input MR images [19] corresponding to mild dementia case are depicted in Fig. 2.

The input MR images corresponding to moderate dementia case [19] are depicted in Fig. 3, and very mild demented cases [19] are depicted in Fig. 4.

The input MR images corresponding to non-demented case [19] are depicted in Fig. 5. The segmentation results corresponding to the multilevel thresholding coupled with Harris Hawks optimization are represented in Figs. 6, 7, 8, 9, and 10.

The output images corresponding to the mild demented case are represented in Figs. 6 and 7.

The output images corresponding to the moderate demented case are represented in Fig. 8, and very mild demented cases are represented in Fig. 9.

The performance metrics are used to validate the multi-thresholding segmentation model.

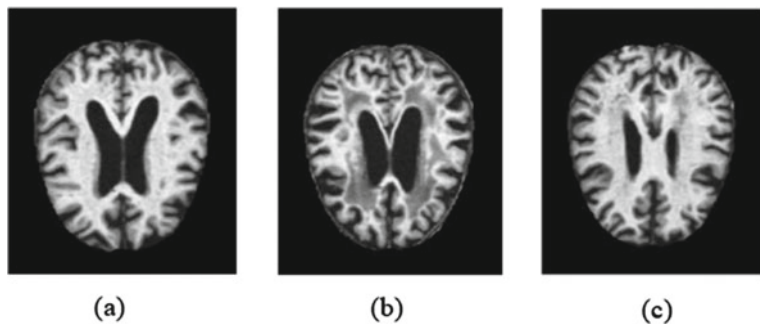


**Fig. 2** Input MR images corresponding to mild demented case (D1–D3)



**Fig. 3** Input MR images corresponding to moderate demented case (D4–D6)



**Fig. 4** Input MR images corresponding to very mild demented case (D7–D9)

Peak signal to noise ratio (PSNR): It gives the quality of the segmentation algorithm; it relies on the input image and segmented image.

$$\text{PSNR} = 20 \log_{10}(255/\text{MSE}) \quad (16)$$

where MSE refers the root mean-squared error

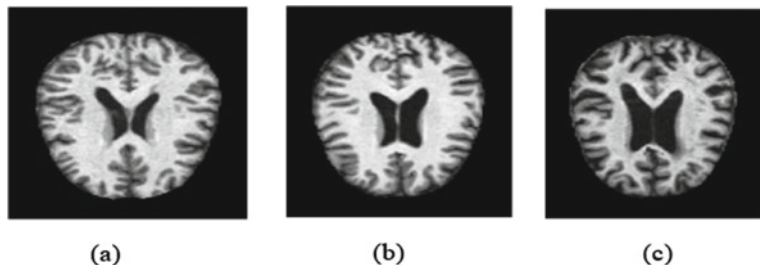


Fig. 5 Input MR images corresponding to non-demented case (D10–D12)

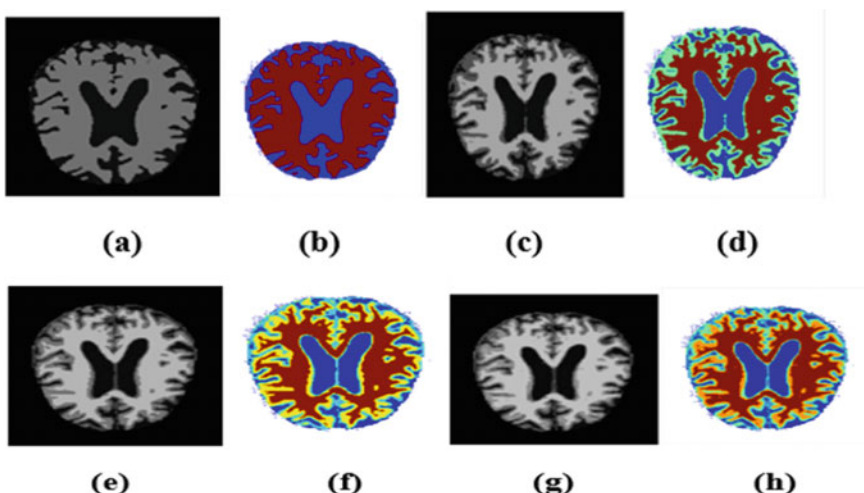


Fig. 6 Segmentation result in case of mild demented for the input (D1)

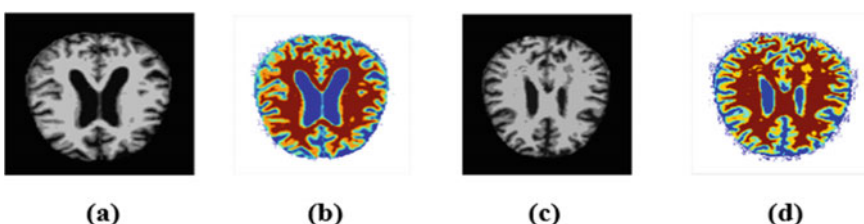
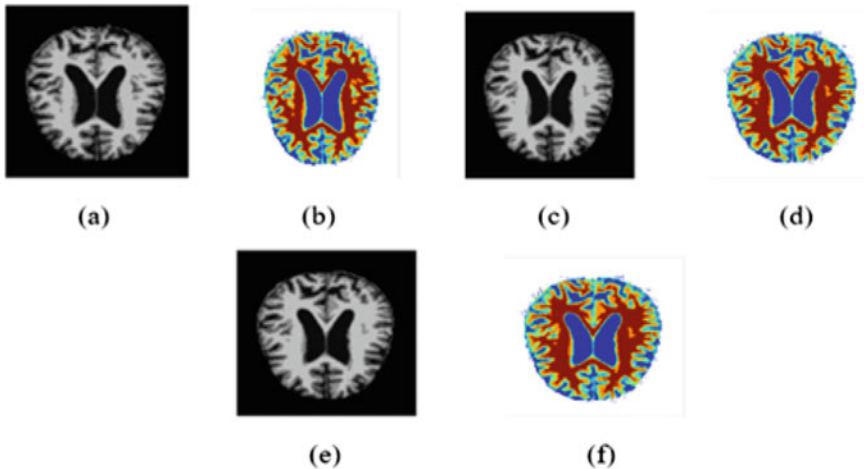


Fig. 7 Segmentation result in case of mild demented for the input (D2, D3)

The output images corresponding to the non-demented case are represented in Fig. 10.

The feature similarity index (FSIM) and structural similarity index (SSIM) are the statistical measures that reflect the quality of the segmentation model. These



**Fig. 8** Segmentation result in case of moderate demented for the input (D4, D5, D6)

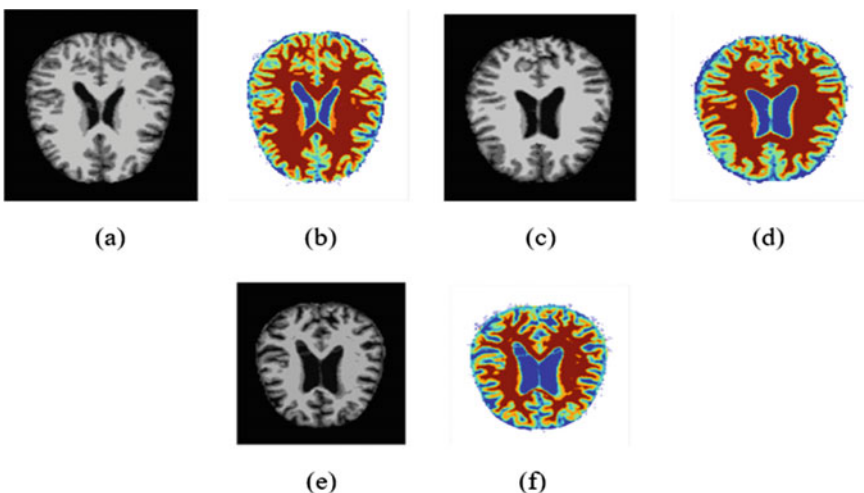


**Fig. 9** Segmentation result in case of very mild demented for the input (D7, D8, D9)

measures compare between the objects of the actual input image and the segmented image.

The SSIM is expressed as follows:

$$\text{SSIM}(C, I) = \frac{(2\mu_p\mu_1 + A_1)(2\delta v A_1 + CA_2)}{(\mu_p 2\mu_1 2 + CA_1)(\delta v_1 2\delta 1^2 1 + CA_2)} \quad (17)$$

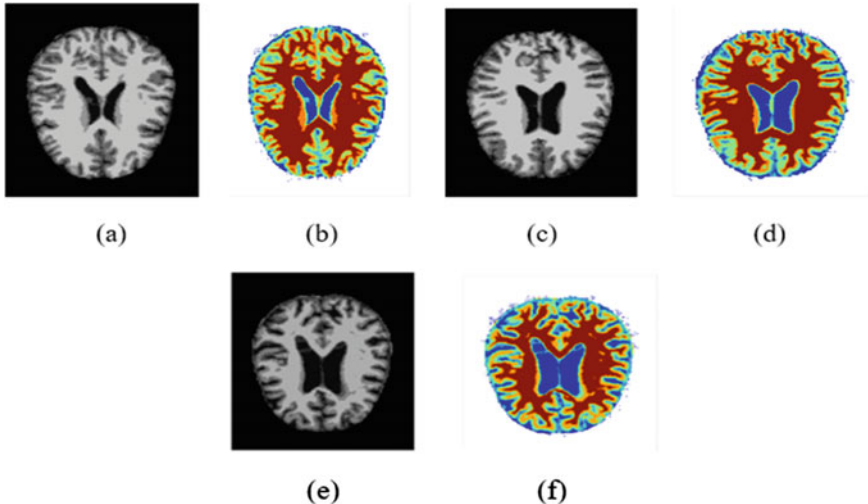


**Fig. 10** Segmentation result in case of non-demented for the input (D10, D11, D12)

where  $\mu_p$  and  $\delta_v$ , respectively, signify the pixel mean and variance of the original image,  $\mu_1$  and  $\delta_1$  give the pixel mean and variance of the segmented image, correspondingly;  $\delta\text{CA}_1$  is the covariance of the actual image and the segmented image, and A1 and A2 are the constants. Here,  $\text{CA}_1 = \text{CA}_2 = 6.5025$ . A higher value of the SSIM indicates better performance.

The FSIM is expressed as follows:

$$\text{FSIM} = \frac{\sum_{h \in \cap} S_{L(h)} PC_m(h)}{\sum_{h \in \cap} PC_m(h)} \quad (18)$$

where

$$DF(h) = D_{JK}(h)D_M(h)$$

$$D_{JK}(h) = \frac{2P\text{JK}_1(x)\text{JK}_2(x) + T_1}{\text{JK}_1^2(x)\text{JK}_2^2(x) + T_1}$$

$$S_M(h) = \frac{2M_1(x)M_2(x) + T_2}{M_1^2(x)M_2^2(x) + T_2}$$

$$\text{JK}_m(h) = \max\{\text{JK}_1(h), \text{JK}_2(h)\}$$

where  $T_1$  and  $T_2$  are constants and  $M(h)$  represents gradient magnitude of an image and  $\text{JK}(h)$  is the phase congruence of an image.

Tables 1, 2, 3, and 4 represent the performance metrics corresponding to the input images corresponding to the various stages of AD for various threshold values. For the threshold value of 5, the performance metric values were found to be good, and hence, 5 level threshold value is chosen for other images (Table 5).

**Table 1** Performance metrics corresponding to mild demented case for various threshold values

ID NO	PSNR	SSIM	FSIM	Fitness	Threshold values
D1	13.7421	0.7047	0.6423	2.3678	15, 112
D1	17.7129	0.8153	0.7452	1.0588	13, 79, 164
D1	20.2269	0.8677	0.8153	0.5850	11, 58, 114, 181
D1	22.2616	0.8926	0.8545	0.4133	10, 51, 92, 139, 191

**Table 2** Performance metrics corresponding to mild demented case

ID NO	PSNR	SSIM	FSIM	Fitness	Threshold values
D1	22.2616	0.8926	0.8545	0.4133	10, 51, 92, 139, 191
D2	21.2886	0.8947	0.8377	0.4469	4, 23, 70, 122, 180
D3	22.8405	0.9034	0.8677	0.4516	11, 55, 97, 141, 187

**Table 3** Performance metrics corresponding to moderate demented case for threshold value = 5

ID NO	PSNR	SSIM	FSIM	Fitness	Threshold values
D4	22.6095	0.8992	0.8613	0.4317	11, 53, 93, 139, 189
D5	22.6522	0.8999	0.8657	0.4157	11, 54, 94, 140, 190
D6	22.5123	0.8976	0.8653	0.4188	11, 53, 92, 138, 190

**Table 4** Performance metrics corresponding to very mild demented case for threshold value = 5

ID NO	PSNR	SSIM	FSIM	Fitness	Threshold values
D7	22.2966	0.8936	0.8608	0.4374	11, 51, 90, 136, 188
D8	23.0351	0.8968	0.8706	0.3931	9, 47, 92, 136, 182
D9	22.1476	0.9023	0.8747	0.3903	10, 54, 101, 148, 199

**Table 5** Performance metrics corresponding to non-demented case for threshold values = 5

ID NO	PSNR	SSIM	FSIM	Fitness	Threshold values
D10	22.6310	0.8995	0.8606	0.3865	12, 62, 105, 147, 194
D11	22.1409	0.9033	0.8810	0.3929	10, 53, 98, 146, 197
D12	22.7300	0.8984	0.8548	0.4244	10, 47, 83, 124, 173

The PSNR, SSIM, and FSIM are found to be satisfactory for the threshold value of 5 with respect to the mild demented case, moderate demented case, very mild demented case, and non-demented case.

## 4 Conclusion

This research work proposes a multilevel thresholding segmentation model based on Harris Hawks optimization. The MR brain images of AD from public source were utilized in this work, and threshold level of 5 generates proficient results. The performance was validated in terms of performance metrics. Four classes of AD images are utilized in this research work, and brain regions were found to extract proficiently through the proposed segmentation model. The optimization algorithm efficiently yields the optimum threshold values and generates robust results than the classical thresholding. The future work will be the estimation of white matter, grey matter, and Cerberro spinal fluid volume for detailed analysis of neuro disorders.

## References

1. Biju KS, Alfa SS, Lal K, Antony A, Akhil MK (2017) Alzheimer's detection based on segmentation of MRI image. *Proc Comput Sci* 1(115):474–481
2. El-Zaart A, Ghosn AA (2013) MRI images thresholding for Alzheimer detection. *Comput Sci Inf Technol* 95–104
3. Lötjönen J, Wolz R, Koikkalainen J, Julkunen V, Thurfjell L, Lundqvist R, Waldemar G, Soininen H, Rueckert D (2011) Alzheimer's disease neuroimaging initiative. Fast and robust extraction of hippocampus from MR images for diagnostics of Alzheimer's disease. *Neuroimage* 56(1):185–196
4. Mirzaei G, Adeli A, Adeli H (2016) Imaging and machine learning techniques for diagnosis of Alzheimer's disease. *Rev Neurosci* 27(8):857–870
5. Kamathe RS, Joshi KR (2018) A novel method based on independent component analysis for brain MR image tissue classification into CSF, WM and GM for atrophy detection in Alzheimer's disease. *Biomed Signal Process Control* 1(40):41–48
6. Rawas S, El-Zaart A (2022) Towards an early diagnosis of Alzheimer disease: a precise and parallel image segmentation approach via derived hybrid cross entropy thresholding method. *Multimedia Tools Appl* 81(9):12619–12642
7. Tuan TA, Pham TB, Kim JY, Tavares JM (2022) Alzheimer's diagnosis using deep learning in segmenting and classifying 3D brain MR images. *Int J Neurosci* 132(7):689–698
8. Deepa N, Chokkalingam SP (2022) Optimization of VGG16 utilizing the arithmetic optimization algorithm for early detection of Alzheimer's disease. *Biomed Signal Process Control* 1(74):103455
9. Suresha HS, Parthasarathy SS (2022) Detection of Alzheimer's disease using grey wolf optimization based clustering algorithm and deep neural network from magnetic resonance images. *Distrib Parallel Databases* 40(4):627–655
10. Barra V, Boire JY (2000) Tissue segmentation on MR images of the brain by possibilistic clustering on a 3D wavelet representation. *J Magn Reson Imag Official J Int Soc Magn Reson Med* 11(3):267–278

11. Alhassan AM (2022) Alzheimer's disease neuroimaging initiative, Australian imaging biomarkers and lifestyle flagship study of ageing. Enhanced fuzzy elephant herding optimization-based OTSU segmentation and deep learning for Alzheimer's disease diagnosis. *Mathematics* 10(8):1259
12. Sindhu TS, Kumaratharan N, Anandan P (2022) Review on automatic detection of Alzheimer disease. In: 2022 International conference on computer communication and informatics (ICCCI). IEEE, pp 1–6
13. Kari N, Singh SK, Velliangiri S (2022) Various machine learning techniques to diagnose Alzheimer's disease—a systematic review. *Sustain Technol Adv Comput Electr Eng* 557–567
14. Kumar LS, Hariharasitaraman S, Narayanasamy K, Thinakaran K, Mahalakshmi J, Pandimurugan V (2022) AlexNet approach for early stage Alzheimer's disease detection from MRI brain images. *Mater Today Proc* 51:58–65
15. Pandey P, Khare A, Srivastava P (2022) Detection of Alzheimer's disease using CNN architectures. *ADBU J Eng Technol* 11(1)
16. Ridha HM, Heidari AA, Wang M, Chen H (2020) Boosted mutation-based Harris hawks optimizer for parameters identification of single-diode solar cell models. *Energy Convers Manage* 1(209):112660
17. Chen H, Heidari AA, Chen H, Wang M, Pan Z, Gandomi AH (2020) Multi-population differential evolution-assisted Harris hawks optimization: framework and case studies. *Futur Gener Comput Syst* 1(111):175–198
18. Heidari AA, Mirjalili S, Faris H, Aljarah I, Mafarja M, Chen H (2019) Harris hawks optimization: algorithm and applications. *Futur Gener Comput Syst* 1(97):849–872
19. <https://www.kaggle.com/datasets/tourist55/alzheimers-dataset-4-class-of-images>

# Applications in Medical Technology for Optimized Convolutional Neural Network Using Differential Evolutionary Algorithm



Vanita S. Buradkar and Asha Ambhaikar

**Abstract** Overall, in the world, most deaths are caused by heart attacks and cancer. Development in medical imaging technology using deep learning algorithms and optimizers is becoming more and more possible. It is a growing area for analytics in the medical field. Medical imaging classification uses convolutional neural networks. It is a difficult effort to choose their hyperparameters and architecture. The CNN is optimized using a variety of evolutionary algorithm versions. Among the evolutionary algorithms are the genetic algorithm, particle swarm optimization, and differential evolutionary algorithms. A straightforward and effective population-based method is a differential evolutionary one to optimize the CNN model, we are using a different evolutionary algorithm. Due to the natural intricacy of medicine, optimization has become an important technique. This article's objective is to provide a thorough summary of applications, methods of CNNs, DE optimizer, and their different versions. The planned algorithm is discussed, and an effort will be made to increase the algorithm's performance to over 90%.

**Keywords** Lungs cancer · Deep learning model · Convolutional neural network (CNN) · Differential evolutionary algorithm · CT images · Genetic algorithm

## 1 Introduction

Billions of cells form a human body structure. Cells are an important part, which absorbs nutrients from food and converts it into energy. A disorder of internal structure or function causes disease. Heart attacks and cancers are fatal diseases and causes of increasing death rates nowadays. That's why the medical field and healthcare centers generated more complex data.

---

V. S. Buradkar (✉) · A. Ambhaikar

Department of Computer Science and Engineering, Kalinga University, Naya Raipur, Raipur, India  
e-mail: [vbsburadkar@gmail.com](mailto:vbsburadkar@gmail.com)

For examining hidden patterns in data sets in the healthcare industry, data abstraction has proven a fantastic tool. It's challenging to extract features from a picture [1]. In order to get important attributes from images, different image classification techniques and data mining techniques play an important role. Various kinds of illnesses have become more prevalent due to the population's fast growth, making the task of diagnosing them a crucial and challenging one [2]. Convolutional neural networks (CNNs) are highly potent technology that has made significant progress in computer-aided detection (CADe) [3]. Nowadays, CNN is a popular deep learning algorithm used in the medical field. CNN is used to detect cancer comprising lungs, breast, brain tumors, and diabetic retinopathy. Optimization helps to improve the efficiency of the objective function and finds the global maximum and minimum. Most of the evolutionary algorithms such as genetic algorithm, differential evolutionary algorithm (DE), Ant Colony Optimization (ACT), and particle swarm optimization are used as optimizers.

The differential evolutionary algorithm invented by Storn and Price is one of the straightforward and effective algorithms. Key elements of DE are Population (NP), Crossover Factor (CR), and Mutation Factor (M) are tuned priorly, the objective function for an optimization issue [4]. DE is an optimizer used for continuous space. Performance is based on improvement in the updated population in each iteration [5]. Organizations may better serve the requirements of millions of people worldwide by developing a computerized system that assists judgment for the identification of different diseases [6]. Tools for comprehending images well are convolutional neural networks (CNNs). CNNs have been effectively used by researchers for a variety of medical image interpretation applications, including the detection of brain tumors and classification [7], the detection of heart disease [8], recognition of eye diseases that are particularly prevalent in Bangladeshis [9], skin cancer detection, and classification of image malignant or benign [10].

The goal of this research article is to show a thorough overview of CNN applications in medical image comprehension. The overarching goal is to encourage experts in medical image understanding to make substantial use of CNNs in their analysis and diagnosis. A succinct overview of CNNs and differential evolutionary algorithms has been given.

## 2 CNN Applications in Medical Image Classification

Convolutional neural has promising properties which work efficiently on real-world applications. To design optimal CNN, evolutionary convolutional neural network method is used [11]. In the past ten years, mammography has benefited from improvements in neural networks to help radiologists to operate more accurately and efficiently. An organized and comprehensive explanation of the computerized classifier and the current convolution model in mammography is covered [12, 13]. In order to navigate the search space, this work proposes a differential evolution technique.

## ***2.1 Lungs Cancer***

In this paper, researchers have used CNN and genetic algorithm to detect lungs cancer. The processing speed of the model is 3.41 ms per image. Automation of this tool increases life and decreases the treatment cost [14]. Pandian et al. used a Google Net, which achieves the efficiency 98% [15]. Sreekumar et al. presented here a model using deep learning. The primary dataset is the LIDC-IDRI. This technique achieved 86% for detecting malignant lung nodules [16]. Li et al. introduce “wavelet dynamic analysis to extract and repair the lung parenchyma” [17]. Venkatesh et al. suggest Otsu thresholding segmentation and achieve an accuracy of 96.97% [18]. Pfeffer et al. combine GA-CNN to check lungs cancer and acquire the 91.3% result [19].

## ***2.2 Skin Cancer***

This CNN model uses a 1D kernel [20]. To reduce the error rate along with CNN, the whale optimization algorithm is [21]. The proposed method is used to detect skin cancer, and deep learning architecture uses 1D CNN to categorize well and unhealthy humans. Based on the clinical report, evaluation of the patient is done which helps in prior. Husan et al. introduced a skin cancer detection model by implementing ML and image processing. The affected part of skin cells is extracted after image segmentation, and CNN is used as a classifier [22].

## ***2.3 Heart Attack***

In the proposed network, overfitting is avoided using a variety of methods [6]. Early-stage diagnosis is important in fatal diseases like cancer, and CNN is very useful in this. Input to CNN is near 13 clinical image features. Convolutional neural network is trained by using back propagation method and gets the accuracy of more than 95% [23]. Conventional three-dimensional (3D) is used in diseases like heart attacks. Automated CNN could improve the comparison between healthy and unhealthy hearts and reduce the mortality rate [24].

## ***2.4 COVID-19***

The worldwide pandemic is being caused by the coronavirus disease 2019 (COVID-19), as identified by the Global Health Organization, and is causing a pandemic that will affect the entire world, which was initially discovered in Wuhan, China, in late

December 2019. Within a few months, the virus had spread to every country in the world. Due to the fact that COVID-19 affects millions of individuals worldwide, it has turned into a global health emergency. In this study, COVID-19 is successfully and precisely diagnosed using CNN trained on datasets of chest X-ray images [25]. Here, researcher compares the exactness of the customized model and the presented study [27].

### 3 Convolutional Neural Network

ConvNet [26] originates from the human nervous system [27]. Convolution operation, ReLU correction, pooling, and fully connected layer are some of the layers that make up the CNN model [28]. Figure 1 shows the layout of CNN.

There are different types of CNN based on the kernels function and used depending on the problem. The size and mobility of the kernel are chosen in accordance with the CNN's dimensions (1D CNN, 2D CNN, and 3D CNN) [29]. The convolutional layer is always the initial layer and the core element of CNN. It carries the lion's share of the network's computation complexity [30]. In convolution, filters are applied to the original picture or to additional feature maps in a deep CNN, and the results are transmitted to the next layer. The most key factors are the volume and size of the kernels [31]. A filter or kernel slides over the 2D input data to perform the element-wise multiplication and form a single output pixel. This produces a two-dimensional image called an activation map. A stride is a name for the kernel's adjustable size (Fig. 2).

**Pooling Layer:** The size of the feature map is lowered. Data reduction will minimize the number of computer resources needed to process the data. It is also useful for spotting dominant characteristics [32]. Three different pooling layers are available. Similar to MIN and average, max pooling returns the greatest number among the region of the picture that the kernel has covered [32]. The max pooling layer performs both denoising and dimension reduction, whereas the average pooling layer performs only dimension reduction (Fig. 3).

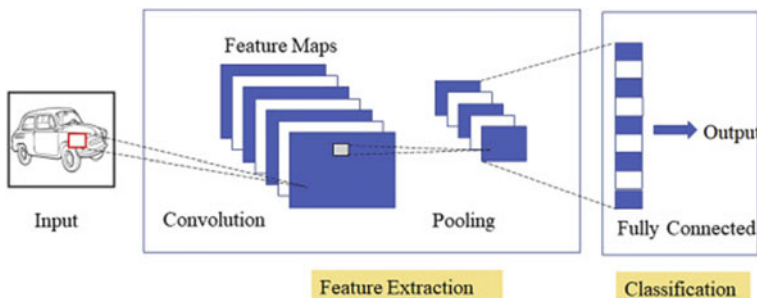


**Fig. 1** Architecture of CNN

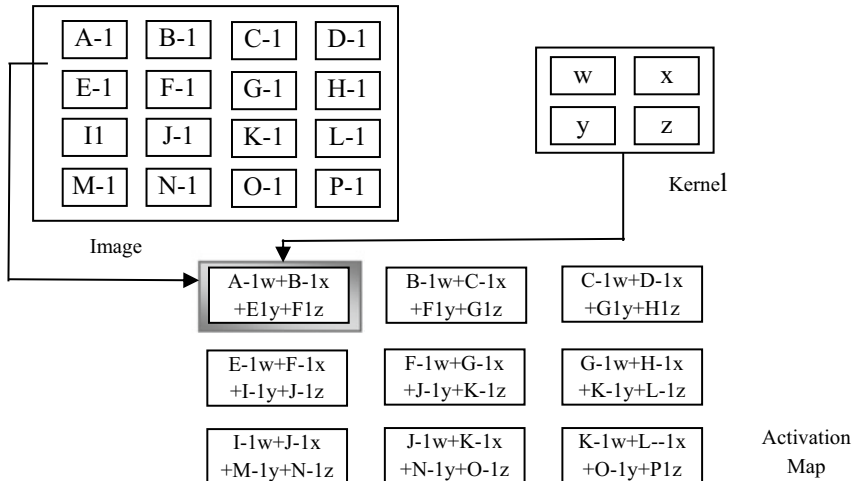
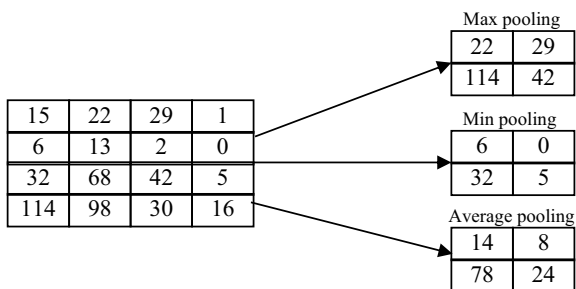


**Fig. 2** Convolution operation

**Fig. 3** Operation of min, max, and average pooling layer with  $2 \times 2$  filter and stride 2



**The Fully Connected Layer:** The final output from the convolution layer and pooling layer serves as the fully linked layer's input. The representation between the input and output images should be mapped.

## 4 Differential Evolution Algorithm

The differential evolution was proposed by Stom and Price in 1977. It is a meta-heuristic technique and is widely used by many researchers. Various fields where DE is used prominently are computer science, decision science, social science, business management, and many more. Every result in DE denotes to genome. So, each chromosome goes through mutation and then recombination.

DE starts with initializing a population.

$$C_{ij} = C_{\min} + (C_{\max} - C_{\min}) \times r1, \quad (1)$$

where the lower and upper limit is declared as  $C_{\min}$  and  $C_{\max}$ , respectively,  $r1$  is a randomly distributed number ranging from 0 to 1 [33]. Every genome will be tested under the fitness function, and the fittest one will be selected. The fittest vector is selected as the target vector. In the mutation operator, three chromosomes are selected randomly to obtain a donor vector. Here,  $F$  is the scaling factor which has defined parameters between 0 and 2.

$$V_{i,g+1} = C_{ri1,g+1} + F \cdot (C_{ri2,g+1} - C_{ri3,g+1}) \quad (2)$$

Once we have completed mutation, the next step will be recombination. Recombination is used to expand the population's variety.

$$\cup_{i,j,g+1} = \left\{ \begin{array}{l} V_{i,j,g+1} \text{if } \text{rand} \leq \text{CR} \\ C_{i,j,g} \text{if } \text{rand} > \text{CR} \end{array} \right\} \quad (3)$$

In recombination, the target vector and donor vector take part to generate the trial vector. Here, Cr is the crossover probability selected by the trial-and-error method during the implementation and rand is the random value between 0 and 1. Donor vectors are regarded as trial vectors if indeed the random value is less than the crossover probability, whereas target vectors are regarded as trial vectors if the random value is larger than CR. So once we have generated the trial vector, the next step is to evaluate the fitness function, and greedy selection will be between target and trial vector. The fittest children can be chosen and included into the original population [34].

The population will be adjusted in this manner for the following iteration. The sections that follow provide descriptions of the six most prevalent mutation schemes [35, 36].

$DE_{\text{rand}/1}$	$V_{i,g+1} = V_{r1,g} + F(C_{r2,g} - C_{r3,g})$	(1)
$DE_{\text{best}/1}$	$V_{i,g+1} = C_{\text{best},g} + F(C_{r2,g} - C_{r3,g})$	(2)
$DE_{\text{rand}/2/\text{bin}}$	$V_{i,g+1} = C_{r1,g} + F(C_{r2,g} - C_{r3,g} + C_{r4,g} - C_{r5,g})$	(3)
$DE_{\text{rand}/1/\text{exp}}$	$V_{i,g+1} = C_{\text{best},g} + F(C_{r2,g} - C_{r3,g})$	(4)
Current – to – rand/1	$V_{i,g+1} = C_{r1,g} + F(C_{r2,g} + C_{r3,g}) + F(C_{r4,g} - C_{r5,g})$	(5)
Current – to – best/1	$V_{i,g+1} = C_{r1,g} + F(C_{\text{best},g} + C_{r3,g}) + F(C_{r4,g} - C_{r5,g})$	(6)

## 5 Optimization of CNN Using DE

One of the most popular layouts and strategies in deep learning is the convolutional neural network (CNN). It indicates a notable advancement in the identification and categorization of items. Convolutional neural networks (CNNs) are highly influenced by their architecture and hyperparameters [36]. Recently, many meta-heuristic methods implemented to improve CNN [37]. This paper uses another type of stochastic population-based differential evolutionary algorithm. The first step is to initialize the population generated randomly.

Once the population is created, the fitness function is assessed and selects the target vector's fittest chromosome. The next step is to compute the donor vector followed by recombination and get the trial vector and finally a selection of the survival fittest and update the population; steps are discussed in the above section. A chromosome is the parameter definition of a convolutional neural network. The chromosome parameters are stride, kernel size, pooling size, activation function, and the number of nodes. The chromosome contains several parameters that may be changed, and each parameter has a vast search space.

The IQ-OTH/NCCD dataset will be used to evaluate the performance of the suggested technique. 1190 pictures altogether, representing slices from 110 instances' CT scans, are included in the collection.

**Algorithm:** Chromosome Evaluation

**Input:**

The Individual Chromosome, the number of training epochs, the training data and Fitness evaluation data from the given image classification dataset.

**Steps:**

The individual with fitness value. Construct CNN model based on information and image dataset.

1. Initialize F,CR and Target vector and population
2. For each epoch
3. do
4. Evaluate fitness function
5. Apply crossover
6. Recombination
7. Selection
8. Set best individual
9. Update Population
10. Satisfy the criterion
11. End do.

## 6 Conclusion

CNN is a well-known technology for solving medical image interpretation difficulties because of its very successful ways of feature extraction and learning differential aspects of an input medical picture. This study's objective is to provide a technique for automatically creating CNN structures using DE. CNN-DE tunes hyperparameters and determines the best optimum CNN architecture to address image classification issues in medical pictures, yielding efficient solutions. The primary benefit of basic DE is that there are only three control variables that need to be altered. The techniques used to generate the trial vectors and the choice of control variables have a big influence on how effectively DE completes a specific optimization assignment.

## References

1. Dubey R, Agrawal J (2022) An improved genetic algorithm for automated convolutional neural network design. *Intell Autom Soft Comput* 32(2). <https://doi.org/10.32604/iasc.2022.020975>
2. Mourya AK, Tyagi P, Bhatnagar A (2016) Genetic algorithm and their applicability in medical diagnostic: a survey. *Int J Sci Eng Res* 7(12):1143. ISSN 2229-5518
3. Hunter Park Innovation Dx, Connor Monahan Innovation DxInc (2019) Genetic deep learning for lung cancer screening. <https://doi.org/10.48550/arXiv.1907.11849>
4. Centeno-Telleria M, Zulueta E, Fernandez-Gamiz U, Teso-Fz-Betóñ D, Teso-Fz-Betóñ A (2021) Differential evolution optimal parameters tuning with artificial neural network. *Mathematics* 9:427. <https://doi.org/10.3390/math9040427>
5. Baioletti M, Bari GB, Milani A, Poggioni V (2020) Differential evolution for neural networks optimization. *Mathematics* 8(1):69. <https://doi.org/10.3390/math8010069>
6. Hussain S, Nanda SK, Barigidad S, Akhtar S, Suai Md. Novel deep learning architecture for heart disease prediction using convolutional neural network
7. Ayumi V, Rasdi Rere LM, Fanany MI, Arymurthy AMA (2016) Optimization of convolutional neural network using microcanonical annealing algorithm. [arXiv:1610.02306v1 \[cs.CV\]](https://arxiv.org/abs/1610.02306v1) 7 Oct 2016
8. Ayadi W, Elhamzi W, Charfi I et al (2021) Deep CNN for brain tumor classification. *Neural Process Lett* 53:671–700. <https://doi.org/10.1007/s11063-020-10398-2>
9. Sarvamangala DR, Kulkarni RV (2022) Convolutional neural networks in medical image understanding: a survey. *Evol Intel* 15:1–22. <https://doi.org/10.1007/s12065-020-00540-3>
10. Tarek Habib Md, Jueal Mia Md, Shorif Uddin M, Siddique MdAA, Ferdose J (2022) Convolutional neural network modeling for eye disease recognition. *Int J Online Biomed Eng (iJOE)* 18(9):115–130. <https://doi.org/10.3991/ijoe.v18i09.29847>
11. Wang Z, Lu D, Wang H, Liu T, Li P (2021) Evolutionary convolutional neural network optimization with cross-tasks transfer strategy. *Electronics* 10:1857. <https://doi.org/10.3390/electronics10151857>
12. Abdelrahman L, Al Ghamdi M, Collado-Mesa F, Abdel-Mottaleb M (2021) Convolutional neural networks for breast cancer detection in mammography: a survey. *Comput Biol Med* 131:104248. ISSN 0010-4825. <https://doi.org/10.1016/j.combiomed.2021.104248>
13. Belciug S (2022) Learning deep neural networks' architectures using differential evolution. Case study: medical imaging processing. *Comput Biol Med* 146:105623. ISSN 0010-4825. <https://doi.org/10.1016/j.combiomed.2022.105623>. (<https://www.sciencedirect.com/science/article/pii/S0010482522004152>)
14. Michael Park H, Monahan C (2019) Genetic deep learning for lung cancer screening. In: Conference on machine intelligence in medical imaging

15. Pandian R, Vedanarayanan V, Ravi Kumar DNS, Rajakumar R (2022) Detection and classification of lung cancer using CNN and Google net. *Measure Sens* 24:100588. ISSN 2665-9174. <https://doi.org/10.1016/j.mesen.2022.100588>. (<https://www.sciencedirect.com/science/article/pii/S2665917422002227>)
16. Sreekumar A, Rajan Nair K, Sudheer S, Nayar HG, Nair JJ (2020) Malignant lung nodule detection using deep learning. In: International conference on communication and signal processing. India
17. Li G et al (2020) Study on the detection of pulmonary nodules in CT images based on deep learning. *IEEE Access* 8:67300–67309. <https://doi.org/10.1109/ACCESS.2020.2984381>
18. Venkatesh C, Ramana K, Lakkisetti SY, Band SS, Agarwal S, Mosavi A (2022) A neural network and optimization based lung cancer detection system in CT images. *Front Public Health* 10:769692. <https://doi.org/10.3389/fpubh.2022.769692>. PMID: 35747775; PMCID: PMC9210805
19. Pfeffer MA, Ling SH (2022) Evolving optimised convolutional neural networks for lung cancer classification. *Signals* 3(2):284–295. <https://doi.org/10.3390/signals3020018>
20. Mostavi M, Chiu YC, Huang Y et al (2020) Convolutional neural network models for cancer type prediction based on gene expression. *BMC Med Genomics* 13:44. <https://doi.org/10.1186/s12920-020-0677-2>
21. Zhang L, Gao HJ, Zhang J, Badami B (2020) Optimization of the convolutional neural networks for automatic detection of skin cancer. *Open Med (Wars)* 15:27–37. <https://doi.org/10.1515/med-2020-0006>
22. Husam M, Barman SD, Islam S, Reza AW (2019) Skin cancer detection using convolutional neural network. In: Conference: the 2019 5th international conference. <https://doi.org/10.1145/3330482.3330525>
23. Singhal S, Kumar H, Passricha V. Prediction of heart disease using CNN. *Am Int J Res Sci Technol Eng Math* ISSN (Print): 2328-3491, ISSN (Online): 2328-3580, ISSN (CD-ROM): 2328-3629
24. Dorner JD, Halicek M, Ma L, Reilly CM, Schreibmann E, Fei B (2018) Proc SPIE Int Soc Opt Eng. Author manuscript; (available in PMC 2018 Sep 5.) Published in final edited form as: Proc SPIE Int Soc Opt Eng. 10575: 1057530. Published online 2018 Feb 27. <https://doi.org/10.1117/12.2293548>
25. NurFu'adah Y et al (2020) IOP Conf Ser Mater Sci Eng 982:012005; Reshi AA, Rustam F, Mehmood A, Alhossan A, Alrabiah Z, Ahmad A, Alsuwailem H, Choi GS (2021) An efficient CNN model for COVID-19 disease detection based on X-ray image classification 2021. Article ID 6621607. <https://doi.org/10.1155/2021/6621607>
26. Uddin A, Talukder B, Khan MM, Zagaria A (2021) Study on convolutional neural network to detect COVID-19 from chest X-rays 2021. Article ID 3366057. <https://doi.org/10.1155/2021/3366057>
27. Pradhan A, Sarma B, Dey BK (2020) Lung cancer detection using 3D convolutional neural networks. In: 2020 International conference on computational performance evaluation (ComPE) North-Eastern Hill University, Shillong, Meghalaya, India
28. Lee S, Kim J, Kang H, Kang D-Y, Park J (2021) Genetic algorithm based deep learning neural network structure and hyperparameter optimization. *Appl Sci* 11:744. <https://doi.org/10.3390/app11020744>
29. Gonsalves T, Upadhyay J. Integrated deep learning for self-driving robotic cars, Chap 8
30. <https://www.freecodecamp.org/news/convolutional-neural-network-tutorial-for-beginners/>
31. <https://towardsdatascience.com/convolutional-neural-networks-explained-9cc5188c4939>
32. <https://towardsdatascience.com/simple-introduction-to-convolutional-neural-networks-cdf8d3077bac>
33. Shaw RN, Ghosh A, Balas VE, Bianchini M (2021) Artificial intelligence for future generation robotics. Elsevier, pp 93–118. ISBN 9780323854986. <https://doi.org/10.1016/B978-0-323-85498-6.00010-1>. (<https://www.sciencedirect.com/science/article/pii/B978032385498600101>)

34. Tonge VG, Kulkarni P (2013) Solving permutation flowshop scheduling problem using improved differential evolutionary algorithm. *Int J Eng Res Technol (IJERT)* 2(10) ISSN: 2278-0181
35. Tonge VG (2012) Performance improvement of differential evolutionary algorithm: a survey
36. Georgioudakis M, Plevris V (2020) A comparative study of differential evolution variants in constrained structural optimization. *Front Built Environ* 6:102. <https://doi.org/10.3389/fbuil.2020.00102>
37. Fatyanosa TN, Aritsugi M (2021) An automatic convolutional neural network optimization using a diversity-guided genetic algorithm. *IEEE Access* 9:91410–91426. <https://doi.org/10.1109/ACCESS.2021.3091729>
38. <https://towardsdatascience.com/a-comprehensive-guide-to-Convolutional-neural-networks-the-eli5-way-3bd2b1164a53>

# Optimization of Different Parameters of One Bit Full Adder Using QCA Technology



Sachindeb Jana, Kisalaya Chakrabarti, and Angsuman Sarkar

**Abstract** One of the newest nanotechnologies is quantum dot cellular automata (QCA). This was an excellent replacement for the traditional complementary metal oxide semiconductor (CMOS) technology. In this technology, logic states do not define voltage levels, those indicates the position of each electrons. Fundamentally, QCA does not imply about the current switch, but it defines binary data by applying a bistable charge configuration. QCA technology covers a great scale of optimization parameters like less power consumption, fast transitions, and an incredibly dense structure. Our paper analyzes about energy flow equations, calculation of power dissipation for adder circuit. This paper defines an optimized circuit of full adder using QCA. Here, only 18 QCA cells have been utilized to create the full adder. The proposed paper analyzes about consumed area, reduced power dissipation, and delay which are significant improvements over the previous papers. The proposed architecture of full adder has been evaluated and simulation been done by using QCA designer tool 2.0.3 and QCADesignerE software tools.

**Keywords** QCA technology · Full adder · Majority voter · Area and power optimization

## 1 Introduction

In modern age, every researchers are trying to optimize power, size, and cost. Recently, several researchers have been suggested to change designs in very large-scale integration (VLSI) technology employing complementary metal oxide semiconductors produced via lithography (CMOS). But due to the tremendous scaling of gadget size, the most basic physical restrictions are practically achieved. According

---

S. Jana (✉) · K. Chakrabarti  
Haldia Institute of Technology, Haldia 721657, India  
e-mail: [mmmsachin@gmail.com](mailto:mmmsachin@gmail.com)

A. Sarkar  
Kalyani Government Engineering College, Kalyani 741235, India

to Moore's law density of the transistor increasing drastically in devices, reducing thickness of wafer. After 10 nm thickness of wafer, working principle of CMOS technology is almost impossible, changing quantum behavior. Several alternative methods to this problem are being introduced which are known as nanotechnologies like QCA, CNT, SET, RTD, molecular electronics, etc. Craig H. Lent developed quantum dot cellular automata (QCA) in the early 1980s. In contrast to traditional CMOS circuits, quantum cellular automata (QCA) uses quantum relations among quantum dots. Quantum dots represent digital data via the places that two different types of electrons occupy instead of being able to convey information as voltage or current. Four numbers of dots and two numbers of electrons form the elementary building block of QCA. Two electrons are present in any two of the four dots, which are arranged in a square. Columbic repulsion causes these dots to always be located in the top right and lower left corner, which is known as state 1 (+1). State 0 (-1) is achieved when 2 electrons align in the left upper and right lower corners. On the other hand, digital gates are designed using cells in QCA technology. The implementation of AND, OR, and NOT gates uses quantum cells. First two gates are realized by using majority voter. The majority voter has five cells connected in a crisscross pattern, while the third one may use two, three, or more cells. Researchers have focused on adders because they are one of the most fundamental computational circuits in digital logic. One of the fundamental components of many VLSI systems, including various microprocessors and processors, are adders. Digital circuits can be significantly simplified by using a full adder/subtractor architecture with a basic topology and low power consumption. A full adder/subtractor design should support both addition and subtraction operations and have a composite calculations circuit.

Previous researchers [1–3] have utilized majority voters (MV) and NOT gates for the realization of adder circuits. But the parameters in terms of cell numbers (area) and power are not fully optimized. In this paper, we have proposed a novel architecture where the space and power is highly optimized described in the later sections.

## 2 QCA Architecture

The quantum cell is fabricated of 2 moving electrons and 4 quantum dots. Is the fundamental building block for the QCA designing. These moving electrons quantum mechanically tunnel between two spots. They can switch positions between neighboring dots, but not amid cells. These electrons are constrained to adopt cross-ways orientations for two stable polarizations and columbic repulsion. According to Fig. 1a, QCA cells can be classified as polarized or non-polarized. As seen in Fig. 1b, 1 polarization,  $P (+1)$  is symbolized as logic “1”, and another,  $P (-1)$  is denoted as logic “0”. As seen in Fig. 1c, by joining cells in sequence, which result in two angular orientations of  $90^\circ$  or  $45^\circ$  rotation, wires are created [4]. Making two cells with opposing polarities (+1 and -1) as shown in Fig. 1d makes it possible to create a NOT gate. As seen in Fig. 1e, a 3-input majority voter (MV) gate [5, 6]

might be created utilizing 5 numbers of cells. By setting 1 input of the MV gate to  $P = -1$  and the OR gate to  $P = +1$ , the AND gate operates. The following logic phrase presents the majority gate.

$$\text{MV}(A, B, C) = AB + AC + BC.$$

Clock is mandatory because of appropriate function of cells and to guide moving of data across QCA circuits. Contrasting sequential circuits, which employ a clock, QCA circuits employ a quasi-adiabatic switching mechanism. As shown in Fig. 2, the clock cycles passes through 4 different states: switch, hold, release, and relax. The QCA cells are initially non-polarized and have a low potential barrier during the switch phase ( $t = 0-t = \pi/2$ ). After then, the potential barrier is raised to a high level by switching. The barrier remains high during the hold phase that follows

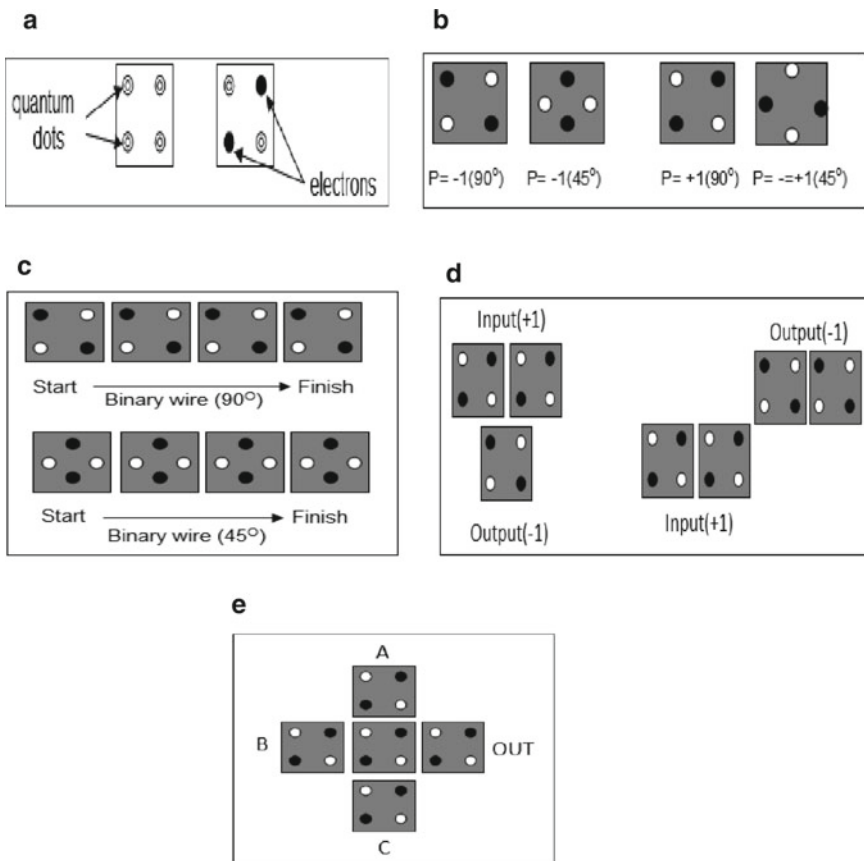


**Fig. 1** **a** Quantum cells (non-polarized and polarized), **b** cell polarization, **c** binary wires, **d** NOT gate, and **e** majority voter

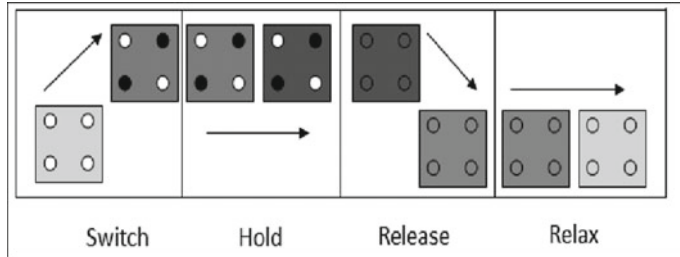


**Fig. 2** Clocking in QCA

( $t = \pi/2 - t = \pi$ ). Next, during the in release phase ( $t = \pi - t = 3\pi/2$ ), the barrier becomes low and the cells lose their polarity. Cells continue their low potential barrier and they stay in an unpolarized state in the final relax phase ( $t = 3\pi/2 - t = \pi$ ). The QCA circuit uses less power since only two electrons are changing positions. By using the clocking parameters, QCA circuits often consume less power.

### 3 Design of 1-bit QCA Full Adder

This section examines several schematic 1-bit full adder [7, 8] formulation and their QCA blueprints that have been obtained in a number of studies. All adders have binary inputs  $A$ ,  $B$ , and  $C_{in}$ , and sum and carry denote the outputs. The first one, introduced in 1994, is seen in Fig. 3a, and it has 5 majority gates and 3 inverters [1]. The design comprises of 192 cells and without any clocking parameters. A modified design is presented in Fig. 3b where 4 majority gates and three inverters formed full adder [9]. One more design of QCA full adder used 3 numbers of majority gates and 2 inverters as in Fig. 3c which has five clock phases and used 145 cells [10]. As shown in Fig. 3d, 3-input majority gate, a NOT gate, and a 5-input majority gate have been used to make this design. Around 2012 a better design was proposed which used 3 clock signals and only 51 cells [11]. Figure 3f shows another design of full adder comprises of 3 majority gates and 2 NOT gates [10, 12]. In this design, there are 82 cells and driven by three clock phases. Further, modification of 1-bit QCA full adder is being shown in Fig. 3f, holding of 3 majority gates and 1 inverter gate [13, 14].

#### 3.1 Proposed Full Adder

Consider a complete adder that has 2 outputs (sum and carry) and 3 inputs ( $A$ ,  $B$ , and  $C_{in}$ ). When the inputs are XORed, the result is the Sum output. The  $C_{in}$  input is the carry bit transmitted from the previous stage. A 3-input majority voter's (Maj3)

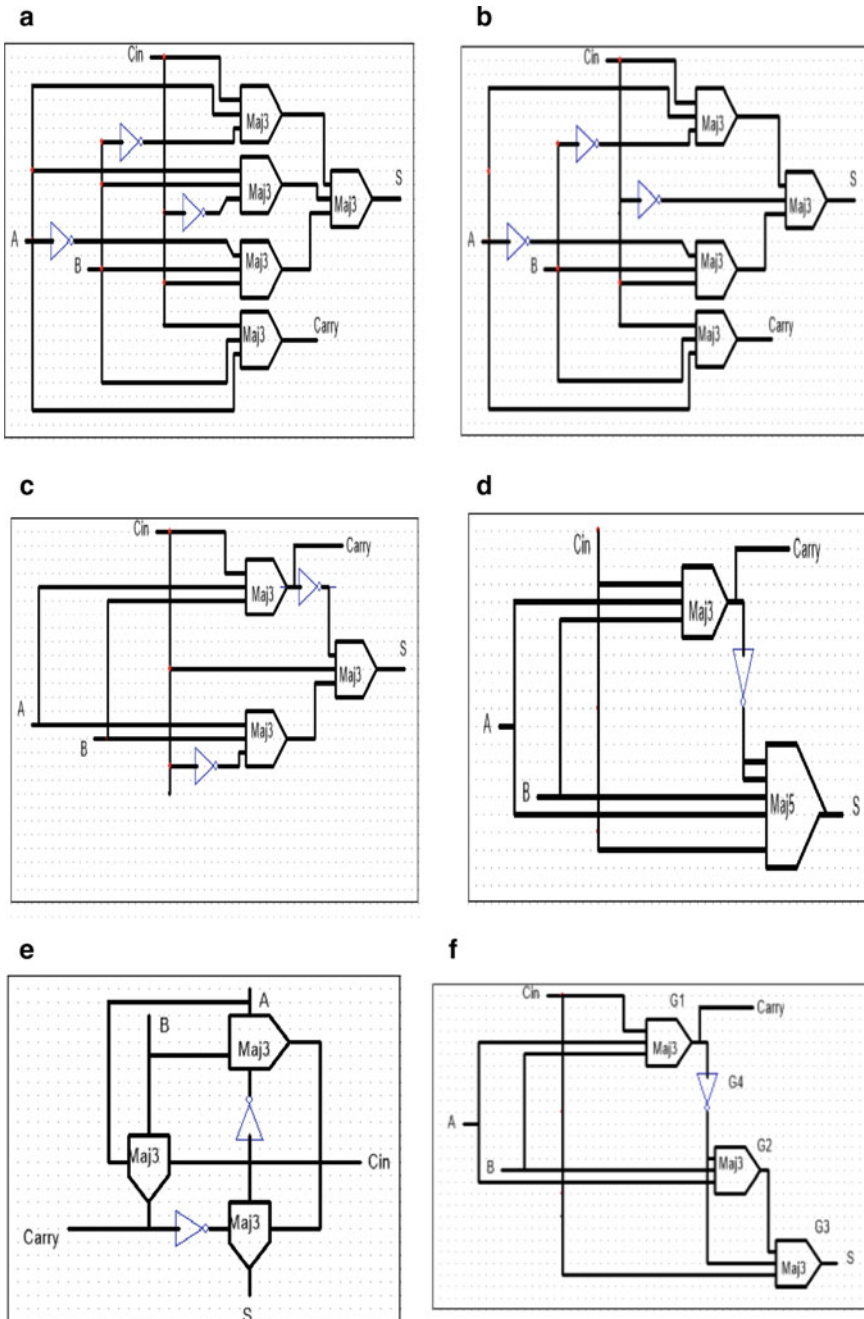


**Fig. 3** **a** 1-bit QCA full adder [1], **b** modified 1-bit QCA full adder [9], **c** modified design of prior QCA full adder [10], **d** modified 1-bit QCA full adder [11], **e** modified 1-bit QCA full adder [12], and **f** modified 1-bit QCA full adder [14]

output is known as “carry” (with  $A$ ,  $B$  and  $C_{in}$  as its inputs). Also, “MV” is the function of majority voter. Therefore, the equation to implement a full adder is as follows:

$$\text{Sum} = A \oplus B \oplus C_{in}$$

$$\begin{aligned}\text{Carry} &= AB + AC_{in} + BC_{in} \\ &= MV(A, B, C_{in})\end{aligned}$$

Design of an optimized full adder in QCA technology can be done by implementing these logics. A single 3-input majority gates are used in the proposed QCA adder’s calculation. The operation of this comprehensive adder is depicted in Fig. 4, which contrasts with the original QCA addition method [15]. This circuit confirms that the consumed area and the number of cells used in the formulated circuit are much less than the previously constructed full adder circuits using 3-input or 5-input majority gates and inverters. Results from comparing a few ideal full adders and the performance metrics of the suggested circuits are shown in Table 1.

**Fig. 4** Proposed design of one bit full adder

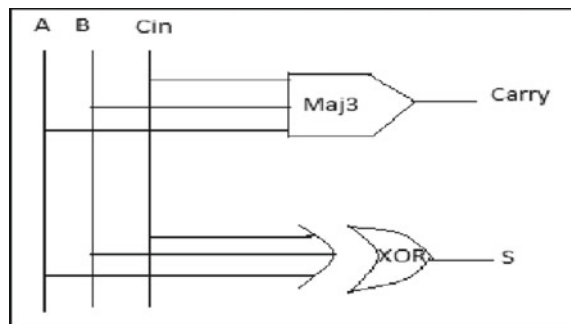
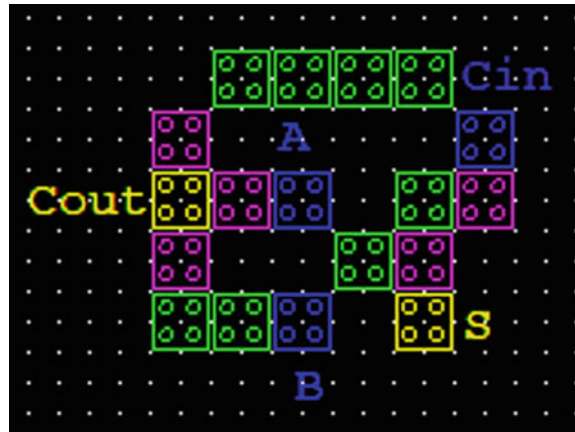


**Table 1** QCA full adder comparisons

Design (Reference No.)	Number of cells	Area ( $\mu\text{m}^2$ )	Latency (clock cycles)	Layer type
[1]	192	0.2	Not applicable	Multilayer
[10]	145	0.17	5	Multilayer
[17]	102	0.09	2	Coplanar
[12]	86	0.10	3	Coplanar
[9]	73	0.04	3	Coplanar
[2]	71	0.06	1.5	Coplanar
[3]	44	0.06	1.25	Coplanar
Proposed	18	0.017	2	Coplanar

**Fig. 5** Proposed model of QCA full adder implemented by using QCA architecture



This table leads us to the conclusion that, in comparison with other circuits, when it has a standard latency, the construction that is suggested is an optimized circuit in terms of occupied area and cell count. It should also be noted that the suggested complete adder is coplanar in design and has a tolerable latency range. The proposed design can be regarded as a more beneficial 1-bit full adder design using the coplanar method as shown in Figs. 5 and 6.

### 3.2 Simulation of Designed Circuit and Experimental Results

#### QCADesigner

QCADesignerE (windows version) software has been used broadly here. Two types of simulation engines are being used in this software, they are known as bistable approximation type engine and the coherence vector with energy engine. Every cell in the bistable approximation engine is seen as a typical two-state system. The interference between cells, which is the degree of interaction between two cells, is used as an approximation by the bistable engine. Based on their respective distances to the fifth power, this strength decreases in the opposite direction. Here, each cell  $i$  is given only the outputs related to the area denoted by the so-called radius of influence  $R$ . The following Hamiltonian mathematically defines the two-state system model for cell  $i$ .

$$H = \begin{bmatrix} -\frac{1}{2} \sum_i E_k S_i f & -\gamma \\ -\gamma & \frac{1}{2} \sum_i E_k S_i f \end{bmatrix} = \begin{bmatrix} -\frac{1}{2}S & -\gamma \\ -\gamma & \frac{1}{2}S \end{bmatrix} \quad (1)$$

$P_j$  is the polarization of cell  $j$ ,  $E_k$  is the kink energy amid the two cells  $i$  and  $j$  and is the tunneling energy.  $E_k$  indicates the energy cost of opposing polarization in the two cells.  $\gamma$  is the geometric part that accounts for electrostatic falloff with

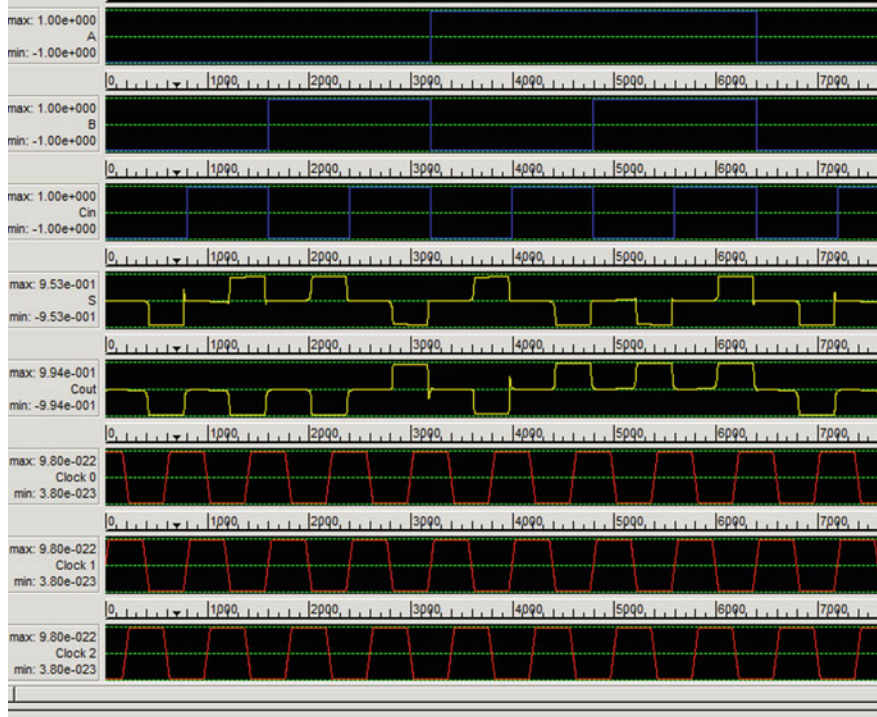


**Fig. 6** Simulated result of proposed 1-bit QCA full adder

cell distance. The  $i$ th adjacent cell's polarization is  $S_i$ . The clocking mechanism regulates the tunneling energy between 2 states of a certain cell, and it is represented by the symbol  $\gamma$ . To determine the ground state of every cell time-independent, Schrödinger equation can be used assuming switching is adiabatic (i.e., at the time of switching the structure remain close to the ground state). The QCADesigner [16] engine is based on Jacobi algorithm to formulate the Eigen values and Eigen vectors of the Hamiltonian. It calculates the polarization of every cell up to the whole system stabilizes. But “coherence vector with energy simulation engine” is a new simulation engine, depending on the density matrix procedure for modeling the power dissipation results and energy analysis of each operation (switching, input, output changes) of QCA circuits. In this mode, the engine employs a time dependent simulation of the desired circuit. Hamiltonian, given in Eq. 1 defines 2 state model of every cell. The equation of motion, which is a partial differential equation with a clear time marching algorithm, is evaluated by the simulation engine. The coherence vector's summation index and equation of motion are determined by cell  $i$ 's adjacent effectiveness.

Comparisons of latency and required area versus number of cells are shown below in Figs. 7 and 8 correspondingly.

**Fig. 7** Comparison of latency versus number of cells

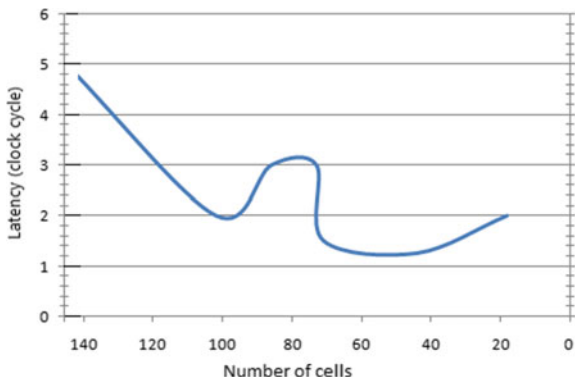
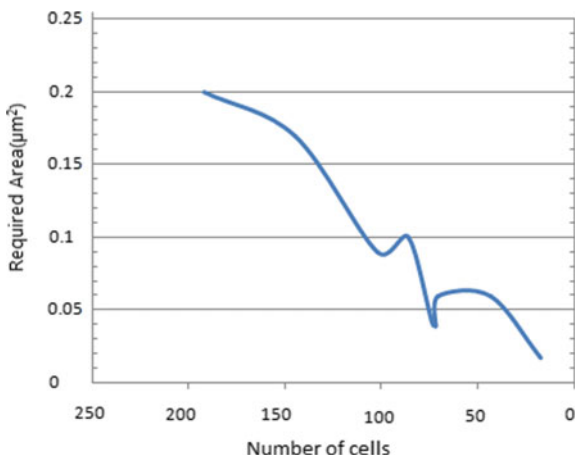


**Fig. 8** Comparison of required area versus number of cells



We have observed from Figs. 7 and 8 that in our proposed design there is an improvement in required area with latency. In the latest design of full adder by Joka et al. [3] used 44 numbers of cells with latency 1.25, but we have designed it using only 18 cells with latency 2. Our proposed design is about the optimization of area and energy consumed of full adders with irreversible adder, whereas Mohammadi et al. [18] has used reversible adder (number of inputs = number of outputs), for that area as well as energy consumed are far more than our proposed work. So our work is simpler and robust in comparison with work of Mohammadi et al. Hence, our model has a tremendous improvement in required area and with moderate latency.

### 3.3 Energy Consumption in One Clock Cycle in QCA

First we will calculate the total power in every clock cycle assuming each cell consumes same power in a QCA circuit followed by summation of power [19, 20]. The mutual effect between cells is carried out by the electrostatic kink energy among them. Assume a circuit of  $N$  cells ( $X_1, X_2, \dots, X_N$ ).  $X_i$  is the polarization of the  $i$ th cell termed as  $X_i \in \{1, -1\}$ . Calculate the power for switching of the input cells considering previous and post polarization of the input cells. Assume  $X_{i/k}$  is the polarization of input ( $i$ th) cell about the  $k$ th input permutation. This computation of polarization is done by any simulation software like QCADesigner. Since in this paper, our motto is to calculate upper bound power (total power consumption), we round up the calculated polarized power to its round value, i.e., 1 or -1. When switching changes from  $k$ th to  $m$ th combination, we have to calculate the effective kink energy of the other cells  $S_{i-}$  and  $S_{i+}$ .

This is calculated as following:

$$S_{i-} = \sum_{j \in \text{Ne}(X_i)} E_k f_j x_{j/k} \quad (2)$$

and

$$S_{i+} = \sum_{j \in \text{Ne}(X_i)} E_k f_j x_{j/m} \quad (3)$$

$f_j$  is distance measuring term which is the fifth power of the distance from cell.  $\gamma L$  and  $\gamma H$  [21] are the powers of low and high clock, respectively. Calculate the leakage power and switching power by applying Eqs. (2) and (3). Now we calculate various design objectives with these evaluated values as given below. It should be mentioned that the quantities computed are actually bounds accordingly. Total dissipated power: transition for  $k$ th state to  $m$ th state is as follows:

$$P_{k \rightarrow m}^{\text{tot}} = \sum_{i=(r+1)}^N P_{i,k \rightarrow m}^{\text{leak}} + P_{i,k \rightarrow m}^{\text{switch}} \quad (4)$$

Average power (all input transitions) is given by

$$P^{\text{avg}} = \frac{1}{2^r} \sum_{k,m} P_{k \rightarrow m}^{\text{tot}} \quad (5)$$

Maximum power (all input transitions) is given by

$$P^{\text{max}} = \max_{k,m} \sum_{k,m} P_{k \rightarrow m}^{\text{tot}} \quad (6)$$

We have calculated total consumed power ( $P_{\text{total}}$ ), total clock energy ( $E_{\text{clk\_total}}$ ), and total error energy ( $E_{\text{Error\_total}}$ ) for different kink energies ( $E_k$ ) for one bit QCA Full adder given in Table 2.  $E_k[0] \dots E_k[10]$  denotes kink energies for combined effect of different input combinations and clock pulses.

Total energy dissipation (Sum\_  $P_{\text{total}}$ ):  $1.51\text{e-}002$  eV (Error:  $\pm -1.58\text{e-}003$  eV).

Average energy dissipation per cycle (Avg\_  $P_{\text{total}}$ ):  $1.37\text{e-}003$  eV (Error:  $\pm -1.43\text{e-}004$  eV). Total simulation time: 8 s

## 4 Conclusion and Future Scopes

In our proposed design, only 18 number of cells are being used to implement one bit full adder which is far less than previous designs. This will obviously reduce the space consumed, total power requirement, clock pulses, etc. But there are challenges in the feasibility of the circuit in view of fabrication problems, working temperature range. Those shortfalls can be evaluated using probability transfer matrix (PTM). On successful evaluation of PTM model, we can apply this proposed model parallel adders, carry look ahead adder (CLA), ripple carry adder, memory unit, etc. Those will be great application of one bit adders in the future days simplifying calculations in electronics and computer science fields.

**Table 2** Energy consumption of 1-bit QCA full adder with different kink energies

Power/ energy	Kink energy ( $E_k$ )	$E_k(1) = -1.021058e-005$	$E_k(2) = -1.021058e-005$	$E_k(3) = 5.727103e-006$	$E_k(4) = -1.974610e-006$	$E_k(5) = 4.413817e-005$
$P_{\text{total}}$	$6.2680e-004$	$1.8027e-003$	$1.9620e-003$	$9.6135e-004$	$7.5380e-004$	$2.0396e-003$
$E_{\text{clk\_total}}$	$1.5256e-003$	$4.2309e-004$	$2.8799e-004$	$1.7421e-003$	$1.7421e-003$	$2.8798e-004$
$E_{\text{Error\_total}}$	$6.3625e-005$	$1.8878e-004$	$2.1192e-004$	$9.7483e-005$	$7.1608e-005$	$2.2020e-004$
Power/ energy	Kink energy ( $E_k$ )	$E_k(6) = 1.483611e-003$	$E_k(7) = 1.483611e-003$	$E_k(8) = -3.225745e-004$	$E_k(9) = -1.021058e-005$	$E_k(10) = 9.284749e-007$
$P_{\text{total}}$	$1.6935e-003$	$8.4120e-004$	$6.2880e-004$	$1.8027e-003$	$1.8027e-003$	$1.9620e-003$
$E_{\text{clk\_total}}$	$4.2309e-004$	$1.5256e-003$	$1.5256e-003$	$4.2309e-004$	$4.2309e-004$	$2.8799e-004$
$E_{\text{Error\_total}}$	$1.7585e-004$	$8.4167e-005$	$6.3625e-005$	$1.8878e-004$	$1.8878e-004$	$2.1192e-004$

## References

1. Tougaw PD, Lent CS (1994) Logical devices implemented using quantum cellular automata. *J Appl Phys* 75:1818–1825
2. Hashemi S, Navi K (2015) A novel robust QCA full-adder. *Proc Mater Sci* 11:376–380
3. Zoka S, Gholami M (2019) A novel efficient full adder–subtractor in QCA nanotechnology. *Int Nano Lett* 9:51–54
4. Ahmad F, Bhat GM, Khademolhosseini H, Azimi S, Angizi S, Navi K (2016) Towards single layer quantum-dot cellular automata adders based on explicit interaction of cells. *J Comput Sci* 16:8–15
5. Balali M et al (2017) Towards coplanar quantum-dot cellular automata adders based on efficient three-input XOR gate. *Results Phys* 7:1389–1395
6. Kong K et al (2010) An optimized majority logic synthesis methodology for quantum-dot cellular automata. *IEEE Trans Nanotechnol* 9(2):170–183
7. Gassoumi I, Touil L, Mtibaa A (2021) An efficient design of QCA full-adder-subtractor with low power dissipation. *Hindawi J Electr Comput Eng* 2021:1–9. Article ID 8856399
8. Karthik R, Jyothi K (2019) Novel design of full adders using QCA approach. *Int J Adv Trends Comput Sci Eng* 8(3):501–506
9. Navi K, Farazkish R, Sayedsalehi S, Mostafa Rahimi A (2010) A new quantum-dot cellular automata full-adder. *Microelectron J* 41:820–826
10. Rumi Z, Walus K, Wang W, Jullien GA (2004) A method of majority logic reduction for quantum cellular automata. *IEEE Trans Nanotechnol* 3:443–450
11. Hashemi S, Tehrani M, Navi K (2012) An efficient quantum-dot cellular automata full-adder. *Sci Res Essays* 7(2):177–189
12. Cho H, Swartzlander EE (2009) Adder and multiplier design in quantum-dot cellular automata. *IEEE Trans Comput* 58(6):721–727
13. Azghadi MR, Kavehei O, Navi K (2007) A novel design for quantum-dot cellular automata cells and full adders. *J Appl Sci* 7:3460–3468
14. Mohammadi M, Mohammadi M (2016) An efficient design of full adder in quantum-dot cellular automata (QCA) technology. *Microelectron J* 50:35–43
15. Jana S, Chakrabarti K, Sarkar A (2020) Optimization of effective area of 3-inputs XOR gate using QCA simulation. *J Crit Rev* 7(6):2816–2823
16. Walus K, Dysart TJ, Jullien GA, Budiman RA (2004) QCADesigner: a rapid design and simulation tool for quantum-dot cellular automata. *IEEE Trans Nanotechnol* 3:26–31
17. Hänninen I, Takala J (2010) Binary adders on quantum-dot cellular automata. *J Signal Process Syst* 58(1):87–103
18. Mohammadi Z, Mohammadi M (2014) Implementing a one-bit reversible full adder using quantum-dot cellular automata. *Quantum Inf Process* 13:2127–2147
19. Chen H, Lv H, Zhang Z, Cheng X (2019) Design and analysis of a novel low-power exclusive-OR gate based on quantum-dot cellular automata. *J Circ Syst Comput* 28(8):1–17. 1950141
20. Sill Torres F, Wille R, Niemann P, Drechsler R (2018) An energy-aware model for the logic synthesis of quantum-dot cellular automata. *IEEE Trans CAD Integr Circ Syst* 37(12):3031–3041
21. Srivastava S, Sarkar S, Bhanja S (2009) Estimation of upper bound of power dissipation in QCA circuits. *IEEE Trans Nanotechnol* 8(1):116–127

# A Robust PID Design for Load Frequency Control Using AEPSO Algorithm with Changing Loads



Souvik Dutta, Alpana Barman, Santigopal Pain, and Parimal Acharjee

**Abstract** This article introduced a new approach known as adaptive exponential particle swarm optimization (AEPSO) for the purpose of load frequency control to damp out the oscillations of frequency response as well as improve the dynamic performance of a single area non-reheat thermal power system. The control parameters of the PID controller are designed using AEPSO with an adaptive inertia weight to overcome the local optima achieving the best solution. The nonlinearity, i.e., governor dead-band (GDB), is considered to make the scheme more realistic. As the load variation is random throughout the year, the performance of the system is rigorously tested for wide load variation, i.e., from 10 to 60%. The performance of AEPSO is compared with general PSO (GPSO) for various loading conditions. Here, it has been found that the proposed technique, i.e., AEPSO endowed better performance compare to GPSO in all respect.

**Keywords** LFC · AEPSO · PID controller · Adaptive inertia weight

## 1 Introduction

Load on a power system fluctuates because of erratic consumer demand, disturbances and/or changing operating conditions and for these the power system becomes extremely unreliable and unstable. So, load variation has a key impact on power system's transient state and steady-state performance. Due to load variation, the power system's frequency and voltage profile will differ from its usual state of operation. The imbalance between voltage and frequency needs to be rectified by using a proper control technique for effective operation under abnormal conditions. Load frequency control (LFC) is a useful tool in the process of power system. This control

---

S. Dutta · A. Barman (✉) · S. Pain  
Haldia Institute of Technology, Haldia, West Bengal 721657, India  
e-mail: [alpana.ee2011@gmail.com](mailto:alpana.ee2011@gmail.com)

P. Acharjee  
National Institute of Technology, Durgapur, West Bengal 713209, India

is very significant for reducing divergences to set up a reliable high-quality electricity. The goal of LFC is to keep the frequency at schedule level, enhance the performance of the system by succeeding zero steady-state error (SSE) with minimal overshoot ( $M_p$ ) and settling time ( $t_s$ ).

Numerous control strategies have been successfully applied over the years to solve the LFC design to enhance the transient and steady-state performance of the system. The traditional proportional-integral (PI) controller is the most often used controller [1]. Despite its simple design and straightforward execution, for the large-scale interconnected power system, it has not produced the desired results. So, to overcome the shortcomings of PI controller, PID controller has been considered. The conventional design method of PID controllers such as Tyreus-Luyben, Ziegler-Nichols has been used for minimizing the oscillations of the frequency of the power system but for the vast and intricate power system networks, these method-based controllers are ineffective [2]. As a result, several control design strategies based on contemporary control theory have been used, including decentralized robust, adaptive, and optimum control systems [3–7]. Due to nonlinearities such as governor dead-band (GDB), generation rate constraint (GRC), and time delay, the system becomes extremely nonlinear [8]. The LFC problem for such a complicated power system cannot be solved by the model-based controller. Therefore, the soft computing tools are more adaptable and reliable. For the LFC of the power system, researchers have suggested a variety of control schemes based on soft computing approaches in order to sustain the system frequency at its true level throughout the operation. One popular soft computing technique, PSO has been widely used to address challenging power system issues [9–12]. PSO, however, sometimes falls short of the global minimum because of inadequate variety and adherence to local minima. Exponential inertia weight ( $w$ ), which has improved the PSO's performance, as reported in [13, 14]. Other control strategies such as genetic algorithm (GA) [2], bacteria foraging optimization algorithm (BFOA) [2], and teaching–learning-based optimization algorithm (TLBO) [15] have been used for load frequency control. These control strategies not only keep the frequency constant in the system but also operate the power system with zero steady-state error. Recently, other evolutionary computation methods and their hybridize forms like gravitational search algorithm (GSA), BAT algorithm, ant lion optimizer algorithm, elephant herding optimization, and fire fly pattern search (FF-PS) algorithm [16–22] have been successfully applied to design LFC challenges with or without constraint scenario. Here, in majority of the papers, crucial physical security constraint governor dead-band (GDB) has partially or completely disregarded when developing the LFC system and putting these design strategies into practice might be challenging. In most of the literature, the load variation study is also inadequate. As power system is highly dynamic, the load changes randomly due to abrupt demand, seasonal effects, and other operating conditions. Therefore, the system must be designed considering the different loading conditions.

The physical constraint increases settling time ( $t_s$ ), overshoot ( $M_p$ ), steady-state error (SSE) of the system and has an impact on both the system's transient and steady-state behavior. Therefore, failing to take this constraint into account while designing the controller would reduce the overall act of the system. An AEPSO-based PID

control technique is projected for an actual single area non-reheat thermal power system. The widely used objective function, i.e., integral square error (ISE), is used to enhance both transient and steady-state performances. In this study, to make the design more useful, load variation has been done from 10 to 60% for both AEPSO and general PSO (GPSO). It is found that the transient response of the system has improved in case of AEPSO compared to GPSO under variable loading conditions.

## 2 System Model

This section presents a simulation model of a single area power system. With variation of load, disturbances, and other changing operating conditions, the dynamic of the power system fluctuates. Hence, the system's frequency and voltage profile differ from operating conditions. The dynamic of the power system can be represented with certain nonlinearities as such GRC, GDB, and time delay. In this work, a realistic single area power system model considering GDB has been developed. The overall magnitude of a persistent speed shift, during which there is no corresponding change in valve position, is referred to as the governor dead-band. Governor dead-band (GDB) is generally stated as the percentage of rated speed per frequency. The steam turbine governor's GDB is 0.06% of the maximum speed. The governor dead-band's impact on LFC performance includes a rise in perceived steady-state frequency control. The proposed system comprises speed governor, turbine system including GDB, PID controller, speed regulation, mass, and load which represent their dynamics, respectively [22]. The traditional LFC of non-reheat single area thermal system has been depicted in Fig. 1.

The command signal is represented by  $\Delta P_{ref}$ ,  $\Delta P_L$  is change in demand power, the time constant of the governor is  $T_G$ , the time constant of the turbine is  $T_T$ , load damping rate is  $D$ ,  $H$  is the inertia constant lies between 2 and 8 s, and the speed regulation of governor is represented by  $R$ . The system parameters are governor time

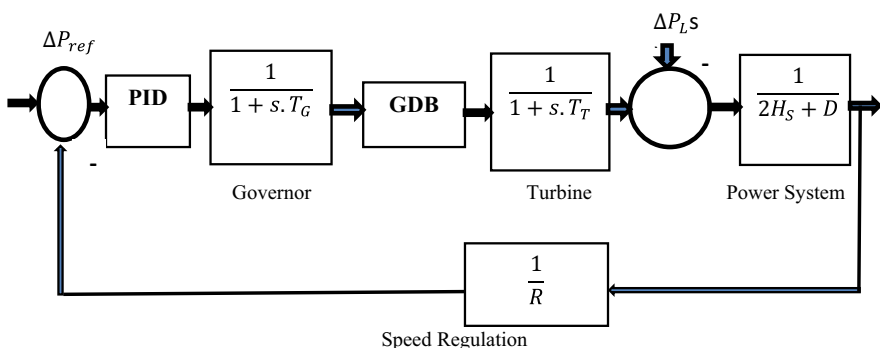


**Fig. 1** LFC transfer function model for single area system

constant ( $T_G$ ) = 0.2 s, turbine time constant ( $T_T$ ) = 0.5 s, generator inertia constant ( $H$ ) = 5 s, speed regulation of governor ( $R$ ) = 0.05 per unit, and governor dead-band (GDB) = 0.0006 pu (0.06% of  $f$ ). The turbine rated power is 250 MW at normal frequency of 60 Hz.

### 3 Objective Function

This study presents a control design for PID load frequency controller with an intelligent technique. The goal of the suggested design is to modulate the frequency in a way that maintains desired system performance despite environmental changes and parameter uncertainty. In case of LFC, the genuine optimum solution is attained by using a specific control technique. True optimality is defined as zero steady-state error, the smallest possible overshoot, the shortest possible settling time, the minimum possible overall oscillation, and the best possible damping of the output frequency. Integral square error (ISE) is utilized as an objective function in order to achieve rapid convergence and real optimum solution. ISE will handle greater mistakes more carefully than smaller ones (as the square of a huge error will be significantly large). Control system's design to minimize ISE has a tendency to swiftly eradicate major mistakes, and this leads to quick response, but with significant low amplitude oscillation. Therefore, the objective function considered in this study is given by

$$\text{ISE} = \int [e(t)]^2 dt \quad (1)$$

### 4 Controller Design

Although PI controller is simple in structure, but it can't give desired transient performance. First order systems can perform well when controlled by a Ziegler-Nichols tuned PI controller (ZNPIC), but higher order systems seldom fail to provide results that are attractive. Sometimes this ZNPIC of a system is not satisfactory owing to significant overshoot and oscillation [23–25].

So, PID controllers are used because of their simple design and ease of implementation. To get a desired result of a real system, a number of PID control strategy are being developed and the most crucial phase for a successful controller design is tuning [26]. Industrial control systems are the primary application for a PID controller. Generally, PID controller is the synthesis of proportional action ( $k_p$ ), integral action ( $k_i$ ), and derivative action ( $k_d$ ). A PID controller measures and determines the needed adjustment based on the proportional, integral, and derivative factors between the desired set point and the measured value. The majority of PID controllers

are employed in feedback systems. The proportional controller does a comparison between the target value and the true value. The output, however, is the product of the resultant error and the proportional constant. Although the steady-state error is constantly maintained, it provides stable system operation. Integral controllers are used to remove a system's steady-state error. The system experiences a lag because of the integration of the error over a period of time, and it will continue until the error value is zero. Derivative controller is used to forecast how the mistake would behave in the future. This D-controller increases the stability of a particular system by mitigating lag brought on by I-action.

So, the three types of controllers are merged together to represent a PID controller having transfer function:

$$C_{\text{pid}(S)} = k_p + k_d S + \frac{K_i}{S} \quad (2)$$

## 5 Proposed Algorithm

In this work, AEPSO has been proposed over GPSO, using conventional proportional-integral-derivative (PID) controller to optimize the system performance in a continuous mode of operation considering ISE as fitness function. GPSO is a stochastic computational method. GPSO technique optimizes a problem iteratively having a population of particles. The algorithm starts with a swarm of randomly created particles with defined range and sizes [8]. Each particle has its own position and velocity which will be updated through previous information. In n-dimensional space, the velocity of  $i$ th particle will be defined using Eq. (3).

$$v_i^{t+1} = w_i \times v_i^t + a_1 \times r_1 \times (\text{pbest}_i^t - x_i^t) + a_2 \times r_2 \times (\text{gbest}_i - x_i^t) \quad (3)$$

In n-dimensional space, the updated position of  $i$ th particle will be defined using Eq. (4).

$$x_i^{t+1} = x_i^t + v_i^{t+1} \quad (4)$$

where  $x_i^t$ ,  $v_i^t$ , and  $\text{pbest}_i^t$  are the position, velocity, and current best position of the  $i$ th particle at  $t$ th iteration. The random numbers such as  $r_1$  and  $r_2$  lie between 0 and 1.  $\text{gbest}_i$  indicates the global best position of the whole swarm and constriction factors such as  $a_1$ ,  $a_2$  are considered as 2.0 to get the better convergence. It is noted that inertia weight is the element that regulates how the prior velocity affects the current velocity. High inertia weight at the start of the iteration will make it easier for global exploration, and low inertia weight at the conclusion of the iteration will make it easier for local exploration. In GPSO, the inertia weight ( $w_1$ ) [27] for the velocity of  $i$ th particle is assigned by

$$w_1 = w_{\max} - \text{iteration.} * \left( \frac{w_{\max} - w_{\min}}{\text{Maximum no. of iteration}} \right) \quad (5)$$

In this work, to achieve better optimal solution, a new inertia weight is formulated. In AEPSO technique, the inertia weight ( $w_3$ ) is assigned as

$$w_3 = \frac{\exp(w_2)}{\text{iteration}} \quad (6)$$

where

$$w_2 = w_{\max} - \text{iteration.} * \left( \frac{w_{\max} - w_{\min} - m_1}{\text{Maximum no. of iteration}} \right) \quad (7)$$

where  $w_{\max}$  and  $w_{\min}$  are maximum and minimum values of  $w$  which are taken as 0.9 and 0.4, respectively. The aforementioned function is nonlinear and rapidly changes with every iteration. This adaptive function enables high ' $w_3$ ' at the beginning and low ' $w_3$ ' at the conclusion, which, respectively, prevent premature convergence and improve local search. The factor  $m_1$  is the control factor whose value is carefully decided as 0.05 by trial and error in order to have the right balance between local exploration and global exploitation.

## 6 Result and Analysis

In this work, an error function known as integral square error (ISE) has been considered as an objective function. GPSO and AEPSO techniques are applied consecutively for optimization of the PID controller. The frequency deviation and the transient response for this system has been observed using above mentioned different techniques with step change in load. The performance of the system is evaluated for load variation of 10–60%. The inertia weight for conventional algorithm is taken as  $w_1$  represented in Eq. (5). The inertia weight for the proposed algorithm is taken as  $w_3$  represented in Eq. (7). The simulation is done using MATLAB/SIMULINK model. The tuned control parameters with variation of load for GPSO and AEPSO are shown in Table 1. The steady state along with transient response specifications is given in Table 2. The dynamic responses of frequency deviation for this single area nonlinear system with variation of loads are depicted in Figs. 2, 3, 4, 5, 6, and 7. Here, both GPSO and AEPSO algorithms have been used to simulate the proposed system to find PID gain values considering 100 particles and 50 iterations in each loading condition.

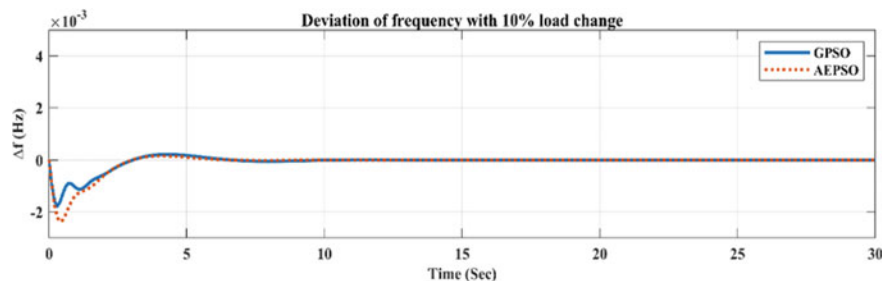
From Table 1, it has been observed that the gain values  $k_p$ ,  $k_i$ ,  $k_d$  are near to each other for both GPSO and AEPSO. From Table 2, it has been observed that the value of maximum overshoot is continuously increasing with increasing loads both for GPSO and AEPSO. It has been also found that the value of maximum overshoot

**Table 1** Tuned control parameters for different algorithms with a step change in load

Change of load in percentage (%)	GPSO			AEPSO		
	$K_{p1}$	$K_{i1}$	$K_{d1}$	$K_{p3}$	$K_{i3}$	$K_{d3}$
10	2.7127	2.6579	2.5192	2.3325	1.8655	1.4586
20	2.7062	2.6189	2.5620	2.3368	1.8284	1.4753
30	2.6769	2.6638	2.5540	2.3496	1.5077	1.3334
40	2.6984	2.6476	2.5186	2.3716	1.7544	1.4505
50	2.7015	2.6408	2.5294	2.3121	1.7834	1.4954
60	2.6824	2.6354	2.5262	2.3132	1.8743	1.5176

**Table 2** Transient and steady-state specifications of LFC for GPSO and AEPSO algorithms with a step change in load

Change of load in percentage (%)	GPSO			AEPSO		
	Max. overshoot ( $M_p$ )	Settling time [ $t_s$ (s)]	Steady-state error (SSE) $\times 10^{-5}$	Max. overshoot ( $M_p$ )	Settling time [ $t_s$ (s)]	Steady-state error (SSE) $\times 10^{-5}$
10	0.0134	15.2	1.7029	0.0095	15.2	1.0041
20	0.0263	15.3	2.0074	0.0119	15.3	1.8446
30	0.0416	15.3	2.6484	0.0127	15.3	1.1836
40	0.0540	15.3	1.3382	0.0305	15.2	1.1589
50	0.0673	15.3	1.7214	0.0468	15.3	1.1008
60	0.0948	15.3	4.2183	0.0623	15.2	2.9946

**Fig. 2** Frequency deviation with 10% load change

for each loading condition is less in AEPSO compared to GPSO. From transient response (Table 2), it is also noticed that the value of steady-state error (SSE) is minimum in case of AEPSO technique compared to GPSO. From Figs. 2, 3, 4, 5, 6, and 7, it is observed that the AEPSO method can converge and attain good optimized value on different loading conditions with less oscillation. Therefore, the proposed AEPSO algorithm is more considerable and robust. As a result, better performance

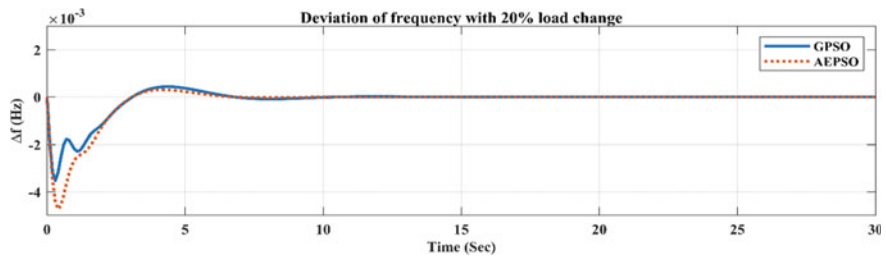


Fig. 3 Frequency deviation with 20% load change

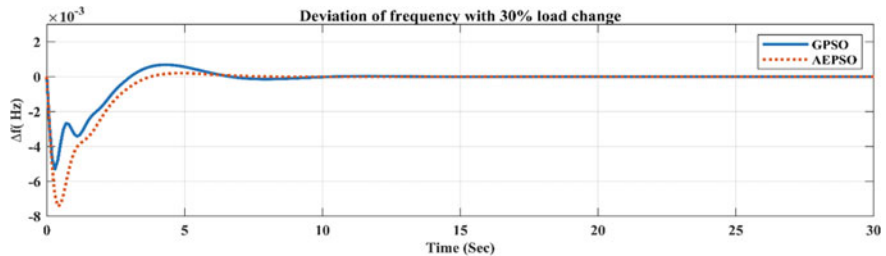


Fig. 4 Frequency deviation with 30% load change

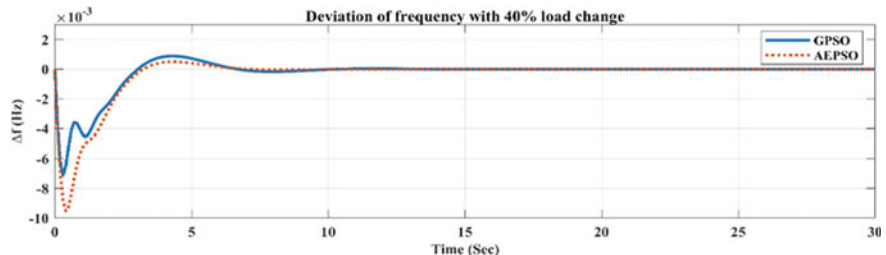


Fig. 5 Frequency deviation with 40% load change

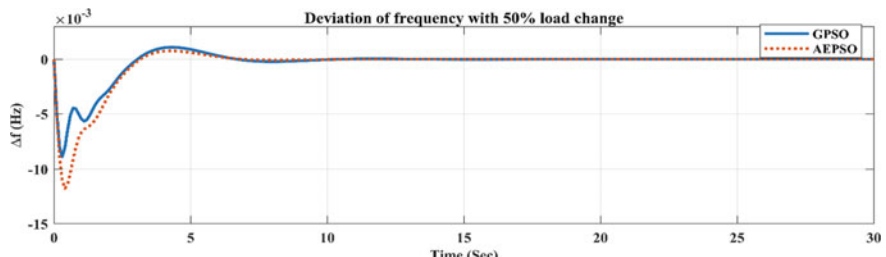
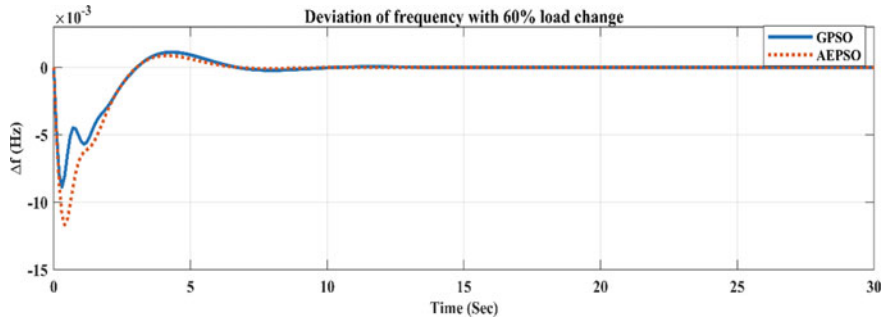


Fig. 6 Frequency deviation with 50% load change



**Fig. 7** Frequency deviation with 60% load change

like improved steady-state and transient response specifications are attained when AEPSO is proposed compare to GPSO.

## 7 Conclusion

In this work, load frequency control using a new approach AEPSO has been suggested. Here, a single area isolated non-reheat realistic power system is considered. The proposed approach optimizes PID controller settings. To achieve optimized PID settings, ISE is used as an objective function. In order to obtain more accurate LFC design, real security constraint GDB is contemplated. To express the excellence and robustness of proposed design, results of AEPSO are compared with GPSO. The simulation results demonstrate that AEPSO is more robust for wide variation of load. AEPSO produces improved transient and steady-state performances such as lower value of  $t_s$ ,  $M_p$ , and SSE compare to GPSO on 10–60% alteration in the power demand caused by step loads perturbation. For further progress of this work, few FACTS devices can be considered to make the system more stable. Similarly, several detection scheme for cyber-physical attacks may be used on LFC and necessary steps can be taken to improve the power quality of the system.

## References

1. Kundur P (1994) Power system stability and control. USA, McGraw-Hill Education, New York
2. Ali ES, Abd-Elazim SM (2013) BFOA based design of PID controller for two area load frequency control with nonlinearities. *Int J Electr Power Energy Syst* 51:224–231
3. Khodabakhshian A, Edrisi M (2008) A new robust PID load frequency controller. *Control Eng Pract* 16:1069–1080
4. Ali T, Malik SA, Hameed IA, Daraz A, Mujlid H, Azar AT (2022) Load frequency control and automatic voltage regulation in a multi-area interconnected power system using nature-inspired computation-based control methodology. *Sustainability* 14:12162

5. Rahmani M, Sadati N (2012) Hierarchical optimal robust load frequency control for power systems. *IET Gener Transm Distrib* 6:303–312
6. Bevrani H, Hiyama T (2009) On load-frequency regulation with time delays: design and real-time implementation. *IEEE Trans Energy Convers* 24:292–300
7. Zhang C, Jiang L, Wu QH, He Y, Wu M (2013) Delay-dependent robust load frequency control for time delay power systems. *IEEE Trans Power Syst* 28:2192–2201
8. Pain S, Acharjee P (2017) Tuning of PID controller for realistic load frequency control system using chaotic exponential PSO algorithm. *Int J Eng Technol (IJET)* 8(6)
9. Uma Mageswaran S, Guna Sekhar NO (2013) Reactive power contribution of multiple STATCOM using particle swarm optimization. *Int J Eng Technol* 5:122–126
10. Bhatt P, Ghoshal SP, Roy R (2010) Load frequency stabilization by coordinated control of thyristor controlled phase shifters and superconducting magnetic energy storage for three types of interconnected two-area power systems. *Int J Electr Power Energy Syst* 32:1111–1124
11. Zare K, Hagh MT, Morsali J (2015) Effective oscillation damping of an interconnected multi-source power system with automatic generation control and TCSC. *Int J Electr Power Energy Syst* 65:220–230
12. Veerasamy V, Abdul Wahab NI, Ramachandran R, Vinayagam A, Othman ML, Hizam H, Satheeshkumar J (2019) Automatic load frequency control of a multi-area dynamic interconnected power system using a hybrid PSO-GSA-tuned PID controller. *Sustainability* 11:6908
13. Chen S, Xu Z, Tang Y, Lee S (2014) An improved particle swarm optimization algorithm based on centroid and exponential inertia weight. *Math Probl Eng* 2014:1–14
14. Jianxin WU, Wenzhi L, Weiguo Z, Qiang LI (2008) Exponential type adaptive inertia weighted particle swarm optimization algorithm. In: Proceedings of second international conference on genetic and evolutionary computing, pp 79–82
15. Sahu RK, Panda S, Rout UK, Sahoo DK (2016) Teaching learning based optimization algorithm for automatic generation control of power system using 2-d of PID controller. *Int J Electr Power Energy Syst* 77:287–301
16. Gupta DK, Jha AV, Appasani B, Srinivasulu A, Bizon N, Thounthong P (2021) Load frequency control using hybrid intelligent optimization technique for multi-source power systems. *Energies* 14:1581
17. Raju M, Saikia LC, Sinha N (2016) Automatic generation control of a multi-area system using ant lion optimizer algorithm based PID plus second order derivative controller. *Int J Electr Power Energy Syst* 80:52–63
18. Dash P, Saikia LC, Sinha N (2015) Automatic generation control of multi area thermal system using bat algorithm optimized PD–PID cascade controller. *Int J Electr Power Energy Syst* 68:364–372
19. Dahiya P, Sharma V, Naresh R (2015) Solution approach to automatic generation control problem using hybridized gravitational search algorithm optimized PID and FOPID controllers. *Adv Electr Comput Eng* 15:23–34
20. Sahu RK, Panda S, Padhan S (2015) A hybrid firefly algorithm and pattern search technique for automatic generation control of multiarea power systems. *Int J Electr Power Energy Syst* 64:9–23
21. Wang GG, Deb S, Coelho LDS (2015) Elephant herding optimization. In: 2015 3rd International symposium on computational and business intelligence (ISCBI), pp 1–5
22. Grover H, Verma A, Bhatti TS (2020) Load frequency control automatic voltage regulation for a single area power system. In: 2020 IEEE 9th power India international conference (PIICON), pp 1–5. <https://doi.org/10.1109/PIICON49524.2020.9112902>
23. Astrom KJ, Hang CC, Person P, Ho WK (1992) Towards intelligent PID control. *Automatica* 28(1):1–9
24. Basilio JC, Matos SR (2002) Design of PI and PID controllers with transient performance specification. *IEEE Trans Educ* 45(4):364–370
25. Hang CC, Astrom KJ, Ho WK (1991) Refinements of Ziegler–Nichols tuning formula. *IEE Proc-D* 138(2):111–118

26. Mudi RK, Dey C, Lee TT (2008) An improved auto-tuning scheme for PI controllers. *ISA Trans* 47(1):45–52
27. Gaing Z-W (2004) A particle swarm optimization approach for optimum design of PID controller in AVR system. *IEEE Trans Energy Convers* 19(2)

# Bilayer Graphene Nanoribbon Transistor for Butane Gas Detection



S. K. Tripathy, J. K. Singh, and G. M. Prasad

**Abstract** Bilayer graphene nanoribbon field effect transistor (BLGNRFET) is simulated, and target molecule was adsorbed in between two graphene layers. BLGNFET device is very new technique and found to be best alternative of the GNRFET device. We have computed the current ( $I$ )-voltage ( $V$ ) characteristics of the proposed device using first-principle calculation. Further, we have calculated the density of states (DOS),  $V$ - $I$  curve, transmission spectra and analysed the performance of BLGNRFET device in presence of butane gas.

**Keywords** ATK VNL · DFT · Graphene nanoribbon · CMOS

## 1 Introduction

Scaling of MOSFET has already reached to nanometre range, and furthermore, scaling will lead to dominate short channel effect (SCE). Therefore, most of researchers are in search of new material technology overcome this issue. Among them, new material technology is easiest technology to overcome the mentioned problem [1]. New emerging technologies includes 2D material transistor, tunnelling transistor, piezoelectric transistor, ferroelectric transistor, and many more. Out of them, graphene-based field effect transistor is turn out to be most interesting device to overcome short channel effect. Nowadays, demand of the sensor device for detection of toxic gases has increased rapidly with the introduction of Internet of things (IOT). These gas sensors are being used in many industries including chemical industry, mining industry, food industry, and so on. Butane is one of two saturated hydrocarbons (alkanes) in the paraffin class having the chemical formula  $C_4H_{10}$ . Carbon

---

S. K. Tripathy (✉)

National Institute of Technology Silchar, Silchar, Assam, India  
e-mail: [sktripathy@ece.nits.ac.in](mailto:sktripathy@ece.nits.ac.in)

J. K. Singh · G. M. Prasad

Intelligent Mining Systems, CSIR-Central Institute of Mining and Fuel Research, Barwa Road, Dhanbad, India

atoms are connected in an open chain in both molecules. The carbon atoms in n-butane (normal) form a side branch, whereas in i-butane (iso), the chain is continuous and unbranched [2]. Graphene-based transistor could be the best candidate for biosensing application in terms of sensitivity and selectivity as compared to solid-state sensor device. Gate voltage controls the electric current flow through the graphene sheet for biosensing application. Target molecules adsorption affects the charge carrier concentration of the graphene sheet and because of which device current changes at constant gate voltage. Some target molecules act as a donor carrier concentration and increases the drain to source current since it is a depletion type n-channel field effect transistor. Similarly, some target molecules act as an acceptor carrier concentration which reduces the drain to source current because of reduced charge carrier in the channel [3]. Variation in drain to source current is used for calculating the sensitivity of the device. Bilayer graphene nanoribbon field effect transistor (BLGNRFET) has been introduced to detect the target molecule. Furthermore, in this paper, sensitivity is computed of bilayer graphene nanoribbon field effect transistor devices.

In Sect. 2, computational methodology used in the entire work has been discussed. Result and discussion explained in detail in Sect. 3. The conclusion of the work is discussed in Sect. 4.

## 2 Computational Details

Quantum Atomistix Toolkit (ATK) Virtual NanoLab (VNL) software version 2016.2 has been used for the simulation of BLGNRFET. We have used extended Huckel approximation within density functional theory (DFT) to optimization of the device property. We have computed the density of states (DOS), IV-curve, band structure, transmission spectrum of the proposed device structure in presence, and absence of target molecule. We have taken k-point sampling and density mesh cut-off are as  $1 \times 1 \times 5$  and 10 Hartree, respectively. We have optimized nitrogen-doped graphene nanoribbon field effect transistor the device with the dimension as depicted in Table 1 and shown in Fig. 1 in presence of butane gas in ATK VNL software.

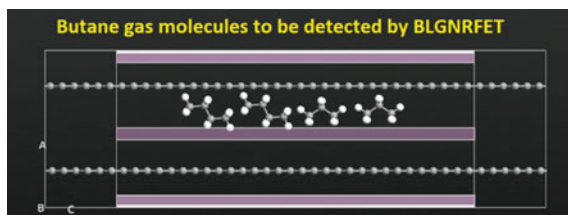
## 3 Results and Discussion

### 3.1 Density of States in Presence of Butane Gas Molecule

Density of states (DOS) represent the number of different orbitals at a given energy levels which is representing the number of electrons present energy level. In other words, DOS is number of electron level states per unit energy per unit volume. It gives the user a clear idea of charge carrier concentration and energy

**Table 1** Parameters used in the simulation of nitrogen-doped graphene nanoribbon field effect transistor

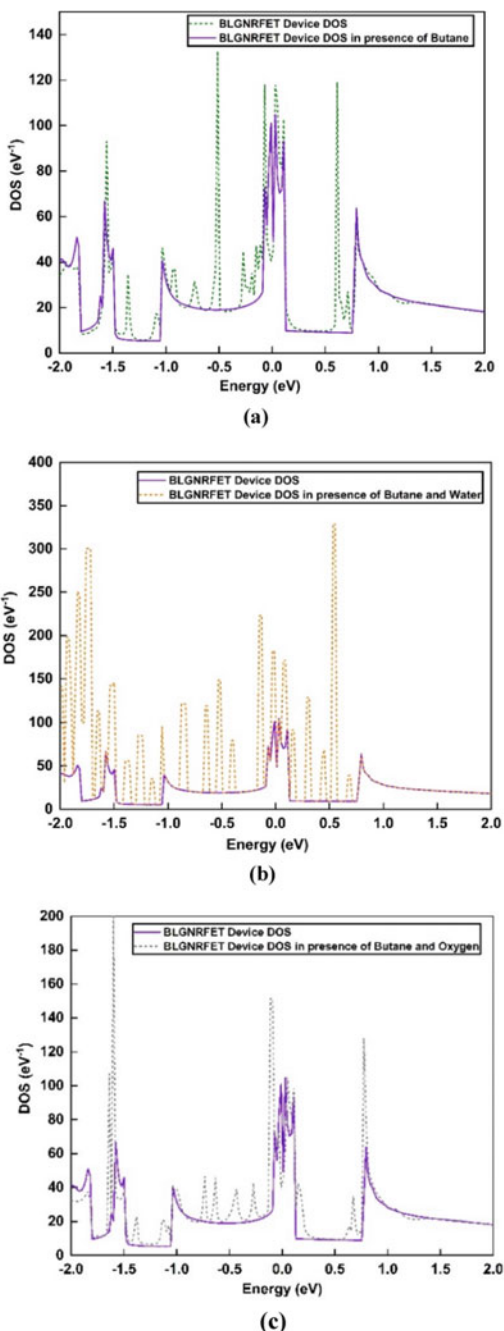
S. No	Parameters	Value
1	Source concentration	$10^{18} \text{ cm}^{-3}$
2	Drain concentration	$10^{18} \text{ cm}^{-3}$
3	Channel concentration	$10^{19} \text{ cm}^{-3}$
4	Channel length	35 nm
5	Dielectric constant	$4\epsilon_0$
6	Gate–source voltage	0 V, -10 V, and -20 V
7	Drain–source voltage	0 V to -1 V (variable)
8	Bandgap of channel (Armchair) region at 0 V	0 eV
9	Bandgap of channel (Armchair) region at -10 V	0.066 eV
10	Bandgap of channel (Armchair) region at -20 V	0.140 eV

**Fig. 1** Bilayer graphene nanoribbon-based field effect transistor for the detection of butane gas molecules

level at every orbital of charge carrier inside the crystal. In this paper, we have computed the density of states for bilayer graphene nanoribbon field effect transistor and compare the results between device in absence and presence of target molecules. A comparison of DOS has been computed between FET device in absence of target molecule and presence of three butane molecule is shown in Fig. 2a. From Fig. 2a, we can clearly see that many new energy levels have been generated by the butane gas molecules in comparison of FET device energy levels. New energy levels are generated below and above of fermi energy level located at 0 eV. From Fig. 2a, clearly new energy levels can be seen in presence of three butane molecule at -1.5 eV, -0.75 eV, -1 eV, -0.5 eV, -0.68 eV, and 0.76 eV.

Further, we have also computed the DOS of FET device in presence of water molecules to find out the atmospheric effect on the simulated FET device. Effect of atmospheric gas can play a vital role in building biosensor device. From Fig. 2b, many new energy levels have been introduced in the DOS versus energy graph below and above of fermi energy levels at -1.6 eV, -1.1 eV, -1.0 eV, -0.53 eV, -0.3 eV, -0.8 eV, 1.19 eV, and 1.9 eV. Similarly, combination of butane and oxygen is also exposed to the BLGNRFET device as shown in Fig. 2c. These new energy levels will

**Fig. 2** Density of states of bilayer graphene nanoribbon FET at  $-20$  V gate-source voltage in the presence of **a** butane molecule, **b** butane and water molecule, **c** butane and oxygen molecule



change the electric current concentration of the device. These DOS will be helpful in detecting the target molecule as there will be change in the device current–voltage characteristics which is used as a parameter for the detection of hazardous gases present in the environment.

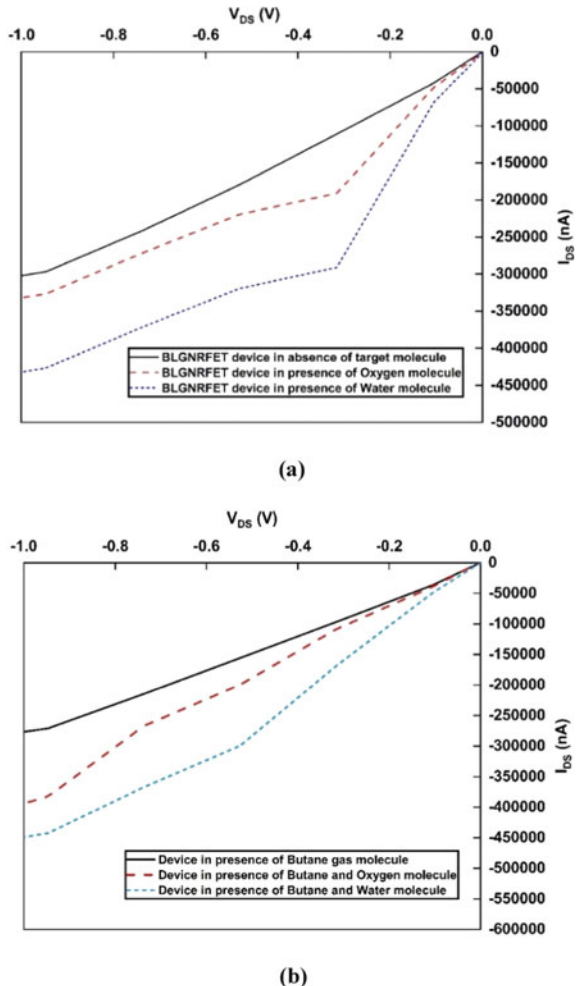
### **3.2 Current (*I*)-Voltage (*V*) Characteristics of BLGNRFET Device in Presence of Oxygen and Water Molecules**

Our proposed FET device is exposed to oxygen gas and water molecule in presence and absence of butane gas. To find out the effect of such gases to our FET device, we have also computed the *V*–*I* characteristics of combination of such gases. Because such gases present in the atmosphere cannot be ignored. Two oxygen molecules have been exposed to the device, and similarly, two water molecules have been exposed too.

Figure 3a shows the *V*–*I* curve of device in absence of target butane molecules. The effect of oxygen and water molecules is shown in Fig. 3a. Our device current varies from  $-50,000$  nA to  $-30,000$  nA at fixed  $-20$  V of gate-source voltage shown in the Fig. 3a. An increase in drain current has been observed when two oxygen gas molecules adsorbed on the graphene sheet of the device and drain current of the device changed significantly from  $-150,000$  nA to  $-290,000$  nA shown in red short, dashed line which means that oxygen gas molecule act like donor carrier concentration to the device and enhanced the current of the device. Similarly, significant increase in the drain can be seen from Fig. 3a when two water gas molecules adsorbed on the device. Drain current of the device changed from  $-290,000$  nA to  $-430,000$  nA approximately shown in blue dotted line.

Further, in this paper, we have computed the drain-source electric current as a parameter for detection of various target molecule at  $-20$  V gate-source voltage. Drain current vs drain-source voltage graph has been plotted for the comparison of the device. We have plotted our graph for drain-source voltage of range  $0$  V to  $-1$  V at constant gate-source voltage of  $-20$  V. Furthermore, we have plotted the *V*–*I* curve of the device in the absence of target molecule at constant gate-source voltage of  $-20$  V. In depletion type n-channel FET device, channel is already present in the device. Since it is a n-channel FET, threshold voltage will be negative for this device. Device will conduct current when gate-source voltage is greater than threshold voltage of the device. We have applied varied the gate-source voltage from  $0$  V to  $-1$  V and found that drain-source current keeps on decreasing with increase of negative gate-source voltage. When negative gate-source voltage is applied to the device, then negative gate field will attract the majority charge carrier from the p-type substrate and since n-channel device have electrons in majority, a recombination of electron–hole will take place and reduces the number of free charge carrier concentration in the device. More is the negative gate-source voltage, lesser will be the drain-source current of the device. Decrease in the drain current with the increase of negative gate-source

**Fig. 3**  $I_D - V_{DS}$  curve of bilayer graphene nanoribbon FET at  $-20$  V gate-source voltage in the presence of **a** only water and oxygen molecule, **b** butane, oxygen, and water molecule



voltage is shown in Fig. 3b. In this paper, this change in the electric current is used to detection of various hazardous gases. Our device current varies from  $-50,000$  nA to  $-280,000$  nA at fixed  $-20$  V of gate-source voltage shown in the Fig. 3b. A decrease in drain current has been observed when butane gas molecules adsorbed on the graphene sheet of the device and drain current of the device changed significantly from  $-46,000$  nA to  $-260,000$  nA shown in blue dotted line which means that butane gas molecule act like acceptor carrier concentration to the device and reduced the current of the device. Further, we have calculated the sensitivity using the relationship  $I = I_{DS} \text{ (Device in the presence of target molecule)} / I_{DS} \text{ (Device in the absence of target molecule)}$  keeping  $V_{GS}$  and  $V_{DS}$  constant and listed in Table 2.

**Table 2** Sensitivity of bilayer graphene nanoribbon in presence of target molecules

S. No	Target molecule	Sensitivity
1	Oxygen	1.18
2	Water	1.66
3	Butane	1.35
4	Propane	1.38
5	Butane and oxygen	1.48
6	Butane and water	1.69
7	Propane and oxygen	1.02
8	Propane and water	1.29
9	Butane and propane	4.15

## 4 Conclusion

In this paper, we have checked the capability of BLGNRFET for biosensing application to detect butane molecules. Apart from that, we have tried to detect butane gas with atmospheric gases like oxygen and water molecule. We have computed sensitivity of oxygen, and water molecules might affect the graphene sheet which might result in changing the drain-source current of the device. To get the correct reading of the biosensor device, we have computed the simulation with very careful precision to reduce the effect of other atmospheric gases. Our device can become a good replacement of silicon-based CMOS device in upcoming future because of very small size, high electrical properties, and high mobility. Theoretically, it is possible to simulate such type of FET sensors. We have observed the better results than [4]. This device could be best alternative of GNRFET as well as CMOS-based device.

**Acknowledgements** The authors are thankful to CSIR, New Delhi, Government of India for grant under Extra Mural Research-II scheme (File No. 70(0076)/19/EMR-II).

## References

1. Rashid MH, Koel A, Rang T (2019) First principles simulations of phenol and methanol detector based on pristine graphene nanosheet and armchair graphene nanoribbons. Sensors (Switzerland) 19(12)
2. Latif U, Dickert FL (2015) Graphene hybrid materials in gas sensing applications. Sensors (Switzerland) 15(12):30504–30524
3. Johnson AP, Sabu C, Swamy NK, Anto A, Gangadharappa HV, Pramod K (2021) Graphene nanoribbon: an emerging and efficient flat molecular platform for advanced biosensing. Biosens Bioelectron 184:113245
4. Rashid MH, Koel A, Rang T (2020) Simulations of graphene nanoribbon field effect transistor for the detection of propane and butane gases: a first principles study. Nanomaterials 10(1)

# Prediction of Far-Field Profile in Optical Kerr Type Nonlinear Triangular Index Profile Fiber of LP<sub>11</sub> Mode Using Simple and Accurate Chebyshev Technique



Kushal Roy, Tilak Mukherjee, and Angshuman Majumdar

**Abstract** In this paper, we present the variation of far-field profile with the angle of view taking into consideration Kerr type practical nonlinear triangular index fiber profile using a very simplified power series expansion method; also known as Chebyshev technique. We restrict our analysis typically for the first higher order LP<sub>11</sub> mode. We have performed the estimation for both linear as well as nonlinear cases and we present the comparative result both graphically as well as in tabular form. Furthermore, we compare our results with the lengthy and cumbersome finite element method to establish the accuracy of our findings and validate our outcomes. As far field is a very important fiber parameter, frequently needed by system designers and field engineers; our simple and accurate technique surely is expected to be of great assistance for them.

**Keywords** Kerr nonlinearity · Dual-mode fiber · Chebyshev technique · Far-field pattern

## 1 Introduction

Optical fibers are emerged as the most efficient type of communication device due to its vast bandwidth and low loss [1]. A most fundamental kind of optical fiber includes a thin cylindrical homogeneous dielectric core that is surrounded in a second coaxial homogeneous dielectric cladding that has a “refractive index” that is marginally less than the core’s. This uncomplicated fiber type is known as step index fiber. Therefore, the fiber core could have an uneven refractive index. Additionally, a fiber might have

---

K. Roy (✉) · T. Mukherjee

Department of Electronics and Communication Engineering, Haldia Institute of Technology, Haldia, West Bengal, India  
e-mail: [kushalroy1979@gmail.com](mailto:kushalroy1979@gmail.com)

A. Majumdar

Department of Electronics and Communication Engineering, Brainware University, Barasat, Kolkata, West Bengal, India

more than one cladding in some circumstances [2]. The corresponding refractive index (r.i) values of the core and cladding region of the optical fiber are narrowly different because the core is constructed of silica, which is widely available, and is doped with appropriate elements like  $\text{GeO}_2$ . Over 20 dB/km of attenuation loss was experienced in silica-composed optical fiber [3]. In the years that followed, technology in this area made considerable strides, allowing attenuation loss to be managed to the tune of 0.15 dB/km at the specific wavelength of  $1.55 \mu\text{m}$  and about 0.35 dB/km at the wavelength of  $1.3 \mu\text{m}$  spectral region. Continuous efforts are being taken to reduce attenuation losses in fibers. Additionally, around the wavelength of  $1.3 \mu\text{m}$ , the material dispersion of optical fiber constructed of silica disappears. To concurrently achieve the lowest possible attenuation loss and material dispersion, wireless signals using silica-made optical fibers are typically operated in the wavelength ranging from  $(1.3\text{--}1.6) \mu\text{m}$ . Different modes in the fiber propagate as a result of optical pulses carrying information across an optical fiber [4, 5]. The aforementioned modes were discovered by using Maxwell's electromagnetic equations to properly analyze optical pulse propagation in a fiber [6]. A mode is a transverse distribution of electromagnetic field that has a set group velocity, a set propagation constant, and a set polarization state. Once more, single-mode fiber is the term for a fiber that only permits the propagation of the basic mode. Multimode fiber is a term used to describe a fiber that propagates multiple modes [7]. The core diameter of single-mode fiber is typically  $5\text{--}10 \mu\text{m}$ , while that of multimode fiber is approximately  $50 \mu\text{m}$ . However, each type of fiber has an outside diameter of about  $125 \mu\text{m}$  [8]. Furthermore, it has been demonstrated successfully that dual-mode optical fiber is important for optical fiber communication systems [9]. Positive dispersion can be eliminated by using the dual-mode optical fiber's first higher order mode, which has a considerable negative waveguide dispersion associated with it. Since the operational wavelength of an erbium-doped fiber amplifier is  $1.55 \mu\text{m}$ , this type of dispersion corrected dual-mode optical fiber can be created for that wavelength. Optical pulses are used to transmit data over the optical fiber. The propagation process excites a variety of modes [10]. A mode is a particular transverse electric or magnetic field with a fixed propagation constant and a fixed polarization state. The electric and magnetic vectors associated with a mode must therefore be found by solving Maxwell's equations while taking into account the pertinent boundary conditions. Furthermore, the core-cladding refractive index difference of graded index fibers utilized in communication technology is quite modest. Scalar wave equations can be used to estimate electromagnetic vector wave equations for certain weakly guiding fiber types [11]. Weakly guiding approximations are what this is. Additionally, it is discovered that parameters assessed using the scalar wave equation and those calculated using the vector wave equation only slightly differ. The results based on the weakly guided approximation demonstrate that the linearly polarized modes in those fibers have a minimal longitudinal component. There are written analytical solutions to the scalar wave equation for step index fiber. But when it comes to other types of fibers, either variation or numerical methods are used to identify the answers to the scalar wave equations [10]. Once more, even when analytical solutions are available, the estimations of the pertinent propagation constants are very difficult since the integrands contain Bessel

functions or modified Bessel functions. The single parameter variation method adds straightforward analysis but is inaccurate. The two parameter variation technique provides accurate estimations of the modal field, but it necessitates significant calculations. It is to be noted that graded index profile fiber propagation characteristics for the whole single-mode region, including the low V zone, can be accurately estimated by using a variation technique employing the Gaussian-exponential-Hankel function. This approach calls for much computation, though. Therefore, it is crucial to create straightforward yet precise equations for the modal fields for both fundamental and higher order modes connected to various types of fibers. The defined formalism must be executed in a user-friendly manner [12]. This simple and accurate user-friendly technique has successfully predicted various fiber parameters like confinement and excitation in various graded index single-mode fibers taking into account linear case as well as with Kerr nonlinearity effect [13], particularly pattern of far field in dispersion managed Kerr type nonlinear optical fibers for LP<sub>11</sub> mode [14]. Since triangular index practical Kerr type nonlinear single-mode fibers have a higher bandwidth as compared to parabolic and step index fiber; it motivates us to use this formalism in determining a very important fiber parameter which is the far-field profile.

## 2 Theory

The expression for the refractive index (r.i) profile in a weakly steered fiber with a circular core is

$$n^2(R) = \begin{cases} (n_1^2)(1 - 2\delta f(R)), & \text{for } R \leq 1 \\ (n_2^2), & \text{for } R > 1 \end{cases} \quad (1)$$

Here,  $R = (r/a)$ ,  $\delta$  = relative r.i difference, and also core radius =  $a$ ,  $f(R) = (R^q)$ ; where exponent term  $q$  can have different values depending upon the nature of the fiber profile.

Since our prime focus is on triangular index fibers; in our work we have taken the value of  $q$  to be 1.

For practical Kerr type nonlinear fibers; the r.i expression (denoted by  $n(R)$ ) is given as,

$$n^2(R) = n_L^2(R) + \left\{ \frac{n_2^2}{\eta_0} n_{NL}(R) \Psi^2(R) \right\} \quad [15] \quad (2)$$

where  $n_L(R)$  is the corresponding linear region value of the refractive index and also  $n_{NL}(R)$  represents the nonlinear Kerr coefficient having the unit (in terms of m<sup>2</sup>/W) along with  $(\eta_0) = (\mu_0/\epsilon_0)^{1/2}$ . According to the current literature, linearly polarized (LP) modes are produced by the solution of the complex and tedious vector and scalar mode wave equations for such weakly steered fibers. The modal field for the LP<sub>11</sub> mode satisfies the scalar wave equation and is set to 0, as denoted by [15, 16],

$$\frac{d^2\psi(R)}{dR^2} + \frac{1}{R} \frac{d\psi(R)}{dR} + (X + Y) = 0 \quad (3)$$

The terms  $X$  and  $Y$  imply,  $X = [V^2\{1 - f(R)\} - W^2]\psi(R) - \frac{\psi(R)}{R^2}$ ;  $Y = V^2g(R)\psi^2(R)$

Also,  $g(R) = \frac{n_2 n_{NL} P}{\pi a^2(n_1^2 - n_2^2)}$  where;  $P$  = optical power,  $n_1$  and  $n_2$  the r.i values for core and cladding respectively, along with other usual terms as stated earlier. The boundary value condition considered satisfies

$$\frac{1}{\Psi} \frac{d\Psi}{dR} = - \left\{ 1 + \left( \frac{W K_0(W)}{K_1(W)} \right) \right\} \text{ at } R = 1 \quad [16] \quad (4)$$

where  $V$  represents the normalized frequency,  $W$  is the cladding decay parameter [17]. The LP<sub>11</sub> modal field in the core and cladding of a graded index fiber can be described as [17–20] using a power series formulation based on the Chebyshev formalism.

$$\begin{aligned} \Psi(R) &= [(a_1 R) + (a_3 R^3) + (a_5 R^5)] \quad \text{for } R \leq 1 \\ &= [(a_1 + a_3 + a_5)] \quad K_1(WR) \quad \text{for } R > 1 \\ &\quad K_1(W) \end{aligned} \quad (5)$$

When Eq. (5) is applied to Eq. (3), the expression obtained is

$$\begin{aligned} a_1 \{V^2(1 - f(R)) - W^2 + V^2g\varphi^2(R)\} \\ + a_3 \{8 + R^2[V^2(1 - f(R)) - W^2 + V^2g\varphi^2(R)]\} \\ + a_5 \{24(R^2) + (R^4)[(V^2)(1 - f(R)) - W^2 + V^2g\varphi^2(R)]\} = 0 \end{aligned} \quad (6)$$

We have taken into account the “2” distinct Chebyshev points (CP) for the respective  $R$  using Eq. (7), and we have expressed “ $a_3$ ”, “ $a_5$ ” in terms of “ $a_1$ ”.

$$R_m = \cosine \left( \left( \frac{2m-1}{2M-1} \right) \frac{\pi}{2} \right) \text{ for } m = (1, 2, 3 \dots (M-1)) \text{ terms} \quad (7)$$

For  $i = 1, 2$  as the value of  $R_i$ , 0.9511 and 0.5878 are obtained with  $M = 3$ . These CP values are further used in aforementioned Eq. (6) to as to get the two (2) distinct equations in terms of  $R_i$  that are mentioned in the literature [21, 22]. The values are determined to be (1.034623 and 0.3890323) respectively. Previous research has shown that the ratio of  $K_1(W)$  with respect to  $K_0(W)$  fluctuates linearly with  $W-1$  within the range from 0.6 to 2.5 [21]. As a result, the least square (LS) line fitting approach is applicable within the aforementioned range.

$$\frac{K_1(W)}{K_0(W)} = \left[ \alpha + \left\{ \frac{\beta}{W} \right\} \right] \quad (8)$$

Equations (5) and (8) in Eq. (4) are also used to derive

$$\begin{aligned} & a_1 \{2(\alpha W + \beta) + W^2\} + a_3 \{4(\alpha W + \beta) + W^2\} \\ & + a_5 \{6(\alpha W + \beta) + W^2\} = 0 \end{aligned} \quad (9)$$

The coefficients;  $a_1$ ,  $a_3$  and  $a_5$  as obtained in Eqs. (6) and (9) will have a “nontrivial solution” [17, 19–21] provided

$$\begin{vmatrix} A_1 & B_1 & C_1 \\ A_2 & B_2 & C_2 \\ A_3 & B_3 & C_3 \end{vmatrix} = 0 \quad (10)$$

where for  $i = 1, 2$

$$A_i = \{V^2(1 - f(R_i)) - W^2 + V^2g\Psi^2(R_i)\}.$$

$$B_i = [8 + R_i^2 \{V^2(1 - f(R_i)) - W^2 + V^2g\Psi^2(R_i)\}]$$

$$C_i = [24R_i^2 + R_i^4 \{V^2(1 - f(R_i)) - W^2 + V^2g\Psi^2(R_i)\}]$$

$$A_3 = \{2(\alpha W + \beta) + W^2\}; B_3 = \{4(\alpha W + \beta) + W^2\}; C_3 = \{6(\alpha W + \beta) + W^2\}$$

Due to the term  $\Psi^2(R)$ , the determinant stated in Eq. (10) is difficult to solve. As a result, in order to simplify the computation, we start by considering the linear situation with  $g(R)$  initially set to 0, and then calculate the respective  $W$  values for each  $V$ . Using the  $W$  values that were previously acquired for the linear case, we compute the values of  $a_3$  and  $a_5$  in the subsequent step. For any nonlinearity value of  $g(R)$  considered and respective  $V$ , the iterative technique is utilized until  $W$  values are achieved at convergence, after which the values of  $a_3$  and  $a_5$  are easily determined in terms of  $a_1$  to take into account the existence of Kerr nonlinearity. Further to add,  $A_3$  and  $A_5$  are the normalized versions of  $a_3$  and  $a_5$ , and they can be simply rewritten as  $A_3 = a_3/a_1$  and  $A_5 = a_5/a_1$ , respectively [23].

Thus the field in core and cladding is given by

$$\begin{aligned} \Psi(R) &= a_1[(R) + A_3R^3 + A_5R^5], \quad \text{when } R \leq 1, \\ &= a_1(1 + A_3 + A_5)K_1(WR)/K_1(W), \quad \text{when } R \geq 1 \end{aligned} \quad (11)$$

The appropriate far field for the optical fiber’s cylindrically symmetric structure is given as,

$$u(\theta) = (2\pi C) \int_0^\infty \Psi(R) J_0(K_0 a R \sin \theta) R dR \quad (12)$$

In this equation, “ $C$ ” stands for a constant, while “ $k_0$ ” is utilized to represent the free space wave number. The angle between the axis of core and measurement direction is depicted by  $\theta$  [22, 25].

$$\begin{aligned} \frac{u(\theta)}{2\pi C} = & \frac{A_1}{B^3} [2BJ_0(B) + (4 - B^2)J_1(B) - 2BJ_2(B)] \\ & + \frac{A_3}{B^5} \left[ 2B^3 J_0(B) + \left( 12B^2 - \frac{B^4}{3} - 32 \right) J_1(B) \right. \\ & \left. + 2B^3 J_2(B) \right] + \frac{A_5}{B^7} \left[ (2B^5 - 8B^3) J_0(B) \right. \\ & \left. + \left( \frac{2}{15} B^6 + \frac{16}{3} B^4 + 8B^2 + 128 \right) J_1(B) + (2B^5 + 8B^3) J_2(B) \right] \\ & - \frac{(A_1 + A_3 + A_5)}{(B^2 + W^2) K_1(W)} [BK_1(W) J_1(B) - W\{(K_2(W) J_0(B))\}] \end{aligned} \quad (13)$$

$$B = k_0 a \sin \theta, \quad A_1 = a_1/a_1 = 1 \quad (14)$$

Putting  $\theta = 0$ ;  $u(0)$  is obtained as below [22, 25, 26].

$$u(0) = 2\pi C \left[ -2 \frac{A_1}{3} - 4 \frac{A_3}{5} - 6 \frac{A_5}{7} \right] \quad (15)$$

The modified Bessel function  $K_i$  and the Bessel function  $J_i$  are both used in the aforementioned expression found in Eq. (13) [24–26].

Therefore, the normalized intensity values of far field are given by

$$I(\theta) = \left| \frac{u(\theta)}{u(0)} \right|^2 \quad (16)$$

### 3 Results and Discussions

Plotting  $I(\theta)$  versus  $B (= K_o a \sin \theta)$  for various  $V$  number ranges for the case of triangular r.i profile fiber while taking into account both linear and nonlinear scenarios allows us to confirm the veracity of our formalism. We have typically chosen the positive and negative variety kinds of nonlinearity values ( $n_{NL}P$ ) as “ $+ 1.5 \times 10^{-14}$  m<sup>2</sup> and  $-1.5 \times 10^{-14}$  m<sup>2</sup>” respectively, in order to account for the “Kerr nonlinearity” impact in our research [17]. Accordingly, Figs. 1, 2 and 3 shows the “far-field pattern” for triangular r.i profile fibers with  $V = 4.5, 5.0$ , and  $5.5$  using our recommended formalism.

For easier comprehension, the pertinent values for Figs. 1, 2 and 3 are presented in Tables 1, 2 and 3, taking the identical optical fiber specifications into account.

**Fig. 1** Variation in the triangular type refractive index profile fiber's "far-field intensity with  $B (= k_0 a \sin)$ " when  $V$  is set to 4.5. (Obtained results are displayed as follows "▲ for linear case, ■ for  $n_{NL}P = + 1.5 \times 10^{-14} m^2$ " ● for " $n_{NL}P = - 1.5 \times 10^{-14} m^2$ " with solid lines denoting the precise simulation results)

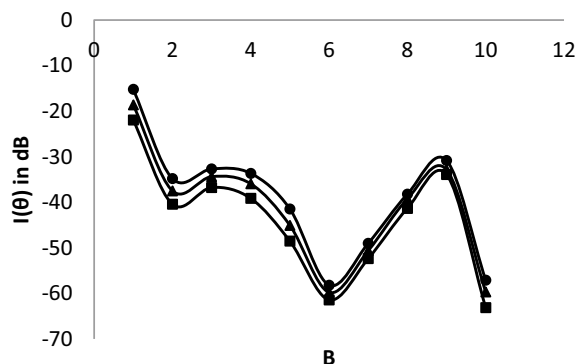


**Fig. 2** Variation in the triangular type refractive index profile fiber's "far-field intensity with  $B (= k_0 a \sin)$ " when  $V$  is set to 5.0. (Obtained results are displayed as follows "▲ for linear case, ■ for  $n_{NL}P = + 1.5 \times 10^{-14} m^2$ " ● for " $n_{NL}P = - 1.5 \times 10^{-14} m^2$ " with solid lines denoting the precise simulation results)

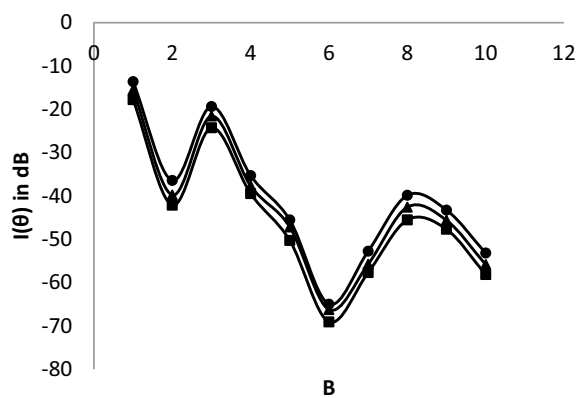
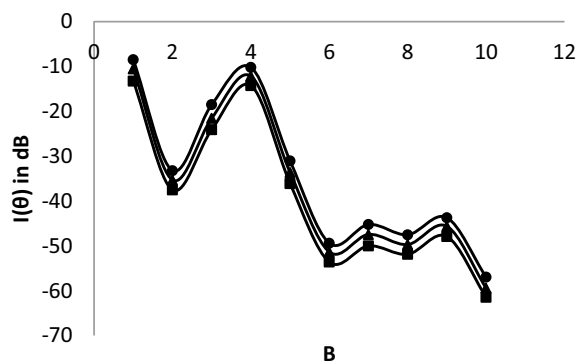


**Fig. 3** Variation in the triangular type refractive index profile fiber's "far-field intensity with  $B (= k_0 a \sin)$ " when  $V$  is set to 5.5. (Obtained results are displayed as follows "▲ for linear case, ■ for  $n_{NL}P = + 1.5 \times 10^{-14} m^2$ " ● for " $n_{NL}P = - 1.5 \times 10^{-14} m^2$ " with solid lines denoting the precise simulation results)



We have used the practical values of  $a = 4 \mu\text{m}$  and  $= 1.5 \mu\text{m}$  because the value of " $B$ " depends on " $k_0 \times a$ ". It is also important to note that the nonlinear fiber medium's refractive index, " $n_{NL}(R)$ ", depends on the product of  $n_{NL}$  ( $\text{m}^2/\text{W}$ ) and optical power  $P$  (expressed in Watts). For the purpose of differentiating the linear

**Table 1** Information pertinent to Fig. 1 depicting the relation between  $B$  ( $k_0 a \sin \theta$ ), “ $\theta$ ” and “ $I$ ”; when  $V = 4.5$ 

$B$	$\theta$	$I(\theta)$ “ $n_{NL}P = 0$ ”	$I(\theta)$ “ $n_{NL}P = + 1.5 \times 10^{-14}$ m $^2$ ”	$I(\theta)$ “ $n_{NL}P = -1.5 \times 10^{-14}$ m $^2$ ”
1	3.2416	-18.6215	-21.9627	-15.2265
2	6.8555	-37.4998	-40.4293	-34.8213
3	10.3144	-34.3762	-36.7619	-32.6825
4	13.8117	-35.9445	-39.1544	-33.6575
5	17.3625	-45.0738	-48.5364	-41.4721
6	20.9835	-59.7796	-61.4463	-58.1998
7	24.6946	-50.6144	-52.3749	-49.0087
8	28.5199	-39.2725	-41.3529	-38.2214
9	32.4897	-32.8661	-33.9124	-30.8373
10	36.6433	-59.6878	-63.1324	-57.1093

**Table 2** Information pertinent to Fig. 2 depicting the relation between  $B$  ( $k_0 a \sin \theta$ ), “ $\theta$ ” and “ $I$ ”; when  $V = 5.0$ 

$B$	$\theta$	$I(\theta)$ “ $n_{NL}P = 0$ ”	$I(\theta)$ “ $n_{NL}P = + 1.5 \times 10^{-14}$ m $^2$ ”	$I(\theta)$ “ $n_{NL}P = -1.5 \times 10^{-14}$ m $^2$ ”
1	3.2416	-15.5295	-17.7725	-13.6179
2	6.8555	-39.7726	-42.1137	-36.4262
3	10.3144	-21.5581	-24.2581	-19.3422
4	13.8117	-37.6532	-39.4587	-35.2782
5	17.3625	-47.1525	-50.2647	-45.5264
6	20.9835	-66.2066	-69.0598	-64.9552
7	24.6946	-55.7316	-57.6716	-52.7488
8	28.5199	-42.5672	-45.5156	-39.8446
9	32.4897	-45.6177	-47.6844	-43.2419
10	36.6433	-55.8173	-58.1346	-53.1644

far-field pattern for the LP<sub>11</sub> mode ( $n_{NL}P = 0$ ), positive kind and negative kind of  $n_{NL}P$  accounting for Kerr type nonlinearity, we provide our results in three alternative notations; accordingly these are for  $n_{NL}P = 0$  (implying linear regime),  $n_{NL}P = (\pm) 1.5 \times 10^{-14}$  m $^2$  for the nonlinear regime respectively. Each case’s precise simulated result is depicted by a solid line. In order to investigate and assess the variation of far-field intensity with such nonlinearity as well as without nonlinearity effect, we have accordingly considered the starting  $V$  number to be 4.5; which is very close to the cut-off  $V$  number for the first higher order (LP<sub>11</sub>) mode and is step wise incremented by 0.5 in each case. From Figs. 1, 2 and 3, it can be seen that the pattern for positive type and negative type nonlinearity values emerges as evenly spaced and is almost

**Table 3** Information pertinent to Fig. 1 depicting the relation between  $B$  ( $k_0a \sin \theta$ ), “ $\theta$ ” and “ $I$ ”; when  $V = 5.5$ 

$B$	$\theta$	$I(\theta)$ “ $n_{NL}P = 0$ ”	$I(\theta)$ “ $n_{NL}P = + 1.5 \times 10^{-14} \text{ m}^2$ ”	$I(\theta)$ “ $n_{NL}P = -1.5 \times 10^{-14} \text{ m}^2$ ”
1	3.2416	-10.5366	-13.2421	-8.4783
2	6.8555	-35.3247	-37.5326	-33.2249
3	10.3144	-21.5581	-24.1021	-18.5131
4	13.8117	-12.1664	-14.2551	-10.1976
5	17.3625	-33.6332	-36.1032	-31.0588
6	20.9835	-51.3688	-53.6158	-49.4136
7	24.6946	-47.4656	-50.0124	-45.2466
8	28.5199	-49.7113	-51.8943	-47.5349
9	32.4897	-45.6532	-47.9245	-43.7312
10	36.6433	-59.4358	-61.4781	-56.9853

equally separated about the corresponding values in the linear regimes. The validity of the functional mathematical model in our work is aptly justified.

## 4 Conclusion

The work presented finally leads us to the conclusion that the formalism we projected in this current paper well captures the far-field intensity variation pattern of the LP<sub>11</sub> mode in triangular refractive index profile kind of fiber. Also shown is the typical Kerr kind nonlinearity influence and its overall impact on the far-field intensity variation and its further repercussions. The methodology as implemented is strikingly straightforward and less computationally complex than other methods described in the literature. Researchers and engineers will benefit greatly from the formalism’s simplicity in precisely calculating the concerned far-field intensity profile of optical Kerr kind nonlinear triangular index type of fibers, and other fiber kinds also with fewer computational steps and a subsequent reduction in mathematical complexity.

## References

1. Kareem FQ, Zeebaree SR, Dino HI, Sadeeq MA, Rashid ZN, Hasan DA, Sharif KH (2021) A survey of optical fiber communications: challenges and processing time influences. Asian J Res Comput Sci 48–58
2. Zhang J, Xiang Y, Wang C, Chen Y, Tjin SC, Wei L (2022) Recent advances in optical fiber enabled radiation sensors. Sensors 22(3):1126–1131
3. Borella MS, Jue JP, Banerjee D, Ramamurthy B, Mukherjee B (1997) Optical components for WDM Lightwave networks. Proc IEEE 85(8):1274–1307

4. Chakraborty S, Mandal CK, Gangopadhyay S (2000) Prediction of first higher order modal field for graded index fiber in presence of Kerr nonlinearity. *J Opt Commun* 41(4):385–391
5. Zhu P, Liu P, Wang Z, Peng C, Zhang N, Soto MA (2021) Evaluating and minimizing induced microbending losses in optical fiber sensors embedded into glass-fiber composites. *J Lightwave Technol* 39(22):7315–7325
6. Okamoto K (2021) Fundamentals of optical waveguides. Elsevier
7. Pan W, Chen X, Zhao K (2022) Cable-partial-discharge recognition based on a data-driven approach with optical-fiber vibration-monitoring signals. *Energies* 15(15):5686
8. Zhao Q, Yuan W, Qu J, Cheng Z, Peng GD, Yu C (2022) Optical fiber-integrated metasurfaces: an emerging platform for multiple optical applications. *Nanomaterials* 12(5):793
9. Cheng L, Cigada A, Lang Z, Zappa E, Zhu Y (2021) An output-only ARX model-based sensor fusion framework on structural dynamic measurements using distributed optical fiber sensors and fiber Bragg grating sensors. *Mech Syst Signal Process* 152:107439
10. Chakraborty S, Mandal CK, Gangopadhyay S (2020) Prediction of first higher order modal field for graded index fiber in presence of Kerr nonlinearity. *J Opt Commun* 41(4):385–391
11. Bose A, Gangopadhyay S, Saha SC (2012) Simple method for study of single-mode dispersion-shifted and dispersion-flattened fibers. *J Opt Commun* 33(4):253–258
12. Hosoki A, Nishiyama M, Watanabe K, Sakurai N (2022) Surface Plasmon resonance sensor using a polarization-maintaining fiber on a hetero-core optical fiber structure with gold thin film. *Opt Express* 30(20):35348–35360
13. Roy K, Majumdar A, Gangopadhyay S (2020) A simple but accurate method for estimation of the effect of Kerr nonlinearity on confinement and excitation of the fundamental mode in single mode graded index fiber. *Optik* 216(2020):164939. <https://doi.org/10.1016/j.ijleo.2020.164939>
14. Roy K, Majumdar A, Gangopadhyay S (2022) An accurate but simple method for estimation of the influence of Kerr nonlinearity on the far field pattern of LP<sub>11</sub> mode in dispersion-shifted and dispersion-flattened fibers. *J Opt Commun.* <https://doi.org/10.1515/joc-2022-0050>
15. Sharma AK, Goyal IC, Ghatak AK (1981) Calculation of cutoff frequencies in single mode fibers for arbitrary profiles using the matrix method. *IEEE J Quant Electron* 16:2317–2320
16. Shijun J (1987) Simple explicit formula for calculating LP<sub>11</sub> mode cutoff frequency. *Electron Lett* 23:534–536
17. Mondal SK, Sarkar SN (1996) Effect of optical Kerr effect nonlinearity on LP<sub>11</sub> mode cutoff frequency of single-mode dispersion shifted and dispersion flattened fibers. *Opt Commun* 127:25–30
18. Patra P, Gangopadhyay S, Goswami K (2008) A simple method for prediction of first-order modal field and cladding decay parameter in graded index fiber. *Optik* 119:209–212
19. Chakraborty S, Mandal CK, Gangopadhyay S (2017) Prediction of fundamental modal field for graded index fiber in presence of Kerr nonlinearity. *J Opt Commun.* <https://doi.org/10.1515/joc-2017-0126>
20. Chakraborty S, Mandal CK, Gangopadhyay S (2018) Prediction of first higher order modal field for graded index fiber in presence of Kerr Nonlinearity. *J Opt Commun.* <https://doi.org/10.1515/joc-20170206>
21. Gangopadhyay S, Sarkar SN (1998) Evaluation of modal spot size in single-mode graded index fibers by a simple technique. *J Opt Commun* 19:173–175
22. Mukherjee T, Majumdar A, Gangopadhyay S (2020) Kerr nonlinearity effect on dimensionless scalar and vector propagation constants of single-mode graded index fiber: estimation by a simple but accurate method. In: IEEE international conference on VLSI DCS. MSIT Kolkata, India, pp 253–257
23. Mukherjee T, Marty S, Majumdar A, Gangopadhyay S (2020) A simple but accurate formalism for study of single-mode graded index fiber directional coupler in presence of Kerr nonlinearity. *Optik* 213:64772
24. Abramowitz M, Stegun IA (1981) Handbook of mathematical functions. Dover Publications, New York

25. Gradshteyn IS, Ryzhik IM (1980) Table of integrals, series and products. Academic Press, London
26. Watson GN (1944) A treatise on the theory of Bessel functions. Cambridge University Press, U.K.

# Design and Fabrication of High-Gain Array Antenna for 5G Communication and Wireless Applications



Arun Raj and Durbadal Mandal

**Abstract** Modern communication demands wide bandwidth, high gain, and efficient reduced size antennas to improve performance over a wide bandwidth range of the frequency spectrum. An array antenna with a circular fractal slot of 3 mm and a circular element antenna with ground dimensions of 17.6 mm by 17.6 mm are proposed in this paper. This paper compares the array antenna's performance to other results that achieve better bandwidth with a smaller size. The modified array antenna has an FR-4 substrate with 25 mm width and 25 mm length, a circular slot through which the antenna has a wide bandwidth, and multiple notches near 26.7, 29.6, and 32 GHz. The proposed antenna has a high peak gain of 8.4 dBi. It covers 5G applications in the range of 26–32.5, 34.28–35.1, and 36.7–37.6 GHz. The proposed antenna has three multiple bands, each with a bandwidth of 6.5, 8.2, and 0.4 GHz. The proposed array antenna covers the 5G millimeter-wave bands n257, n258, n260, and n261; it also covers ground-based radio navigation applications. The proposed antenna was implemented successfully using CST.

**Keywords** Array antenna · Patch array · Fractals · Microstrip antenna

## 1 Introduction

Antennas play an important and emerging role in wireless technology [1]. Researchers are working on new technology for antennas' compactness and reliability [2]. The industry demands a low-profile and compact-sized antenna that can be fabricated easily. During the last few years, researchers have been working toward minimizing the size of antennas that cover a wider range of applications [3]. Due to the fractal shape of the antenna, we get multi-band and cover various applications [4],

---

A. Raj (✉) · D. Mandal  
ECE-Department, National Institute of Technology, Durgapur, India  
e-mail: [arunraj61299@gmail.com](mailto:arunraj61299@gmail.com)

D. Mandal  
e-mail: [durbadal.mandal@ece.nitdgp.ac.in](mailto:durbadal.mandal@ece.nitdgp.ac.in)

5]. Multi-band antennas cover more applications in different bandwidths in different bands than were achieved after simulations.

Due to fractal shape slots, a microstrip patch antenna has high gain and follows multi-band characteristics, by which an antenna covers various applications. When using a single antenna, the radiation pattern is broad, but the gain is low. However, the gain and other properties are improved when using a single-element antenna in an array design [4–7]. Circular slots are cut in each array element to create a ring array in each element to form the following array antenna. In the present paper, an array antenna is more efficient than a fractal antenna due to its minimum size, high gain, and wide bandwidth. And, the proposed array antenna covers the n257, n258, n260, and n261 bands that cover a 5G millimeter wave; the proposed antenna covers ground-based radio navigation applications too [8]. And, all results are measured successfully with the vector network analyzer [9–11].

## 2 Numerical Analysis

In microstrip patch antenna design, the following parameters are calculating like width and length of a patch using following mathematical formulae's:

Calculation of width (W): The width of the patch is given by:

$$W = \frac{C}{2f_r \sqrt{\frac{\epsilon_r + 1}{2}}}, \quad (1)$$

where

$c$ —free space velocity of light =  $3 \times 10^8$  m/s.

$f_r$ —frequency of operation,  $\epsilon_r$ —dielectric constant.

Calculation of effective dielectric constant ( $\epsilon_{\text{eff}}$ ): The effective dielectric constant  $\epsilon_r$  is considered by:

$$W = \frac{1}{2f_r \sqrt{\mu \epsilon}} \sqrt{\frac{2}{\epsilon r + 1}} \quad (2)$$

$$\epsilon_{\text{eff}} = \frac{\epsilon r + 1}{2} + \frac{\epsilon r - 1}{2} \left( 1 + 12 \frac{h}{w} \right)^{-\frac{1}{2}} \quad (3)$$

where  $h$ —height of dielectric substrate in mm.

$w$ —width of patch,  $\epsilon_{\text{eff}}$ —dielectric constant.

The effective length is given by:

$$L_{\text{eff}} = \frac{c}{2f_r \sqrt{\epsilon_r}} - 2\Delta L. \quad (4)$$

Once  $W$  is found using Eq. (2) determine the extension of length.

$$\Delta L = h \frac{(\epsilon_{\text{reff}} + 0.3)(\frac{W}{h} + 0.264)}{(\epsilon_{\text{reff}} - 0.258)(\frac{W}{h} + 0.8)} \quad (5)$$

Actual length of patch:

$$L = \left( \frac{1}{2fr\sqrt{\epsilon}} \times \frac{1}{\sqrt{\mu\epsilon}} \right) - 2\Delta L \quad (6)$$

Effective length  $L^1 = L + 6$  h, effective width  $W^1 = W + 6$  h,

$$\text{Band width \%} = \frac{2(f2 - f1)}{f1 + f2} * 100. \quad (7)$$

The feed point position for  $50 \Omega$  can be calculated as:

$$R_{\text{in}}(y = y_0) = R_{\text{in}}(y = 0) \cos\left(\frac{\pi}{L}y_0\right)^2, \quad (8)$$

where  $R_{\text{in}}(y = y_0)$  is  $50 \Omega$  and  $R_{\text{in}}(y = 0)$  is roughly given as:

$$Z_{\text{in}} = 1/Y_{\text{in}} = R_{\text{in}} = 1/2G_1$$

$$G_1 = \begin{cases} \frac{1}{90}\left(\frac{W}{\lambda}\right)^2 & W \ll \lambda \\ \frac{1}{120}\left(\frac{W}{\lambda}\right) & W \gg \lambda \end{cases}. \quad (9)$$

For array factor,

$$\text{AF} = \{\text{Sin}(N/2)\Phi\}/\{\text{Sin}(\Phi/2)\}, \quad (10)$$

where  $\Phi = k d * \text{Cos } \theta + \beta$ , where  $N$  is the number of elements making the array,  $k = 2\pi/\text{wavelength}$ .

### 3 Antenna Design

Table 1 shows the iteration with element antennas to form the proposed antenna. In simple microstrip patch antenna, the patch height is 0.75 mm with a 1.6 mm substrate height suspended at 17.3 mm length and 17.3 mm width, and the array antenna has a substrate height of 1.6 mm and ground lengths and widths of 25 mm and 25 mm, respectively.

**Table 1** Design parameters for antenna

Antenna description	Element antenna	Array antenna
Ground (Lg*Wg)	17.3 * 17.3 mm	25 * 25 mm
Height of substrate (h)	1.6 mm	1.6 mm
Loss tangent (Tan δ)	0.002	0.002
Frequency range ( $f_r$ )	20–40 GHz	20–40 GHz
Feeding technique	Microstrip line feed	Microstrip line feed
Patch shape	Circular shape	Array

Figure 1 shows the iteration with element antennas to form the proposed array antenna. Here is a microstrip patch element antenna with a 1.6 mm substrate height suspended at 17.3 mm length and 17.3 mm width. In a simple microstrip patch antenna, the patch height is 0.75 mm. Excitation for a simple patch antenna is given with microstrip line feeding. The results are enhanced by the patch antenna line feeding technique. Figure 1 represents a simple microstrip patch element antenna with a line feeding technique. A three-element antenna completes the array antenna with a substrate height of 1.6 mm and ground lengths and widths of 25 mm and 25 mm, respectively.

## 4 Results and Discussion

Figures 2, 3, and 4 show the proposed antenna array results. The return loss graph for a proposed array antenna with center line feeding is shown in Fig. 2, which shows a single wide band with a bandwidth of 6.5 GHz. The maximum return loss is 33.7 dB. The return losses for the three bands are 33.7 dB, 15.7 dB, and 16 dB, respectively. The frequency ranges are 26–32.5 GHz, 34.28–35.1 GHz, and 36.7–37.6 GHz, respectively. Figure 2 shows the VSWR graph with three bands in the VSWR range of 0–2. With the help of the VSWR, return loss [4] is calculated. And, the wide band with multiple notches covers the bandwidth range of 26–32.5 GHz, which covers millimeter-wave applications in the n257, n258, n260, and n261 bands of 5G communication. Figure 3 shows the stimulated and radiated power, power accepted, and total loss, respectively.

$$R(c) = \frac{Z(l) - Z(0)}{Z(l) + Z(0)}$$

$$R(c) = \frac{\text{VSWR} - 1}{\text{VSWR} + 1}$$

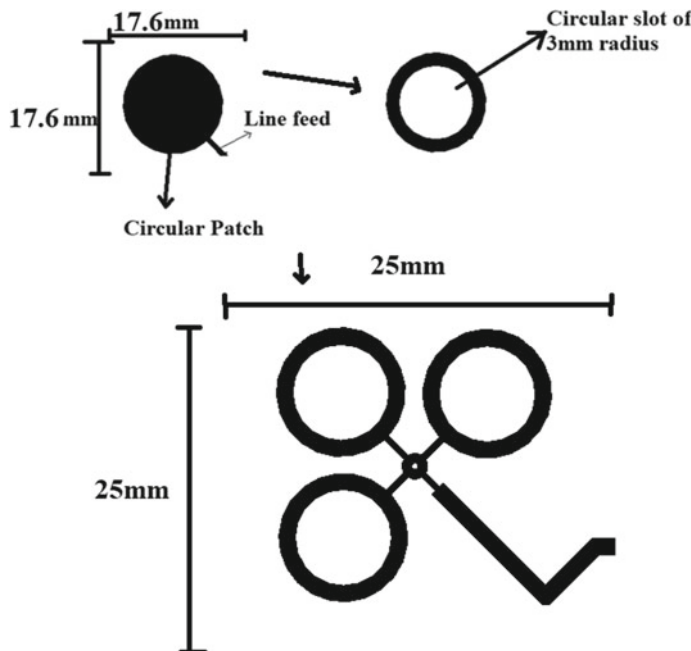


**Fig. 1** Element antenna with circular slot of 3 mm radius, proposed array antenna with respective center feed line

$$R(L) = -20 \log_{10}(R(c)), \quad (11)$$

**Fig. 2** Concerning S11 and VSWR graph of proposed antenna with respect to frequency

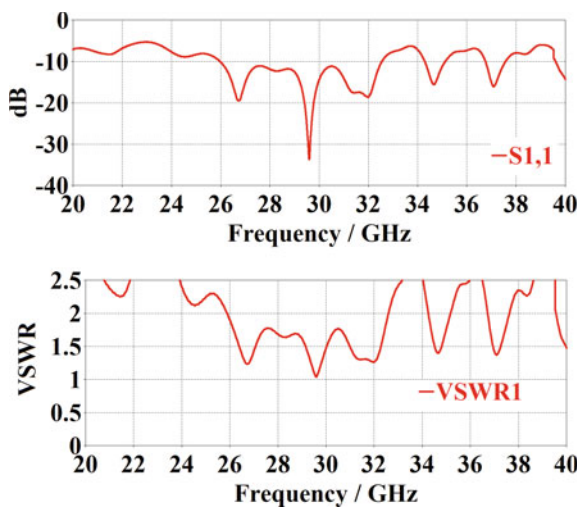


**Fig. 3** Concerning VSWR graph of proposed antenna with respect to frequency

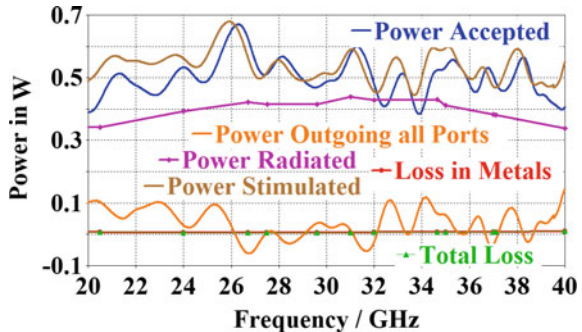
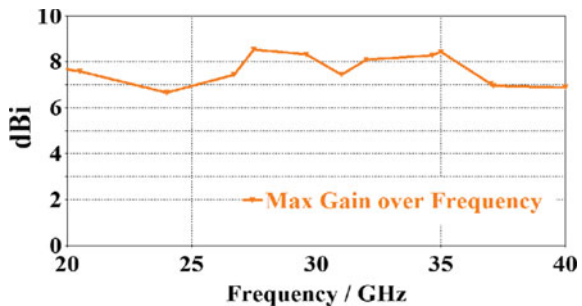


**Fig. 4** Concerning power versus frequency graph for proposed array antenna



where

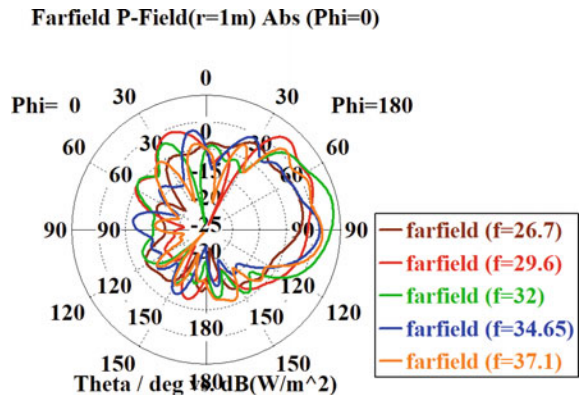
$R(c)$  is reflection coefficient.

$R(L)$  is return loss.

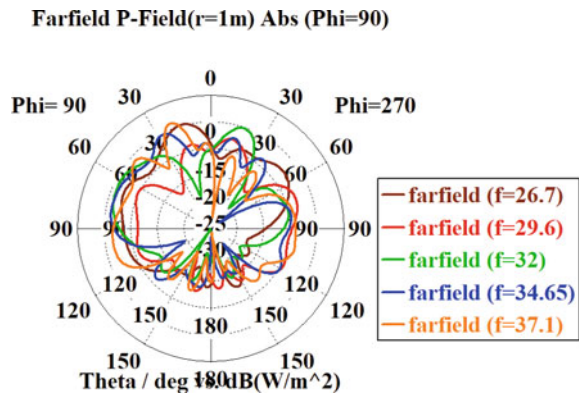
In terms of array antennas, they have a wide bandwidth to cover a wide range of applications in mm-wave and have good resonating notches. Array antenna depicts an ultra-wide band with 6.5 GHz bandwidth and three resonating notches that depict a good radiation pattern; the array antenna gain is increased up to 8.8 dBi. An ultra-wide band and two bands with bandwidths of 0.82 and .4 GHz are among the three bands. Figures 5, 6, 7, and 8 depict the power field radiation pattern of an array antenna with respect to  $\phi = 0$ ,  $\phi = 90$ , and  $\theta = 90$ , respectively, and current distribution of proposed antenna with resonant frequencies of 26.7, 29.6, 32, 34.65, and 37.1 GHz.

Figure 4 shows the maximum gain over frequency in dBi. And, Table 2 depicts the resonating frequency over gain and VSWR, respectively. Figure 8 shows the current flow distribution with different resonating notches over frequencies of 26.7, 29.6, 32, 34.65, and 37.1 GHz. Tables 3 and 4 show the outcomes of the proposed work with respect to bandwidth and return loss. Proposed array antennas have a minimum size as compared to references [1] and [6]. The maximum return loss in the proposed work is 33.7 dB, and the good bandwidth is 6.5 GHz. When proposed work is compared to refereed papers [1, 6], good bandwidth is found in proposed work with respect to size too. Array antenna is a more directive and high-gain antenna with a gain of 8.8

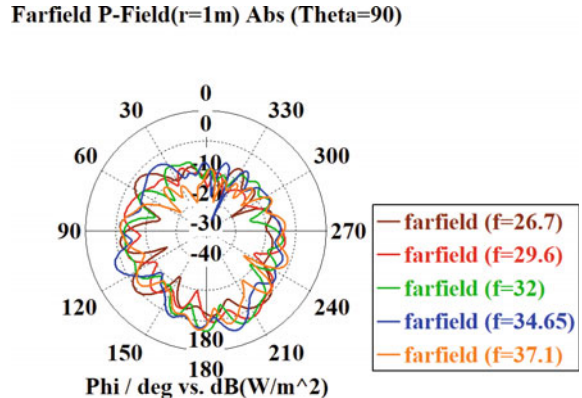
**Fig. 5** Two-dimensional radiation pattern with respect to different resonating frequencies at phi = 0



**Fig. 6** Two-dimensional radiation pattern with respect to different resonating frequencies at phi = 90



**Fig. 7** Two-dimensional radiation pattern with respect to different resonating frequencies at theta = 90



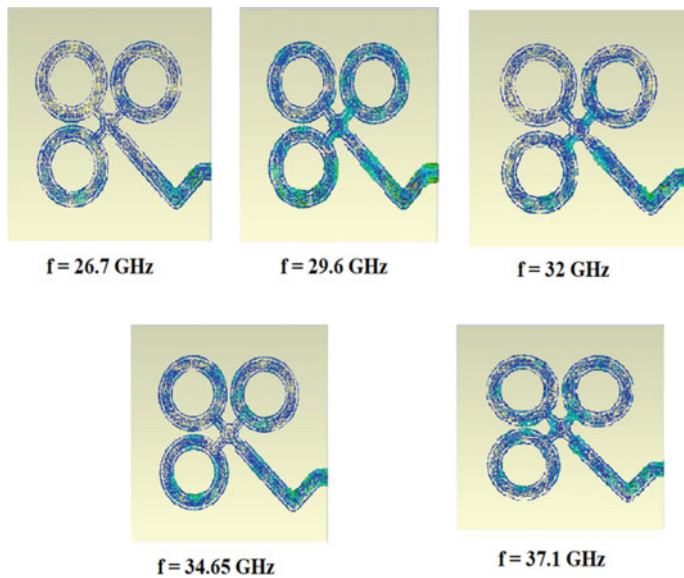


**Fig. 8** Current distribution graph for proposed antenna with respect to different resonating frequencies as 26.7, 29.6, 32, 34.65, 37.1 GHz, respectively

dBi. Another benefit of array antennas is that they have multiple notches for wide bandwidth.

**Table 2** Number of resonant notches with respective Vswr and gain

Band	No. of notches	Resonant frequency (GHz)	VSWR (0–2)	Gain in dBi
Band I	3	26.7, 29.6, 32	1.2, 1.01, 1.3	8.8, 8.5, 8.1
Band II	1	34.65	1.4	8.4
Band III	1	37.1	1.35	6.8

**Table 3** Different parametric results of proposed array antenna

Design	Frequencies [max. and min.]		Parameters		
	F1(GHz)	F2(GHz)	Bandwidth in GHz	Size of antenna	S11 in dB
Array with simple ground	26	32.5	6.5	25 mm * 25 mm	– 33.7
	34.28	35.1	0.82		– 15.7
	36.7	37.6	0.4		– 16

**Table 4** Comparison of proposed array antenna with other published work

Design	Size (mm <sup>2</sup> )	Bandwidth (GHz)
[1]	36 * 32	3.23
[6]	32 * 12	1.41
Proposed work (simulated)	25 * 25	6.5
Proposed work (measured)	25 * 25	1.6, 1.8, 1.7

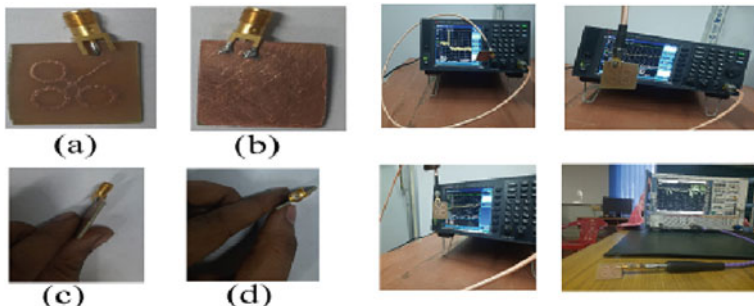


**Fig. 9** Fabricated array antenna with front view (a), back view (b), and side view (c, d), and measurement and measurement setup of different parameters as channel power, PSD, reflection coefficient in spectrum analyzer and vector network analyzer

## 5 Fabrication and Measurement

The antennas are fabricated with a PCB with an Fr<sub>4</sub> substrate. Fabrication is possible with a standard PCB mailing machine. With a substrate height of 1.6 mm, the antenna structure and top view of the fabricated antenna while testing setup with spectrum analyzer and vector network analyzer are shown in Figs. 9 and 10. The proposed array antenna is compared to other published work. The proposed array antenna can achieve a significant reduction in size and an increase in gain and bandwidth. Proposed designs of antennas are successfully designed and tested with the help of the vector network analyzer as shown in Fig. 10. Table 5 shows different parameters with respect to measured result and five bands cover the mm-wave 5G applications.

## 6 Conclusions

In this paper, array antenna designs are successfully fabricated with a height of 1.6 mm, and simulated results show that the bandwidth is increased at the desired mm-wave interval. The proposed antennas have high-gain characteristics, and the current distribution of the fractal antenna and array antenna represents the distribution resulting solely from resistance to current flow in the electrolyte. The 2D polar plot shows the radiation of the designed antenna in how many directions with respect to phi

**Fig. 10** Measured S11 result with vector network analyzer

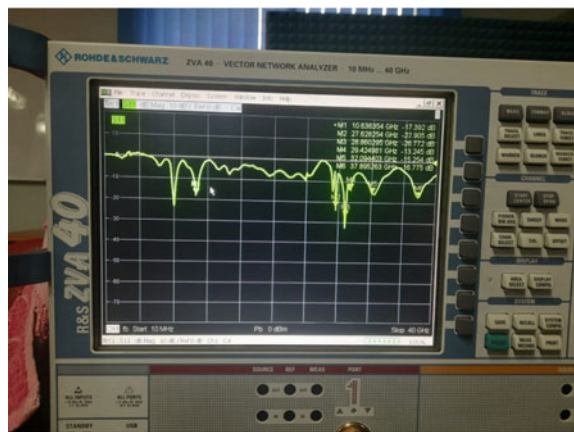


**Table 5** Measured result with respect to different parameters

No. of bands	6
No. of resonating frequency	7
Maximum return loss	26.772 dB
No. of bands cover 5G applications	5

$\phi = 0$ ,  $\theta = 90^\circ$ , and  $\psi = 90^\circ$ . The bandwidths of the proposed antenna are 6.5 GHz, 0.82 GHz, and 0.4 GHz, respectively. Proposed antennas have a high gain of 8.8, 8.5, and 8.1 dBi concerning to their resonating frequencies of 26.7, 29.6, and 32 GHz, respectively. Ultra-wide bands have three resonating notches with return losses of 19.9 dB, 33.706 dB, and 18.2 dB, respectively. When the proposed work is compared to other published work, it shows good bandwidth and a minimum size compared to these references. The proposed antennas are multiband, which means that they can cover the 5G mm-wave region with 26–32.5 GHz, 34.28–35.1–35.1 GHz, and 36.7–37.6 GHz, respectively, which covers millimeter-wave applications in the n257, n258, n260, and n261 bands of 5G communication.

**Acknowledgements** We would like to thank SERB, Department of Science and Technology, Government of India (Sanction Order No: EEQ/2021/000700; Dated 04 March, 2022), for providing the fund that has been required to pursue this research.

## References

1. Bharti G, Sivia JS (2021) A design of multiband nested square shaped ring fractal antenna with circular ring elements for wireless applications. *Prog Electromagnet Res C* 108:115–125
2. Kumar A, Pharwaha APS (2020) Development of a modified Hilbert curve fractal antenna for multiband applications. *IETE J Res*, pp 1–10.

3. Singhal S, Singh AK (2020) Elliptical monopole based super wideband fractal antenna. *Microw Opt Technol Lett* 62(3):1324–1328
4. Karthikeya GS, Abegaonkar MP, Koul SK (2017) Low cost high gain triple band mmWave Sierpinski antenna loaded with uniplanar EBG for 5G applications. In: 2017 IEEE International conference on antenna innovations & modern technologies for ground, Aircraft and Satellite Applications (AIM). IEEE, pp 1–5
5. Garg RK, Nair MVD, Singhal S, Tomar R (2020) A new type of compact ultra-wideband planar fractal antenna with WLAN band rejection. *Microw Opt Technol Lett* 62(7):2537–2545
6. Ullah H, Tahir FA (2020) A novel snowflake fractal antenna for dual-beam applications in 28 GHz band. *IEEE Access* 8:19873–19879
7. Kaur M, Sivia JS (2020) Giuseppe Peano and Cantor set fractals based miniaturized hybrid fractal antenna for biomedical applications using artificial neural network and firefly algorithm. *Int J RF Microwave Comput Aided Eng* 30(1):e22000
8. Singhal S (2020) Four arm windmill shaped superwideband terahertz MIMO fractal antenna. *Optik* 219:165093
9. Khalily M, Tafazolli R, Xiao P, Kishk AA (2018) Broadband mm-wave microstrip array antenna with improved radiation characteristics for different 5G applications. *IEEE Trans Antennas Propag* 66(9):4641–4647
10. Sateaa SD, Hussein MS, Faisal ZG, Abood AM, Satea HD (2022) Design and simulation of dual-band rectangular microstrip patch array antenna for millimeter-wave. *Bull Electr Eng Informat* 11(1):299–309
11. Ghosh S, Baghel GS, Swati MV (2022) A low-profile, high gain, dual-port, planar array antenna for mm-wave powered 5G IoT systems. *AEU-Int J Electron Commun*, p 154354

# An Efficient SEC-DAEC Code for Protecting Data Bits in IoT Devices



Sweta Bijali Maity, Raj Kumar Maity, Jagannath Samanta,  
and Chanchal Kumar De

**Abstract** The design of Internet of Things (IoT)-based systems for various applications is continuously growing worldwide throughout the present and last two decades. The physical devices in IoT-based systems are interconnected through wireless communication. In this communication process, any form of degradation in Signal-to-Noise Ratio can lead to error in data bits which makes the whole system unreliable. Compact, fast and power-efficient Error Correcting Codes (ECCs) have been commonly employed in IoT-based systems to detect and correct bit errors. In this paper, an efficient Single Error Correction-Double Adjacent Error Correction (SEC-DAEC) code has been presented for application in IoT. The encoder and decoder circuits have been constructed based on the proposed  $H$ -matrix. It has been observed that the design of proposed code requires the number of logic gates which are comparable with existing SEC codes. But, the proposed scheme provides better correction capability and better bit error rate performance.

**Keywords** IoT · ECCs · SEC · SEC-DAEC · BER · FPGA

## 1 Introduction

Internet of Things (IoT) [1, 2] has been the most promising technological revolution in recent times. IoT-based systems have been designed for various fields which include but not limited to smart cities [3], agriculture [4] and healthcare [5] applications. The reliability of data in IoT-based devices is greatly influenced by the presence of noise in communication channel. The most common way to protect data from channel noise is the use of suitable Error Correcting Codes (ECCs) with lower encoding and decoding areas, speed and power consumption.

---

S. B. Maity

Department of AEIE, Haldia Institute of Technology, Haldia, West Bengal, India

R. K. Maity (✉) · J. Samanta · C. K. De

Department of ECE, Haldia Institute of Technology, Haldia, West Bengal, India

e-mail: [hitece.raj@gmail.com](mailto:hitece.raj@gmail.com)

The Hamming Single Error Correcting (SEC) codes [6] are proficient of correcting single bit error with lower design constraints, and hence, this code has been popularly employed in IoT applications. Hsiao code [7] is another form of single bit Error Correcting Code which is also capable of detecting double errors. A class of SEC code with lower delay has been presented by Reviriego et al. in [8] for correcting only the data bits. A class of Low Complexity Parity Check (LCPC) codes has been presented by Alabady et al. in [9] for IoT applications. This code is proficient of detecting and correcting consecutive and non-consecutive double bit errors with lower encoding and decoding complexities. But, this code is not competent of correcting all probable double bit errors. In [10], the existing single Error Correcting Codes have been designed and implemented in Cell Design Methodology (CDM) logic style for IoT devices. And it has been reported that CDM logic style is more efficient in power consumption than other logic design styles.

In this paper, a hardware-efficient Single Error Correction-Double Adjacent Error Correction (SEC-DAEC) code has been presented for protecting data bits in IoT devices. The encoder and decoder circuits have been constructed based on the proposed  $H$ -matrix. It has been observed that the design of proposed code requires lesser number of logic gates, but it provides better correction capability.

The rest of this paper is organized as follows. Section 2 describes the basics of SEC-DAEC code. The proposed scheme of SEC-DAEC code has been presented in Sect. 3. The performances of the proposed SEC-DAEC code have been analyzed in Sect. 4, and finally, the paper is concluded in Sect. 5.

## 2 Basics of SEC-DAEC Codes

An  $(n, k)$  Single Error Correction-Double Adjacent Error Correction (SEC-DAEC) code is proficient of correcting single and double consequent errors in any position of its  $n$ -bit codewords. These codewords are formed by the encoder circuit which computes the  $(n, k)$  parity bits and unites them with  $k$  data bits to form the codewords. Decoder of any ECC rectifies the erroneous data bits in the received codewords. The encoding and decoding circuitries of an SEC-DAEC code can be designed based on its parity check matrix ( $H$ -matrix). The  $H$ -matrix of an  $(n, k)$  SEC-DAEC code consists of  $(n, k)$  and  $n$  numbers of rows and columns, respectively. Also, there are  $k$  and  $(n, k)$  numbers of data and parity columns consequently among the  $n$  numbers of columns of  $H$ -matrix. The main characteristics of  $H$ -matrix of SEC-DAEC code are, each column is nonzero and different from one another. And the XOR sums of any two consecutive columns in  $H$ -matrix should be dissimilar from each other and from every column of  $H$ -matrix. These two conditions are incorporated in the  $H$ -matrix creation of SEC-DAEC code for correcting single and double adjacent errors, respectively. The structure of  $H$ -matrix in systematic form has been provided in Eq. (1).

$$H = [ I_{n-k} \ D ]. \quad (1)$$

In Eq. (1),  $D$  consists of  $k$  number of data columns. The generator matrix ( $G$ -matrix) of SEC-DAEC code in systematic form is expressed as:

$$G = [D^T \ I_k], \quad (2)$$

where  $D^T$  represents the transpose of  $D$  sub-matrix. The codewords ( $c$ ) of SEC-DAEC code are obtained by multiplying the  $G$ -matrix with the  $k$ -bit data block ( $d$ ) as shown in Eq. (3).

$$c = d.G. \quad (3)$$

The encoder circuit of SEC-DAEC code generates the codewords for each and every input data block. The encoder circuit is constructed by employing Eq. (3), and only XOR logic gates are needed to design this circuit.

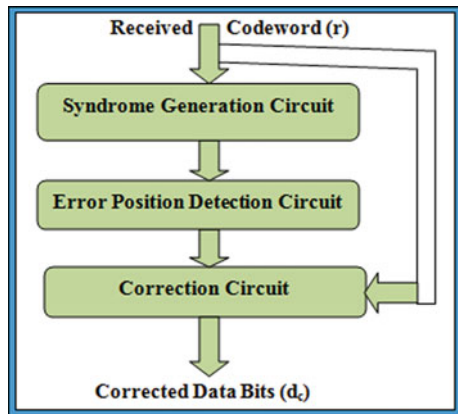
The SEC-DAEC decoder rescues the original data bits from the received erroneous codewords ( $r$ ) and it consists of three functional circuits which are shown in Fig. 1.

The syndrome generation circuit produces the syndromes ( $S$ ) with the help of received codeword ( $r$ ) and the  $H$ -matrix. This circuit is constructed by using XOR gates. Detection of error in the received codeword ( $r$ ) and its exact positions both are determined by the syndrome values. Any error in the received codeword produces nonzero syndromes and zero syndromes indicate no error as shown in Eq. (4).

$$S = \begin{cases} \text{zero.} & \text{no error detected} \\ \text{non-zero.} & \text{error detected} \end{cases}. \quad (4)$$

The error position detection (EPD) circuit of SEC-DAEC decoder locates the precise positions of detected errors in the received codeword. This circuit requires at most three syndrome values for every code bit position to determine the presence of error on it. These syndromes are one single error (SE) and two double consecutive

**Fig. 1** Block diagram of SEC-DAEC decoder



errors' (DCEs) rectification syndromes for each code bit position. These syndromes are represented by using AND and NOT gates and then these are compared by employing OR gates in the error position detection circuit of the SEC-DAEC decoder. Finally, the positioned errors are rectified in correction circuit of the decoder which is designed by means of XOR logic gates.

### 3 Proposed SEC-DAEC Code

In general, the correction capability of SEC-DAEC codes is superior when compared to SEC codes. The main aim of designing the proposed SEC-DAEC code is to decrease the decoding circuitries for SEC-DAEC code so that its area and delay requirements can be made compatible with that of existing SEC codes. The arrangement of parity and data columns in the  $H$ -matrix of proposed SEC-DAEC code has been presented in Fig. 2.

Proposed  $H$ -matrix of SEC-DAEC code has alternate parity and data columns as shown in Fig. 2. Also, the number of parity bits ( $n, k$ ) which are needed to construct the proposed  $(n, k)$  SEC-DAEC code with the  $H$ -matrix structure as shown in Fig. 2 must satisfy Eq. (5). The proposed  $H$ -matrix for  $(n, k) = 5$  has been shown in Fig. 3.

$$n - k = k \text{ or } n = 2k \quad (5)$$

In Fig. 3,  $p_i$  and  $d_i$  for  $i = 1, 2, \dots, 5$  represent parity and data columns, respectively. The expressions of parity bits for proposed SEC-DAEC code have been presented in Eq. (6). The proposed encoder circuit is designed based on Eq. (6) with the help of XOR logic gates.

**Fig. 2** Arrangement of parity and data columns in the proposed SEC-DAEC  $H$ -matrix

**Fig. 3** Proposed  $H$ -matrix for (10, 5) SEC-DAEC code

<b>p<sub>1</sub></b>	<b>d<sub>1</sub></b>	<b>p<sub>2</sub></b>	<b>d<sub>2</sub></b>	<b>p<sub>3</sub></b>	<b>d<sub>3</sub></b>	<b>p<sub>4</sub></b>	<b>d<sub>4</sub></b>	<b>p<sub>5</sub></b>	<b>d<sub>5</sub></b>
1	0	0	1	0	1	0	1	0	1
0	0	1	0	0	1	0	1	0	0
0	1	0	0	1	0	0	1	0	0
0	1	0	0	0	0	1	1	0	1
0	0	0	1	0	0	0	1	1	0

$$\begin{aligned}
 p_1 &= d_2 \oplus d_3 \oplus d_4 \oplus d_5 \\
 p_2 &= d_3 \oplus d_4 \\
 p_3 &= d_1 \oplus d_4 \\
 p_4 &= d_1 \oplus d_4 \oplus d_5 \\
 p_5 &= d_2 \oplus d_4.
 \end{aligned} \tag{6}$$

In the proposed SEC-DAEC decoder, the syndrome circuit generates the syndrome bits by using XOR logic gates. These syndrome expressions are summarized in Eq. (7).

$$\begin{aligned}
 S_1 &= r_1 \oplus r_4 \oplus r_6 \oplus r_8 \oplus r_{10} \\
 S_2 &= r_3 \oplus r_6 \oplus r_8 \\
 S_3 &= r_2 \oplus r_5 \oplus r_8 \\
 S_4 &= r_2 \oplus r_7 \oplus r_8 \oplus r_{10} \\
 S_5 &= r_4 \oplus r_8 \oplus r_9
 \end{aligned} \tag{7}$$

The difference in the proposed and existing DAEC decoders lies in the error position detection (EPD) block of the decoder. In the EPD block of the proposed decoder, only one common error locating syndrome per data bit is used to locate both single and double consequent errors. This common syndrome is determined by comparing the three error locating syndromes and by considering only those syndrome bits which are common for single error (SE) and double consequent errors (DCEs). This fact has been illustrated in Fig. 4 for the first data bit ( $d_1$ ). In this figure, one SE and two DAE situating syndromes for the first data bit ( $d_1$ ) have been presented, and it can be observed that the main variation among these three syndromes is on the first and second bits. So, single and double consecutive errors on the first data bit can be located by considering the last three syndrome bits which are fixed for any type of errors associated with the first data bit ( $d_1$ ). The error position detection (EPD) logic of all the data bits for proposed SEC-DAEC code are expressed in Eq. (8).

**Fig. 4** Determination of error location syndrome for the first data bit ( $d_1$ )

Syndrome	S1	S2	S3	S4	S5
SE Locating	1	0	1	1	0
DAE Locating-I	0	0	1	1	0
DAE Locating-II	0	1	1	1	0
<b>Error Locating Syndrome for <math>d_1=S_3 \&amp; S_4 \&amp; S_5'</math></b>					

$$\begin{aligned}
 EPD_{d_1} &= S_3 \& S_4 \& S_5' \\
 EPD_{d_2} &= S_1 \& S_4' \& S_5 \\
 EPD_{d_3} &= S_1 \& S_2 \& S_5' \\
 EPD_{d_4} &= S_1 \& S_2 \& S_3 \\
 EPD_{d_5} &= S_1 \& S_2' \& S_3' \& S_4
 \end{aligned} \tag{8}$$

The flow diagram of proposed SEC-DAEC decoder has been shown in Fig. 5. The proposed SEC-DAEC decoder starts its operation by computing syndrome bits ( $S$ ). Then, it confirms the occurrence of error in the received codeword by checking nonzero syndrome bits. The error is corrected if the syndromes satisfy the error position detection expressions in Eq. (8). Otherwise, the undetectable error is reported if the error is beyond the error correcting capability of the code.

### 3.1 Theoretical Area Complexity

The comparison of theoretical area complexities which are required to design the encoder and decoder circuits of proposed SEC-DAEC and existing SEC codes in [6] and [8], respectively, has been shown in Table 1. The encoder circuits of proposed SEC-DAEC code require lesser numbers of two-input (i/p) XOR (XOR2) logic gates compared to the encoder circuit of SEC code in [8]. Also, lesser numbers of equivalent 2-i/p NAND (NAND2) logic gates are needed to design the proposed decoder circuit. As shown in Table 1, the Hamming code [6] requires lowest number of equivalent NAND2 logic gates to construct its encoder and decoder circuits.

## 4 Performance Analysis of Proposed Code

The hardware and noise performances of proposed SEC-DAEC code and existing SEC codes in [6] and [8] have been analyzed in this section.

**Fig. 5** Flow diagram of proposed SEC-DAEC decoder

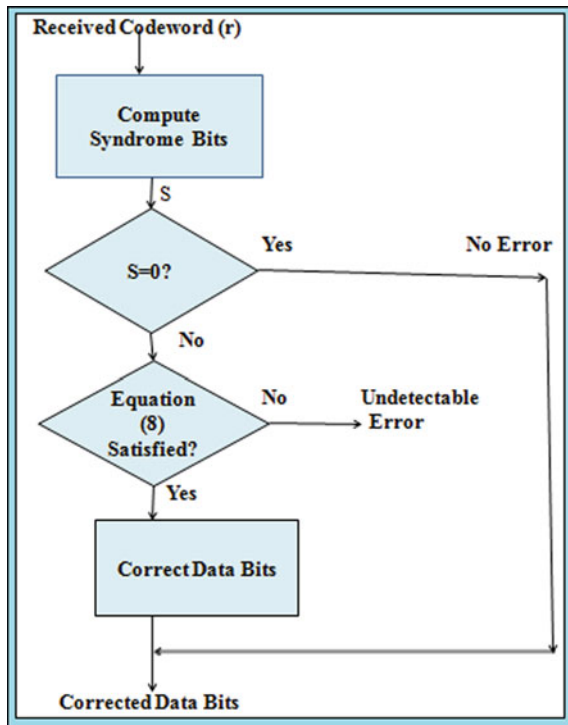


**Table 1** Comparison of theoretical area complexity

Code	Encoder		Decoder			
	XOR2	Equivalent NAND2	XOR2	AND2	NOT	Equivalent NAND2
Hamming (7, 4) SEC [6]	06	24	13	8	8	68
Reviriego. (12, 8) SEC [8]	11	44	24	8	0	112
Proposed (10, 5) SEC-DAEC	08	32	18	11	5	99

#### 4.1 Hardware Performance Analysis

The proposed and existing encoder and decoder circuits have been designed in Verilog Hardware Description Language (HDL) for analyzing the hardware performances. The Field Programmable Gate Array (FPGA)-based Virtex 7 device family has been adopted in this regard. The hardware performance of proposed SEC-DAEC and existing SEC codes has been considered in terms of area (LUTs) and delay (ns). The comparison of area and delay requirements for proposed SEC-DAEC and existing SEC codes in [6] and [8] has been produced in Table 2.

**Table 2** Comparison of FPGA-based synthesis results

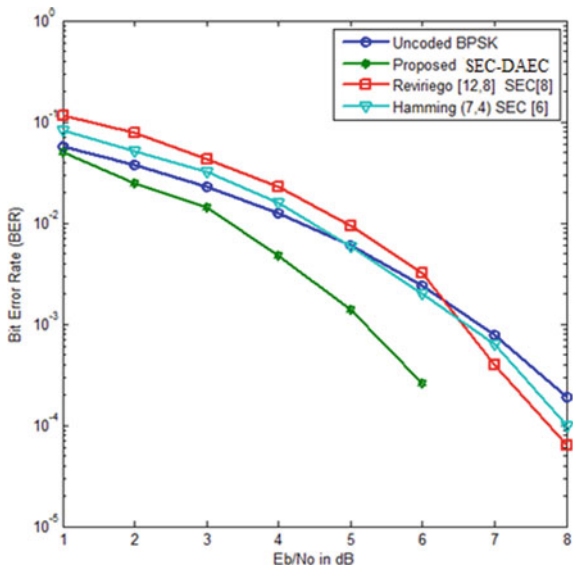
Code	Encoder		Decoder	
	Area (LUTs)	Delay (ns)	Area (LUTs)	Delay (ns)
Hamming (7, 4) SEC [6]	03	1.06	07	1.83
Reviriego (12, 8) SEC [8]	05	1.11	07	1.83
Proposed (10, 5) SEC-DAEC	05	1.11	08	1.86

The area and delay requirement of proposed SEC-DAEC encoder and Reviriego et al. SEC encoder are exactly same as shown in Table 2. But, the proposed and existing SEC decoders have nearly similar tendency in area and delay requirement. Hence, the hardware performance of proposed SEC-DAEC code and existing SEC codes is very much comparable.

## 4.2 Noise Performance Analysis

The noise performance of proposed and existing SEC codes has been measured by simulating Bit Error Rate (BER) of these codes. Binary Phase-Shift Keying (BPSK) modulation scheme and Additive White Gaussian Noise (AWGN) channel have been employed for the simulation of BER by using Monte Carlo simulator. Also, 10,000-bit random input data have been applied to obtain the BER values. The BER of uncoded BPSK, proposed SEC-DAEC code and SEC codes in [6, 8] have been plotted against Eb/No (in dB) in Fig. 6. The existing SEC codes provide slightly better BER performance compared to uncoded BPSK for higher Signal-to-Noise Ratio (SNR). But, the BER performance of the proposed SEC-DAEC code is consistent from lower to higher SNR values. Also, the proposed codes provide the best BER performance compared to the existing codes in [6] and [8]. The proposed SEC-DAEC code provides a coding gain of approximately 1.7 dB with respect to uncoded BPSK at a BER of  $10^{-3}$ . So, the performance of the proposed SEC-DAEC code in the presence of noise is much better compared to existing SEC codes.

**Fig. 6** BER versus Eb/No plot for proposed and existing codes



## 5 Conclusions

In this paper, an efficient Single Error Correction-Double Adjacent Error Correction (SEC-DAEC) code has been presented for protecting data bits in IoT applications. The encoder and decoder circuits have been constructed based on the proposed  $H$ -matrix in FPGA environment. It has been observed that area and delay requirements of designing the proposed SEC-DAEC encoder and decoder are comparable to that of existing SEC codes. But, the proposed code provides better correction capability and hence better coding gain.

## References

1. Ashton K (2009) That ‘internet of things’ thing. *RFID J* 22(7):97–114
2. Gokhale P, Bhat O, Bhat S (2018) Introduction to IOT. *Int Adv Res J Sci, Eng Technol* 5(1):41–44
3. Zanella A, Bui N, Castellani A, Vangelista L, Zorzi M (2014) Internet of Things for smart cities. *IEEE Internet Things J* 1(1):22–32
4. Mohanraj I, Kirthika A, Naren J (2016) Field monitoring and automation using IOT in agriculture domain. *Procedia Comput Sci*, pp 931–939
5. Sandro P, Cabral J, Gomes T (2017) We-care: An IoT-based health care system for elderly people. In: 2017 IEEE International conference on industrial technology (ICIT). IEEE, pp 1378–1383
6. Hamming RW (1950) Error detecting and error correcting codes. *Bell Syst Tech J* 29(2):147–160
7. Hsiao MY (1970) A class of optimal minimum odd-weight column SEC-DED codes. *IBM J Res Develop* 14(4):395–401

8. Reviriego P, Pontarelli S, Maestro JA, Ottavi M (2013) A method to construct low delay single error correction codes for protecting data bits only. *IEEE Trans Comput Aided Des Integr Circuits Syst* 32(3):479–483
9. Alabady SA, Salleh MFM, Al-Turjman F (2018) LCPC error correction code for IoT applications. *Sustain Cities Soc* 42:663–673
10. Gali S, Wauer E, Nikoubin T (2018) Low power and energy efficient single error correction code using CDM logic style for IoT devices. In: 2018 IEEE 13th Dallas circuits and systems conference (DCAS). IEEE, pp 1–5

# Evaluation of Water Quality Index Using Machine Learning Approach



**Moupali Sen, Shreya Basu, Arijit Chatterjee, Anwesha Banerjee, Saheli Pal, Pritam Kumar Mukhopadhyay, Sudipta Sahana, and Stobak Dutta**

**Abstract** Clean water is the fundamental right of all people. The crisis for clean water is everywhere. So there has been an urgent need for clean water. Most people are not aware of clean water and are consuming dirty and infected water, and they suffer from different diseases. In our work, we attempt to analyze the water quality depending on various parameters like pH, temperature, conductivity, nitrate concentration, BOD, fecal coliform, and total coliform. Based on these parameters, our ML model will predict whether the water is clean and safe for consumption or not. To detect the index of the quality of water we have applied the concept of supervised ML techniques, and based on the range, we will be able to state the quality of water to be excellent or good or fair or poor or very poor or unfit for drinking. There has been a use of popular algorithms like support vector machine, K-nearest neighbors, Random Forest Classifier, and decision tree. Through this project, we wanted to create awareness among the people regarding the necessity of clean water.

**Keywords** Water quality · Supervised machine learning · Machine learning model · Water quality index

## 1 Introduction

According to USGS, clean and safe water is defined as “water that will not harm you if you come in contact with it.” When we talk about clean water, we often refer to drinking clean water, but it is also essential for all domestic use. The scarcity of clean water is everywhere. In recent years, the necessity for clean water has increased.

---

M. Sen · S. Basu · A. Chatterjee · S. Pal · P. K. Mukhopadhyay · S. Sahana (✉)  
Department of Computer Science and Engineering, Institute of Engineering & Management  
Kolkata, University of Engineering & Management Kolkata, Kolkata, India  
e-mail: [ss.jisce@gmail.com](mailto:ss.jisce@gmail.com)

A. Banerjee · S. Dutta  
Department of Computer Science and Technology, Institute of Engineering & Management  
Kolkata, University of Engineering & Management Kolkata, Kolkata, India

This is why there is an urgent need for such research as it will help to analyze and diminish the existing problem of clean water to the maximum extent. In 2010, the UN General Assembly recognized the human right for water and sanitation. Everyone has the right to access enough water for personal and domestic use that is available continuously and is safe, acceptable and inexpensive. Water that is safe and easily accessible is essential for maintaining good public health, whether it is utilized for drinking, home use, food production, or leisure activities. Pure and unpolluted water must use for cultivation and farming which maintains cleanliness, hygiene, and disinfection. Clean water is a fundamental right of all people. When dresses are washed in polluted water, it can lead to infection and sickness. Clean water is necessary for healthiness. Consuming clean water also helps to maintain proper body temperature and helps to control blood pressure levels. It also helps to maintain a healthy weight.

In the recent scenario, it has been observed that in this era of artificial intelligence and machine learning, there is a high need of predicting the quality of water for better visualization and sustainability of human lives. Machine learning is implemented on the dataset. Machine learning refers to artificial intelligence (AI) that allows accurate software applications at predicting outcomes by feeding huge amounts of data and training them to implement it. Figure 1 provides the roadmap of our work. There are different types of machine learning algorithms, such as Linear Regression, Logistic Regression, decision tree, SVM, Naive Bayes, kNN, K-Means, Random Forest, etc. We first collected the data. After preprocessing the data, we divided it into train and test data after selecting the target variable. After that, we have chosen and used four popular algorithms. Among them are Logistic Regression, SVM, kNN, and decision tree. Logistic Regression refers to a classification technique that is used in machine learning. Logistic Regression can be defined as a statistical approach that is used to analyze the method to predict a data value that is entirely based on the observations, observed by the data set. It uses a logistic function to make a dependent variable. We have used Logistic Regression here to detect whether the water is clean or not. On the other hand, support vector machine (SVM) is based on the concept of classifying the data by separating those using hyperplanes in the N-dimensional space. Hyperplanes can be defined as decision boundaries that help to classify the data points. K-nearest neighbor (KNN) is another classification algorithm that works on this method of storing all the available information and then classifying the data point based on the similarities of that data. We have fed the whole data into this algorithm and have successfully received the desired classified outcome. A decision tree is an algorithm that uses a tree-like model of decisions, and it predicts a useful outcome based on that predefined result. It is a highly useful algorithm that explicitly represents decision-making. In our work, the dataset is taken from the Central Pollution Control Board from the time range from 2020 to 2021.

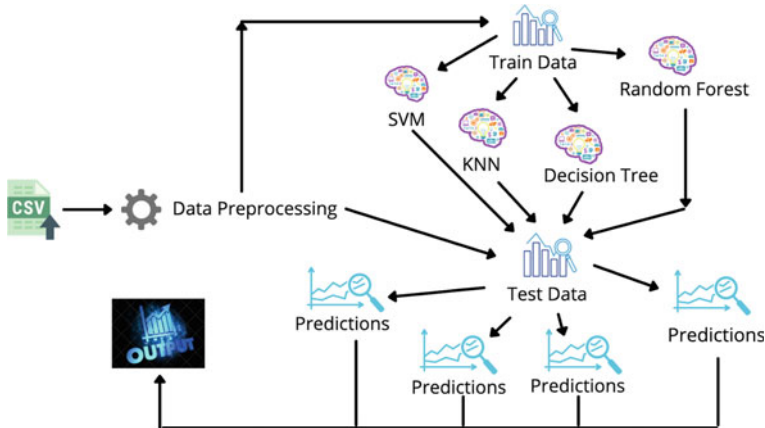


**Fig. 1** Roadmap of our work

## 2 Review of Literature

In 2018, Haghabi et al. [1], the tansig and radial basis functions were discovered to have the highest accuracy among the investigated function while creating the ANN and SVM. While the GMDH model has reasonable performance in the prediction of the elements of water quality, a comparison of its results with those of other used models reveals that it is not quite as accurate as ANN and SVM. SVM was found to be the model with the highest accuracy when applicable models' accuracy was evaluated using error indices. Rawat et al. [2] present a different strategy for predicting water quality using Artificial Intelligence. The WQI is computed utilizing AI methods in this study. Compared to any other IoT framework, it can estimate the water quality using that method quickly and correctly. To verify parameters like pH, temperature, turbidity, and other variables system employs various restrictions. The planned Internet of Things system will identify the proper water quality and send a warning to the concerned professional to take further action. Kurra et al. [3] used decision tree (DT) and K-nearest neighbor as two different classification techniques to estimate the water quality class (KNN). The KNN classifier outperforms other classifiers, according to the outcomes of two different kinds of classifiers. The results show that potability may be predicted with accuracy by machine learning techniques. Index terms include classification, data mining, potability, and water quality parameters. The accuracies were much less than our paper with 58.5% for decision tree and 61.2% for Random Forest, and it was a binary classification. Aldhyani et al. [4], ANN models, specifically LSTM algorithm and NARNET, have been created for the WQI prediction which recommends the error free algorithm demonstrating the quality of water in accordance with improved robustness. According to prediction findings, the LSTM performed marginally better than the NARNET model in predicting WQI values, and the SVM method had the greatest correctness (97.01%) in

predicting WQC. Khan and Soo [5] saw by using ANN and analyzing data point over an interval of time, create a predicting of the quality of water with different parameters. According to Fu [6], the adaptive neuro-fuzzy inference system (ANFIS) is a useful tool for extracting the complex linear and nonlinear relationships concealed in datasets. The ANFIS model has certain drawbacks even though it performs well when predicting water quality. Valcke et al. [7] have confirmed after evaluating the work of a key institutes, the use of noted information to arrive at a point-of-departure (POD) of 25 mg of manganese/kg/day based on neurodevelopmental. According to Fua et al. [8], the stability of an ecosystem depends critically on the monitoring of wastewater quality. The ANFIS model, developed for forecast quality of wastewater, can do so with the greatest degree of accuracy. The outcome suggests the model execute greater than other artificial intelligence models when it comes to forecasting sulfate chloride and total dissolved solids, with R<sup>2</sup> testing values of 0.976, 0.975, 0.988, and 0.986, respectively. Ragi et al. [9] state that Levenberg–Marquardt algorithm is used along with ANN predict using well-known factors like pH, electrical conductivity, TDS, and others, and one may forecast values for unknowable parameters like alkalinity, chloride and sulfate. This aids in further classifying water bodies for various applications. The accuracy of the predictions for chloride, total-hardness, sulfate, and total alkalinity were 83.94%, 87.9%, 81.736%, and 79.48%, respectively. Hu et al. [10], explained to examine the quality of drinking water in Jiaozuo City, China, a novel analytical approach called Grey Relational Analysis (GRA), which was proposed from the grey system theory, is applied is straightforward and better outcomes were obtained. The judgment serves as a scientific guide for Jiaozuo city's integrated plan, managing wise use of its drinking water source. A Survey by Nair and Vijaya [11], building quality of water prediction models, is aided by the modern big data analytics utilizing machine learning and sensor networks with environmental data. In this paper, multiple prediction models for water prediction and evaluation that were created utilizing ML techniques where difficulties and problems are examined, and potential fixes for several research problems are suggested.

## 2.1 Experiment and Observation

Our main aim was to predict the status of each place that is Excellent, Good, Fair, Poor, Very poor, and unfit for drinking on the basis of their WQI index. According [12], we came to know the range of WQI. The WQI range gives the corresponding status of the water (whether it is “excellent”, “good”, “fair”, “poor”, “very poor” or “unfit for drinking”) and its respective possible uses. So in the experiment, we have divided the different places on the basis of the WQI and predicted the possible uses of water like whether it is fit for drinking, irrigation, industrial use, domestic use or not. Our algorithms have six verticals—Excellent, Good, Fair, Poor, Very Poor, or Unfit for drinking. Based on that, we have used Random Forest, decision tree, kNN

algorithm, and SVM algorithm for our classification system. Our data is split into train and test data in ratio 70:30.

#### A. Algorithm 1: Random Forest Classifier

We can see in Fig. 2 from our analysis on the basis of Random Forest Classifier algorithm, we have got precision is 0.64, f1-score is 0.61, and recall is 0.61. The accuracy is 90.50%. This is our benchmark model.

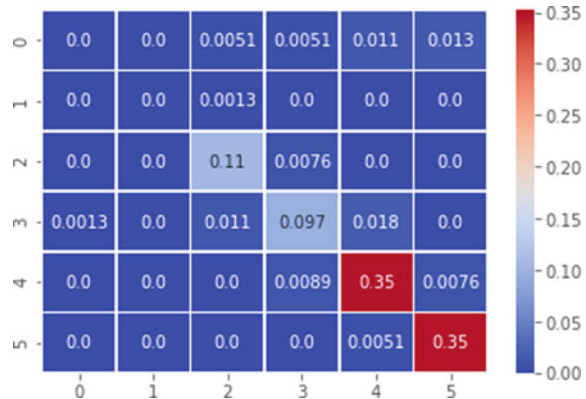
#### B. Algorithm 2: Decision Tree

We can see in Fig. 3 from our analysis on the basis of the decision tree algorithm, we have got precision is 0.71, recall is 0.80, and f1-score is 0.74. The accuracy is 87.85%.

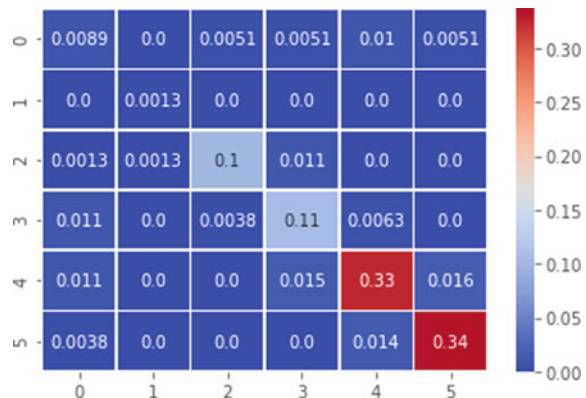
#### C. Algorithm 3: KNN

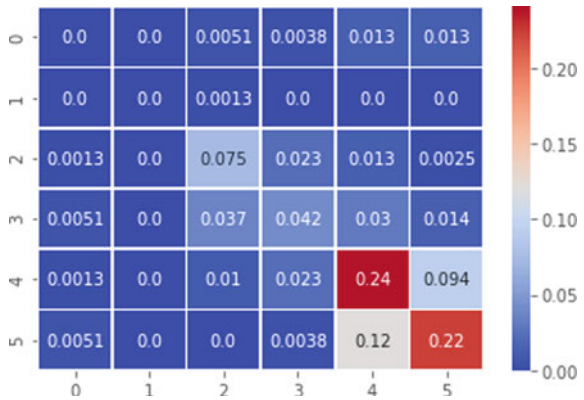
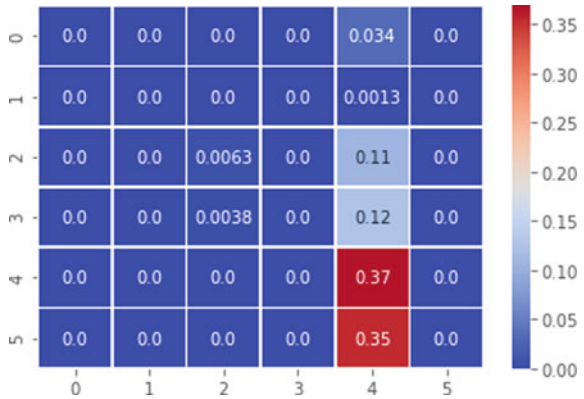
We can see in Fig. 4 from our analysis on the basis of K-nearest neighbors algorithm, we have got the precision is 0.37, recall is 0.38 and f1-score is 0.37. The accuracy is 58.10.

**Fig. 2** Random forest classifier



**Fig. 3** Decision tree



**Fig. 4** KNN**Fig. 5** Support vector machine

#### D. Algorithm 4: Support Vector Machine

We can see in Fig. 5 from our analysis on the basis of support vector machine algorithm, we have got the precision is 0.17, recall is 0.18, and f1-score is 0.11. The accuracy is 37.46.

## 2.2 Formulas

The classifier performance has been expressed in terms of the f1-score and accuracy, in each of the experiments, which is given as

$$\text{f1-score} = (2 * \text{Precision} * \text{Recall}) / (\text{Precision} + \text{Recall})$$

$$\text{Accuracy} = (\text{True Positive} + \text{True Negative}) / (\text{Total Positive} + \text{Total Negative})$$

$$\text{Precision} = (\text{True Positives}) / (\text{True Positives} + \text{False Positives})$$

$$\text{Recall} = (\text{True Positives}) / (\text{True Positives} + \text{False Negatives})$$

### 3 Conclusion

The scarcity of clean water has become an alarming concern for several countries all over the world. Due to the consumption of contaminated water, people are getting more prone to chronic diseases. This is leading to the loss of lives of lakhs of people. In this work, researchers have tried to identify the necessity of clean water and predict the quality of water in different places. It will also detect the water quality index (WQI) and state whether it is excellent or good or fair or poor or very poor or unfit for drinking. It will also predict whether the water is clean and safe for consumption or not. This will help to protect and sustain the livelihood of people. In the near future, we can take our work to the highest domain with additional data from competent authorities so that most of the algorithms can provide an accuracy of 100%.

### References

1. Haghabi AH, Nasrolahi AH, Parsaie A (2018) Water quality prediction using machine learning methods. *Water Qual Res J*
2. Rawat N, Kazembe MD, Mishra PK (2022) Water quality prediction using machine learning. *IJRASET* 44658, 21 June 2022
3. Kurra SS, Naidu SG, Chowdala S, Yellanki SC, Esther Sunanda B (2022) Water quality prediction using machine learning 04(05/May)
4. Aldhyani THH, Al-Yaari M, Alkahtani H, Maashi M (2020) Water quality prediction using artificial intelligence algorithms. *Appl Bionics Biomech*, King Faisal University
5. Khan Y, Chai SS (2021) Predicting and analyzing water quality using machine learning: a comprehensive model. In: 2021 IEEE 23rd international conference on high performance computing & communications; 7th international conference on data science & systems; 19th international conference on smart city; 7th international conference on dependability in sensor, cloud & Big Data systems & application (HPCC/DSS/SmartCity/DependSys), 2021
6. Fu Z (2020) Water quality prediction based on machine learning techniques. UNLV Theses, Dissertations, Professional Papers, and Capstones. 3994
7. Valcke M, Bourgault M-H, Haddad S, Bouchard M, Gauvin D, Levallois P (2018) Deriving a drinking water guideline for a non-carcinogenic contaminant: the case of manganese. *Int J Environ Res Public Health*
8. Fua Z, Chengb J, Yanga M, Batistac J, Jiang Y (2020) Wastewater discharge quality prediction using stratified sampling and wavelet de-noising ANFIS model, 2020 published by Elsevier
9. Ragi NM, Holla R, Manju G (2019) Predicting water quality parameters using machine learning. In: 4th International conference on recent trends on electronics, information, communication & technology (RTEICT), 2019

10. Hu L, Zhang C, Hu C, Jiang G, Use of grey system for assessment of drinking water quality: a case study of Jiaozuo City, China. Springer. [https://doi.org/10.1007/978-3-642-13938-3\\_41](https://doi.org/10.1007/978-3-642-13938-3_41)
11. Nair JP, Vijaya MS (2021) Predictive models for river water quality using machine learning and Big Data techniques—a survey. In: 2021 International conference on artificial intelligence and smart systems (ICAIS), 12 April 2021
12. Karim MA, Uddin MH, Barua S, Nath B Pollution source identification of Halda River water using field observation, laboratory analysis and GIS technique

# Governance of Water and Electricity Sectors in Developing Countries: A Review



**Tsongo P. Kamabu, Eyul'Anki D. Musibono, Banza B. Banza,  
Mowene G. Mayobo, Mukwanga W. Siti, J. Sumaili, Ramesh C. Bansal,  
Ahmed G. Abo-Khalil, Mwana W. K. Mbukani, Diambomba H. Tungadio,  
Kiseya F. Tshikala, T. Madiba, and Nsilulu T. Mbungu**

**Abstract** Against a backdrop of massive population growth, the supply of essential urban services, such as water and power, in developing countries is not growing at nearly the same pace. The critical aspects of this urban development are poorly understood. The main objective of this study was to identify and analyze the different forms of governance in the water and electricity sectors in developing countries based on the

---

T. P. Kamabu

Department of Electrical Engineering, University of Kinshasa, Kinshasa, Democratic Republic of the Congo

E. D. Musibono

Department of Environmental Sciences, University of Kinshasa, Kinshasa, Democratic Republic of the Congo

B. B. Banza · D. H. Tungadio · K. F. Tshikala

Department of Electrical Engineering, School of Engineering, University of Lubumbashi, Lubumbashi, Democratic Republic of the Congo

B. B. Banza · D. H. Tungadio

Department of Electrical Engineering, University of Nouveaux Horizons, Lubumbashi, Democratic Republic of the Congo

M. G. Mayobo

Department of Mechanical Engineering, University of Kinshasa, Kinshasa, Democratic Republic of the Congo

M. W. Siti

Department of Electrical Engineering, Tshwane University of Technology, Pretoria, South Africa

J. Sumaili · N. T. Mbungu (✉)

INESC TEC, Porto, Portugal

e-mail: [ntmbungu@ieee.org](mailto:ntmbungu@ieee.org)

R. C. Bansal · A. G. Abo-Khalil

Department of Electrical Engineering, University of Sharjah, Sharjah, United Arab Emirates

R. C. Bansal · M. W. K. Mbukani · N. T. Mbungu

Department of Electrical, Electronic and Computer Engineering, University of Pretoria, Pretoria, South Africa

existing literature. The synthesis of several studies shows that there is not one mode of governance that fits every time and place. In most cases, municipal authority involves the private sector in water and electricity management. In many countries that have liberalized electricity generation, regulation of municipal utilities is being reformed through the introduction of incentive regulation models. Engaging the population through anti-corruption campaigns is an effective way to improve governance. Given the cost of expanding the conventional power grid, solar PV has proven to be a safe and sustainable way to power urban and peri-urban districts. However, success in promoting this energy source lies in the involvement of the national and/or provincial government through incentive measures. We conclude that the governance of water and electricity in developing countries is successful when the following criteria are applied: decentralization, liberalization, public–private partnerships and community involvement.

**Keywords** Africa · DR Congo · Energy demand · Governance · Essential network services · Developing countries · Private sector · Public sector · Water demand · Water-energy nexus

## 1 Introduction

Urban services in emerging municipalities are often characterized by inadequate and deteriorated infrastructures, poor or irregular services, unequal access, corruption, excessive tariffs and poor governance [1]. As a result, networked technical services have undergone several fundamental reforms for over three decades [2, 3]. Under the influence of the World Bank in the 1990s, most countries liberalized, privatized and modernized the way networked technical services are managed and financed [4, 5].

Several studies have addressed financing and governance issues of essential services [6]. Many researchers agree on the importance of the private sector and decentralization in the administration of urban services [7–12]. This increases operators' accountability, responsiveness and flexibility of action to effectively identify social demands [13, 14]. In Africa, however, some authors argue that there is no automatic correlation between the spatial scale of decision-making and the effectiveness of public action. The standard reform model of decentralizing generation, transmission and distribution, introducing competition at all levels, is never fully implemented because decentralization is only theoretical [15].

---

A. G. Abo-Khalil

Department of Electrical Engineering, College of Engineering, Assuit University, Assuit 71515, Egypt

T. Madiba

Department of Electro-Mechanic, Polytechnic Faculty, University of Lubumbashi, Lubumbashi, Democratic Republic of the Congo

The critical challenge in urban governance is coordinating, playing a leadership role in the marketplace, taking a long-term perspective, and placing equity and citizen voice at the centre of water and electricity provision [16–18]. Unfortunately, although the literature on the governance of water and electricity in developing countries is abundant, few studies have considered governance in a well-defined urban environment. Instead, most researchers have considered some services at the continental, regional, or national level. Another critical weakness is the relatively small number of studies that have systematically attempted to link different governance aspects to electricity or water. Therefore, this research assesses and identifies various governance measures related to water and electricity in developing countries.

## 2 Assessment

Various relevant research works are evaluated using the criteria for inclusion and exclusion to assess their relevance to this topic. Research studies written in English or French and published in peer-reviewed journals are considered. After applying the inclusion and exclusion criteria, the number of papers was reduced, and some relevant and selected published works are presented in Table 1. These were published on the following topics: water and electricity sector reforms, governance modes and/or management of technical services. The date of publication was not considered in the selection criteria. However, after applying the inclusion and exclusion criteria, it was found that all selected studies were published between 2004 and 2022. The inductive approach synthesizes the literature as an appropriate means to condense extensive and diverse texts into a summary.

Governance is used in various ways [19, 20]. This results in multiple definitions, from management to policy [21]. According to Pateman [22], governance is polysemous and often ambiguous. Unlike management, which refers to managing or executing on behalf of others or for oneself, governance inevitably brings to mind the executive power of a state [22]. In the case of a company, Joumard [23] refers to governance as a process rather than an institution or structure. This interconnected system regulates relationships among stakeholders to achieve profits or better management. In this study, governance refers to all the measures, rules, decision-making, information and control bodies that ensure the proper functioning and control of a state, organization or sector [24].

**Table 1** List of works according to their authors, the technical service and the area studied

Topics	References	Electricity	Water	Location
An economic valuation of water connections under various strategies of service governance	[25]		✓	Guatemala
Evaluation of electricity sector reforms in Asia: Georgia, Sri Lanka and Vietnam	[2]			Georgia, Sri Lanka, Vietnam
Reorganisation and control of variety: Urban services in Anglophone Africa	[26]	✓		Africa
Governance of urban energy	[27]	✓	✓	DCs
Governance of basic services in Tangier and Tetouan (Morocco)	[28]		✓	Morocco
Governance of the electricity sector in India	[29]		✓	India
Governance and public services	[30]	✓	✓	Africa
Impacts of corporate governance on corporations in Brazil's power sector	[31]	✓		Brazil
The Philippine electricity sector reform and the urban question	[32]	✓		Philippine
The extension of essential service networks in the irregular neighbourhoods of Delhi and Lima	[1]	✓		Delhi and Lima
Governance of Public Enterprises in Morocco	[33]	✓		Morocco
Governance of urban service networks: The case of the reforms of the electricity network of the National capital territory of Delhi	[4]	✓	✓	Delhi
Governance of water services in Tunisia	[34]	✓	✓	Tunisia
Water governance in the context of scarcity	[8]	✓	✓	Morocco
Networked urban services in Arab countries: diversity of liberal reforms	[3]	✓		Arab countries

(continued)

**Table 1** (continued)

Topics	References	Electricity	Water	Location
Liberalization of the energy sector	[35]	✓	✓	DCs
Public–private partnerships: Lessons from experiences in developing countries	[21]	✓	✓	DCs
Public–private partnerships in the water sector: A review	[36]		✓	World
Reform of the electricity sector in Africa	[37]	✓		Africa
Tensions in the transition: The politics of electricity distribution in South Africa	[38]	✓		South Africa
Roles of electricity regulators in the efficiency of this service in developing countries	[39]	✓	✓	DCs
The power supply industry in the Democratic Republic of the Congo	[40]	✓		DR Congo

Source Compilation of authors, based on the literature

### 3 Governance and Its Different Forms in Developing Countries

#### 3.1 Public and Private Governance

Studies on the governance of networked technical services have addressed the issue from different perspectives. These are mainly the institutional and regulatory aspects [6, 26], management [31], mobilization [41], valorization [32], financing [25], information, training and research and development [8]. Thus, there is no universal governance model in which effectiveness and efficiency would be recognized at any time and place [42]. Public sector decisions regarding managing a basic network service must therefore be pragmatic and consider the needs of the public interest and the local context [43]. The advantage of this study is also to support digitalization throughout the implementation of sustainable development goals in developing countries [44].

In the electricity sector, the vertically integrated public monopoly was the standard model adopted by developing countries [45]. This model consisted of a single company managing the public service generation, transmission and distribution [33]. The statement substantiates the benefit of this domination style that the cost of a single company in the market is lower than in a competitive environment [45]. In addition, the monopolist can ensure a scale that benefits consumers because the tariffs for the energy supplied are lower [30].

However, in the water sector, the model of the centralized system that delivers large quantities of water to all households through a network is insufficient, especially in developing countries, because it implicitly assumes a homogeneous city and a general salary [46].

In most cases, the public sector decides to involve the private sector in service delivery because of difficulties in using existing infrastructure and expanding infrastructure to meet the demand of new users [47].

Private sector participation in urban service provision is an arrangement between the public and private sectors to provide services in the public interest. In this arrangement, the private sector provides financial investment, and the risks are shared between the public and private sectors [48]. Table 2 describes different forms for effective business development of public–private partnerships [36]. Several authors have analysed the above models in many cases, which leads to the fact that the participation of the private sector results in higher costs and connection rates [47]. Regarding the privatization of networked public services, the authors' opinions differ. Some try reconciling private management and poverty reduction [4, 49]. Others take a more radical view, arguing that the various forms of commercialization and privatization are incompatible with universal service to the poor [4]. Megginson and Netter [50] provide an extensive literature review on privatization, including 61 empirical studies. They conclude that privately managed enterprises are more productive and profitable than public enterprises in developed and developing countries. In three studies examining 204 privatization cases in 41 countries, one-third of privatized firms experienced a minimal improvement in a difficult situation. In all other cases studied, privatization tends to improve firm performance. The impact of privatization of electricity distribution of 116 scenarios in ten Latin American countries has shown that privatization brings improvements in labour productivity, efficiency, and quality of life of the product or service [51].

**Table 2** Public–private partnership form for effective business development

Form	Features
Privatization	Infrastructures are sold to private investors
Concession	The tasks of operation and investment are entrusted to a private operator
Leasing	A newly established private company operates public facilities and collects revenues that it shares with the public owner, who remains responsible for the investments
Management contract	Services are provided by a public company managed by a private operator
Mixed-economy company	A private operator acquires a minority stake in a water company and manages the company on behalf of local authorities, sharing financial profits with the public partner

### ***3.2 Reform of the Governance of Networked Technical Services***

The need to strengthen the governance of technical services in developing countries is reported, analysed or even proposed in several cases by several authors [37]. As a result, the lack of proper governance leads to criticism of governments' ability to dispose of energy resources [42]. In addition, reforms initiated in developing countries have been less technically and financially effective due to fewer resources and weaker institutions [52].

As in the electricity sector, political, economic, and structural reforms have occurred [53]. However, most of these reforms were initiated when international experience with such initiatives was limited. As a result, these reforms have taken different forms and followed different paths [54]. Most countries that have initiated reforms in the energy sector have been found to lack regulatory models, experience and skilled human resources [55]. However, there is a limit to those whose form of governance is effective: electricity systems vary significantly in size, structure, and resources, making it difficult to compare and transfer experiences with other regions [56].

In most reform cases, the following three steps have been observed:

- i. Unbundling the state and creating new institutional arrangements;
- ii. Restructuring of the electricity sector;
- iii. Change of ownership: partial or full privatization.

Regardless of the model chosen, restructuring aims to achieve a market logic for the electricity sector and rationalize costs in the long term [36]. However, several models for power sector reforms have emphasized market-oriented reforms based on private sector participation [57]. However, the essential elements of reform are [58]: (i) regulation, (ii) restructuring and (iii) privatization. In addition, several studies have discussed different aspects of water sector reforms [4]. Overall, it has been estimated that the reforms that have led to public-private partnerships in the water sector have enabled more than 24 million people in developing countries to access safe water supplies since 1990 [58].

In theory, decentralizing the water supply to local governments improves resource allocation because local governments know best what their citizens need. Some authors even suggest that local governments have political incentives to provide better water services because their re-election depends on the perceived quality of municipal services [59].

Regardless of the nature of urban service, it is notable in developing countries that when public administration fails, the people tend to take matters into their own hands. This form of organization involves the participation of small private operators (POPs), which some describe as the "informal sector" [3]. In most studies, POPs are described as flexible and responsive actors resulting from pure competition that should not be hindered [60]. From this perspective, the public sector must limit itself to the role of "facilitator" and let supply be driven by demand (Kariuki & Schwartz,

2005). Some analysts even believe that a regulatory framework is not essential for POPs, as they are used to developing in a hostile legal environment [45].

### **3.3 Case Study of Water and Electricity Sector Governance**

#### **3.3.1 Water Sector Governance**

In sub-Saharan Africa, water governance does not follow a coherent model. Most French-speaking countries have retained the unique public enterprise model, while most English-speaking countries have undertaken some decentralization to local jurisdictions [26]. Where services are centralized, a significant minority have chosen to combine water and electricity distribution into a single national entity [61].

In Tunisia, for example, water policy has shifted from supply management, an extensive hydropower infrastructure implemented, to demand management over the past three decades [8]. The provision of services in Tunisia is centred on two leading national operators: the national sanitation board (ONAS) and the national company of exploitation and distribution of water (SONEDE). Private sector participation in the water sector remains limited. However, neither SONEDE nor ONAS has attempted to use the private sector to supplement its operations [62].

Private sector participation has been used less in the water supply sector. In 2011, SONEDE delegated some tasks to the private sector, such as leakage inspection (up to 34%). This is the same model of governance seen in Jordan [63]. However, several authors agree that water sector governance based on solid centralization of responsibilities and decision-making powers also has limitations when reaching the population in remote neighbourhoods [28]. Moreover, in Niger, it has been shown that the state has maintained the option of “hybrid” agriculture, in which the farmer must participate in investments in the sector in addition to farming. Still, only Law No. 2000-12 of 14, August, 2000, concretizes institutional reform [64]. In contrast to the Ivory Coast, where the Ministry of Water directly manages the investments, Niger established a body solely accountable for funds to guarantee transparency and monitor donor commitments and assets [42].

Due to differences in political and demographic circumstances, Niger and Senegal have opted for leasing rather than concessions. Therefore, Senegal claims to have the highest rate of urban connectivity in all of Sub-Saharan Africa [42]. The same approach (leasing), where a wealthy company makes investments, has produced excellent results in Ivory Coast: nearly three million people have had access to clean water in their homes since 1990, with connections funded entirely from bill revenues, without any public funding [58].

In this respect, the observation made in Maputo [65] differs from that of Marin [58] in Ivory Coast. In Maputo (Mozambique), the operator Aguas de Mozambique (AdeM) provides the water supply, which is particularly weakened in peri-urban areas where the network has often not been developed. The private and independent informal operators (Pequeños Operadores Privados, POPs) have invested since the

late 1980s in realising small food systems fed by local groundwater resources, a unique situation in Africa [65].

However, the scenario of water sector governance in Venezuela is exemplary: water co-production policies between public institutions and organized communities have expanded and improved access to this basic technical service [32]. The same observation is made in Mali, where water user associations (WUAs) have been formed in rural villages (about 3–10,000 inhabitants) as part of water sector investment programmes.

In Guatemala, for example three forms of water sector coexist to provide water to urban households: municipal, private, and community-managed public service [25]. According to the current water legislation, two municipalities are the leading water supplier in urban areas, reaching almost 74% of urban households. This form of governance places Guatemala second among Central American countries, behind Costa Rica, where 100% of urban households have access to piped water [66].

Unlike other urban service sectors in Vietnam, the water sector is decentralized at the provincial level [67]. For example, in Ho Chi Minh City, official drinking water services are provided by two institutions: a public enterprise for the dense urban areas and the rural water supply centre; for the intense urban regions in the remote periphery. Overall, the cases where water supply management has improved have come about either through individualistic practises (at the household level) or through community practises (at the neighbourhood level) and even through authoritarian intervention by the state [68].

### **3.3.2 Governance of the Electricity Sector**

In DR Congo, for example, the government has controlled the electricity sector since independence through the National Electricity Company (SNEL). This national company is under the direct control of the Ministry of Energy. The Ministry of Public Enterprises controls the financial aspect of SNEL. The government does not have a regulatory structure for the electricity sector [40]. In many developing countries that have recognized the need to involve the private sector in electricity, this type of governance is disappearing. Attempts to reform the electricity sector in DR Congo are only theoretical. The recent Law No. 14/011 of 17, June, 2014, on the electricity sector, provides for effective measures:

- an effective liberalization of the electricity sector;
- promotion and harmonious development of electricity supply in urban, peri-urban and rural areas and compliance with safety and environmental standards;
- creating;
- the institutional framework and favourable economic conditions;
- ensuring and implementing profitable investments in the electricity sector and the emergence of a national energy supply system within the framework of a public–private partnership;

- ensuring fair competition among operators and respecting users' rights [69].

Interesting proposals for the Katanga region in DR Congo were made by Eberhard et al. [70]. To solve their problems, mining companies could work with SNEL [71]. If the efforts of the mining companies and SNEL in Katanga were successful, the beneficiaries would be the mines themselves and the population. Local industry and the people would have a surplus of electricity to boost the economy.

In Ivory Coast, private sector participation in electricity does not only concern the production sector [72]. The state arranged with a private company responsible for operating the entire industry. This model has responded positively even during the period of political crisis. This impressive increase is a response to the growing demand and cannot be achieved without the participation of the private sector [73]. However, the public–private partnership can cause fundamental problems if it is not adequately structured and coordinated [74].

The energy produced by independent generators must first be purchased, which can cause constraints in the optimal programming of the plants' production [75]. Therefore, a fleet consisting solely of independent producers with a take-or-pay obligation is not feasible, as the entire production system would be constrained [74]. Moreover, energy is under four ministries (coal, electricity, oil and gas, and new and renewable energy). The Ministry of Atomic Energy has been under the Prime Minister since its establishment in 1954 [75].

The governance of electricity supply in Delhi provides an interesting case study. In a situation of public sector failure, the Delhi Electricity Supply Board has opted for unbundling the state agency and privatizing electricity distribution [4]. The first phase is unbundling the national electricity company into several small, concentrated, state-controlled companies [76]. The second phase must be the privatization of the resulting companies. The National Capital Territory government began restructuring Delhi's electricity industry to meet the goals of the Delhi Electricity Reform Act of 2000. After learning from the unbundling and privatization experiences of other states and receiving advice from the Regulatory Commission, the Delhi government opted for a restructuring plan that followed the spirit of the 2000 Act and allowed for the smooth transition of an organization integrated into a group of unbundled entities that were reconfigured along functional lines [77]. The national breakup authority is unbundled into six companies: a holding company, a generation company, a transmission company, and three distribution companies. The three distribution companies, which are critical to improving consumer services and economic profitability, were privatized on 31, May, 2002 [4]. The share purchase agreements are signed with Tata Electricity Company. This type of management has improved the electricity situation in the Indian capital [1].

Verdeil's work [3] shows that EDL (the national company) has a virtual monopoly on electricity generation, transmission and distribution in the country, except for four small private concessions and private/semi-private hydroelectric plants. From a technical perspective, there is a large gap between national demand and supply. Frequent power outages have led households to resort to private generators, which

impose additional costs. These deficits amount to billions of dollars in annual losses for the Lebanese economy [3].

In Brazil, independent power producers were formalized by Law 9074 and are either public or private power generation companies. In addition, the electricity sector reform defined some enforcement bodies.

Another form of governance that has proven to be very effective in most developing countries where rapid urban growth is uncontrolled is the use and promotion of renewable energy [78]. Some governments have taken the necessary measures to facilitate the access and adoption of solar PV, especially in the electrification of remote areas [79]. There are two photovoltaic (PV) systems: islanded and non-islanded [80]. In scattered residential areas, the stand-alone type is recommended [79, 81]. In PV promotion, the role of the government in implementing incentives is of utmost importance. Nepal, for example has exempted some technologies, such as solar PV and hydropower, from import duties. China and India have reduced VAT rates for renewable energy installations.

Other measures demonstrating strengthening governance include fighting corruption through public education, information, and whistleblowing. For example, public information campaigns fighting against harmful practices such as electricity theft and corruption have produced significantly productive results in several cases [53]. Indeed, these information campaigns have helped educate the population and those in power to adopt positive behaviours.

Several authors suggest using the media, including regular media interventions, public service announcements on television, websites, religious sermons and information directly on consumers' electricity bills [82, 83]. Indeed, the media can combat corruption by informing policymakers and authorities, raising public awareness about corruption, its causes, consequences, and possible remedies, exposing corrupt officials, and prompting investigations by official bodies [82]. In addition, three strategies have been proposed to inform the public [84]: (i) raise public awareness of the economic dimension of illegal electricity use, (ii) communicate the social harm of illegal electricity use to the public and (iii) communicate the link between illegal electricity use and religious and moral values. Finally, socio-economic factors that significantly influence electricity theft are mentioned in [85]:

- the misconception of some consumers who believe that theft is a dishonest act only if it is committed at the neighbour's house and not at a national company like SNEL;
- unemployment and the poor economic situation of some customers;
- ignorance/absence of laws and crimes related to electricity theft;
- company employees are sometimes corrupt and responsible for billing irregularities.

### 3.4 Discussion and Prospective

Figure 1 shows the components of a successful model of water and electricity sector governance in developing countries. The Venn diagram shows that water and electricity consumers are at the centre of governance. They are the ultimate beneficiaries and are usually organized into local organizations to fight corruption and promote good governance. In addition, private and public companies are regulated by municipal and regional authorities. Above all, there is the national government. In the successful models of the water and electricity sectors, the national government, whose primary role is to set the legal framework, has implemented decentralization and liberalization of production and supply. As part of these incentive measures, regional governments can regulate public and private companies in their regions. Besides, private and public companies can operate separately to promote competition or in partnerships to join forces. At the municipal level, local authorities can regulate civil organizations (NGOs and communities) that form groups to promote water and electricity supply and good governance. Involving consumers in governance (as civil organizations) has the advantage of promoting the fight against corruption, illegal and abusive use, and monitoring facilities. Implementing such policies can assist countries, such as DR Congo, with a critical water potential, for instance, the congo river, etc., to implement energy-water nexus to increase the resilience of power and water supply systems [86].

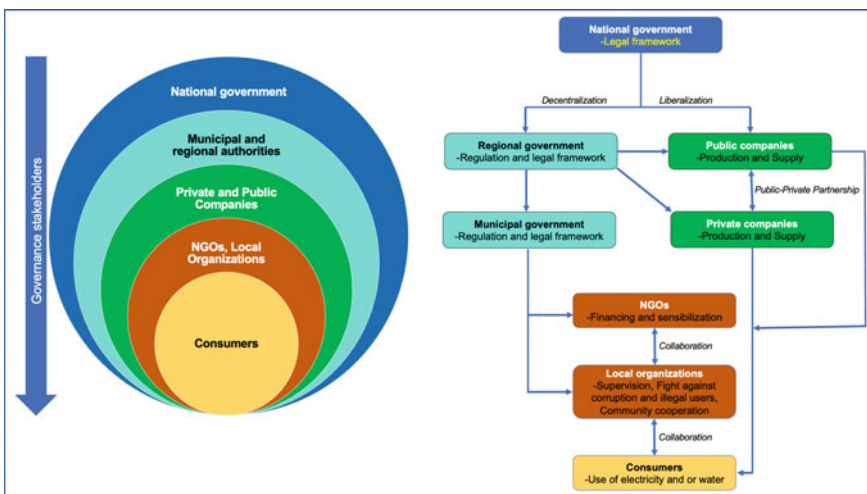


**Fig. 1** Conceptual model of water and power sector governance in developing countries

## 4 Conclusion

The governance of urban services in developing cities has been the subject of this review. The synthesis of several studies shows no appropriate form of government at every time and place. In most cases, the public sector involves the private sector in water and electricity management. Many countries that have liberalized electricity generation have reformed utility regulations by introducing incentive regulation models.

Both positions criticize public and private utility systems mainly in terms of two main objectives: supply efficiency at acceptable prices and inclusive and accountable governance, capable of meeting the demand of the poorest. The way the private sector intervenes in the management of technical services depends, in most cases, on political (instability), demographic (solid urban growth), economic (poverty) and historical factors (no experience in the delegation of public services). However, at the metropolitan level, some policies may provide appropriate solutions in developing countries. Indeed, engaging the population through anti-corruption training campaigns is an effective way to improve governance. Given the cost of expanding the conventional electricity grid, solar PV has proven to be a safe and sustainable way to power urban and peri-urban communities. However, success in promoting this environmentally friendly energy source lies in government involvement through incentives. This work opens a door for future research. Studies should be conducted to assess the impact of socio-economic conditions on the governance of water and electricity. This is crucial to propose governance models adapted to the different realities of developing countries. In addition, the scientific research component in water and electricity governance should be highly prioritized to encourage innovation.

## References

1. Criqui L (2020) Sociotechnical alternatives and controversies in extending water and sanitation networks in Lima, Peru. *Water-alternatives.org* 1(13):160–181
2. Nam KY, Asian Development Bank (2015) Assessment of power sector reforms in Asia: experience of Georgia, Sri Lanka, and Viet Nam—synthesis report. ASian Dev. Bank, p 99
3. Verdeil É (2009) Électricité Et Territoires : Un Regard Sur La Crise Libanaise. *Rev. Tiers Monde* 198(2):421
4. Dementhon T (2011) La gouvernance des réseaux de services urbains: Le cas des réformes du réseau électrique du Territoire de la capitale nationale de Delhi, Institut d'urbanisme de Lyon Université Jean Moulin Lyon 3. Institut d'urbanisme de Lyon Université Jean Moulin Lyon 3
5. “World Development Report 1994,” World Dev. Rep. 1994
6. Barbier E (2013) Valuing ecosystem services for coastal wetland protection and restoration: progress and challenges. *Resources* 2(3):213–230
7. Madiba T, Bansal RC, Mbungu NT, Bettayeb M, Naidoo RM, Siti MW (2021) Under-frequency load shedding of microgrid systems: a review. 42(4):653–679. <https://doi.org/10.1080/02286203.2021.1964061>
8. Tazi Sadeq H (2020) Water governance in a context of scarcity. <http://journals.openedition.org/factsreports>, no. Special Issue 22:34–39

9. Wilder M, Romero Lankao P (2006) Paradoxes of decentralization: water reform and social implications in Mexico. *World Dev.* 34(1):1977–1995
10. Azaroual M, Mbungu NT, Ouassaid M, Siti MW, Maaroufi M (2022) Toward an intelligent community microgrid energy management system based on optimal control schemes. *Int J Energy Res*
11. Jaglin S (2022) Urban electric hybridization: exploring the politics of a just transition in the Western Cape (South Africa). <https://doi.org/10.1080/10630732.2022.2111176>
12. Hamid AK, Mbungu NT, Elnady A, Bansal RC, Ismail AA, AlShabi MA (2022) A systematic review of grid-connected photovoltaic and photovoltaic/thermal systems: benefits, challenges and mitigation. *Energy Environ*
13. D'Afrique SJ (2007) Décentralisation et gouvernance de la diversité. *Gouv les villes Local, Gouv*
14. Jamasb T, Nepa R (2015) Energy sector Liberalisation: pricing and subsidy reform and the poor. In: 38th IAEE international conference, 2015, pp 5–6
15. Foster V, Rana A (2019) Rethinking power sector reform in the developing world. World Bank Publ
16. Burke MJ, Stephens JC (2018) Political power and renewable energy futures: a critical review. *Energy Res Soc Sci* 35:78–93
17. Tortajada C (2010) Water governance: some critical issues 26(2):297–307. <https://doi.org/10.1080/07900621003683298>
18. Mulugetta Y et al (2022) Africa needs context-relevant evidence to shape its clean energy future. *Nat Energy* 2022 711, 7(11):1015–1022
19. Le Galès P (2016) Neoliberalism and urban change: stretching a good idea too far? 4(2):154–172. <https://doi.org/10.1080/21622671.2016.1165143>
20. Orum A (2019) The Wiley-Blackwell Encyclopedia of Urban and Regional Studies
21. “La contractualisation: une clé pour la gestion durable des services essentiels | AFD—Agence Française de Développement 2008. [Online]. Available: <https://www.afd.fr/fr/ressources/la-contractualisation-une-cle-pour-la-gestion-durable-des-services-essentiels>. Accessed 10-Dec-2022
22. Bialès C (2000) La gestion. *Cah. D' Économie Gest.* 65:1–12
23. Joumard R (2009) Le concept de gouvernance. *Rev. Interdiscip. d'études Juridiques* 65(2)
24. Commission E (2009) European Commission Sustainability Report 13:2009
25. Vásquez WF (2013) An economic valuation of water connections under different approaches of service governance. *Water Resour Econ* 2–3:17–29
26. Jaglin S (2007) Décentralisation et gouvernance de la diversité. *Les Serv urbains en Afrique anglophone Arch* 21–34
27. Rutherford J, Jaglin S (2015) Introduction to the special issue-urban energy governance: local actions, capacities and politics. *Energy Policy* 78:173–178
28. Legrouri A, Sendide K, Kalpakian JV (2019) Enhancing integrity in water Governance in Morocco: opportunities and challenges. *J Gov Integr* 3(1):1–9
29. Mahalingam S, Jairaj B, Washington SN, undefined DC, and undefined 2006, “Electricity sector governance in India: an analysis of institutions and practice. academia.edu
30. Zoé LS (2020) Plural governance for the management of local public services: an empirical investigation on the French Car Park Industry. *M@n@gement* 23(4):28–43
31. de Castro NJ, Soares I, Rosental R, Sellare AJ, TDSE (2010) Impacts of corporate governance on companies im Brazil's Electricity Sector N°24. *GESEL—Grup. Estud. Do Set. Elétrico*
32. Moretto L (2015) Application of the ‘urban governance index’ to water service provisions: between rhetoric and reality. *Habitat Int* 49:435–444
33. Erramli N, MK-I J of Applied, and undefined (2017) Governance of public enterprises in Morocco: measuring efficiency by combining the Sugeno integral method and the AHP method. *ripublication.com* 12:10249–10257
34. “Recommendation of the Council on Principles for Public Governance of Public-Private Partnerships,” 2012

35. Jamasb RN (2015) T Energy Sector Liberalisation: pricing and subsidy reform and the poor. In: Proceedings international association for energy economics, Antalya Special Issue
36. Lima S, Brochado A, Marques RC (2021) Public-private partnerships in the water sector: a review. *Util Policy* 69:101182
37. Jamasb T (2006) Between the state and market: electricity sector reform in developing countries. *Util Policy* 14(1):14–30
38. Baker L, Phillips J (2018) Tensions in the transition: the politics of electricity distribution in South Africa. *Environ Plan C Polit Sp* 37(1):177–196
39. Berg SV (2015) Energy efficiency in developing countries: roles for sector regulators. *Energy Sustain Dev* 29:72–79
40. Lukamba-Muhiya JM, Uken E (2006) The electricity supply industry in the Democratic Republic of the Congo. *J Energy South Africa* 17(3):21–28
41. “An AMCOW Country Status Overview Water Supply and Sanitation in Burkina Faso Turning Finance into Services for 2015 and Beyond,” 2011
42. AFD, “Accès à l’électricité en Afrique subsaharienne: retours d’expérience et approches innovantes | AFD—Agence Française de Développement. Document de Travail, 2012. [Online]. Available: <https://www.afd.fr/fr/ressources/acces-lelectricite-en-afrique-subsaharienne-retours-dexperience-et-approches-innovantes>. Accessed: 20-Dec-2022
43. G. Weynand EGAT (2005) Improving power distribution company operations to accellerate power sector reform. USAID
44. Mondejar ME et al (2021) Digitalization to achieve sustainable development goals: steps towards a smart green planet. *Sci Total Environ* 794:148539
45. “La contractualisation: une clé pour la gestion durable des services essentiels by Agence Française de Développement—Issuu,” 2008. [Online]. Available: <https://issuu.com/objectif-developpement/docs/43-notes-documents>. Accessed: 20-Dec-2022
46. Zérah M-H (2003) Dix ans de libéralisation de l’économie indienne : les effets limités de la gouvernance dans le secteur de l’eau et de l’assainissement en ville. *Autrepart* 27(3):91–106
47. Mustafa D, Reeder P (2009) ‘People is all that is left to privatize’: water supply privatization, globalization and social justice in Belize City, Belize. *Int J Urban Reg Res* 33(3):789–808
48. Bult-Spiering M, Dewulf G (2008) Strategic issues in public-private partnerships: an international perspective. *Strateg. Issues Public-Private Partnerships An Int. Perspect*
49. McGranahan G, Satterthwaite D (2006) Governance and getting the private sector to provide better water and sanitation services to the urban poor
50. Megginson WL, Netter JM (2001) From state to market: a survey of empirical studies on privatization. *J Econ Lit* 39(2):321–389
51. Andres LA, Foster V, Guasch JL (2006) The impact of privatization on the performance of the infrastructure sector: the case of electricity distribution in Latin American countries. 01-Jun-2006
52. “Electricity Sector Deregulation in the APEC Region, 2000 | APEC.” [Online]. Available: <https://www.apec.org/publications/2000/03/electricity-sector-deregulation-in-the-apec-region-2000>. Accessed: 20-Dec-2022
53. Banza BB, Mbungu NT, Siti MW, Tungadio DH, Bansal RC (2022) Critical analysis of the electricity market in developing country municipality. *Energy Rep* 8:329–337
54. Bacon RW, Besant-Jones J (2003) Global electric power reform, privatization, and liberalization of the electric power industry in developing countries. 26:331–359. <https://doi.org/10.1146/annurev.energy.26.1.331>
55. Ahmad A, McCulloch N, Al-Masri M, Ayoub M (2022) From dysfunctional to functional corruption: the politics of decentralized electricity provision in Lebanon. *Energy Res Soc Sci* 86:102399
56. Trotter PA, McManus MC, Maconachie R (2017) Electricity planning and implementation in sub-Saharan Africa: a systematic review. *Renew Sustain Energy Rev* 74:1189–1209
57. Wamukonya A, Davidson N, Brew-Hammond O (2008) Réformes du secteur de l’énergie électrique en Afrique subsaharienne : principales leçons et priorités. *Liaison Energie-Francophonie*. *Liaison Énergie-Francophonie* 73:39–44

58. Marin P (2009) Public private partnerships for urban water utilities: a review of experiences in developing countries
59. Bardhan P (2002) Decentralization of governance and development. *J Econ Perspect* 16(4):185–205
60. Allen A, Dávila JD, Hofmann P (2016) The peri-urban water poor: citizens or consumers? *Environ Urban* 18(2):333–351
61. Johnson RC et al (2014) Situation of water, hygiene and sanitation in a peri-urban area in Benin, West Africa: the case of S&#232;m&#232;-Podji. *J Environ Prot (Irvine Calif)* 05(12):1277–1283
62. Renou Y (2009) La gouvernance des services de l'eau à l'aune du XXIe siècle: une analyse en termes de stratification de l'action. LEPPI - Lab d'Economie la Prod l'Intégration Int
63. “La gouvernance par la gestion intégrée des ressources en eau au Maroc : Levier fondamental de développement durable,” *Conseil Economique, Social et Environnemental - Rabat - Maroc*. [Online]. Available: <https://www.pseau.org/outils/biblio/resume.php?d=10311>. Accessed: 21-Dec-2022
64. Dupont V (2022) Financement des services d'eau en milieu urbain au Niger | OIEau – Eaudoc. Développer les compétences pour mieux gérer l'eau, 2010. [Online]. Available: <https://www.oieu.fr/eaudoc/oai/Financement-des-services-d-eau-en-milieu-urbain-au-Niger> [Accessed: 21-Dec-2022]
65. Blanc E, Cavé J, Chaponniere E (2009) Les Petits opérateurs privés de la distribution d'eau à Maputo: d'un problème à une solution? Regards croisés. Doc Trav—AFD 85:54
66. Lentini MR, Fraser SI, Scott Sumner H, Davies RJ (2010) Geodynamics of the central South Atlantic conjugate margins: implications for hydrocarbon potential. *Pet Geosci* 16(3):217–229
67. “Basic Services for All in an Urbanizing World - Google Books.” [Online]. Available: [https://books.google.ae/books?hl=en&lr=&id=SR0WBAAAQBAJ&oi=fnd&pg=PP1&dq=Basic+services+for+all+in+an+urbanizing+world&ots=8fNMyQ5STl&sig=NvVQgSdHbIO63WQOpbc24C\\_jvIQ&redir\\_esc=y#v=onepage&q=Basicservices](https://books.google.ae/books?hl=en&lr=&id=SR0WBAAAQBAJ&oi=fnd&pg=PP1&dq=Basic+services+for+all+in+an+urbanizing+world&ots=8fNMyQ5STl&sig=NvVQgSdHbIO63WQOpbc24C_jvIQ&redir_esc=y#v=onepage&q=Basicservices) for all in an urbanizing world&f=false. Accessed: 21-Dec-2022
68. Botton S, Blanc A (2010) Accès de tous aux services d'eau: le rôle des petits opérateurs privés à Hô Chi Minh ville, Vietnam
69. “Journal Officiel de la RD. (2018). La loi n° 14/011 du 17 juin 2014 relative au secteur de l'électricité”
70. A. Eberhard, O. Rosnes, M. Shkaratan, and H. Vennemo (2011) Africa's power infrastructure: investment, integration, efficiency. The Word B. The Word Bank
71. Maennling N , Toledano P, Thomashausen S, Natural resource charter case study mine power: partnering to upgrade energy infrastructure in the DRC
72. Banerjee S, Skilling H, Foster V, Briceno-Garmendia C, Morella E, Chfadi T (2008) Africa—Ebbing Water, Surging Deficits : Urban Water Supply in Sub-Saharan Africa. World Bank, Washington, DC
73. Eberhard A, Gratwick K, Morella E, Antmann P (2017) Independent power projects in sub-Saharan Africa: investment trends and policy lessons. *Energy Policy* 108:390–424
74. Gangwar R, Raghuram G (2015) Framework for structuring public private partnerships in railways. *Case Stud Transp Policy* 3(3):295–303
75. Giraud P (2008) La croissance urbaine soutenable des villes du Sud. Quelques remarques. *Réalités Ind* 20(1):32–36
76. Phillips J, Newell P (2013) The governance of clean energy in India: the clean development mechanism (CDM) and domestic energy politics. *Energy Policy* 59:654–662
77. Racine JL (2014) The geopolitics of Indian energy. *Herodote* 155(4):114–134
78. Mbungu NT, Milambo KD, Siti MW, Bansal RC, Naidoo RM, Kiseya FT (2022) Assessing and mapping electricity access patterns in developing countries. In 7th International conference on renewable energy and conservation, ICREC 2022 November 18–20, 2022
79. Birajdar P, Bammani S, Shete A, Bhandari R, Metan S, Assessing the technical and economic feasibility of a stand-alone PV system for rural electrification: a case study. *Int J Eng Res Appl* 3:2525–2529

80. Siti MW, Mbungu NT, Tungadio DH, Banza BB, Ngoma L, Tiako R (2022) Economic dispatch in a stand-alone system using a combinatorial energy management system. *J Energy Storage* 55
81. Poti KD, Naidoo RM, Mbungu NT, Bansal RC (2022) Intelligent solar photovoltaic power forecasting. In: 7th International conference on renewable energy and conservation, ICREC 2022 November 18–20, 2022
82. Bhatia B, Gulati M (2004) Reforming the power sector: controlling electricity theft and improving revenue
83. Mutebi RM, Otim JS, Okou R, Sebitosi B (2015) Electricity theft in kampala and potential ICT solutions. *Lect Notes Inst Comput Sci Soc Telecommun Eng LNICST* 147(April 2018):198–206
84. Onat N (2010) Recent developments in maximum power point tracking technologies for photovoltaic systems. *Int J Photoenergy* 2010
85. Depuru SSSR, Wang L, Devabhaktuni V (2011) Electricity theft: overview, issues, prevention and a smart meter based approach to control theft. *Energy Policy* 39(2):1007–1015
86. Mbungu NT, Bansal RC, Naidoo RM, Siti MW, Tungadio DH (2020) Modelling of a smart hybrid water-power system for freshwater and energy supply network. In: 2020 1st International conference on power, control and computing technologies, ICPC2T 2020, pp 6–9, 2020

# Far-Field Radiation Pattern Synthesis of Elliptical Antenna Arrays Using GA and PSO



Satish Kumar, Gopi Ram, Durbadal Mandal, and Rajib Kar

**Abstract** In this paper, Genetic Algorithm (GA) and Particle Swarm Optimization (PSO) are used to solve a design challenge for non-uniform elliptical antenna arrays (EAAs) in a single ring with the best sidelobe level (SLL). An optimal combination of inter-element spacing and current excitation for EAA that provides an array pattern with the greatest possible reduction in SLL is determined using these techniques. It is assumed that an EAA is placed on an X-Y plane. A 12-, 16- and 20-element elliptical array is optimized using PSO and GA. On the basis of various simulation results, the performances of sidelobe level have been analyzed. The maximum reduced sidelobe level is getting for 12, 16 and 20 elements using PSO as compared to GA.

**Keywords** Elliptical arrays · Sidelobe level · GA · PSO

## 1 Introduction

In order to integrate the radiations from a group or array of identical antennas when the phenomenon of wave interference is present, one typical technique is the antenna array. Antenna arrays are extensively used in modern radar and communication technologies. The first antenna array is operated in the kilohertz range. Nowadays, arrays can function at nearly any frequency. Antenna array research and development began more than a century ago. In the last few decades, research has been done on various antenna arrays to optimize the radiation pattern. Antennas with strong directional

---

S. Kumar (✉) · D. Mandal · R. Kar

Department of Electronics and Communication Engineering, National Institute of Technology  
Durgapur, Durgapur, India

e-mail: [sk.ece.nitdgp@gmail.com](mailto:sk.ece.nitdgp@gmail.com)

G. Ram

Department of Electronics and Communication Engineering, National Institute of Technology  
Warangal, Warangal, India

e-mail: [gopi.ram@nitw.ac.in](mailto:gopi.ram@nitw.ac.in)

characteristics are frequently needed to meet the need for long-distance communication. The antenna array is made up of radiating components that are organized in a geometrical or electrical manner. The fields generated by a current excitation element for each individual antenna are added to determine the overall field of the antenna array [1, 2]. The array's fields must add effectively in the intended direction, add destructively in the opposite way and cancel out each other in the continuing space to give a very directed pattern [3, 4]. The radiation pattern can be altered by adjusting a number of parameters like individual element patterns, different geometrical configurations, inter-element spacing, amplitude excitation and phase excitation [5, 6]. It is extensively employed in many high-performance radio systems, including radar, which operates in the microwave frequency spectrum chart, communication, navigation, etc., to give exceptionally competent antenna features with increasingly strict constraints like high gain, wideband, radical low sidelobes and so on with the rapid advancement of technology [7]. SLL can be decreased by increasing thinning percentage [8].

In the present case, the current excitation levels and antenna inter-element separations of the elements are utilized to determine the variable that would change the radiation pattern of SLL with a maximum decrease. The GA and PSO techniques are used to solve the design problem for implementation in an application with a wide range.

The remaining part of the paper is described as follows: in Sect. 2, the description of the design equation of non-uniform EAA. Then, in Sect. 3, a brief description of the evolutionary optimization technique which are GA and PSO. Computation results and convergence curve are discussed in Sects. 4 and 5, respectively. In Sect. 6, conclusion of the paper with a work summary. Finally, in Sect. 7, the description of acknowledgments is mentioned.

## 2 Design Equations

Let us consider  $N$  isotropic sources of an elliptical array (EA) in the  $x$ - $y$  plane in Fig. 1 having ' $a$ ' and ' $b$ ' which is the length of semi-major axis and semi-minor axis, respectively, and in the far field, searching at a point P. Assuming that the elements constitute an isotropic source, the array factor of the non-uniform EAA may be used to depict its radiation pattern. The array factor for the elliptical array is defined by [9].

$$AF(\theta, \phi) = \sum_{n=1}^N I_n e^{j[k \rho_n \sin \theta \cos(\phi - \phi_n) + \alpha_n]}, \quad (1)$$

where

$$k = 2\pi/\lambda.$$

$\lambda$  = Operational wavelength.

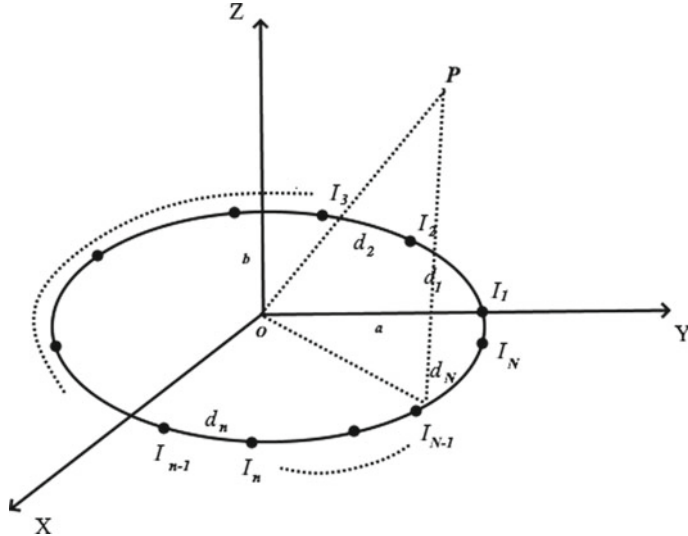


**Fig. 1** Schematic of non-uniform elliptical array scanning at a point P with N isotropic elements

$\theta$  = An elevation angle.

$\phi$  = Azimuthal angle.

$a$  = Radius of the circular array.

$I_n$  = The excitation amplitude of the  $n$ th element.

$\phi_n$  = The angular position of the  $n$ th element.

$$\phi_n = \frac{2\pi(n-1)}{N}. \quad (2)$$

$\alpha_n$  = The excitation phase of the  $n$ th element.

$$\rho_n = \frac{ab}{\sqrt{(b \cos(\phi_n))^2 + (a \sin(\phi_n))^2}}. \quad (3)$$

$$\alpha_n = -k\rho_n \sin(\theta_o) \cos(\phi_o - \phi_n). \quad (4)$$

From Eqs. (1) and (4), the array factor may be defined as:

$$AF(\theta, \phi) = \sum_{n=1}^N I_n e^{jk \rho_n [\sin(\theta) \cos(\phi - \phi_n) - \sin(\theta_o) \cos(\phi_o - \phi_n)]}. \quad (5)$$

$I = [I_1, I_2, \dots, I_N]$ , and  $d = [d_1, d_2, \dots, d_N]$ , where  $I_n$  and  $d_n$  represent the  $n$ th excitation element and gap from the element  $n$  to  $n+1$  of the array, respectively. In our design, global maximum is obtained at greatest radiation angle  $\phi_0 = 0$  degrees

in  $\phi = [-\pi, \pi]$ . In order to achieve the array pattern with the best minimization of SLL in the intended direction  $\phi$ , the objective of the study is to identify the ideal set of  $I_n$  and  $d_n$  values with which the antenna design is modified.

The next phase is to define the minimized objective function. The objective function  $f$  can be defined as

$$f = W_1 \times |\text{AF}(\phi_{\max \text{ sl}}, I_n)| / |\text{AF}(\phi_0, I_n)|, \quad (6)$$

where  $\phi_{\max \text{ sl}}$  is the angle at which the main beam's sidelobe on either side reaches its maximum sidelobe  $\text{AF}(\phi_{\max \text{ sl}}, I_n)$ .  $W_1$  is weighting factors that are chosen such that the optimal value of sidelobe level remains more and  $f$  never be negative. The GA and PSO techniques are applied for optimizing  $I_n$  and  $d_n$  for minimization of  $f$ .

### 3 Evolutionary Optimization Method Used

#### 3.1 Genetic Algorithm (GA)

The heuristic search and optimization methods known as Genetic Algorithms imitate the process of natural evolution based on Darwin's principal. This optimization technique draws inspiration from the well-known biological processes of genetics and evolution. In this process, the strongest elements become stronger, while the weaker elements are terminated. A GA will start with a population of initial solutions generated at random. Chromosome refers to the input of an objective function  $f$ . The cost is the result of the goal function. A chromosome is made up of distinct variables. A population of chromosomes is a matrix with each row representing a chromosome and is referred to as a collection of chromosomes. An objective function  $f$  uses each chromosome as an input, and it determines the cost for each chromosome either sequentially or concurrently. An individual's fitness in the population is determined by their cost. A low cost for a minimization issue suggests a high fitness value. The following steps involve in GA [10, 11]:

- A random sample of solutions is used to construct the initial population.
- Depending on how near a solution really comes to fixing the problem, a fitness score is given to each one.
- Solutions with higher fitness values have a higher propensity to create offspring that are susceptible to mutation after reproduction.
- The issue is resolved if the new generation has a solution that results in an output that is sufficiently close to or equal to the intended response.

A GA has some limitation which is given below.

- Complexity increases slowly for genetic algorithms. In other words, the search space size typically grows exponentially in areas where there are many components that are susceptible to mutation.
- Being stochastic, there are no guarantees on the optimality or the quality of the solution.

### 3.2 Particle Swarm Optimization (PSO)

PSO is a bioinspired optimization approach based on population with a uniformity that performs effectively with non-differential objective functions. PSO is developed in three-dimensional space from a simulation of the motion of fish schooling. The specific objective function is optimized through fish schooling. Each particle (fish) is aware of its latest optimal value ( $pbest$ ). This information relates to each particle's individual experiences. However, each fish knows the optimum value, in the  $gbest$  (group best) of  $pbests$  so far, and attempts to improve its location using the methods described below:

- The separation between the  $pbest$  and the current location.
- The separation between the  $gbest$  and the current location.

In the Particle Swarm Optimization technique, let us assume the particle vectors of the population are  $n_{pop}$ . In the EAA design, each particle vector has the necessary number of components for inter-element spacing weights and current excitation.

Mathematically, modify the particle vector's speed and location as the following equations [12–14]:

$$V_i^{k+1} = w \times V_i^k + a_1 \times rd_1 \times (pb_i^k - X_i^k) + a_2 \times rd_2 (gb_i^k - X_i^k), \quad (7)$$

$$X_i^{k+1} = X_i^k + V_i^{k+1}, \quad (8)$$

where  $rd_1$  and  $rd_2$  are the random values that lie between zero and one;  $a_1$  and  $a_2$  are the local acceleration and the global acceleration constants of the particle, respectively;  $w$  is a weighting factor;  $V_i^k$  is the velocity in the  $k$ th iteration of  $i$ th particle;  $pb_i^k$  is the  $i$ th particle's local best in  $k$ th iteration;  $gb_i^k$  is the global best of all particles in  $k$ th iteration;  $X_i^k$  is the current position in the  $k$ th iteration of  $i$ th particle.

## 4 Computational Result

This section presents the simulation results for several EAA designs utilizing GA and PSO methodologies of SLL. This scenario considers the radiation pattern of the EAA, with the primary lobe at  $\phi_0 = 0^\circ$ . It is assumed that there are three non-uniform EAAs with 12, 16 and 20 elements. The population size is maintained at 120 and the algorithm has been run 400 times. The PSO and GA algorithms are initiated with random values. Figures 2, 3 and 4 compare the radiation patterns ( $d = \lambda/2$ ) of uniform and asymmetrical elliptical antenna arrays that were optimized using the GA and PSO algorithms for elliptical arrays with 12, 16 and 20 elements. The inter-element spacing  $d$  in an elliptical antenna array is the distance in an arc between two subsequent elements placed in an ellipse having an eccentricity  $e$  ( $e = \sqrt{1 - (b^2/a^2)}$ ).

Figure 2 demonstrates the argument for  $N = 12$ . Given that, in Table 1 using the GA and PSO techniques, an  $I_n$  and  $d_n$  set is obtained that produces a radiation pattern that has  $-8.96$  dB and  $-11.84$  dB SLL, respectively, which is a maximum SLL reduction in comparison to those in [9]. Figure 3 indicates the case for  $N = 16$ . Given that, in Table 1 using the GA and PSO techniques, an  $I_n$  and  $d_n$  set is obtained that produces a radiation pattern that has  $-11.17$  dB and  $-11.49$  dB SLL, respectively, which is a maximum SLL reduction. The simulation result for 16-element EAA is not reported in [9]. Figure 4 demonstrates the argument for  $N = 20$ . Given that, in Table 1 using the GA and PSO techniques, an  $I_n$  and  $d_n$  set is obtained that produces a radiation pattern that has  $-12.99$  dB and  $-14.40$  dB SLL, respectively, which is a maximum SLL reduction in comparison to those in [9].

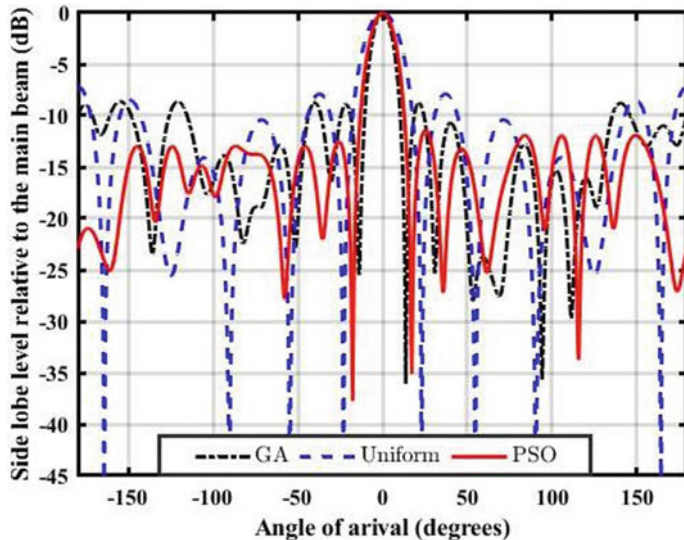


**Fig. 2** Array pattern for non-uniform 12-element elliptical array

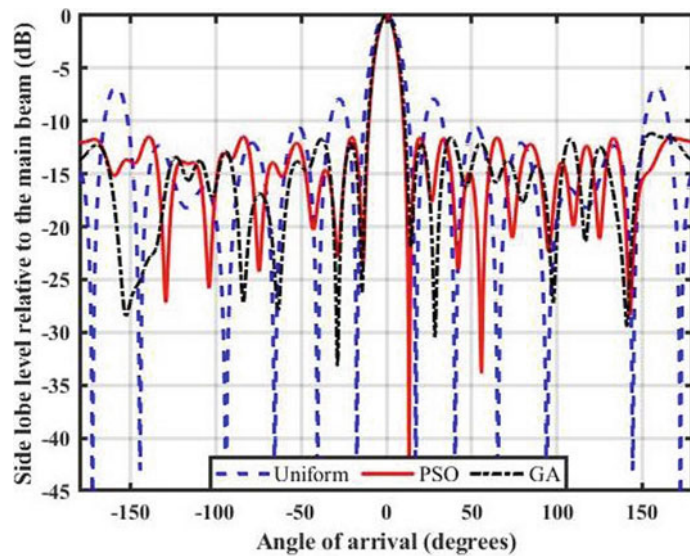


**Fig. 3** Array pattern for non-uniform 16-element elliptical array

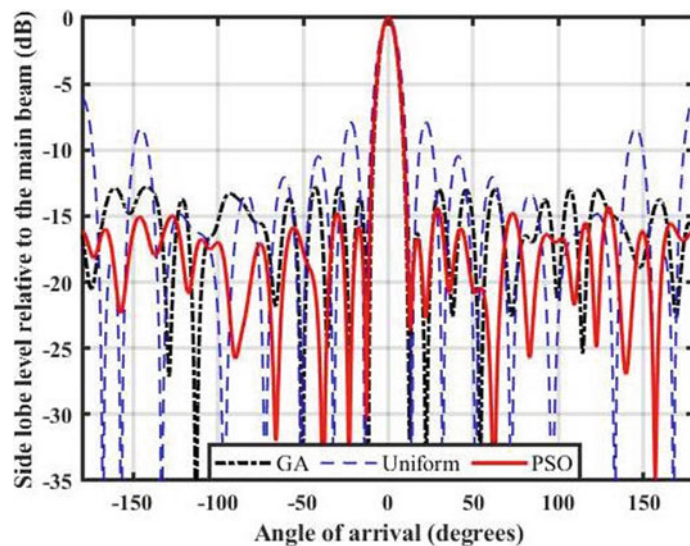


**Fig. 4** Array pattern for non-uniform 20-element elliptical array

**Table 1** Excitation amplitude and inter-element spacing distribution for non-uniform elliptical antenna array obtained by GA and PSO

No. of elements	SLL (dB) using GA	SLL (dB) using PSO in [9]	SLL (dB)	$[I_1, I_2, \dots, I_N]$ ; using GA	$[I_1, I_2, \dots, I_N]$ ; using PSO	$[d_1, d_2, \dots, d_N]$ in $\lambda$ 's using GA	$[d_1, d_2, \dots, d_N]$ in $\lambda$ 's using PSO
12	- 8.96	- 11.84	- 7.90	0.4599 0.5734 0.4762 0.2131 0.8381 0.6990 0.6876 0.9600 0.5469 0.4689 0.6547 0.5691	0.5912 0.6793 0.3843 0.3673 0.4602 0.2894 0.4771 0.7832 0.7387 0.3844 0.5744 0.5678	0.5949 0.6865 0.8946 0.8244 0.7855 0.9677 0.5925 0.6364 0.7632 0.6701 0.8419 0.5567	0.5507 0.5239 0.5593 0.7783 0.6820 0.5716 0.7561 0.8717 0.5049 0.6338 0.9600 0.5009
16	- 11.17	- 11.49	NR	0.8951 0.6294 0.2474 0.5804 0.4584 0.8020 0.8905 0.9850 0.9079 0.4983 0.4704 0.7412 0.2444 0.3596 0.8610 0.7187	0.6602 0.6917 0.2026 0.1605 0.3995 0.8562 0.1735 0.9790 0.5002 0.0727 0.7717 0.5045 0.8394 0.5020 0.8831 1.1271	0.8648 0.5135 0.8077 0.6485 0.6686 0.8882 0.5063 0.7774 0.5448 0.6661 0.8773 0.6280 0.6960 0.5224 0.9544 0.7083	0.6491 0.6105 0.7957 0.8077 0.8593 0.7114 0.5358 0.6989 0.8845 0.9519 0.6411 0.6721 0.5837 0.7251 0.9171 0.6869
20	- 12.99	- 14.40	- 11.48	0.9042 0.9992 0.5330 0.6373 0.4569 0.4562 0.1071 1.0000 0.0077 0.7785 0.9652 0.6151 0.5645 0.4554 0.8415 0.4180 0.0055 0.7709 1.0000 0.9988	0.9050 0.6332 0.7829 0.4550 0.2372 0.3679 0.5875 0.7734 0.8660 0.9690 0.9252 0.2892 0.2591 0.2157 0.7521 0.4019 0.5790 0.6348 0.7009 0.9323	0.5753 0.6020 0.8579 0.6903 0.8003 0.8609 0.9733 0.6355 0.5281 0.5000 0.5064 0.8635 0.7163 0.5657 0.7405 0.5833 0.6402 0.7180 0.9000 0.5338	0.6117 0.5813 0.6045 0.9538 0.9434 0.5297 0.8991 0.9673 0.5075 0.6122 0.5720 0.5816 0.6332 0.9020 0.5122 0.7740 0.5864 0.9582 0.6665 0.5969

NR—not reported

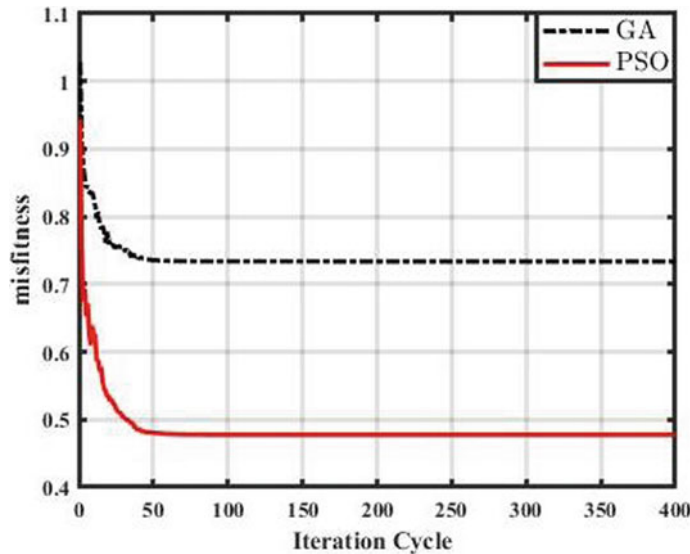


**Fig. 5** Convergence curve for non-uniform 12-element elliptical array

The result also shows that SLL reduced as per increasing the number of an antenna array elements.

It should be mentioned that the size of the EAA achieved in this study is somewhat greater than that obtained in [9] because the inter-element spacing is being kept at a minimal distance ( $\lambda/2 < d < 2\lambda$ ) to prevent the mutual coupling effect.

## 5 The Convergence Curves of GA and PSO

In order to determine the convergence curve for each array, the minimum values of the cost function are input in the relation to the number of iteration cycles. Figures 5, 6 and 7 show the convergence curves of the cost function for 12-, 16- and 20-element EAAs, respectively.

**Fig. 6** Convergence curve for non-uniform 16-element elliptical array

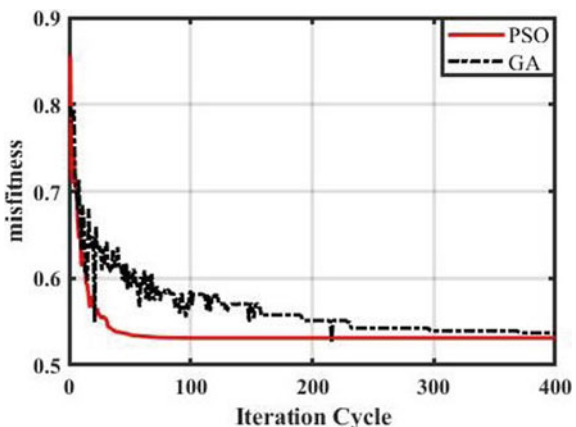
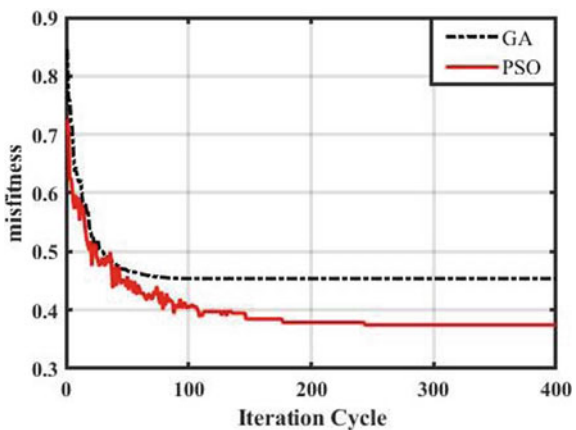


**Fig. 7** Convergence curve for non-uniform 20-element elliptical array



## 6 Conclusion

This work demonstrates non-uniform EAA design modeling strategies for the greatest amount of SLL decrease. Techniques like GA and PSO are suggested for this design issue in place of Symbiotic Organisms Search (SOS) and Antlion Optimization (ALO). The PSO technique successfully computed the optimal configuration of inter-element spacing and current excitation to produce a radiation pattern with the lowest sidelobe level. Experimental results provide the information about comparison of GA and PSO. It also provides the information about comparison with [9] in which SOS and ALO algorithms are used.

It will be planned for future study to design different geometries like hexagonal and concentric circular structures and also planned to minimize the sidelobe level and FNBW of these structures using different evolution algorithms.

**Acknowledgements** We would like to thank SERB, Department of Science and Technology, Government of India (Sanction Order No: EEQ/2021/000700; Dated 04 March 2022), for providing the fund that has been required to pursue this research.

## References

1. Balanis CA (2005) Antenna theory analysis and design, 3rd edn. John Wiley and Sons Inc., UK
2. Ram G, Mandal D, Kar R, Ghoshal SP (2016) Hybrid GSADe algorithm for optimization of far-field radiation pattern of circular arrays. *Ann Telecommun*, pp 61–71
3. Murthy K, Kumar A (1976) Synthesis of linear antenna arrays. *IEEE Trans Antennas Propag AP-24*:865–870
4. Zainud Deen S, Mady E, Awadalla KH (2006) Controlled radiation pattern of circular antenna array. In: IEEE antennas and propagation symposium, pp 3399–3402
5. Wang LL, Fang DG (2003) Synthesis of nonuniformly spaced arrays using genetic algorithm. In: Asia Pacific conference on environmental electromagnetics, pp 302–305
6. Das P, Roy J (2014) Thining of elliptical antenna arrays using genetic algorithm. *Int J Eng Res Appl* 4:225–229
7. Sainath M, Chaitanya K, Raju S (2017) Comparative analysis of reduction of side lobe level for concentric elliptical array and cylindrical elliptical array using differential evolution. *Int J Adv Electron Comput Sci* 4(1):70–74
8. Misra B, Mahanti GK (2021) Teaching learning based optimization algorithm for synthesis of a thinned elliptical array antenna. In: International conference on communication and electronics systems, pp 451–454
9. Dib N, Amaireh A, Al-Zoubi A, On the optimal synthesis of elliptical antenna arrays. *Int J Electron*. <https://doi.org/10.1080/00207217.2018.1512658>
10. Sivanandam SN, Deepa SN (2011) Principles of soft computing, 2nd edn. John Wiley and Sons Inc., UK
11. Haupt RL, Werner DH (2007) Genetic algorithms in electromagnetics. IEEE Press Wiley Interscience
12. Mandal D, Ghoshal SP, Bhattacharjee AK (2009) A novel particle swarm optimization based optimal design of three-ring concentric circular antenna array. In: IEEE International conference on advances in computing, control, and telecommunication technologies, 2009, ACT'09, pp 385–389
13. Mandal D, Ghoshal SP, Bhattacharjee AK (2009) Determination of the optimal design of three ring concentric circular antenna array using evolutionary optimization techniques. *Int J Recent Trends Eng.* 2(5):110–115
14. Eberhart RC, Shi Y (2001) Particle swarm optimization: developments, applications and resources. *Proc IEEE Conf Evol Comput, ICEC* 1:81–86

# CVD-Grown MoS<sub>2</sub> Nanosheets-Based Gas Sensor for Low-Limit Detection of NO<sub>2</sub> Gas



Shreerupa Biswas and Sapana Ranwa

**Abstract** Here, the gas sensor's performance of NO<sub>2</sub> gas based on MoS<sub>2</sub> nanosheets with controlled 3D edge-enrich growth by chemical vapor deposition (CVD) method has been optimized. By controlling deposition process parameters (operating temperature 800 °C for Zone 2 heating, Ar gas flow at 180 sccm for 40 min deposition time), nanostructures transform into 3D edge-enriched nanosheets, which are uniformly distributed throughout the substrates and well interconnected. Surface morphology and crystal structures of the MoS<sub>2</sub> nanosheets were confirmed by FESEM and XRD characterization. Raman spectra further confirm the deposition of MoS<sub>2</sub> nanostructures with confirmed in-plane and out-of-plane A<sub>1g</sub> and E<sup>1</sup><sub>2g</sub> peaks which indicates the growth planes of MoS<sub>2</sub> nanostructures. These MoS<sub>2</sub> nanosheet-based sensors exhibit high sensitivity of ~ 37.68% at 75 °C optimum operating temperature for 100 ppm NO<sub>2</sub> gas concentration. This sensor demonstrates fast response and recovery time (48 and 142 s). Even at room temperature, nanosensors could detect 100 ppm NO<sub>2</sub> gas concentration with 19.7% sensor response.

**Keywords** TMD material · MoS<sub>2</sub> · 2D materials · Gas sensor · Sensor response · Limit of detection (LOD)

## 1 Introduction

As a result of the rapid industrialization of wastes and combustion of fossil fuels used in cars, NO<sub>2</sub> gas has become a significant health hazard. Therefore, developing a NO<sub>2</sub> gas sensor with enhanced sensitivity, low limit of detection (LOD), high selectivity, minimum cost, and operation near room temperature (RT) is urgently needed.

In the beginning, many gas sensors like conductometric, optical, electrochemical, thermoelectric, and acoustic were invented to achieve efficient gas sensors [1–5].

---

S. Biswas (✉) · S. Ranwa

Nano-Device Laboratory, Department of Electronics and Communication Engineering, National Institute of Technology Durgapur, Durgapur 713209, India  
e-mail: [sb.19ec1102@phd.nitdgp.ac.in](mailto:sb.19ec1102@phd.nitdgp.ac.in)

For gas sensing applications, metal oxide semiconductors have been used for many years for their minimum cost, affordability of fabrication, and high sensitivity to target gas [6]. However, metal oxide-based devices have high working temperatures of nearly 100–450 °C as well as high recovery times and lack of selectivity, which restrict their practical applications [7–10]. Furthermore, graphene [11–14], graphene oxide [15–17], and reduced graphene [18–20]-based gas sensors had been extensively studied over the past decade. With excellent electron transport properties, and high conductivity, graphene and its derivatives have been considered to be superior gas sensors. The main disadvantage of graphene-based gas sensors was the long recovery time [21]. Therefore, researchers started searching for a new material due to the functional limitations of existing gas sensors.

Among various TMD materials based gas sensor's, MoS<sub>2</sub> is most commonly used [22–24]. Its multilayered structure, tunable bandgap, high surface-to-volume ratio, excellent adsorption coefficient, and unique physical–electrical properties make it suitable for gas sensing applications. This typical layered structural arrangement and the d-orbital electron numbers in the atom influence the excellent mechanical, optical, and unique electronic properties of 2D MoS<sub>2</sub> [25]. MoS<sub>2</sub> has outstanding electrical properties compared to graphene for this tuning bandgap nature. So far, many methods have been developed to synthesize MoS<sub>2</sub> nanospheres, nanofilms, nanoparticles, nanoflowers, and nanosheets. These methods are mechanical exfoliation, liquid-phase exfoliation, and electrochemical and hydrothermal syntheses. Among these methods, the CVD process is a superior method for MoS<sub>2</sub> synthesis as it can produce large single-crystal 2D MoS<sub>2</sub> with large lateral dimensions and high crystallinity, as well as multilayer MoS<sub>2</sub> as compared to hydrothermal. Kumar et al. [26] reported a MoS<sub>2</sub> nanowire network that was synthesized using a CVD method. The CVD method was performed in a turbulent vapor flow environment. The high-density nanowires and vertically oriented flakes of the MoS<sub>2</sub> network exhibited high performance in gas sensing. However, at 60 °C optimum working temperature, the device showed complete recovery with a response of 18% for 6 ppm of NO<sub>2</sub> gas. In [27], a unique two-step CVD method was defined to deposit a bilayer MoS<sub>2</sub> nanosheet for the NO<sub>2</sub> gas sensor. During the process, MoO<sub>3</sub> was deposited and sulfurized. They reported that this new method produced an atomic layer of MoS<sub>2</sub> with a 50–100 μm large lateral grain size, which showed better sensitivity of 2.5% to RT for 1 ppm NO<sub>2</sub>. Furthermore, Cho et al. [28] reported a bifunctional sensor using MoS<sub>2</sub> film deposition via the CVD method to detect gas molecules.

In this work, we fabricated a unique MoS<sub>2</sub> nanosheet-based gas sensor deposited by a one-step CVD method on a SiO<sub>2</sub>/p-Si substrate. The crystallinity, morphology of MoS<sub>2</sub> investigations have been confirmed by XRD, Raman spectroscopy, and FESEM, respectively. In addition, at 75 °C optimum operating temperature, the MoS<sub>2</sub> gas sensor exhibits a sensitivity of 37.68% to concentrations of 100 ppm NO<sub>2</sub>.

### 1.1 Experimental Section

In this work, a chemical vapor deposition (CVD) method was used to grow MoS<sub>2</sub> nanosheets on p-Si/SiO<sub>2</sub> substrates. A standard chemical process was used to clean the substrate. The substrate was placed on the top of the alumina boat of MoO<sub>3</sub> (0.04 g powder). Another boat with sulfur powder (1.4 g) was placed 20 cm away from MoO<sub>3</sub>. To grow the uniformly distributed MoS<sub>2</sub> nanostructures, MoO<sub>3</sub> was heated at 800 °C for 40 min, with an argon (Ar) gas flow of 180 sccm, and heat of 200 °C was applied to the sulfur powder. The schematic diagram of the CVD method for MoS<sub>2</sub> deposition is shown in Fig. 1. For gas sensing measurement, Ti/Au (5 nm/200 nm) IDE's contact (100-micron distance between fingers) had been deposited using the e-beam/thermal evaporation method.

## 2 Results and Discussion

Crystalline growth and surface morphology of deposited MoS<sub>2</sub> nanostructures were confirmed by XRD and FESEM techniques. Surface morphology was confirmed with different magnification images of well-connected and uniformly distributed 3D edge-enrich MoS<sub>2</sub> nanosheets throughout the substrate.

Figures 2a–b depict low- and high-magnification FESEM images used to characterize the sample's morphology. Figure 2a shows the uniformly distributed nanosheet-like morphology throughout the substrate. Figure 2b shows a high-magnified image of interconnected nanosheets. These nanosheets are well connected, and 3D edge-enrich growth has been achieved.

The energy-dispersive X-ray (EDX) mapping images are used to know the chemical composition of the nanosheets. Figures 3a–d EDX images and spectra shows the element analysis of as-prepared MoS<sub>2</sub> nanosheets. The presence of only Mo and S elements in mapping images and EDX spectra confirms the crystalline growth of MoS<sub>2</sub> nanosheets without impurities.

The XRD analysis of MoS<sub>2</sub> nanosheets had been confirmed their crystalline structure and phase purity. As shown in Fig. 4a, the small diffraction peak (002) was observed at  $2\theta = 14.65^\circ$ . It was well matched with a pure hexagonal MoS<sub>2</sub> (JCPDS 37-1492) [29]. Additional peaks (110) corresponding to MoO<sub>3</sub> and (111) and (211)

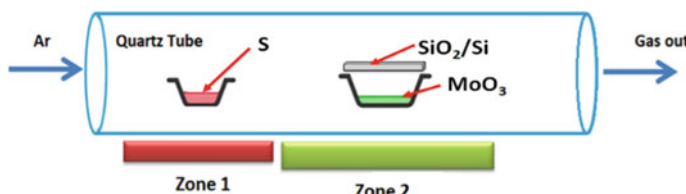


**Fig. 1** Schematic diagram of CVD method for MoS<sub>2</sub> deposition

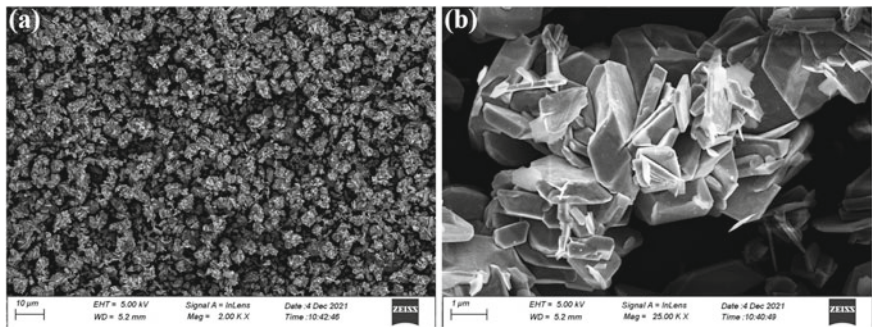


**Fig. 2** **a** Low and **b** high-magnification FESEM images of uniformly distributed  $\text{MoS}_2$  nanosheets

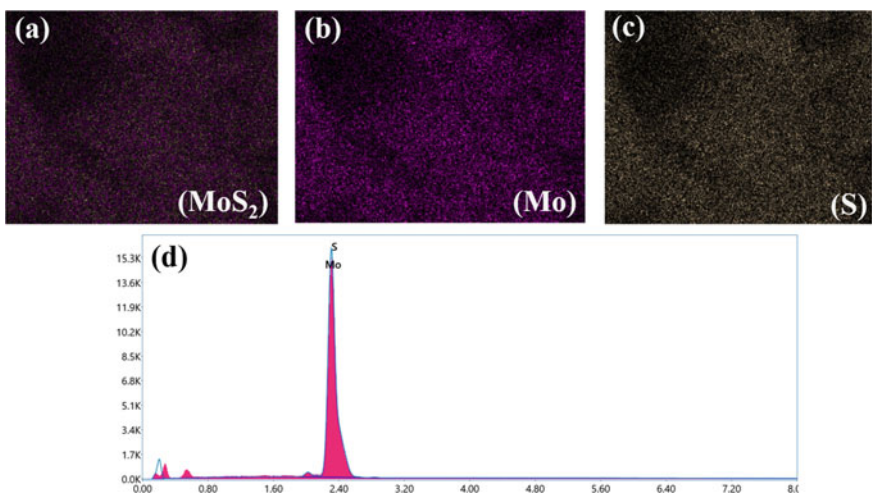


**Fig. 3** FESEM—energy-dispersive X-ray (EDX) mapping of **a**  $\text{MoS}_2$ , **b** Mo, **c** S elements' distribution in scanned area, **d** EDX spectra analysis of  $\text{MoS}_2$

corresponding to  $\text{MoO}_2$  are present in XRD spectra. Further verification of the crystal structure growth of a sample is carried out using Raman spectroscopy. Figure 4b reveals two typical peaks, the out-of-plane vibration of the S atom ( $A_{1g}$ ) and the in-plane vibration ( $E^{1\ 2g}$ ). The presence of two strong peaks  $E^{1\ 2g}$  at  $377.35\ \text{cm}^{-1}$  and  $A_{1g}$  at  $403.83\ \text{cm}^{-1}$  confirmed the deposition of  $\text{MoS}_2$  nanosheets throughout the  $\text{SiO}_2/\text{p-Si}$  substrate.

For gas sensor response measurements, temperature-dependent I-V characteristics had been recorded. I-V characteristics of  $\text{MoS}_2$  sensing devices were investigated at increasing operating temperatures varying from room temperature to  $125\ ^\circ\text{C}$ . Figure 4a shows the temperature-dependent voltage versus current (I-V) curve, indicating that sensor conductance increases with increasing temperature from RT to  $125\ ^\circ\text{C}$ . With increased temperature, the device's current was observed to be enhanced

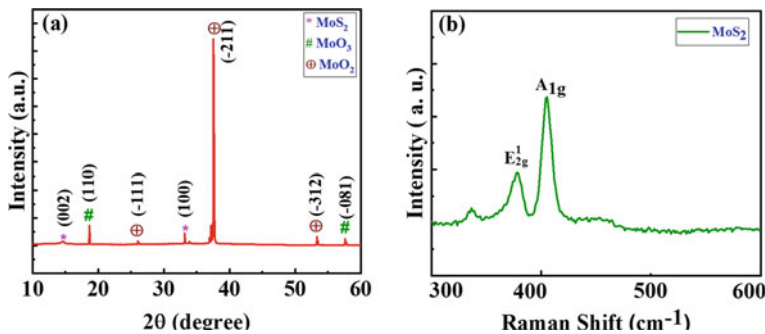


**Fig. 4** **a** XRD diffraction pattern of MoS<sub>2</sub> nanosheets, **b** Raman spectroscopy of MoS<sub>2</sub> nanosheets

and shows ohmic behavior. Meanwhile, we investigated how MoS<sub>2</sub> responds to different NO<sub>2</sub> concentrations at RT to 125 °C temperatures. The calculation of sensor response is based on the relative response, which is formulated as  $(\Delta R/R_a) \times 100\% = (R_a - R_g)/R_a \times 100\%$ , where  $R_a$  is the resistance of the device in the air environment and  $R_g$  is the resistance of the device in the presence of the gas.

Meanwhile, the pristine MoS<sub>2</sub> device showed sensor response which increases from 19.7 to 37.68% for 100 ppm NO<sub>2</sub> exposure when the temperature varies from RT to 75 °C. Furthermore, from Fig. 5b, we can find the optimum operating temperature of the device, as at 75 °C temperature, the sensor showed the highest relative response, which should be the working temperature of the device for 100 ppm NO<sub>2</sub> concentration. Figure 5c shows the relative response of the MoS<sub>2</sub> sensor under exposure to 100 ppm NO<sub>2</sub> gas at different temperatures. With increasing temperatures, the relative response of the device has changed. For further increasing temperatures higher than the optimum working temperature (75 °C), target gas molecules' adsorption and desorption rate decreased, leading to reduced sensor response.

In Figs. 6a, b, we observed that as temperature changes, the resistance values also changed with time. It is known that oxidizing gas NO<sub>2</sub> atoms' adsorption increases sensor resistance. However, it has been observed that at RT Fig. 6a, the MoS<sub>2</sub> device shows incomplete recovery and a low desorption rate of gas molecules because NO<sub>2</sub> is strongly bound to the active site on MoS<sub>2</sub> nanosheets. However, the device recovered completely at 75 °C, meaning that 75 °C is the minimum operating temperature for desorbing the gas molecules from MoS<sub>2</sub> nanosheets.

In order to understand the recovery as well as response behavior of the MoS<sub>2</sub> nanosheets, the calculated response time is 48 s (10–90% of maximum value) and the recovery time is 142 s to 100 ppm NO<sub>2</sub> concentration at the optimum operating temperature of 75 °C, as shown in Fig. 6c.

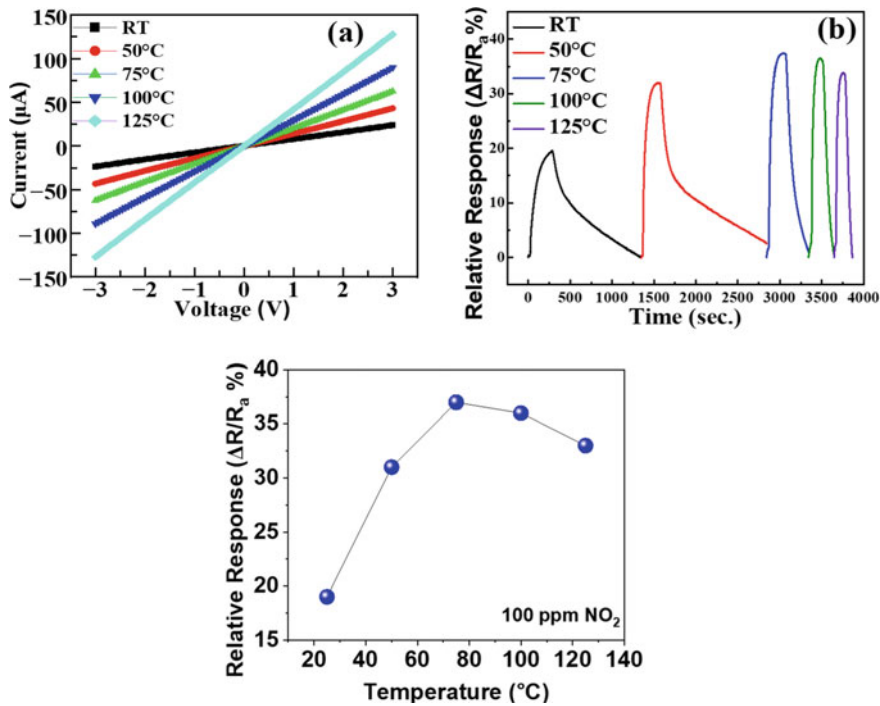


**Fig. 5** **a** Temperature-dependent I-V characteristics of the device at different temperatures ranging from RT to 125 °C, **b** the relative response of the  $\text{MoS}_2$  nanosheet-based sensors with increasing operating temperatures at 100 ppm  $\text{NO}_2$  concentration, **c** relative response versus temperature of the device under exposure to 100 ppm  $\text{NO}_2$  concentration

## 2.1 Gas Sensing Mechanism

In general, the TMD 2D  $\text{MoS}_2$  bases' sensor senses gas by transferring charge between target gas molecules and sensing materials as shown in Fig. 7. The charge transfer depends on the nature of oxidizing and reducing target gas which leads toward increasing or decreasing gas sensor resistance. Furthermore, it is known that  $\text{NO}_2$  gas has an unpaired electron, which behaves as an oxidizing gas. In presence of an air environment, oxygen molecules has been adsorbed on the surfaces of  $\text{MoS}_2$  nanosheets. Because of the oxygen adsorption on the  $\text{MoS}_2$  nanosheet's surface, the resistance of the device increases. With loading to  $\text{NO}_2$  gas, the  $\text{NO}_2$  atom extracts electrons from the conduction band, further increasing the sensor's resistance. The electron interaction between the  $\text{MoS}_2$  and  $\text{NO}_2$  gas changes the resistivity or conductivity of the material. Furthermore, the N-type  $\text{MoS}_2$  and the electrode at their interface form a Schottky junction which plays an important role in gas sensors response towards targeted gases.

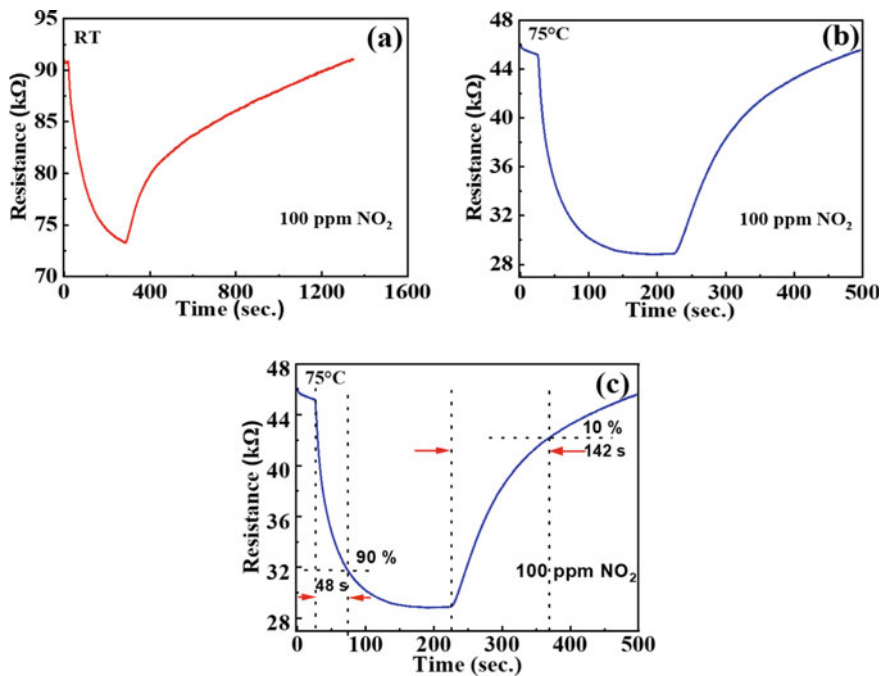


**Fig. 6** Resistance versus time plot at operating temperature **a** RT, **b** 75 °C of MoS<sub>2</sub> nanosheet-based sensor during loading and unloading of 100 ppm target gas, **c** response and recovery time calculation at optimum operating temperature 75 °C

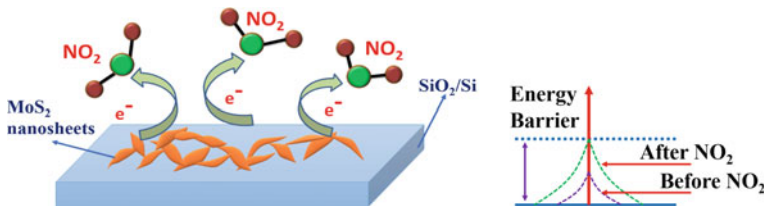


**Fig. 7** Proposed schematics for sensing mechanism of the sensor

### 3 Conclusion

In summary, the atmospheric pressure one-step CVD process had been used for the uniform growth of MoS<sub>2</sub> nanosheets throughout the substrate (SiO<sub>2</sub>/p-Si substrates). Ti/Au IDEs' contact had been deposited to fabricate MoS<sub>2</sub> nanosheets-based gas sensor. The XRD, FESEM, and Raman Spectroscopy were performed to analyze the crystalline structure and structural morphology of prepared MoS<sub>2</sub> nanosheets. The highly crystalline structure of MoS<sub>2</sub> has been confirmed by XRD spectra. Uniform distribution of edge-enriched interconnected nanosheets' morphology had

been confirmed by FESEM, and EDX analysis confirms element analysis. These MoS<sub>2</sub> nanosheets exhibit high sensitivity of 37.68% at 75 °C operation toward 100 ppm NO<sub>2</sub> with fast response and recovery time. The limit-of-detection (LOD) range of this nanosensor is 100 parts per million of NO<sub>2</sub> gas balance in inert gas.

**Acknowledgements** Support for this work has been provided in part by DST-SRG project file no-SRG/2019/000945 dated 18/12/2019 and ‘Centre of Excellence in Advanced Materials’ NIT Durgapur. We also want to thank Mr. Sumit Kumar and Dr. Mahesh Kumar, IIT Jodhpur, for their measurement support for this work.

## References

1. Francia GD, Alfano B, Ferrara VL (2009) Conductometric gas nanosensors. *J Sens* 2009, 659275(1–18). <https://doi.org/10.1155/2009/659275>
2. Hodgkinson J, Tatam RP (2013) Optical gas sensing: a review. *Meas Sci Technol* 24(1):012004 (59 pp). <https://doi.org/10.1088/0957-0233/24/1/012004>
3. Williams DE (2020) Electrochemical sensors for environmental gas analysis. *Curr Opin Electrochem* 22:145–153. <https://doi.org/10.1016/j.colelec.2020.06.006>
4. Champier D (2017) Thermoelectric generators: a review of applications. *Energy Convers Manag* 140:167–181. <https://doi.org/10.1016/j.enconman.2017.02.070>
5. Jakubik WP (2011) Surface acoustic wave-based gas sensors. *Thin Solid Films* 520(3):986–993. <https://doi.org/10.1016/j.tsf.2011.04.174>
6. Dey A (2018) Semiconductor metal oxide gas sensors: a review. *Mater Sci Eng B* 229:206–217. <https://doi.org/10.1016/j.mseb.2017.12.036>
7. Moseley PT (2017) Progress in the development of semiconducting metal oxide gas sensors: a review. *Meas Sci Technol* 28(8):082001. <https://doi.org/10.1088/1361-6501/aa7443>
8. Fine GF, Cavanagh LM, Afonja A, Binions R (2010) Metal oxide semi-conductor gas sensors in environmental monitoring. *Sensors* 10(6):5469–5502. <https://doi.org/10.3390/s100605469>
9. Wang C, Yin L, Zhang L, Xiang D, Gao R (2010) Metal oxide gas sensors: Sensitivity and influencing factors. *Sensors* 10(3):2088–2106. <https://doi.org/10.3390/s100302088>
10. Ponzoni A et al (2017) Metal oxide gas sensors, a survey of selectivity issues addressed at the SENSOR lab, Brescia (Italy). *Sensors* 17(4). <https://doi.org/10.3390/s17040714>
11. Geim AK, Grigorieva IV (2013) Van der Waals heterostructures. *Nature* 499(7459):419–425. <https://doi.org/10.1038/nature12385>
12. Leenaerts O, Partoens B, Peeters FM (2008) Adsorption of H<sub>2</sub>O, NH<sub>3</sub>, CO, NO<sub>2</sub>, and NO on graphene: a first-principles study. *Phys Rev B* 77(12):125416. <https://doi.org/10.1103/PhysRevB.77.125416>
13. Ko G, Kim H-Y, Ahn J, Park Y-M, Lee K-Y, Kim J (2010) Graphene-based nitrogen dioxide gas sensors. *Curr Appl Phys* 10(4):1002–1004. <https://doi.org/10.1016/j.cap.2009.12.024>
14. Yoon HJ, Jun DH, Yang JH, Zhou Z, Yang SS, Cheng MMC (2011) Carbon dioxide gas sensor using a graphene sheet. *Sens Actuators B Chem* 157(1):310–313. <https://doi.org/10.1016/j.snb.2011.03.035>
15. Prezioso S et al (2013) Graphene oxide as a practical solution to high sensitivity gas sensing. *J Phys Chem C* 117(20):10683–10690. <https://doi.org/10.1021/jp3085759>
16. Peng Y, Li J (2013) Ammonia adsorption on graphene and graphene oxide: a first-principles study. *Front Environ Sci Eng* 7(3):403–411. <https://doi.org/10.1007/s11783-013-0491-6>
17. Tang S, Cao Z (2011) Adsorption of nitrogen oxides on graphene and graphene oxides: Insights from density functional calculations. *J Chem Phys* 134(4):044710. <https://doi.org/10.1063/1.3541249>

18. Robinson JT, Perkins FK, Snow ES, Wei Z, Sheehan PE (2008) Reduced graphene oxide molecular sensors. *Nano Lett* 8(10):3137–3140. <https://doi.org/10.1021/nl8013007>
19. Lipatov A, Varezhnikov A, Wilson P, Sysoev V, Kolmakov A, Sinitskii A (2013) Highly selective gas sensor arrays based on a thermally reduced graphene oxide. *Nanoscale* 5:5426–5434. <https://doi.org/10.1039/C3NR00747B>
20. Wang DH, Hu Y, Zhao JJ, Zeng LL, Tao XM, Chen W (2014) Holey reduced graphene oxide nanosheets for high performance room temperature gas sensing. *J Mater Chem A* 2(41):17415–17420. <https://doi.org/10.1039/c4ta03740e>
21. Mohan VB, Lau K-T, Hui D, Bhattacharyya D (2018) Graphene-based materials and their composites: a review on production, applications and product limitations. *Compos Part B Eng* 142(1):200–220. <https://doi.org/10.1016/j.compositesb.2018.01.013>
22. Wilson JA, Yoffe AD (1969) The transition metal dichalcogenides discussion and interpretation of the observed optical, electrical and structural properties. *Adv Phys* 18(73):193–335. <https://doi.org/10.1080/00018736900101307>
23. Lee E, Yoon YS, Kim DJ (2018) Two-dimensional transition metal dichalcogenides and metal oxide hybrids for gas sensing. *ACS Sens* 3(10):2045–2060. <https://doi.org/10.1021/acssensors.8b01077>
24. Manzeli S, Ovchinnikov D, Pasquier D, Yazyev OV, Kis A (2017) 2D transition metal dichalcogenides. *Nat Rev Mater* 2:17033. <https://doi.org/10.1038/natrevmats.2017.33>
25. Li T, Galli G (2007) Electronic properties of MoS<sub>2</sub> nanoparticles. *J Phys Chem C* 111(44):16192–16196. <https://doi.org/10.1021/jp075424v>
26. Kumar R, Goel N, Kumar M (2018) High-performance NO<sub>2</sub> sensor using MoS<sub>2</sub> nanowires network. *Appl Phys Lett* 112(5):053502. <https://doi.org/10.1063/1.5019296>
27. Xu T et al (2017) High-response NO<sub>2</sub> resistive gas sensor based on bilayer MoS<sub>2</sub> grown by a new two-step chemical vapor deposition method. *J Alloys Compd* 725(2):253–259. <https://doi.org/10.1016/j.jallcom.2017.06.105>
28. Cho B et al (2015) Bifunctional sensing characteristics of chemical vapor deposition synthesized atomic-layered MoS<sub>2</sub>. *ACS Appl Mater Interfaces* 7(4):2952–2959. <https://doi.org/10.1021/am508535x>
29. Niu Y et al (2015) MoS<sub>2</sub> graphene fiber based gas sensing devices. *Carbon* 95:34–41. <https://doi.org/10.1016/j.carbon.2015.08.002>

# A Linear Array of Dropper-Shaped Wideband Printed Radiators for Ku-band Applications



Kalyan Sundar Kola and Anirban Chatterjee

**Abstract** A two-element linear array for various wireless or satellite-related applications under the Ku-band is reported in this article. Its dropper-shaped architecture gives rise to a single antenna with a high impedance bandwidth and a resonance frequency of 16.00 GHz. The antenna is constructed with a combination of regular squares, triangular and rectangular shape geometries. The linear array has been presented for the intended applications in order to get better parametric performances. To minimize losses and maximize isolation at the target frequency, the Wilkinson power divider network was implemented into the feed architecture of the array. The array has a gain of 9.70–10.48 dBi across the entire frequency range of operation under the Ku-band. The envisaged array has tremendous radiation efficiency, is electromagnetically compatible and has a low cross-pol. level along its primary beam path. Both antennas are well suited for various wireless, direct broadcast satellite or high-frequency satellite communications in the Ku-band.

**Keywords** Antenna · Circuit model · Correction factor · Ku-band · Wilkinson

## 1 Introduction

The satellite and the wireless applications are two major parts of the communication era where the use of antennas is quite apparent. The main challenge is to develop a single antenna or the array which can be used for both side applications simultaneously. The printed antennas [1, 2] have ample range of applications for the modern wireless or satellite communications. The patch antennas are used for such applications due to several benefits they provide like robustness, less weight, compact, low cost, ease to fabricate, ease to make balance with the other microwave devices, etc.

---

K. Sundar Kola (✉)

Department of ECE, GMR Institute of Technology, Rajam, Andhra Pradesh 532127, India  
e-mail: [kalyankola12@gmail.com](mailto:kalyankola12@gmail.com)

A. Chatterjee

Department of ECE, National Institute of Technology Goa, Goa 403401, India  
e-mail: [snanirban@nitgoa.ac.in](mailto:snanirban@nitgoa.ac.in)

The fundamental drawback of microstrip patch antennas is their limited bandwidth; hence, there is a growing need to improve this characteristic for use in real-world applications. Several solutions have been proposed to this issue, including increasing the thickness of the dielectric material and reducing the substrate dielectric constants, both of which have been shown to improve the x-pol. performance of antennas. The following is a brief overview of some of the published works on microstrip antennas.

A brief idea about microstrip antenna related to theoretical and practical methods has been carried out in the literature [3]. Few printed antennas like slotted, substrate integrated and split quadrilateral miniaturized antennas for Ku-band applications have been investigated in [6–9]. Dual-band printed antennas for X and Ku-band based applications like direct broadcast satellite are reported in the literature [10–12]. Printed array for Ku-band satellite applications is investigated in [13–27]. Several wireless communications, vehicular applications and direct broadcast satellite applications-based printed antennas have been investigated by authors in literatures [28–31]. A partial ground plane-based meta-surface antenna has been proposed by Behera et al. [32] Several printed antennas have been invented for the Ku-band-related applications and discuss their advantageous features in [33–35].

The authors have been developed an array of compact printed dropper-shaped wideband antennas for Ku-band applications and carried out in this article. The oddities of the suggested and developed antennas are listed as follows:

- The small-sized sole radiator is derived from a dropper-shaped geometry.
- It offers wide-impedance bandwidth with immense gain and very low x-pol.
- The Wilkinson power divider [36]-based array is very compact and less weight.
- The array offers immense absolute gain and high level of x-pol. suppressions.

Both the antennas give good radiation efficiency, acceptable aperture efficiency [37] and desirable correction factor at the desired frequency. Both are ideal for applications under Ku-band.

## 2 Single Radiator

The intended sole radiator [1, 2] is designed based on a medical, non-commercial, breakable ‘dropper’. A regular dropper is shown in Fig. 1. Based on this, a printed antenna has been proposed in which the ‘rubber-bulb’ portion is considered as the ‘radiator’, the ‘glass-tube’ portion is treated as ‘feedline’, and the ‘nozzle’ is contemplated as ‘the source port’ of the antenna, respectively. The detailed design procedure, current path calculation and circuit equivalent approach of the antenna are discussed in the following subsections.

**Fig. 1** Dropper

## 2.1 Formation Details

This subsection is going to cover the detailed description about the stepwise formation of the proposed geometry followed by the complete embodiment.

- **Step-by-step construction**

A simple dropper-shaped geometry has been constructed by using regular square and triangular-shaped structures. Those basic blocks have been arranged in a particular manner to make the one-sided structure of the intended geometry. In order to achieve symmetric pattern at the desired direction, the same structure has been flipped concerning the  $y$ -axis and Boolean theorem. In addition, as indicated in Fig. 2, one little rectangle-shaped geometry has been installed in the middle of the construction to deliver the power, arriving from the source port to the top portion. Further, a tapered rectangular-shaped structure has been added with the Boolean geometry, and in turn, we achieved the proposed ‘dropper’-shaped compact geometry.

- **Complete embodiment**

The ‘dropper’-shaped structure has been printed on the top layer of the PCB laminated Roger 5880 material. The radiating layer is made of copper. In order to achieve large impedance bandwidth, two-thirds of the metal ground plane had to be etched away to make the structure a monopole, and it has been clearly indicated in Fig. 2. The desired geometry was designed with the use of the SONNET EM simulator [38], and the CST microwave studio [39] was utilized in order to cross-verify the design. The caption of Fig. 2 provides a comprehensive overview of the antenna’s physical layout, while the figure offers a comprehensive list of dimensions.

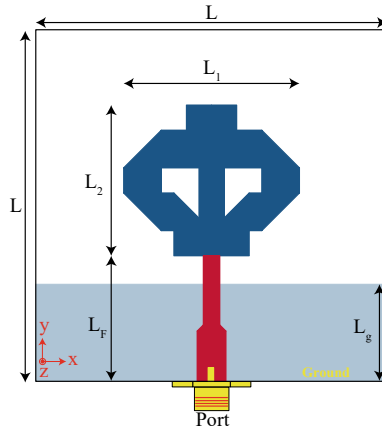


**Fig. 2** Proposed printed antenna ( $L = 28$ ,  $L_1 = 14$ ,  $L_2 = 12.04$ ,  $L_F = 10.02$ ,  $L_g = 8$ ; unit:mm)

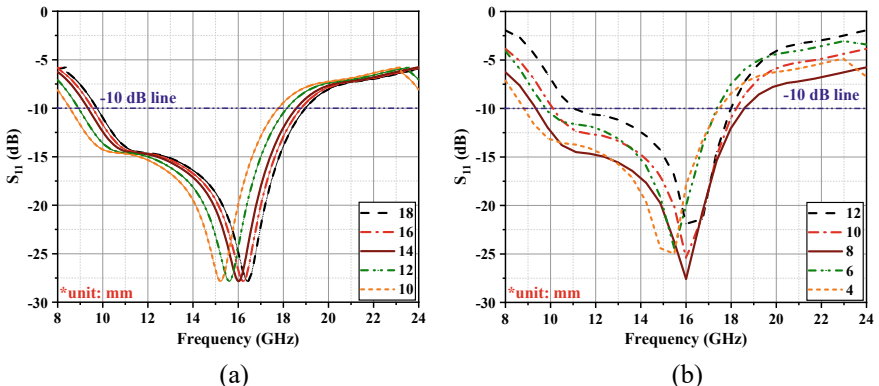


**Fig. 3**  $S_{11}$  characteristics for different values of **a**  $L_1$  and **b**  $L_g$

## 2.2 Parametric Study

The impedance behaviour like return loss and impedance bandwidth of the proposed compact antenna have been carried out in this section. The simulated results are shown in Fig. 3.

### Effects of $L_1$

The return loss characteristics of the antenna have been analysed for the different values of the patch length ( $L_1$ ). The values of the  $L_1$  have been varied from 10 to 18 mm with the span of 2 mm. For  $L_1 = 14$  mm, the proposed antenna offers better return loss at the desired frequency compared to the other values as obtained from Fig. 3a.

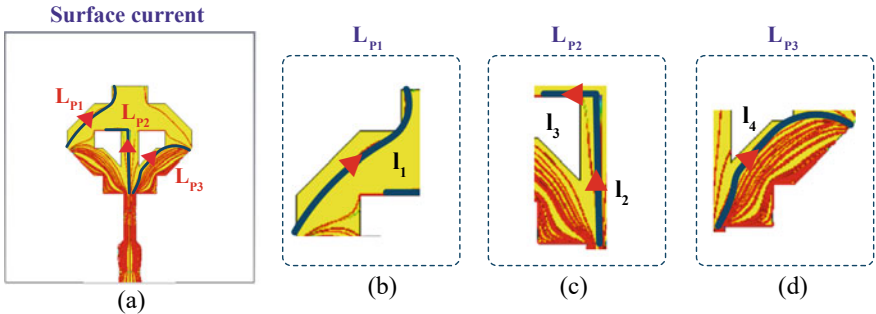


**Fig. 4** **a** Path of surface currents, **b–d** highlighted current paths.

### Effects of $L_g$

The impedance bandwidth response of the antenna has been analysed for the different values of the length of the ground plane ( $L_g$ ). For the proof of concept, the values of the ground length have been varied from 4 to 12 mm with the span of 2 mm. For  $L_g = 8$  mm, the proposed antenna offers maximum impedance bandwidth at the desired frequency compared to the other values as obtained from Fig. 3b.

### 2.3 Current Path Computation

On the surface of the antenna, the current is distributed as shown in Fig. 4a, with three numbers of streamlines indicated by the labels  $L_{P1}$ ,  $L_{P2}$  and  $L_{P3}$ , respectively. Figure 4b–d shows the intricate motion of the streamlines. The line length of those mentioned streamlines can be computed [40] as follows:

$$L_{P1} = l_1 = 10.20 \text{ mm} \quad (1)$$

$$L_{P2} = l_2 + l_3 = 4 + 3 \text{ mm} \quad (2)$$

$$L_{P3} = l_4 = 5.03 \text{ mm} \quad (3)$$

Therefore, we can get the median current route length ( $L_{PL}$ ) by using the formula [40]:

$$L_{PL} = \frac{1}{3} \sum_{n=1}^3 L_{Pn} = 7.41 \text{ mm} \quad (4)$$

The effective patch length of **7.41** mm is needed to produce resonant behaviour with the suggested structure at the target frequency of 16 GHz, which is quite close to the prediction of the average current path length ( $L_{PL}$ ).

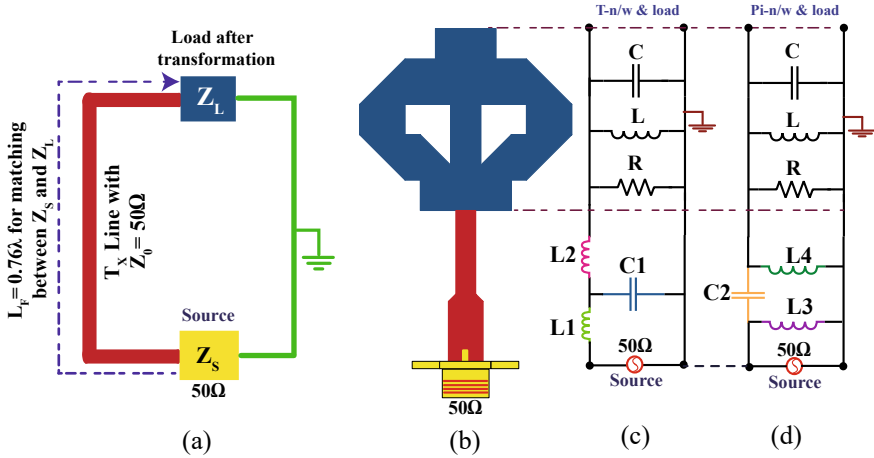


**Fig. 5** **a** Primitive model of an antenna, **b** circuit model of antenna **c-d** T and Pi models ( $R = 50.21 \Omega$ ,  $L = 0.41 \text{ nH}$ ,  $C = 0.164 \text{ pF}$ ,  $L_1 = 2.65 \text{ nH}$ ,  $L_2 = 2.21 \text{ nH}$ ,  $C_1 = 0.05 \text{ pF}$ ,  $L_3 = 0.05 \text{ nH}$ ,  $L_4 = 0.06 \text{ nH}$ ,  $C_2 = 0.54 \text{ pF}$ ).

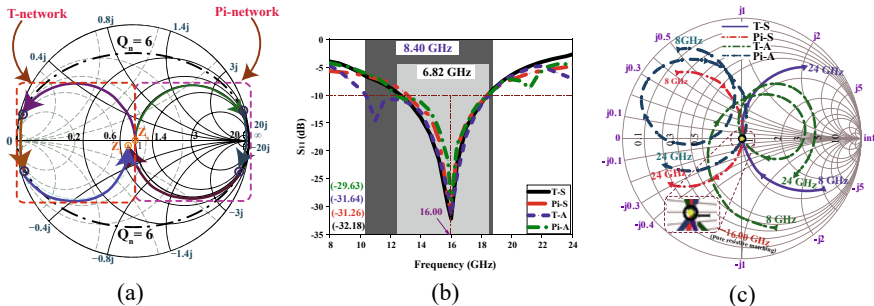


**Fig. 6** **a**  $Q_n$  circle representation, **b-c**  $|S_{11}|$  and impedance transformation of antenna's lumped models

## 2.4 Representation of an Equivalent Circuit

According to transmission line theory, a circuit equivalent approach to the suggested antenna has been studied. The antenna's radiator section is represented as a parallel RLC circuit, while the feedline is modelled as a T and Pi-type matching network. In Fig. 5a, we see a simple circuit model of the single radiator in which the source impedance is matched with the load impedance through the  $0.76\lambda$  transmission line. The antenna with port is depicted in Fig. 5b. The lumped model of the antenna radiator part and the corresponding T and Pi-type matching networks are depicted in Fig. 5c and d, respectively. To generate  $|S_{11}|$  like graphs using antenna circuit models, the nodal-quality factor  $Q_n$  [41] is emphasized. The parallel RLC [1] load is taken into account for the proposed antenna, and its parameters are as indicated in Fig. 6a.

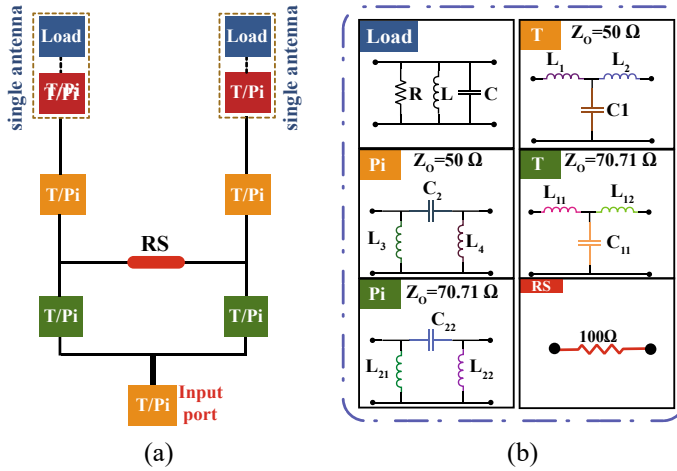


**Fig. 7** **a** Lumped model of the array and **b** its individual element ( $L_{11} = 1.82 \text{ nH}$ ,  $L_{12} = 1.36 \text{ nH}$ ,  $C_{11} = 0.05 \text{ pF}$ ,  $L_{21} = 0.04 \text{ nH}$ ,  $L_{22} = 0.05 \text{ nH}$ ,  $C_{22} = 0.92 \text{ pF}$ )

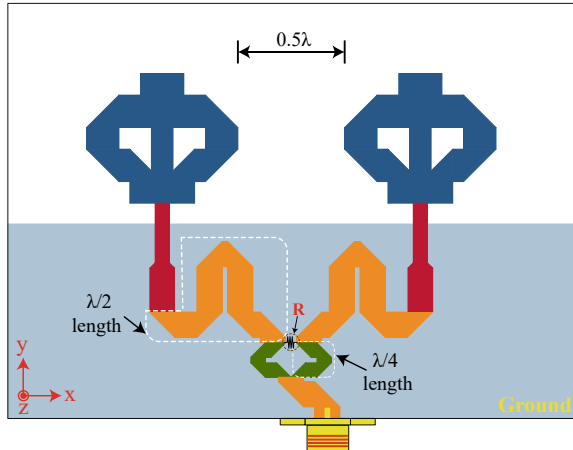
As stated in caption of Fig. 5, the values of the lumped elements are calculated in this manner. T/Pi network performance measured in terms of  $|S_{11}|$  is described in Fig. 6b using the Cadence simulator to mimic the circuit architecture. The impedance bandwidth response of the model is found to be good, and it has been discovered that the model resonates perfectly at 16.00 GHz. Figure 6c shows the input impedance behaviour of the corresponding circuit model of the antenna. Both antennas have a perfect  $50\Omega$  resistive match, as shown in the enlarged section of Fig. 6c.

### 3 Antenna Array

In order to achieve more improved parametric results at the desired frequency, a two-element linear array has been proposed for wireless and satellite applications under Ku-band. The array's lumped equivalent model and feed network have been thoroughly investigated in the following subsections.

#### 3.1 Model Using Lump Elements

The circuit model of the array is shown in a simplified form in Fig. 7a. The array's feed network serves as the input for the Wilkinson power divider, which then uses the T and Pi sub-blocks represented by the feedlines to construct the final design. The lumped equivalent circuit model for each sub-block is shown in Fig. 7b. Lumped element

**Fig. 8** Proposed linear array

weights for all sub-blocks are determined using the array's schematic model and are then referred to in Fig. 7 legend. Figure 6b and c shows the  $|S_{11}|$  and impedance responses of the array model, respectively; these values provide a proper resonance of 16.00 GHz. With the proposed array design, the impedance bandwidth may be increased to 8.40 GHz. Since the circuit model does not take into consideration fringing fields, dielectric material or the mutual coupling impact of the antenna, the relatively large bandwidth seen in actuality is likely owing to these factors. After seeing some encouraging results in the model, the array was constructed in Sonnet simulator [38] and cross-verified in CST microwave studio [39].

### 3.2 Construction of the Array

CST microwave studio has created a two-element linear array using the circuit equivalent approach (v2019). The intended array of dropper-shaped printed radiators is shown in Fig. 8. The mutual coupling effect is mitigated by maintaining a constant spacing of  $0.5\lambda$  between the components. A transmission line approach and a custom Wilkinson power divider are used to build the feed network for the array. Specifically, both the  $50\Omega$  line length and the quarter-wave transmission line length are maintained at integer multiples of  $\lambda/2$  and  $\lambda/4$ , respectively. A  $100\Omega$  chip resistor is placed at the junction of a  $70.7\Omega$  line to achieve a low degree of isolation. The Wilkinson power divider helps to get the required frequency with little loss while decreasing the array's overall size.

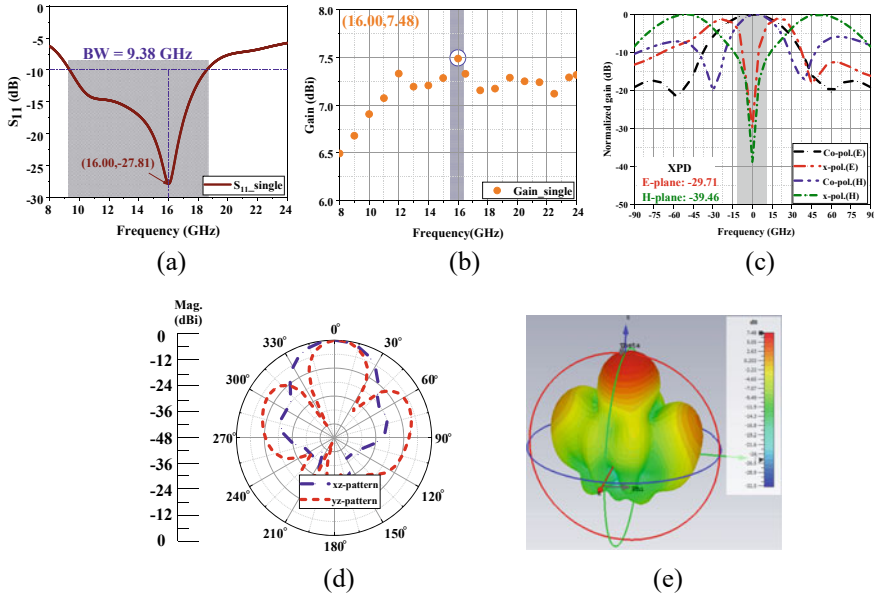


**Fig. 9** Simulated outcomes of single antenna: **a**  $S_{11}$ , **b** gain, **c** E and H-field, **d** xz–yz and **e** 3D radiation patterns (XPD: cross-pol. discrimination).

## 4 Results and Discussion

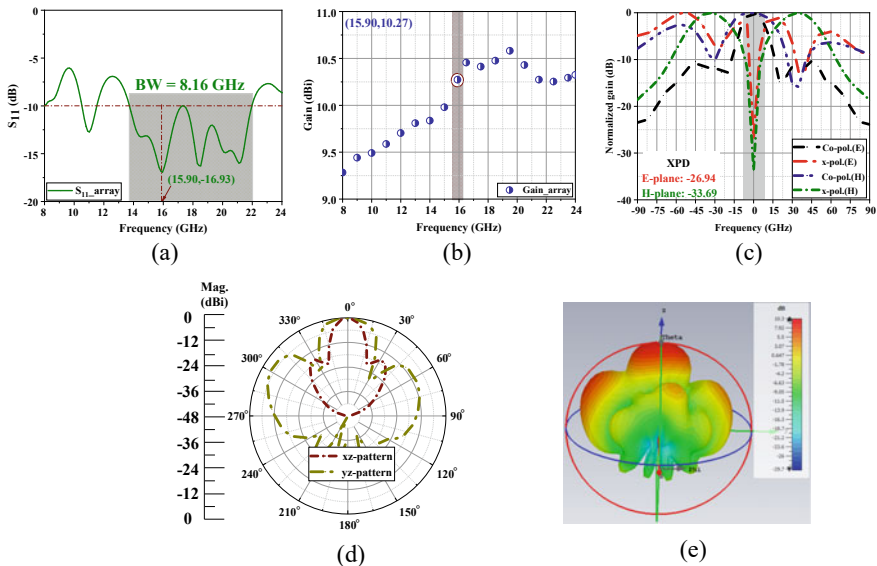
A dropper-shaped printed antenna and its two-element linear arrays simulated outcomes are graphically presented in this section. All the simulated outcomes of the sole radiator are conferred in Fig. 9. From Fig. 9a, it can be clearly observed that the antenna is resonated at 16.00 GHz and offers 27.81 dB return loss along with 9.38 GHz impedance bandwidth, which is helpful for Ku-band-related applications. The gain characteristic of the antenna is conferred in Fig. 9b, and it offers 7.48 dBi gain at the particular resonating frequency. The E and H-field patterns of the antenna are shown in Fig. 9c. It is clear to observe that the antenna gives  $-29.71$  dB cross-pol. discrimination at the desired frequency, which is quite acceptable for particular applications. Radiation characteristics for two cut angles ( $\phi = 0^\circ, 90^\circ$ ) are presented in Fig. 9d, demonstrating that the antenna provides a symmetric radiation pattern with minimal back radiations. Similarly, the 3D radiation pattern is also reflected in Fig. 9e. The antenna offers 97% radiation efficiency and -26 dB side lobe level, respectively.

An antenna's aperture efficiency [37] can be determined using the following formula:

$$\eta_{ap} = \frac{D}{D_{max}} \quad (5)$$

**Table 1** Performance parameters of proposed antennas

Parameter(s)	Single antenna	Antenna array
$f_r$ (GHz)	16.00	15.90
$S_{11}$ (dB)	-27.81	-16.93
IBW (GHz)	9.38	8.16
Gain (dBi)	7.48	10.27
Directivity (dBi)	8.62	11.94
SLL (dB)	-26	-18
XPD (dB)	-29.71	-26.94
$\eta$ (%)	97	86
$\eta_{ap}$ (%)	63	66
CF (dB/m)	46.86	44.02

**Fig. 10** Simulated outcomes of antenna array: **a**  $S_{11}$ , **b** gain, **c** E and H-field, **d** xz–yz and **e** 3D radiation patterns.

$$D_{\max} = \frac{4 \times \pi \times A_r}{\lambda^2} \quad (6)$$

where  $D$  represents the antenna's directivity,  $D_{\max}$  represents its maximum directivity,  $A_r$  represents its area, and  $\lambda$  represents its free-space wavelength. The antenna's aperture efficiency becomes 63% which is computed using above equation.

To assess an antenna or array's electromagnetic compatibility (EMC) [42], the surface equivalence technique is used to calculate the correction factor (CF). Using a perfect matching system, the CF can be calculated as follows.

**Table 2** Relative performance of existing and proposed antenna

References	Substrate	$\epsilon_r$	$f_r$ (GHz)	$S_{11}$ (dB)	Gain (dBi)	x-pol. (dB)	$\eta$ (%)
[4]	Cu-clad	2.16	12.5	-15	7.02	-20	NR
[5]	RO-5870	2.3	15.46	-26	3.94	NR	89
[8]	FR-4	4.4	12.2	-15	4.81	NR	NR
[9]	FR-4	4.4	13.5	-20	4.20	NR	86
[18]	Ceramic-P	10.2	13	-32.5	2.03	-30.00	75
[19]	FR-4	4.4	15.06	-22.7	6.01	NR	NR
[20]	RO5880	2.2	14.6	-30.5	4.70	-12.00	82
[23]	FR-4	4.4	17.5	-20	5.52	NR	NR
<b>Prop.</b>	RO-5880	2.2	16	-27.8	7.48	-29.71	97

NR: Not reported

$$CF = \frac{|\mathbf{E}^{INC}|}{|V_r|} = 20 \log \left( \frac{9.73}{\lambda \sqrt{G_a}} \right) \quad (7)$$

where  $|\mathbf{E}^{INC}|$ ,  $|V_r|$  and  $G_a$  denote the magnitude of the incident field, the terminal voltage and the antenna's absolute gain, respectively. It is stated that the antenna's electromagnetic interference is low, making it an attractive choice for Ku-band use (the antenna has a correction factor of 46.86 dB/m). Table 1 lists all the settings for the single radiator. Simulated results for the antenna array built using Wilkinson power dividers are visually shown in Fig. 10. Array return loss is shown in Fig. 10a, which displays a resonant frequency of 15.90 GHz, a return loss of 16.93 dB and a bandwidth of 8.16 GHz. Figure 10b displays the array's absolute gain, showing that at the chosen frequency, it provides a gain of 10.27 dBi. Figure 10c shows the antenna's E and H-field patterns and provides a cross-pol. level of -26.94 dB in the primary emission direction. It is claimed that the array's xz–yz radiation patterns, as shown in Fig. 10d, provide a desired radiation pattern in addition to low SLL (-18 dB). Figure 10e similarly presents the array's 3D radiation pattern, claiming that the array provides a symmetric radiation pattern in the preferred orientation. Both the array's radiation and aperture efficiencies are rather high at 86% and 66%, respectively. When operating at the target frequency, the array provides a correction factor of 44.02 dB/m, which is within acceptable range. For your convenience, we have provided all of the array's antenna parameters in Table 1. A comparative performance between the proposed and few existing antennas is carried out in Table 2. It can be clearly observed that the proposed antenna offers better simulated results compared to the other existing antennas operating in Ku-band.

## 5 Conclusion

A linear array of wideband printed antennas for Ku-band-related applications has been reported in this article. A single radiator with a dropper-shaped design is used in the suggested array, and its features include a gain of 7.48 dBi, a broad impedance bandwidth, a low x-pol. level, high radiation efficiency and a manageable correction factor. The length of the current route has been calculated to demonstrate that the antenna operates at a certain frequency. More specifically, both antennas' circuit equivalent models have been explored in depth. The ground plane of the antennas does not include any flawed geometries other than the monopole structure, which is the primary cause of frequency drift. Wilkinson power division allows for a smaller array to provide the same or better parametric performance. Gain is quite high, and both cross-pol. and radiation efficiency are good thanks to the array's design. Several wireless and satellite applications are possible because of the Ku frequency range that both antennas cover.

## References

1. Balanis CA (1997) Antenna theory: analysis and design. Wiley, New York
2. Haupt RL (2010) Antenna arrays: a computational approach. Wiley-IEEE Press (2010)
3. Carver KR, Mink JW (1981) Microstrip antenna technology. IEEE Trans Antennas and Propag. AP-29(1):2–24
4. Tong KF, Luk KM, Lee KF (2001) Wideband Pi-shaped aperture-coupled U-slot patch antenna. Microw Opt Technol Lett 28(1):70–72
5. Islam MM, Islam MT, Faruque MRI (2013) Dual-band operation of a microstrip patch antenna on a duroid 5870 substrate for Ku- and K-Bands. Hindawi Publishing Corporation, The Scientific World Journal, pp 1–10
6. Ahsan MR, Habib Ullah M, Mansor F, Misran N, Islam T (2014) Analysis of a compact wideband slotted antenna for Ku, vol applications. Hindawi Publishing Corporation, The Scientific World Journal, pp 1–6
7. Kumar A, Raghavan S (2017) Wideband slotted substrate integrated waveguide cavity backed antenna for Ku band application. Microw Opt Technol Letter 59(7):1613–1619
8. Vijayvergiya PL, Panigrahi RK (2017) Single-layer single-patch dual band antenna for satellite applications. IET Microwaves, Antennas Propag 11(5):664–669
9. Alam MJ, Faruque MRI, Hasan MM, Islam MT (2017) Split quadrilateral miniaturised multi-band microstrip patch antenna design for modern communication system. IET Microwaves, Antennas Propag 11(9):1317–1323
10. Lakrit S, Ammor H, Matah S, Karli R, Saadi A, Terhzaz J, Tribak A (2018) A new small high-gain wideband rectangular patch antenna for X and Ku bands applications. J Taibah Univ Sci 12(2):202–207
11. Samantaray D, Bhattacharyya S, Srinivas KV (2019) A modified fractal-shaped slotted patch antenna with defected ground using meta-surface for dual band applications. Int J RF Microw Comput Aided Eng 29:1–9
12. Kola KS, Kousalya R, Mahalakshmi BNS, Chatterjee A (2021) A high-gain and low cross-polarized wave-fractal shaped printed antenna for DBS application. J Electromagn Waves Appl 36(5):607–625
13. Wang H, Huang XB, Fang DG (2008) A single layer wideband U-slot microstrip patch antenna array. IEEE Ant Wireless Propag Lett 7:9–12

14. Awida MH, Fathy AE (2009) Substrate-Integrated Waveguide Ku-Band Cavity-Backed  $2 \times 2$  microstrip patch array antenna. *IEEE Ant Wireless Propag Lett* 8:1054–1056
15. Bilgic MM, Yegin K (2014) Low profile wideband antenna array with hybrid microstrip and waveguide feed network for Ku-band satellite reception systems. *IEEE Trans Antns Prop* 62(4):2258–2263
16. Jin H, Chin K, Che W, Chang C, Li H, Xue Q (2014) Differential-fed patch antenna arrays with low cross polarization and wide bandwidths. *IEEE Ant Wireless Prop Lett* 13:1069–1072
17. Jin H, Chin K, Che W, Chang C, Busuioc D, Safavi-Naeini S (2015) A broadband patch antenna array with planar differential L-shaped feeding structures. *IEEE Ant Wireless Prop Lett* 14:127–130
18. Ahsan MR, Islam MT, Ullah MH, Aldhaheri RW, Sheikh MM (2015) A new design approach for dual-band patch antenna serving Ku/K-band satellite communications. *Int J Satellite Commun Network* 1–11
19. Naik KK, Vijaya Sri PA (2018) Design of hexa-decagon circular patch antenna with DGS at Ku band for satellite communications. *Prog Electromag Res M* 63:163–173
20. Kumar A, Raghavan S (2018) Broadband SIW cavity-backed triangular-ring-slotted antenna for Ku-band applications. *Int J Electron Commun* 1–14
21. Kong L, Xu X (2018) A compact dual-band dual-polarized microstrip antenna array for MIMO-SAR applications. *IEEE Trans Antennas Propag* 66(5):2374–2381
22. Kola KS, Patanvariya D, Naik SB, Reddy MV, Chatterjee A (2018) A novel two-element linear array for DSRC band. In: International conference on computing, communication and networking technologies (ICCCNT), pp. 1–5
23. Bag B, Biswas P, De S, Biswas S, Sarkar PP (2019) A wide multiband monopole antenna for GSM/WiMAX/ WLAN/XBand/KuBand applications. *Wireless Pers Commun* 1–17
24. Patanvariya D, Kola KS, Chatterjee A (2019) Left-handed circularly polarized two-element antenna array for vehicular communication. In: International Conference on Communication and Signal Processing (ICCSP), pp 27–32
25. Kola KS, Chatterjee A, Patanvariya D (2020) Design of a compact high gain printed octagonal array of spiral-based fractal antennas for DBS application. *Int J Microw Wireless Technol* 12(8):769–781
26. Kola KS, Chatterjee A, Patanvariya D (2020) Design of a wideband right-handed circularly polarized array of miniaturized mushroom-shaped antennas for direct broadcast satellite application. *Microw Opt Technol Lett* 62(11):3542–3555
27. Kola KS, Chatterjee A (2020) A linear array of christmass-tree shaped antennas for DBS applications. In: International conference on computer, electrical and communication engineering (ICCECE), pp 1–6
28. Kola KS, Chatterjee A (2021) A high-gain and low cross-polarized printed fractal antenna for X-band wireless application. *Int J Commun Syst* 34(10):1–25
29. Kola KS, Chatterjee A (2021) Design of a right-handed circularly polarized printed antenna for vehicular communication. *Wireless Personal Commun* 121(4):2735–2756
30. Kola KS, Chatterjee A (2021) A  $1 \times 2$  array of high-gain radiators for direct broadcast satellite (DBS) services under Ku-band. In: 8th International conference on signal processing and integrated networks (SPIN), pp 297–302
31. Kola KS, Chatterjee A (2021) An array of tulip-flower shaped printed radiators for direct broadcast satellite (DBS) applications. In: IEEE international conference on advanced communication technologies and signal processing (ACTS), pp 1–6
32. Behera BR, Meher PR, Mishra SK (202) Meta-surface superstrate inspired printed monopole antenna for RF energy harvesting application. *Prog Electromagnet Res C* 110:119–133
33. Kola KS, Chatterjee A (2022) A highly directive array of nature-inspired based patch antennas. *Int J RF and Microw Comput-Aided Eng* 32(8):1–20
34. Kola KS, Chatterjee A (2022) A highly-directive hybrid-fractal radiator-based printed array for X-band amateur radio applications. *Int J Electromag Waves Appl* 36(14):1935–1956
35. Monebi AM, Lee C, Ahn B, Choi S (2023) Design of a Ku-Band monopulse antenna with a truncated reflector and an open-ended waveguide feed. *Sensors* 23(1):1–11

36. Wilkinson EJ (1960) An N-way hybrid power divider. *IRE Trans Microw Theory Tech* 8(1):116–118
37. Vosoogh A, Kildal P S (2016) Simple formula for aperture efficiency reduction due to grating lobes in planar phased arrays. *IEEE Trans Antennas Propag* 64(6):2263–2269
38. High Frequency Electromagnetic Software SONNET (v14), North Syracuse, NY 13212, April (2013)
39. CST STUDIO SUITE, CST AG, Germany(2018)
40. Kreyszig EO (1983) Advanced engineering mathematics. Wiley, New York
41. Ludwig R, Bretschko P (2000) RF circuit design, theory and applications. Prentice-Hall, Upper Saddle River, NJ
42. Paul CR (2006) Introduction to electromagnetic compatibility, 2nd edn. Wiley

# Sentiment-Based Simplification of Legal Text



Cinu C. Kiliroor, Som Sagar, and Swani Sundara Didde

**Abstract** Legal documents have always played an important role for liabilities and safety, but the length of the document and the use of complex terms have become a complication for apprehension. Hence, if one possesses a tool to facilitate improvement in understanding, it could be a possible way of securing impartiality. The legal text is challenging since it is entirely different from the ordinary natural language in vocabulary, morphology, syntax, and semantics. Thus, a text simplification method that is to the legal domain can help make the legal text more accessible and save people from taking time to read legal documents. Thus, this study aims to find a text simplification method that would best suit legal text conversion. The proposed model is identifying complex words with the help of statistics and then replacing them with simpler and readable phrases or words which would be done with the help of a word2Vec model and sentiment analysis. The model is trained using a dataset that contains combined data from Indian Legal Documents Corpus (ILDC<sub>single</sub> and ILDC<sub>multi</sub>) which has a corpus count of 1,906,365 which groups vectors of similar words together in the vector space. We propose an approach that successfully detects complex words in a paragraph and replaces it with a less complex word with the same sentiment as the complex word.

**Keywords** Word2Vec · Sentiment analysis · Corpus

## 1 Introduction

Reading a legal document has always been a hassle for the common man, they are tough to understand due to the use of a foreign language such as Latin phrases and a sentence structure different from plain English. There is the usual use of center-embedded clauses which is standard practice in legal documents that makes it tough to read, and this practice is memory intensive. Understanding a legal text is important,

---

C. C. Kiliroor · S. Sagar (✉) · S. S. Didde  
Indian Institute of Information Technology, Kottayam, India  
e-mail: [somsagar2019@iiitkottayam.ac.in](mailto:somsagar2019@iiitkottayam.ac.in)

it would help the underprivileged understand what law has to offer and also opens a gateway for transparency and accountability. The proposed model used is Word2Vec which can read a large corpus that gives us a set of vectors as an output. Word2Vec groups vectors of similar words together in the vector space. Therefore, this approach aids the basic requirement of complex word identification and replacement.

In the following sections, Sect. 2 conveys the literature survey on related works, Sect. 3 is the proposed approach, and Sect. 4 is the experimental setup and result and finally the conclusion.

## 2 Related Works

A framework based on BERT was introduced by Qiang, Jipeng, which focuses on the context of the complex word on all steps of lexical simplification without relying on the parallel corpus or any linguistic database. Since BERT can be trained in raw text, this method can be applied to many languages for lexical simplifications [1]. The problem with this model is that it only generates a single-word replacement for the complex word. Other methods like text simplification systems combining semantic structures and neural machine translation are done using a semantic component that performs sentence splitting without relying on a specialized corpus but only an off-the-shelf semantic parser. After splitting, neural machine translation (NMT)-based simplification is performed, using the NTS system [2]. One major problem we see is the lack of data set but there are few like the ILDC is a sizable corpus of 35,000 judgments from the Indian Supreme Court that are annotated. A component of the corpus (a distinct test set) has gold-standard justifications annotated by legal professionals. Many approaches exist now like the hybrid approach for term frequency-inverse document frequency (tf-idf) word vectorizer and k-means clustering algorithm for automatic text summarization of legal cases [3]. Many framework based on BERT has been developed that aims to understand the context of complex words at all stages of lexical simplification. These framework does not rely on parallel corpus or any linguistic database [4]. Bert was further investigated in BERTopic for topic modeling in legal documents and shows that taking statute law references into account during the text embedding process enhances topic modeling quality [5].

The authors [6] suggest the task of Court Judgment Prediction and Explanation based on ILDC (CJPE). The task calls for an automated system to forecast a case's explainable outcome. They test various fundamental models for case predictions and explainability, proposing a hierarchical occlusion-based paradigm. Their best prediction model's performance is 78% compared to human legal experts' accuracy of 94%, demonstrating the difficulty of the prediction task. The investigation of the proposed algorithm's explanations reveals a large divergence between the algorithm's and legal experts' explanations of the judgments, suggesting areas for further study.

There are nascent ways that integrate various natural language processing techniques to derive rules from legal documents [7]. The method employed combines linguistic data from WordNet with a syntax-based extraction of rules from legal

writings and a logic-based extraction of connections between chunks of such texts. As a result, powerful techniques for extracting machine-readable rules from legal documents are developed. Topic modeling in legal documents can be considered for simplification aspects such as the usage of BERTopic for topic modeling in legal documents and shows that taking statute law references into account during the text embedding process enhances topic modeling quality [8]. A survey was conducted to explore the existing work in the area of Indian Legal NLP, and the survey puts forward ideas for creating new benchmarks to enhance Indian legal natural language processing and discusses various legal NLP applications like factoid Q/A, question generation, judgments summarization, timeline extraction, context-specific summary, relationship extraction, find similar cases, find supporting paragraphs for new judgements, influential case law extraction, predicting relevant acts based on case facts, statement contradiction discovery, sentence rhetorical roles prediction, argument generation, autocomplete of judgements, and documents how benchmarks can be created and used for these applications [9].

From the existing approaches, we can reasonably infer that complex legal word identification and simplification are a crucial step for Legal NLP. And since there is a corpus of Indian legal cases, it can be useful for training the model to identify complex words. This is beneficial for all people who are non-native speakers of the English language and can change the aspect and understanding of legal documents. It is useful since a common man can detect loop holes and understand contracts in an efficient and simple way.

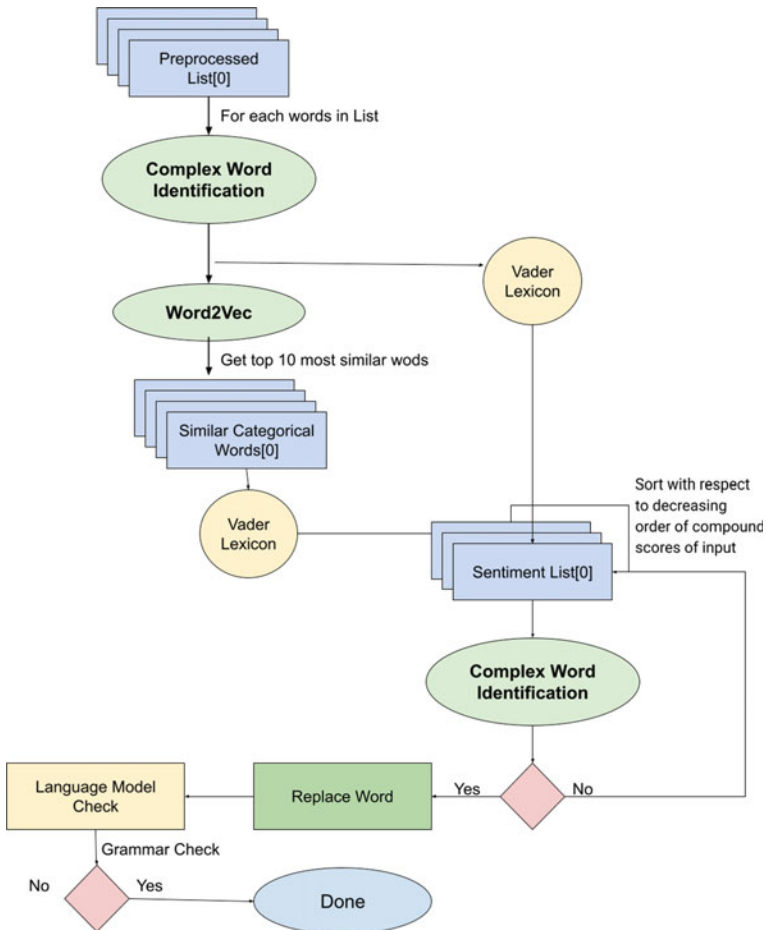
### 3 Proposed Sentiment-Based Word2Vec Text Simplification

See Fig. 1.

#### 3.1 Method

##### 3.1.1 Complex Word Identification

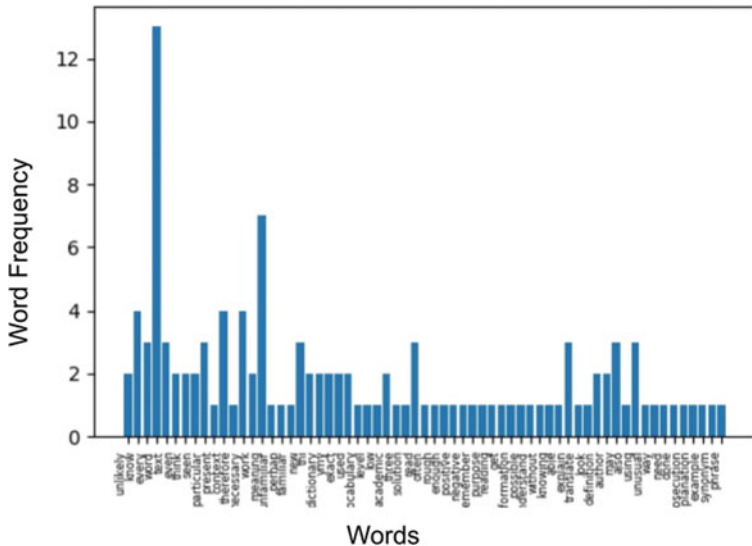
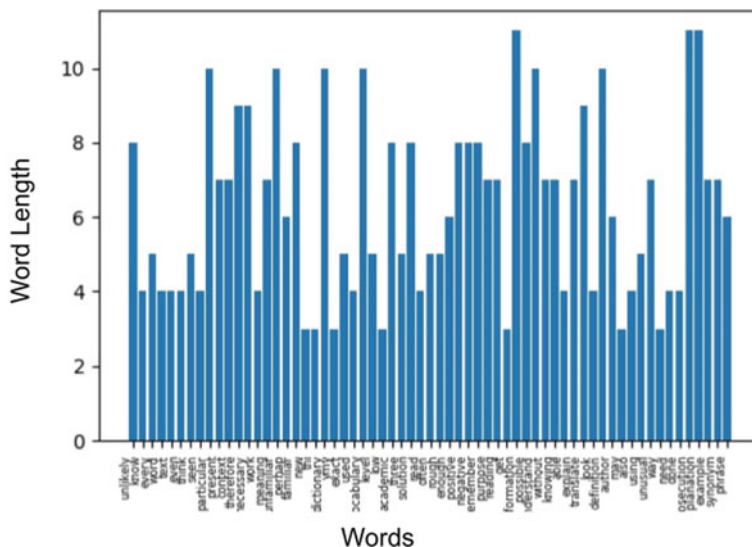
In this study, a dataset and model are developed for complex word identification. The model uses an ensemble of two classifiers: multinomial Naive Bayes (MNB) and gradient boosting (GB). Multinomial Naive Bayes is a probabilistic algorithm that is based on the Bayes theorem. It is commonly used in text classification problems where the features are discrete values such as the frequency of words in a document. The MNB algorithm makes the assumption that each feature is independent of the other features given the class label. It then uses the frequency of the words in each class to calculate the probability of a given class. The class with the highest probability is then assigned to the input text. MNB is simple to implement, fast, and highly



**Fig. 1** Workflow of the proposed model

scalable, making it a popular choice for text classification tasks. The two parameters considered for complex words dataset were

1. Frequency: Due to parts of speech, counting does not satisfy the first consistency requirement. To function, a program must identify words by compiling all potential word forms, just like a linguist would.
2. Word Length: If word parts can be used to infer meaning, long words do not necessarily have to be complex. Include a morphological (word part) analyzer in your program rather than relying only on a standard-length analyzer (Figs. 2 and 3).

**Fig. 2** Word frequency distribution**Fig. 3** Word length distribution

### 3.1.2 Word2Vec

Upon the completion of the preprocessing stage, Word2Vec is used to construct the word vector representation. Using training data, the Word2Vec model first generates a vocabulary. It then figures out the vector representation of each word. The classification features will be taken from the generated word vector. Because comparable words have similar vectors in Word2Vec, it can generally aid in enhancing classification results.

### 3.1.3 Sentiment Analysis

Ultimately, the reviews are classified as favorable or negative in the final stage. The categorization work in this study is performed using the VADER Lexicon. The VADER sentiment analysis, despite being computationally complex, can effectively perform sentiment analysis tasks with the help of its lexicon that assigns sentiment scores to lexical elements based on their emotional intensities. By summing up the intensity scores of each word in a text, VADER can accurately calculate the sentiment score of the text.

## 3.2 Algorithm

**Function:** sentiment\_compund\_score(m)

**Input:** paragraph

**Output:** simplified paragraph

**Begin**

```

1:   Frequency = Lemmatization(words)
2:   Length = len(words)
3:   n = CWI(words,Length,Frequency)
4:   for each word in n:
5:     m = similar_words(n)
6:     Sentiment = sentiment_compund_score(m)
7:     Sort( m - sentiment_compund_score(word)) in decreasing order
8:   for each word in m:
9:     if word is not complex then
10:      replace n
11:    end if
12:    if replaced_text.check == True then
13:      break
14:    end if
15:   end for
16: end for
```

**End**

## 4 Experimental Setup and Result

### 4.1 Experimental Setup

For implementation purposes, there is a use of Python language. The implementation would be carried out using the Gensim library with the TensorFlow framework and with other libraries like Pandas and NumPy. Keras is a Python-based open-source framework that includes many implementations of commonly used neural network building components including as layers, activation functions, optimizers, and tools for preprocessing pictures and text data. Using the Google Colab platform, all implementations were ran on AMD Ryzen 7 3700U with Radeon Vega Mobile Gfx, a 2.30 GHz processor with 12.0 GB (9.94 GB usable) RAM.

### 4.2 Dataset

**Indian Legal Document Corpus (ILDC).** The dataset used is the Indian Legal Document Corpus (ILDC), which is a compilation of Supreme Court of India case proceedings. This is a corpus of 35 K Indian Supreme Court cases with original court judgements annotated. ILDC papers are longer and feature a more sophisticated vocabulary than normal corpora used for training text classification algorithms and language models. This information has been compiled for CJPE. The dataset that is being used for the model is separated into 2 sets—ILDC<sub>single</sub>, and ILDC<sub>multi</sub>. ILDC<sub>single</sub> contains all the documents where there is a single petition (and, thus, a single decision) or multiple petitions, but the decisions are the same across all those petitions. While ILDC<sub>multi</sub> is a superset of ILDC<sub>single</sub> and has multiple appeals leading to different decisions. The model used for this model is Word2Vec, and since our aim is to get word vectors, only the text used in the document is relevant to this model is. To obtain a corpus consisting of legal words only, the ILDC<sub>single</sub> and ILDC<sub>multi</sub> datasets were merged into a single corpus. As a result, legal words from both datasets were combined and used for further analysis. The ILDC<sub>single</sub> dataset contains 939,571 case records, and the ILDC<sub>multi</sub> contains 11,960 case records. Later combined them while removing null values to get a dataset of 951,531 case records.

**English Word Frequency.** The frequency of a word in a language is critical information for linguists and natural language processing. In natural language processing, very common terms are often removed during preprocessing since they are less informative than less frequent ones. Human language users are also aware of word frequency. The frequency of use of a word affects how individuals process language. For instance, words with a high frequency of occurrence can be read and interpreted more rapidly and are easier to understand in noisy environments.

**Complex Words.** To determine the complexity of words in a text corpus, we first used the natural language toolkit (nltk) library to tokenize the text and remove stop words from the ILDC dataset. The stop words were determined using the stop words

corpus from the nltk library. The words were then processed and scored based on their frequency of occurrence and length. We created a dictionary created to store the word frequency, with words as keys and their frequency as values. For each text in the corpus, the words were tokenized, and stop words were removed. The frequency of each word is then updated in the frequency dictionary. Next, a score is assigned to each word in the frequency dictionary based on its frequency and length, using the following formula:  $\text{frequency} * (1/\text{length})$ . This scoring function is created with the objective of capturing the idea that complex words tend to be less frequent and longer in length. Words with a score less than 0.5 were considered complex, while words with a score greater than or equal to 0.5 were considered simple. These words were then combined into a single list, with labels assigned as ‘complex’ or ‘simple’ based on their complexity score.

### **4.3 Data Preparation**

Initially, the use of a new dataset that contained news titles and content from which content is extracted and preprocessed; the steps taken here are as follows:

1. Tokenization: The process of transforming a string or text into a collection of tokens is referred to as tokenization. Tokens are parts in the same way that a word is a token in a sentence, and a phrase is a token in a paragraph.
2. Stop Words Removal: Removing words that appear frequently in all of the corpus documents Articles and pronouns are typically classified as stop words.
3. Singularize: The plural words are changed to their respective singular phrases so that later when a process like frequency count or duplicate removal is used the plural, and singular will result as separate words to avoid this problem

### **4.4 Complex Word Identification**

We first balanced the dataset by resampling the minority class using the resample method from the imbalanced-learn library. The resulting dataset has an equal number of samples from both the majority and minority classes. We trained two classifiers on the preprocessed data: MNB and GB. The MNB classifier is trained using the fit method from the MultinomialNB class in the scikit-learn library. The GB classifier is trained using the fit method from the GradientBoostingClassifier class in the scikit-learn library. We then ensembled the two classifiers using the VotingClassifier class in the scikit-learn library. The ensemble method used a ‘hard’ voting scheme, where the majority vote of the two classifiers determines the final prediction.

```

array([-2.93274593e+00, -6.75747681e+00, -2.41958246e-01, 1.19422734e+00,
-5.90108156e+00, -1.99230909e+00, 4.19672155e+00, -4.19123220e+00,
-8.37560534e-01, -1.08981284e+00, -4.27308750e+00, -1.31374419e+00,
5.03259945e+00, 2.51002216e+00, 4.70668459e+00, -8.28086555e-01,
4.37550879e+00, 4.40181780e+00, 1.57484257e+00, 4.85246849e+00,
2.43877506e+00, 3.57117033e+00, 1.38127315e+00, -1.00630260e+00,
9.539191532e-01, 2.47777653e+00, -3.63964891e+00, 1.63715327e+00,
6.07199764e+00, -6.99488770e+00, -1.78389287e+00, -1.55733371e+00,
-1.78748883e+00, -4.30674523e-01, 2.45191622e+00, -6.29993105e+00,
-2.90111756e+00, -1.35444009e+00, 3.14902616e+00, -1.70277834e+00,
-4.36926603e+00, 1.73181020e+00, -5.32921016e-01, -2.37786531e+00,
3.57486796e+00, 3.79688096e+00, 2.93443060e+00, 3.43609023e+00,
-1.98322996e-01, 4.98237324e+00, -1.54932964e+00, -6.96247637e-01,
-1.86761034e+00, -8.86986136e-01, -4.51446819e+00, 2.98392749e+00,
4.75042969e-01, -3.87275243e+00, -1.66596913e+00, -9.08595603e-03,
2.20501304e+00, 3.06466985e+00, -1.17274964e+00, 2.18687868e+00,
1.63325870e+00, -7.42867887e-01, 5.19318104e+00, -2.09369016e+00,
-2.59023213e+00, -4.29291695e-01, -1.82072818e+00, 3.53625131e+00,
1.11131411e+01, -5.42456545e-02, -2.08971709e-01, 2.25748229e+00,
-2.56328607e+00, -6.95670605e-01, -2.14211369e+00, -4.05776888e-01,
2.40912008e+00, -6.04700232e+00, 2.35183656e-01, -3.02307218e-01,
5.85123062e+00, 1.11719632e+00, -1.24848984e-01, -5.92985861e-02,
6.97398961e-01, 5.39910913e-01, 2.57330227e+00, -4.78034496e+00,
-7.80621409e-01, -2.44534755e+00, 1.88412592e-01, 6.91371346e+00,
4.19141436e+00, 3.94341230e+00, 2.55795789e+00, -3.61543632e+00],
dtype=float32)

```

**Fig. 4** Vector of the word ‘prosecution’

“It is unlikely that you will know every word in a text and even if you think you have seen every word before, it is unlikely that you will have seen a particular word in its present context. It is therefore necessary to work out the meaning of unfamiliar words in context and, perhaps, familiar words in new contexts. This is necessary even if you have a dictionary as your dictionary does not know the exact context in which the word is being used. If you think your vocabulary level is too low for academic work there are three solutions: read, read and read. A. Is it necessary to know the exact meaning of a particular word? Often a rough meaning is enough (does the word have a positive or negative meaning?). Remember that the purpose of reading an academic text is to get information and it is possible to understand the text without knowing the meaning of every word. It is not necessary to be able to explain, or translate, the meaning of a word. B. Look for definitions. The author may know a particular word may be new so it explains. The author may also be using the word in a new, or unusual way so will need to explain how it is being used. This will be done by using a definition, prosecution, explanation, example, or by using a synonym (a word with the same meaning). The phrases”

**Fig. 5** Input given for complex word identification

## 4.5 Result

The Word2Vec model is trained on a combined dataset of ILDC<sub>single</sub> and ILDC<sub>multi</sub>, totaling 1,906,365 corpora. Word2Vec’s vocabulary is 170,728 words long. There are key-value pairs in the vocabulary. The key is the word, and the value is the vector map of the word, e.g., the vector of the word ‘prosecution’ (Fig. 4 ).

### 4.5.1 CWI Evaluation

This section contains the results of our study. We used the multinomial Naive Bayes (MNB) algorithm and gradient boosting (GB) classifier and combined them using

**Table 1** Truth table confusion matrix

	Positive	Negative
Positive	113,845	7724
Negative	20,674	46,007

the voting classifier. We evaluated the performance of our classifier using a confusion matrix and other metrics such as accuracy, precision, recall, and F1-score (Table 1).

The confusion matrix obtained from our study is shown in Table 1. The results indicate that the classifier has 113,845 true positive predictions, 7724 false positive predictions, 20,674 false negative predictions, and 46,007 true negative predictions (Fig. 5).

The CWI step example on the text sentence:

For which the following are identified as complex: ['unlikely', 'imlead', 'particular', 'present', 'unfamiliar', 'familiar', 'dictionary', 'vocabulary', 'academic', 'understand', 'without', 'knowing', 'translate', 'definition', 'prosecution', 'explanation', 'example', 'synonym', 'phrase'].

#### 4.5.2 Simplification

The results showed that our CWI method was effective in identifying complex words in the legal text, providing a step toward simplifying legal documents for better understanding. The proposed method for simplification of legal documents involves the use of Word2Vec, a widely-used word embedding technique, that has been trained on a legal dataset. The trained Word2Vec model is used to generate similar words for a given input word. This step helps in identifying synonyms or related phrases for the complex legal terms present in the document. Next, the sentiment analysis is applied on the generated similar words to determine if the sentiment of the similar word matches the sentiment of the original complex word. If the sentiment of the similar word is found to be in alignment with the original word, then the next step is to check if the similar word is less complex compared to the original word.

If the similar word is found to be less complex, it is then considered as a candidate for replacement. The proposed model leverages this approach to replace complex legal terms in a document with their less complex synonyms or related phrases, thereby simplifying the document. This approach of using Word2Vec and sentiment analysis for simplifying legal documents can help make the legal documents more accessible and understandable for a wider audience. The use of the trained Word2Vec model on the legal dataset ensures that the synonyms or related phrases that are generated are semantically relevant to the legal domain and are not generic terms. The use of sentiment analysis helps ensure that the replacement words maintain the intended meaning of the original complex legal terms.

Inputs for word replacement are taken as the detected complex words, e.g., word 'prosecution', the word is fed into the Word2Vec model which gives output of most similar vectors with respect to the vector of 'prosecution' (Fig. 6).

**Fig. 6** Words with similar vector as prosecution

```
[('accused', 0.7369358539581299),
 ('cution', 0.681521475315094),
 ('approver', 0.6333706378936768),
 ('prosecution', 0.6248856782913208),
 ('companyplainant', 0.6178526878356934),
 ('companycocted', 0.6170843839645386),
 ('jawanaram', 0.6163038015365601),
 ('pws', 0.6017733216285706),
 ('prose', 0.5991949439048767),
 ('alibi', 0.5882930159568787)]
```

**Fig. 7** Sentiment compound of similar word result of prosecution

		θ	compound
0	accused	-0.296	
1	cution	0.000	
2	approver	0.000	
3	prosecution	0.000	
4	companyplainant	0.000	
5	companycocted	0.000	
6	jawanaram	0.000	
7	pws	0.000	
8	prose	0.000	
9	alibi	0.000	

After getting most similar words, the logic that the replaced word should have the same sentiment as the word has been replaced with, later with the use of sentiment analyzer VADER lexicon to get sentiment compound scores of all the words in the similar words list. The word is replaced only if the similar word is detected as simple and not complex (Figs. 7, 8, 9, 10 and 11).

From the above sentiment table, top 3 words are taken with the least sentiment difference from the input words sentiment.

Python uses a language model called language tool Python, which is accessed via LanguageTool('en-US'). We use this library to find grammatical and spelling errors. We loop over the top 3 similar words as output and replace them with the input complex word. Until the LanguageTool gives a no grammar mistake message.

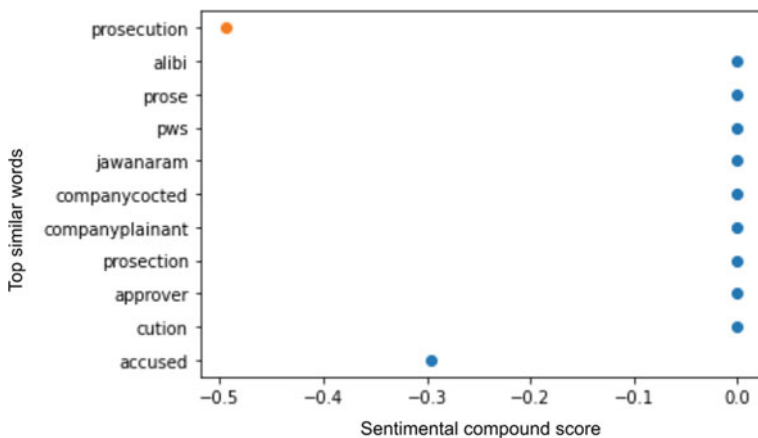


**Fig. 8** Sentiment compound scores of words similar to prosecution

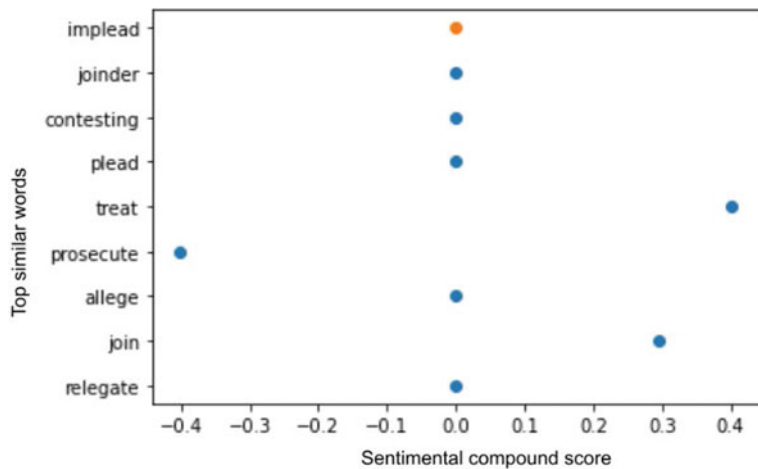


**Fig. 9** Sentiment compound scores of words similar to implead

**Fig. 10** Words for  
prosecution

0	accused
1	cution
2	approver

**Fig. 11** Words for implead

0	relegate
1	allege
2	plead

## 5 Conclusion

The results of our study show that the multinomial Naive Bayes (MNB) algorithm and gradient boosting (GB) classifier combined using the voting classifier are able to correctly classify complex and simple words with high accuracy and precision. The high accuracy and precision results indicate that the classifier is able to distinguish between complex and simple words with a high degree of confidence. The dataset for this study is a compilation of Supreme Court of India case proceedings. This is a corpus of 35 K Indian Supreme Court cases annotated with original court rulings. When compared to usual corpora used for training text classification models and language models, ILDC texts are longer and feature a more specialized vocabulary. This data was compiled for Court Judgment Prediction and Explanation (CJPE). Our approach involves the replacement of complex words in the legal documents with simpler synonyms or related phrases, leveraging the sentiment analysis and Word2Vec models trained on the ILDC dataset. The proposed model has the potential to aid in summarization tasks and can be used in future works for this field.

## References

1. Qiang J et al (2021) LS Bert: lexical simplification based on BERT. IEEE/ACM transactions on audio, speech, and language processing 29:3064–3076
2. Sulem E, Abend O, Rappoport A (2018) Simple and effective text simplification using semantic and neural methods. In: Proceedings of the 56th annual meeting of the association for computational linguistics, (vol 1: Long Papers), Association for Computational Linguistics, Melbourne, Australia, pp 162–173
3. Cemri M, Çukur T, Koç A (2022) Unsupervised simplification of legal texts. ArXiv preprint [arXiv:2209.00557](https://arxiv.org/abs/2209.00557)
4. Qiang J, Li Y, Zhu Y, Yuan Y-H, Wu X (2020) LS Bert: a simple framework for lexical simplification. ArXiv preprint [arXiv:2006.14939](https://arxiv.org/abs/2006.14939)
5. Ma, S, Sun X (2017) A semantic relevance based neural network for text summarization and text simplification. ArXiv preprint [arXiv:1710.02318](https://arxiv.org/abs/1710.02318)
6. Malik V, Sanjay R, Nigam SK, Ghosh K, Guha SK, Bhattacharya A, Modi A (2020) ILDC for CJPE: Indian legal documents corpus for court judgment prediction and explanation. In: Proceedings of the 59th annual meeting of the association for computational linguistics and the 11th international joint conference on natural language processing, volume 1: Long Papers, Online. Association for Computational Linguistics, pp 4046–4062
7. Dragoni M et al (2016) Combining NLP approaches for rule extraction from legal documents. In: 1st workshop on MIning and REasoning with legal texts (MIREL 2016)
8. Silveira R et al (2021) Topic modelling of legal documents via legal-bert. In: Proceedings <http://ceur-ws.org>. ISSN 1613:0073
9. Kalamkar P, Venugopalan J, Raghavan V (2021) Benchmarks for Indian legal NLP: a survey

# Prediction of Dew Point Temperature and Relative Humidity for Nashik Region Using LSTM



Mandal Nabanita and Sarode Tanuja

**Abstract** Predicting the climate parameters has been a challenging task over the years. These climate parameters like temperature, rainfall, and humidity are affected by other parameters like dew point temperature and wind speed. Nashik region has seasonal variation in the humidity which is associated with the dew point temperature. An LSTM model which predicts humidity and dew point temperature is proposed in this paper. The trend and seasonality present in the data is depicted using data visualization, and the missing values are handled by data imputation. It is observed that when 90% of the entire data is provided to the model for training and only 10% is used for testing, it gives better accuracy as compared to the model which utilizes 80% of training data and 20% of testing data.

**Keywords** Machine learning · Deep learning · Prediction · Data imputation · Data visualization

## 1 Introduction

Deep learning methods are applicable to different areas these days. The impact of applying these techniques on the climate data gives good results because it identifies the pattern occurring in it and learns from it. The data pertaining to climate consists of past data as well as present data which can be used for prediction. This voluminous data helps the machine learning models to train properly and give suitable results. The models created through this can be tested on data which is completely unknown to the model to give the future predictions. Weather forecasting is done for a shorter period of time, whereas climate prediction is done considering larger period of time. The climate of any region is affected by various factors like temperature, pressure,

---

M. Nabanita (✉) · S. Tanuja  
Thadomal Shahani Engineering College, Mumbai, India  
e-mail: [nabanita.mandal@thadomal.org](mailto:nabanita.mandal@thadomal.org)

S. Tanuja  
e-mail: [tanuja.sarode@thadomal.org](mailto:tanuja.sarode@thadomal.org)

rainfall, etc. These factors are related to each other, and different techniques can be used to establish correlation between them. Understanding the seasonality and trend of these parameters over a longer period of time helps in creating a model which gives appropriate predictions. Many statistical models exist which are used in forecasting. Machine learning and deep learning models [1] can be applied to classification as well as regression. Prediction of climate parameters is a regression problem. The supervised learning technique is used here. In this paper, prediction of relative humidity and dew point temperature is shown. This prediction is based on multiple parameters. The results of prediction in deep learning depend majorly on the data. If the data is consistent, then the predictions are quite remarkable. The major challenge of any real-time meteorological data is the presence of missing values. For this research, climate data is collected from India Meteorological Department, Pune, Maharashtra, India [2]. After the data is collected, its pre-processing is an important task. Data pre-processing [3] includes data imputation and scaling. Three techniques of data imputation are implemented. Meteorological data consists of time as an important parameter on the basis of which it can be further processed. The data is organized in the time series format to implement the long short-term memory (LSTM) [4, 5] technique. LSTM has the capability to learn from the data which has some long-term temporal dependencies. In this research, mean data imputation, iterative data imputation, and KNN data imputation methods are used for handling missing values [6]. LSTM technique is implemented on the pre-processed data set. The results are evaluated based on performance metrics which are mean squared error, root mean squared error, and mean absolute error. This paper has the following sections: related work, climate data, prediction, results, and conclusion.

## 2 Related Work

In this section, the previous work done by other researchers in this field is described. ARIMA model and artificial neural networks-based model for forecasting weather have been studied by Namratha and Usha [7]. In their research, they are predicting humidity for Karnataka Region. Hewage et al. have proposed a model for forecasting short-term weather which is based on LSTM [5]. Temperature prediction using ANN-based technique has been proposed by Santhosh and Kadar in their paper [8]. They have implemented back propagation technique which gives good predictions with low error rate. For forecasting weather, Kumar et al. have implemented artificial neural network-based model. They have implemented the different models for predicting the maximum temperature by varying the number of hidden layers. They have made different combinations by changing number of neurons [9]. But the main component of all these models is the data. These models are data driven, and hence, data pre-processing is an important step. Antony et al. have discussed about the various data processing techniques for time series data. In their paper [3], they have depicted various data visualization techniques like scatter plot, box plot, etc., to show the time series data. Absence of values in the data set is also a challenge. Dimitris et al. have

shown some methods for handling missing values. Filling up these missing values is known as data imputation. They have demonstrated different data imputation techniques in their research [10]. Nuran and Cemalettin have proposed a hybrid data imputation technique using random forest and DataWig [11]. They have compared the performance with KNN, MICE, and PCA. Humidity is also an important climate parameter, and its efficient prediction is challenging. Marlyna et al. have implemented LSTM-based model for humidity prediction [12]. The results show significant improvement as compared to other methods. Based on these related work, we have made an attempt in this research to implement an LSTM model for prediction of humidity.

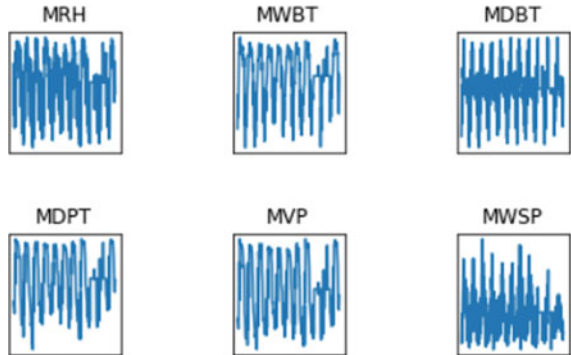
### 3 Climate Data

This section describes the climate data and its pre-processing. The climate of any region gets affected by a lot of parameters. These parameters are wind precipitation, temperature, pressure, humidity, etc. Although each of these parameters have a different unit of measurement, but they are very much correlated to each other. The data is obtained from India Meteorological Department, Pune, Maharashtra, India from the year 2007 onwards for two synoptic hours [13] for the Nashik station. The Synoptic hour is the time which is agreed upon internationally for making meteorological observations. Nashik comes under Madhya Maharashtra Meteorological Substation of Maharashtra. The humidity parameter is closely related to the dew point. If the dew point temperature is high, then it feels like humidity is more, and if the dew point temperature is less, then it feels like the weather is dry. The climate of Nashik is mostly dry except for monsoon season. There is extreme variation in the humidity [14]. This variation is seasonal. So, before predicting the relative humidity and dew point temperature, understanding the seasonality of the data is important.

#### 3.1 Data Set

The data set contains monthly data for two synoptic hours 3 and 12. It consists of various parameters like mean sea level pressure, evaporation, dry bulb temperature, average wind speed, wet bulb temperature, mean sunshine duration, vapor pressure, dew point temperature, maximum and minimum temperature, relative humidity, total cloud amount, etc. The research is conducted for two target variables. The target variables are relative humidity and dew point temperature which is to be predicted. In the data set, it is denoted by MRH which stands for mean relative humidity and MDPT which stands for mean dew point temperature. It is correlated to some other variables such as mean vapor pressure (MVP), mean wet bulb temperature (MWBT), mean dry bulb temperature (MDBT), and mean wind speed (MWSP). This correlation factor helps in feature selection. If the correlation value is positive, then it signifies

**Fig. 1** Trend and seasonality of target variable and input features



that both variables are showing change in the same direction. If it is negative, then it signifies that both variables are showing change in opposite direction to each other. So, these five variables are the input features.

### 3.2 Data Visualization

To understand the data, various data visualization techniques are available [3]. These techniques help in better understanding of the data. Here, we are using line plots which shows the time series plot. Before implementation of the machine learning algorithms to predict any of these parameters, it is important to understand trend and seasonality.

### 3.3 Trend and Seasonality

The increase and decrease in the values of these parameters with respect to time refer to trend. The repetition of these patterns periodically refers to seasonality. Figure 1 shows the trend and seasonality of target variables and input features: MRH, MWBT, MDBT, MDPT, MVP, and MWSP.

It is observed that the input features, MWBT, MDBT, MDPT, MVP, and MWSP, exhibit the same trend and seasonality like the target variable.

### 3.4 Missing Values

Handling the missing values is also one of the important steps of pre-processing of the data. The missing values are shown using time plots.

Figure 2 shows the absence of values in MRH. From the figure, it can be observed that some data is missing between 2018 and 2020.

In the target variable MDPT, also some values are not present in between 2018 and 2020 as shown in Fig. 3.

After applying K-nearest neighbor (KNN) [15] data imputation technique, the inconsistency in the data is removed. This approach uses the K-nearest neighbor to impute the missing value. The value of k is considered as 5 here.

From Fig. 4, we can see that for the year 2018, the rows corresponding to month number 5–9 and 11, 12 for both synoptic hours 3 and 12 are empty. The data was not recorded for these months. So, these missing values are filled up using the KNN data imputation method.

The plot shown in Fig. 5 depicts that the missing values are replaced by the imputed values in the data set.

The discontinuity present in graph of Fig. 2 is removed here in the plot of Fig. 5 due to the imputation of values.

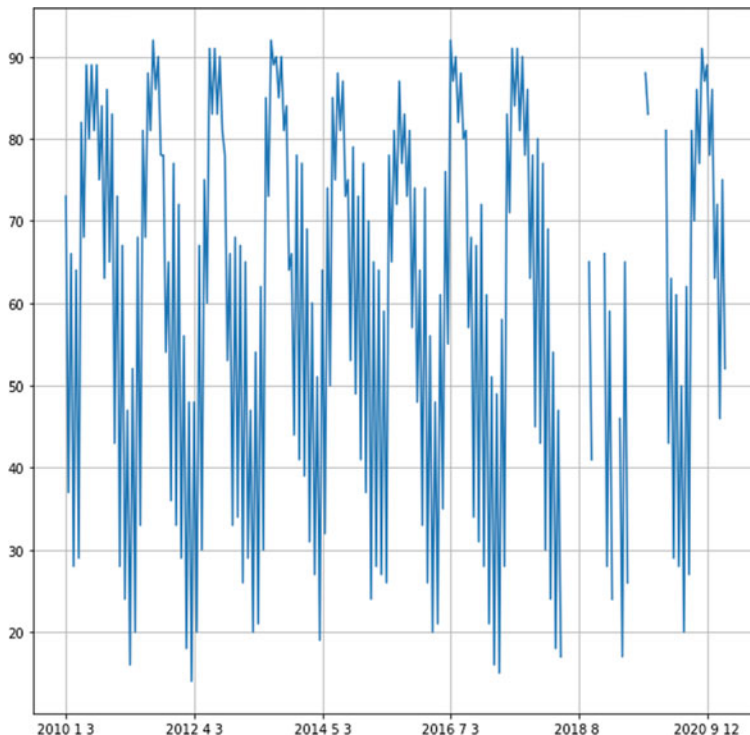


**Fig. 2** Plot of missing values in the target variable MRH

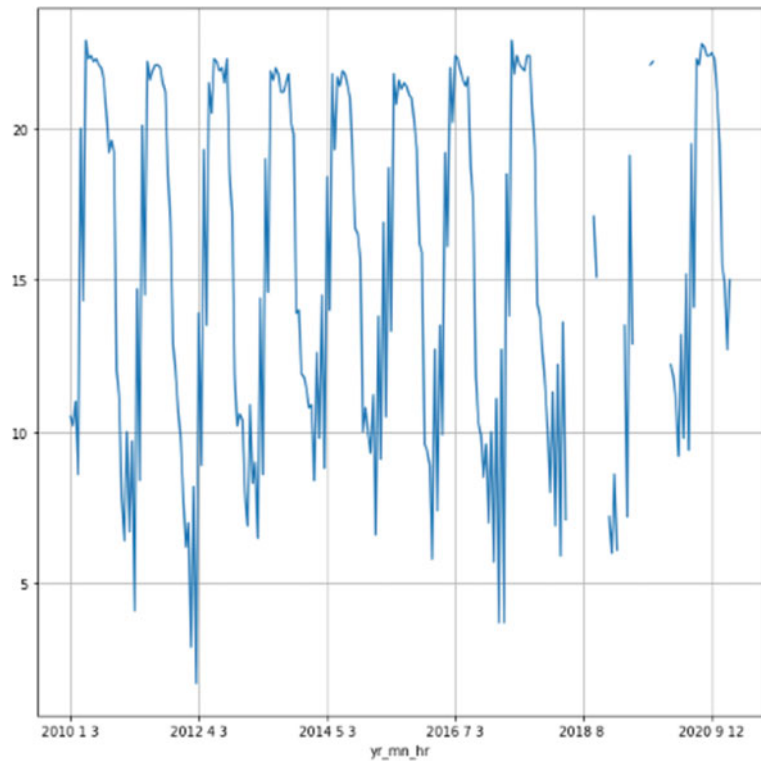


**Fig. 3** Plot of missing values in the target variable MDPT

YEAR	MN	HR	MDBT	MWBWT	MDPT	MRH	MVP	MWSP	Imputed MBDT	Imputed MWBWT	Imputed MDPT	Imputed MRH	Imputed MVP	Imputed MWS
2018	4	3	25.9	18.5	13.6	47	15.9	1.9	25.9	18.5	13.6	47	15.9	1.9
2018	4	12	36	19.4	7.1	17	10.4	7.2	36.0	19.4	7.1	17	10.4	7.2
2018	5	3							25.3682	19.3830	15.3430	60.1522	18.6978	4.2622
2018	5	12							25.3683	19.3830	15.3430	60.1522	18.6978	4.2622
2018	6	3							25.3683	19.3830	15.3430	60.1522	18.6978	4.2622
2018	6	12							25.3683	19.3830	15.3430	60.1522	18.6978	4.2622
2018	7	3							25.3683	19.3830	15.3430	60.1522	18.6978	4.2622
2018	7	12							25.3683	19.3830	15.3430	60.1522	18.6978	4.2622
2018	8	3							25.3683	19.3830	15.3430	60.1522	18.6978	4.2622
2018	8	12							25.3683	19.3830	15.3430	60.1522	18.6978	4.2622
2018	9	3							25.3683	19.3830	15.3430	60.1522	18.6978	4.2622
2018	9	12							25.3683	19.3830	15.3430	60.1522	18.6978	4.2622
2018	10	3	23.8	19.6	17.1	65	19.9	1.1	23.8	19.6	17.1	65	19.9	1.1
2018	10	12	30.1	20.7	15.1	41	17.7	3.8	30.1	20.7	15.1	41	17.7	3.8
2018	11	3							25.3683	19.3830	15.3430	60.1522	18.6978	4.2622
2018	11	12							25.3683	19.3830	15.3430	60.1522	18.6978	4.2622
2018	12	3							25.3683	19.3830	15.3430	60.1522	18.6978	4.2622
2018	12	12							25.3683	19.3830	15.3430	60.1522	18.6978	4.2622
2019	1	3	13.6	10.4	7.2	66	10.3	0.7	13.6	10.4	7.2	66	10.3	0.7

**Fig. 4** Imputed values in the target variable

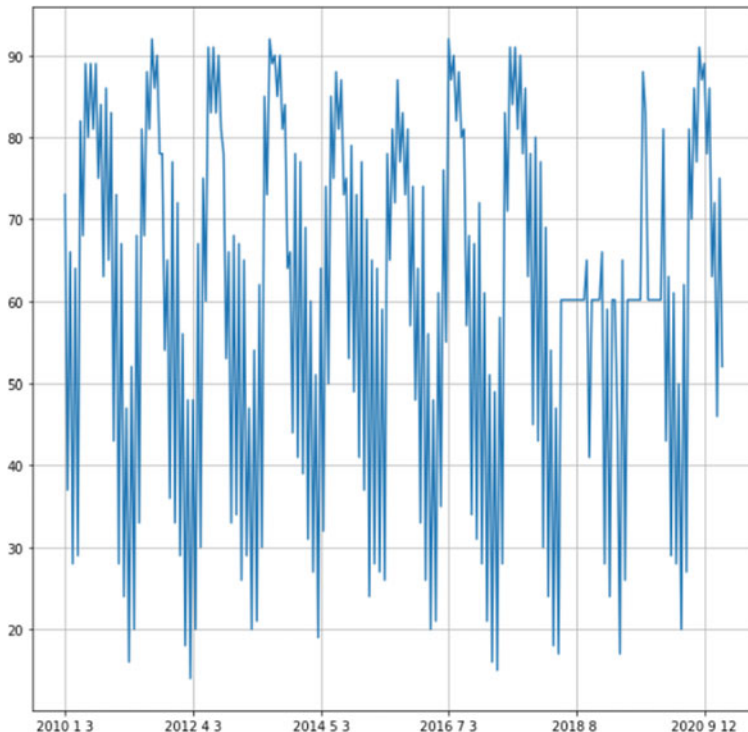


**Fig. 5** Plot of imputation values in the target variable

## 4 Prediction

This section describes the machine learning techniques that are implemented on the data set after data imputation. Long short-term memory (LSTM) is applied to get the prediction of relative humidity [9, 12]. Long short-term memory (LSTM) is a type of recurrent neural network (RNN) which learns from recurring sequence of data. An LSTM module contains one cell state. It also contains three gates which are input gate, the forget gate, and the output gate. The data needs to be arranged in time series format.

### 4.1 Model Configuration

The input is arranged in a group of three tuples, namely batch size, timesteps, and features. The batch size is 32 and timesteps are 2 because we are considering 2 synoptic hours for each month and the features. The output is based on values of features at the previous timesteps along with current state values. The model

comprises of two hidden layers along with one input and one output layer. The model is built considering the training testing split for 90–10% and 80–20%. The model performance is analyzed for these different training–testing split.

## 4.2 Model Evaluation

The different evaluation metrics that are used for evaluating the model performance includes root mean square error, mean squared error, and mean absolute error. The graph of Fig. 6 represents the training and testing loss for 500 epochs when the model is predicting MRH.

The loss of training and testing after the model is trained for 500 epochs to predict MDPT is depicted by the plot of Fig. 7.

To evaluate the model, we have used some performance metrics. Let us consider that  $y_i$  be the actual  $i$ th value and  $\hat{y}$  be the predicted  $i$ th value of the target variable MRH. Let  $n$  be the total number of observations. The average of squared difference between the observed and predicted values gives the mean squared error.

$$\text{MSE} = \frac{1}{n} \sum_{i=1}^n (y_i - \hat{y})^2 \quad (1)$$

If we take the square root of the mean squared error, then it gives the root mean squared error.

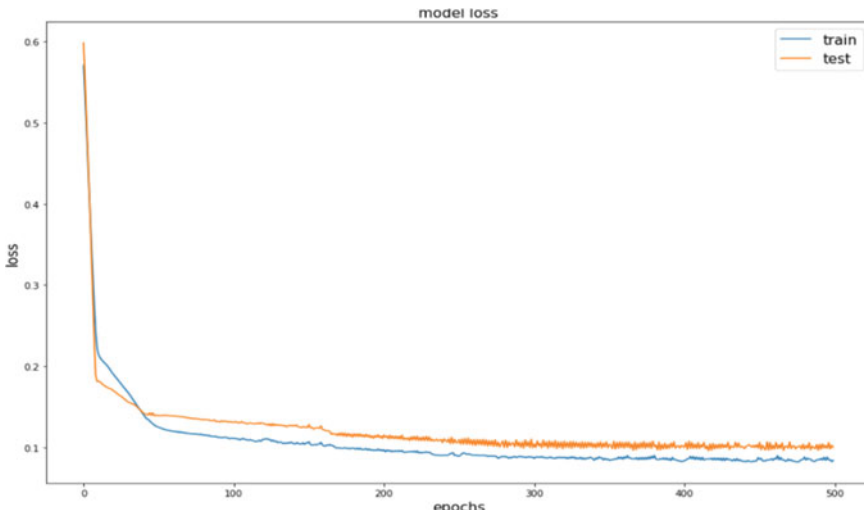


**Fig. 6** Plot of training–testing loss of the model for predicting MRH

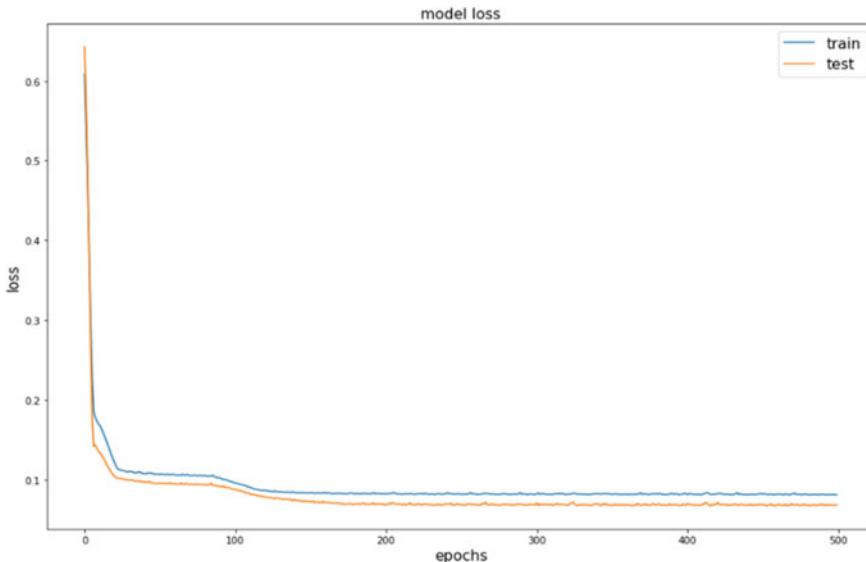


**Fig. 7** Plot of training–testing loss of the model for predicting MDPT

$$\text{RMSE} = \sqrt{\frac{1}{n} \sum_{i=1}^n (y_i - \hat{y})^2} \quad (2)$$

When we consider the prediction errors taken individually for all data in the test set and then find the mean of the absolute values of these errors, then it is the mean absolute error.

$$\text{MAE} = \frac{1}{n} \sum_{i=1}^n |y_i - \hat{y}|^2 \quad (3)$$

## 5 Results

This section shows the results obtained for prediction of MRH and MDPT after applying LSTM technique.

Table 1 shows the values of the evaluation parameter when the training is done considering 90% of data, and testing is done on 10% of data for prediction of MRH.

The results show that the prediction of MRH is better when the model training is done with 90% of the data. The MSE, RMSE, and MAE are less as compared to the model which is trained with 80% of data.

**Table 1** Prediction error for MRH

Evaluation metrics	90–10%	80–20%
MSE	0.01912813	0.03877632
RMSE	0.13830450	0.19691704
MAE	0.10007467	0.14422816

For MDPT, the prediction error using different evaluation parameters is shown in Table 2.

The model trained at 90% of the data and tested with 10% data gives better results than the model which is trained with 80% of data and tested with 20% of data.

The actual and predicted values of the target variable, MRH, are represented in Fig. 8. When the training is done with 90%, testing is done with 10% of data.

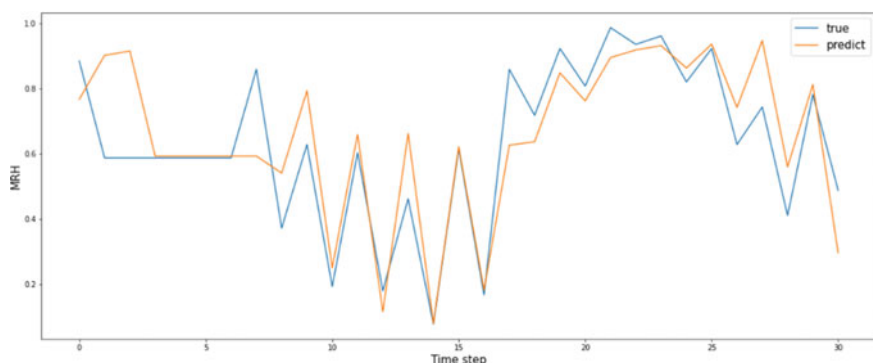
Figure 9 shows the actual and predicted values of MRH when the 80% of data is given to training and 20% of data is used for testing. It can be seen that the predicted values almost follow the same trend as the actual ones.

In Fig. 10, the actual and predicted values of MDPT are represented when the training is done with 90% and testing is done with 10% of data.

In Fig. 11, it can be seen that initially, there is much difference between actual and predicted values of MDPT. This difference gradually reduces with time. This result is obtained when the 80% of data is given to training and 20% of data is used for testing.

**Table 2** Prediction error for MDPT

Evaluation metrics	90–10%	80–20%
MSE	0.01153078	0.02038463
RMSE	0.10738149	0.14277476
MAE	0.06774333	0.11014693

**Fig. 8** Plot of actual and predicted MRH for 90 and 10%

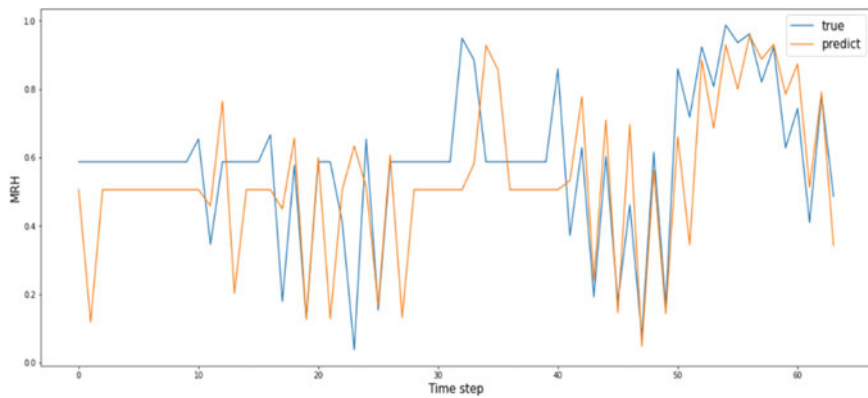


**Fig. 9** Plot of actual and predicted MRH for 80 and 20%

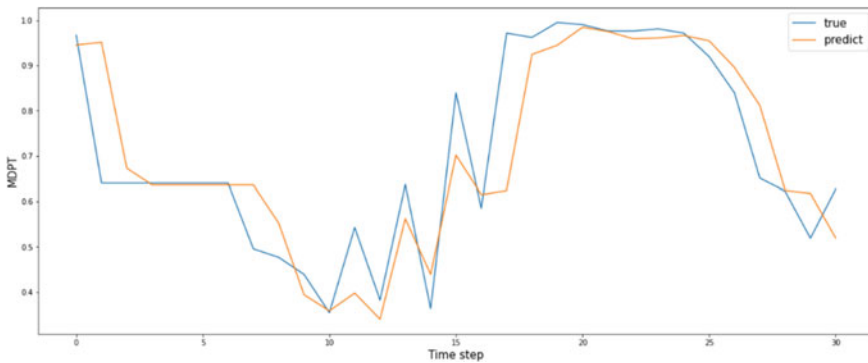


**Fig. 10** Plot of actual and predicted MDPT for 90% and 10%

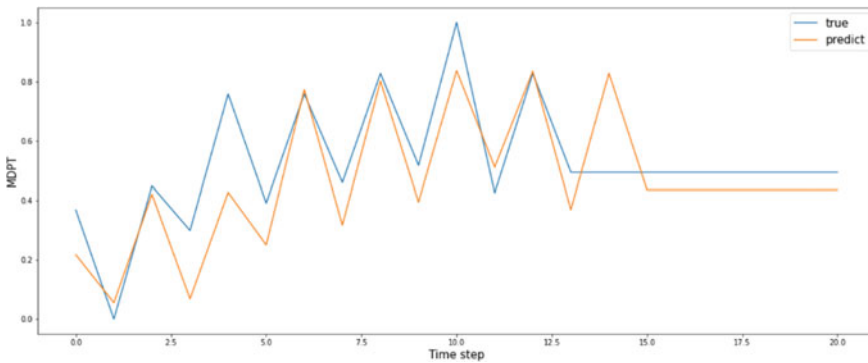


**Fig. 11** Plot of actual and predicted MDPT for 80 and 20%

## 6 Conclusion

After analysis of the data set, it can be concluded that there is a seasonal variation in the humidity of Nashik. This is shown using time plot. To predict the humidity and the dew point, we have used the data pre-processing approaches which includes handling the missing values and scaling before creating the model. The model is trained for 500 epochs. The best results are observed when the LSTM model is trained at 90% training data and 10% test data. The MSE, RMSE, and MAE values are less in this model, and hence, the accuracy is more. For prediction of both MRH and MDPT, this model gives good results. The deep learning models mostly rely on large amount data for giving good results. Since maximum percentage of data is fed to training, and less data is kept for testing, so the prediction accuracy is high. This model can be further used for prediction of other climate parameters like rainfall, temperature, and wind speed.

**Acknowledgements** This research would not have been possible without the data obtained from India Meteorological Department, Pune, Maharashtra, India. We are extremely thankful to them for sharing the data with us.

## References

1. Rasp S, Pritchard M, Gentine P (2015) Deep learning to represent subgrid processes in climate models. In: Proceedings of national academy of sciences, pp 1–6
2. India meteorological department. <https://www.imdpune.gov.in/>
3. Antony E, Sreekanth NS, Sunil Kumar RK et al (2021) Data preprocessing techniques for handling time series data for environmental science studies. Int J Engg Trends Tech 69(5):196–207
4. Solgi R, Loáiciga HA, Kram M (2021) Long short-term memory neural network (LSTM-NN) for aquifer level time series forecasting using in-situ piezometric observations. J Hydro 601
5. Hewage P, Behera A, Trovati M, Pereira E (2019) Long-short term memory for an effective short-term weather forecasting model using surface weather data. In: MacIntyre J, Maglogiannis I, Iliadis L, Pimenidis E (eds) Artificial intelligence applications and innovations. AIAI 2019. IFIP advances in information and communication technology, vol 559. Springer, Cham
6. Biessmann F, Naidu P, Rukat et al (2020) DataWig: missing value imputation for tables. J ML Res
7. Namratha V, Murthy U (2020) Arima model based relative humidity prediction analysis. Int J Sci Engg Res 11(7):1484
8. Santhosh B, Kadar S (2010) An efficient weather forecasting system using artificial neural network. Int J Env Sci Dev 1(4)
9. Kumar A, Singh MP, Ghosh S, Anand A (2012) Weather forecasting model using artificial neural network. Procedia Technol 4:311–318
10. Dimitris B, Colin P, Ying Z (2018) From predictive methods to missing data imputation: an optimization approach. J ML Res 18:1–39
11. Nuran P, Cemalettin K (2021) A hybrid modified deep learning data imputation method for numeric data sets. Int J Int Syst Appl Engg 9:6–11
12. Marlyna H, Yolanda P, Indra S et al (2020) Prediction of relative humidity based on long short-term memory network. In: AIP Conference of Proceeding 2221, 060003

13. Patwardhan S, Sooraj KP, Varikoden H et al (2020) Synoptic scale systems. In: Assessment of climate change over the Indian region
14. Climate and average weather year around in Nashik, India. <https://weatherspark.com/y/107612/Average-Weather-in-Nashik-India-Year-Round>. Accessed 12 Aug 2022
15. Gustavo B, Maria M (2002) A study of K-nearest neighbour as an imputation method. In: Soft computing systems—design, management and applications, HIS, Santiago, Chile

# Optimization in the Method of Choosing Quasi-Optimal Values of the Regularization Parameter



Van Huyen Le

**Abstract** This work is devoted to narrowing down the set of solutions to the inverse problem, found using a combination of the Tikhonov's regularization method and the method of choosing quasi-optimal values of the regularization parameter (next, it will be called the method to find the quasi-optimal regularization parameter or the method FqORP). First, a mathematical model described by a system of differential equations is studied. Then, an inverse problem was posed: by the given values of the unknown functions of the studied mathematical model at different points in time, determine its parameters. Further, to solve this inverse problem, the Tikhonov's regularization method is used. The values of the regularization parameter are determined by the method FqORP. As a result, a set of approximations to the solution of the inverse problem is found. Finally, two optimization criteria are used to optimize this set. In this method, two optimization criteria are used to select the approximate parameters of the studied mathematical model. The practical implication of this work is that, by solving the direct problem with the found approximate parameters, it is possible to predict the change over time in the properties and behavior of the mathematical model.

**Keywords** Inverse problem · Regularization parameter · Mathematical model · Tikhonov's regularization method · Approximate parameters · Optimization

## 1 Introduction

In the middle of the twentieth century, the first studies on the inverse problem appeared in physics, geophysics and other areas of natural science. The inverse problem is understood as the process of identifying unknown parameters of the direct problem on the basis of information obtained from a series of observations.

---

V. H. Le (✉)

Peter the Great St. Petersburg Polytechnic University, Politekhnicheskaya Ulitsa 29, 195251 St. Petersburg, Russia

e-mail: [huyenlevan120193@gmail.com](mailto:huyenlevan120193@gmail.com)

Problems of mathematical physics are divided into direct and inverse on the basis of cause-and-effect relationships. Usually, inverse problems are formulated on the basis of direct problems.

In recent decades, with the advent and development of powerful computers, the inverse problem has become a popular area of research in the field of computational and applied mathematics. Due to its great practical applicability, it is turning into an interdisciplinary science, developing as a new promising area of research. That is why the inverse problem is attracting more and more attention of many scientists. In practice, finding solutions to inverse problems often faces the greatest difficulty, which is the instability of the solution for small errors in the data measurements. The Soviet mathematician A. N. Tikhonov in 1943 introduced the regularization method for solving ill-posed inverse problems, named after him [1]. This method allows to find approximate solutions of inverse problems with approximate initial data [2–7]. Determining the value of the regularization parameter plays an important role in applying the Tikhonov's regularization method. There are several methods for choosing the regularization parameter. In this paper, we will consider the method FqORP [8–10].

## 2 Inverse Problem of Restoring Parameters in a Mathematical Model

We will consider a following mathematical model:

$$\left\{ \begin{array}{l} \frac{dx_1}{dt} = a_{11}x_1(t) + a_{12}x_2(t) + \dots + a_{1n}x_n(t), \\ \frac{dx_2}{dt} = a_{21}x_1(t) + a_{22}x_2(t) + \dots + a_{2n}x_n(t), \\ \dots, \\ \frac{dx_n}{dt} = a_{n1}x_1(t) + a_{n2}x_2(t) + \dots + a_{nn}x_n(t), \end{array} \right. \quad (1)$$

where  $a_{ij}$ , where  $i, j = 1, \dots, n$ , are parameters (constant coefficients) of the mathematical model (1);  $x_i(t)$ , where  $i = 1, \dots, n$ , are unknown functions depending on time  $t$ . Let us assume that  $x_i(t)_{t=0} = x_i(0)$  at the time  $t = 0$ .

It is possible to transform (1) in the form  $\frac{d\mathbf{X}(t)}{dt} = \mathbf{A}\mathbf{X}(t)$ , where  $\mathbf{A}$  is a matrix of parameters;  $\mathbf{X}(t)$  is a solution vector of the system (1),  $\mathbf{X}(t) = (x_1(t), x_2(t), \dots, x_n(t))^T$ .

Within the framework of the studied mathematical model (1), the following two tasks will be posed.

**Task 1.** According to the given coefficients  $a_{ij} = a_{ij}^0$ , where  $i, j = 1, \dots, n$ , and  $\mathbf{X}(0)_{t=0} = \mathbf{X}(0)$ , it is necessary to determine  $\mathbf{X}(t)$ .

Task 1 will be called a direct problem within the framework of a mathematical model (1). It is a problem of constructing a solution to the Cauchy problem. The solution of problem 1 shows the change over time in the properties  $\mathbf{X}(t)$  of the object under study.

**Task 2.** Based on the given values  $\mathbf{X}(t_k)$  at time points  $t_k$ , where  $k = 1, 2, \dots, m$ , it is necessary to determine the coefficients  $a_{ij} = a_{ij}^0$ , where  $i, j = 1, 2, \dots, n$ .

Task 2 will be called the inverse problem with respect to problem 1 within the mathematical model (1). The solution of task 2 is denoted by  $\mathbf{K}^0$ ,  $\mathbf{K}^0 = (a_{11}^0, a_{12}^0, \dots, a_{1n}^0, \dots, a_{n1}^0, a_{n2}^0, \dots, a_{nn}^0)^T$ .

### 3 Method to Solve the Inverse Problem

In [11–16], the authors presented a technique used to solve the task 2 and illustrative examples. This technique builds on the following series of methods: the method of finite differences, the interpolation method, the Tikhonov's regularization method. We will describe this technique in more detail below.

Applying the method of finite differences, from (1) we will get a system of equations:

$$\begin{cases} \frac{x_1(t+h)-x_1(t-h)}{2h} - o(h^3) = x_1(t) a_{11} + x_2(t) a_{12} + \dots + x_n(t) a_{1n}, \\ \frac{x_2(t+h)-x_2(t-h)}{2h} - o(h^3) = x_1(t) a_{21} + x_2(t) a_{22} + \dots + x_n(t) a_{2n}, \\ \dots, \\ \frac{x_n(t+h)-x_n(t-h)}{2h} - o(h^3) = x_1(t) a_{n1} + x_2(t) a_{n2} + \dots + x_n(t) a_{nn} \end{cases} \quad (2)$$

with respect to unknowns  $a_{ij}$ . Here, stride  $h$  is a very small positive number.

Substituting  $t = t_k$ , where  $k = 1, 2, \dots, m$ , into (2), we obtain an “exact” system of algebraic equations (in the form of mathematical symbols):

$$\begin{cases} x_1(t_k) a_{11} + \dots + x_n(t_k) a_{1n} = \frac{x_1(t_k+h)-x_1(t_k-h)}{2h} - o(h^3), \\ x_1(t_k) a_{21} + \dots + x_n(t_k) a_{2n} = \frac{x_2(t_k+h)-x_2(t_k-h)}{2h} - o(h^3), \\ \dots, \\ x_1(t_k) a_{n1} + \dots + x_n(t_k) a_{nn} = \frac{x_n(t_k+h)-x_n(t_k-h)}{2h} - o(h^3) \end{cases} \quad (3)$$

with respect to unknowns  $a_{ij}$ . We can represent (3) in matrix–vector form  $\mathbf{X}\mathbf{K} = \mathbf{B}$ , where  $\mathbf{X}$  is a matrix with elements that are “exact” values of  $x_i(t)$  at points in time  $t_k$ , i.e.,  $\mathbf{X}(t_k)$ ;  $\mathbf{K}$  is a vector with unknown elements  $a_{ij}$ , where  $\mathbf{K} = (a_{11}, a_{12}, \dots, a_{1n}, \dots, a_{n1}, a_{n2}, \dots, a_{nn})^T$ ;  $\mathbf{B}$  is the vector of the “exact” right side (vector with free terms).

The desired solution  $\mathbf{K}^0 = (a_{11}^0, a_{12}^0, \dots, a_{1n}^0, \dots, a_{n1}^0, a_{n2}^0, \dots, a_{nn}^0)^T$  of the task 2 is an exact solution of system (3).

Neglecting  $o(h^3)$ , from (3) we will get a system of equations:

$$\begin{cases} x_1(t_k)a_{11} + \dots + x_n(t_k)a_{1n} = \frac{x_1(t_k+h)-x_1(t_k-h)}{2h}, \\ x_1(t_k)a_{21} + \dots + x_n(t_k)a_{2n} = \frac{x_2(t_k+h)-x_2(t_k-h)}{2h}, \\ \dots, \\ x_1(t_k)a_{n1} + \dots + x_n(t_k)a_{nn} = \frac{x_n(t_k+h)-x_n(t_k-h)}{2h} \end{cases} \quad (4)$$

with respect to unknowns  $a_{ij}$ . The given values  $x_1(t_k), x_2(t_k), \dots, x_n(t_k)$  may contain measurement and rounding errors. The values  $\mathbf{X}(t_k + h), \mathbf{X}(t_k - h)$  will be determined by the cubic spline interpolation method, so they may contain interpolation errors and rounding errors. Therefore, we will call system (4) an “approximate” system. We can rewrite (4) in the form  $\mathbf{X}_\eta \mathbf{K} = \mathbf{B}_\delta$ , where  $\mathbf{X}_\eta$  is an approximation to matrix  $\mathbf{X}$ ,  $\|\mathbf{X}_\eta - \mathbf{X}\| \leq \eta$ ;  $\mathbf{B}_\delta$  is an approximation to vector  $\mathbf{B}$  with respect to  $\|\mathbf{B}_\delta - \mathbf{B}\| \leq \delta$ ;  $\eta, \delta$  are small positive numbers.

The problem of solving system (4) may be incorrect. If it has a unique solution, it is also impossible to conclude that this solution depends continuously on all small changes in the original data  $\{\mathbf{X}_\eta, \mathbf{B}_\delta\}$ . To eliminate this difficulty, Tikhonov’s regularization method will be used. In the course of this method, we will not look for a solution to system (4), but we will look for an approximation to the desired solution  $\mathbf{K}^0$ , which uniquely and continuously depends on  $\{\mathbf{X}_\eta, \mathbf{B}_\delta\}$ . To do this, let us first consider the following problem: Find the value of  $\mathbf{K}$  such that

$$\mathbf{M}(\mathbf{K}) = \|\mathbf{X}_\eta \mathbf{K} - \mathbf{B}_\delta\|^2 + \alpha \|\mathbf{K}\|^2 \rightarrow \min_{\alpha} \min_{\mathbf{K}}, \quad (5)$$

where  $\alpha = \text{const} > 0$  is the regularization parameter.

From (5) follows the regularizing system of equations:

$$\mathbf{X}_\eta^* \mathbf{X}_\eta \mathbf{K} + \alpha \mathbf{K} = \mathbf{X}_\eta^* \mathbf{B}_\delta, \quad (6)$$

where  $\mathbf{X}_\eta^*$  is the conjugate to the matrix  $\mathbf{X}_\eta$ . The solution of system (6) has the following form:  $\mathbf{K}^\alpha = (\mathbf{X}_\eta^* \mathbf{X}_\eta + \alpha \mathbf{E})^{-1} \mathbf{X}_\eta^* \mathbf{B}_\delta$ . This solution will be denoted in form:  $\mathbf{K}^\alpha = (a_{11}^\alpha, a_{12}^\alpha, \dots, a_{1n}^\alpha, \dots, a_{n1}^\alpha, a_{n2}^\alpha, \dots, a_{nn}^\alpha)^T$ . Here, we note that  $\mathbf{K}^\alpha$  does not approximate  $\mathbf{K}^0$  for all values of the regularization parameter  $\alpha$ . If  $\mathbf{K}^\alpha$  approximates  $\mathbf{K}^0$ , then it is called a regularized solution of system (4) [2–7].

## 4 The Method FqORP

The most important task in the Tikhonov’s regularization method is to find such a value of the parameter  $\alpha > 0$  that  $\mathbf{K}^\alpha$  approximates the desired solution  $\mathbf{K}^0$ . There are several methods to find this parameter. Due to the fact that error estimates when specifying input data are often unknown and poorly controlled, it is difficult to use a well-tested and theoretically developed residual method. Therefore, other methods to determine the parameter  $\alpha > 0$  are more widely used in practical problems. In

this paper, we will consider the method FqORP, which is not directly related to the level of errors  $\eta$  and  $\delta$  [8–10].

Let us consider the Tikhonov's regularization method in the general case, when a trial solution of the inverse problem is given [8–10]. In this case, let us consider the following problem: Find the value of  $\mathbf{K}$  such that

$$\mathbf{M}(\mathbf{K}) = \|\mathbf{X}_\eta \mathbf{K} - \mathbf{B}_\delta\|^2 + \alpha \|\mathbf{K} - \mathbf{K}^*\|^2 \rightarrow \min_{\alpha} \min_{\mathbf{K}}, \quad (7)$$

where  $\alpha = \text{const} > 0$  is the regularization parameter;  $\mathbf{K}^*$  is a trial solution.

From (7) follows the regularizing system of equations:

$$\mathbf{X}_\eta^* \mathbf{X}_\eta \mathbf{K} + \alpha \mathbf{K} = \mathbf{X}_\eta^* \mathbf{B}_\delta + \alpha \mathbf{K}^*, \quad (8)$$

where matrix  $\mathbf{X}_\eta^*$  is a conjugate to the matrix  $\mathbf{X}_\eta$ .

The solution of system (8) is the solution of problem (7) and has the form:

$$\mathbf{K}^\alpha = (\mathbf{X}_\eta^* \mathbf{X}_\eta + \alpha \mathbf{E})^{-1} \mathbf{X}_\eta^* \mathbf{B}_\delta + \alpha (\mathbf{X}_\eta^* \mathbf{X}_\eta + \alpha \mathbf{E})^{-1} \mathbf{K}^*.$$

Note that if there is no information about the trial solution, then we can put  $\mathbf{K}^* = 0$ . In this case, it is obvious that problem (7) becomes (5).

Consider problem (5). Let, for some value of the regularization parameter  $\alpha$ , we have that  $\mathbf{K}_1^\alpha = (\mathbf{X}_\eta^* \mathbf{X}_\eta + \alpha \mathbf{E})^{-1} \mathbf{X}_\eta^* \mathbf{B}_\delta$  which is a regularized solution of (4) ( $\mathbf{K}_1^\alpha$  approximates  $\mathbf{K}^0$ ,  $\mathbf{K}_1^\alpha \cong \mathbf{K}^0$ ,  $\|\mathbf{K}_1^\alpha - \mathbf{K}^0\| \approx 0$ ).

Consider problem (7) with  $\mathbf{K}^* \equiv \mathbf{K}_1^\alpha$ . Let, also for the value of the parameter  $\alpha$ , we have that  $\mathbf{K}_2^\alpha = (\mathbf{X}_\eta^* \mathbf{X}_\eta + \alpha \mathbf{E})^{-1} \mathbf{X}_\eta^* \mathbf{B}_\delta + \alpha (\mathbf{X}_\eta^* \mathbf{X}_\eta + \alpha \mathbf{E})^{-1} \mathbf{K}_1^\alpha$  which is a regularized solution of the system of (4) ( $\mathbf{K}_2^\alpha$  approximates  $\mathbf{K}^0$ ,  $\mathbf{K}_2^\alpha \cong \mathbf{K}^0$ ,  $\|\mathbf{K}_2^\alpha - \mathbf{K}^0\| \approx 0$ ).

From  $\|\mathbf{K}_1^\alpha - \mathbf{K}^0\| \approx 0$  and  $\|\mathbf{K}_2^\alpha - \mathbf{K}^0\| \approx 0$ , it follows that  $\|\mathbf{K}_2^\alpha - \mathbf{K}_1^\alpha\| \approx 0$ . Thus, the value  $\alpha$  will be found so that  $\|\mathbf{K}_2^\alpha - \mathbf{K}_1^\alpha\| \approx 0$ . We will transform  $\mathbf{K}_2^\alpha$  into the following form:

$$\mathbf{K}_2^\alpha = (\mathbf{X}_\eta^* \mathbf{X}_\eta + \alpha \mathbf{E})^{-1} \mathbf{X}_\eta^* \mathbf{B}_\delta + \alpha (\mathbf{X}_\eta^* \mathbf{X}_\eta + \alpha \mathbf{E})^{-1} \mathbf{K}_1^\alpha.$$

We have that  $\|\mathbf{K}_2^\alpha - \mathbf{K}_1^\alpha\| = \left\| -\alpha \frac{d\mathbf{K}_1^\alpha}{d\alpha} \right\|$ . Next, we will look at a method for choosing parameters  $\alpha$ —the method FqORP. The idea of this method is that the value  $\alpha$  will be found so that  $\left\| -\alpha \frac{d\mathbf{K}_1^\alpha}{d\alpha} \right\| \approx 0$ . We will consider a geometric sequence with a given initial value of the parameter  $\alpha$  such that  $\alpha = \alpha_1$  and a progression denominator  $q$  that satisfies the following conditions:  $q = \frac{\alpha_{i+1}}{\alpha_i} \in (0, 1)$ , where  $i = 1, 2, \dots, N$ . Based on the sequence  $\{\alpha_i\}$ , a sequence  $\{\mathbf{K}_1^{\alpha_i}\}$  will be built. In the sequence  $\{\alpha_i\}$ , the quasi-optimal values of the regularization parameter are considered to be such an element  $\alpha_i$  for which  $\left\| -\alpha_i \frac{d\mathbf{K}_1^{\alpha_i}}{d\alpha_i} \right\| \rightarrow \min_i$ . We have that  $\left\| -\alpha_i \frac{d\mathbf{K}_1^{\alpha_i}}{d\alpha_i} \right\| = \frac{1}{(1-q)} \|\mathbf{K}_1^{\alpha_{i+1}} - \mathbf{K}_1^{\alpha_i}\|$ . Therefore, the condition  $\left\| -\alpha_i \frac{d\mathbf{K}_1^{\alpha_i}}{d\alpha_i} \right\| \rightarrow \min_i$  is

equivalent to the condition  $\|\mathbf{K}_1^{\alpha_{i+1}} - \mathbf{K}_1^{\alpha_i}\| \rightarrow \min_i$ , where  $i = 1, 2, \dots, (N - 1)$ . In practice, we will choose the value  $\alpha_i$  so that  $\left\| -\alpha_i \frac{d\mathbf{K}_1^{\alpha_i}}{d\alpha_i} \right\| \rightarrow \min_i$  and  $\left\| -\alpha_i \frac{d\mathbf{K}_1^{\alpha_i}}{d\alpha_i} \right\| \approx 0$ . As a result of calculations, a set  $\mathbf{Q}$  of all elements that satisfy the conditions  $\left\| -\alpha_i \frac{d\mathbf{K}_1^{\alpha_i}}{d\alpha_i} \right\| \rightarrow \min_i$  and  $\left\| -\alpha_i \frac{d\mathbf{K}_1^{\alpha_i}}{d\alpha_i} \right\| \approx 0$  will be obtained [8, 9].

Here, we note that if  $\alpha$  arbitrarily tends to zero, then the regularized solutions  $\mathbf{K}^\alpha$  may, generally speaking, not approximate the desired solution  $\mathbf{K}^0$ , although  $\|\mathbf{X}_\eta \mathbf{K} - \mathbf{B}_\delta\|$  can be arbitrarily small. Let us analyze (5). If the value of the parameter  $\alpha$  increases, then  $\|\mathbf{K}^\alpha\|^2$  decreases, but the discrepancy  $\|\mathbf{X}_\eta \mathbf{K} - \mathbf{B}_\delta\|^2$  increases.

Further, the following optimization problem will be considered: to find an element of the set  $\mathbf{Q}$  so that

$$\begin{cases} \|\mathbf{X}_\eta \mathbf{K} - \mathbf{B}_\delta\|^2 \rightarrow \min_{\mathbf{K} \in \mathbf{Q}}, \\ \|\mathbf{K}\|^2 \rightarrow \min_{\mathbf{K} \in \mathbf{Q}}. \end{cases} \quad (9)$$

Hence, from all values of the parameter  $\alpha_i$  that satisfy the conditions  $\left\| -\alpha_i \frac{d\mathbf{K}_1^{\alpha_i}}{d\alpha_i} \right\| \rightarrow \min_i$  and  $\left\| -\alpha_i \frac{d\mathbf{K}_1^{\alpha_i}}{d\alpha_i} \right\| \approx 0$ , we will choose the values of the parameter  $\alpha$  such that  $\|\mathbf{X}_\eta \mathbf{K} - \mathbf{B}_\delta\|^2$  and  $\|\mathbf{K}\|^2$  are as small as possible. Then, instead of  $N$ , another value of  $N_i$  will be chosen so that  $\left\| -\alpha_i \frac{d\mathbf{K}_1^{\alpha_i}}{d\alpha_i} \right\| \rightarrow \min_i$ .

## 5 Numerical Example

Within the framework of this work, we will consider a mathematical model that describes the kinetics of the oil refining process. Let the initial mixture consists of one heavy hydrocarbon **C**. Under the action of temperature and collisions, hydrocarbon **C** decomposes into hydrocarbons **B** and also turns into isomer **D** with the same number of carbon atoms as in the original molecule. Substance **D** also decomposes into **A** and **B** or turns back into **C**. Let the reaction products **A**, **B** are lighter hydrocarbons, and no further transformations occur with them.

The mathematical model of the catalytic cracking reaction is a system of differential equations [12, 13, 17]:

$$\left\{ \begin{array}{l} \frac{dy_1(t)}{dt} = k_5 y_2(t) + k_1 y_3(t) + k_4 y_4(t); \\ \frac{dy_2(t)}{dt} = -k_5 y_2(t) + k_1 y_3(t) + k_4 y_4(t); \\ \frac{dy_3(t)}{dt} = -(k_1 + k_2) y_3(t) + k_3 y_4(t); \\ \frac{dy_4(t)}{dt} = k_2 y_3(t) - (k_2 + k_4) y_4(t), \end{array} \right. \quad (10)$$

where  $k_1, k_2, k_3, k_4, k_5$  are reaction rate constants,  $s^{-1}$  [18];  $y_i(t)$ , where  $i = 1, 2, 3, 4$ , are the concentrations of substances **A**, **B**, **C**, **D** at a point in time  $t$ ,  $\frac{\text{mol}}{L}$ . Suppose that at the initial time  $t = 0$  the concentrations of substances **A**, **B**, **C**, and **D** are equal to  $y_i(0)$ , where  $i = 1, 2, 3, 4$ .

**Direct task.** Based on the given reaction rate constants  $k_1 = k_1^0, k_2 = k_2^0, k_3 = k_3^0, k_4 = k_4^0, k_5 = k_5^0$  and the concentrations of the initial substance, products **A**, **B**, **C**, and **D** at  $t = 0$  determine  $y_i(t)$ , where  $i = 1, 2, 3, 4$ .

**Inverse task.** According to the given concentrations of the initial substance, products **A**, **B**, **C**, and **D** at time points  $t_i, i = 1, 2, \dots, 10$ , determine  $k_1, k_2, k_3, k_4, k_5$  (i.e.,  $k_1^0, k_2^0, k_3^0, k_4^0, k_5^0$ ).

Let us know the concentrations of substances **A**, **B**, **C**, **D** at different points in time (see Table 1).

The “exact” system of algebraic equations for  $k_1, k_2, k_3, k_4, k_5$  has the form:

**Table 1** Measured concentrations of substances **A**, **B**, **C**, **D**

$t(s)$	$y_1(t)$	$y_2(t)$	$y_3(t)$	$y_4(t)$
0	0	0	90	10
30	77.76206	12.47561	48.11464	6.76653
60	132.29327	7.46789	25.74512	4.37430
90	162.81084	4.12939	13.78771	2.74217
120	179.58861	2.26780	7.39035	1.68145
150	188.79792	1.24467	3.96468	1.01403
180	193.85216	0.68309	2.12871	0.60366
210	196.62600	0.37489	1.14389	0.35567
240	198.14831	0.20574	0.61518	0.20779
270	198.98377	0.11291	0.33111	0.12055

$$\begin{cases} y_3(t_i)k_1 + y_4(t_i)k_4 + y_2(t_i)k_5 = \frac{y_1(t_i + h) - y_1(t_i - h)}{2h} - o(h^3), \\ y_3(t_i)k_1 + y_4(t_i)k_4 - y_2(t_i)k_5 = \frac{y_2(t_i + h) - y_2(t_i - h)}{2h} - o(h^3), \\ -y_3(t_i)k_1 - y_3(t_i)k_2 + y_4(t_i)k_3 = \frac{y_3(t_i + h) - y_3(t_i - h)}{2h} - o(h^3), \\ [y_3(t_i) - y_4(t_i)]k_2 - y_4(t_i)k_4 = \frac{y_4(t_i + h) - y_4(t_i - h)}{2h} - o(h^3), \end{cases} \quad (11)$$

where  $h = 0.001$ ,  $i = 1, 2, \dots, 10$ . We supply the values  $y_2(t_i)$ ,  $y_3(t_i)$ ,  $y_4(t_i)$  and  $y_1(t_i + h)$ ,  $y_1(t_i - h)$ ,  $y_2(t_i + h)$ ,  $y_2(t_i - h)$ ,  $y_3(t_i + h)$ ,  $y_3(t_i - h)$ ,  $y_4(t_i + h)$ ,  $y_4(t_i - h)$  into (11). The “approximate” system of algebraic equations with respect to  $k_1, k_2, k_3, k_4, k_5$  has the form:

$$\begin{cases} y_3(t_i)k_1 + y_4(t_i)k_4 + y_2(t_i)k_5 = \frac{y_1(t_i + h) - y_1(t_i - h)}{2h}, \\ y_3(t_i)k_1 + y_4(t_i)k_4 - y_2(t_i)k_5 = \frac{y_2(t_i + h) - y_2(t_i - h)}{2h}, \\ -y_3(t_i)k_1 - y_3(t_i)k_2 + y_4(t_i)k_3 = \frac{y_3(t_i + h) - y_3(t_i - h)}{2h}, \\ [y_3(t_i) - y_4(t_i)]k_2 - y_4(t_i)k_4 = \frac{y_4(t_i + h) - y_4(t_i - h)}{2h}, \end{cases} \quad (12)$$

The system of Eq. (12) will be solved. Having set some “suitable” value of the parameter  $\alpha_1 = 1$ , we calculate  $\mathbf{K}_1^{\alpha_1} = 0.081532$ . Having constructed in its neighborhood a geometric grid along  $\alpha_1$  such that  $\alpha_{i+1} = 0.9\alpha_i$ ,  $i = 1, 2, \dots, 100$ , we calculate  $\mathbf{K}_1^{\alpha_{i+1}}$  and construct sequences  $\{\mathbf{K}_1^{\alpha_i}\}$ . Figure 1 shows how the estimate of the norm of the difference  $\mathbf{Si} = \left\| -\alpha_i \frac{d\mathbf{K}_1^{\alpha_i}}{d\alpha_i} \right\|$ ,  $i = 1, 2, \dots, 99$ , changes at two adjacent iterations.

It is obvious that for  $i = 1, 2, \dots, 100$ , the condition  $\mathbf{Si} \approx 0$  is satisfied. For  $i > 45$ , the value of  $\left\| -\alpha_i \frac{d\mathbf{K}_1^{\alpha_i}}{d\alpha_i} \right\|$  changes very little (it can be considered unchanged). In what follows, we will only look at the values of  $\left\| -\alpha_i \frac{d\mathbf{K}_1^{\alpha_i}}{d\alpha_i} \right\|$  for  $i \leq 45$ . The set of all elements  $\mathbf{K}_1^{\alpha_i}$ , where  $i = 1, 2, \dots, 45$ , will be denoted by  $\mathbf{Q}$ . Next, the optimization problem (9) will be solved. Figure 2 shows how the norms  $\mathbf{S1} = \|\mathbf{X}_\eta \mathbf{K}^{\alpha_i} - \mathbf{B}_\delta\|^2$  and  $\mathbf{S2} = \|\mathbf{K}^{\alpha_i}\|^2$ , where  $i = 1, 2, \dots, 45$ , change depending on the values of the parameter  $\alpha$ .

Obviously,  $\mathbf{S1}$  is continuously increasing and  $\mathbf{S2}$  is continuously decreasing as  $\alpha$  decreases. Therefore, in this case, there is no pareto optimality. For  $\alpha \leq 0.047101287$  (i.e.,  $i \geq 30$ ), the values of  $\mathbf{S1}$  and  $\mathbf{S2}$  change very little (can be considered unchanged). Therefore, we will consider only the values of the regularization parameter  $\alpha_i$ ,  $30 \leq i \leq 40$ .

Consider the case  $\alpha = \alpha_{30} = 0.047101287$ . In this case,  $N = 30$  will be chosen instead of  $N = 100$ . Conditions  $\left\| -\alpha_i \frac{d\mathbf{K}_1^{\alpha_i}}{d\alpha_i} \right\| \rightarrow \min_i$  and  $\left\| -\alpha_i \frac{d\mathbf{K}_1^{\alpha_i}}{d\alpha_i} \right\| \approx 0$

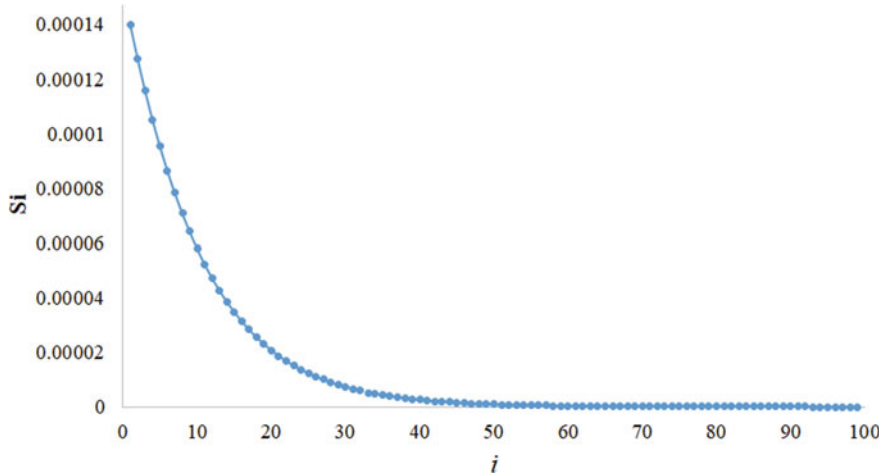


Fig. 1 Change in the estimates of the norm of the difference  $S_i$  at two adjacent iterations

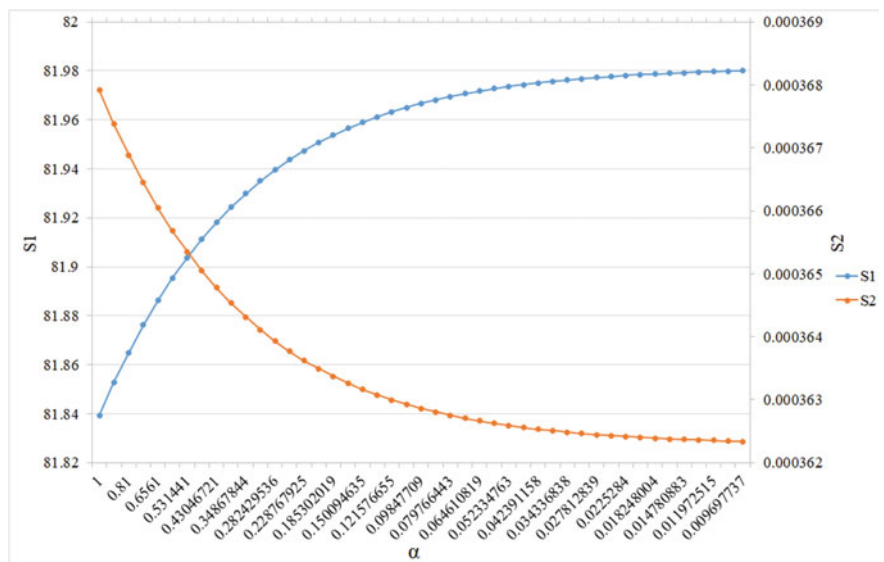
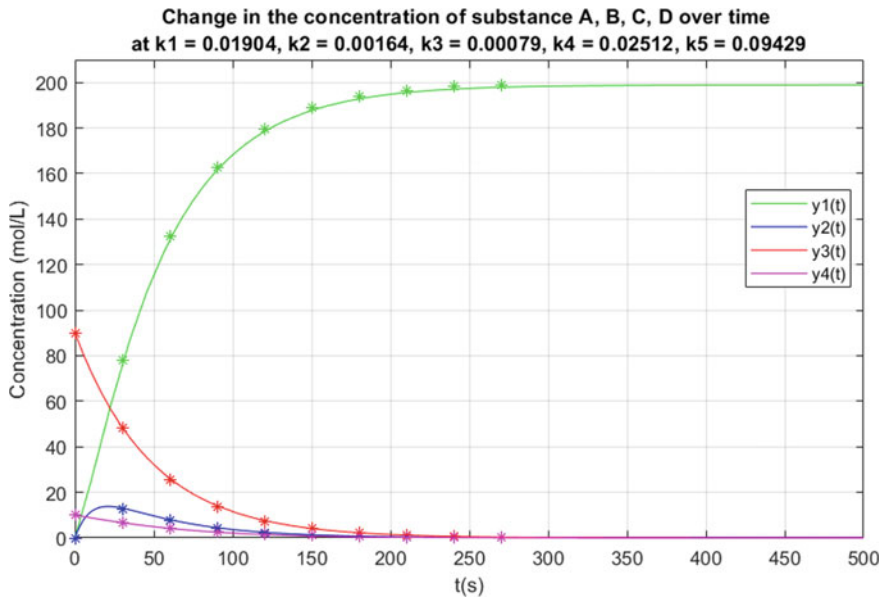


Fig. 2 Changing the norms  $S_1$  and  $S_2$  depending on the values of the regularization parameter

are met when  $N = 30$ . For  $\alpha = \alpha_{30} = 0.047101287$ , we have that  $\mathbf{K}^\alpha = (0.01904, 0.00164, 0.00079, 0.02512, 0.09429)^T$ . Next, the direct problem will be solved with approximate reaction rate constants  $k_1^\alpha = 0.01904$ ,  $k_2^\alpha = 0.00164$ ,  $k_3^\alpha = 0.00079$ ,  $k_4^\alpha = 0.02512$ ,  $k_5^\alpha = 0.09429$ . Figure 3 shows how the concentration of substances **A**, **B**, **C**, **D** changes over time. Asterisks indicate the measured concentrations **A**, **B**, **C**, **D** (initial data). Curves  $y_i(t)$ , where  $i = 1, 2, 3, 4$ , represent the



**Fig. 3** Change in the concentration of substance, products A, B, C, and D over time at  $k_1 = 0.01904$ ,  $k_2 = 0.00164$ ,  $k_3 = 0.00079$ ,  $k_4 = 0.02512$ ,  $k_5 = 0.09429$

changes in the calculated concentration of substance A, B, C, D over time. It is easy to see that the measured values are very close to the curves. Therefore,  $k_1^\alpha = 0.01904$ ,  $k_2^\alpha = 0.00164$ ,  $k_3^\alpha = 0.00079$ ,  $k_4^\alpha = 0.02512$ ,  $k_5^\alpha = 0.09429$  can be taken as approximate parameters of the mathematical model (10) and used in practical problems for analysis and prediction of substance concentrations over time.

## 6 Conclusion

In the presented work, the possibility of narrowing the set of solutions to the inverse problem was studied. The inverse problem of restoring the parameters of a mathematical model was posed and solved. To solve this inverse problem, the finite difference method, the cubic spline interpolation method, the Tikhonov's regularization method, and the method for choosing quasi-optimal values of the regularization parameter were used. The set of possible solutions were obtained. To narrow this set, the optimization problem was solved according to two criteria. As a numerical example, a mathematical model of the oil refining process was investigated. As a result of calculations, approximate reaction rate constants were found.

## References

1. Tikhonov AN (1943) *Ob ustojchivosti obratnyh zadach* [On the stability of inverse problems]. Doklady Akademii Nauk SSSR [Reports of the Academy of Sciences of the USSR]. 39(5):195–198
2. Tikhonov AN, Arsenin VY (1979) *Metody reshenija nekorrektnyh zadach* [Methods for solving ill-posed problems]. Nauka, Glavnaja redakcija fiziko-matematicheskoy literatury, Moscow (in Russian)
3. Ivanov VK, Vasin VV, Tanana VP (1978) *Teoriya linejnyh nekorrektnyh zadach i ejo prilozhenija* [Theory of linear ill-posed problems and its applications]. Nauka, Moscow (in Russian)
4. Kabanikhin SI (2011). Inverse and Ill-Posed Problems DE Gruyter. <https://doi.org/10.1515/9783110224016>
5. Zhdanov MS (2009) Principles of Ill-posed problem solution. Methods Geochem Geophys 43(8):299–319
6. Morozov VA (1984) Methods for solving incorrectly posed problems. Springer New York, New York (1984). <https://doi.org/10.1007/978-1-4612-5280-1>
7. Tikhonov AN, Goncharsky AV, Stepanov VV, Yagola AG (1995) Numerical methods for the solution of Ill-posed problems. Springer Netherlands, Dordrecht (1995). <https://doi.org/10.1007/978-94-015-8480-7>
8. Liskovets OA (1982) *Teoriya i metody reshenija nekorrektnyh zadach* [Theory and methods for solving ill-posed problems]. Itogi nauki i tehniki. Serija «Matematicheskiy analiz» [Results of science and technology. Series “Mathematical Analysis”]. 20:116–178 (1982). (in Russian)
9. Morozov VA (1987) *Metody reguljarizacii neustojchivih zadach* [Regularization Methods for Unstable Problems]. Publishing House of Moscow State University, Moscow (in Russian)
10. Morozov VA (20003) *Algoritmicheskie osnovy metodov reshenija nekorrektno postavlennyh zadach* [Algorithmic foundations of methods for solving ill-posed problems]. Numerical Methods and Programming 4(1):130–141 (2003). (in Russian)
11. Van Huyen L, Chernenkaya LV (2022) Method for finding an approximate solution for the coefficient inverse ill-posed problem. News of the Tula state university. Tech Sci 10:274–282. <https://doi.org/10.24412/2071-6168-2022-10-274-282>. (in Russian)
12. Van Huyen L (2022) Coefficient inverse problem in the mathematical model of the refining process kinetics. Bullet Voronezh State Tech Univ 18(5):64–72 (2022). <https://doi.org/10.36622/VSTU.2022.18.5.008>. (in Russian)
13. Van Huyen L, Firsov AN (2022) Tikhonov’s regularization method for solving the inverse problem in a mathematical model of the kinetics of oil refining process. Proc Cybernet 48(4):49–58 (2022). <https://doi.org/10.34822/1999-7604-2022-4-49-58>. (in Russian)
14. Van Huyen L (2022) Stability of a dynamical system with approximate parameters found by the tikhonov regularization method. News of the Tula state university. Tech Sci 12:429–435 (2022). <https://doi.org/10.24412/2071-6168-2022-12-429-436>. (in Russian)
15. Van Huyen L, Chernenkaya LV (2023) Investigation of the stability of regularized solutions of the coefficient inverse problem. Part 1. News of the Tula state university. Tech Sci 1:8–14 (2023). <https://doi.org/10.24412/2071-6168-2023-1-8-14>. (in Russian)
16. Van Huyen L, Chernenkaya LV (2023) Investigation of the stability of regularized solutions of the coefficient inverse problem. Part 2. News of the Tula state university. Tech Sci 1:239–247 (2023). <https://doi.org/10.24412/2071-6168-2023-1-239-247>. (in Russian)
17. Lysenkova SA (2018) On mathematical modeling of catalytic cracking. Proc Cybernet 4:107–110 (in Russian)
18. Kolinko PA, Kozlov DV (2013) *Himicheskaja kinetika v kurse fizicheskoy himii* [Chemical kinetics in the course of physical chemistry]. Novosibirsk State University, Novosibirsk (in Russian)

# Analysis and Comparison of Real-Time Data Set with Generation of Networks for Underwater Wireless Sensor Networks



**D. Ruby, J. Jeyachidra, T. Logesh, P. Ranjani, G. Umamaheswari, and K. Nandhini**

**Abstract** A wireless communication system is providing secured, reliable, and quality communications. The evolution of the network starts with first generation to fifth generation. Each generation have a set of standards to utilize the networks in any applications. In underwater communication, lot of data missed due to very low bandwidth, intermittent channel, and hardware problems. The sensor nodes are deployed in underwater in a long distance. The coverage area is restricted due to the bandwidth level of the networks. Compared to 4G networks, the 6G networks are to be useful for underwater and underground communication and result in decrease the data loss intern minimize the utilization of energy level. In the TAO Project, the sensors are deployed from the distance of 1.5–500 m and 10 years of data collected from the project. The root mean square error analysis depicts the lot of data loss which is occurred for each year for a particular distance. This loss of data is identified due to very low-level bandwidth and loss of intermittent channel requirements. Hence, the loss of data may be avoided by updating the generation of networks.

---

D. Ruby (✉) · J. Jeyachidra · T. Logesh · P. Ranjani · G. Umamaheswari · K. Nandhini  
Department of Computer Science and Applications, Periyar Maniammai Institute of Science and Technology, Vallam, Tamil Nadu, India  
e-mail: [rubymca@pmu.edu](mailto:rubymca@pmu.edu)

J. Jeyachidra  
e-mail: [chithu\\_raj@pmu.edu](mailto:chithu_raj@pmu.edu)

T. Logesh  
e-mail: [logeshmca@pmu.edu](mailto:logeshmca@pmu.edu)

P. Ranjani  
e-mail: [ranjani@pmu.edu](mailto:ranjani@pmu.edu)

G. Umamaheswari  
e-mail: [umamaheswari@pmu.edu](mailto:umamaheswari@pmu.edu)

K. Nandhini  
e-mail: [nandhinik@pmu.edu](mailto:nandhinik@pmu.edu)

**Keywords** Intermittent channel · Climate change · Error rate analysis · Consumption of energy · Propagation delay · Node density

## 1 Introduction

Wireless sensor networks (WSNs) consist of a huge number of spatially dispersed sensor nodes that are intrinsically resource constrained. These networks are used to collect and forward the readings to the focal center efficiently. It is used to measure environmental conditions like pressure, humidity, temperature, sound, contamination levels, and wind.

The standardization of 1G to 5G has been completed, and it is installed in world wide. The networks up to 5G provide the variety of services of broadband connection and low-latency communication. But, the traffic, volume of data transfer, and number of connections are high within a cubic meter in the wireless environment. But, in the sixth generation, communication networks are aimed to afford a huge coverage in the sensor networks and also support high-speed data transfer rate.

Since 1980 onwards, every 10 years, the generation networks emerge in the industrial world are mentioned by the author [1]. The researcher briefed about the first generation networks introduced in 1981, second generation networks emerged in 1992, third generation networks offered in 2001, and fourth generation networks used from 2011 [2]. In the last decades, tremendous changes in the technological advancement in mobile applications, wireless communications, video streaming, online transaction, etc. [3]. The 5G networks are standardized in South Korea. 75% of the people in the world will be benefitted around on 2025. The author [4] narrated the requirements, vision, and features of 5G wireless communication networks. The challenges, risk, and advancements in 5G represented in [5]. The variety of service provided by the 5G networks [6].

In the 6G, the artificial intelligence and machine learning algorithms are used for analysis of data with Internet of things for the efficient data transfer by [7]. The researcher [8] described about to providing the 6G communication standards to satisfy the future demands. The researcher [9] narrated the discussion of 6G based on the coverage, data rate and speed of 5G. The protocols, architecture, and operation of the 6G networks standard is proposed. The holographic messaging to AI using subTHz and VLC is proposed [10]. The new vision, integration, security, and intelligence of 6G is explained and also challenges for the development 6G technology and the solution for the development is also proposed [11]. The comparison of different versions, practice, and theory of 4G, 5G, and 6G communication networks is narrated by [12]. The merits and demerits of 6G are mentioned by [13]. The emerging technology and applications in 6G mobile networks are explained by [14, 14]. The application, challenges, requirements, and research directions in 6G wireless communications are explained by [16]. The resolution of the display device

and the correlation of the visual angle to be improved by the way of using holographic optical element and projection technique for the message communication in three-dimensional displays is expressed by [17].

The 5G-enabled tactile Internet, challenges, problems, and research issues and its standards are explained by [18, 19]. The researcher [20] demonstrated the Aerosol transmission through breath. The architecture and requirements of networks in 2030 are explained by [21]. The opportunities and challenges for 6G and beyond for the communication above 100 GHz are explained by [22]. The researcher [23] illustrated the RF spectrum puzzle for communication systems. The consumption of power becomes reduced using the STAR-RIS-aided wireless communication [25].

## 2 Wireless Sensor Networks and Its Types

In real-time, various types of sensor networks are used in different applications relevant to their environment. The types of networks are chosen based on domain types. Sensors are deployed in the underwater, underground, terrestrial, or in any other real-time applications. The different types of such networks are listed below:

- TWSNs-Terrestrial WSNs
- UGWSNs-Underground WSNs
- UWWSNs-Underwater WSNs
- MMWSNs-Multimedia WSNs
- MWSNs-Mobile WSNs.

### 2.1 *Terrestrial Wireless Sensor Networks*

TWSNs are suitable for imparting the information center proficiently. They comprise a large number of SNs assembled either in an unstructured (ad hoc) or in a structured (pre-planned) arrangement. The sensor nodes are arbitrarily arranged inside the bounded area by dropping from a fixed surface in an unstructured arrangement. The pre-planned or organized arrangement includes the optimal deployment and position of the nodes in 2D and 3D situation models. In TWSNs, every sensor node is equipped with a battery having limited power. The battery is rechargeable, and the solar cells provide an additional power. The low duty cycles, minimizing the delay, and the better routing path are needed to preserve the energy.

### 2.2 *Underground Wireless Sensor Networks*

Compared to TWSNs, the underground wireless sensor networks are costlier for the deployment, maintenance, and installation. The cost of the hardware is high

because the device is installed under the ground. Hence, it must be secured. In it, large numbers of sensor nodes are invisible and fixed underground to monitor the data on environmental changes. The sink nodes are installed over the ground. The sink nodes are receive the readings from the SNs deployed underground.

It is tough to energize the nodes continuously because of their deployment. Each sensor nodes (SNs) configured with a restricted power battery. It is very difficult to recharge the battery immediately. The loss of signal and higher attenuation of communication are the challenges of UGWSNs, because of fast depleting energy of the sensors.

### **2.3 Underwater Wireless Sensor Networks**

70% of the earth is covered by water. The architecture static two-dimensional UWWSNs, static three-dimensional UWWSNs, and 3D with autonomous underwater vehicles (AUVs) are used for efficient communication of data in the networks. Lot of problems in UWWSNs are signal fetching, long-distance communication, energy depletion, environmental changes, and aquatic animal movements.

### **2.4 Multimedia Wireless Sensor Networks (MMWSNs)**

Multimedia wireless sensor networks are mainly needed to observe unstructured multimedia data. It is used for tracking and monitoring the actions of multimedia data like video and audio ones. In these networks, the sensor nodes are equipped with cameras and microphones for tracking and monitoring the entire scenario. Each multimedia sensor node is interconnected with one another through a wireless association for information recovery and data compression. The limitations of multimedia wireless sensor networks are high-energy utilization and high-speed data transfer from the source to the destination, which increases the cost of the network.

### **2.5 Mobile WSNs**

Mobile wireless sensor networks are positioned on the dynamic nature of deployment of nodes. The mobile WSNs comprise a cluster of sensor nodes that are operated with mobile transferring the information in the form of signals. The mobile nodes can identify and transfer the signals between them. In mobile WSNs, the dynamic sensor nodes are more adaptable compared to the static sensor networks. These dynamic networks provide a maximized version of coverage, energy consumption, and channel requirement.

### 3 Underwater Wireless Sensor Networks

Underwater wireless sensor networks (UWWSNs) contain lot of equipments such as sensors or underwater vehicles that are configured in an exact acoustic region for data collection, data analysis, and collaborative monitoring tasks. In UWWSNs, the communication channel for underwater is water. A typical UWWSNs consist of a receiver and transmitter part. It uses optical, acoustic, and electromagnetic waves for communication. For such communication, optical waves are better suited, since less range communication and electromagnetic waves require higher power for transmission. Hence, the acoustic waves are selected for use in underwater communications.

#### 3.1 *Comparison of TWSNs and UWWSNs*

In general, UWWSNs have differed from normal terrestrial networks in terms of deployment, communication signal, cost of the equipment, channel requirement, storage space, size of data, and utilization of energy and delay. UWWSNs are located in undersea in the sub-marine environment with nearby surroundings for collecting the readings and environmental study. The comparative study of TWSNs and UWWSNs is as mentioned below:

**Deployment, Manufacturing Cost and Size:** In TWSNs, the communication medium for communicating the packet is through the air. For UWWSNs, the communication medium is water. Cost is inexpensive for terrestrial sensors due to a smaller size, but underwater devices are more expensive. The hardware needs to protect in underwater, and hence, the devices are costly to deploy and maintain.

**Sensors Deployment:** Large numbers of sensors are deployed densely in terrestrial networks. For underwater networks; the nodes are deployed sparsely. The deployment in underwater involves a higher cost.

**Communication Power:** In underwater communication, the power needed for transforming the packet is higher compared to the terrestrial communication because of the long distance between the sending and receiving nodes and also due to more complicated signal processing used at the destination. Better signal processing is essential in underwater due to complex channel conditions. In underwater networks, because of higher energy consumption, a higher capacity battery is required which leads to increasing the cost of the network.

**Storage Space:** The terrestrial wireless sensor nodes require very limited storage capacity. But, the underwater sensor nodes require more storage capacity because of intermittent channel requirements. Table 1 displays the comparison of TWSNs and UWWSNs.

**Table 1** Comparison between TWSNs and UWWSNs with 4G

Quality of service	Parameters	TWSNs	UWWSNs	Challenges in UWWSNs
Clustering	Communication	Electromagnetic waves	Acoustic waves	<ul style="list-style-type: none"> <li>Manual recharging of battery is not possible</li> <li>Loss of data is followed due to the communication medium</li> </ul>
Location	GPS aware	Non-GPS		
Speed of the signal	Speed of light	1500 m/s		
Medium	Air	Water		
Recharging process	Can be done	Not can be done		
Coverage	Coverage	Up to the miles (approximately 5000 m)		<ul style="list-style-type: none"> <li>Hardware failure is occurred due to the position of the node in underwater</li> </ul>
Node deployment	Static	Static or dynamic		<ul style="list-style-type: none"> <li>Need more energy for effective communication</li> <li>Cost of the deployment is high</li> </ul>
Node position	Any environment	Underwater		
Node density	Dense	Sparse		
Connectivity	Link process	Stable	Unstable	<ul style="list-style-type: none"> <li>The propagation delay is high</li> <li>It requires more memory because of channel intermittent</li> <li>The error rate is increased compared to other similar measurements</li> </ul>
	Communication	$\leq 150$ mt	$\leq 10$ km	
	Propagation delay	Low	High	
	Deployment	2D environment	2D and 3D are possible	
	Frequency	(908–928) MHz	(10 Hz to 1 MHz)	
	Error rate	Moderate2	High	

## 4 UWWSNs Architecture

The UWWSNs transmitting the data through electromagnetic, optical, and acoustic waves. Contrasted with the electromagnetic and optical wave, the acoustic waves are the most favored signal mode for some applications pertinent to submerged ones because the signals travel longer with less absorption. The static two-dimensional UWWSNs, static three-dimensional UWWSNs, and three-dimensional with autonomous underwater vehicles are the kinds of UWWSNs technologies adopted in the sea-based research. These architectures are support up to 6G networks.

### 4.1 Static Two-Dimensional UWWSNs

In a static two-dimensional UWWSNs, a UW-sink gathers information from the sensor nodes by the horizontal connection and afterward forwards the packet to the sink node by the vertical connection. The on-shore and surface sink is communicated with the surface station via radio frequency signal. The direct or multi-hop link is used to determine the routing path to forward the data from the source node to the sink. In a direct link, the SN sends the reading directly to the selected destination node. This method is not energy efficient. In a multi-hop method, a relay node is positioned between the source and destination nodes.

### 4.2 Static Three-Dimensional UWWSNs

In a static 3D UWWSNs; each node is linked with a hanging float that can be extended by a siphon. The sensors are pulled by the float toward the sea surface. The detected information is transmitted to the focal station by the drift-based sensor signal. The sensors are haphazardly disseminated at the base. The sensor is tied together with a handle by different lengths of the wire depending upon the depth of the sensor, so that, the sensor depth is synchronized.

### 4.3 3D with Autonomous Underwater Vehicles

The 3D with AUVs comprises static sensors together with some autonomous underwater vehicles (AUVs). AUVs are considered as supernodes, having higher energy, moving freely switching between nodes. This architecture is energy efficient and robust.

**Table 2** Comparison of various communication concepts with 4G networks

Attributes	EM	Acoustic	RF	OWC
Range	$\leq 10$ m	$\leq 10$ km	Few meters	10–100 m
Propagation delay	High	Low	Moderate	Moderate
Data rate	A few Mbps—moderate	$\leq 100$ Kbps—low	$\leq 10$ Mbps—high	$\leq 1$ Gbps—very high
Battery recharge-ability	Possible	Not possible	Not possible	Possible
Coverage area	Limited range	Very long distance	Long distance	Very short distance
Bandwidth	MHz	KHz	30-300 Hz	10-150 MHz
Transmission power	Moderate	Moderate	High	Moderate
Marine life	Not affected	Affected	Affected	Not affected

## 5 Communication Techniques in Underwater Up to 4G

Underwater wireless communication technology is used to transfer the information through various communication modes like electromagnetic waves (EM), acoustic waves (AW), radio frequency (RF), and optical wave communication (OWC) for shallow water, coastal ocean, and seawater. Table 2 shows [24] the comparison of various communication concepts in underwater.

## 6 Protocols in UWWSNs

In UWWSNs, the routing protocols are selected for the optimal path of transmitting the quality packet to the destination in consideration with the energy utilization. By default, it maximizes the lifespan of the networks. In a routing process, sending a packet from a node to the destination node is a difficult task for every node. At the hour of routing the information, mobility and energy are considered. There are three classifications of protocols to routing the packet, and they are geographical, reactive, and proactive. The proactive protocol used to route the packet periodically. Reactive kind of protocol might be utilized in dynamic networks; however, they cause enormous postponements to sense and forward the packets. The geographical protocol sends the packets to any geographical region in which the nodes are deployed. The information sent from a node to the destination node or some other nearest node can be classified as any-to-any, all-to-any, any-to-all, and all-to-all, and the entire routing protocols are categorized into three classifications: i.e., vector, directional, and hierarchical.

The routing is the essential part of the network layer used to decide the path between the sensor nodes. At the time of routing the packet, the network layer is

responsible for routing the messages inside the systems. In underwater WSNs; routing a packet is not quite the same as the TWSNs due to restricted measures of transmission capacity, node portability, and transmission delay during the transmission of the packet. Along with these parameters together in the entire network, there is a need to build up the routing procedures. A lot of researchers have analyzed various protocols to create an effective routing protocol while thinking about the exceptional parameters of the underwater networks. They are basically three classifications as mentioned earlier, i.e., geographical, reactive, and proactive.

### ***6.1 Proactive Routing Protocols (Table Driven)***

In the proactive routing protocols (PRP), the routing table keeps all routing data to discover paths from a node to the nearest neighboring node. It decreases the message redundancy received by routing nodes. The proactive routing protocol first creates a signal on the predefined path and enables the path for communication. The routing table is updated by the nodes with a new routing path. The protocol creates a new path each time whenever the network design is adjusted because of lost connectivity and node troubled in underwater wireless sensor networks. In UWWSN, storage space and energy consumption are principle motivations to be considered in the proactive routing protocol.

### ***6.2 Reactive Routing Protocols***

In reactive routing protocols, each sensor node starts to frame a new routing procedure for identifying the path needed to forward the data to the destination. Whenever the new path is framed, it is kept up and maintained in the routing table until it is required. This protocol is increasingly reasonable for dynamic situations, and it is normally utilized by the source node initiated by flooding technique.

### ***6.3 Geographical Routing Protocols***

The geographical routing protocol is to find the routing path from the sender to the receiver. This protocol has mainly used for controlling the location information of the sensor nodes. Hence, the source node chooses the next nearest node that depends on the location information of the nearest neighbor node. In the underwater conditions, the exact information about the node position is identified.

## 7 Clustering Process

Clustering in UWWSNs is recent and modern on account of the derived features that separate them from different wireless systems, for example, ad hoc networks, mobile ad hoc networks, or cellular networks. First, the SNs are deployed densely. Receiving the readings from every deployed node is difficult task. Besides, these sensor nodes should reorganize in a self-organizing system setting up associations and exchange data. Cluster-based conventions include a proactive foundation of fundamental structure among nodes or relay node through distinguishing targets.

### 7.1 *Clustering Objectives*

In UWWSNs, the cluster architecture ensures the accomplishment of fundamental execution together with the simultaneous utilization of network assets to enhance the framework's capacity. In clustering, dynamic routing is applied within the cluster, and the cluster heads (CHs) are used to manage the data among various clusters and forward to the collector node. The aim of clustering in UWWSNs is summarized as:

**Improved Scalability:** Compared with the flat topology, the clustered network topology is simpler and can be effectively rearranged relying upon ecological events. Because of the various tasks of assignments to an independent cluster, the nearby paths can be built up inside the nodes, designating out the need of putting away the whole routing path table at every node.

**Data Aggregation:** Out of different aggregation strategies, clustering approach is engaged as the most encouraging decision. The detected data from the cluster members are aggregated in the head of each cluster. Each cluster member utilizes the multi-hop transmission for forwarding the information to other heads and the base station.

**Avoid the Overhead:** In the clustering approach, the minimal numbers of nodes are used to collect the reading. The remaining nodes are forward the information to the next level. CHs are utilized for long-distance correspondence and inter-cluster routing bringing about minimum energy utilization at the independent node in the cluster. Thus, it, in-turn, helps in setting up energy proficient systems.

**More Robustness:** The whole clustered networks show profoundly vigorous conduct and are tolerant of a clustering network. The changes in the clustering networks, it may emerge because of energy level or unforeseen dislocation of sensors. These issues are handled inside the clusters without influencing the efficiency of the entire network.

**Collision Avoidance:** The less amount of resources are distributed and reused by the sensors in a wireless medium in a multi-hop flat networks. In the multi-hop clustered system, solve these problems and provide better utilization of resources during the data collection and transmission between the nodes.

**Load Balancing:** In order to reduce the consumption of energy, every cluster is assigned with fixed number of nodes, and also CHs are selected with the rotation basis by different algorithms. The lifetime of the sensor node is increased. The routing of the information among the clusters uses the multipath communication.

**Minimizing Bottleneck:** The cluster head consumes maximum energy for transforming bulk information toward the sink node without losing the packets. The remaining members use limited energy level compared with the cluster head. Hence, the uses of the clustering approach solve the bottleneck related to energy conservation.

## 8 Cluster-Based Data Aggregation in UWWSNs Using 4G Networks

The data aggregation process involves eliminating the redundant packet transmission and only relevant fewer packets transmission to the destination to conserve network energy. The following are three concepts important to data aggregation process:

**Aggregation functions:** It specifies the set of functions applied in the data aggregation node and cluster head to aggregate the data.

**Routing scheme:** It describes the data on which routing takes place, and it is aggregated.

**Data aggregation scheduling:** It mentions the scheduling period of each node is sensed, and the sensed data are aggregated.

## 9 Drawbacks in UWWSNs with 4G

Underwater communication is essential for scientific applications like monitoring the seismic activities, algae bloom, climate change, navigation, tactical surveillance, aquatic animals, and oil leakages. In an earlier model, the underwater monitoring system was to monitor the ocean environment and faced a lot of problems like:

- Communication of signals from the underwater sensor to on-shore systems is not effective always.
- It is very difficult to detect the failures in the equipment be recovered after several days, weeks, or months. Since real-time data about the environment are crucial, losing instruments is a real problem.
- It has a limited storage capacity.
- The cost of deploying the sensors is high.
- High power is needed for communication.

## 10 Generation of Networks

Table 3 exhibits the assessment of various attributes of first generation networks to sixth generation networks. In 6G, the high-frequency bands are used in fast communication with high security rate.

## 11 Features of 6G

- Provide the large coverage of area with an extremely large bandwidth (THz waves)
- More reliable data transmission with high end security framework
- Less consumption of energy due to large bandwidth
- Three-dimensional unmanned aerial vehicle and satellite communication for underwater
- Use the tactile, holographic, and human-bond communications
- 6G operate at 95 GHz to 3 THz
- The frequency bandwidth between 7 and 20 GHz.

## 12 Benefits of 6G in UWWSNs

A huge number of challenges occurred at the time of designing the underwater sensor networks because the communication media for underwater is water. So, it requires many networking paradigms encountered with the following benefits are:

- High bandwidth
- Decrease the propagation delay in underwater
- Reduce the intermittent channel requirement due to multipath communication
- Less loss of connectivity at the place of shadow zones
- Failure rate of sensors due to corrosion and erosion may be decreased
- Localization problems to be avoided
- High packets reliability.

UWWSNs consist of self-governing SNs arbitrarily and sparingly installed to monitor and collect the oceanographic information. It is equipped with batteries having limited power. Hence, the lifetime of battery-powered UWWSNs is strictly limited by the lifespan of batteries. So, a lot of research efforts have focused on with high end next generation networks like 6G which are:

- Energy-efficient deployment techniques with high bandwidth
- Designing of the routing protocol to limit the consumption of power
- Framing an optimal clustering model to minimize collisions and loss of energy
- Creating efficient-energy aware scheduling algorithms
- Marine bed mine processing

**Table 3** Comparison of various parameters of first generation networks to sixth generation networks

Attributes	Generation of networks				
	First	Second	Third	Fourth	Fifth
Spectrum	< 894 MHz	< 960 MHz	< 2170 MHz	< 2670 MHz	3–300 GHz
Mobility	Few meters	< 100 m	< 100 m	< 100 m	< 500 km/h
Access	FDMA	TDMA, FDMA	WCDMA	OFDMA	WCDMA OFDMA
Bandwidth	30 kHz	200 kHz	5 MHz	< 20 MHz	< 1 GHz
Transfer rate	2.4 Kbps	9.6–200 Kbps	0.3–30 Mbps	0.07–1 Gbps	Up to 20 Gbps
Features	Voice call	Voice call and communication (messaging)	Voice call, video call, messaging	Broadcasting	Video chat, IoT, smart city 3D integrated communication, tactile/ haptic Internet

- Underwater robots development and use.

## 13 Real-Time Data Study

Experiments on the real-time data collected from the TAO project for saving the energy and for minimizing the vast volume of data in real-time applications of UWWSNs are addressed. TAO positioned a huge number of sensors scattered over the oceans that collect salinity, temperature, currents, etc., at the depth of 3000 m with 4G networks. The subsurface temperature data are collected with different distances from 1 to 500 m and analyzed.

Figure 1 shows the percentages of similar data analyzed for the period from 2008 to 2018. The data are sensed by the sensor node and sent to its cluster head positioned in the floating buoy on the sea surface at the consecutive periods. It highlights that around 80–90% of similar data are sent to the information center. This proves that the subsurface temperature measures collected at each time period by every sensor have a high level of similarity data. It consumes excessive energy for sensing, forwarding to the information center and by default, it reduces the active life span of the sensor node. The energy depletion is highly dependent on the volume of data sent by the sensor to the cluster head, which include the duplicate ones.

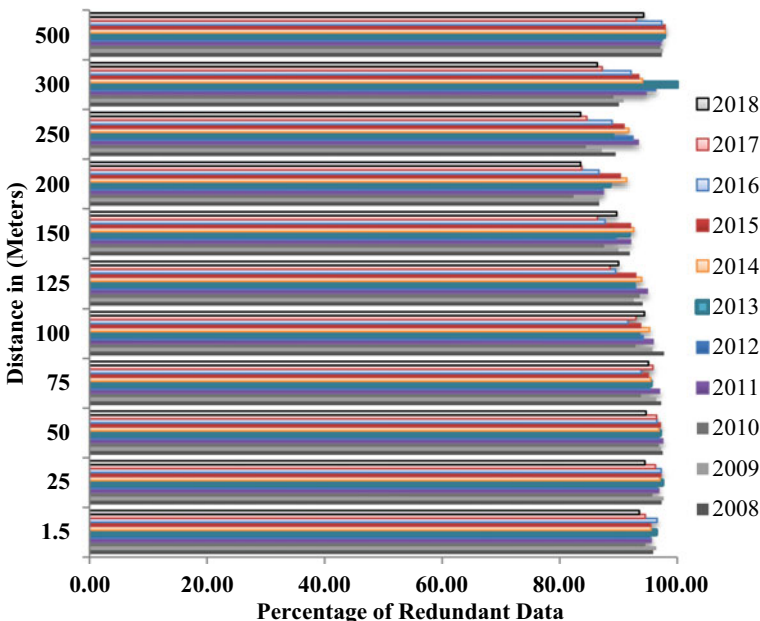


**Fig. 1** Percentage of similar readings

### 13.1 Root Mean Square Error Analysis

RMSE analysis is the standard deviation of the residuals. The residuals are measures of how far the data are fit into the threshold value. Let  $x_i$  is the observed value obtained from the sensor node  $s_i$  for a particular distance  $d_i$ ,  $n$  is the total number of observed values collected.  $x_j$  is the forecasted value; it is substituted with the null value. The  $R_e$  is the root mean square error value calculated by

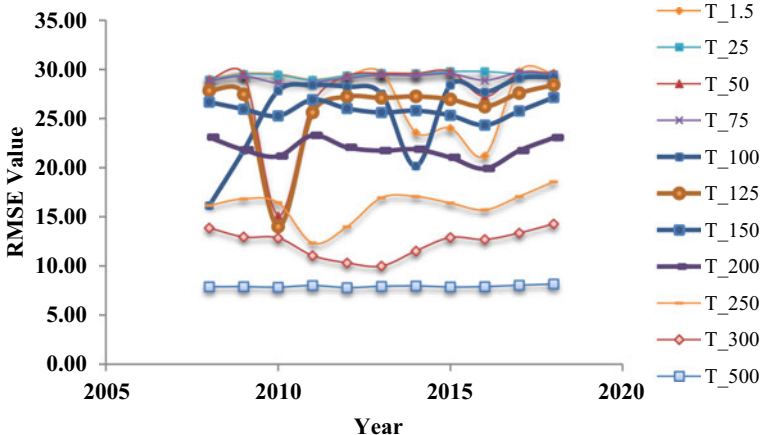
$$R_e = \sqrt{\frac{\sum_{i=1}^n (x_i - x_j)^2}{n}} \text{ with respect to } d_{(ti)} \quad (1)$$

Table 4 displays the calculated value of the root mean square error analysis of sensor reading from 2008 to 2018 deployed in various distances 1.5, 25, 50, 75, 100, 125, 150, 200, 250, 300, and 500 m. RMSE is used to analyze the real-time data with various distances based on year wise. The RMSE value for 1.5, 25, and 50 m is approximately 29. The RMSE values are less than 29, then the sensor fails to sense the readings on month-wise or may be year wise. Similarly, the RMSE value for the 200 m is 23, with any other value less than these values, the sensor does not send the data to the information center due to dry energy, hardware failures.

Figure 2 displays the RMSE values calculated with various distances on year wise. It shows that the analyzes of variations in the sensed data are of good quality or any error data sent by the sensor node. In the graphical representation, the sensed reading on the 500 m distance is smoothly narrow in all the years without much deviation. It shows that the deployment distance increases due to sensor which are not affected by currents or wave movements. At distance 300 m, there is a little bit deviation from 2012 to 2014, indicating that the sensor has failed to sense the data due to signal

**Table 4** Root mean square error analysis (RMSE)

Year	Distance in meters										
	1.5	25	50	75	100	125	150	200	250	300	500
2008	29.05	28.95	28.95	28.82	16.13	27.83	26.68	23.09	16.16	13.87	7.88
2009	29.59	29.50	29.50	29.31	21.75	27.48	25.95	21.81	16.83	12.96	7.89
2010	29.53	29.43	15.14	28.60	27.81	14.00	25.27	21.17	16.43	12.85	7.84
2011	28.97	28.91	26.49	28.67	28.40	25.62	26.91	23.28	12.33	11.06	8.01
2012	29.40	29.35	29.35	29.14	28.24	27.22	26.03	22.07	13.99	10.32	7.80
2013	29.70	29.61	29.61	29.43	27.50	27.11	25.61	21.73	16.94	10.00	7.93
2014	23.59	29.58	29.61	29.39	20.16	27.25	25.80	21.86	17.07	11.53	7.97
2015	24.03	29.79	29.80	29.56	28.40	26.95	25.32	21.04	16.40	12.90	7.86
2016	21.23	29.80	27.23	28.90	27.68	26.20	24.33	19.90	15.71	12.70	7.90
2017	29.80	29.53	29.62	29.66	29.11	27.58	25.76	21.73	17.08	13.36	8.04
2018	29.63	29.44	29.60	29.54	29.22	28.42	27.15	23.05	18.57	14.28	8.16



**Fig. 2** Comparison of RMSE value on year wise

loss. For the distance 125 m, the graphical representation displays a very low value on the year 2010, the sensor failed to sense the data. Also, a long time was spent to recover the sensors. In a underwater wireless communication, the data loss rate is increased due to less frequency bandwidth, signal loss, etc. The high end networks may reduce the data loss.

## 14 Conclusion

Environmental prediction of the nation is unpredictable due to lot of changes in the life style of the people and usage of materials, product in their day-to-day activities. Maximum of the unwanted waste are deposited in the river, ponds, sea, etc. It creates a lot of environmental changes in the underwater. It is very difficult to monitoring these changes by manually and also with low end networks. Hence, the sensor technologies are used to measure the changes with the help of high end networks like 6G. For a short-distance communication, the low end networks are useful. The long-distance communication and the high end networks like 6G are useful for better data collection. The early prediction of environmental changes in the underwater and underground is very useful for the entire society. Mostly, the technology becomes changing day by day. Even though, the analysis and challenges of an environment changes are also increased. The technology upgradation becomes very useful for analyzing the unforeseen environment. This paper shows the loss of data may be avoided by migrating the generation of networks from 4 to 6G.

**Acknowledgements** The authors thank the TAO project office of NOAA/PMEL for allowing the use of the TAO data in the present study.

## References

1. Alsharif MH, Nordin R (2017) Evolution towards fifth generation (5G) wireless networks: Current trends and challenges in the deployment of millimetre wave, massive MIMO, and small cells. *Telecommun Syst* 64:617–637
2. Albreem MA, Alsharif MH, Kim S (2020) A robust hybrid iterative linear detector for massive MIMO uplink systems. *Symmetry* 12:306
3. Mohammed SL, Alsharif MH, Gharghan SK, Khan I, Albreem M (2019) Robust hybrid beamforming scheme for millimeter-wave massive-MIMO 5G wireless networks. *Symmetry* 11:142
4. Albreem M, Juntti M, Shahabuddin S (2019) Massive MIMO detection techniques: a survey. *IEEE Commun Surv Tutor* 21:3109–3132 [CrossRef]
5. Parikh J, Basu A (2020) Technologies assisting the paradigm shift from 4G to 5G. *Wirel Pers Commun* 1–22
6. Mallat NK, Ishtiaq M, Rehman AU, Iqbal A (2020) Millimeter-wave in the face of 5G communication potential applications. *IETE J Res* 1–9
7. Alsharif MH, Kelechi AH, Yahya K, Chaudhry SA (2020) Machine learning algorithms for smart data analysis in internet of things environment: taxonomies and research trends. *Symmetry* 12:88
8. Letaief KB, Chen W, Shi Y, Zhang J, Zhang Y-JA (2019) The roadmap to 6G: AI empowered wireless networks. *IEEE Commun Mag* 57:84–90
9. Chen S, Liang Y-C, Sun S, Kang S, Cheng W, Peng M (2020) Vision, requirements, and technology trend of 6G: how to tackle the challenges of system coverage, capacity, user data-rate and movement speed. *IEEE Wirel Commun* 1–11 [CrossRef]
10. Strinati EC, Barbarossa S, Gonzalez-Jimenez JL, Kténas D, Cassiau N, Dehos C (2019) 6G: the next frontier: from holographic messaging to artificial intelligence using subterahertz and visible light communication. *IEEE Veh Technol Mag* 14:42–50
11. Gui G, Liu M, Kato N, Adachi F, Tang F (2020) 6G: opening new horizons for integration of comfort, security and intelligence. *IEEE Wirel Commun* 1–7. *Symmetry* 12, 676 18 of 21
12. Chen S, Sun S, Xu G, Su X, Cai Y (2020) Beam-space multiplexing: practice, theory, and trends-from 4G TD-LTE, 5G, to 6G and beyond. ArXiv:2001.05021
13. Dang S, Amin O, Shihada B, Alouini M-S (2020) What should 6G be? *Nat Electron* 3:20–29
14. Liang Y-C, Larsson EG, Niyato D, Popovski P (2020) 6G mobile networks: emerging technologies and applications. *China Commun* 17:1–6
15. Yuan Y, Zhao Y, Zong B, Parolari S (2019) Potential key technologies for 6G mobile communications. ArXiv:1910.00730
16. Chowdhury MZ, Shahjalal M, Ahmed S, Jang YM (2019) 6G wireless communication systems: applications, requirements, technologies, challenges, and research directions. ArXiv:1909.11315v1
17. Wakunami K, Hsieh P-Y, Oi R, Senoh T, Sasaki H, Ichihashi Y, Okui M, Huang Y, Yamamoto K (2016) Projection-type see-through holographic three-dimensional display. *Nat Commun* 7:1–7
18. Aggarwal S, Kumar N (2019) Fog computing for 5G-enabled tactile internet: research issues, challenges, and future research directions. *Mob Netw Appl* 1–28
19. Holland O, Steinbach E, Prasad R, Liu Q, Dawy Z, Ajiaz A (2019) The IEEE 1918.1 “Tactile Internet” standards working group and its standards. *Proc IEEE* 107:256–279
20. Khalid M, Amin O, Ahmed S, Shihada B, Alouini M-S (2019) Communication through breath: aerosol transmission. *IEEE Commun Mag* 57:33–39
21. Yastrebova A, Kirichek R, Koucheryavy Y, Borodin A, Koucheryavy A (2030) Future networks 2030: architecture and requirements. In: Proceedings of the 2018 10th international congress on ultra-modern telecommunications and control systems and workshops (ICUMT), Moscow, Russia, 5–9 November pp 1–8

22. Rappaport TS, Xing Y, Kanhere O, Ju S, Madanayake A, Mandal S, Alkhateeb A, Trichopoulos GC (2019) Wireless communications and applications above 100 GHz: Opportunities and challenges for 6G and beyond. *IEEE Access* 7:78729–78757
23. Elayan H, Amin O, Shihada B, Shubair RM, Alouini M-S (2019) Terahertz band: the last piece of RF spectrum puzzle for communication systems. *IEEE Open J Commun Soc* 1:1–32
24. Yadav S, Kumar V (2017) Optimal clustering in underwater wireless sensor networks: acoustic, EM and FSO communication compliant technique, digital object identifier. *IEEE Access* 5:12761–12776. <https://doi.org/10.1109/ACCESS.2017.2723506>
25. Mu X, Liu Y, Guo L, Lin J, Schober R (2021) Simultaneously transmitting and reflecting (STAR) RIS aided wireless communications. *IEEE Trans Wireless Commun* 21(5):3083–3098

# Deep Ear Biometrics for Gender Classification



Ritwiz Singh, Keshav Kashyap, Rajesh Mukherjee, Asish Bera,  
and Mamata Dalui Chakraborty

**Abstract** Human gender classification based on biometric features is a major concern for computer vision due to its vast variety of applications. The human ear is popular among researchers as a soft biometric trait, because it is less affected by age or changing circumstances and is non-intrusive. In this study, we have developed a deep convolutional neural network (CNN) model for automatic gender classification using the samples of ear images. The performance is evaluated using four cutting-edge pre-trained CNN models. In terms of trainable parameters, the proposed technique requires significantly less computational complexity. The proposed model has achieved 93% accuracy on the EarVN1.0 ear dataset.

**Keywords** Convolutional neural network (CNN) · Gender classification · Ear biometric · Soft biometrics

## 1 Introduction

Gender identification has become a major concern due to its vast variety of applications, including social communication and connection, commercial visual supervision, banking transactions, illness prognosis, demographic data collection, artificial

---

R. Singh · K. Kashyap · R. Mukherjee (✉)

Department of Computer Science and Engineering, Haldia Institute of Technology, Haldia, WB, India

e-mail: [rajeshmukherjee.cse@gmail.com](mailto:rajeshmukherjee.cse@gmail.com)

A. Bera

Department of Computer Science and Information Systems, Birla Institute of Technology and Science Pilani, Pilani Campus, Rajasthan 333031, India

e-mail: [asish.bera@pilani.bits-pilani.ac.in](mailto:asish.bera@pilani.bits-pilani.ac.in)

M. D. Chakraborty

Department of Computer Science and Engineering, National Institute of Technology, Durgapur, West Bengal, India

e-mail: [mamata.dalui@cse.nitdgp.ac.in](mailto:mamata.dalui@cse.nitdgp.ac.in)

intelligence (AI)-based user interface for customization, consumer analysis for business growth, and many more [17, 35]. Biometric traits have proven their suitability in gender classification as they are non-intrusive, remain invariant with time, and are less influenced by emotions and circumstances. Several approaches have been proposed using various biometrics traits and their fusion. Biometrics can be broadly categorized into the conventional (aka hard) biometrics (e.g., face, hand, etc.) [5, 18] and soft biometrics (e.g., ear, gait, etc.) [26, 34].

In classifying human gender, based on the iris samples, Bansal and Sharma [2] have employed wavelet transforms and statistical methods. A technique to identify the gender of complete body photographs using part-based gender recognition is proposed in [7]. To determine the dialect and gender from parlance data, supervised machine learning techniques have been employed [13]. Tapia et al. [30] used the local binary patterns (LBP) and Histograms of Gaussian (HOG) descriptors for gender identification from iris images. Gait-based gender categorization methods are suggested by Yu et al. [36] and Li et al. [22]. Shan [28] has used real-world facial pictures and the LBP description to categorize gender. A novel patch-based LBP with adjustable weights is presented by Chen and Jeng [9] for the classification of gender on the person's face.

Moreover, a human ear is an unique evidence among the existing biometric traits for gender identification. The anatomy of the human ear is regarded to be equally significant as compared to other biometric traits like the face, iris, and gait, for identifying an individual. Additionally, it is less affected by aging when compared to other biometric traits like the face [16] and gait [22]. Other biometric traits may change with age or changing circumstances, but the ear simply scales up. Numerous methods for ear identification have been proposed. Anwar et al. [1] use geometrical information from human ear images for identification. Various image descriptors have been studied including LPQ, BSIF, LBP, HOG, and surface descriptors in [27]. Gender classification from ear images has also been studied in [11, 12, 19, 34].

However, the effectiveness of ConvNet for gender identification is yet to be researched thoroughly. In this study, we suggest a basic yet successful CNN-based model that is computationally lightweight. For the experiment, we have considered the EarVN1.0 large-scale ear dataset and achieved significantly good accuracy.

## 2 Related Work

Existing works on gender identification can be divided into three types: appearance-based approaches [3, 4, 7, 14, 28, 33], biological feature-based approaches [6, 8, 29, 31, 32], and interpersonal information-based approaches [10, 23, 25]. External traits of an individual, such as the face, eye brows, hands, fingernails, attire, and footwear, are focused on an appearance-based approach. The biological feature-based techniques make use of biometric characteristics (e.g., fingerprint, ear, iris, etc.) and

biosignals to determine gender (ECG, EEG, etc.). The interpersonal information-based strategy uses email, blogs, handwriting, and other types of interpersonal information.

Nowadays, the research community has recently demonstrated a growing interest in biological feature-based techniques approaches since unique biological information of individuals does not change over long periods of time, is non-intrusive, is less influenced by emotions, and is appropriate for applications requiring real-time recognition. [20]. Because of various distinctive features, the ear has gained increased interest in biometric research for identification. Several works on gender categorization based on ear biometrics have been conducted. In [12], the authors considered measurements between the ear hole within the ear hole and seven ear features computed from the masked ear image for identification. Over 342 samples, they examined KNN, Bayes, and neural networks for classification accuracy. KNN performed the best, with a classification accuracy rate of 90.42%. Histogram intersection kernel is employed to classify profile face and ear images in [37]. To increase accuracy, they used Bayesian analysis to achieve score-level fusion. The trials were carried out using 2D images. Face and ear attained 95.43% and 91.78% perfection, respectively, while fusion achieved 97.68% precision. Yaman et al. [35] shows that much higher accuracy in gender identification (99%) can be achieved through fusion with facial profiles. Authors in [19] suggested a sparse representation-based method for identifying gender from ear images. They added Gabor filters for feature extraction to enhance accuracy. The authors in [21] have investigated the use of 3D ear images for gender identification. The authors have exploited curvature and indexed shapes of ears for the classification. In [34], authors with the aid of geometrical and appearance-based features identified age, gender, and other biometric traits. A methodology to identify gender and kinship using geometric aspects of ear pictures has been developed in [24]. The proposed model has an accuracy of 67.2% in gender classification.

In this study, a straightforward, but, effective CNN model is proposed and tested for gender classification using the EarVN1.0 [15] ear dataset, and performance is evaluated in contrast with four cutting-edge models.

### 3 Methodology

A novel CNN-based architecture is proposed for gender detection using ear images to increase classification accuracy and reduce model size. The proffered model's architecture is portrayed in Fig. 1, and Table 1 displays the output shape and parameters for each layer of the proposed model. Let, the input color image is  $X \in I^{h \times w \times 3}$ , where  $h, w, 3$  represent height, width, and the number of channels. A sequel of convolutional extraction blocks  $C(\sum_n \omega_n \cdot x_n + b)$  (where  $\omega_n$ ,  $x_n$ , and  $b$  are weight, input, and bias at  $n$ th layer) is employed for the extraction of deep feature map  $FM = C(X) \in I^{h \times w \times c}$  from  $X$ . The resultant feature map is then split into two channels, one for global average pooling  $Pool_{avg}$  (GAP) and another for global max pooling  $Pool_{max}$

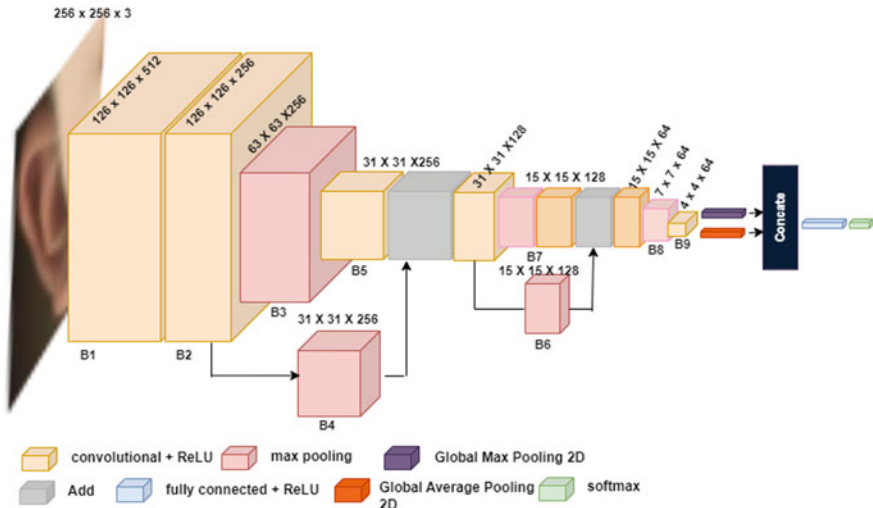


**Fig. 1** Proposed deep model for ear biometrics

(GMP), in order to decrease the spatial aspects by identifying key features along both the pathways,  $FM_a = \text{Pool}_{\text{avg}}(\text{FM})$  and  $FM_m = \text{Pool}_{\text{max}}(\text{FM})$ . It retains translation invariance while providing a summary of the feature maps. Then, a high-level feature map is created by fusing these two feature maps  $FM_c = FM_a \oplus FM_m$ , where  $\oplus$  represents linear concatenation function. And lastly, the Softmax estimates the likelihood ( $\rho$ ) of gender classification from the input image,  $\rho[0, 1] = \text{softmax}(FM_c)$ . ‘0’ is designated as the ‘female’ class in the binary classification issue, while ‘1’ is designated as the ‘male’ class.

$$\text{FM} = C(X); \text{ where } \text{FM} \in I^{h \times w \times c}; X \in I^{h \times w \times 3}; \text{ and } C\left(\sum_n \omega_n \cdot X_n + b\right) \text{ is a CNN}, \quad (1)$$

$$FM_a = \text{Pool}_{\text{avg}}(\text{FM}) \text{ and } FM_m = \text{Pool}_{\text{max}}(\text{FM}), \quad (2)$$

$$FM_c = [FM_a \oplus FM_m]; \text{ and } \rho = \text{softmax}(FM_c). \quad (3)$$

**Implementation:** The proposed model comprises a sequel of convolution extraction blocks to extract the feature maps. Next, GAP and GMP are applied independently on the extracted feature map (Fig. 1). Finally, Softmax is applied to calculate output probabilities by concatenating the two acquired feature maps. To optimize the training job, binary cross-entropy ( $\gamma$ ) is employed as a loss function.

**Table 1** Layer outputs and parameters of proposed model

Blks	Layer (type)	Output shape	Parameter
	Input layer	(None, 256, 256, 3)	0
B1	Conv 2D 1	(None, 126, 126, 512)	38,912
B2	Conv 2D 2	(None, 126, 126, 256)	1,179,904
B3	Maxpooling 2D 1	(None, 63, 63, 256)	0
B4	Maxpooling 2D 2	(None, 31, 31, 256)	0
B5	Conv 2D 3	(None, 31, 31, 256)	590,080
	Add 1	(None, 31, 31, 256)	0
	Conv 2D 4	(None, 31, 31, 128)	295,040
B6	Maxpooling 2D 3	(None, 15, 15, 128)	0
B7	Maxpooling 2D 4	(None, 15, 15, 128)	0
	Conv 2D 5	(None, 15, 15, 128)	65,664
	Add 2	(None, 15, 15, 128)	0
	Conv 2D 6	(None, 15, 15, 64)	73,792
B8	Maxpooling 2D 5	(None, 7, 7, 64)	0
B9	Conv 2D 6	(None, 4, 4, 64)	36,928
GAP	GlobalAvgPooling 2D	(None, 64)	0
GMP	GlobalMaxPooling 2D	(None, 64)	0
Concat	Concatenate	(None, 128)	0
Dense	Dense	(None, 2)	258

$$\gamma = \frac{1}{n} \sum_{t=1}^k -[y_t \cdot \log(P_t) + (1 - y_t) \cdot \log(1 - P_t)], \quad (4)$$

where  $P_t$  and  $(1 - P_t)$  denote the likelihood of female and male classes, respectively.  $y_t$  and  $\bar{y}_t$  indicate the actual and predicted class labels, and  $n$  represents the number of data samples. With a learning rate of 0.001, the Adaptive Moment Estimation (ADAM) optimizer is employed. The model is trained for 100 epochs with 32 mini-batch size.

The input shape is  $256 \times 256 \times 3$ , and also, the suggested model is trained over 100 epochs in 32-batch iterations. The data augmentation process is used to increase the data's size and diversity by including  $\pm 0.2$  horizontal flips and  $\pm 0.2$  rotations. The output feature dimension (FM) is  $4 \times 4 \times 64$ . Pooling reduces the size of a feature map from  $w \times h \times c$  to  $1 \times 1 \times c$ . Then, the feature map is further reduced to 64 ( $FM_a = FM_m = 64$ ) by using the GAP and GMP layers in two distinct channels. Finally, feature maps from both channels (GAP and GMP) are concatenated ( $FM_c = 128$ ). To avoid the overfitting problem, a dropout rate of 0.2 is used in the experiment as regularization.

## 4 Experiments and Result

In this section, we present the outcomes of the proposed model. In order to compare the performance of the proposed model, we have used four base models in which four CNNs, namely, VGG19, Xception, ResNet50, and MobileNet have been used as the backbone and tuned with the target dataset. For faster learning convergence, pre-trained ImageNet weights are employed in the considered base models. Features are extracted from the last layers of the backbone CNNs, and then, subsequent dense layer is applied for the classification. To assess the model's performance, we have used the EarVN1.0 [15] dataset. The dataset contains the large-scale ear images of 164 subjects and a total of 28,412 images.

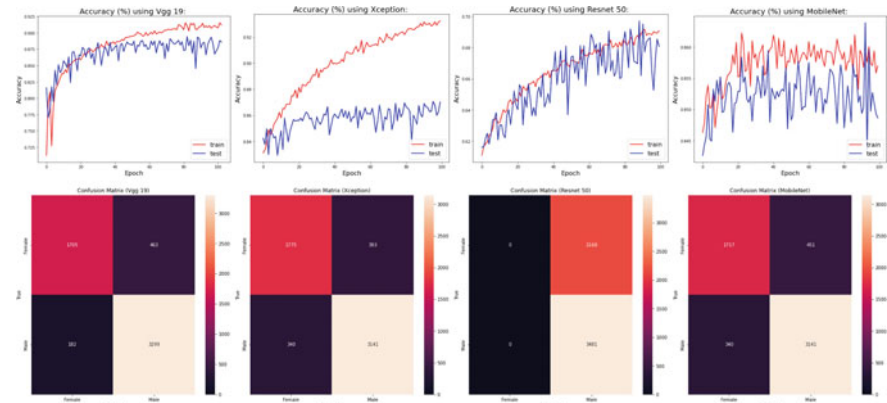
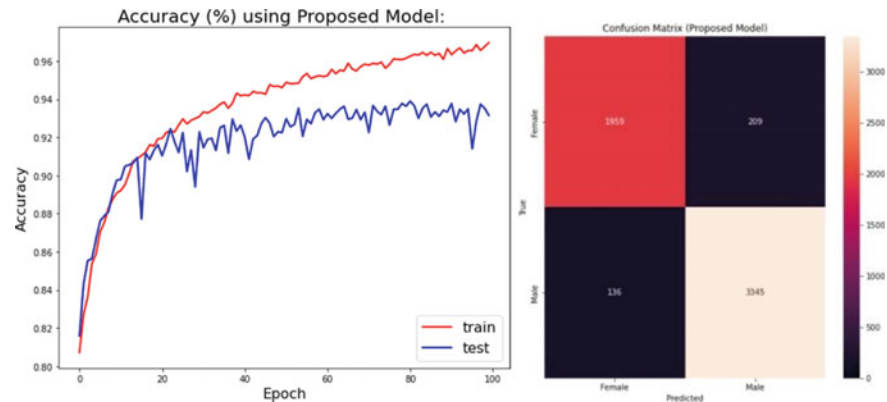
For assessment, the Receiver Operator Characteristic (ROC) curve is used. AUC, which serves as a summary of the ROC curve, calculates the capacity to differentiate between the classes. In order to discriminate between the male and female categories, a higher AUC is indicative of greater performance. The accuracy (%) and AUC (%) metrics are employed. Model parameters of the CNN models are expressed in millions (M). Furthermore, both accuracy and recall are taken into account in order to properly assess the efficacy of the proposed framework. Higher recall demonstrates a higher likelihood that a specific category may be identified, whereas higher precision suggests the efficiency of a model used to predict a certain category.

The experiments are conducted on the Kaggle notebook platform equipped with an NVIDIA Tesla T4 GPU. We have tested and compared the performance of all four state-of-the-art pre-trained models and the proposed model on the EarVN1.0 [15] ear dataset with a 70:30 train–test ratio, and the results are displayed in Table 2. The accuracy indicates that our method outperforms four well-known state-of-the-art classification models, as stated above. Additionally, it should be highlighted that the computational complexity of the proposed model is considerably lower than the state-of-the-art models. We achieved 93% accuracy in the proposed model on the EarVN1.0 dataset, whereas only VGG-19 and MobileNet ensure the maximum 85% accuracy among the examined state-of-the-art models. The confusion matrix is used to assess a model's utility and envision its performance. In a confusion matrix, diagonal values correspond to predicted labels that are identical to actual labels, whereas non-diagonal values correspond to classifier erroneously classified labels. Figure 2 depicts the confusion matrix and training–testing accuracy during the training process for state-of-the-art models. Figure 3 depicts the same for the proposed model. The test results imply that our proposed deep architecture performs better than state-of-the-art computationally heavy models in the context of precision and recall metrics.

**Feature Map Representation:** Figure 4 displays the feature maps from various layers of the proposed model. The low-level features depict an ear shape with earlier levels having more distinct details. On the other hand, the network pipeline's deeper levels depict high-level characteristics with fewer details.

**Table 2** Efficacy of the considered base models along with the proposed model

CNN model	Female		Male		Accuracy	Model parameters (M)
	Precision	Recall	Precision	Recall		
VGG-19	86	73	84	93	85	20.07
ResNet50	67	31	68	89	68	23.59
Xception	78	83	89	85	84	20.86
MobileNet	83	77	86	91	85	3.23
Proposed model	92	89	93	95	93	2.46

**Fig. 2** Accuracy and confusion matrix of VGG-19, Xception, ResNet-50, and MobileNet (left to right)**Fig. 3** Gender recognition performance of the proposed model

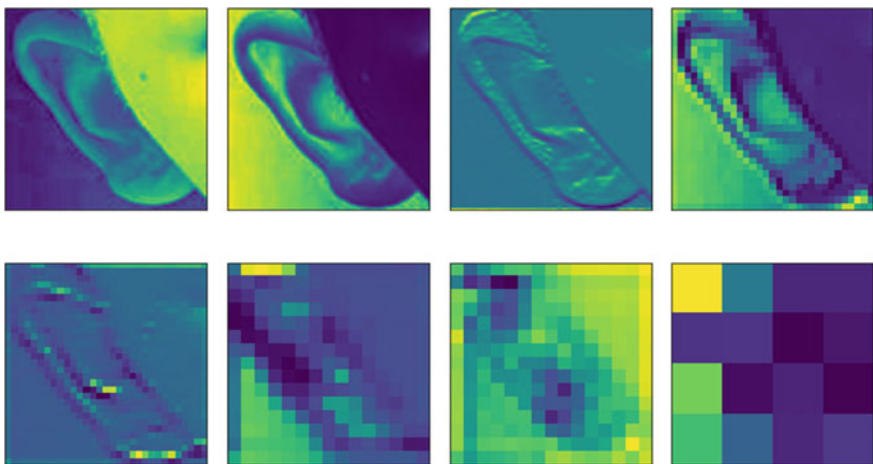


**Fig. 4** Feature map representation of proposed model at different convolutional layers

## 5 Conclusion

In this paper, a simple and novel deep CNN method is devised for gender classification using ear biometric samples. The proposed model is tested on EarVN1.0 ear dataset. The proposed model outperforms four computationally demanding state-of the-art model CNNs, namely VGG-19, Xception, ResNet-50, and MobileNet. Thus, the proposed approach makes the gender categorization more practical. We intend to develop a new deep model for soft biometric features and a fusion of them, to broaden the method's usefulness for real-world applications.

## References

1. Anwar AS, Ghany KKA, Elmahdy H (2015) Human ear recognition using geometrical features extraction. *Proc Comput Sci* 65:529–537
2. Bansal A, Agarwal R, Sharma R (2012) SVM based gender classification using iris images. In: 2012 fourth international conference on computational intelligence and communication networks. IEEE, pp 425–429
3. Basha AF, Jahangeer GSB (2012) Face gender image classification using various wavelet transform and support vector machine with various kernels. *Int J Comput Sci Issues (IJCSI)* 9(6):150
4. Bekios-Calfa J, Buenaposada JM, Baumela L (2014) Robust gender recognition by exploiting facial attributes dependencies. *Pattern Recogn Lett* 36:228–234
5. Bera A, Bhattacharjee D (2017) Human identification using selected features from finger geometric profiles. *IEEE Trans Syst Man Cybernet: Syst* 50(3):747–761
6. Bera A, Bhattacharjee D, Nasipuri M (2014) Person recognition using alternative hand geometry. *Int J Biometr* 6(3):231–247
7. Cao L, Dikmen M, Fu Y, Huang TS (2008) Gender recognition from body. In: Proceedings of the 16th ACM international conference on Multimedia, pp 725–728

8. Carrier J, Land S, Buysse DJ, Kupfer DJ, Monk TH (2001) The effects of age and gender on sleep EEG power spectral density in the middle years of life (ages 20–60 years old). *Psychophysiology* 38(2):232–242
9. Chen WS, Jeng RH (2020) A new patch-based lbp with adaptive weights for gender classification of human face. *J Chin Inst Eng* 43(5):451–457
10. Corney M, De Vel O, Anderson A, Mohay G (2002) Gender-preferential text mining of e-mail discourse. In: 18th Annual computer security applications conference, 2002. Proceedings. IEEE, pp 282–289
11. Emersic Z, Struc V, Peer P (2017) Ear recognition: more than a survey. *Neurocomputing* 255:26–39
12. Gnanasivam P, Muttan S (2013) Gender classification using ear biometrics. In: Proceedings of the fourth international conference on signal and image processing 2012 (ICSIP 2012). Springer, pp 137–148
13. HaCohen-Kerner Y, Hagege R (2017) Language and gender classification of speech files using supervised machine learning methods. *Cybern Syst* 48(6–7):510–535
14. Hadid A, Pietikainen M (2009) Combining appearance and motion for face and gender recognition from videos. *Pattern Recogn* 42(11):2818–2827
15. Hoang VT (2019) Earvn1. 0: a new large-scale ear images dataset in the wild. *Data in brief* 27
16. Iannarelli A (1989) Forensic identification series: ear identification. Paramount, California 5
17. Kamboj A, Rani R, Nigam A (2022) A comprehensive survey and deep learning-based approach for human recognition using ear biometric. *Vis Comput* 38(7):2383–2416
18. Kar A, Pramanik S, Chakraborty A, Bhattacharjee D, Ho ES, Shum HP (2020) Lmzmpm: local modified zernike moment per-unit mass for robust human face recognition. *IEEE Trans Inf Forens Secur* 16:495–509
19. Khorsandi R, Abdel-Mottaleb M (2013) Gender classification using 2-d ear images and sparse representation. In: 2013 IEEE workshop on applications of computer vision (WACV). IEEE, pp 461–466
20. Kumar A, Wu C (2012) Automated human identification using ear imaging. *Pattern Recogn* 45(3):956–968
21. Lei J, Zhou J, Abdel-Mottaleb M (2013) Gender classification using automatically detected and aligned 3d ear range data. In: 2013 International conference on biometrics (ICB). IEEE, pp 1–7
22. Li X, Maybank SJ, Yan S, Tao D, Xu D (2008) Gait components and their application to gender recognition. In: IEEE transactions on systems, man, and cybernetics, part C (Applications and Reviews) 38(2):145–155
23. Liwicki M, Schlapbach A, Loretan P, Bunke H (2007) Automatic detection of gender and handedness from on-line handwriting. In: Proceedings of 13th conference of the graphonimics society. Citeseer, pp 179–183
24. Meng D, Nixon MS, Mahmoodi S (2019) Gender and kinship by model-based ear biometrics. In: 2019 International conference of the biometrics special interest group (BIOSIG). IEEE, pp 1–5
25. Mukherjee A, Liu B (2010) Improving gender classification of blog authors. In: Proceedings of the 2010 conference on empirical methods in natural language processing, pp 207–217
26. Mukherjee R, Bera A, Bhattacharjee D, Nasipuri M (2021) Human gender classification based on hand images using deep learning. Tech Rep, EasyChair
27. Pflug A, Paul PN, Busch C (2014) A comparative study on texture and surface descriptors for ear biometrics. In: 2014 International Carnahan conference on security technology (ICCST). IEEE, pp 1–6
28. Shan C (2012) Learning local binary patterns for gender classification on real-world face images. *Pattern Recogn Lett* 33(4):431–437
29. Shue YL, Iseli M (2008) The role of voice source measures on automatic gender classification. In: 2008 IEEE international conference on acoustics, speech and signal processing. IEEE, pp 4493–4496

30. Tapia J, Viedma I (2017) Gender classification from multispectral periocular images. In: 2017 IEEE international joint conference on biometrics (IJCB). IEEE, pp 805–812
31. Thomas V, Chawla NV, Bowyer KW, Flynn PJ (2007) Learning to predict gender from iris images. In: 2007 First IEEE international conference on biometrics: theory, applications, and systems. IEEE, pp 1–5
32. Tripathy RK, Acharya A, Choudhary SK (2012) Gender classification from ECG signal analysis using least square support vector machine. *Am J Sig Proc* 2(5):145–149
33. Ueki K, Komatsu H, Imaizumi S, Kaneko K, Sekine N, Katto J, Kobayashi T (2004) A method of gender classification by integrating facial, hairstyle, and clothing images. In: Proceedings of the 17th international conference on pattern recognition, 2004. ICPR 2004. vol 4. IEEE, pp 446–449
34. Yaman D, Eyiokur FI, Sezgin N, Ekenel HK (2018) Age and gender classification from ear images. In: 2018 International workshop on biometrics and forensics (IWBF). IEEE, pp 1–7
35. Yaman D, Irem Eyiokur F, Kemal Ekenel H (2019) Multimodal age and gender classification using ear and profile face images. In: Proceedings of the IEEE/CVF conference on computer vision and pattern recognition workshops, pp 0–0
36. Yu S, Tan T, Huang K, Jia K, Wu X (2009) A study on gait-based gender classification. *IEEE Trans Image Process* 18(8):1905–1910
37. Zhang G, Wang Y (2011) Hierarchical and discriminative bag of features for face profile and ear based gender classification. In: 2011 International joint conference on biometrics (IJCB). IEEE, pp 1–8

# Design of Smart IoT-Based Gas Leakage Detection and Prevention Devices for Hydrogen Station



**Tapan Maity, Pranabendu Giri, Rohit Sasmal, Niladri Biswas, Sourav Das, Raj Kumar Maity, Prabir Saha, and Jagannath Samanta**

**Abstract** Air pollution directly affects our health and has an awful impact on the environment. Currently, people are becoming more aware of the environmental protection and health monitoring in order to ensure the future generations healthier lives. Air quality is a crucial factor in raising public awareness. Controlling air pollution has become a top priority for the urban population. The air quality also degrades due to gas leakage from different industries. The development and design of an IoT-based simple and low-cost air quality monitoring system (AQMS) based on Arduino microcontrollers and the Blynk cloud platform are the primary focus of this paper. This device can detect and measure the concentration of carbon dioxide, carbon monoxide, hydrogen, ammonia, toluene, and acetone. It can also measure the amount of dust particle ( $PM_{2.5}$ ), humidity, and temperature present in the environment. The MQ series sensors (MQ135 and MQ6) collect the data of the harmful and flammable gases present in the air, and the DHT11 and GP2Y101 sensors collect the humidity, temperature level, and particular material present in the atmosphere, respectively. The proposed device can be employed in a hydrogen station for detection and prevention of gas leakage purposes.

**Keywords** MQ135 · MQ6 · DHT11 · GP2Y101 · Atmega328P · IoT · Hydrogen station

---

T. Maity · P. Giri · R. Sasmal · N. Biswas · S. Das · R. K. Maity · J. Samanta (✉)  
Department of ECE, Haldia Institute of Technology, Haldia, India  
e-mail: [jagannath19060@gmail.com](mailto:jagannath19060@gmail.com)

P. Saha  
Department of ECE, NIT Meghalaya, Shillong, India  
e-mail: [prabir.saha@nitm.ac.in](mailto:prabir.saha@nitm.ac.in)

## 1 Introduction

Hydrogen station is a location where hydrogen is stored or refilled. There is about 550 gas hydrogen refuelling stations available worldwide as of 2021. There are two types of hydrogen refuelling stations: off-site stations, where hydrogen is transported by pipeline or truck, and on-site stations, where hydrogen is produced and compressed specifically for the vehicles [1]. From this hydrogen refuelling stations, different gases emit which is the major concern for air pollution. The air pollution is a major risk to today's emergent world. The amount of air pollution in the atmosphere is quickly rising each day. Based on this, the Government has already taken certain steps to outlaw high pollution-emitting items including air conditioners, motorcycles with single or two stroke engines, smoking, and forest fires. Chemicals and gases that contribute to air pollution can be dangerous to the health of people, animals, and plants. Fourteen out of the twenty most polluted cities in the world are situated in India, according to the World Health Organization's most recent database on air pollution. The city of New Delhi is noted for having the highest air quality in the world, with readings above 300PPM [2]. The pollutants can be gases, spheres of solid matter, or drops of liquid. There are several ways that pollution reaches the atmosphere. Anthropogenic sources account for the majority of air pollution. Numerous illnesses, such as stroke, chronic obstructive pulmonary disease, trachea, bronchus, and lung cancer, worsened asthma, and lower respiratory infections, can be brought on by this bad air quality. It is challenging for humans to measure the air's quality or detect any dangerous particles that may be present. People therefore do not understand when or how their actions can cause air pollution or expose them to it. People can avoid a significant quantity of pollution or infection by the air by taking easy precautions if they are aware of the air quality in their immediate surroundings.

The IoT is a smart and intelligent infrastructure which allows static and dynamic environmental objects to communicate and update the real situations [3, 4]. The different objects of IoT are able to interact with each other and cooperate with their neighbours to reach their common goals through unique addressing schemes [5].

Technology is essential for expediting the hydrogen energy shift, in addition to more investment, government assistance, and a workforce with more advanced skills. Through real-time monitoring and data analytics, the Internet of things offers hydrogen-generating plants great prospects to enhance and automate systems.

We are focussing on a few of the gases in this paper that the WHO has identified as the most dangerous gases in the atmosphere. To test the air quality, we use sensors from the MQ series as well as some specific matter detectors. In this paper, we have design an IoT-based AQMS device which can measure different gases like ammonia, sulphur, carbon dioxide, and carbon monoxide using gas sensors. LPG, isobutane, propane, and a few other flammable gases are frequently detected using the MQ6 sensor.

Remaining paper is organized as follows. Basics of AQMS are discussed in Sect. 2. Proposed design is described in Sect. 3. Parameters are calculated in Sect. 4. Results and discussion are discussed in Sect. 5. The paper has been concluded in Sect. 6.

## 2 Basics of AQMS

All private, public, and local organizations can accomplish their air quality goals and difficulties with the aid of the air quality monitoring system. Testing and collecting air pollutants are done by an air quality monitoring system. Every application's unique requirements are taken into account whilst designing air quality monitoring systems. Our eco energies engineers have been developing, creating, and modernizing tomorrow's air quality monitoring system (AQMS) solutions over the years to meet all environmental regulations, and the problems posed by climate change. The AQMS is available to assist you, whether you need it for a single monitoring location or a whole city. Due to both natural and human influences, air quality has substantially declined worldwide. The quantity of both natural and human activity in an area is strongly correlated with the quality of the air there.

### 2.1 Related Work

A high-quality air pollution monitoring system is made up mostly of numerous advanced instruments that employ challenging measurement techniques. Researchers must employ a variety of sensors and control tools to ensure the accuracy and quality of the data. As a result, air quality monitoring systems are frequently expensive, energy-intensive, bulky, and heavy. No low-cost portable sensor can attain the same data accuracy and quality as the conventional monitoring system, despite the efforts of many researchers to introduce fixed point arrangements and moveable monitoring approaches. Researchers are currently working on small and quick-responding ambient sensors that are low cost and size, and they are attempting to use microcontrollers in the field of embedded systems. It has been examined how the indoor and outdoor air quality are being monitored in [6]. A system of pervasive distributed sensing units, information systems for data aggregation, reasoning, and context awareness that the author proposes to monitor temperature, humidity, and light intensity [2]. The sensor data's dependability is encouraging. Recently, a number of monitoring systems have been proposed for the monitoring of air pollution. Some monitoring devices are designed specifically for CO<sub>2</sub> monitoring [3]. However, we also track other gases including CO<sub>2</sub>, CO, acetone, toluene, NH<sub>3</sub>, LPG, and CH<sub>4</sub>. In the Ref. [7], authors proposed a suggestion for a real-time indoor air quality monitoring system. Seven sensors in the system are keeping an eye on seven distinct gases. However, authors merely employ two gas sensors to track seven separate gases. In addition to providing relevant data for the general public's end users, the goal of air quality monitoring is to offer the information needed for scientists, policy-makers, and planners to enable them to make educated decisions about managing and enhancing the environment [8]. As demonstrated in Fig. 2, creating a schematic range is the initial step in system design. We employ four different types of sensors, namely MQ7, MQ1131, MQ135, and PM<sub>10</sub>, to measure various sorts of particles

in the air [9, 10]. Then use the Arduino IDE to programme the Arduino Uno. An editor called Arduino IDE is used to create programmes for Arduino [11]. Create a channel in ThingSpeak so that you may collect the measurement data that the Arduino sends. By visiting the ThingSpeak API URL, we acquired after creating a channel to receive data, and we may transmit data from Arduino. Arduino makes use of the WIFI ESP8266 module to access the ThingSpeak API [12]. Numerous initiatives have been documented in the literature that makes use of affordable air pollution sensor equipment that may be transported by people or by various vehicles [13]. A semiconductor sensor is further employed at the vehicle's emission outlet to measure the level of pollutants and relay that level to the microcontroller [14]. The authors of a different study [15] offer a cloud-based system that searches for real-time air quality data using knowledge-based discovery. Monitoring stations positioned in various geo-locations gather the data. Mobile clients are used in this system for monitoring purposes.

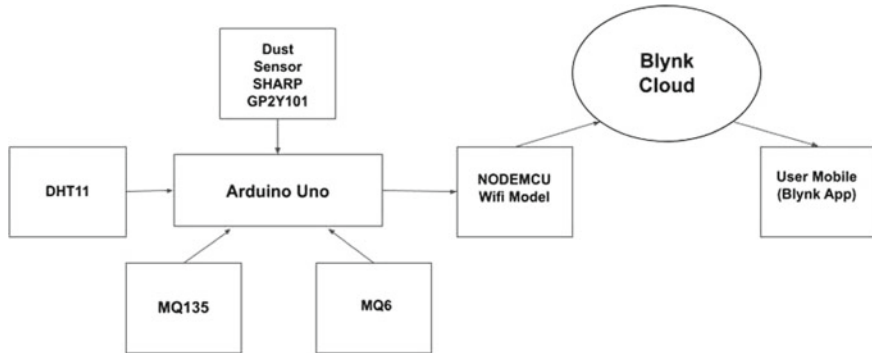
### 3 Proposed Work

#### 3.1 Block Diagram

Figure 1 shows the different blocks of IoT-based proposed AQMS systems. This device can detect and measure the concentration of different gases of environment like hydrogen, carbon dioxide, carbon monoxide, ammonia, toluene, and acetone. It can also measure the dust particle ( $PM_{2.5}$ ), humidity, and temperature present in the environment. The MQ series sensors MQ135 and MQ6 collect the data of the harmful and flammable gases present in the air; and the DHT11 and GP2Y101 sensors collect the humidity, temperature level, and particular material present in the atmosphere, respectively. The receiving data then transfer to the user's device where user can monitor the air quality of any place by enabling the remote monitoring. This is especially significant for developing a low-cost movable real-time monitoring gadget which can overcome the real-time monitoring limits.

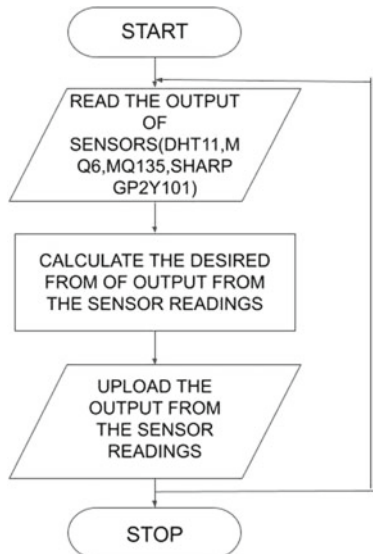
#### 3.2 Flow Chart of Proposed AQMS

Figure 2 shows the flow chart of air quality monitoring system based on IoT.



**Fig. 1** Block diagram of proposed IoT-based AQMS

**Fig. 2** Flow chart of proposed IoT-based AQMS



### 3.3 Algorithm of Proposed AQMS

1. Read the analogue output of the MQ135 and MQ6 sensors, the digital output of the DHT11 sensor, and the analogue output of the SHARP GP2Y101 sensor.
2. Calculate the concentration of the gases (NH<sub>3</sub>, CO, CO<sub>2</sub>, toluene, acetone, LPG, CH<sub>4</sub>, H<sub>2</sub>) using the derived equation which are written in the parameter calculation from Sects. 4.1 and 4.2.
3. Send the data using Wi-Fi module (ESP8266) to the Blynk cloud platform.
4. The data are shown in the user's device.

### 3.4 Circuit Diagram

Figure 3 shows the circuit diagram of proposed AQMS system.

Here, we use one Arduino Uno and four sensors for fetching the data with using three analogue read output and one digital read output. In the dust sensor (SHARP GP2Y101), we are using one capacitor and one resistor. A Wi-Fi module (ESP8266) is employed for uploading the data through the Blynk platform into the cloud. So, it will be helpful for giving the air quality of the particular area.

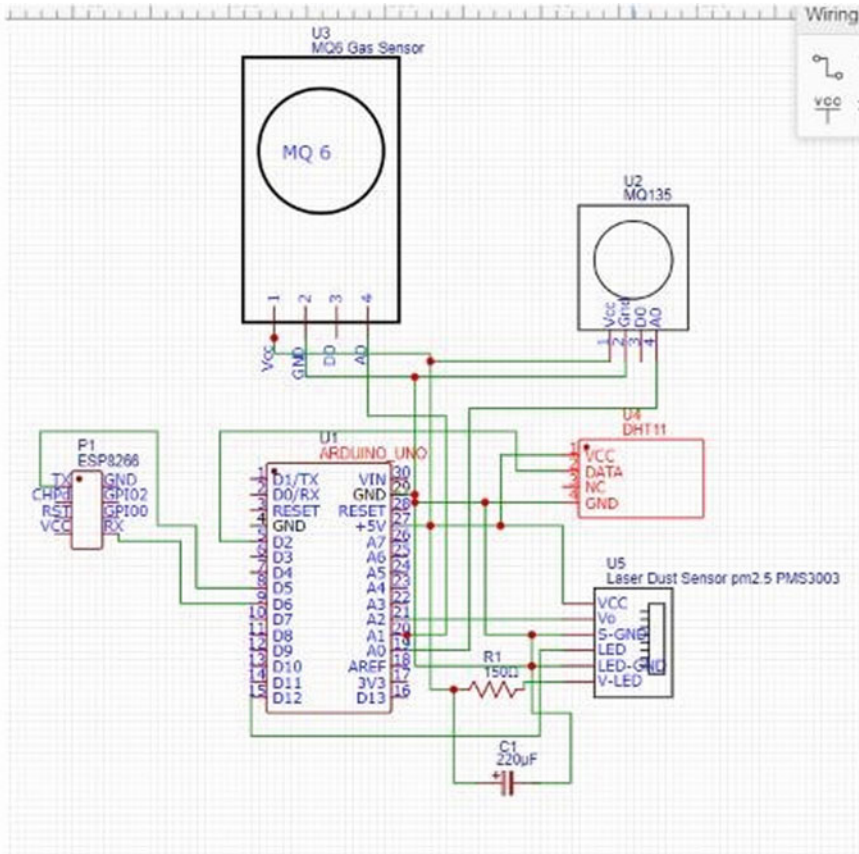


**Fig. 3** Circuit diagram of the proposed AQMS

**Table 1** Hardware components required

S. No.	Name of components	Purpose
1	MQ series gas sensors (MQ135, MQ6)	To detect alcohol, smoke, methane, LPG, hydrogen, NH <sub>3</sub> , benzene, propane
2	Dust sensor (SHARP GP2Y101)	To detect dust particles
3	Humidity and temperature sensor	To detect humidity, temperature
4	Microcontroller (UNO_R3_Wi-Fi_ATMEGA328P_ESP8266)	To process and control the sensed data

### 3.5 List of Components

The different hardware components which are employed our design are presented in Table 1.

## 4 Parameter Calculation of Proposed AQMS

### 4.1 MQ135 Sensor Calibrations for Detection of Different Gases

Figure 4 describes about the gases and their concentrations which are calculated by using the graph through the straight line equation. We can only detect the gases which are present on the above graph. We take two points for the line equations and put these two points on the line equation and calculate the concentration of gases. It is a logarithmic graph so we use log<sub>10</sub> as base. In the following, the expression of different gases like NH<sub>3</sub>, acetone, CO<sub>2</sub>, CO, and toluene has been written as follows:

#### 4.1.1 Expression for NH<sub>3</sub>

From the database of MQ135 shown in Fig. 4, we can determine the equation of NH<sub>3</sub> line using the formula of a straight line,

$$y - y_1 = (y_2 - y_1)/(x_2 - x_1) \times (x - x_1) \quad (1)$$

where all the values are in log<sub>10</sub> from according to the datasheet, so from the datasheet, we take (x<sub>1</sub>, y<sub>1</sub>) = (10, 2.6) and (x<sub>2</sub>, y<sub>2</sub>) = (100, 1).

Thus, according to the Eq. (1), the NH<sub>3</sub> line equation will be

$$\begin{aligned} \log(y) - \log(2.6) &= [(\log(1) - \log(2.6))/(\log(100) - \log(10))] \\ &\times (\log(x) - \log(10)) \end{aligned} \quad (2)$$

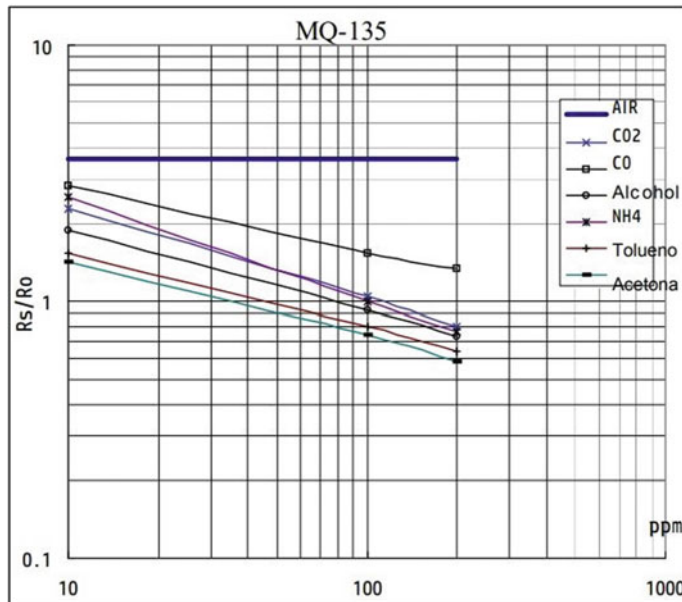


**Fig. 4** MQ135 different gases graph from the given datasheet [8]

Equation number (2) can be simplified as  $x(\text{gas})$  in the form of  $y$  and some constant terms.

$$x = (10)^{(2 - 2.41 \log(y))} \quad (2a)$$

where  $y$  is ( $Rs/Ro$ ), so the equation for  $\text{NH}_3$  concentration becomes

$$x = (10)^{(2 - 2.41 \log(Rs/Ro))} \quad (2b)$$

#### 4.1.2 Expression for Acetone

So from the datasheet, we obtain the points of  $(x_1, y_1) = (10, 1.5)$  and  $(x_2, y_2) = (100, 0.75)$ .

Thus, with according to the Eq. (1), the acetone line equation will be

$$\begin{aligned} \log(y) - \log(1.5) &= \left[ (\log(0.75) - \log(1.5)) / (\log(100) - \log(10)) \right] \\ &\times (\log(x) - \log(10)) \end{aligned} \quad (3)$$

Equation (3) can be simplified as follows:

$$x = (10)^{(1.58 - 3.3 \log(y))} \quad (3a)$$

where  $y$  is  $(Rs/Ro)$ , so the equation for acetone concentration becomes

$$x = (10)^{(1.58 - 3.3 \log(Rs/Ro))} \quad (3b)$$

#### 4.1.3 Expression for CO<sub>2</sub>

Two points  $(x_1, y_1) = (10, 2.4)$  and  $(x_2, y_2) = (100, 1.1)$  are obtained from datasheet. Thus, with according to the Eq. (1), the CO<sub>2</sub> line equation will be

$$\begin{aligned} \log(y) - \log(2.4) &= [(\log(1.1) - \log(2.4)) / (\log(100) - \log(10))] \\ &\times (\log(x) - \log(10)) \end{aligned} \quad (4)$$

Equation (4) can be simplified as follows:

$$x = (10)^{(2.124 - 2.958 \log(y))} \quad (4a)$$

where  $y$  is  $(Rs/Ro)$ , so the equation for CO<sub>2</sub> concentration becomes

$$x = (10)^{(2.124 - 2.958 \log(Rs/Ro))} \quad (4b)$$

#### 4.1.4 Expression for CO

The points  $(x_1, y_1) = (10, 2.9)$  and  $(x_2, y_2) = (100, 1.6)$  have been obtained from datasheet. Now according to the Eq. (1), the CO line equation will be

$$\begin{aligned} \log(y) - \log(2.9) &= [(\log(1.6) - \log(2.2)) / (\log(100) - \log(10))] \\ &\times (\log(x) - \log(10)) \end{aligned} \quad (5)$$

The Eq. (5) can be represented as follows:

$$x = (10)^{(2.792 - 3.876 \log(y))} \quad (5a)$$

where  $y$  is  $(Rs/Ro)$ , so the equation for CO concentration becomes

$$x = (10)^{(2.792 - 3.876 \log(Rs/Ro))} \quad (5b)$$

#### 4.1.5 Expression for Toluene

From the datasheet, we take the two points  $(x_1, y_1) = (10, 1.6)$  and  $(x_2, y_2) = (100, 0.8)$ .

Thus, with according to the Eq. (1), the toluene line equation will be

$$\begin{aligned} \log(y) - \log(1.6) &= [(\log(0.8) - \log(1.6)) / (\log(100) - \log(10))] \\ &\times (\log(x) - \log(10)) \end{aligned} \quad (6)$$

After simplification, the Eq. (6) can represent as follows:

$$x = (10)^{(1.678 - 3.322\log(y))} \quad (6a)$$

where  $y$  is  $(Rs/Ro)$ , so the equation for toluene concentration becomes

$$x = (10)^{(1.678 - 3.322\log(Rs/Ro))} \quad (6b)$$

## 4.2 MQ6 Sensor Calibrations for Detection of Different Gases

Figure 5 describes about the gas concentrations which are calculated by using the graph through the straight line equation. We can only detect the gases which are present on the above graph. We take two points for the line equations and put these two points on the line equation and calculate the concentration of gases. Here, we calculate the expression of gases like LPG,  $\text{CH}_4$ , and  $\text{H}_2$ .

#### 4.2.1 Expression for LPG

So from the datasheet shown in Fig. 6, we obtain the two points  $(x_1, y_1) = (200, 2)$  and  $(x_2, y_2) = (1000, 1)$ .

Thus, with according to the Eq. (1), the LPG line equation will be

$$\begin{aligned} \log(y) - \log(2) &= [(\log(1) - \log(2)) / (\log(1000) - \log(200))] \\ &\times (\log(x) - \log(200)) \end{aligned} \quad (7)$$

Simplifying the Eq. (7), we can get the value of  $x$ (gas) in the form of  $y$  and some constant terms, like..

$$x = (10)^{(3 - 2.325\log(y))} \quad (7a)$$

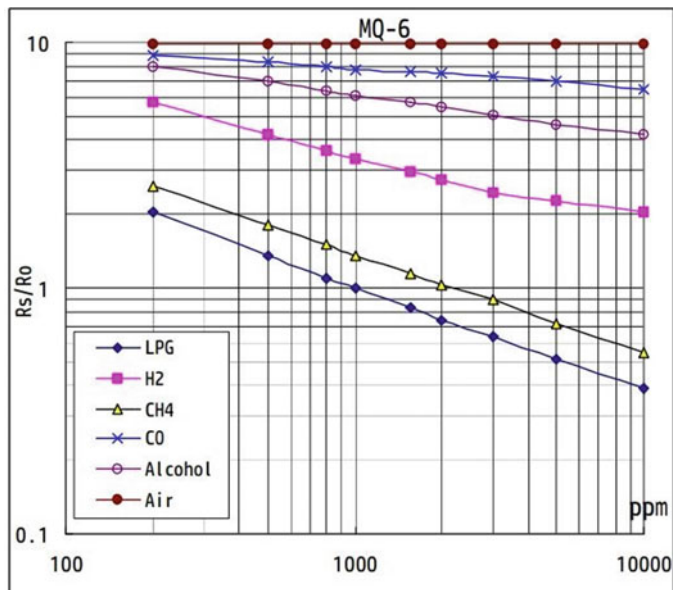


**Fig. 5** MQ6 sensor different gases graph from the datasheet [16]

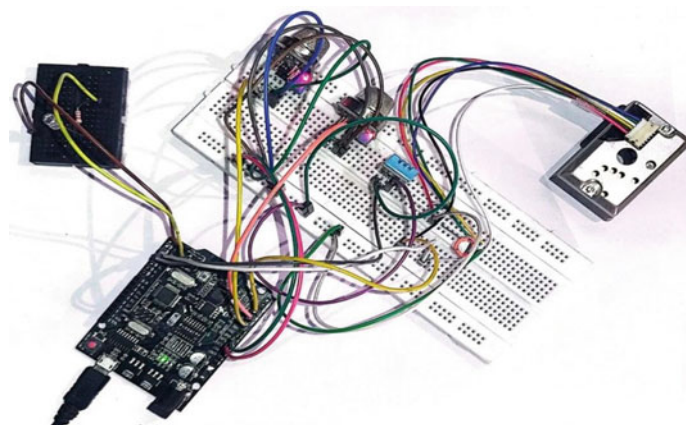


**Fig. 6** Snapshot of the proposed AQMS model

where  $y$  is  $(Rs/Ro)$ , so the equation for LPG concentration becomes

$$x = (10)^{(3 - 2.325 \log(Rs/Ro))} \quad (7b)$$

#### 4.2.2 Expression for CH<sub>4</sub>

From datasheet, we obtain two points  $(x_1, y_1) = (200, 2.5)$  and  $(x_2, y_2) = (1000, 1.5)$  for CH<sub>4</sub>. The expression for CH<sub>4</sub> is written as follows:

$$\begin{aligned} \log(y) - \log(2.5) &= [(\log(1.5) - \log(2.5)) / (\log(1000) - \log(200))] \\ &\times (\log(x) - \log(200)) \end{aligned} \quad (8)$$

Upon simplification of the Eq. (8), we can get the value of  $x$ (gas) in the form of  $y$  and some constant terms, like

$$x = (10)^{(3.55 - 3.125\log(y))} \quad (8a)$$

where  $y$  is (Rs/R<sub>o</sub>), so the equation for CH<sub>4</sub> concentration becomes

$$x = (10)^{(3.55 - 3.125\log(Rs/R_o))} \quad (8b)$$

#### 4.2.3 Expression for H<sub>2</sub>

Upon observing the characteristics line of hydrogen in the Fig. 6, we obtain the points  $(x_1, y_1) = (200, 5.9)$  and  $(x_2, y_2) = (1000, 3.3)$  for CH<sub>4</sub>. The expression for H<sub>2</sub> is written as follows:

$$\begin{aligned} \log(y) - \log(5.9) &= [(\log(3.3) - \log(5.9)) / (\log(1000) - \log(200))] \\ &\times (\log(x) - \log(200)) \end{aligned} \quad (9)$$

Upon simplification of the Eq. (9), we can get the value of  $x$ (gas) in the form of  $y$  and some constant terms, like..

$$x = (10)^{(4.44 - 2.77\log(y))} \quad (9a)$$

where  $y$  is (Rs/R<sub>o</sub>), so the equation for H<sub>2</sub> concentration becomes

$$x = (10)^{(4.44 - 2.77\log(Rs/R_o))} \quad (9b)$$

### 4.3 Calibration for Dust Sensor Density Calculation

Through the monitoring of the output voltage of the sensor [14] with respect to change of dust density in air, we can came up with the linear relationship between



**Fig. 7** Snapshot of Web dashboard using Blynk

the sensor output voltage and the dust density ( $D$ ) which is given as [1]:

$$D = 170 * V_{\text{out}} - 1 \quad (10)$$

## 5 Result and Discussion

### 5.1 Implementation of AQMS

Figure 6 represents the snapshot of our proposed AQMS system.

Figure 7 shows the Web dashboard snapshot using Blynk.

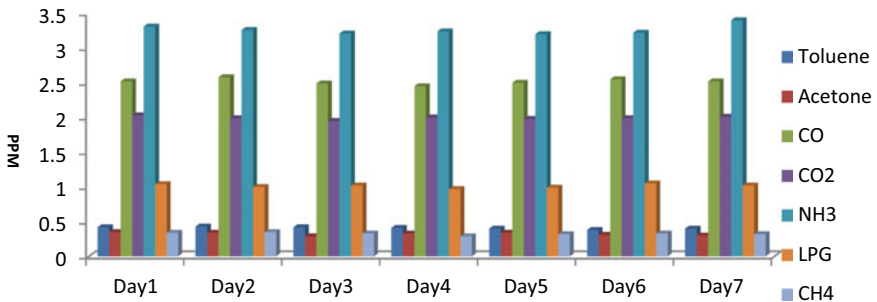
### 5.2 Observation

We have performed our experiment during one week time period, and the observation table is shown in Table 2. Measurement of gases concentration has been observed in Table 2 for duration of one week. All of the values are taken at the same time (@11AM) every day.

Observation of different gases concentration has been shown in Fig. 8 for duration of one week.

**Table 2** Measurement of gases concentration for a duration of one week

Parameters	Day1	Day2	Day3	Day4	Day5	Day6	Day7
Toluene (ppm)	0.42	0.43	0.42	0.41	0.4	0.38	0.4
Acetone (ppm)	0.35	0.34	0.29	0.33	0.34	0.31	0.3
CO (ppm)	2.52	2.58	2.49	2.45	2.5	2.55	2.52
CO <sub>2</sub> (ppm)	2.03	1.99	1.95	2	1.98	1.99	2.01
NH <sub>3</sub> (ppm)	3.31	3.26	3.21	3.24	3.2	3.22	3.4
LPG (ppm)	1.04	1	1.02	0.97	0.99	1.05	1.02
CH <sub>4</sub> (ppm)	0.34	0.35	0.33	0.29	0.32	0.33	0.32
PM <sub>2.5</sub> (ppm)	45.55	45.38	44.72	58.84	63.82	58.01	52.19
H <sub>2</sub> (ppm)	52.9	53.45	54.17	50.24	51.54	56.26	52.54
Temp (°C)	28.2	26.5	20	22	23.6	29	27.2
Humidity (%)	67	65	68	60	62	65	66

**Fig. 8** Different gases concentration

### 5.3 Comparison Table

Our proposed AQMS has been compared with two existing works which is shown in Table 3.

**Table 3** Comparison with existing works

Topics	Proposed work	Ref. [9]	Ref. [10]
Gas sensors	MQ135, MQ6	MQ7, MQ3, MQ135	MQ135
Temperature and humidity sensor	DHT11	–	DHT11
Dust sensor	SHARP GP2Y101	–	–
Cloud platform	Blynk	Ubidots	–

## 6 Conclusion and Future Work

In this work, an outdoor and indoor low-cost air quality monitoring sensor system are successfully developed and designed. This system utilizes a microcontroller board to obtain the concentration of different gases, relative humidity, temperature, and the dust particle present in the air. This system is portable, convenient, and cost effective for monitoring the gases anywhere. So this device is suitably employed for gas leakage detection and prevention in the hydrogen stations.

The proposed work can be improved in a variety of ways in the future. (1) Integration of more sensors which may provide the precise composition of all gases in the air. (2) Creation of a Webpage and uploading information to it with the date and time. (3) Connect a GPS module to the Website for the general public in order to track pollution at its specific location.

## References

1. Zhang H, Qi W, Hu Z, Song Y (2017) Planning hydrogen refueling stations with coordinated on-site electrolytic production. In: 2017 IEEE power & energy society general meeting. IEEE, pp 1–5
2. López-Rodríguez FM, Andruino-A1 CF (2016) Low-cost educational mobile robot based on Android and Arduino. *J Intell Robot Syst* 81:63–76. <https://doi.org/10.1007/s10846-015-0227-x>
3. Lo Re G, Peri D, Vassallo SD (2014) Urban air quality monitoring using vehicular sensor networks. In: Advances onto the Internet of Things. Springer, pp 311–323
4. Gaglio S, Lo Re G, Martorella G, Peri D, Vassallo SD (2014) Development of an IoT environmental monitoring application with a novel middleware for resource constrained devices. In: Proceedings of the 2nd conference on mobile and information technologies in medicine (MobileMed 2014)
5. Atanasovski V, Leon-Garcia A (2015) Future access enablers for ubiquitous and intelligent infrastructures, vol 8. Springer, Berlin
6. Kelly S, Suryadevara N, Mukhopadhyay S (2013) Towards the implementation of IoT for environmental condition monitoring in homes. *IEEE Sens J* 13(10):3846–3853
7. Kim JY, Chu CH, Shin S-M (2014) ISSAQ: an integrated sensing systems for real-time indoor air quality monitoring. *IEEE Sens J* 14(12):4230–4244
8. [https://www.electronicoscaldas.com/datasheet/MQ-135\\_Hanwei.pdf](https://www.electronicoscaldas.com/datasheet/MQ-135_Hanwei.pdf)
9. Dhingra S et al (2019) Internet of Things mobile–air pollution monitoring system (IoT-Mobair). *IEEE Internet of Things J* 6(3):5577–5584
10. Ayele TW, Mehta R (2018) Air pollution monitoring and prediction using IoT. In: 2018 second international conference on inventive communication and computational technologies (ICICCT). IEEE
11. <http://www.howmuchsnow.com/arduino/airquality/>
12. Zheng Y, Chen X, Jin Q, Chen Y, Qu X, Liu X, Chang E, Ma W-Y, Rui Y, Sun W (2014) A cloud-based knowledge discovery system for monitoring fine-grained air quality. Prep. Microsoft technical report. <http://research.microsoft.com/apps/pubs/default.aspx>
13. Kadri A, Yaacoub E, Mushtaha M, AbuDayya A. Wireless Sensor network for real-time air pollution monitoring. Qatar Mobility Innovations Centre (QMIC), Qatar Science and Technology Park, Doha, Qata
14. [https://www.sparkfun.com/datasheets/Sensors/gp2y1010au\\_e.pdf](https://www.sparkfun.com/datasheets/Sensors/gp2y1010au_e.pdf)

15. <https://www.mouser.com/datasheet/2/758/DHT11-Technical-Data-Sheet-Translated-Version-1143054.pdf>
16. <https://www.sparkfun.com/datasheets/Sensors/Biometric/MQ-6.pdf>

# Efficient and Novel Architecture of Golay Encoder and Decoder for McEliece Cryptosystem



Tirthadip Sinha and Jaydeb Bhaumik

**Abstract** As technology advances, it is projected that the development of a quantum computer may jeopardize various existing public key cryptosystems. The integrity and confidentiality of communications will be negotiated. Code-based cryptosystems are compatible with existing networks and communication protocols as well as secure against any attacks. Security and effectiveness are traded off in the use of code-based cryptography. In the first part of this work, a McEliece cryptosystem is successfully designed employing an extended Golay code. In the second part of this work, efficient encoder and decoder architecture for extended binary Golay code have been developed and employed after validating the proposed algorithm for McEliece cryptosystem. The synthesis results show that the proposed hardware structures for Golay code are superior to those already in use considering various performance metrics. High throughput, minimal latency and low area are achieved for both hardware modules. For secure high-speed communications, the proposed Golay encoder and decoder is a promising option in the McEliece cryptosystem.

**Keywords** Golay code · Encoder · Decoder · Architecture · McEliece cryptosystem

## 1 Introduction

It is anticipated that as technology develops, various existing public key cryptosystems could be compromised by the advancement of a quantum computer. The integrity and confidentiality of communications will be negotiated. Public key cryptosystems, which include the RSA, Diffie-Hellman, Elliptic curve cryptosystems and digital signature algorithm (DSA), have grown to be an essential part of cyber

---

T. Sinha (✉)  
HIT, Haldia, WB, India  
e-mail: [tirthadip.sinha@gmail.com](mailto:tirthadip.sinha@gmail.com)

J. Bhaumik  
JU, Kolkata, WB, India

security throughout the years. Given its potential use in breaking through numerous cryptosystems, including the RSA algorithm and elliptic curve cryptography [1], Shor's algorithm is popular in cryptography. Using Shor's method, any of these public key cryptosystems can be broken. Other significant categories of cryptosystems include those that use codes, lattices, hashes, multivariate quadratic equations and secret key. Security and effectiveness are traded off in the use of code-based cryptography. The objective of post-quantum cryptography is to create cryptosystems which are compatible with existing networks and communications protocols as well as secure against any attacks. The current status of various cryptosystems is shown in Table 1. Golay codes [2], which were developed in 1949, have seen extraordinary growth in recent years and implemented as a linear error-correcting code in communication links. Bit interleaving technology can be used with Golay codes to fix burst errors. McEliece [3] suggested an asymmetric encryption cryptosystem using Goppa codes in 1978, and it is still in use today due to its uncrackable security criteria. By employing alternate error-correcting codes, such as convolutional, low-density parity check (LDPC) or algebraic geometric codes (AGC) in place of Goppa codes, many scholars developed improved McEliece cryptosystems. All of these plans have turned out to be vulnerable later. The comparison of different codes used in cryptosystem is shown in Table 2. A McEliece cryptosystem using extended Golay code is implemented in the first part of this work.

There are many different encoding-decoding techniques available. Although [7–9] deal with many algorithms, hardware implementation is not possible with these due to higher complexity. For hardware implementation, linear feedback shift register (LFSR)-based [10–13] approaches are suitable, although they are not acceptable due to high latency and less throughput. CRC-based hardware implementation is suggested in [14]. Several hardware architectures [15–19] have been developed based on various Golay code decoding methods. Efficient encoder and decoder architecture is presented for extended Golay code in the second part of this work. The synthesis outcomes demonstrate that the proposed architectures for Golay codes are superior to those already in use.

**Table 1** Current status of various cryptosystems [4]

Cryptographic algorithm	Year of introduction	Impact of quantum computing
Diffie-Hellman	1976	Cracked
RSA	1978	
McEliece	1978	Not cracked
Niederreiter	1986	
Elliptic curve	1987	
Buchmann-Williams	1988	
Sidelnikov	1994	
NTRU	1998	
Lattice-based	1998	

**Table 2** Comparison of different codes used in cryptosystem [5, 6]

Codes	Parameter	Merits	Observations
Hammimg	Security	2 bit error detection and 1 error bit correction	Fail to detect uncorrected errors
Reed-Solomon		Multiple symbol errors detection and correction	Non-binary cyclic code
Reed-Muller		Multiple bit errors detection and correction	Low transmission rate
Convolutional		Appropriate for large data	Computational and decoding complexity is high
Turbo		Performs well at low SNR and uses interleaver to reduce burst errors	Decoding complexity and latency is high; poor performance at low BER
LDPC		Performs well and attains near Shannon capacity	High complexity
Polar		Performs well for short blocklengths and attains near Shannon capacity	High complexity
Golay		Detect 7 bit error and correct 3 error bits	Low complexity

The rest of this paper is organized in the given fashion. Overview of Golay coding is briefly introduced in Sect. 2. McEliece cryptosystem implementing extended Golay code is presented in Sect. 3. Proposed encoder and decoder design for extended Golay code is shown in Sect. 4. The synthesis outcomes are provided and compared in Sect. 5. In Sect. 6, conclusions are drawn.

## 2 Golay Codes

Ternary and binary Golay codes are two different types of Golay codes. In addition, binary Golay codes are classified into perfect binary and extended versions. The perfect binary Golay code is denoted as  $(23, 12, 7)$  that describes 23 bits codeword length, 12 bits information length and Hamming distance of 7 bits or error detection of 7 bits with error correction ability of any 3 bits. One of the following generator polynomials produces the perfect binary Golay code and they are  $g_1(X) = 1 + X^2 + X^4 + X^5 + X^6 + X^{10} + X^{11}$  and  $g_2(X) = 1 + X + X^5 + X^6 + X^7 + X^9 + X^{11}$ . These polynomials can produce the same cycle codewords since they are reversible of one another. Thus, the perfect binary Golay code can be produced using a  $12 \times 23$  generator matrix  $G_{23} = [I, B_{23}]$ , where  $I$  is  $12 \times 12$  identity matrix and  $B_{23}$  is  $12 \times 11$  matrix.

$$B_{23} = \begin{bmatrix} 0 & 1 & 1 & 1 & 1 & 1 & 1 & 1 & 1 & 1 & 1 & 1 \\ 1 & 1 & 1 & 0 & 1 & 1 & 1 & 0 & 0 & 0 & 1 \\ 1 & 1 & 0 & 1 & 1 & 1 & 0 & 0 & 0 & 1 & 0 \\ 1 & 0 & 1 & 1 & 1 & 0 & 0 & 0 & 1 & 0 & 1 \\ 1 & 1 & 1 & 1 & 0 & 0 & 0 & 1 & 0 & 1 & 1 \\ 1 & 1 & 1 & 0 & 0 & 0 & 1 & 0 & 1 & 1 & 0 \\ 1 & 1 & 0 & 0 & 0 & 1 & 0 & 1 & 1 & 0 & 1 \\ 1 & 0 & 0 & 0 & 1 & 0 & 1 & 1 & 0 & 1 & 1 \\ 1 & 0 & 0 & 1 & 0 & 1 & 1 & 0 & 1 & 1 & 1 \\ 1 & 0 & 1 & 0 & 1 & 1 & 0 & 1 & 1 & 1 & 0 \\ 1 & 1 & 0 & 1 & 1 & 0 & 1 & 1 & 1 & 0 & 0 \\ 0 & 0 & 1 & 1 & 0 & 1 & 1 & 1 & 0 & 0 & 0 \end{bmatrix}$$

To generate extended Golay code (24,12,8), a parity bit is added to the binary Golay code (23,12,7). The parity bit is zero if binary Golay codeword has even weight, otherwise parity bit is 1. The extended Golay code also has error detection of 7 bits with error correction upto 3 bits for 12 bit message length having a codeword of 24 bits. Extended Golay codes were employed for error correction on the Voyager spacecraft missions in 1977. The  $12 \times 24$  generator matrix  $G_{24} = [I, B_{24}]$  produces the extended Golay code, where  $I$  is  $12 \times 12$  identity matrix and  $B_{24}$  is  $12 \times 12$  matrix.

$$B_{24} = \begin{bmatrix} 1 & 1 & 0 & 1 & 1 & 1 & 0 & 0 & 0 & 1 & 0 & 1 \\ 1 & 0 & 1 & 1 & 1 & 0 & 0 & 0 & 1 & 0 & 1 & 1 \\ 0 & 1 & 1 & 1 & 0 & 0 & 0 & 1 & 0 & 1 & 1 & 1 \\ 1 & 1 & 1 & 0 & 0 & 0 & 1 & 0 & 1 & 1 & 0 & 1 \\ 1 & 1 & 0 & 0 & 0 & 1 & 0 & 1 & 1 & 0 & 1 & 1 \\ 1 & 0 & 0 & 0 & 1 & 0 & 1 & 1 & 0 & 1 & 1 & 1 \\ 0 & 0 & 0 & 1 & 0 & 1 & 1 & 0 & 1 & 1 & 1 & 1 \\ 0 & 0 & 1 & 0 & 1 & 1 & 0 & 1 & 1 & 1 & 0 & 1 \\ 0 & 1 & 0 & 1 & 1 & 0 & 1 & 1 & 1 & 0 & 0 & 1 \\ 0 & 1 & 0 & 1 & 1 & 0 & 1 & 1 & 1 & 0 & 0 & 1 \\ 1 & 0 & 1 & 1 & 0 & 1 & 1 & 1 & 0 & 0 & 0 & 1 \\ 0 & 1 & 1 & 0 & 1 & 1 & 1 & 0 & 0 & 0 & 1 & 1 \end{bmatrix}$$

### 3 McEliece Cryptosystem Employing Extended Golay Code

The McEliece cryptosystem generates public and private keys using a linear error-correcting code. The error-correcting code in the McEliece cryptosystem is binary Goppa code [3]. The different alternative codes can be used to determine the secret key. Several variants of the McEliece cryptosystem were put forth employing different secret codes. McEliece cryptosystem using extended Golay code functions similarly to the standard McEliece cryptosystem using Goppa code, however it creates the secret matrix  $G$  in a different fashion and employs different decoding methods. The second row of the cyclic Golay coding matrix  $B$  is created by shifting the first component to the last location. Similar to this, every row of matrix  $B$  may be created by right-shifting the row before it, with the exception of the final row. The matrix  $B$  is a component of the extended Golay code's generator and parity check matrices, and its decoding is fairly straightforward. As long as  $S$  is the selected sparse random matrix, the constructed system is efficient and secure. Each codeword can have up to 3 bit errors corrected. It can be compressed significantly and is effective thanks to sparse matrices. Additionally, a finite state machine is developed for the decoding part and used extended Golay code to create the McEliece cryptosystem. McEliece cryptosystem using extended binary Golay code is tested by MATLAB program and the description of the extended Golay code-based McEliece cryptosystem's detailed algorithm is given below. Figure 1 depicts the McEliece cryptosystem based on extended Golay code.

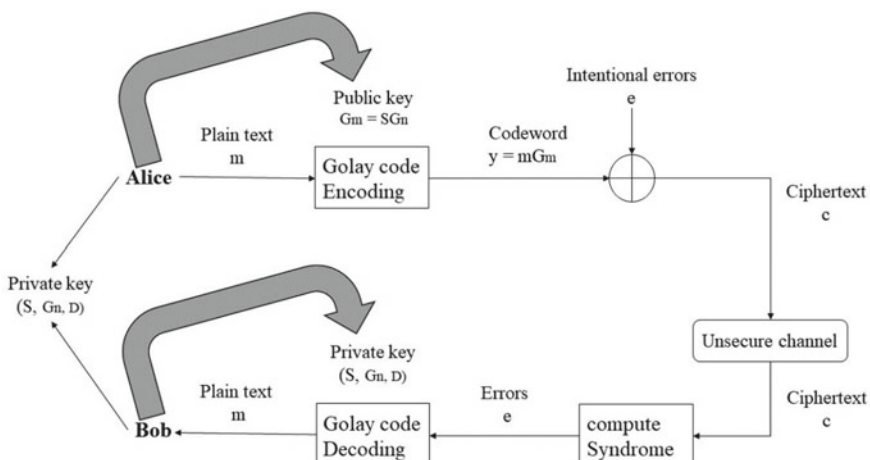


**Fig. 1** McEliece cryptosystem implementing extended Golay code

**Algorithm 1** Key generation**Parameter:**

$F$  = family of  $t$ -error-correcting  $(n,k,d)$  codes with  $t < n$ ;

$S$  = non-singular invertible matrix;

Public key:  $G_m$ ; Private key:  $(S, G_n, D)$ ;  $D$  = efficient decoding algorithm

**Input:**

Extended Golay code  $(24,12,8)$  with message length  $k = 12$  bit, codeword length  $n = 24$  and  $t = 3$  bit error correction ability

**Output:**

- 1) Generate  $k \times n$  generator matrix  $G \leftarrow [I, B]$
- 2) Generate  $n \times n$  permutation matrix  $P$  having exactly 1 in each row & column with other entries as 0
- 3) Compute  $G_1 \leftarrow GP$
- 4) Arrange  $G_1$  in systematic format of generator matrix;  $G_n \leftarrow G_1$
- 5) Generate  $S \in F^{k \times k}$
- 6) Compute  $G_m \leftarrow SG_n$
- 7) Return  $G_m$  &  $(S, G_n, D)$

**Algorithm 2** Encoding**Parameter:**

$G_m$  = Public key;  $m$  = Message;  $e$  = Error vector;  $c$  = Ciphertext

**Input:**

- 1)  $G_m \in F^{k \times n}$
- 2)  $m \in F^k$
- 3)  $e \in F^n$

**Output:**

- 1) Compute codeword  $y \leftarrow mG_m$
- 2) Compute  $c \leftarrow y + e$
- 3) Return  $c$

**Algorithm 3** Decoding**Parameter:**

Private key =  $(S, G_n, D)$ ;  $m$  = Message;  $e$  = Error vector;  $c$  = Ciphertext

**Input:**

- 1)  $(S, G_n, D)$
- 2)  $c \in F^n$

(continued)

(continued)

---

**Output:**

- 1) Calculation of  $e$  by calling subroutine D ( $c, G_n$ )
  - 2) Compute encoded message  $y_1 \leftarrow c + e$
  - 3) Compute  $y_1 \leftarrow mSG_n + e$
  - 4) Compute  $mS$  by row reducing  $[G_n' | (mSG_n)']$
  - 5)  $m \leftarrow (mS)S^{-1}$
  - 6) Return  $m$
- 

**Algorithm 4** Subroutine D ( $c, G_n$ )

---

**Parameter:**

Generator matrix (Private) =  $G_n$ ;  $e$  = Error vector;  $c$  = Ciphertext;  
 $l_i$  = the word of length 12 with 1 in  $i$ th place and 0 elsewhere in I matrix

---

**Input:**

- 1)  $G_n$
  - 2)  $c \in F^n$
- 

**Output:**

- 1) Compute first syndrome  $S_1 \leftarrow cG_n$
  - 2) If weight( $S_1$ )  $\leq 3$ , Return  $e \leftarrow [S_1, 000000000000]$
  - 3) Else If weight( $S_1 + B_i$ )  $\leq 2$ , Return  $e \leftarrow [S_1 + B_i, l_i]$
  - 4) Else Compute second syndrome  $S_2 \leftarrow S_1B$
  - 5) If weight( $S_2$ )  $\leq 3$ , Return  $e \leftarrow [000000000000, S_2]$
  - 6) Else If weight( $S_2 + B_i$ )  $\leq 2$ , Return  $e \leftarrow [l_i, S_2 + B_i, ]$
- 

## 4 Proposed Design for Extended Golay Code

### 4.1 Proposed Encoding Structure

Figures 2, 3 and 4 depict optimized structures for encoders. The entire structure is split into two sections, one displaying the generation of G23 and the other the transformation from G23 to G24.

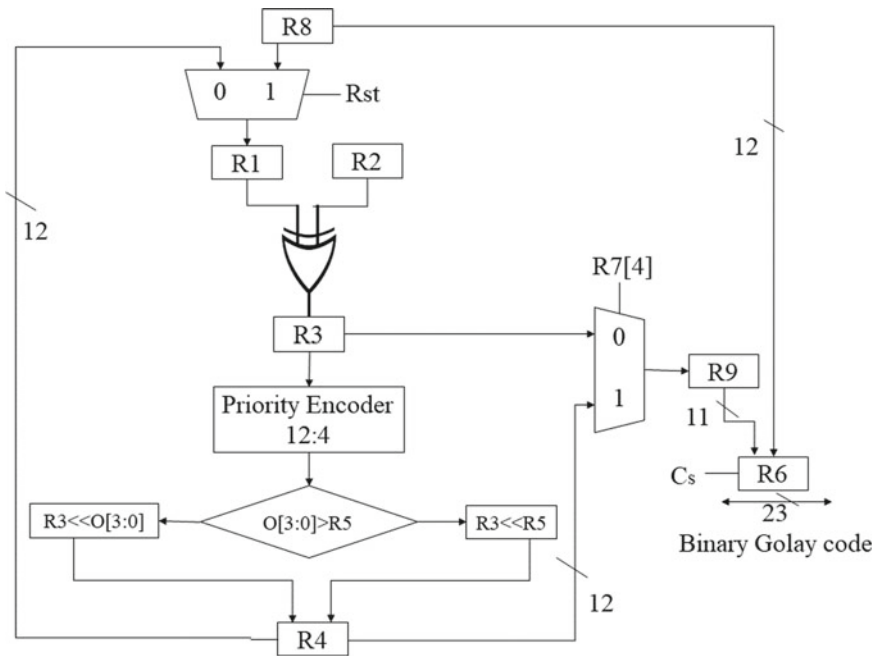


**Fig. 2** Proposed structure for producing binary Golay code

**Fig. 3** Proposed structure for iteration control unit

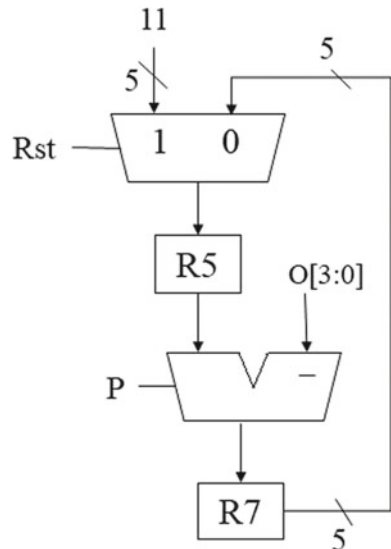
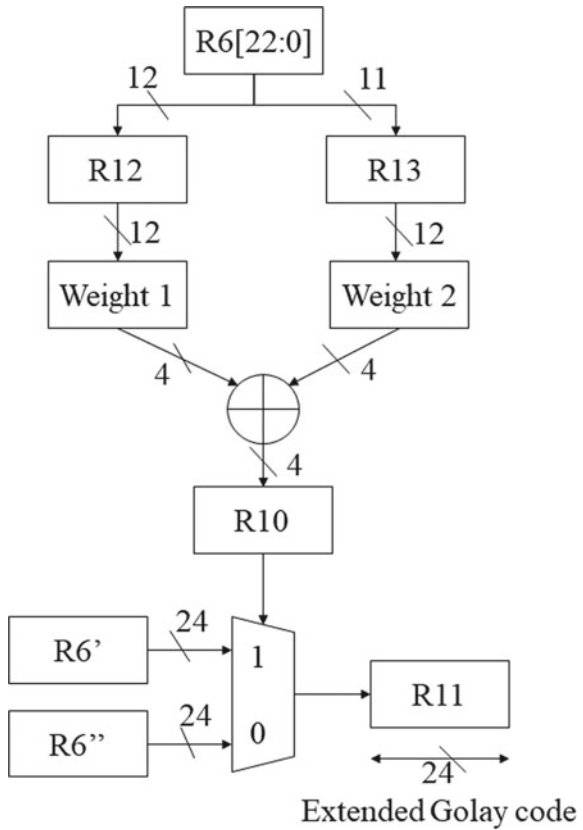


**Fig. 4** Proposed structure for extended Golay code generation from binary Golay code



## 4.2 Proposed Decoding Structure

Assume that  $e$  represents the error pattern,  $b_i$  is the  $i$ th row of  $B_{24}$ , and  $y$  is the received codeword. Due to the potential of two parity check matrices (either  $[I|B]$  or  $[B|I]$ ), two syndromes ( $S$  and  $SB$ ) are feasible.

### (i) Syndrome measurement unit

By multiplying the received codeword  $r$  with the parity check matrix  $H$ , syndrome  $S$  is assessed. As a result, the following is the logical statement for computing the MSB bit of syndrome vector:

$$\begin{aligned}
 S[11] &= r[23] \text{ } XOR \text{ } r[11] \text{ } XOR \\
 &r[10] \text{ } XOR \text{ } r[8] \text{ } XOR \text{ } r[7] \text{ } XOR \\
 &r[6] \text{ } XOR \text{ } r[2] \text{ } XOR \text{ } r[0].
 \end{aligned}$$

The logical statement above can be used to determine other bits of the syndrome measuring unit. Figure 5 depicts the delay optimization construction for the  $S[11]$  bit of the syndrome vector.

### (ii) Weight measurement unit

Utilizing weight measurement units, one may determine how many binary 1 s are there in the sequence. Figure 6 depicts the structure of a weight measurement unit.

### (iii) $s + b_i$ and $\text{SB} + b_i$ calculation and selection

By flipping part of the bits in registers S and SB or leaving them unaltered, this unit computes  $S + b_i$  and  $\text{SB} + b_i$  ( $1 \leq i \leq 12$ ).  $S + b_1$ 's logical contents are given by

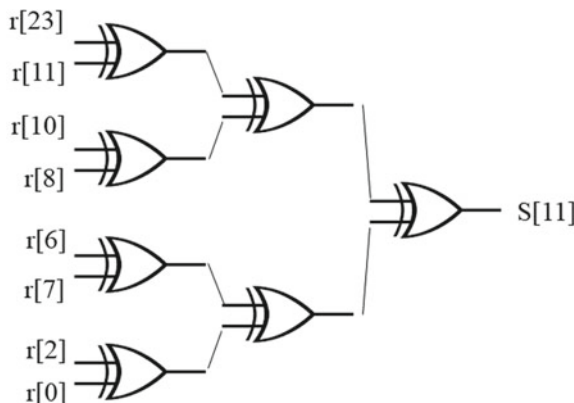


**Fig. 5** Syndrome measurement unit

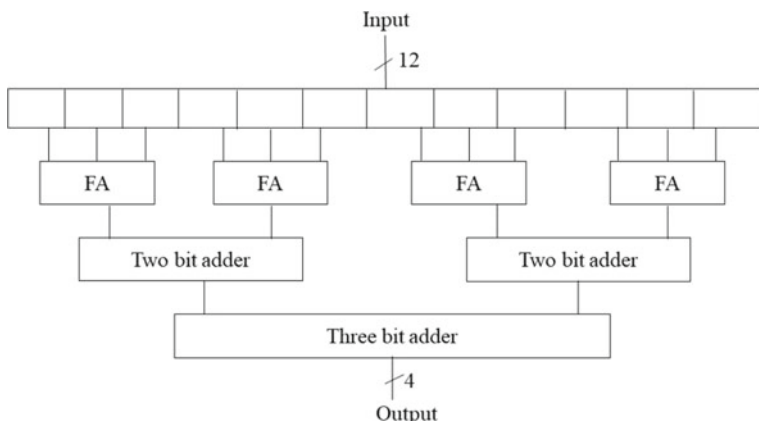
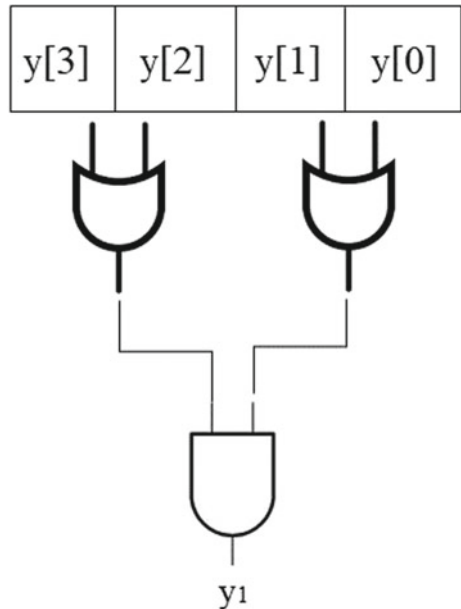


**Fig. 6** Weight measurement unit

**Fig. 7** Construction to evaluate the weight constraint



$$S + b_1 = \left\{ \begin{array}{l} \sim S[11], \sim S[10], S[9], \\ \sim S[8], \sim S[7], \sim S[6], S[5], S[4], S[3], \\ \sim S[2], S[1], \sim S[0] \end{array} \right\}$$

where symbol  $\sim$  stands for logical NOT.

$S$  is switched out for SB in each expression to calculate  $SB + b_i$ . According to the logic stated in Figs. 7, 8 and 9,  $S + b_i$  or  $SB + b_i$  is chosen for weight  $\leq 2$ .

## 5 Synthesis Results of Golay Encoder and Decoder

Utilizing the Xilinx ISE tool, the structure of the Golay encoder and decoder has been built on the Field Programmable Gate Array (FPGA)-based vertex 4 platform. Contrary to [10], Table 3 shows that the suggested encoder architecture does not have any additional clocking mechanisms, which minimizes both area and power consumption. Additionally, as opposed to the 23 clock cycles shown in [10], the proposed architecture's latency is 12 clock cycles. Table 4 demonstrates that the proposed encoder architecture outperforms existing in terms of LUT usage percentage while retaining the same latency. Comparison of LUT, Slices or Area and Synthesized frequency of proposed encoder architecture with existing is shown in Table 5. The designed encoder architecture can handle MSB messages with '0' and '1' inputs, which is crucial for error-correcting codes. The implementation results,

**Fig. 8** Priority encoder for producing the multiplexer's selection signal

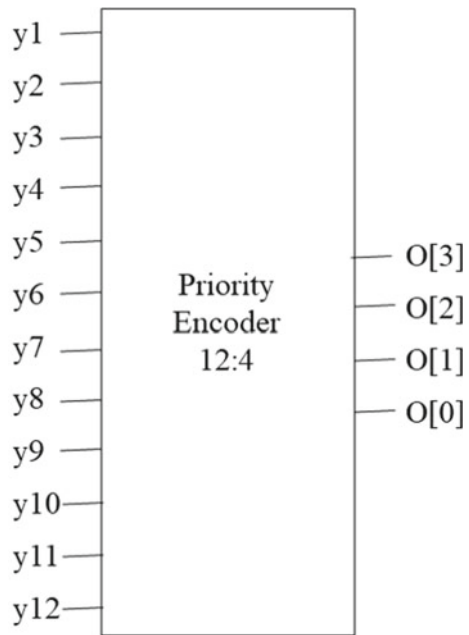
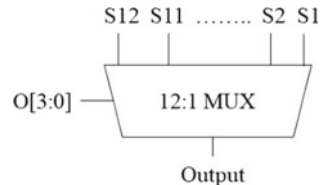


**Fig. 9** Multiplexer to choose a register that adheres to the weight constraint



which came at a acceptable area and delay time overhead, confirmed the accuracy of the designed architecture.

Table 6 compares the throughput and latency metrics. The proposed decoder design is promising for systems with high data rates. Table 7 demonstrates that the proposed decoder design uses resources more efficiently and operates more quickly

**Table 3** Comparison of the Golay encoder structure's clocking and latency mechanisms

Reference	Latency (clock cycles)	Clocking mechanism
[10]	23	System clock + clock doubler
[14]	12	System clock
[18]	12	
Proposed	12	

**Table 4** Comparison of LUT utilization and latency of Golay encoder structure

Reference	LUT utilization (%)	Latency (clock cycles)
[11]	1.33	12
[12]	1.72	12
[15]	1.42	12
[14]	0.14	12
Proposed	0.05	12

**Table 5** Comparison of the Golay encoder structure's LUT, slices and synthesized frequency

Reference	Number of LUT	Number of slices (Area)	Synthesized frequency (MHz)
[14]	187	103	238.575
[18]	149	85	380.967
[19]	191	102	162.425
Proposed	119	73	344.827

**Table 6** Latency and throughput comparison of Golay decoder structure

Reference	Latency (clock cycles)	Throughput
[16]	576	1 output/ 144 clock cycle
[17]	48	1 output/ 24 clock cycle
[14]	27	1 output/ clock cycle
[18]	24	
Proposed	24	

than existing available works. Comparison of LUT, Slices or Area and Synthesized frequency of proposed decoder architecture with existing is shown in Table 8.

**Table 7** Comparison of slices utilization and synthesized frequency of Golay decoder structure

Reference	Slices utilization (%)	Synthesized frequency (MHz)
[15]	2.3	217.3
[14]	1.9	195.08
Proposed	0.5	318.47

**Table 8** Comparison of LUT, slices (Area) and synthesized frequency of Golay decoder structure

Reference	Number of LUT	Number of slices (Area)	Synthesized frequency (MHz)
[14]	785	230	195.08
[18]	113	60	220.6
Proposed	121	56	318.47

## 6 Conclusion

Efficient hardware structure for extended binary Golay code have been developed and employed after validating the proposed algorithm for McEliece cryptosystem. The shortcomings of the existing architectures are omitted by the proposed structures and outperforms in terms of synthesis results considering various performance metrics. High throughput, minimal latency and low area are achieved for both hardware modules. For secure high-speed communications, the proposed Golay encoder and decoder is a promising option in the McEliece cryptosystem.

## References

- Chen L, Chen L, Jordan S, Liu Y-K, Moody D, Peralta R, Perlner R, Smith-Tone D (2016) Report on post-quantum cryptography. US Department of Commerce, National Institute of Standards and Technology
- Golay MJE (1949) Notes on digital coding. In: Proceedings IRE, vol 37. pp 657
- McEliece RJ (1978) A public-key cryptosystem based on algebraic Coding Thv 4244:114–116
- Bernstein DJ (2009) Introduction to post-quantum cryptography. In: Post-quantum cryptography. Springer, pp 1–14
- Sinha T, Bhaumik J (2020) Performance analysis of CRC-aided Polar codes with SCL decoding algorithm for the binary deletion channel. In: Proceedings 2nd international conference communication, devices and computing, Lecture notes in electrical engineering (LNEE), vol 602. Springer, Singapore, pp 13–23
- Sinha T, Nayek S, Bhaumik J (2020) On relative performances and decoding of CRC concatenated polar codes with different lists for solid state drives. In: Proceedings 2nd international conference communication, devices and computing, Lecture Notes in Electrical Engineering (LNEE), vol. 602. Springer, Singapore, pp 377–389
- Peng XH, Farrell PG (2006) On construction of the (24, 12, 8) Golay codes. IEEE Trans Inf Theory 52(8):3669–3675
- Honary B, Markarian G (1993) New simple encoder and trellis decoder for Golay codes. Electron Lett 29(25):2170–2171
- Classon BK (2001) Method, system, apparatus, and phone for error control of Golay encoded data signals. U.S.Patent 6 199 189
- Weng MI, Lee LN (1983) Weighted erasure codec for the (24, 12) extended Golay code. U.S.Patent 4 397 022
- Sprachmann M (2001) Automatic generation of parallel CRC circuits. IEEE Des Test Comput 18(3):108–114
- Campobello G, Patane G, Russo M (2013) Parallel CRC realization. IEEE Trans Comput 52(10):1312–1319
- Nair R, Ryan G, Farzaneh F (1997) A symbol based algorith for hardware implementation of cyclic redundancy check(CRC). In: Proceedings VHDL international users forum, pp 82–87
- Sarangi S, Banerjee S (2015) Efficient hardware implementation of encoder and decoder for Golay code. IEEE Trans VLSI 23(9):1965–1968
- Alimohammad A, Fard SF (2014) FPGA-based bit error rate performance measurement of wireless systems. IEEE Trans Very Large Scale Integr (VLSI) Syst 22(7):1583–1592
- Abbaszadeh AD, Rushforth CK (1988) VLSI implementation of a maximum-likelihood decoder for the Golay (24, 12) code. IEEE J Sel Areas Commun 6(3):558–565
- Adde P, Bidan R Le (2012) A low-complexity soft-decision decoding architecture for the binary extended Golay code. In: Proceedings 19th IEEE international conference electronics, circuits, systems (ICECS), pp 705–708

18. Bhoyar P (2016) Design of encoder and decoder for Golay code. In: 2016 International conference communication signal process (ICCSP), pp 1491–1495
19. Nazeri M, Rezai A, Azis H (2018) An efficient architecture for golay code encoder. In: 2018 2nd East Indonesia conference on computer and information technology (EIConCIT), pp 114–117

# Blockchain-Based Dynamic Pricing Framework for Electric Vehicle Charging



Brijmohan Lal Sahu and Preeti Chandrakar

**Abstract** The number of electric vehicle purchases has grown recently. Electric vehicles (EVs) use electricity as fuel which directly impacts the amount of carbon emission. In EVs, the carbon emission is negligible, and now, governments are promoting the use of EVs. Batteries used in EVs require some time to charge after discharging. As the number of EVs grows, the huge demand for electricity at a particular time, like office or school time, creates a problem for power grids. For charging stations, it is challenging to handle such demand and satisfy all EVs. The slow charging rate and long waiting time for EVs become a huddle. This paper proposes a duration-based charging and penalty mechanism inspired by the Stackelberg game model to counter the issue of long waiting times and balance the sudden increase in electricity demand. By controlling the demand, grid stability can be achieved. The numerical analysis shows that the EV has to pay a fixed price for a fixed duration. Beyond that duration, a penalty has to be paid by the EV. The smart contract-based blockchain protocol acts as a neutral intermediate between EVs and charging stations. To create a transparent and safe environment for energy transactions, Ethereum blockchain-based smart contract solution is proposed. This paper illustrates the significance of the blockchain for transaction transparency and reliability on the network, as well as preserving the private information of network participants.

**Keywords** Blockchain · Dynamic pricing · Electric vehicle · Power grid · Smart contract

---

B. L. Sahu · P. Chandrakar (✉)

Department of Computer Science and Engineering, National Institute of Technology, Raipur, India  
e-mail: [pchandrakar.cs@nitrr.ac.in](mailto:pchandrakar.cs@nitrr.ac.in)

B. L. Sahu  
e-mail: [blsahu.phd2020.cse@nitrr.ac.in](mailto:blsahu.phd2020.cse@nitrr.ac.in)

## 1 Introduction

The entire physical structure and infrastructure are changing because of the quick growth of huge data and Internet technologies. The issues caused by the usage of the centralized system can be resolved with the help of a decentralized blockchain system. Blockchain technology is a well-known building block of cryptocurrencies (like Bitcoin) [1] but has many other potential applications [2–5]. Blockchain is mainly a peer-to-peer distributed ledger that is cryptographically secure and immutable, which means very difficult to change, easily verifiable, and can only be added after consensus among its users. The number of electric vehicles is growing daily. To charge electric vehicles, numerous charging stations are being constructed. The issue arises when more users demand full charge of their vehicles during a specific time. The load on the grid will rise, resulting in a power crisis. In the future, electric vehicles will experience a charge shortage and high electricity prices. In the existing system, EV users control demand, resulting in a high load on charging stations and power grids. The demand for charging at charging stations proliferates during office and school time, which impacts power generation and storage on the power grid. Also, the waiting time at the charging station increases as charging a vehicle for a high quantity requires higher time. This paper aims to minimize the waiting time for electric vehicles at charging stations, enhance the charging experience, and secure transactions to build trust in the energy network. Serve the maximum number of electric vehicles in a short time span so that the long waiting vehicles at the charging station can be controlled.

### 1.1 Research Contribution

The objectives of this paper are as follows:

1. Control the demand for power during higher demand times by imposing penalties for overtime charging. Doing so will minimize the waiting time for another vehicle, waiting for charging. As a result the demand pressure on the power grid will also reduce.
2. Enhance the efficiency of the existing electricity trading in the energy network using blockchain and make all transactions secure and transparent. EV charging infrastructure could be further boosted if blockchain is integrated into the energy system.
3. Smart contract for unbiased transactions and automated execution of requests.

## 1.2 Paper Organization

The rest of the paper is structured as follows. Section 2 presents the related work. Section 3 describes the blockchain-enabled dynamic pricing mechanism along with the proposed system model. Section 4 explains the results. Finally, we conclude the paper in Sect. 5.

## 2 Related Work

Blockchain is also reforming many different domains, including banking, education, law, and energy section. Many other researchers are trying to infuse blockchain into electric vehicular networks to make them better. Electric vehicles outperform traditional vehicles in terms of energy conservation, emission reduction, and lowering reliance on fossil fuels [6]. A decentralized tamper-proof authentication mechanism using a smart contract for the mobile vehicular network [7]. To reduce the power demand pressure on the power grid, several other renewable sources are also used to get power at charging stations. P2P energy trading is promoted and secured by the blockchain to make it happen [8]. The prosumers create a community of prosumers then can supply to the charging stations or they can supply individually or can sell it to the power grid [12]. A consensus mechanism for V2V energy trading in the vehicular network has been designed using blockchain and deployed in the Internet of electric vehicles to reduce buyers costs and increase the utility of seller. Many experts have been looking into ways to protect EV users' privacy in recent years [10, 13]. Different encryption methods and hash values research in cryptography has all been used to secure the personal information of EV users. When an EV needs to be charged, its owner creates a charging request to charge service providers or charging stations. Authors in [11] applied smart contracts for energy trading in EVN to create an automated bias-free environment for all EVs. Also, provide privacy to all the network members for secure transactions and transparency [14]. The power demand varies throughout the day and night. Residential areas, industries, and educational institutes have a special pattern of power consumption which grows and falls during different periods of day and night. The power demand also depends on temperature, humidity, and season in different area shown by authors in [9]. As the driving fuel in EVs is electricity it also consumes electricity. The pressure on the power grid and power network increase when all the power-consuming areas demand power simultaneously. Authors [16] proposed a method using blockchain, along with a zero-sum game-based dynamic pricing scheme for charging electric vehicles. Table 1 summarizes the related work, majorly stating objectives, contributions, pros, cons, and other parameters.

**Table 1** Current state-of-the-art blockchain-based approaches

Ref.	Year	Objective	1	2	3	4	5	Pros.	Cons.
[9]	2016	To understand the power demand during day and night	N	Y	N	N	N	Analyze the residential power consumption and factors affecting it	Only residential power consumption is analyzed, electric vehicle consumption is not considered
[10]	2018	To provide transaction security in smart grid energy trading without relying on trusted third parties	Y	Y	N	N	A secure transaction framework	No dynamic pricing	No dynamic pricing
[11]	2019	To develop smart contract-based charging station system	Y	Y	N	Y	Energy trading system using smartcontract is proposed for electric vehicles	Charging station charging and dynamic pricing is not included	(continued)

**Table 1** (continued)

Ref.	Year	Objective	1	2	3	4	5	Pros.	Cons.
[12]	2020	To understand the latest state-of-the-art system in peer-to-peer electricity network	N	N	N	N	Y	Summarized work of many state-of-the-art systems	Theoretical information only
[13]	2020	To create a secure authentication framework using zero knowledge proof	Y	Y	N	Y	Secure communication system is proposed for electric vehicles	Dynamic charging pricing is not considered	
[14]	2020	Developing a secure blockchain-based privacy preservation system for charging station selection	Y	Y	N	Y	A secure blockchain-based privacy preservation system is proposed for charging station selection	Electric vehicle charging is not the considered	(continued)

**Table 1** (continued)

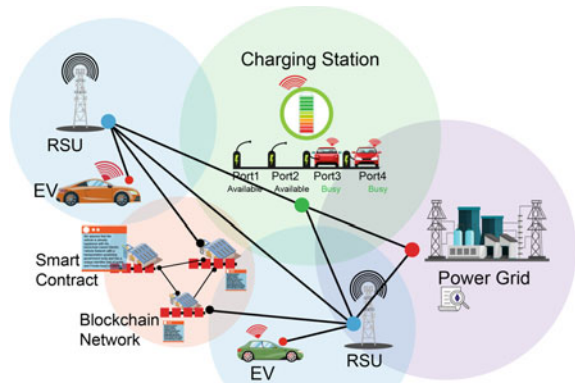
Ref.	Year	Objective	1	2	3	4	5	Pros.	Cons.
[15]	2022	To create a consensus mechanism for blockchain-enabled v2v energy trading	Y	Y	N	Y	Y	No dynamic pricing	Proof-of-reputation based consensus mechanism
[16]	2022	To develop a zero-sum game-based dynamic pricing	Y	Y	Y	Y	Y	6G communication network is considered	Zero-sum game-based dynamic pricing scheme is proposed

1 : Encryption key, 2 : Smart contract, 3 : Framework, 4 : Dynamic pricing, 5 : Electric vehicle, Y : yes and N : no

### 3 System Description

In this section, we will explain the entire vehicular energy network (VEN) model, as shown in Fig. 1. The components of the network model are trusted authority (TA), EVs, charging stations, power grid, RSUs, and Ethereum blockchain smart contracts. In our work, we have created a TA who is responsible for creating a digital certificate for the EVs and also controls the duration of validation of the digital certificate generated. The power grid is the source of electricity, EVs are the consumers in this network, and charging stations are the distributors of power generated at the power grid. Blockchain is the digital ledger used to record the demand and supply of electricity; smart contract makes it automated and transparent. The EVs make charging requests, and the charging stations give responses. The response of the charging station depends on the electricity available at the charging station and the demand load on the charging station. The RSUs are connecting links to bind all the network components together. The charging price varies over the duration as per the power load on the charging station. The TA also handles the deployment of the smart contract, and the smart contract monitors all the requests and responses in the network. The smart contract keeps a record of registered EVs and charging stations. Smart meters are used to check the charging status of the EVs and how much charge they are getting from the charging station. We have applied a modified version of the Stackelberg game theory to restrict the EVs power demand during the high demand time. Here, the charging station is acting as the leader, while the electric vehicles are the followers, adhering to the leader's instructions.

**Fig. 1** Blockchain-based vehicular energy network



### 3.1 Problem Formulation

Every electronic and electric device requires some source of energy. Devices in houses, industries, banks, colleges, and offices have a special power demand pattern. All these sectors generally start consuming more power in the morning and less power in the night hours. After EVs grow in number, the power demand at night is also growing, and the load on power grids is increasing. When people start for office or school in the morning, all the homes, industries, and banks demand power. At the same time, EVs also demand power at charging stations. In this paper, the following two significant problem statements are addressed:

- The sudden load on the power grid is making the grid unstable.
- The long waiting time for charging at charging stations consumes EV drivers valuable time and costs indirect financial loss.

To control the waiting time as well as the demand pressure on the power grid, a penalty-based cost function is proposed. The proposed model is based on game theory to bring the demand and supply balance in the vehicular energy blockchain network. The Stackelberg game model [15] inspires the proposed model to achieve a demand balance.

### 3.2 Proposed Model

The components of network model are EVs, Road Side Units (RSUs), Charging stations (CSs), Power Grid (PG), and Blockchain network. In this vehicular energy network (VEN), EVs are buyers of energy, and charging stations are sellers of energy. The symbols used in the paper are listed in Table 2.

Let,

$$u_i \in U = \{u_1, u_2, u_3 \dots u_n\}, \text{ a set of Users.}$$

$$e_i \in E = \{e_1, e_2, e_3 \dots e_n\}, \text{ a set of EVs.}$$

$$c_i \in C = \{c_1, c_2, c_3 \dots c_n\}, \text{ a set of charging stations.}$$

In the vehicular energy network, every EV requires an identity certificate which the TA issues to verify itself as an authentic EV.

TA generate his public key cryptosystem keys:

$$\text{TA} = \{\text{TA}_{privk}, \text{TA}_{pubk}\} \quad (1)$$

User generate his public key cryptosystem keys:

$$u_i = \{u_{privk}, u_{pubk}\} \quad (2)$$

**Table 2** Notation used in the paper

Variable	Description
$e_i$	$i$ th vehicle
ID	ID of the vehicle
$u_{privk}$	Private key of the user
$u_{pubk}$	Public key of the user
$e_{dem}$	User electricity demand
$e_{certi}$	Certificate by TA
$e_{iper}$	$i$ th vehicle charging percentage
$c_i$	$i$ th charging station
$c_{privk}$	Private key of charging station
$c_{pubk}$	Public key of charging station
$E_{epubk}$	Encryption by charging station
$D_{eprivk}$	Decryption by charging station
$E_{cprivk}$	Encryption by vehicle $e_i$
$D_{vprivk}$	Decryption by vehicle $e_i$
$T_c$	Token generated by charging station
$t_{ri}$	Reporting time of $i$ th vehicle on token
$\alpha$	Service charge by CSs
$P_{base}$	Base price of 1 KW electricity
$w_{add}$	Wallet address
$\delta$	Penalty factor

Every EV has his identity to uniquely identify it:

$$e = \{\text{ID}\} \quad (3)$$

User request for network certificate generation through TA:

$$r_{req} = u_i \rightarrow \{u_{pubk}, \text{ID}\} \quad (4)$$

Certificate generation by TA is demonstrated in Algorithm 1. When a request is received, the TA checks to see if a certificate for the EV already exists or not; if it does, the TA will refuse the request. This indicates that for each EV in the network, only one certificate is present.

So, the identity of an EV becomes

$$e_i = \{u_{pubk}, \text{ID}, e_{certi}, w_{add}\} \quad (5)$$

**Algorithm 1:** Certificate generation by TA

---

```

Data:  $r_{req}$ 
Result:  $e_{certi}$ 
if  $e_{certi}$  exist then
|   reject  $r_{req}$ 
else
|   status="active"
|    $e_{certi} = generateCertificate(E_{taprivk}(u_{pubk}, ID, t_{stamp},$ 
|    $t_{exp}, status))$ 
|   return  $e_{certi}$ 
end

```

---

EVs create requests for charging to the smart contract. After verifying EVs' validity, smart contracts create a time-based token for the requested EV.

$$e_{req} = e_i \rightarrow \{E_{cpubk}(e_{certi}, e_{dem}, e_{iper})\} \quad (6)$$

$$(e_{certi}, e_{dem}, e_{iper}) = c_i \rightarrow \{D_{cprivk}(e_{req})\} \quad (7)$$

$$c_i : \text{verify} = \{e_{certi}\} \quad (8)$$

Token generation by CSs

$$T_c = c_i \rightarrow \{E_{epubk}(e_{dem}, t_{ri}, T_{wait}, e_{iper}, U_{pay}, e_{certi})\} \quad (9)$$

EVs on receiving token

$$(e_{dem}, t_{ri}, T_{wait}, e_{iper}, U_{pay}, e_{certi}) = e_i \rightarrow \{D_{eprivk}(T_c)\} \quad (10)$$

Reporting for charging means EVs have to report to the charging station within  $t_{ri}$  time, otherwise the token will get expired.

EV report:

$$e_{rep} = e_i \rightarrow \{E_{cpubk}(e_{dem}, e_{iper}, t_{ri}, e_{certi})\} \quad (11)$$

At CSs:

$$(e_{dem}, e_{iper}, t_{ri}, e_{certi}) = D_{cprivk}\{e_{req}\} \quad (12)$$

Verification of request:

$$c_i : \text{compare} = \{t_{ri}, t_c\} \quad (13)$$

If  $t_{ri} \leq t_c$  : true, valid token

If  $t_{ri} \leq t_c$  : false, EV token is expired.

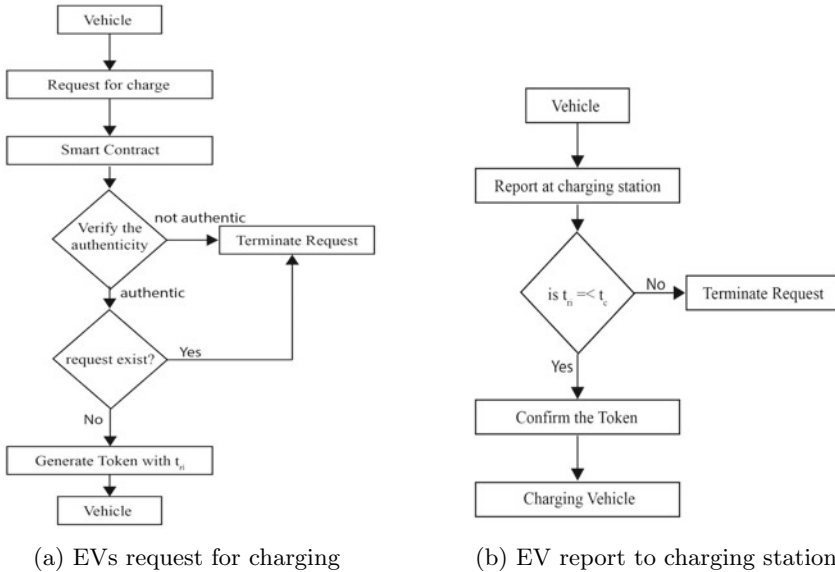
**Fig. 2** Smart contract functionalities

Figure 2a illustrates the process of request creation by EVs, submission to the smart contract, and token generation by the smart contract. Smart contract also check for any active existing request to prevent network from DoS attack situation. In case of already active request contract rejects the new request for charging. When the charging station verifies the EVs token it allows it to charge as per the demand mentioned in the token. EV owner makes the payment as per the charging done:

$$U_{pay} = P * e_{dem} + \alpha \quad (14)$$

Figure 2b shows the reporting process of an EV at a charging station and checking the validity of the charging token. As the charging token is time-based the EV must report before time to report  $t_{ri}$ .

### 3.3 Penalty Mechanism

In this paper a penalty mechanism for EVs to restrict the charging demand at charging stations during high load times. As per the research on the power demand curve [9] for every day during different times of day and night, and considering the office and school time, the most electricity demand time can be calculated. This means the time when the electricity demand at charging stations spikes up every day. This sudden increase in power demand creates a power crisis situation at the charging

station and the power grid. It also directly impacts the waiting time at the charging station. High charging time is also required to complete high charging demand, and the rest of the vehicles have to wait for charging. By controlling the duration of charging during such a situation the demand for electricity can be controlled. The penalty mechanism penalizes the EVs that demand more charging time than the fixed charging time during such a situation.

$$\text{Cost function: } P' = P_{base} + \left( \frac{t - \beta}{2 * \beta} \right) * P_{base} \quad (15)$$

$$\text{Cost function: } P' = P_{base} + \delta * P_{base} \quad (16)$$

$$\text{Penalty factor } \delta = \left( \frac{t - \beta}{2 * \beta} \right) \quad (17)$$

$$U_{pay} = P' * e_{dem} + \alpha \quad (18)$$

### 3.4 Charging Duration Selection

During high demand times for electricity, the demand pressure of electricity on the power grid increases. The waiting time at the charging station also increases as the number of EVs demand charging increases, and charging EVs require time. To control the demand, this paper proposed a penalty-based restrictive charging scheme. From Eq. 15 the method has a variable  $\beta$ , fixed time for charging during such heavy demand. As shown in Fig. 3, all the CSs create their proposal after analyzing the

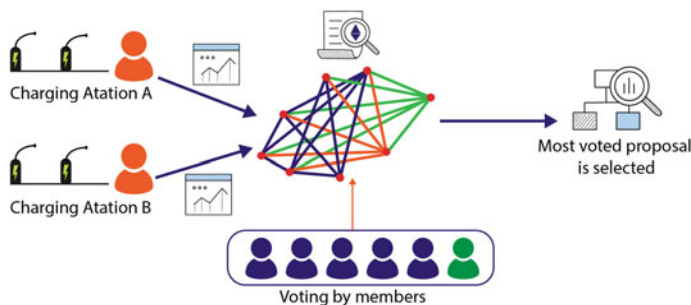


**Fig. 3** Selection of proposal

peak demand time of day and night and broadcast the table on the network, along with the value of  $\beta$ . All the members of the network vote for the suitable proposal as per their decision. The value of  $\beta$  that gets the most vote will be selected as the base time for the network. The selection of  $\beta$  may differ depending on the seasons and geographical location. The durations and the charges per unit may vary depending on the load on the grid, availability of electricity, weather, and electricity demand. The charging station's objective is to satisfy as many requests as possible and reduce the waiting time at the charging station. The EVs objective is to charge as much as possible and avoid the penalty for the over-demand duration.

When the EV selects the fixed duration by network, the penalty factor will be  $\delta = 0$  as the time selected by the EV is  $t$  which is equal to network time  $\beta$  from Eq. 17

$$\text{Penalty factor } \delta = \left( \frac{t - \beta}{2 * \beta} \right)$$

$$\text{Penalty factor } \delta = \left( \frac{0}{2 * \beta} \right)$$

$$\text{Penalty factor } \delta = 0$$

That means the Eq. 18 becomes equal to Eq. 14

$$\text{Cost function: } P' = P_{base} + \delta * P_{base}$$

$$P' = P_{base} + 0 * P_{base}$$

Now,

$$P' = P_{base}$$

So,

$$P = P'$$

The EV does not need to pay any penalty.

### 3.5 Smart Contract

The smart contract for this paper is deployed on the Ethereum network and written in Solidity version 0.8. Figure 2a shows the function of the smart contract. The smart contract can verify the EVs certificate and monitor the number of requests it has created. To protect the VEN from DoS attack. The smart contract allows EVs to check their previous charging transactions and payment history. It also checks

**Table 3** Electric vehicles of different brand and model

S. No.	Brand	Model	Capacity (KWh)	Range (km)	km/KWh
1	Chevrolet	Volt	10.3	85	8.25
2	Volkswagen	e-up	18.7	160	8.55
3	BMW	i3 (60 Ah)	18.8	190	10.10
4	Renault	Fluence Z.E.	22	185	8.40
5	CITROËN	Berlingo Electric	22.5	170	7.55
6	Ford	Focus Electric	33.5	225	6.71
7	Hyundai	Kona Elektro 100 kW	42	305	7.26
8	Hyundai	Kona Elektro 150 kW	64	484	7.56
9	Audi	e-tron 55	95	409	4.30
10	Tesla	Model x 100D	100	565	5.65

whether the EV owner or wallet address has sufficient balance. For secure and safe payment at the charging station. Before generating the charging token, the smart contract checks the available balance of the wallet address and locks the amount. After charging, releases the payable amount to the charging station. In some case if some amount remain at smart contract after paying due to some issue, the contract returns to the wallet address associated with the EV.

## 4 Result and Discussion

From the Indian perspective, the EVs charging speed considered in this paper are 15, 22, and 100 KW [18]. The average rate for 1KWh of electricity is 8 Rs in India [19]. Considering the selected value of  $\beta$  during office time is 10 min for ease by the VEN. Table 3 shows different EVs along with the models and capacity in KWh, the range distance they can cover on a full charge, and the average distance it covers per KWh. From Tables 4, 5, and 6 it can be seen that after a fixed time ( $\beta$ ), the penalty that an EV has to pay grows very high. Figure 4 illustrates the behavior of the penalty function and its growth for  $\beta = 10$ . Figure 5a–c show the variation in actual price for the charging and proposed method with 15, 22, and 100 KW speed charging. For different duration show the normal charging price and price with penalty considering the value of  $\beta=10$ . It shows the penalty price is significantly higher than the normal price for charging.

**Table 4** Charging with 15 KW charger

Time	15 KW	Normal price	Proposed method price	Penalty (%)
1 min	0.25	2	2	0
5 min	1.25	10	10	0
10 min	2.5	20	20	0
15 min	3.75	30	37.5	25
30 min	7.5	60	120	100
60 min	15	120	420	250
2 h	30	240	1560	550
3 h	45	360	3420	850
4 h	60	480	6000	1150

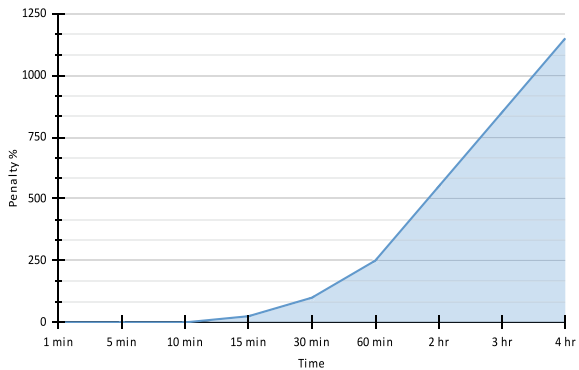
**Table 5** Charging with 22 KW charger

Time	22 KW	Normal price	Proposed method price	Penalty (%)
1 min	0.36	2.93	2.93	0
5 min	1.83	14.66	14.66	0
10 min	3.66	29.33	29.33	0
15 min	5.5	44	55	25
30 min	11	88	176	100
60 min	22	176	616	250
2 h	44	352	2288	550
3 h	66	528	5016	850
4 h	88	704	8800	1150

**Table 6** Charging with 100 KW charger

Time	100 KW	Normal Price	Proposed method price	Penalty (%)
1 min	1.66	13.33	13.33	0
5 min	8.33	66.66	66.66	0
10 min	16.66	133.33	133.33	0
15 min	25	200	250	25
30 min	50	400	800	100
60 min	100	800	2800	250
2 h	200	1600	10400	550
3 h	300	2400	22800	850
4 h	400	3200	40000	1150

**Fig. 4** Penalty graph for  $\beta = 10$  min



As the EV user cannot demand more duration to charge because of the dynamic pricing method proposed in this paper, the waiting time for charging will be significantly reduced. Also, because of the very high many EVs users will try to schedule the charging during low penalty durations. The paper's problem statement can be solved in this manner.

## 5 Conclusion

In this paper, we proposed a cost function and penalty factor to create a dynamic pricing mechanism for energy delivery in VEN, to restrict EVs from charging for a long duration. Smart contract-based model for EVs charging and secure payment. Due to the incredible increase in the usage of electric vehicles, there is a growing need for charging services and a growing pressure on the power grids. To minimize the load on the grid and shorten the wait time for electric vehicles, we devised the concept of restrictive charging based on a predetermined duration. The Stackelberg game model inspired us to design a restrictive charging model. To restrict EV users by penalizing them for over-duration charging. The numerical analysis shows that the EV has to pay a fixed price for a fixed duration, and beyond that duration, a penalty has to be paid by the EV.

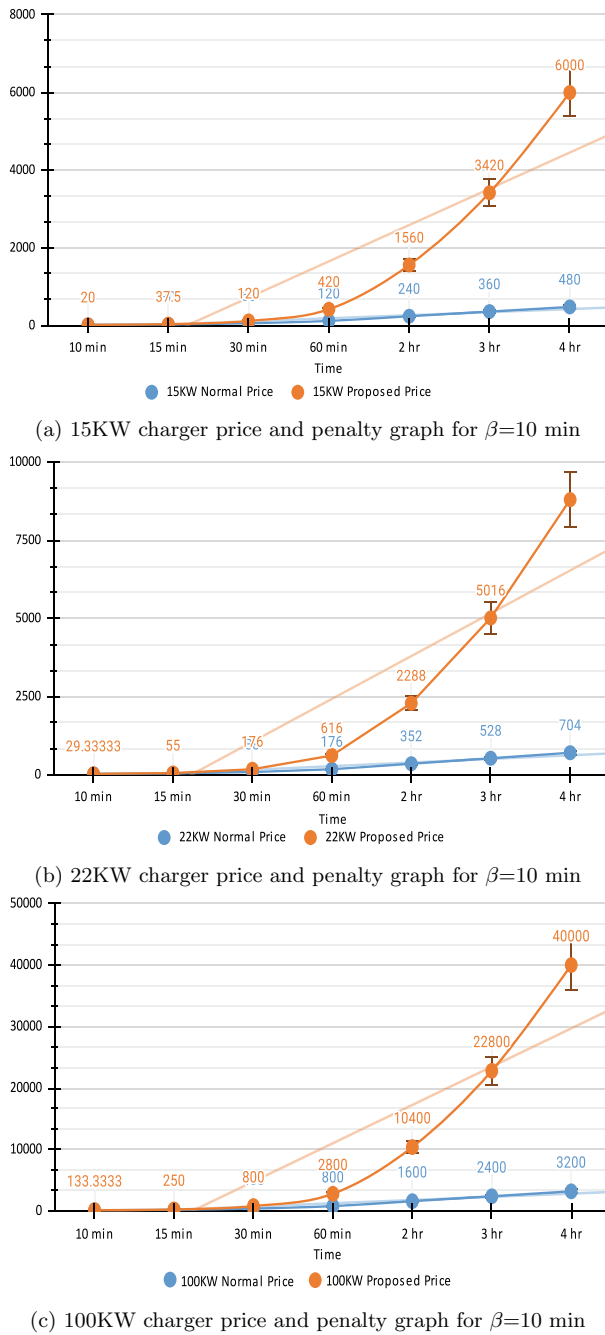


Fig. 5 The behavior of the proposed penalty system for different charging speed

## References

1. Nakamoto S (2008) Bitcoin: a peer-to-peer electronic cash system. <https://bitcoin.org/bitcoin.pdf>
2. Dewangan NK, Chandrakar P (2022) Patient-centric token-based healthcare blockchain implementation using secure internet of medical things. In: IEEE transactions on computational social systems. <https://doi.org/10.1109/TCSS.2022.3194872>
3. Dewangan NK, Chandrakar P, Kumari S et al (2022) Enhanced privacy-preserving in student certificate management in blockchain and interplanetary file system. *Multimed Tools Appl.* <https://doi.org/10.1007/s11042-022-13915-8>
4. Chandraka, P, Dewangan, NK, Chandrakar K (2022) Decentralized energy management in smart cities using blockchain technology. In: Panda SK, Rout RR, Sadam RC, Rayanothalala BVS, Li KC, Buyya R (eds) Computing, communication and learning. CoCoLe 2022. Communications in computer and information science, vol 1729. Springer, Cham. [https://doi.org/10.1007/978-3-031-21750-0\\_9](https://doi.org/10.1007/978-3-031-21750-0_9)
5. Dewangan NK, Chandrakar P (2022) Patient feedback based physician selection in blockchain healthcare using deep learning. In: Woungang I, Dhurandher SK, Pattanaik KK, Verma A, Verma P (eds) Advanced network technologies and intelligent computing. ANTIC 2021. Communications in computer and information science, vol 1534. Springer, Cham. [https://doi.org/10.1007/978-3-030-96040-7\\_17](https://doi.org/10.1007/978-3-030-96040-7_17)
6. Clement-Nyns K, Haesen E, Driesen J (2010) The impact of charging plug-in hybrid electric vehicles on a residential distribution Grid. *IEEE Trans Power Syst* 25(1):371–380. <https://doi.org/10.1109/TPWRS.2009.2036481>
7. Xue K, Luo X, Ma Y, Li J, Liu J, Wei DSL (2022) A distributed authentication scheme based on smart contract for roaming service in mobile vehicular networks. *IEEE Trans Veh Technol* 71(5):5284–5297. <https://doi.org/10.1109/TVT.2022.3148303>
8. Sampath LPMI, Paudel A, Nguyen HD, Foo EYS, Gooi HB (2022) Peer-to-peer energy trading enabled optimal decentralized operation of smart distribution grids. *IEEE Trans Smart Grid* 13(1):654–666. <https://doi.org/10.1109/TSG.2021.3110889>
9. Gaur K, Kumar H, Agarwal RPK, Baba KVS, Soonee SK (2016) Analysing the electricity demand pattern. In: National power systems conference (NPSC), pp 1–6. <https://doi.org/10.1109/NPSC.2016.7858969>
10. Aitzhan NZ, Svetinovic D (2018) Security and privacy in decentralized energy trading through multi-signatures, blockchain and anonymous messaging streams. In: IEEE transactions on dependable and secure computing, vol 15, no 5, 1 Sept–Oct 2018, pp 840–852. <https://doi.org/10.1109/TDSC.2016.2616861>
11. Asfia U, Kamuni V, Sheikh A, Wagh S, Patel D (2019) Energy trading of electric vehicles using blockchain and smart contracts. In: 2019 18th European control conference (ECC), Naples, Italy, 2019, pp. 3958–3963. <https://doi.org/10.23919/ECC.2019.8796284>
12. Tushar W, Saha TK, Yuen C, Smith D, Poor HV (2020) Peer-to-peer trading in electricity networks: an overview. *IEEE Trans Smart Grid* 11(4):3185–3200. <https://doi.org/10.1109/TSG.2020.2969657>
13. Gabay D, Akkaya K, Cebe M (2020) Privacy-preserving authentication scheme for connected electric vehicles using blockchain and zero knowledge proofs. *IEEE Trans Veh Technol* 69(6):5760–5772. <https://doi.org/10.1109/TVT.2020.2977361>
14. Danish SM, Zhang K, Jacobsen HA (2020) A Blockchain-Based Privacy-Preserving Intelligent Charging Station Selection for Electric Vehicles. In: IEEE international conference on blockchain and cryptocurrency (ICBC), vol 2020, pp 1–3. <https://doi.org/10.1109/ICBC48266.2020.9169419>
15. Abishu HN, Seid AM, Yacob YH, Ayall T, Sun G, Liu G (2022) Consensus mechanism for blockchain-enabled vehicle-to-vehicle energy trading in the internet of electric vehicles. *IEEE Trans Veh Technol* 71(1):946–960. <https://doi.org/10.1109/TVT.2021.3129828>

16. Kakkar R, Agrawal S, Gupta R, Tanwar S (2022) Blockchain and zero-sum game-based dynamic pricing scheme for electric vehicle charging. In: IEEE INFOCOM 2022—IEEE conference on computer communications workshops (INFOCOM WKSHPS), pp 1–6. <https://doi.org/10.1109/INFOCOMWKSHPS54753.2022.9797894>
17. Knirsch F, Unterweger A, Engel D (2018) Privacy-preserving blockchain-based electric vehicle charging with dynamic tariff decisions. Comput Sci Res Dev 33:71–79. <https://doi.org/10.1007/s00450-017-0348-5>
18. Government of India, Niti Aayog (2022) e-AMRIT. <https://e-amrit.niti.gov.in/standards-and-specifications>
19. GlobalPetrolPrices (2022) Price of 1 KWh in India. <https://www.globalpetrolprices.com/India/>

# Movie's-Emotracker: Movie Induced Emotion Detection by Using EEG and AI Tools



Sima Das, Siddhartha Chatterjee, Sutapa Bhattacharya, Solanki Mitra, Arpan Adhikary, and Nimay Chandra Giri

**Abstract** The proposed work “Movie’s-Emotracker” has been designed to track movie induced emotions by using electroencephalography signals and artificial intelligence tools. Electrodes placed with human brain scalp while watching movies and send through BrainTech Traveler system to store data as numerical form. In this procedure of data acquisition, we used 25 video clips applied on 20 participations for detecting a distinct emotional state using brain signals. Due to watching movie occipital lobe is active, due to listen movie temporal lobes is active, parietal due to thinking about the movie and frontal lobe for emotion detection. 1–30 Hz band-pass filter used for filtering, for artifact removal used independent component analysis, feature extraction by Root mean square, classification done by Self-assessment Manikins and Back propagation neural network. Finally, movie induced emotions categorized as negative, natural and positive emotion. Observations are analyzed by proposed system and movie rating will be send to the user’s smart phone, based on previous rating the users also be alert about the movie type. Average test accuracy of our proposed work is 90% and above. The current system can be used for weak old

---

S. Das (✉)

Department of Computer Science and Engineering, Bengal College of Engineering and Technology, Durgapur, West Bengal 713212, India

e-mail: [simadascse@gmail.com](mailto:simadascse@gmail.com)

S. Chatterjee

Department of Computer Science and Engineering, NSHM Knowledge Campus, Durgapur, India

S. Bhattacharya

Department of Computer Science and Engineering, Siliguri Institute of Technology, Siliguri 734009, India

S. Mitra

School of Computing Science, University of Glasgow, 18 Lilybank Gardens, Glasgow G12 8RZ, UK

A. Adhikary

Haldia Institute of Technology, Hatiberia, ICARE Complex, Haldia, West Bengal 721657, India

N. C. Giri

Department of Electronics and Communication Engineering, Centurion University of Technology and Management, Jatni, Odisha 752050, India

aged peoples, teenagers and also used for psychological guide, and the system will be prodigious impression on the world.

**Keywords** Electroencephalography · Artificial intelligence · Brain-computer interaction · Emotion detection · Human–computer interaction

## 1 Introduction

Emotion is the basic characteristics of human; emotions can be influenced by human nature, others response, temperament, surrounding environment. According to human behavior emotion can be categorized as positive or negative. Emotion are difficult by nature, but it is essential to maintain psychological well-being. Depression, anxiety, mental disorder are symptoms for cognitive load, in that condition one can pay attention for observe their daily routine to identify the correct reason for mental imbalance. Watching a movie will attach as to the movie's characters and we see the movie from their point of view like scared when they threatened, we also getting hurt when they get hurt and wounded, when they are succeeded [1, 2], we also glad and pleased. So, movie and the actors are very closed to us and as a viewer their(actors) activity effects on our brain. The electroencephalography (EEG) [3–8] is harmless, painless procedure that can diagnose, monitored brain activity and used to estimate different kinds of brain ailments. EEG is the current demanded technology for stress detection, data acquisition, feature extraction and classifications are the basic procedure for detecting mental stress [9]. Liu et al. [10], designed EEG-based method for real time movie's emotion detection, they used 2 segment windows for valence and arousal discrete emotion detection with average 86.3% accuracy. In our previous paper [11] we discussed how movie effect human hearts by using electrocardiography (ECG) signal, and the movie rating send to the user's mobile by using Telegram Bot, in this paper we used EEG instead of ECG for observe how movie effects on human brain, so based on previous rating peoples can understood about the movie type. In another paper [12], the system was built for observe gaming effects on human brain, for this artificial intelligence tool were used. The cognitive load classified as low, medium and high when participate involved with game. Özerdem et al. [13], used EEG for data acquisition for emotion detection during movie and for classification multilayer perceptron neural network with 77.14% testing accuracy and k-nearest neighbor algorithm testing accuracy was 72.92%, for automatic emotion detection Self-Assessment Manikins was used. Espenahn et al. [14], they compose EEG system with somatosensory-evoked potentials (SEPs) alpha/beta event-related desynchronization (ERD) for observe effects on movie watching.

The main contributions of the proposed method are as follows:

- Analyzing emotion detection by comparing training dataset with movie induced testing dataset which collected from EEG.

- Bandpass filter used to remove unwanted frequency which collected from raw dataset.
- Independent component analysis used for remove eye induced artifact while collect data from testing purposes.
- For feature selection Root mean square method will be used.
- Self-assessment Manikins is the technique which automatically detect emotions as arousal and valence.
- To classified emotion as positive, neutral and negative Backpropagation neural network was used.
- The rating of the movie will be calculated as per classification result.

The objective of the proposed method are as follows:

- The paper designed to detect movie induced emotions for teenager's so their parent can guide their children which movie is not suitable for their child.
- The system will be helpful for old aged peoples too to avoid negative rating movies and enjoy suitable one.
- One can visit previously movie rating for which movie is best for their instead emotion.
- Weak hearted peoples can avoid negative rating movies to avoid stress which also good for their heart.
- The system will be helpful for young and individuals and working people can observe their child and old aged parents' movie induced activity from anywhere. So, the system can relief their stress too and works as parental guide.
- The system also can be used as stress relief tool for stressful peoples, so the system will be used as rehabilitation tool also.

Rest of the paper are as follows: 2 for related works, 3 for proposed work, 3 for result and 4 for conclusion and future work.

## 2 Related Works

Iyer et al. [15] proposed a new approach to recognize human sentiment using electroencephalogram (EEG) signals. For this work, they considered three types of emotions, i.e., positive, neutral and negative. The recorded EEG signals were separated into five frequency band components. For this research, long short-term memory (LSTM) and convolution neural network (CNN)-based hybrid model was developed to detect the human emotions accurately. These extracted features were taken into consideration to feed all the models. Eventually, the predictions of the three models were combined using an ensemble model. Two datasets, i.e., SEED and DEAP were taken to validate the approach. The researchers achieved 97.16% of accuracy for SEED dataset.

Murugappan et al. [16] classified six emotions, i.e., surprise, disgust, fear, happiness, sadness and anger in this work. Two types of strokes, i.e., right-brain damage

(RBD) and left-brain damage (LBD) were also classified in this research, they have collected EEG signals from 19 subjects of RBD, normal control (NC) and LBD at 128 Hz sampling rate. For noise and artifact effects reduction, IIR Bandpass filter and amplitude thresholding methods were used. The collected signals were extracted into five EEG frequency bands named, alpha, beta, gamma, beta to gamma, alpha to gamma using discrete wavelet packet. Recurrent quantification analysis was taken into consideration to extract a set of non-linear features from five different EEG frequency ranges. Finally, the extracted features were mapped to six corresponding emotions. Three non-linear classifiers, i.e., K-nearest neighbor (KNN), random forest (RF) and probabilistic neural network were taken into consideration for this step. The result exhibited that LBD subjects have critical emotional disablement than that of RBD subjects. The maximum accuracy of 85.24% was achieved using RF classifier.

Subasi et al. [17] proposed an automated emotion identification system that uses EEG signals. Their methodology is consisted of four major phases, i.e., preprocessing, feature extraction, feature dimension reduction and classification phase. In this paper, multiscale principal component analysis (MSPCA) was using for noise reduction during preprocessing phase. To extract the features, a tunable Q Wavelet transform (TQWT) was taken into consideration. In the classification step, rotation forest ensemble (RFE) classifier was utilized with other classification algorithms like support vector machine (SVM), KNN, artificial neural network (ANN), RF and decision tree (DT). The proposed system got over 93% of classification accuracy with RFE and SVM.

Tavakkoli et al. [18] introduced a new technique in symbolic time series analysis (STSA) for symbol sequence generating and signal phase space partitioning. The symbolic sequences were produced next to spherical partitioning of phase space. Then, these sequences were compared and classified based on the maximum value of similarity index. To solve the generalization problem, a subject-independent protocol was introduced. DEAP dataset was taken for this study, which included recorded peripheral and EEG signals of 32 subjects. The signal was taken based on the music videos watched by the subjects. These signals were sampled at the rate of 512 Hz and were down sampled to 128 Hz for further processing. The researchers obtained the accuracy of 98.44% for happiness and sadness classification, when there were only two emotion groups. The accuracy was decreased to 93.75% when three emotion groups were included.

Panda et al. [19] proposed a emotion recognition multimodal system and sentiment analysis. They have used four types of emotions, i.e., happy, sad, anger and relaxed for their work. Both EEG signals and spatial (comments and customer reviews) were taken as input parameters. Then, the emotion was created while watching the product on computer. Their proposed structure learnt about spatial and temporal discriminative features using text encoder and EEG encoder. The two of these encoders transformed the text and EEG features into a common feature space. An accuracy of 98.27% was achieved by the researchers for this study.

### 3 Proposed Works

In this section we will be discussed about the proposed work for movie induced emotion detection. Proposed system shown in Fig. 1, in this EEG used for data acquisition while watching movies, bandpass filtering range 1–30 Hz, for artifact removing ICA method will be used, feature extraction done by Root mean square, Back propagation neural network and self-assessment Manikins classified the emotions as negative, natural, positive emotion. The movie rating will be calculated as per classification result.

#### 3.1 Experimental Setup for Data Collection

Figure 2 shows that data acquisition standard 10–20 system EEG channels was used for proposed work, 15 EEG channels was as follows: AF3-AF4, F3-F4-F8, FC5-FC6, T7-T8, P3-P4, P7-P8, O1-O2 as shown in Fig. 2. Where F represented for frontal lobe, T for temporal lobe, P for parietal, O for occipital, A1-A2 used for Reference. In this procedure of data acquisition, we used 20 video clips applied on 25 participations for detecting a distinct emotional state using brain signals by BrainTech Traveler system.

**Sample Heading (Third Level).** Only two levels of headings should be numbered. Lower-level headings remain unnumbered; they are formatted as run-in headings.

#### 3.2 Data Acquisition Epochs

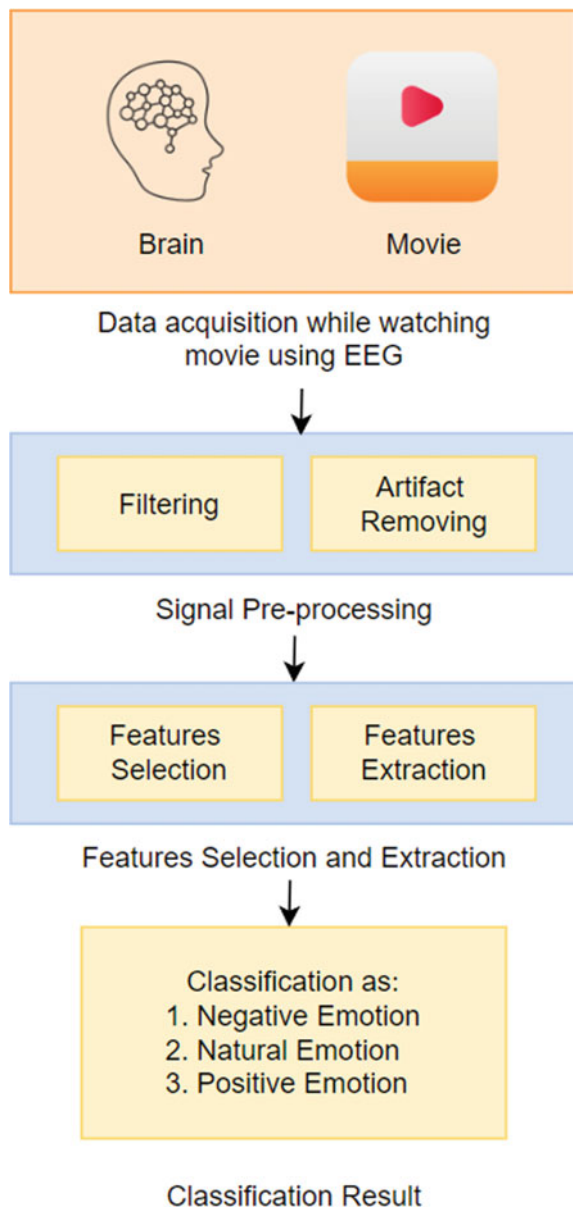
EEG placed on 20 participations scalp of 25 video clips applied for detecting a distinct emotional state using brain signals. In every epoch of acquisition EEG signal have 4 conditions to collect EEG-based datasets, the conditions are: hint of start, during movie clip, self-assessment and rest conditions as shown in Fig. 3.

#### 3.3 Signal Preprocessing

The signal processing has 2 sub methods: filtering and artifact removing. The procedure will be discussed below:

##### 3.3.1 Filtering

In this current work 1–30 Hz bandpass filter was used to filter raw dataset in 250 Hz down sampling.

**Fig. 1** Proposed work

### 3.3.2 Artifact Removal

During dataset collection eye blink, movement of eyes are captured, to remove this type of artifact independent component analysis will be used.

**Fig. 2** Electrode placement in 10–20 EEG system

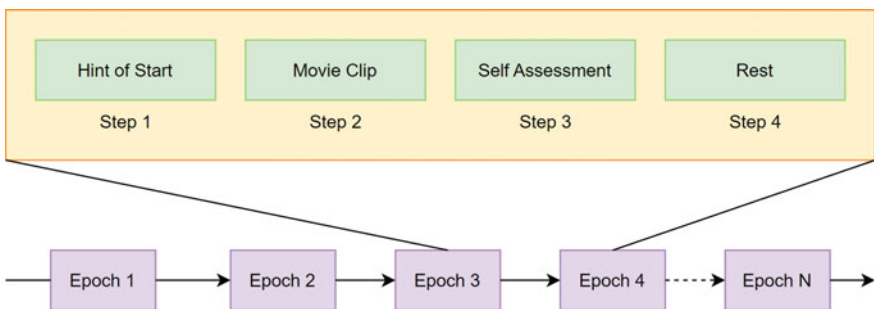
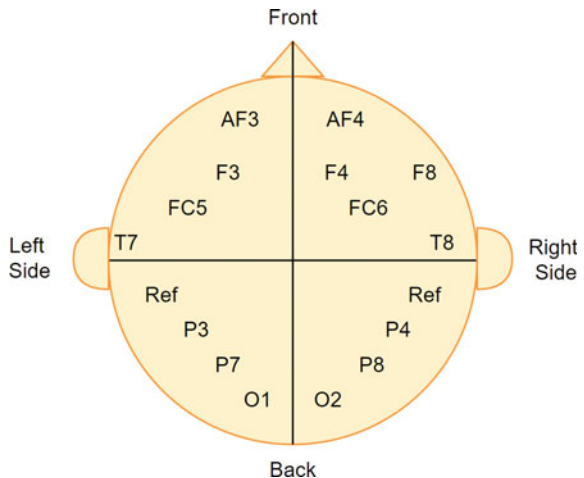


**Fig. 3** Data acquisition Epochs for collecting EEG dataset while watching movies

### 3.4 Feature Selection and Extraction

Features selection and extraction are important method in signal processing. In this paper we used Root mean square method for feature selection.

In Eq. 1, set of n numbers of inputted values are  $\times 1, \times 2, \dots, \times_n$

$$\text{RMS} = \sqrt{\left( \frac{1}{n} (x_1^2 + x_2^2 + \dots + x_n^2) \right)} \quad (1)$$

From Eq. 2,  $f(t)$  defined over the interval  $T1 \leq T \leq T2$

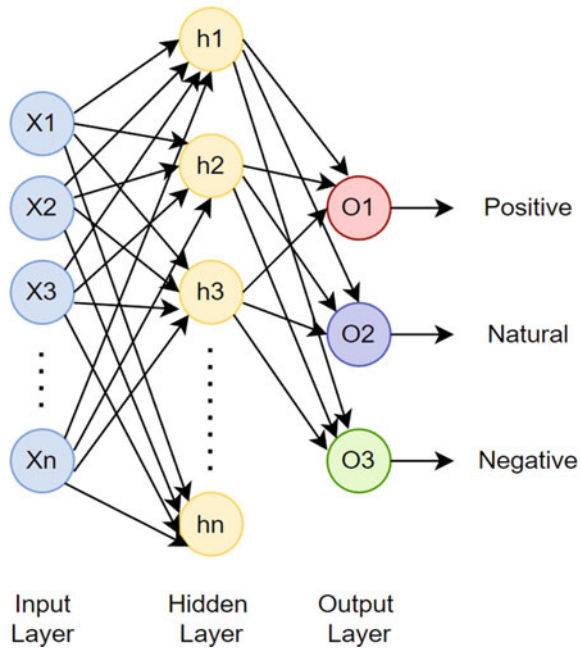
$$\text{fRMS} = \lim_{T \rightarrow \infty} \left( \sqrt{\frac{1}{2T} \int_{-T}^{T} [f(t)]^2 dt} \right) \quad (2)$$

### 3.5 Classification

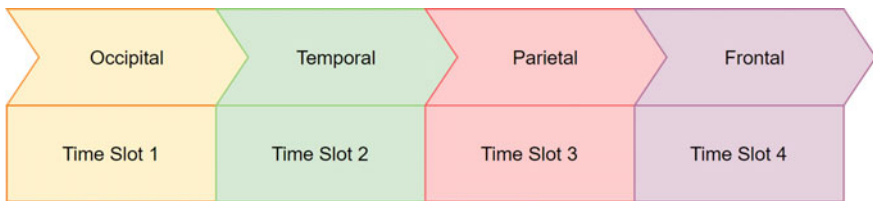
Self-assessment Manikins is the technique which automatically detect emotions as arousal and valence, after that BPNN will be used to categorized the system as positive, natural and negative as shown in Fig. 4. In Fig. 4,  $x_1, x_2, \dots, x_n$  are input layer,  $h_1, h_2, \dots, h_n$  are hidden layer and  $O_1, O_2$  and  $O_3$  are classification result as positive, natural and negative. In Eq. 3,  $i$  is the initial epoch and  $n$  is the numbers of epochs,  $D_o$  is the desired output and  $A_o$  is the actual output.

$$\text{Cumulative Error} = \frac{1}{2} \sum_{i=1}^n (D_o - A_o)^2 \quad (3)$$

**Fig. 4** Classification using back propagation neural network



AF3-A1	F3-A1	FC5-A1	T7-A1	P3-A1	P7-A1	O1-A1	AF4-A2	F4-A2	F8-A2	T8-A2	FC6-A2	P4-A2	P8-A2	O2-A2
0	0	0	0	0	0	0	0	0	0	0	0	0	0	0
0	0	0	0	0	0	0	0	0	0	0	0	0	0	0
0	0	0	0	0	0	0	0	0	0	0	0	0	0	0
12	14	15	16	14.5	18	14	62	21	36	47	24	13	17	15
32	42	15	17	25	34	16	17	24	26	32	28	24	19	18
17	18	35	19	22	26	27	30	30.5	32.1	38.2	40.3	25.6	29.3	30
35	42.3	45	43	46	41	50	12	16	36	42	34	28	26	18

**Fig. 5** Dataset collection while watching movies**Fig. 6** Brain lobe activation during movie watching

## 4 Result

### 4.1 Data Acquisition

The dataset collects from 20 participants for 25 different movie clips in 4 different moods. AF3-A1, F3-A1, FC5-A1, T7-A1, P3-A1, P7-A1, O1-A1, AF4-A2, F4-A2, F8-A2, T8-A2, FC6-A2, P4-A2, P8-A2, O2-A2 are the channels selected for movie induced EEG signal collection with 250 Hz down sampling as shown in Fig. 5.

### 4.2 Brain Activation Detection

During watching movies occipital lobe will be activated for watch the movie, due to listen movie temporal lobes is active, parietal due to thinking about the movie and frontal lobe for emotion detection as shown in Fig. 6.

### 4.3 Feature Extraction

Table 1, shows that EEG features with respect to emotional states and frequency band, here delta, theta, alpha, beta, gamma is the frequency band and emotional states are mentioned column wise.

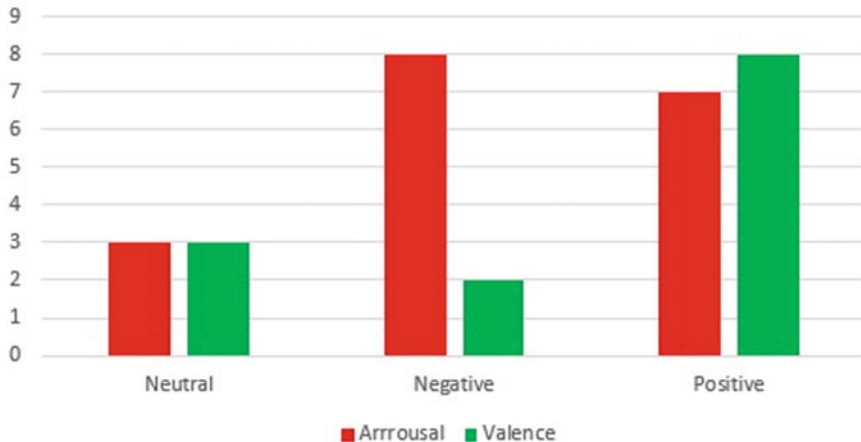


**Fig. 7** Emotion detection for arousal and valence

**Table 1** EEG features with respect to emotional states and frequency band

Emotional states	Frequency band				
	Delta	Theta	Alpha	Beta	Gamma
Positive and negative	F3-F4,F8		FC5-FC6, F3-F4	AF4, F4, F8	
Non-neutral and neutrality		T7-T8, FC5	P3, P7	F4, F8	
Amusement, joy, tenderness	F4, F8		AF3-AF4, F3, F4, F8	P4, P8, O1-O2	
Anger, disgust, fear, sadness	F4, F8	P3-P4, P7-P8		O1-O2	T7, T8

#### 4.4 Classification

Self-assessment Manikins automatically classified emotion as arousal and valence and for classification Back propagation neural network was used. Finally, movie induced emotions categorized as negative, natural and positive emotion as shown in Fig. 7. Testing accuracy of the proposed system is 90% and above using BPNN which is shown in Table 2.

#### 4.5 MCNEmar's Test

Table 3, analyzed the proposed method by McNemar's test. In this A is the proposed algorithm by using BPNN and others machine learning sets are B. The null hypothesis

**Table 2** Classifier performance analysis

Participants	Training accuracy			Testing accuracy		
	Neutral	Negative	Positive	Neutral	Negative	Positive
P1	89	85.2	90	91	88.2	91
P2	94	93.3	88	92	91.3	87
P3	91	94.5	84	91	87.5	90
P4	87	88.1	86	78	81.6	96
P5	85	93.6	82	85	86.2	89
P6	93	85.3	89	96	88.3	85
P7	88	90.1	93	98	95.3	80
P8	91	85.3	90	91	88.9	91
P9	88	93.2	88	92	91.02	87
P10	95	94.5	84	91	87.3	90
P11	98	88.6	86	78	81.5	96
P12	97	93.1	82	85	86.2	89
P13	84	85.6	89	96	88.6	85
P14	88	90.5	93	98	95.2	80
P15	85	85.8	90	91	88.7	91
P16	91	90.1	88	92	91.01	87
P17	95	92.6	84	91	87.60	90
P18	94	85.2	90	91	88.69	91
P19	96	93.2	88	92	91.3	87
P20	82	94.5	84	91	87.6	90
Average	90.2	90.5	90.8	90.1	90.3	90.8

is rejected, z goes beyond the 3.84. After analyzed we came to the conclusion that A have better controlled system than B.

**Table 3** Performance analysis using McNemar's test

Machine learning procedures (B)	BPNN controlled proposed system(A)			
	$N_{0I}$	$N_{25}$	Z	Comment
Support vector machine	5	30	12.02	Reject
K-nearest neighbor	7	28	16.3	Reject
Linear discriminant analysis	3	24	11.5	Reject
Quadratics discriminant analysis	6	27	14.3	Reject
Multilayer neural network	7	26	13.8	Reject

## 5 Conclusion and Future Work

The proposed system is designed with an EEG-based data acquisition method captured by EEG signal. The bandpass filter used for filtering and for artifact removing ICA was used self-assessment Manikins automatically classified emotion as arousal and valence and for classification Back propagation neural network was used, movie induced emotions categorized as negative, natural and positive emotion which testing accuracy is greater than 90%. The system will be helpful for young individuals and working people to observe their child and old aged parent's movie induced activity from anywhere. So, the system can relieve their stress too and works as a parental guide for their child. So, we can see the system will be helpful for society.

In the future we extend the work with more movie clips and deep learning techniques. The extended work also will apply to different ages more peoples during doing different tasks.

## References

1. Tan ES (2018) A psychology of the film. *Palgrave Commun* 4:82. <https://doi.org/10.1057/s41599-018-0111-y>
2. Qiao N (2021) Does perceived stress of university students affected by preferences for movie genres? an exploratory cross-sectional study in China. *Front Psychol* 12:761340. <https://doi.org/10.3389/fpsyg.2021.761340.PMID:34899504;PMCID:PMC8660665>
3. Li Q et al. (2021) EEG signal processing and emotion recognition using convolutional neural network. In: 2021 international conference on electronic information engineering and computer science (EIECS), 2021, pp 81–84. <https://doi.org/10.1109/EIECS53707.2021.9587900>
4. Sarikaya MA, Ince G (2017) Emotion recognition from EEG signals through one electrode device. In: 2017 25th signal processing and communications applications conference (SIU), 2017, pp 1–4. <https://doi.org/10.1109/SIU.2017.7960390>
5. Wang K-Y, Ho Y-L, Huang Y-D, Fang W-C (2019) Design of intelligent EEG system for human emotion recognition with convolutional neural network. In: 2019 IEEE international conference on artificial intelligence circuits and systems (AICAS), 2019, pp 142–145. <https://doi.org/10.1109/AICAS.2019.8771581>
6. Dommez H, Ozkurt N (2019) Emotion classification from EEG signals in convolutional neural networks. In: 2019 innovations in intelligent systems and applications conference (ASYU), 2019, pp 1–6. <https://doi.org/10.1109/ASYU48272.2019.8946364>
7. Kul S, Durdu PO, Akbulut O (2019) Performance comparison of EEG channels in emotion recognition. In: 2019 27th signal processing and communications applications conference (SIU), 2019, pp 1–4. <https://doi.org/10.1109/SIU.2019.8806538>
8. Li X, Zhang X, Yang H, Duan W, Dai W, Yin L (2020) An EEG-based multi-modal emotion database with both posed and authentic facial actions for emotion analysis. In: 2020 15th IEEE international conference on automatic face and gesture recognition (FG 2020), 2020, pp 336–343. <https://doi.org/10.1109/FG47880.2020.00050>
9. A. Ghosh & S. Das & Srip. (2022). Stress detection for cognitive rehabilitation in COVID-19 scenario. [https://doi.org/10.1049/PBHE042E\\_ch12](https://doi.org/10.1049/PBHE042E_ch12).
10. Liu Y-J, Yu M, Zhao G, Song J, Ge Y, Shi Y (2018) Real-time movie-induced discrete emotion recognition from EEG signals. *IEEE Trans Affect Comput* 9(4):550–562. <https://doi.org/10.1109/TAFFC.2017.2660485>

11. Das S, Bhattacharya A (2021) ECG assess heartbeat rate, classifying using BPNN while watching movie and send movie rating through telegram. 465–474. [https://doi.org/10.1007/978-981-15-9774-9\\_43](https://doi.org/10.1007/978-981-15-9774-9_43)
12. Das S, Ghosh L, Saha S (2020) Analyzing gaming effects on cognitive load using artificial intelligent tools. <https://doi.org/10.1109/CONECCT50063.2020.9198662>
13. Özerdem MS, Polat H (2017) Emotion recognition based on EEG features in movie clips with channel selection. *Brain Inf* 4:241–252. <https://doi.org/10.1007/s40708-017-0069-3>
14. Espen'hahn S, Yan T, Beltrano W, Kaur S, Godfrey K, Cortese F, Bray S, Harris AD (2020) The effect of movie-watching on electroencephalographic responses to tactile stimulation. *NeuroImage* 220:117130. ISSN 1053-8119. <https://doi.org/10.1016/j.neuroimage.2020.117130>
15. Iyer A, Das SS, Teotia R, Maheshwari S, Sharma RR (2022) CNN and LSTM based ensemble learning for human emotion recognition using EEG recordings. *Multimedia Tools and Appl* 1–14
16. Murugappan M, Zheng BS, Khairunizam W (2021) Recurrent quantification analysis-based emotion classification in stroke using electroencephalogram signals. *Arab J Sci Eng* 46:9573–9588
17. Subasi A, Tuncer T, Dogan S, Tanko D, Sakoglu U (2021) EEG-based emotion recognition using tunable Q wavelet transform and rotation forest ensemble classifier. *Biomed Signal Process Control* 68:102648
18. Tavakkoli H, Motie Nasrabadi A (2022) A spherical phase space partitioning based symbolic time series analysis (SPSP—STSA) for emotion recognition using EEG signals. *Front Hum Neurosci* 16:936393
19. Panda D, Chakladar DD, Dasgupta T (2020) Multimodal system for emotion recognition using EEG and customer review. In: Proceedings of the global ai congress 2019, Springer, Singapore, pp 399–410

# Models for Analysis of Factors Influencing Economic Development



Dung Nguyen Thi Thu and V. Chernenkaya Ludmila

**Abstract** Data processing in research in general and in economics in particular is extremely important. Data analysis is the basis for researchers to draw efficient and accurate, conclusions from which appropriate judgments and recommendations for economic development can be drawn. In recent years, many multivariate statistical analyzes have been applied to analyze general practice, including economics, such as correlation-regression analysis, factor analysis, cluster analysis. However, in Vietnam, the use of these analysis methods is still limited. In this study, the method of factor analysis in the Matlab environment is applied, aimed at identifying problems that affect the economic development of Thai Binh of Vietnam. This research is the basis to help Thai Binh find the most effective plan to promote economic development, and at the same time, this result could be applied to perform other analyzes in the future for the purposes of researchers.

**Keywords** Multivariate statistics · Factor analysis · Model for analysis · Economic development of Vietnam

## 1 Introduction

Factor analysis is one of the statistical success stories in the social sciences. Factor analysis has been around for nearly 120 years since the publication of psychologist and statistician Charles Spearman's important 1904 paper introducing the key elements of this invaluable statistical tool and many variations of factor analysis were developed over the following century [1].

The reader cannot hope to get a comprehensive view of the development of factor analysis over the past three years from this review. This is even too much to hope

---

D. N. T. Thu (✉) · V. Chernenkaya Ludmila  
The Great St. Petersburg Polytechnic University, Saint Petersburg, Russia  
e-mail: [thudung.mta.tb@gmail.com](mailto:thudung.mta.tb@gmail.com)

V. Chernenkaya Ludmila  
e-mail: [ludmila@qmd.spbstu.ru](mailto:ludmila@qmd.spbstu.ru)

for from any one of the recent reviews of factor analysis methods [2]. The field has grown too broad and too deep to allow study of it either indirectly or from a summary.

There are many excellent books on factor analysis. Practical examples and application advice can be found, for example, in Stevens [3]; a more detailed description is provided by Cooley and Lohnes [4]; Harman [5]; Kim and Mueller [6]; Lawley and Maxwell [7]; Lindeman, Merenda and Gold [8]; Morrison [9] and Mulaik [10]. Interpretation of secondary factors in hierarchical factor analysis, as an alternative to the traditional rotation of factors, is given by Wherry [11].

Based on critical reviews of the use of factor analysis in a number of different research areas [12], most studies of factor analysis have at least one critical error. Common problems include sample sizes being too small and not reporting enough numerical results for work to be taken seriously. Those errors are fixed in this research paper.

When working with factor analysis, it is common to apply several methods together: principal component analysis (PCA), principal axis factoring (PAF), maximum likelihood, image factoring, unweighted least squares, alpha factoring, generalized least squares, and canonical [13]. The main task, then, served by factor analysis reflects in the extraction of factors that are given out by the above methods.

In practice, the most applied methods are principal component analysis and principal axis factorization. The method PAF and PCA carry out one difference in the form of the analyzed data matrix. With a large number of factors (thirty or more) and a high quality of reliability of the collected data, these differences are not significant.

In this paper, the method of factor analysis is also applied with principal component analysis. Factor analysis can be applied to reduce data and classify factors. Factor analysis is a step-by-step process where a separate task is performed at each step. The method consists of six steps, in which the researcher with the ability to decide the question of the number of repetitions of the sequence of analysis or to skip some extra steps to quickly obtain the result.

The advantages and disadvantages of software products for data analysis were compared, such as: R, Matlab, SPSS, Stata, SAS. Overall, R and Matlab get the most advantage and are suitable for factor analysis in [14–16]. And Matlab was chosen to be used for analysis in this study because in addition to its more powerful features than other software it is more common and easier to use.

The subject of this research is the economic development of Thai Binh, which is a province in the North of Vietnam. According to the assessment of economic experts, Thai Binh has a lot of potential for economic development, but until many years now, the economic development of Thai Binh is still low compared to other regions.

Based on methods factor analysis in the MatLab environment, a model has been built to analyze the factor affecting the development of the economy of the Thai Binh of Vietnam, groups of new factors are classified with reducing the number of factors, the new factors are called by more suitable new names, that are used for practical analysis of the development of the economy of Thai Binh.

## 2 Model for Analysis

The factor analysis method based on the method of principal components consists in decomposing (using an orthogonal transformation) a k-dimensional random vector

$$\mathbf{X} = (X_1, X_2, \dots, X_k)^T$$

Canonical factor analysis model for a centered vector  $\widehat{\mathbf{X}} = \mathbf{X} - \mathbf{M}\mathbf{X}$  has the following form:

$$\widehat{\mathbf{X}} = \mathbf{AF} + \widehat{\varepsilon} \quad (1)$$

where  $\mathbf{F} = (F_1, F_2, \dots, F_m)^T$ —centered and normalized random vector  $m(m < k)$  of uncorrelated common factors for all original random variables;  $X_i(i = 1, 2, \dots, k)$ ,  $\mathbf{A} = (a_{ij}) \in \mathbb{R}^{k \times m}$ —non-random matrix of loads of random variables  $X_i$  on factors  $F_j$ ;  $\widehat{\varepsilon} = (\widehat{\varepsilon}_1, \widehat{\varepsilon}_2, \dots, \widehat{\varepsilon}_k)^T$ —a centered vector of specific factors  $\widehat{\varepsilon}_1, \widehat{\varepsilon}_2, \dots, \widehat{\varepsilon}_k$  distributed according to the k-dimensional normal law, uncorrelated both with each other and with common factors.

Let  $\Sigma_{\mathbf{X}} = \mathbf{M}(\widehat{\mathbf{X}} \widehat{\mathbf{X}}^T)$ —covariance matrix of vector  $\mathbf{X}$ , and  $\Sigma_{\varepsilon} = \mathbf{M}(\widehat{\varepsilon} \widehat{\varepsilon}^T)$ —covariance matrix of the vector  $\widehat{\varepsilon}$  with diagonal entries equal to  $\mathbf{M}\widehat{\varepsilon}_i^2 = \mathbf{D}\widehat{\varepsilon}_i^2 = v_i$ .

Let construct a system of equations for determining the matrices  $\mathbf{A}$  and  $\Sigma_{\varepsilon}$ . Taking into account (1) and the conditions on the vectors  $\mathbf{F}$  and  $\widehat{\varepsilon}$  we obtain:

$$\begin{aligned} \Sigma_{\mathbf{X}} &= \mathbf{M}[(\mathbf{AF} + \widehat{\varepsilon})(\mathbf{AF} + \widehat{\varepsilon})^T] = \mathbf{M}(\mathbf{AFF}^T \mathbf{A}^T) \\ &\quad + \mathbf{M}(\mathbf{AF} \widehat{\varepsilon}^T) + \mathbf{M}(\widehat{\varepsilon} \mathbf{F}^T \mathbf{A}^T) + \mathbf{M}(\widehat{\varepsilon} \widehat{\varepsilon}^T) \\ &= \mathbf{M}(\mathbf{AIA}^T) + \mathbf{AM}(\mathbf{F} \widehat{\varepsilon}^T) + \mathbf{A}^T \mathbf{M}(\widehat{\varepsilon} \mathbf{F}^T) + \Sigma_{\varepsilon} \\ &= \mathbf{AA}^T + \Sigma_{\varepsilon} \end{aligned}$$

$$\text{Either } \left\{ \begin{array}{l} \text{cov}(X_i, X_p) = \sum_{j=1}^m a_{ij} a_{pj} \quad (i = 1, 2, \dots, k, \quad p = 1, 2, \dots, k, \quad p \neq i), \\ \text{cov}(X_i, X_i) = \mathbf{DX}_i = \sum_{j=1}^m a_{ij}^2 + v_i \quad (i = 1, 2, \dots, k). \end{array} \right. \quad (2)$$

Thus, here, the covariances of the initial random variables are completely reproduced by the load matrix, and in order to reproduce their variances, in addition to the loads, the variances  $v_i$  of specific factors are needed.

From here,  $\mathbf{D}X_i = h_i^2 + v_i$ , where  $h_i^2$ —community, part of the dispersion due to common factors,  $v_i$ —specificity of variable  $X_i$ .

Thus, if the covariance matrix of variables is known, then finding the loadings of factors on features is a matter of solving Eq. (2) with respect to  $\mathbf{A}$  and  $v_i$ . This solution is not unique.

In particular, if  $\mathbf{A}$  is a solution, then  $\tilde{\mathbf{A}} = \mathbf{AB}^{-1}$ , where  $\mathbf{B}$  is an orthogonal matrix, is also a solution.

It is in line with other factors associated with the old formula

$$\tilde{\mathbf{F}} = \mathbf{BF} \quad (3)$$

Since  $\mathbf{B}$  is an orthogonal matrix, (3) means the rotation of the coordinate system. It is possible to select  $\mathbf{B}$  in such a way that in  $\tilde{\mathbf{A}}$  the loadings of factors are large for some features and close to zero for others (the VARIMAX procedure). This will facilitate the interpretation of new factors.

The factor analysis in this study was carried out in 7 steps, which are shown in the (Fig. 1), and are detailed in the following sections of this paper, including:

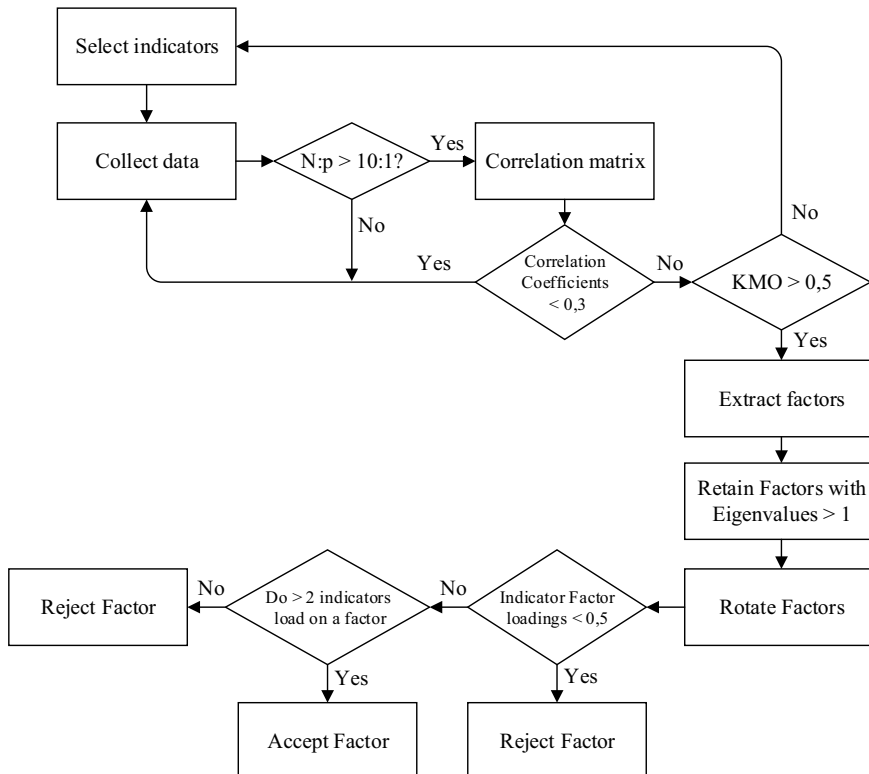


**Fig. 1** Factor analysis model

1. Initial data collection.
2. Checking the correlation coefficients between factors:
3. Kaiser–Meyer–Olkin Measure of Sampling Adequacy.
4. Selecting the number of components to extract.
5. Rotation method.
6. Interpret Factor Analysis Results.

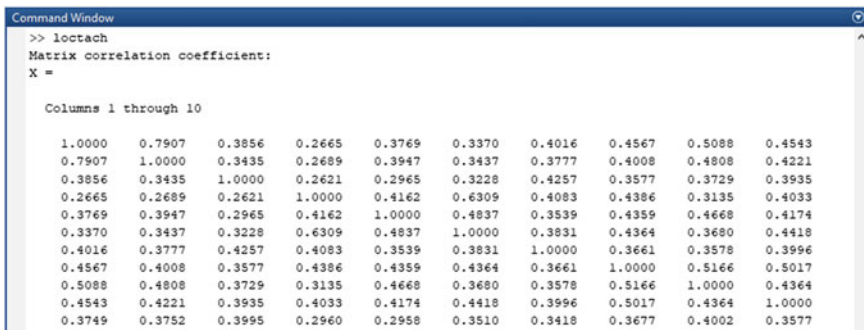
## 2.1 Initial Data Collection

First, in collecting data for analysis, the initial items that are believed to affect the economic development of Thai Binh, include 13 measure items (Fig. 2), which are divided into 44 variables in the scale, which are collected data from the Vietnam Statistical Office.

For factor analysis, sample size plays a big role. Many publications suggest many methods for determining an appropriate sample size, and the issue of sample size is also unresolved [13]. As early as 1973, Libo Comrie stated sample sizes: 100 as bad, 200 as fair, 300 as good, 500 as very good, and 1000 or more as excellent. In 1995, Hare and Anderson wrote in their paper that the sample size should be 100 or more. Meanwhile, Tabacnik and Fidell in 2001 thought 100 was not enough and suggested that the sample size should be 300 or more. In this paper, the sample size is 1000 observations with 44 variables, which is sufficient for sample size rules.

**Fig. 2** Initial measure items

Factors
1. Market demand for products
2. Access to tangible and intangible
3. Access to land and housing
4. Business climate
5. Local taxes
6. Local school systems
7. Utilities
8. Environmental awareness
9. Sports and culture
10. The quality of the workforce
11. Transport infrastructure
12. Government policy for economic
13. Others.



```

Command Window
>> loctach
Matrix correlation coefficient:
X =

Columns 1 through 10

1.0000    0.7907    0.3856    0.2665    0.3769    0.3370    0.4016    0.4567    0.5088    0.4543
0.7907    1.0000    0.3435    0.2689    0.3947    0.3437    0.3777    0.4008    0.4808    0.4221
0.3856    0.3435    1.0000    0.2621    0.2965    0.3228    0.4257    0.3577    0.3729    0.3935
0.2665    0.2689    0.2621    1.0000    0.4162    0.6309    0.4083    0.4386    0.3135    0.4033
0.3769    0.3947    0.2965    0.4162    1.0000    0.4837    0.3539    0.4359    0.4668    0.4174
0.3370    0.3437    0.3228    0.6309    0.4837    1.0000    0.3831    0.4364    0.3680    0.4418
0.4016    0.3777    0.4257    0.4083    0.3539    0.3831    1.0000    0.3661    0.3578    0.3996
0.4567    0.4008    0.3577    0.4386    0.4359    0.4364    0.3661    1.0000    0.5166    0.5017
0.5088    0.4808    0.3729    0.3135    0.4668    0.3680    0.3578    0.5166    1.0000    0.4364
0.4543    0.4221    0.3935    0.4033    0.4174    0.4418    0.3996    0.5017    0.4364    1.0000
0.3749    0.3752    0.3995    0.2960    0.2958    0.3510    0.3418    0.3677    0.4002    0.3577

```

**Fig. 3** Correlation matrix

## 2.2 *Checking the Correlation Coefficients Between Factors*

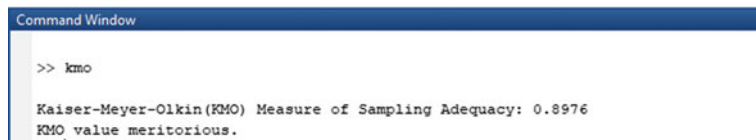
Checking the correlation coefficients is used to make sure that all items have some extent of correlation with the other items. The table (Fig. 3) shows the pairwise correlation coefficient between the variables, if the correlation coefficient is 0.3, it shows the eligibility to apply factor analysis, if the correlation coefficient reaches 0.4, it is the important, and if it is 0.5 then the expression gives the actual value. If the correlation coefficient is less than 0.30, it should be reconsidered whether factor analysis is an appropriate method for the data collected.

In this research, a satisfactory correlation matrix was obtained (Fig. 3). The values in the table are all greater than 0.3, most are between 0.4 and 0.5. That shows that these studies have practical significance.

## 2.3 *Kaiser–Meyer–Olkin Measure of Sampling Adequacy*

After checking the correlation of the coefficients, the question that must be answered is the adequacy of the sample and the suitability of the data for factor analysis. This requires estimating the ratio of correlation coefficient values to partial correlation coefficient values. The Kaiser–Meyer–Olkin index (KMO) is a good measure of this relationship. Large KMO values are a good indicator because research factors can be predicted by other factors.

The value of the KMO coefficient is in the range from 0 to 1. If the KMO is below 0.5, then using factor analysis is not accommodated with this data. On the other hand, the data with KMO value above 0.8 is considered adequate for analyzing with FA. The KMO in this research is reached with 0.8976, and it shows that the data are acceptable for the FA (Fig. 4).



```
Command Window

>> kmo

Kaiser-Meyer-Olkin(KMO) Measure of Sampling Adequacy: 0.8976
KMO value meritorious.
```

**Fig. 4** KMO measure of sampling adequacy

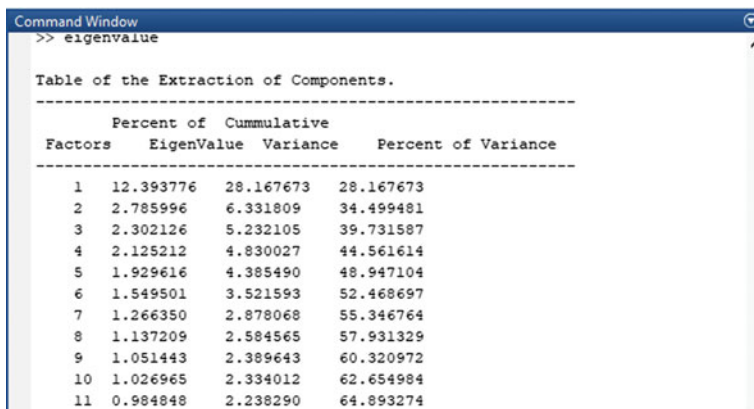
## 2.4 Selecting the Number of Components to Extract

The most common methods used to solve this problem are two main methods: Cumulative percent of variance extracted, Kaiser's criteria (eigenvalue > 1 rule) and Parallel Analysis. In some cases, they also give inconsistent results, so it is better for the analyst to use both methods at the same time.

According to the K1—Kaiser's method, the Eigenvalue is the total variance explained by the common factor. Any factor that has an Eigenvalues of less than one does not have enough total variance explained to depict a unique factor, and is therefore rejected. The eigenvalue for the exploratory data matrix is displayed on Fig. 5.

To determine the number of factors retained, Scree's graph was constructed (Fig. 6). The Scree plot is a graph illustrating the total variance associated with each factor. It is a visual graph of how many factors are contained in the data. The number of saved factors is the number of factors over the discontinuity of the Scree plot. The point at which discontinuity occurs does not count.

As can be seen from Figs. 5 and 6 that, although there are 10 factors have eigenvalues over one, so expect to find 10 principal components in the data.



Factors	EigenValue	Cumulative Variance	Percent of Variance
1	12.393776	28.167673	28.167673
2	2.785996	6.331809	34.499481
3	2.302126	5.232105	39.731587
4	2.125212	4.830027	44.561614
5	1.929616	4.385490	48.947104
6	1.549501	3.521593	52.468697
7	1.266350	2.878068	55.346764
8	1.137209	2.584565	57.931329
9	1.051443	2.389643	60.320972
10	1.026965	2.334012	62.654984
11	0.984848	2.238290	64.893274

**Fig. 5** Extraction of components

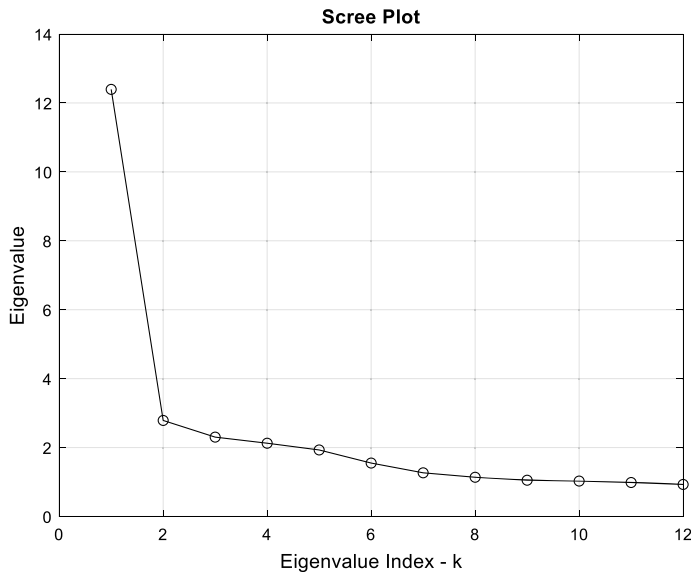


**Fig. 6** Scree plot

## 2.5 Rotation Method

The main purpose of the rotation method is to align the variables with the factor with which it is most relevant by maximizing high item loadings and minimizing low item loadings. The Rotated Factor Matrix represents the factor loadings for each variable on the components or factors after rotation. The rotated solution provides a bright indication of how each item correlates with each factor. There are 2 basic rotation techniques, which are oblique and orthogonal rotations. The methods often used in the oblique rotation technique are quartimin, forward oblique rotation, and promax. Also in orthogonal rotations, including quartimax, varimax, and equamax. It has been argued that orthogonal rotation produces more easily interpretable results and is simpler in complexity than oblique rotation.

In this research, there are 3 times to rotate the data before a solution has been found. The results of third factor loading matrix is shown (Fig. 7).

Suppress values of factor loading of 0.5 or even less, and still match each item with its corresponding factor. After distributing the factor loadings, the factor transformation matrix is obtained, which redefines each variable that measures precisely one factor.

Factorloadings3 =										
0.4731	0.0788	0.1196	0.1610	0.0771	0.1277	0.1212	0.0684	0.0261	-0.6654	
0.4681	0.1511	0.0901	0.1916	0.0454	0.1358	0.1628	0.0081	-0.0391	-0.6232	
0.6677	0.1201	0.1831	0.0228	0.0353	0.0322	0.0420	0.0276	0.1211	-0.0403	
0.2405	0.0518	0.0371	-0.0049	0.0563	0.1086	0.7731	0.0719	0.0649	-0.0024	
0.3012	0.0333	0.0915	0.1979	0.0827	0.1013	0.5731	0.1343	0.0484	-0.1684	
0.3287	0.0357	0.1138	0.0424	-0.0066	0.0230	0.7364	0.0598	0.0460	-0.0448	
0.5448	0.1159	0.0554	0.0989	0.0164	0.1493	0.2871	0.1213	-0.0006	-0.0545	
0.3736	0.0109	0.1646	0.0389	0.0400	-0.0031	0.3856	0.3363	0.1951	-0.2929	
0.4055	0.0649	0.1272	0.2068	0.1280	0.1418	0.2703	0.1758	0.2713	-0.3308	
0.5027	0.1118	-0.0167	0.0266	-0.0294	0.1161	0.3294	0.1947	0.1632	-0.2341	
0.6147	0.0127	0.0239	0.1022	0.0179	0.1726	0.1782	0.0619	0.1381	0.0339	
0.7440	0.0483	0.0550	0.0850	0.0527	0.0937	0.1563	0.1362	0.0206	-0.0131	
0.6536	0.1439	0.1014	0.0380	0.0833	-0.1404	0.0632	0.1075	0.0872	-0.1929	

**Fig. 7** Rotated factor matrix

## 2.6 Interpret Factor Analysis Results

After obtaining 10 groups of factors including corresponding sub-factors, the next task is to identify the names of those factors, looking for what each factor represents. The results are presented in the figure below (Fig. 8). This is the research process for selecting variables that relate to a construct and naming that construct.

Thus, the factors affecting economy of Thai Binh include: Corporate environment, utilities and local taxes; Development to tangible and intangible resources, Living environment, opportunity, and quality of workers and employees; Local politics, transportation, and availability of organized sporting events; Availability of places of worship, communication, quality of water transport services; Government policy in the field of economic development; The right to work, access to natural gas; Market demand for products; Literacy rate of the available labor force; Quality of area highways, wage rates compared to other potential locations, in which the initial factors that need to be focused are: Corporate environment, utilities, and local taxes, in which, special attention should be paid to: Crime level; Access to marketing and advertising services; Local taxes on businesses (property, sales); Government taxes on businesses and individuals; Availability of unskilled labor; Availability of high-speed telecommunication services; The quality of life; Power quality; Affordable water supply; Land value; Quality of higher education and research institutions; General business climate. These 10 factors consist of 33 sub-factors, which are shown in detail in the chart above, each row represents a factor and the sub-factors it contains [15, 16].

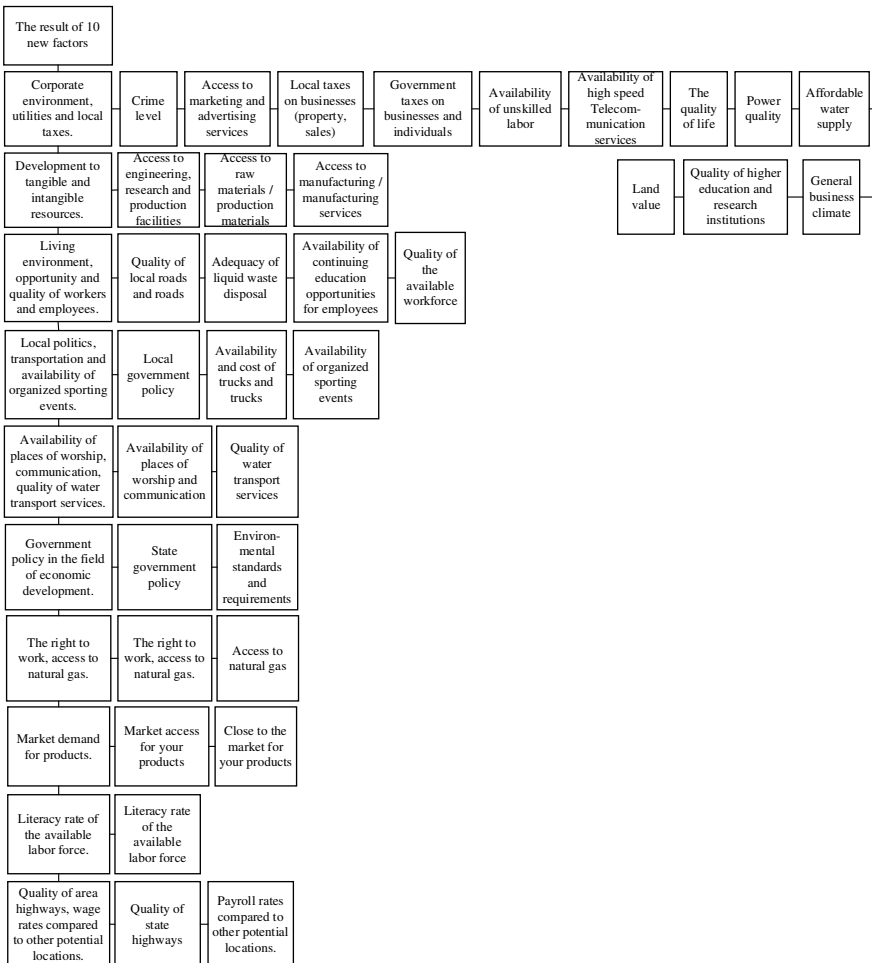


**Fig. 8** Factor analysis results

### 3 Conclusion

By using the factor analysis method in the Matlab environment, the results obtained are the selection, classification, and discovery of new factors and contact with reality to give the direction of Thai Binh economic development. Create a model with the help of Matlab to analyses economic development, defining factors, which influences with economic development, based on mathematical multivariable statistical methods applied to the economic regions of Vietnam. From the initial data consisting of 13 items including 44 measure variables, the result obtained 10 new factors including 33 sub-factors that affect the economic development of Thai Binh. This result is the basis to help Thai Binh find the most effective plan to promote economic development, and

this result could be applied to perform other analyzes in the future for the purposes of researchers.

## References

1. Volkova VN, Loginova AV, Chernenkaya LV, Romanova EV, Chernyy YY, Lankin VE (2018) Problems of sustainable development of socio-economic systems in the implementation of innovations. In: Proceedings of the 3 rd international conference ERGO-2018: human factors in complex technical systems and environments, ERGO, 2018, pp 53–56
2. Kaiser H (1960) The application of electronic computers to factor analysis. *Educat Psychol Measur* 141–151
3. Hillsdale JS (1986) NJ: Erlbaum applied multivariate statistics for the social sciences. 8 + 515
4. Cooley WW, Lohnes PR (1973) Review of multivariate data analysis. *J Royal Statist Soc Series A (General)* 136(1):101–103
5. Harman HH, Jones WH (1966) Factor analysis by minimizing residuals (Minres). *Psychometrika* 31:351–369
6. Kim JO, Mueller CW (1978) Factor analysis: statistical methods and practical issues. Sage, Beverly Hills, CA
7. Lawley DN, Maxwell AE (1971) Factor analysis as a statistical method, 2nd edn. Butterworths, London
8. Lindeman RH, Merenda PF, Gold RZ (1980) Introduction to bivariate and multivariate analysis. Glenview, IL, Scott, Foresman and Company
9. Morrison DF (1967) In: Multivariate statistical methods. New York, McGraw-Hill, pp 16 + 338
10. Mulaik SA (1972) In: The foundations of factor analysis. New York, McGraw-Hill. pp 16 + 453
11. Wherry RJ (1984) In: Contributions to correlational analysis. Academic Press. <https://doi.org/10.1016/C2013-0-11694-7>
12. Fabrigar LR, Wegener DT, MacCallum RC, Strahan EJ (1999) Evaluating the use of exploratory factor analysis in psychological research. *Psychol Methods* 4(3). <https://doi.org/10.1037/1082-989X.4.3.272>
13. Taherdoost H, Sahibuddin S, Jalaliyoon N (2014) Exploratory factor analysis: concepts and theory. *Advances in applied and pure mathematics*. pp 375–382
14. Leonova TI, Mager VE, Mikeladze BD, Chernenkaya LV, Chernenkii AV (2017) Support of decision-making in organization's quality management. In: Proceedings of 2017 XX IEEE international conference on soft computing and measurement (SCM-2017). pp 843–845
15. Nguyen Thi TD, Chernenkaya LV (2020) A model for analyzing the development of the economy of the Thai Bing region (Vietnam) based on mathematical methods of multivariate statistics. In the collection: system analysis in design and management. collection of scientific papers of the XXIV International scientific and educational-practical conference. St. Petersburg, pp 497–505
16. Nguyen TTD, Chernenkaya LV (2020) Models for analyzing the development of the economy of several regions of Vietnam based on mathematical methods of multivariate statistics. In the collection: impulse of organizational innovations. Collection of competitive works of the 1st interuniversity competition of students, undergraduates and graduate students. Moscow, (2020), pp 301–324

# Password Scheme: Amalgamation of Characters with Picture



Sk Sahnawaj and Apratim Mitra

**Abstract** Since the inception of computer system security has been an issue. To secure the computerized system password verification is prime objective. Traditional system of character-based password is vulnerable to various attacks. For more secure authentication, picture is used as password. Instead of using character or picture as password, an amalgamation of both picture and character is more secure authentication system. The image is divided into the user specified number of rows and columns. Considering the number of rows is  $m$  and number of columns is  $n$ , then the selected image is of  $m \times n$  grids. The character set is also divided into  $m \times n$  matrix. User selects at least 8 grids from portioned image which produces a sequence of  $(a_m, a_n)$ . Each value of  $(a_m, a_n)$  maps to the value of  $(a_i, a_j)$  of character matrix which forms a sequence of characters. This set of characters formed the password. This paper explores the combination of character and picture as a potential solution to overcome the different kinds of attack. This work also achieves better secure authentication system.

**Keywords** Identity verification · Shoulder surfing · Grid · Password

## 1 Introduction

Password authentication is the technique of identifying the intended user who requests to utilize the resources. Most extensively used authentication system is text-based which suffers from security issues. Text-based identification is more susceptible to beat. In order to defeat the pitfalls of text-based verification scheme, picture-based verification scheme is used. Picture-based authentication consists of an image or a sequence of images set as password. Text-based and picture-based authentication are two categories of knowledge-based technique which depends upon the

---

S. Sahnawaj (✉) · A. Mitra

Department of Computer Applications, Haldia Institute of Technology, Haldia, West Bengal 721657, India

e-mail: [sahnawaj.sk@gmail.com](mailto:sahnawaj.sk@gmail.com)

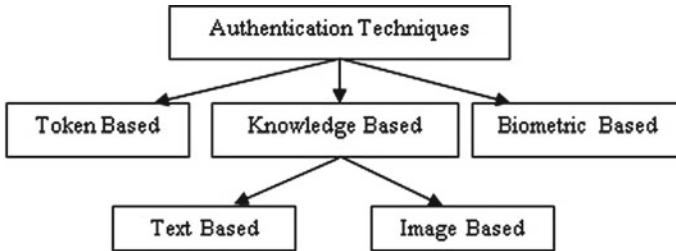


**Fig. 1** Classification of authentication techniques

data supplied by the user. In 1996, Blonder [1] first proposed the graphical password scheme which demonstrates to select one or more point from the image as password. Here, the key issue is the memorization of points. In [2], proposed that click on any point in the picture and define as password. This scheme is more secure than Blonder's scheme. In Draw-A-Secret (DAS) scheme, lines are drawn in NxN grid and set as password, proposed in [2], which is vulnerable to dictionary attack. Déjà vu scheme, proposed by Dhamija et al. [3], in 2000, allowed the users to set abstract pictures as password. As the image is abstract, it is hard to guess but hard to remember. In PassFaces scheme, users allowed to select human face as password, proposed by Brostoff et al. [4, 5]; selecting face is an issue to memorize. In [6], demonstrated the combination of text and graph as password focus on security of authentication. In [7, 8], proposed image identification method to resist shoulder surfing attack. Limitations of literatures deal with secure authentication technique motivate to design a new approach of secure identification scheme which also defy shoulder surfing attack. The shoulder surfing attacks employ surveillance over one's shoulder or apply video-capture technology or any other venue to collect one's secret information [8, 9] (Fig. 1).

In this paper, we proposed a scheme which challenges to resist the different kind of attacks, namely shoulder surfing, guessing, phishing, and dictionary attack. This scheme beats the memorability issue. Traditionally, characters are used as password, and alternative approach is image which is used as password. Our scheme is the amalgamation of both characters and images which is used as password which enhances security aspect. The scheme uses picture-matrix and character-matrix. User chooses grids from picture-matrix. As a consequence, a sequence of grid value is generated; then according to the sequence, user selects characters from character-matrix. This scheme consists of three phases.

The paper is structured as follows: Sect. 2 demonstrates the amalgamation of characters with picture scheme. Section 3 illustrates the proposed scheme. The result analysis is discussed in Sect. 4. The conclusion of the paper is introduce in Sect. 5.

## 2 Creating Image Password

### 2.1 Phase 1

User imports any picture to be used as the verification of identity. The picture is partition into the specific number of rows and columns. For example, we divide the picture into 5 rows and 6 columns; as a result, we get  $5 \times 6$  grids. So the picture is divided into 30 different sections. This partition of picture refers as  $5 \times 6$  matrixes, named as picture-matrix. This procedure divides the picture into 30 different cells (Figs. 2 and 3).

#### 2.1.1 Phase 2

User uses a set of characters. The characters are arranged into  $5 \times 6$  matrix format, named as character-matrix. As a result, the characters are placed into 30 cells (Fig. 4).

**Fig. 2** Picture registered by the user

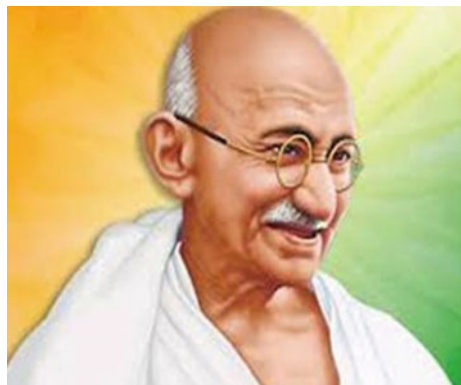


**Fig. 3** Picture-matrix: picture is portioned into  $5 \times 6$  matrix

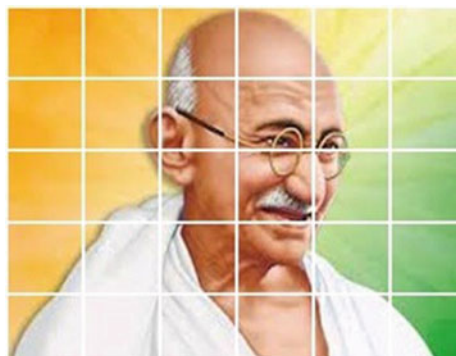
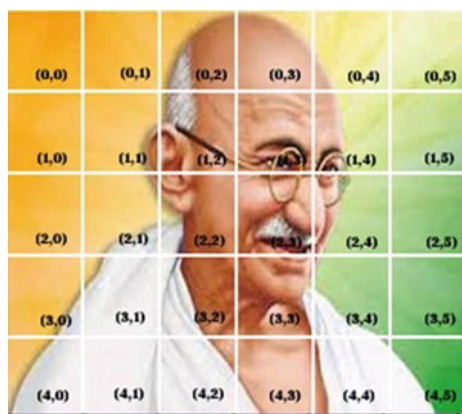


**Fig. 4** Character-matrix:  
characters arranged into  
 $5 \times 6$  matrix

q	w	e	r	t	y
u	i	o	p	a	s
d	f	g	h	j	k
l	z	x	c	v	b
n	m	!	#	@	\$

**Fig. 5** Value of each cell of  
picture-matrix



### 3 Creating Character Password

#### 3.1 Phase 3

From picture-matrix, user selects at least 8 cells. The value of each cell ( $a_m, a_n$ ) of picture-matrix corresponds to the value of each cell ( $a_i, a_j$ ) of character-matrix. This procedure produces the sequence of characters which is used as password (Fig. 5).

### 4 Analysis and Discussion of this Scheme

User selects cell ( $a_m, a_n$ ) form picture-matrix. From character-matrix, match the ( $a_i, a_j$ ) with the ( $a_m, a_n$ ). Consider the value of ( $a_m, a_n$ ) = (0, 3), so ( $a_i, a_j$ ) = (0, 3),

**Fig. 6** Selected grids from picture-matrix

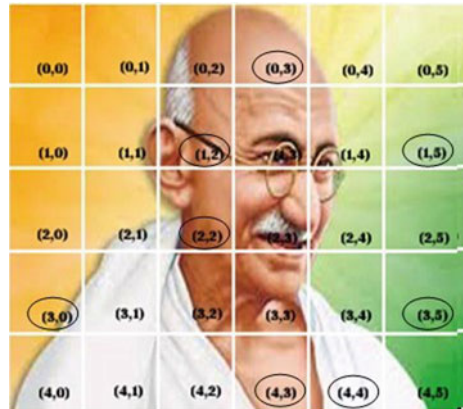


**Fig. 7** Corresponding characters of selected grids

q	w	e	r	t	y
u	i	o	p	a	s
d	f	g	h	j	k
l	z	x	c	v	b
n	m	!	#	@	\$

which is the character “e”. Following the same method, user selects 8 or more grids from picture-matrix  $(a_m, a_n)$ , where  $m = 0 \dots 5$  and  $n = 0 \dots 6$ , corresponding 8 or more characters from  $(a_i, a_j)$  form the desired password. If selecting grids from picture-matrix is the sequence  $((4, 4), (0, 3), (1, 2), (2, 2), (1, 5), (3, 0), (3, 5), (4, 3))$ , then corresponding sequence of characters from character-matrix @rogslb# forms the password (Figs. 6 and 7).

#### 4.1 Space of Password

The scheme enhances the space of password. Let  $n$  be the number of sections or grids of the picture portfolio. Let  $k$ , which set as password by the user, be the number of grids selected randomly from the picture-matrix. The entropy of the password is  $\log_2(n!/(n - k)!)$  bits, since grids maintained an order. Considering an example,

**Table 1** Comparison of different attacks

Scheme	Shoulder surfing	Guessing	Phishing	Dictionary
Picture password [6]	No	Yes	Medium	Yes
PassFaces [5]	No	No	Medium	No
Déjàvu [4]	No	Yes	Medium	Yes
Story [8]	No	Yes	Medium	Yes
Proposed scheme	Yes	Yes	Hard	Yes

$n = 30$  and  $k = 8$ , entropy =  $\log_2(30!/22!) = 44.8(\text{aprx})$  bits. So if  $k$  increases, then entropy increases. Let  $A$  be the number of characters of character-matrix and  $c$  be the number of corresponding characters, then entropy is  $(c \cdot \log_2(A))$  bits. Taking into account the above example,  $n = 30$  means  $A = 30$ , and  $k = 8$  means  $c = 8$ . Hence, entropy is  $8\log_2(30) = 40(\text{aprx})$ . When  $k$  increases, the value of  $c$  also increases, resulting entropy of character increases significantly.

## 4.2 Mitigating Several Attacks

Table 1 illustrates the comparison of different attacks of our scheme with other well-known schemes. The schemes are specified in the first column. The various attacks are mentioned in other columns which contain the value “Yes” and “No”. The column value “Yes” represents that the scheme is resistant to the hit, while the column value “No” indicates that the scheme is not resistant to the hit. Instead of selecting characters as password, user selects grids from the picture-matrix, so it is not possible for an invader to watch and remember the entry of password. As a consequence, our scheme overcomes shoulder surfing problem. The picture may be known to the invader but it is not possible to guess the grids selected by the user. Since specific characters are not used, dictionary attack is not possible in our scheme. Also phishing attack is hard to implement in our scheme as user choose grids instead of characters.

## 5 Conclusion

This work offers a secure approach for identification. The prime focus of our scheme is to overcome the shoulder surfing attack which stand firm by this scheme. Considering security aspect, our scheme resists different kind of attacks. The pass-

word space is much larger as picture is used. This work has potential to offer assurance to develop more secure password. It is easy to remember the image and no need to remember the characters which set as password. Also it is very simple to implement and no need to train the general users.

## References

1. Blonder GE (1996) Graphical password nonlinear. US patent 5,559,961
2. Jermyn I (1999) The design and analysis of graphical passwords. In: Proceedings of the 8th conference on USENIX security symposium, vol 8, issue 2, pp 244–248
3. Perrig A, Dhamija R (2000) A user study using images for authentication. In: USENIX security symposium, Denver, Colorado, USA
4. Brostoff S, Sasse MA (2000) Are passfaces more usable than passwords? a field trial investigation. In: Sharon McDonald GC, Waern Y (eds) People and computers XIVUsability or else! Proceedings of HCI 2000. Springer, pp 405–424
5. Morgan K, University of Bergen N, Spector JM (2000) Authenticating mobile device users through image selection. In: Morgan K, University of Bergen N, Spector JM, Syracuse University U (eds) The internet society: advances in learning, commerce and security. WITPress, pp 183–194
6. Akinyele A, Joseph E, Abdul OIS (2022) An efficient and secured graphical authentication system. *Acta Informatica Malaysia* 6:17–21. <https://doi.org/10.26480/aim.01.2022.17.21>
7. Bostan H, Bostan A (2021) Shoulder surfing resistant graphical password schema: randomized pass points (RNN). In: 2021 International conference on information security and cryptology (ISCTURKEY), pp 81–86. <https://doi.org/10.1109/ISCTURKEY53027.2021.9654422>
8. Sun H-M, Chen S-T, Yeh J-H, Cheng C-Y (2018) A shoulder surfing resistant graphical authentication system. *IEEE Trans Depend Secur Compu* 15(2):180–193. <https://doi.org/10.1109/TDSC.2016.2539942>
9. Kwon T, Shin S, Na S (2014) Covert attentional shoulder surfing: Human adversaries are more powerful than expected. *IEEE Trans Syst Man Cybern: Syst* 44(6):716–727. <https://doi.org/10.1109/TSMC.2013.2270227>

# Performance Analysis of Energy Harvesting-Based CR Network Assisted by Full-Duplex Relays Under Joint Underlay/Overlay Mode



Dipak Samanta, Chanchal Kumar De, and Abhijit Chandra

**Abstract** In this paper provides a energy harvesting-based cognitive radio network (CRN) that evaluates the end-to-end outage performance of secondary user communications under a full-duplex relay network through a joint underlay/overlay protocol. Secondary transmitters simultaneously Switch between overlay and underlay mode based on sensing results; if primary users (PUs) are not active, they run in overlay mode with the maximum allowed transmit power; otherwise, they operate in underlay mode with transmit power limitation. A dynamically adaptable amalgamation of the underlay/overlay protocol is created based on channel occupancy to improve the efficiency of the spectrum. A radio frequency (RF) energy detector circuit is present in each secondary transmitter node, allowing it to detect energy from the transmitters of several primary users. The FD relays together with the hybrid functioning of joint mode transmission allows for an improvement in system throughput. We devised a mathematical study to jointly assign power at each transmitting node in such a way that improves the throughput of the system. The existence of self-interference (SI) at an FD relay network and interference effect from multiple PUs transmitter has also been addressed. Lastly, all analytical mathematical statements in closed form have been verified using Monte Carlo simulations.

**Keywords** Cognitive radio · Full-duplex relay · Joint underlay/overlay · Self-interference

---

D. Samanta (✉) · C. K. De

Department of ECE, Haldia Institute of Technology, Haldia, WB 721657, India  
e-mail: [dipak.ecehit@gmail.com](mailto:dipak.ecehit@gmail.com)

A. Chandra

Department of IEE, Jadavpur University, Jadavpur, WB 700032, India

## 1 Introduction

Spectrum scarcity is one of the most difficult concerns in wireless communication owing to the tremendous rise in data traffic, and it must be managed appropriately. The Federal Communications Commission's assessments, however, showed that the spectrum, particularly in wireless sensor networks, is underutilised [1]. This is the driving force behind the development of cognitive radio (CR) technology, which enables spectrum reuse [2]. The spectrum allotted to licensed users, i.e. primary users (PU), can occasionally be accessed by non-licensed users, i.e. secondary users (SU). Spectrum sensing, spectrum management, spectrum sharing, and spectrum mobility are major functions in CR technology. The fundamental goal of spectrum sensing is to identify the presence of PU spectrum, whether it is inactive or active [3]. Cognitive radio technology incorporates an overlay or underlay mode for secondary users to access the licensed spectrum in order to enhance spectrum usage [4–6]. During the overlay method, the secondary transmitter (ST) uses the available spectrum of PU, which is not accessible by PU. When the interference from ST to the primary receiver (PR) stays below a specific threshold, ST and the primary transmitter (PT) can communicate jointly with their respective receivers in underlay mode [7]. The underlay and overlay mode for CR networks are smartly chosen by ST after detection of the PU spectrum [3]. In [6], the outage analysis of secondary receiver (SR) networks has been evaluated for the multi-antenna, multi-relay-based CR networks that are operated in joint underlay/overlay mode. Green communication networks have gained a lot of attention as a viable way to deal with the worldwide energy shortfall and environmental problem [8]. In [9] authors illustrated the energy harvesting (EH) approach at the ST from radio frequency (RF) signal of active PU transmitters. Here calculation for transmission probability and maximum throughput under outage constraints for secondary receiver is explored apparently. The performance of cooperative spectrum sharing networks is considerably enhanced when employing alternative relay selection schemes, such as amplify-and-forward (AF), decode-and-forward (DF), and adaptive hybrid relays (AHR) relaying protocols [10–12]. Cognitive radio, in conjunction with Full-Duplex (FD) transmission technology, improves spectrum use and network efficiency [13]. The transmission in a half-duplex relaying network involves two hops, from the source to the relay and then from the relay to the destination. For such relay networks, the FD transmission method has been crucial in overcoming the problems of spectral inefficiency. The use of FD methods has enabled the relay node to transmit and receive signals simultaneously at the expense of self-interference (SI), which is undesirable. The active and passive cancellation of SI factor with several FD relays in a multi-user spectrum sharing environment has been proposed in [14].

### **1.1 Major Contribution**

The aforementioned studies encourage finding to construct a model and to analyse the system performance of energy harvesting-based CR network communicated via full-duplex relays under joint underlay/overlay protocol.

The important contributions of this paper are summarised as follows:

- It has been addressed how a CR network can operate in underlay, overlay, or joint underlay/overlay mode in the presence of an FD relay network.
- Multiple primary users of CRN and an adaptive joint underlay or overlay transmission technique are taken into consideration.
- Impact of self-interference at each FD relay along with all the transmitting interference at each receiving nodes have been thoroughly discussed. A comparison between an FD relaying protocol and a traditional HD relaying protocol has been made.
- The effects of self interference at each FD relay as well as all of the transmitting interference at each receiving node have been thoroughly discussed.
- The secondary outage performance is evaluated at various channel occupancy factor values.
- The impacts of modifying the efficiency factor of the energy harvesting circuit on secondary outage performance have been properly examined.
- Final closed-form mathematical equations for the probability of SU outage during adaptive transmission via a CR network with FD relays are assessed.

The rest of the article is organised as follows: The system architecture and underlying assumption are illustrated in Sect. 2. Section 3 gives a concise explanation of their compact power allocation techniques in an energy harvesting environment. The evaluation of the performance and mathematical analysis, which includes the closed-form expressions, comes next in Sect. 4. The simulation results and associated discussion are shown in Sect. 5. Finally, the conclusion of this paper is described in Sect. 6.

## **2 System Model**

Figure 1 depicts the system architecture of a cognitive radio network where a secondary user ( $SU_{TR}$ ) make to communicate with secondary user receiver ( $SU_R$ ) via multi-FD relays ( $R_l; l = 1, 2 \dots L$ ) in presence of multi-primary users ( $PU_m; m = 1, 2 \dots M$ ). Here a assumption is made on an FD relay that each are incorporated with one transmitting and one receiving antenna except all other nodes with single antenna. It is also assumed that in the suggested system model there is no direct connectivity between  $SU_{TR}$  and  $SU_R$  due to excessive shadowing and multipath propagation loss. The EH-enabled circuits are attached on both FD relays and ( $SU_{TR}$ ), allowing them to draw power from RF signals in the surrounding area. The interference source of

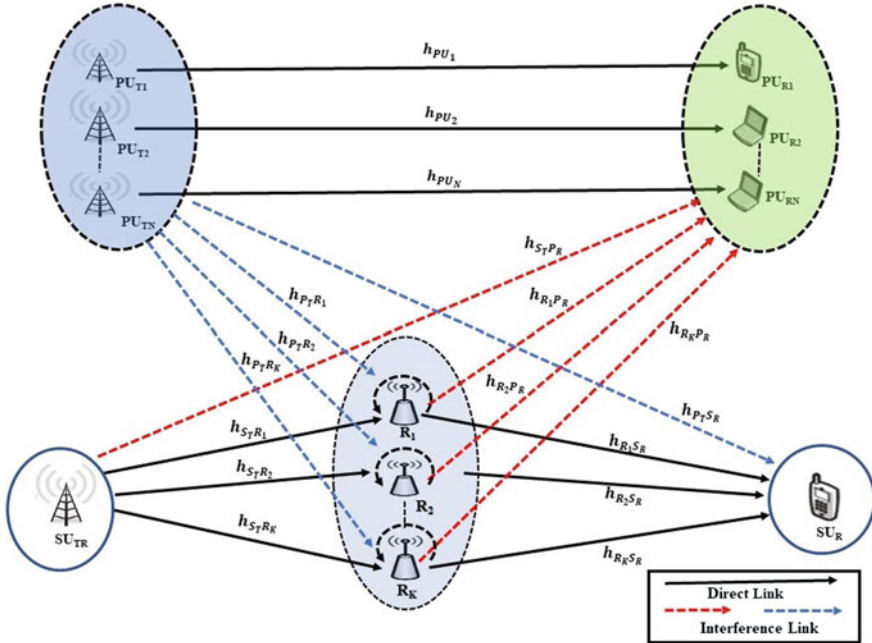


**Fig. 1** System model

the  $M$  active PUs can be used by the secondary transmitting nodes (i.e.  $SU_{TR}$ , FD relays) to generate some amount of their energy. The  $SU_{TR}$  connects with the  $SU_R$  over the FD relay network in a concurrent transmitting-receiving procedure. All of the channel coefficients are considered by  $h_{x,y}$ , which obeys the Rayleigh distribution and the equivalent power gains are expressed as  $g_{x,y}$ , this follows an Exponential distribution with mean  $\lambda_m$ , where ‘ $x, y$ ’ represents the relevant channel pathway with suffix  $m = a, ., h$  from each node. The distinct path specifications are displayed in the following Table 1. In the proposed system, the transmission procedure is considered to be of a dual-hop nature. The first hop is concerned with transmitting data from  $SU_{TR}$  to  $R_L$ , where the best relay  $R_L$  is selected in accordance with the relay section scheme and channel quality, respectively.

The principle operation is based on two phases of time slots as in phase one, where the secondary transmitters takes part in sensing as well as energy harvesting (EH) activity by energy detector and EH circuit, respectively. Additionally, in phase two all the secondary transmitters actively takes part in data transmission. The optimal relay is selected using this relaying selection combination (SC) strategy based on a process to optimise the minimum of the weighted channel strength between the links from the source to the relays and from the relays to the destination. As the relay  $R_L$  has been assumed to operate in full-duplex mode, it is receiving and transmitting data at the same time, which is what mostly causes self-interference (SI) at the receive antenna

**Table 1** Path-with channel gain parameter chart

Path-with channel gain parameter chart		
Path- $(i, j)$ , channel coefficient( $h_{i,j}$ )	gain $g_{i,j}$	Parameter chart $\lambda_m$
$\text{PU}_{TM}\text{-}\text{PU}_{RM}, h_{p_m}$	$g_{p_n}$	$\lambda_a$
$\text{SU}_{TR}\text{-}\text{PU}_{RM}, h_{STP_R}$	$g_{STP_R}$	$\lambda_b$
$R_L\text{-}\text{PU}_{RM}, h_{R_LP_R}$	$g_{R_LP_R}$	$\lambda_c$
$\text{PU}_{TM}\text{-}R_L, h_{P_T R_L}$	$g_{P_T R_L}$	$\lambda_d$
$\text{PU}_{TM}\text{-}\text{SU}_R, h_{P_TS_R}$	$g_{P_TS_R}$	$\lambda_e$
$\text{SU}_{TR}\text{-}R_L, h_{S_T R_L}$	$g_{S_T R_L}$	$\lambda_f$
$R_L\text{-}\text{SU}_R, h_{R_L S_R}$	$g_{R_L S_R}$	$\lambda_g$
$R_L\text{-}R_L, h_{R_L}$	$g_{R_L}$	$\lambda_h$

of  $R_L$ . This SI is being modelled as an independent Rayleigh distributed channel. The implementation of the successive interference cancellation (SIC) process is unable to fully eliminate SI at the relay.

In order to increase the spectrum efficiency of the CR network, this study provides an adaptive hybrid underlay/overlay transmission system.  $\text{SU}_{TR}$  and all relays can detect PU activity using an energy detector circuit built into them. Relays and  $\text{SU}_{TR}$  made wise decisions by switching between underlay and overlay mode depending on the outcome of the PU activity to communicate with secondary receiver. If the PU is engaged after detecting it,  $\text{SU}_{TR}$  shifts to underlay mode; if not,  $\text{SU}_{TR}$  functions at its maximum power overlay mode, assisted by a number of active FD relays. According to data from the FCC [1], average channel occupancy for the measuring period was close to 15%, while peak utilisation was close to 85%. It is assumed that  $\vartheta$  represent probability of channel occupancy ( $0 \leq \vartheta \leq 1$ ), which depicts the busyness of PUs. As a result, the probability of PU being busy is  $\vartheta P_d$ , while the probability of PU being inactive is  $(1 - \vartheta) P_d$ , where this probability of detection  $P_d$  identifies the probability of the presence of primary signal.

### 3 Compact Power Allocation at Every Nodes

Time Switching Relaying (TSR) protocol is used by the secondary source  $\text{SU}_{TR}$  and the relays  $R_L$  for manual energy harvesting and signal transfer. It is presumed that  $T$  is the entire amount of time needed for message packet to be transmitted from  $\text{SU}_{TR}$  to the secondary destination. Additionally, the assumption has been made that secondary transmitting nodes requires  $\tau$  amount of time to sense as well as gather energy from the  $M$  number of PU transmitter. The remaining time ( $T - \tau$ ) is utilised to transmit data.

Over a given time  $\tau$ , the total harvested energy from  $M$  active primary transmitters at secondary sources are calculated as described below.

The amount of harvested energy at  $SU_{TR}$  is given by:

$$E_{S_{TR}}^H = \eta \tau \left( \sum_{m=1}^M P_m g_{m_s} \right) \quad (1)$$

where,  $P_m$  represents the transmitted power from a single  $PU_{TR}$  and  $g_{m_s}$  is the associated channel gain.  $\eta$  specifies the energy harvesting circuit's efficiency factor at each secondary transmitter node. The amount of transmission power at  $SU_{TR}$  during the time  $(T - \tau)$  is expressed as,

$$P_{S_{TR}}^H = \left( \frac{E_{S_{TR}}^H}{T - \tau} \right) \quad (2)$$

The amount of harvested energy at  $R_L$  relay during  $\tau$  time from  $M$  active primary transmitters and secondary source  $SU_{TR}$  is given by

$$E_{R_L}^H = \eta \tau \left( P_{st} g_{S_{TR} R_L} + \sum_{m=1}^M P_m g_{P_{TR} R_L} \right) \quad (3)$$

where,  $P_{st}$  represents the underlay mode transmitted power by  $SU_{TR}$ , that maintains the outage constraint of primary. In a similar way  $R_L$  operates with its transmit power at time  $(T - \tau)$ , accompanied by EH circuit is expressed as:

$$P_{R_L}^H = \left( \frac{E_{R_L}^H}{T - \tau} \right) \quad (4)$$

The peak interference parameter  $I_p$  of the primary network limits the simultaneous transmit power from  $SU_{TR}$  and  $R_L$  as in the following equation also we are depending on the idea of sharing spectrum with  $R_L$  operating in full-duplex communication process [15]

$$I_p \geq (P_{st} g_{S_{TR} P_R} + P_{R_L} g_{R_L P_R}) \quad (5)$$

From above expression, assuming non-optimal condition for  $P_{st}$  and  $P_{R_L}$  for simplicity, with the necessary condition that the transmit power of  $SU_{TR}$  and  $R_L$  are maintained that the communication of SUs does not cause any PUs to be overly interfered.

The received signal at  $n$ th PU face the signal-to-interference-noise-ratio (SINR) defined as:

$$\gamma_n = \frac{P_m g_{P_m}}{P_{st} g_{S_{TR} P_R} + P_{R_L} g_{R_L P_R} + N_0} \quad (6)$$

The SU<sub>TR</sub> and R<sub>L</sub> transmit powers should be maintained in order to prevent any PUs from experiencing severe interference from the SU's transmission.

Therefore, the outage value at the PU receiver can be expressed as:

$$P_O^p = Pr \left[ \min_{m=1,\dots,M} \left( \frac{P_m g_{P_m}}{P_{st} g_{S_T P_R} + P_{R_L} g_{R_L P_R} + N_0} \leq \gamma_{th}^{Pr} \right) \right] \leq \varepsilon \quad (7)$$

here,  $\gamma_{th}^{Pr} = 2^{R_{Pr}} - 1$  including  $\varepsilon$  signify the outage threshold and constraint of a primary receiver (PU<sub>Re</sub>), respectively. Let us assume PU transmits data at the rate of  $R_{Pr}$ .

After considering non optimal power condition in Eq. (6) can be modified as

$$\begin{aligned} P_O^p &= Pr \left[ \min_{m=1,2,\dots,M} \left( \frac{P_m g_{P_m}}{2P_{st} g_{S_T P_R} + N_0} \leq \gamma_{th}^{Pr} \right) \right] \leq \varepsilon \\ &= 1 - \sum_{m=1}^M \left[ 1 - \underbrace{Pr \left( \frac{P_m g_{P_m}}{2P_{st} g_{S_T P_R} + N_0} \leq \gamma_{th}^{Pr} \right)}_{P^w} \right] \leq \varepsilon \end{aligned} \quad (8)$$

The aforementioned expression can be used to demonstrate the outage probability of  $P^w$  as [16]

$$P^w = 1 - \exp \left( -\frac{\gamma_{th}^{Pr} N_0}{P_p \lambda_a} \right) \left( \frac{P_p \lambda_a}{P_p \lambda_a + 2\gamma_{th}^{Pr} P_{st} \lambda_b} \right) \quad (9)$$

Consequently, after solving Eq. (8), the primary receiver's final outage behaviour is as follows:

$$P_O^p = 1 - \left[ \exp \left( -\frac{\gamma_{th}^{Pr} N_0}{P_p \lambda_a} \right) \left( \frac{P_p \lambda_a}{P_p \lambda_a + 2\gamma_{th}^{Pr} P_{st} \lambda_b} \right) \right]^N \leq \varepsilon \quad (10)$$

Given the aforementioned expression, the transmitted power by SU<sub>TR</sub> should be sufficient to prevent a PU receiver outage, which is expressed as

$$P_{st} = \frac{P_p \lambda_a}{2\gamma_{th}^{Pr} \lambda_b} \left[ \frac{\exp \left( -\frac{\gamma_{th}^{Pr} N_0}{P_p \lambda_a} \right)}{(1 - \varepsilon)^{\frac{1}{N}}} - 1 \right] \quad (11)$$

In similar manner R<sub>L</sub> would transmit power satisfying outage performance criteria of PU can be expressed as:

$$P_{R_L} = \frac{P_p \lambda_a}{2\gamma_{th}^{Pr} \lambda_c} \left[ \frac{\exp \left( -\frac{\gamma_{th}^{Pr} N_0}{P_p \lambda_a} \right)}{(1 - \varepsilon)^{\frac{1}{N}}} - 1 \right] \quad (12)$$

The output power of the secondary-source transmitter in underlay mode is determined by,

$$P_s^u = \min(P_{S_{TR}}^H, P_{st}) \quad (13)$$

The transmitting power from the secondary FD relay  $R_L$  in underlay mode is given by,

$$P_r^u = \min(P_{R_L}^H, P_{R_L}) \quad (14)$$

The transmitting power from  $SU_{TR}$  and FD relay  $R_L$  under overlay mode is expressed as:

$$P_s^o = P_{S_{TR}}^H \quad (15)$$

$$P_r^o = P_{R_L}^H \quad (16)$$

According to the mode of transmission which on opportunistically switching between underlay or overlay is based on sensing result that monitors the transmission power policies.

## 4 Performance and Mathematical Analysis

The received signal at the  $L^{th}$  relay during the underlay mode of operation is provided by:

$$y_{R_L}^u(t) = \sqrt{P_s^u} h_{S_{TR} R_L} x_s(t) + \sqrt{P_r^u} h_{L R_L} x_r(t) + \sum_{m=1}^M \sqrt{P_m} h_{P_T R_L} x_p(t) + n_o(t) \quad (17)$$

Thus, SINR at  $L^{th}$  FD relay under underlay transmission mode is derived from the above expression as:

$$\gamma_F^u = \frac{P_s^u g_{S_{TR} R_L}}{P_r^u h_L + \sum_{m=1}^M P_m g_{P_T R_L} + N_o} \quad (18)$$

The received signal at  $SU_R$  from the  $L^{th}$  FD relay in underlay mode is expressed by

$$y_{Re}^u(t) = \sqrt{P_r^u} h_{R_L R} x_r(t) + \sum_{m=1}^M \sqrt{P_m} h_{P_T S_R} x_p(t) + n_o(t) \quad (19)$$

Thus at underlay transmission mode the SINR at secondary receiver is given from the above expression as:

$$\gamma_{\text{Re}}^u = \frac{P_r^u g_{R_L}}{\sum_{m=1}^M P_m g_{P_T S_R} + N_o} \quad (20)$$

The end-to-end outage at receiver of secondary network under the performance of underlay protocol is calculated using selection combination technique and can be expressed as:

$$P_O^{un} = Pr \left[ \left\{ \max_L (\min (\gamma_F^u, \gamma_{\text{Re}}^u)) \right\} < \gamma_{\text{th}}^{\text{Re}} \right] \quad (21)$$

here,  $\gamma_{\text{th}}^{\text{Re}} = 2^{R_{Tr}} - 1$ , SU<sub>TR</sub> transmits data at the rate of  $R_{Tr}$ .

By using order statistics [17],

$$Pr [\min (\gamma_F^u, \gamma_{\text{Re}}^u) < \gamma_{\text{th}}^{\text{Re}}] = Pr [\gamma_F^u < \gamma_{\text{th}}^{\text{Re}}] + Pr [\gamma_F^u > \gamma_{\text{th}}^{\text{Re}}] Pr [\gamma_{\text{Re}}^u < \gamma_{\text{th}}^{\text{Re}}] \quad (22)$$

$$\begin{aligned} P_O^{un} = & \left[ 1 - \exp \left( -\frac{\gamma_{\text{th}}^{\text{Re}} N_0}{P_s^u \lambda_f} \right) \left( \frac{P_S^u \lambda_f}{P_s^u \lambda_f + \gamma_{\text{th}}^{\text{Re}} P_n \lambda_d} \right) \right. \\ & \left( \frac{P_r^u \lambda_h}{P_r^u \lambda_h - P_n \lambda_d} \right)^N + \left\{ \exp \left( -\frac{\gamma_{\text{th}}^{\text{Re}} N_0}{P_s^u \lambda_f} \right) \right. \\ & \left( \frac{P_S^u \lambda_f}{P_s^u \lambda_f + \gamma_{\text{th}}^{\text{Re}} P_n \lambda_d} \right) \left( \frac{P_r^u \lambda_h}{P_r^u \lambda_h - P_n \lambda_d} \right)^N \left. \right\} \times \\ & \left. \left\{ 1 - \exp \left( -\frac{\gamma_{\text{th}}^{\text{Re}} N_0}{P_r^u \lambda_g} \right) \left( \frac{P_r^u \lambda_g}{P_r^u \lambda_g + \gamma_{\text{th}}^{\text{Re}} P_n \lambda_e} \right)^N \right\} \right]^K \end{aligned} \quad (23)$$

Now during overlay mode of operation the received signal at  $k^{\text{th}}$  relay being transmitted from SU<sub>TR</sub> is given by:

$$y_{R_L}^o(t) = \sqrt{P_s^o} h_{S_T R_L} x_s(t) + \sqrt{P_r^o} h_{R_L} x_r(t) + n_o(t) \quad (24)$$

Thus at overlay transmission mode the SINR at  $k^{\text{th}}$  FD relay is given from the above expression as:

$$\gamma_F^o = \frac{P_s^o g_{S_T R_L}}{P_r^o g_{R_L} + N_o} \quad (25)$$

During overlay mode of operation the received signal at SU-Rx from  $k^{\text{th}}$  FD relay is given by:

$$y_{\text{Re}}^o(t) = \sqrt{P_r^o} h_{R_L} x_r(t) + n_o(t) \quad (26)$$

Thus at overlay transmission mode the SINR at secondary receiver is given from the above expression as:

$$\gamma_{\text{Re}}^o = \frac{P_r^o g_{R_L}}{N_o} \quad (27)$$

Similar way SC technique is used at the destination thus the end-to-end outage probability at the secondary receiver during overlay mode is found out to be:

$$P_O^{ov} = Pr \left[ \left\{ \max_k (\min (\gamma_F^o, \gamma_{Re}^o)) \right\} < \gamma_{th}^S \right] \quad (28)$$

So, the end-to-end outage at  $SU_R$  as mentioned here for overlay transmission mode can be expressed as:

$$\begin{aligned} P_O^{ov} = & \left[ 1 - \exp \left( -\frac{\gamma_{th}^{\text{Re}} N_0}{P_s^o \lambda_f} \right) \left( \frac{P_s^o \lambda_f}{P_s^o \lambda_f + \gamma_{th}^{\text{Re}} P_r^o \lambda_h} \right) \right. \\ & + \left\{ \exp \left( -\frac{\gamma_{th}^{\text{Re}} N_0}{P_s^o \lambda_f} \right) \left( \frac{P_s^o \lambda_f}{P_s^o \lambda_f + \gamma_{th}^{\text{Re}} P_r^o \lambda_h} \right) \right\} \\ & \times \left. \left\{ 1 - \exp \left( -\frac{\gamma_{th}^{\text{Re}} N_0}{P_r^o \lambda_g} \right) \right\} \right]^K \end{aligned} \quad (29)$$

Finally, based on the activity of sensing, the detection of the primary user, and their state of channel occupancy with their outage constraint (i.e. QoS) maintained by the secondary user, their overall outage probability during adaptive switching of underlay or overlay mode is achieved. Therefore, the outage probability under the joint underlay/overlay protocol at the secondary receiver can be expressed as:

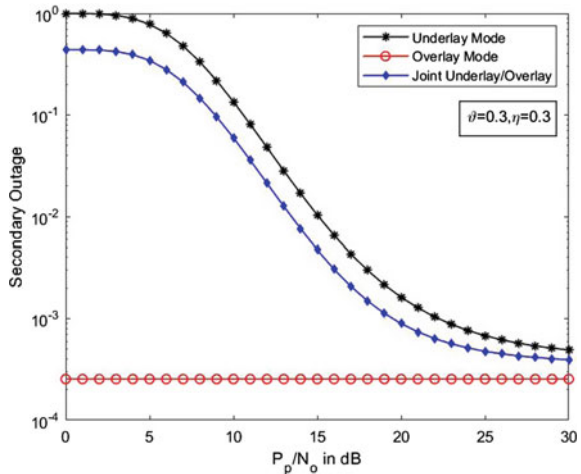
$$P_O^{\text{Joint}} = [(1 - P_d) + \vartheta P_d] P_O^{\text{un}} + (1 - \vartheta) P_O^{ov} \quad (30)$$

## 5 Result Analysis and Discussion

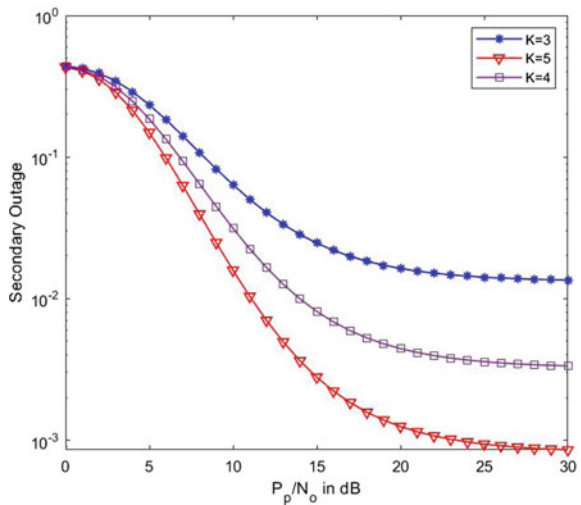
In this section, we examine the system performance results using a MATLAB simulation testbed, and then we discuss the behaviour of the system performance based on these results. The numerical outcomes shown here demonstrate the performance enhancement attained while using the suggested relay-assisted adaptive joint underlay /overlay spectrum access approach. Additionally, it has been demonstrated that FD relay-based CR networks outperform half-duplex (HD) relay-based CR networks in terms of performance. Here we have considered the following system parameters to verify the performance of the system:  $R_p$  and  $R_s$  are the target rates for both PU and SU, with values of 0.15 bits/s/Hz and 0.1 bits/s/Hz, respectively. The outage constraint for PU is set to  $\varepsilon = 0.1$ . The power of the noise is standardised to a unit value. In this study, the EH circuit's efficiency factor ( $\eta$ ) value is taken as 0.3. Here it is also assumed that the initial energy harvesting time  $\tau$  is allocated as 20 ms out of total estimated time  $T = 100$  ms.

Figure 2 depicts the  $SU_R$  outage performance as a function of  $P_p/N_0$  for various protocols, including underlay, overlay, and joint underlay and overlay. The probability of channel occupancy ( $\vartheta$ ), no of PUs (N), probability of detection ( $P_d$ ) and no

**Fig. 2** Comparison of outage performance under underlay, overlay, and joint underlay/overlay mode



**Fig. 3** Comparison of outage performance of joint underlay/overlay mode under varying  $K$  with respect to  $P_p/N_0$



of relays ( $K$ ) are maintained constant value at 0.3, 0.8, 4, and 5, respectively. It has been found that the overlay mode's outage performance is independent of the PU's ( $P_p$ ) transmitting power. Therefore, this overlay method alone cannot participate in the model of spectrum sharing. Furthermore, it has been demonstrated that the joint underlay/overlay scheme outperforms the current underlay scheme for this proposed model during outages. As the reason for this,  $SU_T R$  detects the PUs are busy it operate underlay mode otherwise it works in overlay mode.

The outage probability of  $SU_R$  is also shown in Fig. 3 as a function of  $P_p/N_0$  in the joint underlay/overlay mode for varied numbers of relays  $K = 3, 4$  and  $5$ . It has been noticed that as the number of relays increases, the outage performance improves accordingly. Figure 4 shows that the secondary network's outage perfor-

**Fig. 4** Comparison of SU outage performance with respect to  $P_p/N_0$  under full-duplex versus half-duplex relaying mode

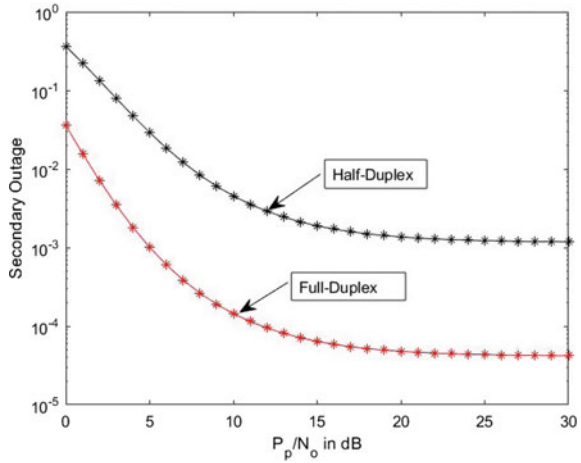
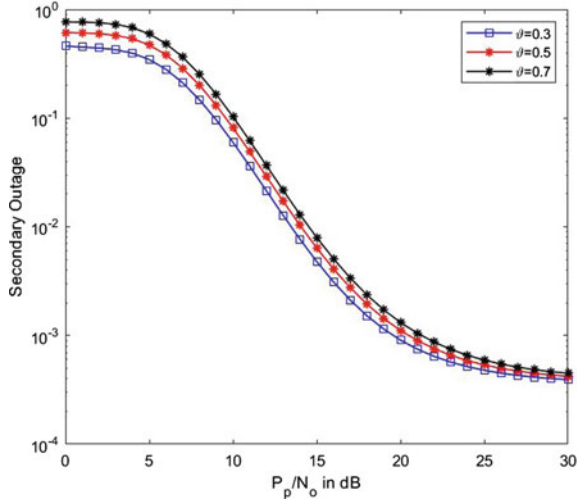


**Fig. 5** Comparison of outage under adaptive underlay/overlay mode under varying probability of channel occupancy ( $\vartheta$ ) with reference to  $P_p/N_0$



mance is affected by the joint underlay/overlay mode under the FD relay network in comparison to the HD relay network. The results precisely depict that the outage performance of secondary receivers under the FD relay network is improved compared to the HD relay network under multiple PUs.

The outage probability of  $SU_R$  is also depicted in Fig. 5 as a function of  $P_p/N_0$  in the joint underlay/overlay mode under varying probability of channel occupancy ( $\vartheta$ ). It has been observed that as the values of  $\vartheta$  increases, the outage performance deteriorate accordingly. The outcome we got reflects that the more and more channel occupancy factor which signifies more traffic involved results in drop of outage performance at secondary network.

**Fig. 6** Comparison of outage performance of joint underlay/overlay mode under varying probability of detection ( $P_d$ )

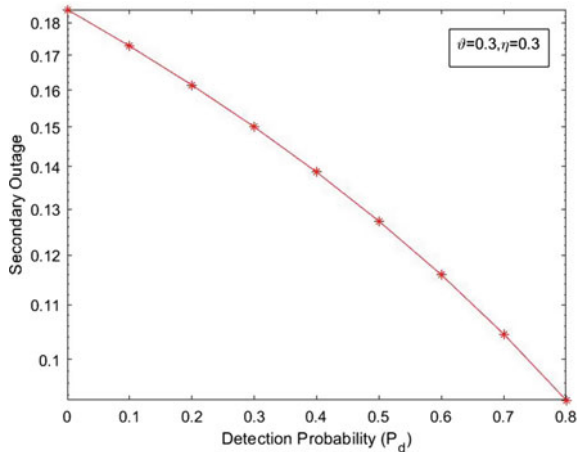
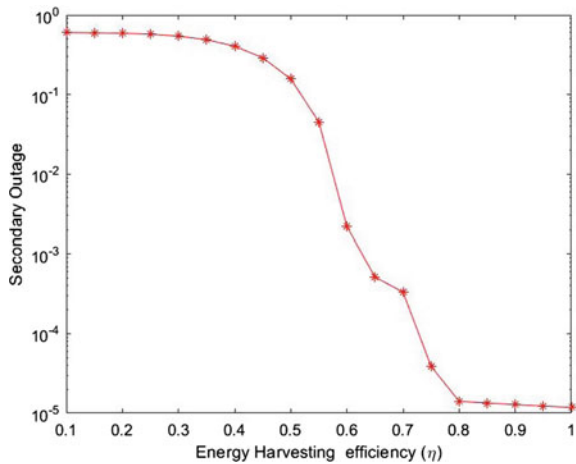


**Fig. 7** Outage probability at secondary network with respect to efficiency factor  $\eta$  of the EH circuit



The secondary receiver outage performance of the combined underlay/overlay mode is shown in Fig. 6 as a function of variations in probability of detection values ( $P_d$ ). It is precisely illustrated that increasing the value of  $P_d$  reflects on the results of secondary receiver outage performance. A higher  $P_d$  value provides the most accurate information on the activity of the PUs, as a result, there is a lower probability of error at the secondary receiver, which improves outage performance.

As a final illustration, Fig. 7 depicts outage probability at  $SU_R$  as a function of the EH circuit's efficiency factor ( $\eta$ ) in an FD relay mode. Here, we noticed that as the efficiency factor ( $\eta$ ) grows, the system's outage performance gets better. This indicates that the outage improves when the EH efficiency is higher because the SU transmitter can capture more energy from the RF environment. However, it subsequently stabilises as a result of the transmit power limitation to preserve the PUs' QoS.

## 6 Conclusion

In this study, we have suggested and explored a joint underlay/overlay full-duplex relaying mode with a multi-user scenario in an energy harvesting environment. The operation is built on a cognitive radio network that detects whether PUs are active or idle and then transmits signals in an underlay or overlay mode in accordance with the results of the sensing. Here, residual self-interference at every FD relay node and all other interfering sources at every receiving node are handled. The research study shows that FD relaying outperforms HD relaying in terms of throughput improvement. Furthermore, the spectrum utility in a CR network is increased by the opportunistically adaptive switching mode of transmission between the underlay and overlay. It has been observed that the FD relaying mode excels the HD relaying protocol in terms of outage performance. Additionally, this hybrid manner of transmission provides superior throughput performance compared to the underlay protocol. This secondary outage performance, taking into account SI and more from the primary network, nonetheless produces the intended result despite high channel occupancy. This secondary interrupt performance, taking into account SI and more from the primary network, nonetheless produces the intended result despite high channel occupancy.

## References

1. Force SPT (2002) Spectrum policy task force report et docket no. 02-135. US Federal Communications Commission
2. Mitola J, Maguire GQ (1999) Cognitive radio: making software radios more personal. *IEEE Pers Commun* 6(4):13–18
3. Subhedar M, Birajdar G (2011) Spectrum sensing techniques in cognitive radio networks: a survey. *Int J Next-Gener Netw* 3(2):37–51
4. Senthuran S, Anpalagan A, Das O (2012) Throughput analysis of opportunistic access strategies in hybrid underlay-overlay cognitive radio networks. *IEEE Trans Wirel Commun* 11(6):2024–2035
5. Zheng K, Liu X-Y, Liu X, Zhu Y (2019) Hybrid overlay-underlay cognitive radio networks with energy harvesting. *IEEE Trans Commun* 67(7):4669–4682
6. Samanta D, Kumar Bag J, De Kumar C, Chandra A (2021) A smart spectrum utilization approach using multiantenna-based cognitive relays in cognitive radio network. *Int J Commun Syst* 34(1):4671
7. Usman M, Koo I (2014) Access strategy for hybrid underlay-overlay cognitive radios with energy harvesting. *IEEE Sens J* 14(9):3164–3173
8. Cai LX, Liu Y, Luan TH, Shen XS, Mark JW, Poor HV (2014) Sustainability analysis and resource management for wireless mesh networks with renewable energy supplies. *IEEE J Sel Areas Commun* 32(2):345–355
9. Lee S, Zhang R, Huang K (2013) Opportunistic wireless energy harvesting in cognitive radio networks. *IEEE Trans Wirel Commun* 12(9):4788–4799
10. Yan Y, Huang J, Wang J (2012) Dynamic bargaining for relay-based cooperative spectrum sharing. *IEEE J Sel Areas Commun* 31(8):1480–1493

11. Bao VNQ, Duong TQ, da Costa DB, Alexandropoulos GC, Nallanathan A (2013) Cognitive amplify-and-forward relaying with best relay selection in non-identical Rayleigh fading. *IEEE Commun Lett* 17(3):475–478
12. Bag JK, Samanta D, De CK, Chandra A (2022) Outage analysis of joint underlay/overlay CR network. In: Proceedings of the 3rd international conference on communication, devices and computing. Springer, pp 537–550
13. Liao Y, Song L, Han Z, Li Y (2015) Full duplex cognitive radio: a new design paradigm for enhancing spectrum usage. *IEEE Commun Mag* 53(5):138–145
14. Zhang Z, Chai X, Long K, Vasilakos AV, Hanzo L (2015) Full duplex techniques for 5g networks: self-interference cancellation, protocol design, and relay selection. *IEEE Commun Mag* 53(5):128–137
15. Doan X-T, Nguyen N-P, Yin C, Da Costa DB, Duong TQ (2017) Cognitive full-duplex relay networks under the peak interference power constraint of multiple primary users. *EURASIP J Wirel Commun Netw* 2017(1):1–10
16. Tran H, Zepernick H-J, Phan H (2013) Cognitive proactive and reactive DF relaying schemes under joint outage and peak transmit power constraints. *IEEE Commun Lett* 17(8):1548–1551
17. Shrestha S, Chang K (2010) Closed-form solution of outage capacity for cooperative DF and AF relay network. *Wirel Pers Commun* 54(4):651–665

# Secure Sharing of Student Credentials Using Blockchain



**Puja Sarkar, Psarag Jyoti Kalita, Mugdhatanu Dev Goswami, Sanchita Saha, and Amitava Nag**

**Abstract** Sharing students' credentials is an essential process for any educational ecosystem that includes diverse stakeholders such as students, teachers, various committees of institutes, administrations, government agencies, and many more. All of these stakeholders take extensive measures to ensure the authenticity and confidentiality of students' testimonials when those are being shared. In spite of these concerns, the distribution of students' credentials is a vulnerable, potentially complex, and sometimes insecure process. The goal is to reduce the existing security-related issues when sharing the students' credentials with the help of blockchain technology. The technology of blockchain can be used effectively to solve the issue of securely exchanging student credentials. We proposed a secure, immutable, authentic, tamper-proof, privacy-preserving, and easily shareable blockchain-based mechanism for securely exchanging students' credentials. In order to make the process of sharing credentials scalable, we proposed a secure off-chain store mechanism. A decentralized application based on Ethereum technology is used for conducting an analysis of the architecture with regard to its performance as well as its potential feasibility.

**Keywords** Blockchain · IPFS · Student credentials · Decentralized application · Web 3.0 · Smart contracts · Ethereum

---

P. Sarkar (✉) · P. J. Kalita · M. D. Goswami · S. Saha · A. Nag

Department of Computer Science and Engineering, Central Institute of Technology, Kokrajhar, Assam 783370, India

e-mail: [p.sarkar@cit.ac.in](mailto:p.sarkar@cit.ac.in)

M. D. Goswami

e-mail: [u19cse1001@cit.ac.in](mailto:u19cse1001@cit.ac.in)

A. Nag

e-mail: [amitava.nag@cit.ac.in](mailto:amitava.nag@cit.ac.in)

S. Saha

Department of Computer Science and Engineering, Haldia Institute of Technology, Haldia 721657, India

## 1 Introduction

Nowadays, the online method is chosen for document sharing due to its many benefits, including being quick (nearly instantly), simple, accessible worldwide, and constantly available. However, the online exchange of credentials does not always guarantee the privacy, veracity, integrity, security, or accessibility of shared files. Even in the existence of a dedicated facility like a password-based trustworthy server, which is vulnerable to attacks [1], it is challenging to ensure these features. In recent years, blockchain has developed as a technology that has the potential to be promising for many kinds of information systems where the highest priority is placed on security and privacy. This paper's focus is on the secure exchange of student credentials among various educational stakeholders using blockchain technology. Blockchain provides a novel way to store information, carry out transactions, complete tasks, and establish trust [2]. Blockchain is widely regarded as a ground-breaking cybersecurity and cryptographic technology. This paper suggests a blockchain-based system for safely and securely managing student records.

### 1.1 Motivation of the Work

Complications arise in any institution that handles certificates from students, such as companies and educational institutes. A common example can be the job application process: When a student provides their application for a job, it becomes the responsibility of the company staff to carefully authenticate the certificate received. If necessary, it is also conceivable that the business will need to get in touch with the specific school to ask about the validity of the certificate. Despite being so drawn out, the system as a whole is not secure and makes it challenging to deal with fraud and tampering [3]. Additionally, the credentials of students contain private information, and when it comes to disclosing this information, privacy becomes quite important. The need to preserve the privacy of personal information is made legal in particular by new privacy rules (such as the general data protection regulation (GDPR)) [4]. In order to ensure a high level of privacy, the system for managing and sharing student credentials must do so.

### 1.2 Our Contributions

The purpose of the study is to address the underlying problems with student credentials security. The concept of this article is how to share and manage student credentials using blockchain technology in conjunction with an off-chain storage system.

1. We have proposed a blockchain-based architecture to ensure the secure sharing of students' credentials.
2. To maintain the privacy of students' credentials, we have proposed a mechanism for data protection.
3. We have also employed a mechanism for off-chain storage to improve the system's scalability.
4. We have used Ethereum to create a decentralized application (DApp) that serves as a prototype for the suggested architecture.
5. Our system uses smart contracts, and cost computation is done based on the execution time of key processes.

## 2 Related Work

Numerous advantages that come from using blockchain in the education system include immutability and the origin of uploaded credentials, peer-to-peer, and secure interactions between parties, transparency, trust, and distributed digital ledgers. These advantages have led to a large amount of research, some of which are mentioned briefly in this section.

Arenas and Fernandez [5] proposed a mobile application for storing and validating student certificates using hyperledger (permissioned) blockchain. However, proper testing of the mobile app in terms of computational cost and execution time is not shown. Also, the certificates are stored on-chain, which makes it difficult to scale further. Andreev and Daskalov [6] proposed a blockchain framework that enables the exchange of student registration data from schools to learners to businesses (and vice versa). However, it uses a central database to store data, which makes their proposed model partially decentralized. The paper also does not provide implementation or experimental evaluation. Similar issues arise with the work of Young and Verhulst [7]. Their work is a case study that involves a blockchain platform for storing student degrees, implemented by the Massachusetts Institute of Technology (MIT). Each credential has a unique URL that can be shared with others. The recipient of the URL can verify its authenticity by visiting the official Website and checking the URL for authenticity.

Han et al. [8] presented a blockchain-based architecture for storing educational records on the blockchain. However, the work does not include implementation or test-based results. The student certificate management architecture proposed by Gräther et al. [9] uses a distributed file system to store the profile information of the certificate authority. However, the actual certificate (plain text) appears to be stored in a central system. Another problem is that every time a student wants to share his/her credentials, the request must be approved by the agency that manages the central system.

The author Hope [10] reported that Central New Mexico Community College uses blockchain to store student credentials, allowing students to be the owners of their educational certificates. Students can download their credentials to any device

using their wallet address. However, the implementation is not included. Their work uses on-chain storage, which is costly and hence not scalable. The work presented by Kanan et al. [11] uses a blockchain-based prototype consisting of two types of users: administrators and students. Administrators can add certificates to student accounts, and students can view them. However, their work does not include the costs of various smart contracts.

Ocheja et al. [12] proposed that each institution provides access via smart contracts to its data stores used to store student files and protect student privacy. This architecture leads to many security and privacy issues as the stored data is clear text, and the database is centralized. Additionally, even after the institution has granted access to the student, it may still allow other students access to his/her learning logs. Therefore, the student does not have full control over his or her personal information. Furthermore, how the entry of new users is permitted which is not addressed in this work.

The authors Kalani and Aditya [13] proposed to store student credentials on Ethereum blockchain and analyzed the complexity of the smart contracts in terms of cost computation and time taken to mine the transactions. The certificates seem to be stored directly in the blockchain, which gives it scalability issues. Duong et al. [14] presented IU-SmartCert, a blockchain-based system, and process for the issuance, verification, and exchange of educational credentials with selective disclosure characteristics. However, the actual certificates seem to be stored on-chain which makes it difficult to scale further.

In this paper, we have tried to solve the issues mentioned in the related work section by making the system fully decentralized to maintain confidentiality, integrity, and authenticity and storing the certificates in an off-chain distributed server to make the system scalable.

### 3 Proposed Architecture

In this paper, we have tried to present a secure and tamper-proof structure for sharing students' credentials. The purpose of the proposed structure is to ensure both protection and privacy. It uses core blockchain technology and makes use of off-chain storage to enhance scalability. This paper considers an academic environment that is composed of three different parties or stakeholders. These stakeholders play one-of-a-kind roles, which are stated below:

1. **Educational Institutions:** Educational institutions of any kind, like schools, colleges, universities, etc., are represented by the stakeholder "educational institutions." Their role is both that of an issuer and a viewer. The reason for this is that institutions will issue certificates to enrolled students when they meet the requirements and also refer to other students' certificates issued by other institutions. Registered institutions are responsible for publishing and verifying credentials,

as well as revoking certificates if the certificate was issued incorrectly or the student is engaged in dishonest behavior.

2. **Students:** Credentials must be displayed and securely stored in the academic portfolio for future use. Students are required to show credentials upon admission to a particular university or during a recruitment process. Thus, the roles of the student are both a viewer and to provide access to the certificate.
3. **Companies and Other Stakeholders:** At the time of hiring, the company will most likely need to view the credentials of the applicant. Also, when a student completes their training or internship with the organization or a particular company, it is the responsibility of the respective company to issue a corresponding certificate. Similar to institutions, companies can also be publishers and viewers.

### **3.1 System Architecture**

The corresponding architecture of our proposed model for secured sharing of student credentials is shown in Fig. 1. This architecture includes different parties or stakeholders, the process, and also distributed file storage with an off-chain mechanism(i.e., IPFS). To record the interactions taking place between the various stakeholders, blockchain is used in the form of transactions that are immutable. The accomplishment of such transactions is achieved by deploying smart contracts on the blockchain to manage all the necessary interactions between the stakeholders and provide various functionalities.

The core features of the proposed architecture are as follows:

1. **Registration of Institutes:** Registration of institutes is done by the Central Authority. The Central Authority enables institutes to register themselves on the network with a lifelong permanent account on the blockchain. The registration includes the institute's permanent network address, institute name, institute acronym, institute's official Website, and the courses it provides.
2. **Log In:** After successful registration, institutes can log in with the same network address they used while registering. Institutions go through a one-time registration process, which would simplify subsequent logins.
3. **Student Enrollment:** This is utilized by the academic organization at the time of admission. For enrolling the student, the institution appears to confirm the existence of the student's account using the blockchain's public key. After verification, the institute enlists the student by using the public key. Additionally, this is displayed on the student's account.
4. **Uploading of Credentials:** If students meet the course or program requirements, the institute will issue credentials to enrolled students. These credentials (degrees, certificates, transcripts, etc.) are sizeable pieces of data, so storing them immediately on the blockchain becomes a steeply-priced proposition. In this view, credentials are stored using distributed record storage (off-chain storage) in the proposed architecture. Credential upload is done in 3 steps.

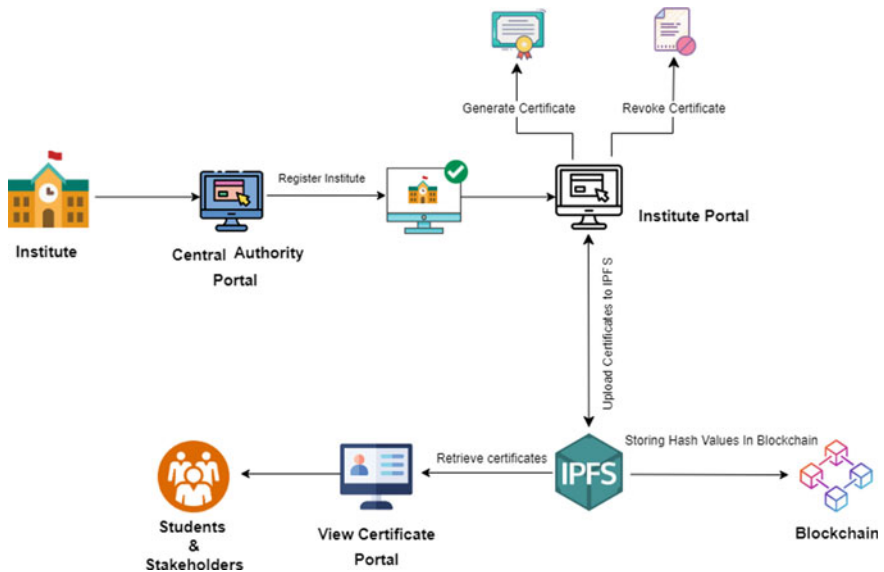


**Fig. 1** System architecture

**Step 1:** The institution publishes credentials by uploading them to the distributed file store. In return, the institute receives the address where the credentials are stored.

**Step 2:** Creation of data (address, metadata, public key) is done by the institute. Certificate metadata includes the name of the certificate and other information such as the date of issue, course, and program.

**Step 3:** The final step is to create the digital signature that is to sign the message and then upload the result to the blockchain. Therefore, this function is available to two stakeholders: the institute and the company.

5. **Retrieval and Viewing of Credentials:** This allows the student to retrieve (and view) credentials uploaded by the participant. To retrieve and look at the uploaded credentials, the student can log into their account, and then from the blockchain, they can retrieve the address of the particular credential. Students will use this address to view and download their credentials.

## 4 Implementation

The implementation of our prototype is explained in this segment. The prototype of our proposed system is a decentralized application (DApp) for the secure sharing of students' credentials.

## 4.1 Backend Technologies

Given that blockchain application development is still immature, DApps can be made in a variety of ways. The approach we take in our work makes use of the subsequent technologies:

1. Metamask: A browser extension gives us the ability to interact with Ethereum. MetaMask version used in our paper is 10.23.2.
2. Web3.js: Through the remote procedure call protocol, Web3.js connects MetaMask to the client application. These libraries offer a number of crucial features, including the ability to install smart contracts, transmit ether from one account to another, read and write data to/from smart contracts, and call methods from deployed smart contracts. Web3 version used in this paper is 1.7.4.
3. React is a frontend JavaScript library that is open-source and free to use when developing user interfaces based on UI components. React version used in this paper is 18.2.0.
4. Crypto: A built-in module for Node.js offers cryptographic features like message verification, hash generation, encryption, and decryption. Crypto version used in this paper is 4.1.1.
5. IPFS: A distributed file system for peer-to-peer data sharing. It functions according to the concept of content-based addressing. Data is returned as a hash when it is uploaded, and this hash can be used to later access the data. The version used in this paper is 0.16.0.

## 4.2 Application Stack

Our prototype DApp's application stack consists of a frontend running on a backend distributed server.

1. Frontend: Users communicate with the DApp using the MetaMask browser extension, which links the application to the blockchain. Next.js is the foundation of the user interface. The DApp sends various kinds of queries to the distributed servers on the backend by utilizing the capability offered by Web3.js and MetaMask. The frontend also uses crypto to generate a SHA256 hash.
2. Decentralized server: The smart contracts set up on Ethereum handle requests produced by users. The IPFS responds to some requests.

## 5 Experimental Results

The overall performance of the prototype DApp is calculated by forming distinctive checks. To carry out the evaluation, a local host test network is used. Ganache pro-

vides us with this environment host installation. It is a private Ethereum blockchain environment that permits us to emulate the Ethereum blockchain in order that allows one to interact with smart contracts privately for testing and development purposes. It uses proof-of-authority (PoA) consensus set of rules.

## 5.1 *Cost Computation and Execution Time of the Smart Contracts*

The decentralized peer-to-peer network can be safely managed and to achieve that the blockchain needs to give certain incentives to the miners. The miners get rewarded for validating the transactions and also for mining the new nodes or blocks on the blockchain network. The computational capability of the system that is required to validate the transactions generally decides the reward on Ethereum. The rewards are paid to the prevailing miner in the form of gas by the sender. Therefore, to ensure profitability, it is necessary to execute the smart contract and the cost calculation of the important functions.

Deploying smart contracts on the blockchain requires two types of costs: transaction costs and execution costs. The smart contract and the data which is required for verification are sent together, and the transaction cost is basically just the gas used. Transaction charges are based totally on the cost of sending data to the blockchain. Execution costs are based totally on the cost of the computational operations that are completed due to the transaction. Remix is used to calculate values for each charge.

The expenses of smart contracts are indicated in Table 1, and cost transactions required by the essential functions are indicated in Table 2.

The execution time for the application comprises mining the blocks, time for transmission, and the time associated with the execution of smart contracts. Processing of a large number of requests is handled by the Dapp, so utmost importance needs to be given to the overall time required for the execution of user requests. The transmission requests of any particular user can be of two types. The two types are reading and writing data. Reading data is done almost instantly. However, the transactions need to be validated first before the block gets mined, so writing to the blockchain requires some time. The time to process a transaction on a local host is almost immediate. But the average time to process a transaction on other networks will vary.

## 5.2 *Comparison with Related Works*

Table 3 distinguishes our work from existing related studies. Data size is paramount to securely issuing, viewing, and sharing all types of educational credentials. Using on-chain data storage incurs prohibitive costs that may not be affordable for stakeholders, especially students. Therefore, our proposed architecture uses off-chain distributed

**Table 1** Cost of smart contracts

Contract	Execution cost (gas)	Transaction cost (gas)
Students	1,014,967	1,387,679
Institute	1,680,954	2,269,244
Share files	556,381	791,677
Request	919,455	1,272,875
Company	894,242	1,242,750

**Table 2** Transaction cost of important functions

Transaction	Cost in Gwei	Cost in ether	Cost in USD
Registering an institute	72,230	0.00007214	0.015
Uploading a credential <sup>a</sup>	158,413	0.000158413	0.034
Certificate retrieval <sup>a</sup>	158,288	0.000156499	0.032

<sup>a</sup> Depends on the title and description length

file storage. This reduces costs and improves scalability. Unlike other works, our proposed work includes important features such as confidentiality, integrity, authenticity, and scalability. Once a certificate is issued, the student fully owns the certificate. Our work also reveals the implementation information of the DApp and conducts experiments to affirm its feasibility.

### 5.3 Working of Proposed DApp

The major use cases that our implemented DApp provides are a central authority portal for allowing the registration of institutes, issuing of certificates after successful registration of institutes, revoking of certificates by the registered institutes, and allowing the students to access and share their required certificates.

1. **Interface to register institutes:** The interface for the institutes to register themselves in the central authority portal and only the registered institutes can issue certificates is shown Fig. 2a.
2. **Successful Registration of Institutes:** A dialog box will appear regarding the successful registration of an institute along with the information related to that institute like the institute address, name, and institute Website link which is shown in Fig. 2b.
3. **Issuing of certificates:** After the registration of institutes, the institute portal becomes accessible, and the institute can issue the requested certificates for the students which are then stored in the IPFS. The interface for the registered institutes to issue certificates to their students as shown in Fig. 2c.

Table 3 Comparison with related work

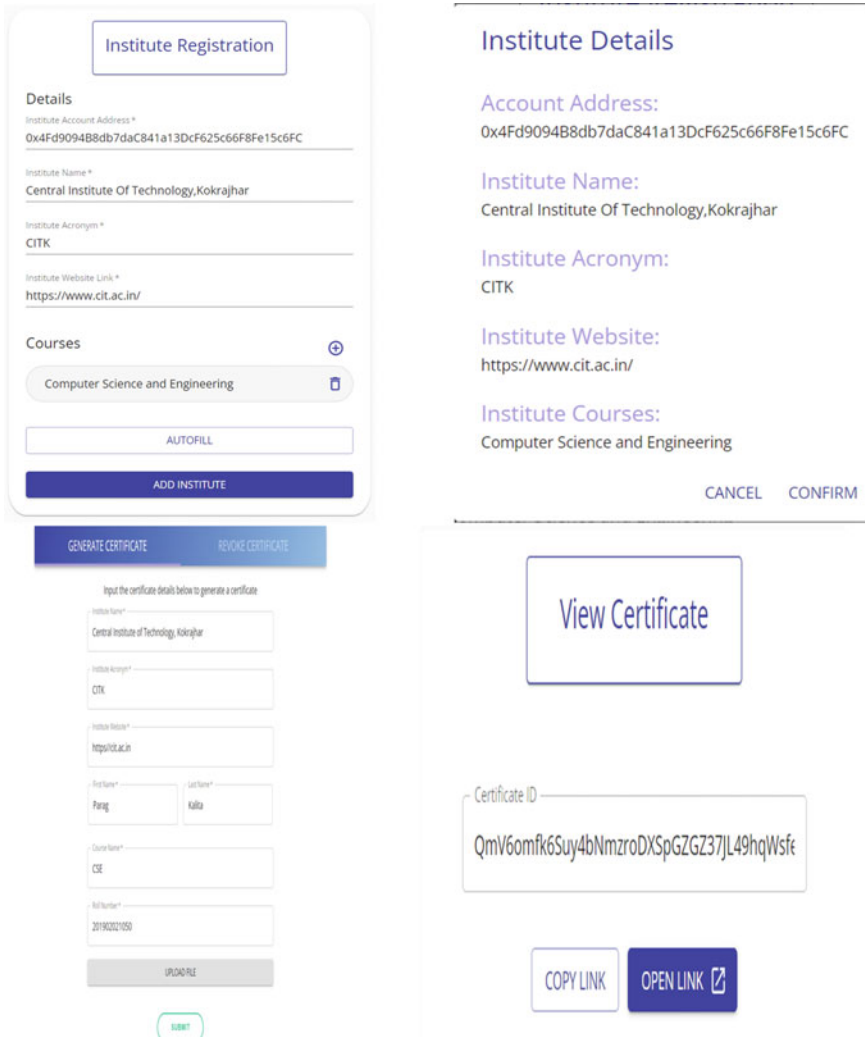


**Fig. 2** Some screenshots of the proposed DApp

4. **Revoking of certificates:** If the institute wants to revoke any particular certificate of a student, it can do so by providing the certificate ID which will attach a revoked message to that particular certificate.
5. **Viewing Certificates:** Figure 2d shows the interface to view the certificates. The student can view their certificates via the student portal by providing the certificate ID which the student can receive after the institute issues that particular certificate.

## 6 Conclusion

The technology of blockchain can be effectively used to solve the issue of securely exchanging student credentials. In this paper, we have introduced a simple and workable architecture that enumerates the various stakeholders, their roles, and their functionalities. A decentralized application (DApp) is developed as a proof-of-concept. Smart contracts are created and deployed as core components of the DApp. Testing is done using the Ethereum blockchain. Additionally, experiments to calculate costs show that the proposed system is feasible. Therefore, using the DApp makes all students' credentials authentic, immutable, and easy to share. The proposed architecture uses off-chain distributed storage and has two major advantages over the traditional method: One is that it improves scalability, and the second is the reduction of transaction costs. Moreover, the proposed framework may be extended to other domains. Our future plan is to enhance the security of the stored credentials in the IPFS server by using security mechanisms such as secret sharing. Introducing secret sharing and encrypting the certificates before storing them on the IPFS server act as an additional layer of security for off-chain storage.

## 7 Future Work

Our future plan is to enhance the security of the stored credentials in the IPFS server by using security mechanisms such as secret sharing. Introducing secret sharing and encrypting the certificates before storing them on the IPFS server act as an additional layer of security for off-chain storage.

## References

1. Singh A, Chatterjee K (2017) Cloud security issues and challenges: a survey. *J Netw Comput Appl* 79:88–115
2. Shuaib M, Hassan NH, Usman S, Alam S, Bhatia S, Mashat A, Kumar A, Kumar M (2022) Self-sovereign identity solution for blockchain-based land registry system: a comparison. *Mob Inf Syst* 2022
3. Børresen LJ, Meier E, Skjerven SA (2020) Detecting fake university degrees in a digital world. In: *Corruption in higher education*. Brill, pp 102–107
4. Voigt P, von dem Bussche A (2017) Enforcement and fines under the GDPR. In: *The EU general data protection regulation (GDPR)*. Springer, pp 201–217
5. Arenas R, Fernandez P (2018). CredenceLedger: a permissioned blockchain for verifiable academic credentials. In: *2018 IEEE international conference on engineering, technology and innovation (ICE/ITMC)*. IEEE, pp 1–6
6. Andreev O, Daskalov H (2018) A framework for managing student data through blockchain. In: *Proceedings of X international scientific conference e-governance and e-communications*
7. Young A, Verhulst S (2018) Creating immutable, stackable credentials through blockchain at MIT

8. Han M, Li Z, He J, Wu D, Xie Y, Baba A (2018) A novel blockchain-based education records verification solution. In: Proceedings of the 19th annual SIG conference on information technology education, pp 178–183
9. Gräther W, Kolvenbach S, Ruland R, Schütte J, Torres C, Wendland F (2018) Blockchain for education: lifelong learning passport. In: Proceedings of 1st ERCIM blockchain workshop 2018. European Society for Socially Embedded Technologies (EUSSET)
10. Hope J (2019) Give students ownership of credentials with blockchain technology. Enroll Manage Rep 23(2):6–7
11. Kanan T, Obaidat AT, Al-Lahham M (2019) SmartCert blockchain imperative for educational certificates. In: 2019 IEEE Jordan international joint conference on electrical engineering and information technology (JEEIT). IEEE, pp 629–633
12. Ocheja P, Flanagan B, Ueda H, Ogata H (2019) Managing lifelong learning records through blockchain. Res Pract Technol Enhanced Learn 14(1):1–19
13. Kalani A (2021) Student credential sharing system using blockchain DApp. Ph.D. thesis, California State University San Marcos
14. Tran T-T, Le H-D (2021). IU-SmartCert: a blockchain-based system for academic credentials with selective disclosure. In: International conference on future data and security engineering. Springer, pp 293–309

# An Optimal Circular Antenna Array Design for an Efficient 5G Communication System Using Krill Herd Optimization



Rajrup Saha, Avishek Das, Durbadal Mandal, and Rajib Kar

**Abstract** The work in this study illustrates a precise non-uniform circular antenna array design for synthesizing the ideal far-field radiation pattern in the spectrum of 5G communication frequency by utilizing an evolutionary optimization technique called krill herd (KH) optimization. Here, the side lobe level and the 3 dB beamwidth are decreased by using the KH technique to identify the exact values of the feeding current and the inter-elemental spacing among the array elements. It is assumed that  $x$ - $y$  plane contains all the elements of CAA. The values of the SLL and 3 dB beamwidth are reported after several executions of the KH algorithm. This research reports two distinct design examples of CAA (8 elements and 10 elements) in contemplation of comparing the achievement of KH optimization-based results to those of other previously released articles.

**Keywords** Circular antenna array · Krill Herd optimization · 3 dB beamwidth · Side lobe level

## 1 Introduction

An exact antenna array structure design is necessary for wireless devices to transmit and receive radio frequency signals. For the past few years, numerous research projects have been working to synthesize an antenna array's ideal far-field radiation pattern [16]. A reduced side lobe level and a narrow 3 dB beamwidth antenna array were designed as a result of the increased electromagnetic environment traffic [1]. A lower SLL is important for reducing intervention from other systems using the same frequency range, and a narrower beamwidth is necessary for improving

---

R. Saha · D. Mandal · R. Kar

Department of Electronics and Communication Engineering, NIT Durgapur, Durgapur 713209, India

A. Das (✉)

Department of Electronics and Communication Engineering, HIT Haldia, Haldia 721657, India  
e-mail: [avishek.uit0408@gmail.com](mailto:avishek.uit0408@gmail.com)

directivity [1–6]. The radiation pattern can be altered by adjusting some important parameters like the geometry of the antenna array, the inter-elemental separation among the elements of the array, amplitude excitations, and the phase excitation weights [7–9]. Here, all the elements are arranged in a circular fashion around a circle's circumference.

Here, the primary goal is to construct a CAA with a lower SLL and narrower HPBW. In this situation, the array elements' inter-elemental separation and the current excitation amplitude weights can be used to achieve the convenient radiation pattern while maintaining a zero-phase difference. KH algorithm is employed here for the optimization of the design problem for the implementation of the CAA. The results obtained from different evolutionary algorithms [15–26] like GA [8, 9, 11], and PSO [10] are compared in this article.

The resting portion of the article is standardized in this fashion: in part II, the design equation of non-uniform CAA has been described, in part III, a short description of the KH algorithm has been described, in part IV, the collected results from the simulation are discussed. In part V, the paper has been concluded.

## 2 Design Equation

Figure 1 displays a non-uniformly excited CAA with  $N$  elements scanning a far-field point PP. The radius of the array is “ $a$ .” The  $x$ – $y$  plane contains the elements of CAA. Here, all the CAA's components are regarded as isotropic sources. Therefore, an array factor, which is depicted in (1), is used to express the radiation properties.

$$AF(\theta, \varphi) = \sum_{n=1}^N I_n \exp[j(ka \sin \theta \cos(\varphi - \varphi_n) + \alpha_n)] \quad (1)$$

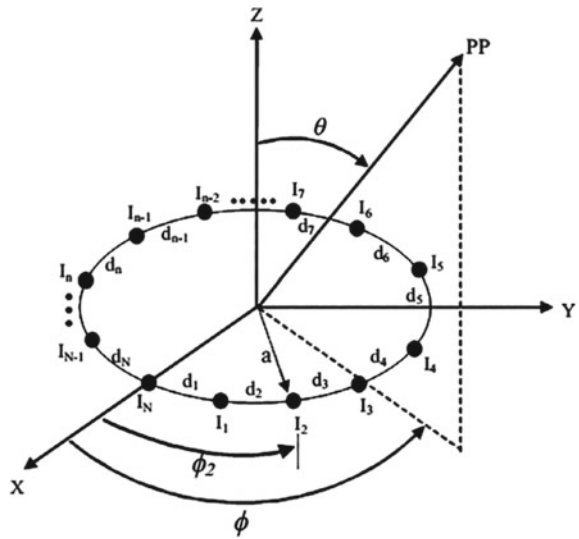
$$\text{where, } ka = \frac{2\pi a}{\lambda} = \sum_{j=1}^N d_j \quad (2)$$

$\lambda$ , denotes the operational wave length,  $\theta$  and  $\varphi$  are the elevation angle, and the azimuthal angle,  $a$  is the radius of the circular array. The feeding current of  $n$ th element is represented by  $I_n$ ,  $\varphi_n$  is the angular position of the  $n$ th element and  $\alpha_n$  is the excitation phase of  $n$ th element.

$$\varphi_n = \left( \frac{2\pi}{ka} \right) \sum_{j=1}^n d_j \quad (3)$$

$$\alpha_n = -ka \cos(\varphi_0 - \varphi_n) \quad (4)$$

**Fig. 1** Schematic diagram of non-uniform CAA scanning at a point ‘PP’ with  $N$  isotropic elements



From Eqs. (1) and (3), the radiation pattern is expressed by the array factor as follows,

$$AF(\theta, \phi) = \sum_{n=1}^N I_n \exp[j(ka \sin \theta \cos(\phi - \varphi_n) - ka \cos(\phi_0 - \varphi_n))] \quad (5)$$

where  $I_n$  denotes the  $n$ th element of the array's feeding current, and the inter-elemental distance between elements “ $n$ ” and “ $n + 1$ ” is  $d_n$ .  $\phi_0$  is the main beam's direction, which is set as 0.

In this study, the global best is accomplished at the greatest radiation angle  $\phi_0 = 0$  degrees in  $\phi = [-\Pi, \Pi]$ . To attain the desired radiation pattern with the highest minimization of SLL and HPBW in the intended direction  $\phi$ , the main objective of the study is to determine the exact values of  $I_n$  and  $d_n$ .

In the next phase, the minimization is achieved by defining a suitable cost function. The objective function  $f$  can be represented as,

$$f = W_1 \times |AF(\varphi_{\max sl}, I_n)| / |AF(\phi_0, I_n)| + W_2 \times (\text{HPBW(Computed)} - |\text{HPBW}|_{I_n=1}) \quad (6)$$

Here, the weighting factors are represented by  $W_1$  and  $W_2$ .  $\varphi_{\max sl}$  represents the angle at which the highest side lobe level is compassed on both sides (below and upper) of the main beam. HPBW for non-uniform and uniform excitation is represented by and, respectively. The SLL is reduced using the first term of the  $f$ , and HPBW is decreased using the second term of the  $f$ . To decrease the  $f$ , the KH optimization is

utilized to find the optimal feeding currents and the inter-elemental separation among the array elements.

### 3 Krill Herd (KH) Optimization

Krill Herd [14, 15] optimization is applied here for the design of CAA. KH is inspired by biological environments, and swarm intelligence algorithms that are established on a particular biological, environmental process that involves the herding behavior of krill swarms. The fitness of each krill is influenced by its proximity to the location of the food and the point of maximum density of the swarm. After calculating the motion of the swarm, the KH technique also incorporates the adaptive genetic reproduction mechanism.

The crossover and mutation procedure, which are followed by the operation to update the krill's position in the solution space, improve the achievement of the KH algorithm. The KH method models the herding of krill swarms scientifically and goes into detail about it in [14, 15].

## 4 Results and Discussion

In this article, the KH optimization technique has been incorporated to conduct a thorough analysis of 8 and 10-element CAA to find the exact set of feeding current and inter-elemental separation. The KH optimization technique is used to achieve the finest results after 50 test runs in MATLAB 7.5 on an Intel Core (TM) 2 processor running at 3.00 GHz with 3 GB RAM.

### 4.1 Numerical Results

The radiation pattern (uniformly excited) and the results of the newly reported literature have both been compared with the results produced by employing the KH technique for CAA design.

The SLL values of CAA (uniform pattern) (8 and 10 elements) are found in Table 1 to be  $-4.17$  dB and  $3.59$  dB, respectively, and the 3 dB beamwidths of the aforementioned arrays are  $32.32$  deg and  $25.84$  deg, respectively. According to Table 1, the 3 dB beamwidth values of the CAA (uniform pattern) (8 and 10 elements) steadily drop with the increase in the number of elements.

For an 8-element and 10-element CAA design, the KH-based results are shown in Table 2. Table includes the parametric study that was produced for an 8-element and 10-element CAA design utilizing optimization.

**Table 1** Different parameters for uniform CAA (8, 10 elements)

No. of element	SLL (dB)	3 dB beamwidth (deg)
8	- 4.17	32.32
10	- 3.59	25.84

**Table 2** Results attained by employing KH for CAA (8 and 10 elements)

Number of elements	Currents		Distance		SLL (dB)	3 dB beamwidth (deg)
8	0.2602	0.0015	0.3613	0.5849	- 15.91	32
	0.1461	0.3220	0.7785	0.9020		
	0.3354	0.1459	0.5446	0.9034		
	0.2625	0.1950	1.3874	0.3422		
10	0.7191	0.1659	0.3616	0.7600	- 15.63	24.8
	0.3777	0.8955	0.5510	0.9715		
	0.2878	0.8747	0.3064	0.3190		
	0.336	0.2309	0.9232	0.6600		
	0.7071	0.7177	0.7110	0.3583		

Figure 2 shows the outcomes of the 8-element CAA design using various algorithms. Figure 2 shows that, when compared to other well-known algorithms, the KH approach surpasses the other meta-heuristic method in terms of side lobe level and HPBW (3 dB beamwidth) reduction. The figure illustrates how the KH approach outperforms other algorithms.

The results based on KH, GA [8], and PSO [10] are compared in Table 3. The results of Table 3 depict that in comparison to other well-known algorithms, the results achieved by employing the KH approach are much better.

The radiation pattern produced by several evolutionary techniques for the CAA (10-element) design is depicted in Fig. 3. The plot demonstrates how much better the KH-based results are than other reported results attained using various methods.

## 4.2 Convergence Plots

The convergence curve as given in Fig. 4 shows the minimum value of the cost function ( $f$ ) over the iteration cycles. This curve represents the KH algorithm's convergence profile for an 8, 10-element CAA design.

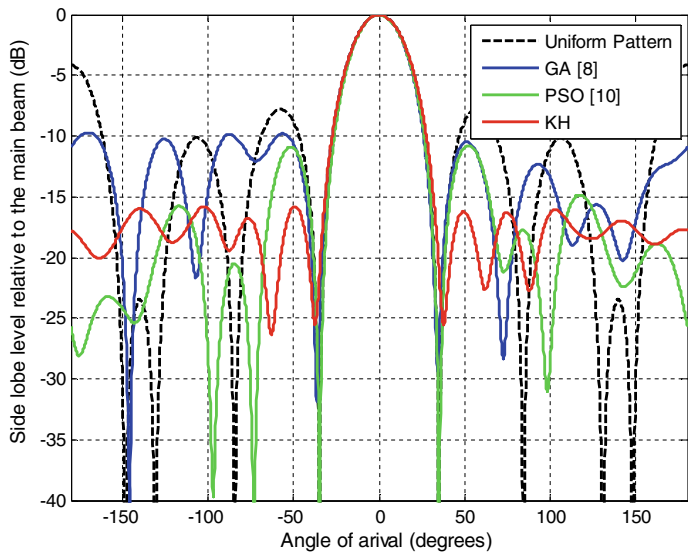


**Fig. 2** Radiation patterns of CAA (8 elements)

**Table 3** Results attained by employing KH in comparison with other algorithms

Number of elements	Algorithms	SLL (dB)	3 dB beamwidth (deg)
8	GA [8]	- 9.811	32
	PSO [10]	- 10.799	32
	KH	- 15.910	32
10	GA [8]	- 9.811	24.4
	PSO [10]	- 12.307	24.1
	KH	- 15.630	24.8

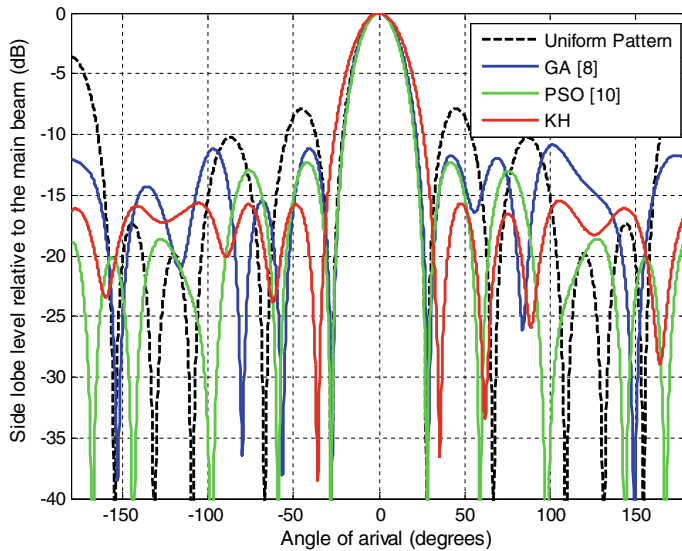
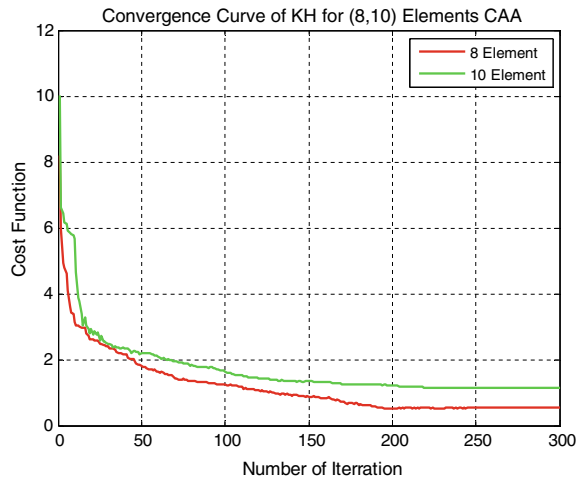


**Fig. 3** Radiation patterns of CAA (10 elements)

**Fig. 4** Convergence plots attains by the designed CAA



## 5 Conclusion

This study presents a CAA's optimal design approach for the highest reduction of SLL and HPBW by using an evolutionary technique known as Krill Herd optimization. The results obtained in this study show that it is leading to a better design concerning the reduction of SLL and HPBW in comparison to those of the results obtained by using some other evolutionary techniques like GA and PSO. So, in this article, the

obtained results depict that the KH optimization has the potential to be used as an effective optimizer and a viable alternative to the existing optimization methods for designing an efficient single-ring non-uniform CAA structure.

## References

1. Ballanis CA (1997) Antenna theory analysis and design, 2nd edn. Willey, New York
2. Elliott RS (2003) Antenna theory and design, Revised. IEEE Press, New Jersey
3. Lui HS, Hui HT, Leong MS (2009) A note on the mutual-coupling problems in transmitting and receiving antenna arrays. *IEEE Antennas Propag Mag* 51(5)
4. Gupta IJ, Ksienki AA (1983) Effect of mutual coupling on the performance of adaptive arrays. *IEEE Trans Antennas Propag* ap-31(5):785–791
5. Chakravorty P, Mandal D (2016) Radiation pattern correction in mutually coupled antenna arrays using parametric assimilation technique. *IEEE Trans Antennas Propag* 64(9):4092–4095
6. Mandal D, Ghoshal SP, Bhattacharjee AK (2011) Wide null control of symmetric linear antenna array using novel particle swarm optimization. *Int J RF Microwave Comput Aided Eng* 21(4):376–382
7. Haupt RL, Werner DH (2007) Genetic algorithms in electromagnetics. IEEE Press and Wiley-Interscience
8. Panduro M, Mendez A, Dominguez R, Romero G (2006) Design of non-uniform antenna arrays for side lobe reduction using the method of genetic algorithm. *Int J Electron Commun (AEU)* 60(7):713–717
9. Haupt RL (1995) An introduction to genetic algorithm for electromagnetics. *IEEE Antenna Propag Mag* 37(2):7–15
10. Sahib M, Najjar Y, Dib N, khodier M (2008) Design of non-uniform circular antenna arrays using the partical swarm optimization. *J Electr Eng* 59(4):216–200
11. Boeringer DW, Werner DH (2004) Particle swarm optimization versus genetic algorithm for phased array synthesis. *IEEE Trans Antenna Propag* 52(3):771–779
12. Kennedy J, Eberhart R (1995) Particle swarm optimization. In: Proceedings of the IEEE international conference on neural network, Perth:1942–1948
13. Tizhoosh HR (2005) Opposition-based learning: a new scheme for machine intelligence. In: Proceedings International conference on computational intelligence for modelling control and automation 1:695–701
14. Gandomi AH, Alavi AH (2012) Krill herd: a new bio-inspired optimization algorithm. *Commun Nonlinear Sci Numer Simul* 17:4831–4845
15. Das A, Mandal D, Ghoshal SP, Kar R (2018) A heuristic approach to design linear and circular antenna array for side lobe reduction. *Iranian J Sci Technol, Trans Electr Eng* 43(1):67–76. Springer. <https://doi.org/10.1007/s40998-018-0147-4>
16. Das A, Mandal D, Kar R (2019) An optimal far-field radiation pattern synthesis of time modulated linear and concentric circular antenna array. *Int J Numer Model Electron Netw Dev Fields* 32(6):1–20. Wiley. <https://doi.org/10.1002/jnm.2658>
17. Das A, Mandal D, Ghoshal SP, Kar R (2019) An optimal mutually coupled concentric circular antenna array synthesis using ant lion optimization. *Ann Telecommun* 74(11–12):687–696. Springer. <https://doi.org/10.1007/s12243-019-00729-3>
18. Das A, Mandal D, Kar R (2022) Side lobe suppression of concentric circular antenna array using social spider algorithm. *IETE J Res* 68(6):4198–4207. Taylor and Francis. <https://doi.org/10.1080/03772063.2020.178842>
19. Das A, Mandal D, Kar R (2022) An optimal radiation pattern synthesis and correction of mutually coupled circular dipole antenna array. *Scientia Iranica* 29(3):1455–1474. Sharif University of Technology. <https://doi.org/10.24200/SCI.2020.53745.3393>

20. Das A, Mandal D, Kar R (2020) An optimal circular antenna array design considering the mutual coupling employing ant lion optimization. *Int J Microwave Wirel Technol* 13(2):164–172. Cambridge University Press. <https://doi.org/10.1017/S1759078720000914>
21. Das A, Mandal D, Kar R (2020) An optimal circular antenna array design considering mutual coupling using heuristic approaches. *Int J RF Microwave Comput-Aided Eng* 30(11):1–14. Wiley. <https://doi.org/10.1002/mmce.22391>
22. Das A, Mandal D, Kar R (2021) An optimal compact time-modulated circular antenna array synthesis using krill herd optimization. *Ann Telecommun* 76:467–482. Springer. <https://doi.org/10.1007/s12243-020-00827-7>
23. Das A, Mandal D, Kar R (2021) An optimal time modulated compact circular antenna array design using a stochastic optimization technique. *J Electromagn Waves Appl* 35(8):1025–1045. Taylor and Francis. <https://doi.org/10.1080/09205071.2020.1868353>
24. Das A, Mandal D, Kar R (2021) An optimal radiation pattern synthesis of mutually coupled antenna array using an efficient compensation method. *IET Microwaves, Antennas Propag* 15(9):1054–1062. IET Digital Library. <https://doi.org/10.1049/mia2.12109>
25. Das A, Mandal D, Kar R (2022) An optimal far field radiation pattern synthesis of mutually coupled antenna arrays. *Int J RF Microwave Comput-Aided Eng* 32(7):1–24. Wiley. <https://doi.org/10.1002/mmce.23198>
26. Gandomi AH, Alavi AH (2016) An introduction of Krill Herd algorithm for engineering optimization. *J Civ Eng Manag* 22(3):302–310

# Impact of Stress Concentrated Region on MEMS-Based Piezoelectric Energy Harvester



Satyana Rayana Talam, Ayesha Begum, M. B. Chakravarthi,  
Tilak Mukherjee, Poornaiah Billa, and Rambabu Busi

**Abstract** To manage solar power demand, various types of energy harvesting systems have been developed. Day-by-day different models are being reported with piezoelectric materials to improve efficiency. The present work reports the influence of stress concentrated regions in the form of rectangle, square and circle on the cantilever provided with three different piezoelectric materials: quartz, lithium niobate and lithium tantalite. Modeling and simulation have been carried out for the applied boundary load ranging from 50 to 200N. From the analyses of simulation results, it is observed that the induced electric potential found to be 5.02 V for the square shape punching against the load of 200N with Quartz material. Thus, maximum efficiency is exhibited for this in comparison with remaining attempts. The reasons for such variations among other materials and loads have been discussed in detail. For modeling and simulation, COMSOL Multiphysics software is used.

**Keywords** Stress · Regions · MEMS cantilever · Piezoelectric · Efficiency

---

S. Talam (✉) · P. Billa · R. Busi

Department of ECE, Lakireddy Bali Reddy College of Engineering, Affiliated to Jawaharlal Nehru Technological University Kakinada, Mylavaram, NTR District, Andhra Pradesh 521230, India  
e-mail: [drtsatyam@gmail.com](mailto:drtsatyam@gmail.com)

A. Begum · M. B. Chakravarthi

Department of EEE, Lakireddy Bali Reddy College of Engineering, Affiliated to Jawaharlal Nehru Technological University Kakinada, Mylavaram, NTR District, Andhra Pradesh 521230, India

T. Mukherjee

Department of ECE, Haldia Institute of Technology, ICARE Complex, Hatibera, Haldia, West Bengal 721657, India

## 1 Introduction

Energy harvesting is gripping technology that expands opportunities to achieve long-term wireless sensor networks [1–3]. The energy which converts ambient energy into electrical energy is known as piezoelectric energy harvesting. The principle behind this effect is those positive ions and negative ions are uniformly distributed in a crystal. Piezoelectric ceramic materials are not piezoelectric until the random ferroelectric domains are aligned by a process called polling. When the pressure is impacting the object, a negative charge is produced on the expanded side and positive charges are produced on the compressed side. Once the pressure is applied, electric current flows across the material. Micro electro mechanical systems (MEMS) are micro-electronic systems that incorporate chemical, magnetic, and radiant heat micromechanical sensors and actuators. MEMS represent a family of diverse designs, devices with simple cantilever beam to develop several sensors. The micro or nanoscale devices are used to design a simple unimorph cantilever beam in order to achieve the optimized conversion efficiency using different piezoelectric, piezoresistive, etc., materials. Several investigations are being carried out to improve the efficiency of microscale-based energy harvesting systems.

Cook-Chennault and his co-researchers [4] have investigated the powering MEMS portable devices for the analysis of the output power varying with the elastic layer thickness which is about  $300\text{ }\mu\text{m}$ . Do [5] has investigated a high-efficiency piezoelectric energy harvesting system, for changing the boundary loads with respect to different materials. The maximum electric potential found in their study was 3.3 V. Dallage et al. [6] have investigated a self-supplied integrable high-efficiency AC-DC converter for piezoelectric Energy scavenging systems for the considerations of applied boundary loads in the range of 100 to 200N and subsequently, the maximum electric potential was observed as 2.3 V.

From the literature review, it has been thoroughly understood that still there is a scope for further investigations and carry out few modeling attempts to realize and improve the efficiency of the piezoelectric energy harvesters. Most importantly, the optimization can be achieved by varying the dimensions of punching objects on the cantilever, three piezoelectric materials and the applied loads on the boundaries varying from 50 to 200N. Here, the new concept of stress concentrated region (SCR) is introduced to improve efficiency in which a simple unimorph cantilever beam is punched with square, rectangle and circle shapes four in number. The generated electric potential in accordance with the applied loads for all the punched objects are discussed in detail, and the optimized attempt resulting high conversion efficiency is suggested for real-time applications.

## 2 Software Tool Used

For the study of COMSOL Multiphysics, version 5.2 was used with the required interfaces such as electrostatics, structural mechanics, and different piezoelectric materials those are available from built-in materials library. It facilitates preferring and adding of the required piezoelectric material to the virtual model and simulates the energy harvester to explore the efficiency with respect to different punched objects for the various loads. The software tool has provision of adding multiple physical interfaces which is quite interesting to perform variety of investigations; pertaining to present work, electric potential has been evaluated against the applied load for different piezoelectric materials as it combines both electrostatics and structural mechanics interfaces.

## 3 Geometry Details

A simple cantilever beam is designed in 2D modeling. Various attempts have been made by changing the dimensions of unimorph cantilever, punching objects, and piezoelectric materials for the applied loads of 50–200N. After such attempts, the dimensions are fixed for the current investigation as follows: for rectangles of width: 10  $\mu\text{m}$  and height: 5  $\mu\text{m}$ , width: 2  $\mu\text{m}$  and height: 1  $\mu\text{m}$ , for square of side length: 1  $\mu\text{m}$  and finally circle with radius: 0.7  $\mu\text{m}$ . The geometries designed for the current work are presented in Fig. 1. It is essential to make sure that one side of the cantilever is fixed and other side is to be free so that it bends and in turn causes electric potential generation. This is done by fixing the constraints on right side of the cantilever. In addition to this, piezoelectric materials are added to the punched objects and cantilever by taking the appropriate domains of relevant shapes along with applying boundary loads as mentioned earlier.

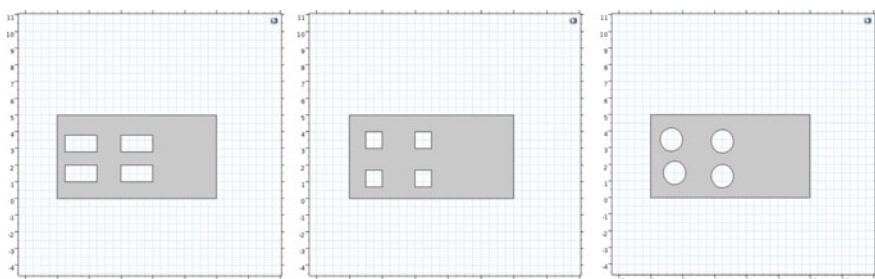


**Fig. 1** Piezoelectric cantilever punched with stress-concentrated regions such as four rectangles, squares and circles, respectively, from right to left

## 4 Simulation Results and Discussion

As part of preliminary investigation to select suitable piezoelectric materials, some modeling investigations were carried out and our study has been limited to three piezoelectric materials: quartz, lithium niobate, and lithium tantalate as they found to exhibit highest electric potential rather than PZT-4, PZT-5H for the same set of applied loads. To estimate the optimized efficiency, different steps in terms of varying loads and changing of cantilever material are carried out for SCR with rectangle, square, and circle. The investigation has been carried out in three basic steps. In the first step, SCR with different shapes like rectangle, square, and circle on simple unimorph cantilever beam. The input boundary load is applied on total surface area covering domains of punched objects ranging from 50 to 200N in the second step. Both first and second steps are executed by adding selective piezoelectric material, namely quartz, lithium niobate, and lithium tantalate. Based on the analyses of simulation results, the model which will give optimized efficiency will be selected for real time application.

The electric potential details for the lithium tantalite were not shown as the values were extremely low in comparison with quartz and lithium niobate at any applied loads [7–9]. The studies were depicting the electric potential at applied load 200N only as it exhibits high potential than any other loads. The maximum electric potential is observed 5.02 V for the quartz material under the boundary load of 200N, while 3.07 V for the niobate material. The results are depicted in the Fig. 2 that has been generated from the software tool. Further, the comparison electric potential values against different arc lengths of various punched objects is also presented [10] (Figs. 3 and 4).

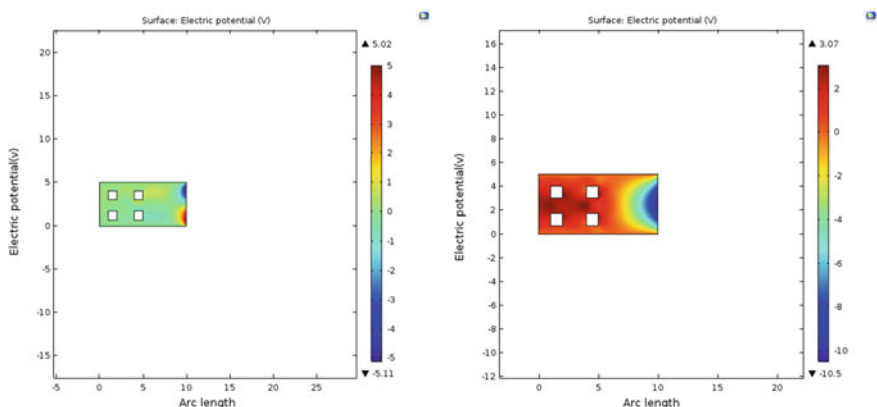


**Fig. 2** Induced electric potential against 200N load for the cantilever punched with square provided with quartz and lithium niobate materials (from Top to Bottom)

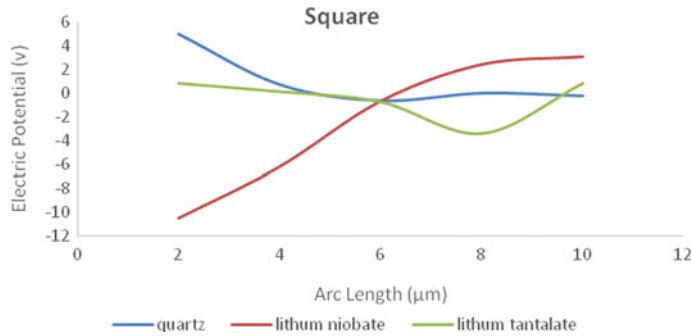


**Fig. 3** Variation of electric potential for three different materials for punched square against 200N applied force

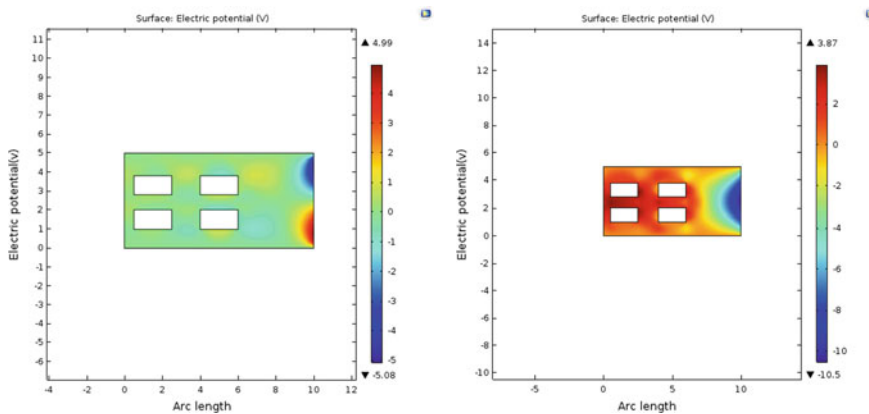


**Fig. 4** Induced electric potential against 200N load for the cantilever punched with square provided with quartz and lithium niobate materials (from Top to Bottom)

The maximum electric potential for the punched rectangle is found to be 4.99 V for the quartz material under boundary load of 200N. Similarly, electric potential is observed to be 3.87 for the lithium niobate with 200N force is applied (Fig. 5).

In order to understand the variation of electric potential with respect to applied load for different piezoelectric materials, the following physical properties are summarized in Table 1.

The maximum electric potential for the punched circle is observed as 4.99 V for the quartz material for the boundary load of 200N which is equal to case of rectangle. Similarly, electric potential is observed 3.27 for the lithium niobate material is used with 200N force. The physical properties such as poisson's ratio, young's modulus and density found to be low for quartz than remaining two materials. It could be the reason for optimized performance in addition to punching object of square than rectangle and circle [11, 12] (Figs. 6 and 7).

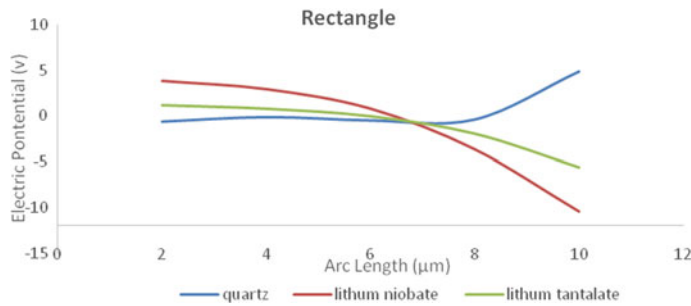


**Fig. 5** Variation of electric potential for three different materials for punched rectangle against 200N applied force

**Table 1** Comparison of physical properties of piezoelectric materials under investigation

Piezoelectric material	Density ( $\text{Kg/m}^3$ )	Young's modulus (GPa)	Poisson's ratio
Quartz	2651	97.2	0.17
Lithium niobate	4700	170	0.35
Lithium tantalate	7450	160	0.25

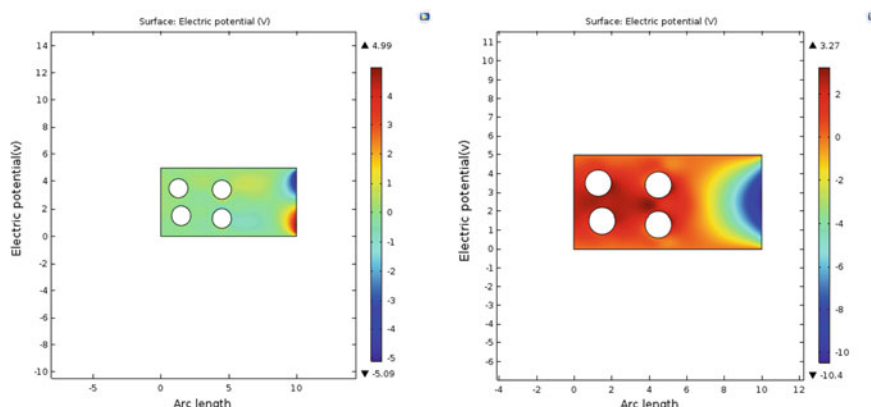


**Fig. 6** Induced electric potential against 200N load for the cantilever punched with circles provided with quartz and lithium niobate materials (from top to bottom)

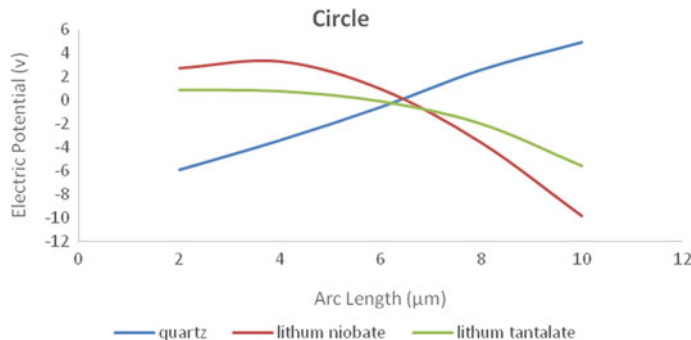


**Fig. 7** Variation of electric potential for three different materials for punched circles against 200N applied force

## 5 Conclusion

The unimorph piezoelectric cantilever beam is customized with a finite shape. The dimension is optimized after performing various try-out and error attempts with the simple square, rectangle and circle shaped with stress concentrated regions. Three different materials are used for simulation, among them quartz with square punches has given away a maximum electric potential of 5.02 V and a minimum electric potential of 1.26 V for boundary loads 200N and 50n respectively. Similarly, quartz with rectangular punches has given a maximum electric potential of 4.99 V and the minimum electrical potential as 1.25 for boundary load 200N to 50N. Similarly, quartz with circle punches has given maximum electric potential as 4.99 V and the minimum electric potential as 1.25 V. These variations are absolutely associated with physical properties of piezoelectric materials and punching objects dimensions.

**Acknowledgements** The authors would like to thank National MEMS Design Centre (NMDC) at LBRCE that facilitates to carry out this work.

## References

1. Song J, Sun G, Zeng X et al (2022) Piezoelectric energy harvester with double cantilever beam undergoing coupled bending-torsion vibrations by width-splitting method. *Sci Rep* 12:583
2. Satyanarayana T, Vasu Babu M, Venkata Lakshmi D, Rama Koti Reddy DV (2016) Modelling and deformation analysis of piezoresistive cantilever for bio-sensing applications. *Indian J Sci Technol* 9(S1)
3. Wang JL, Bao BH, Wen F, Gong YZ (2010) Modelling and analysis of bimorph piezoelectric cantilever generators with the finite element simulation. *Mech Des Manuf*:3–5
4. Cook-Chennault KA, Thambi N, Sastry AM (2008) Powering MEMS portable devices—a review of non-regenerative and regenerative power supply systems with special emphasis on piezoelectric energy harvesting systems. *Smart Mater Struct* 17

5. Do XD et al (2011) A high efficiency piezoelectric energy harvesting system. Int Soc Des Conf:9–11
6. Dallage E, Miaton D, Venchi G, Frattini G, Ricotti G (2007) Self-supplied integrable high-efficiency AC-DC converter for piezoelectric energy scavenging systems. IEEE Int Symp Circ Syst Conf:1633–1636
7. Nabavi S, Zhang L (2019) T-shaped piezoelectric structure for high-performance MEMS vibration energy harvesting. J Microelectromech Syst 28:1100–1112
8. Wang QP, Wang Q, Jiang SL (2012) Research status of piezoelectric energy collector. Electron Comp Mater:72–76
9. Zou HX, Zhang WM, Li WB, Hu KM, Wei KX, Peng ZK, Meng G (2017) A broadband compressive-mode vibration energy harvester enhanced by magnetic force intervention approach. Appl Phys Lett 110:163904
10. Lefevre E, Badel A, Richard C, Pettit L, Guyomar D (2006) A comparison between several vibration-powered piezoelectric generators for standalone systems. Sens Actuator A 126:405–416
11. Roundy S, Wright PK (2004) A piezoelectric vibration-based generator for wireless electronics. Proc Smart Mater Struct 13
12. Li N, Yi Z, Ma Y, Xie F, Huang Y, Tian Y, Dong X, Liu Y, Shao X, Li Y et al (2019) Direct powering a real cardiac pacemaker by natural energy of a heartbeat. ACS Nano 13:2822–2830

# Color based Classification of Products Using Internet of Things



**Meenaxi M. Raikar, S. M. Meena, Siddaraj Hubballi, Anirudh Kulkarni, Vinayak Merawade, and Yash Deshpande**

**Abstract** Classification is a primary task in different sectors such as industry, agriculture, retail, and healthcare. Automation of this primary task reduces the manpower required and thereby increases productivity. Internet-connected devices will enable the user to manage the resources from remote locations. Classification of products is performed using various features, namely size, weight, length, color, and many more attributes. In this paper, color-based classification of products using the Internet of Things (IoT) is proposed. The system is able to classify the products into three categories such as red, green, and black (defective). The color sensor and infrared sensor are used. The infrared sensor is used to locate the product and initiate the actuation process using the servo motor. The products move on the conveyor belt using a DC motor. The wireless connectivity to the things is provided using the HC-05 a Bluetooth module. The MIT application inventor is used to develop a mobile application that records the count of red, green, and black products. The cloud-based storage of the data is provided for analysis that aid in decision-making and thereby increases profit. The promising results are obtained with 97% accuracy in classifying the products.

---

M. M. Raikar (✉) · S. M. Meena · S. Hubballi · A. Kulkarni · V. Merawade · Y. Deshpande  
School of Computer Science and Engineering, K. L. E. Technological University, Hubballi, India  
e-mail: [mmraikar@kletech.ac.in](mailto:mmraikar@kletech.ac.in)

S. M. Meena  
e-mail: [msm@kletech.ac.in](mailto:msm@kletech.ac.in)

S. Hubballi  
e-mail: [hubballisiddaraj@gmail.com](mailto:hubballisiddaraj@gmail.com)

A. Kulkarni  
e-mail: [anirudhkulkarni2002@gmail.com](mailto:anirudhkulkarni2002@gmail.com)

V. Merawade  
e-mail: [vinayak8928merawade@gmail.com](mailto:vinayak8928merawade@gmail.com)

Y. Deshpande  
e-mail: [yash.myinbox@gmail.com](mailto:yash.myinbox@gmail.com)

**Keywords** Color sensor · Infrared sensor · Conveyor belt · Actuation · Microcontroller

## 1 Introduction

Color forms a distinguishing attribute in the classification of products. The other primary attributes for the classification of products are size, shape, weight, and texture. IoT-enabled classification of products aids in process automation used in different sectors such as the manufacturing, textile, and food industry. Automation of product classification enables a reduction in labor costs and system downtime.

### 1.1 Applications of Color-Based Classification

In [7], the color sensor is used to identify the iodine level in the salt. The robotic arm picks the blocks based on the color sensed by the sensor using the microcontroller [8]. A manipulator arm to pick and place the objects used color based sensor is designed [9]. The color of the wall is detected using the TCS230 sensor [10]. In [11] voice-assisted guidance for color detection is provided to the color blind person using the TCS3200 sensor. In [4] the surface color of the tomatoes is one of the decisive factors for the ripeness of fruits. The coloring indexes of the tomatoes are considered to judge the ripeness of the fruit.

RGB color sensor is used for detecting occupants instead of using passive infrared (PIR) sensor [15]. The occupant is found out by measuring the color shift in the background. The TCS3200 sensor is used in the production line to fill the box with the different materials based on the color in industry [16]. An electro pneumatic system is developed using TCS3200 sensor for moving and positioning of objects in packing industry [17]. The model using color sensor is proposed in [18] for accurate color measurement and matching that is used in textile and paper industries. The products are classified based on the color by using robotic arm in industrial application [19]. In manufacturing industry, the color sensor is used to guide the vehicle in following a black colored line [20].

## 2 Related Work

### 2.1 Color-Based Classification

The RGB model is used to classify the products based on the color.

**Table 1** Basic RGB color values [6]

S. No.	Value			Basic colors
	Red	Green	Blue	
1	> 250	> 250	> 250	White
2	< 25	< 25	< 25	Black
3	< 200	< 200	> 250	Blue
4	> 250	< 200	< 200	Green
5	< 200	> 250	< 200	Red

### *RGB color model*

Red, green, and blue are the primary colors represented using three integers, each of eight bits. The value of each integer ranges from 0 to 255. In Table 1, the range of values used to identify the basic colors using TCS3200 sensor is presented.

## **2.2 Color Sensor Used for Classification**

The authors proposed a system that sorts tomatoes based on their ripeness level, using the TCS3200 color sensor, which uses three colors, red, blue, and green (RBG), to differentiate the colors of tomatoes. The SG90 servo motors are used to push the tomatoes into the appropriate container [1]. The study in [2] aimed to develop an automatic color sorting apparatus for tomatoes by utilizing a microcontroller, color sensor array, servo motors, and mechanical components. The system automatically separated tomatoes of a particular color into three subclasses, green, red, and yellow, as per their color values. A servo motor is used to push colored tomatoes into separate collecting tins. The authors in [3] proposed a system to sort tomatoes based on the colors red, green, and yellow. Conveyor belts are used to push the tomatoes into separate storage boxes for grading.

## **2.3 Machine Vision-Based Classification**

In [5], machine vision-based classification using texture features (Entropy, Inverse Difference Moment—IDM), color features (Angular Second Moment-ASM, a measure of homogeneity), and shape features (circularity) are performed.

### 3 Proposed System

The proposed system is able to classify and count the products based on the color as shown in Fig. 2. The proposed system architecture is formed of physical, network, database, application, and security/management layer.

#### *Physical/Device Layer*

The device layer is composed of different sensors namely the TCS3200 color sensor, infrared (IR) sensor, DC motor, and servomotor as represented in Fig. 3.

- (1) *Color sensor*: The TCS3200 color sensor is used to detect the color of the products. The light intensity of the primary colors is converted to frequency using photodiodes for filtering and convertor. The microcontroller pins 4, 5, 6, 7, and 8 are used for color sensing. The initial values of these pins are as presented in Fig. 4a.
- (2) *Infrared sensor*: The infrared ray is blocked when the product is detected on the conveyor belt. Two IR sensors are used, one for red and the other for green product detection. The state of the IR sensor is read on pin 11; if it is zero, the servomotor is actuated.
- (3) *Conveyor belt*: The products are carried on the conveyor belt to classify and place in the appropriate containers. The DC motor is used for rotating the conveyor belt on the pulleys.
- (4) *Actuation*: The servomotor is actuated on identification of the product by the IR sensor. Upon identification the servomotor pushes the product to the respective containers.

#### *Network Layer*

The Bluetooth connectivity is provided to the devices connected to the system using the HC-05 module. Pin 1 and 0 of the microcontroller are used to transmit and receive the data for the establishment of the connection to the devices remotely.

#### *Data/Database Layer*

The data acquired is stored in the cloud platform using the real-time firebase DB. The count of red, green, and black products is stored batch wise. The user can query the count of products for data analysis and further processing.

#### *Application Layer*

The block-based programming is performed for its ease of design and deployment capabilities. The user interface is provided for connecting through Bluetooth, product count, reset, and disconnects using the button as presented in Fig. 5.

#### *Security/Management Layer*

The security to the system can be provided by adding the access control using pattern matching or biometric authentication features, for enabling only the authenticated users to control the system [13].

### 3.1 Problem Statement

To design an IoT-based classification of the products using color sensor providing the count of different products on the mobile application. The hardware components used for prototype development of the model are:

- Acrylic sheets used in design of conveyor belt
- Two plastic bearings with grooves
- A belt with grooves
- Two couplings
- A DC motor
- Relay
- 12 V DC Adapter
- Arduino Uno
- Tower pro 9 g micro servo motor × 2
- Two IR sensors
- TCS3200 color sensor
- HC-05 Bluetooth module

The software components to build the prototype of the model are:

- Online circuit diagram tool using [www.circuito.io](http://www.circuito.io)
- Arduino IDE software
- MIT app inventor

### 3.2 Colour-Based Classification Pseudo Code

**Algorithm 1:** Colour-based classification and counting of products using IoT.

1: Assumption: HC-05 for Bluetooth Connectivity establishment, Arduino Uno used as microcontroller; the blocks as presented in Fig 1, are assumed as products.

2: Input: Products placed on the conveyor belt, Mobile app interface to count the number of products.

3: Pins Defined: TCS3200 Color sensor (4, 5, 6, 7, 8), Servomotor (2), DC motor (9, 10), Two IR sensors (11, 12), HC-05 (1, 0)

Initialization: Microcontroller pin 4, 5, 6, 7, 9, 10 are set as OUTPUT, Pin 8 set as INPUT to obtain color sensed and PIN 2, 3 is set to 0 degree, Pin 11, 12 set as INPUT, Pin 4—Set to HIGH, Pin 5 set to LOW, Baud rate set to 9600.

Output: The system is able to classify the products into three different categories.

Loop until

Pin 9—Set to HIGH, Pin 10—set to LOW, for continuous movement of the conveyor belt.

Attach pin 2 and 3 to the servomotor, used for sliding the product on detection.



**Fig. 1** IoT-based product classification using color sensor

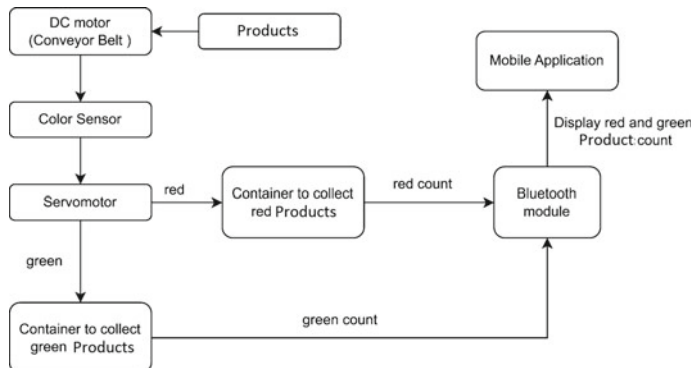


**Fig. 2** Proposed color sensor based classification of products using IoT

For Color classification: RED, GREEN, BLACK set the PIN values as presented in Table 2.

Obtain the frequency of the color, RED Frequency, GREEN Frequency.  
If the RED Frequency lies in the range of red color

IR Sensor enabled detection of the product,  
Servo motor sliding the RED product into container 1.

If the GREEN Frequency lies in the range of green color

IR Sensor enabled detection of the product,  
Servomotor sliding the GREEN product into container 2.

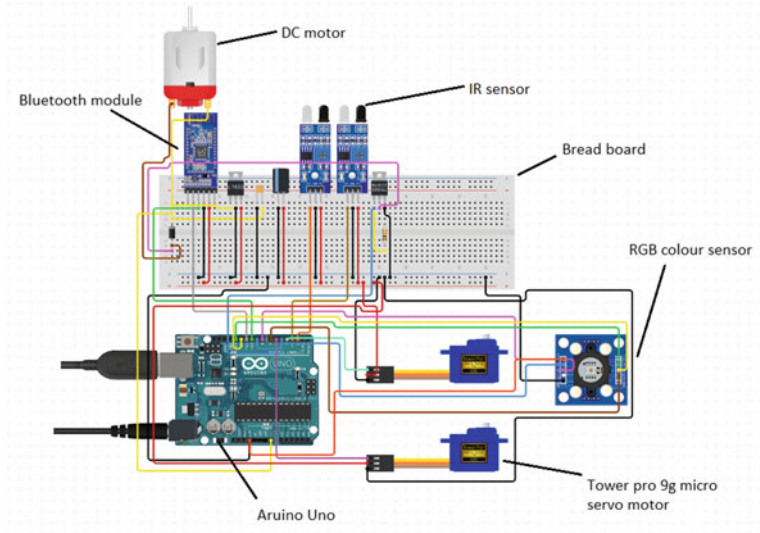


**Fig. 3** Circuit diagram for classification of the products using IoT

Display the count of product upon the button press using the mobile app  
 Store the timestamp, count of products in the Cloud database.  
 end-loop.

#### 4 Methodology

The product classification machine uses an RGB color sensor to sense the color of the product and give information about the color to the microcontroller; based on the input, the actuators can be controlled to slide the products into different containers. The flow diagram for color-based classification of products is presented in Fig. 4b. Two actuators and three containers are used to classify the products; the first container collects red products, the second container collects green products, and the third container is used to collect black or rotten products. A conveyor belt is used to carry the products to the respective container. The servo motors are used at respective positions to push the products to the appropriate container. The algorithm to classify and count the number of red, green, and black products is presented in algorithm 1.

The conveyor belt requires a hard material to be able to hold the pulley and belt; the material used is an acrylic sheet which is durable and strong; two pulleys are fixed at both ends, and the belt is wrapped around one end of the conveyor belt has a setup where the color sensor is placed, two infra-red sensors are fixed along the conveyor belt to detect the object incoming, two containers are fixed along edges of the conveyor belt, and the entire conveyer belt is fixed on an acrylic sheet

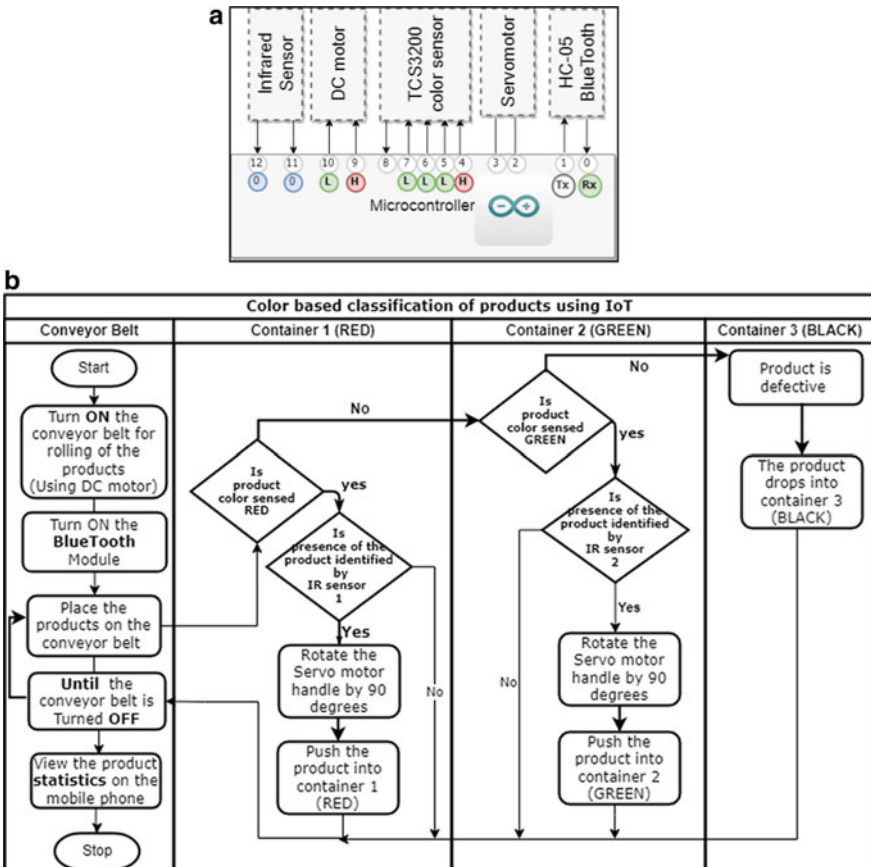


**Fig. 4** **a** Microcontroller PIN state for product classification using color sensor, **b** flow diagram for color-based classification of product

platform. The design and prototype developed for color-based product classification is as represented in Fig. 6a and b respectively.

## 5 Result Analysis

The mobile application to count the number of red and green color products is designed using the MIT app inventor available online, as shown in Fig. 5 using block programming. Proficiency in programming is not required to develop IoT prototype using block-based programming [21]. The timestamp, batch information, and count of the products are stored in the firebase cloud platform for further data analysis. The

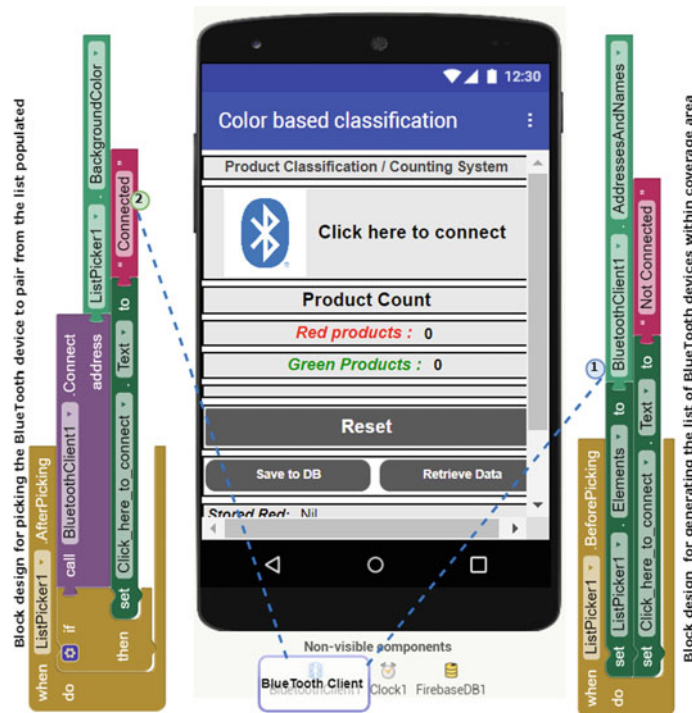


**Fig. 5** Mobile application design to count the number of products

**Table 2** Microcontroller pin state for product color identification

S. No.	Pin		Color
	7	6	
1	L	L	Red
2	H	H	Green
3	L	H	Blue
4	H	L	-

limitation of the system is shape, weight, and sizes of the product are not considered for classification.

The management of IoT devices is efficient by integrating with software-defined networking technology as presented in [12]. The integration of the cloud platform to the IoT system helps in achieving scalability, as presented in [14]. The energy efficiency is increased by using the lightweight protocol, Message Queue Telemetry Transfer (MQTT), for communication.

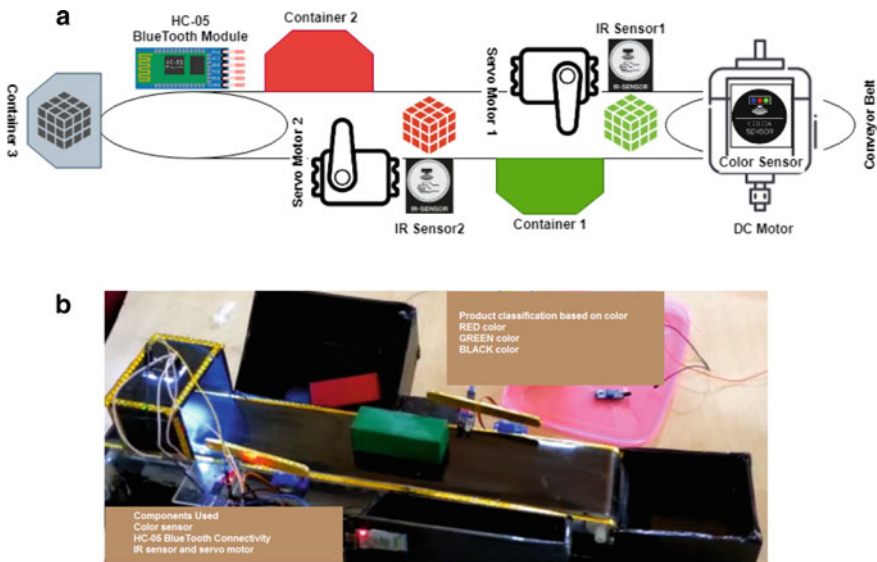


**Fig. 6** **a** Design of IR sensor-based detection of product and sliding into the appropriate containers, **b** prototype of IR sensor-based detection of product and sliding into the appropriate containers

## 6 Conclusion

The products are classified based on the color sensed by the TCS3200 sensor. IoT-enabled product classification and counting systems are designed. The system classifies the products into three categories, namely red, green, and black color. The user is able to count the number of products in the different categories using the mobile application designed. The product statistics are stored in the cloud platform to support data analysis. The future plan is to use a camera that captures the product images and uses them for classification. The machine learning model is to be built for training the system to classify the products.

## References

- Putra F, Rizaldi T (2019) Application of color sensor in the determination of tomato fruit ripeness (*Solanum Lycopersicum*, L) in gravitation type fruit sorting tool (gravitation type). Indonesian J Agric Res 2(1):13–20. <https://doi.org/10.32734/injar.v2i1.862>
- Adamu A, Shehu A (2018) Development of an automatic tomato sorting machine based on color sensor
- Sari M, Fajar R, Gunawan T, Handayani R (2022) The use of image processing and sensor in tomato sorting machine by color, size, and weight. JOIV: Int J Inf Vis 6:244. <https://doi.org/10.30630/joiv.6.1-2.944>.

4. Edan Y, Pasternak H, Shmulevich I, Rachmani D, Guedalia D, Grinberg S, Fallik E (2006) Color and firmness classification of fresh market tomatoes. *J Food Sci* 62:793–796. <https://doi.org/10.1111/j.1365-2621.1997.tb15457.x>
5. Pavithra V, Pounroja R, Bama BS (2015) Machine vision based automatic sorting of cherry tomatoes. In: 2015 2nd international conference on electronics and communication systems (ICECS), pp 271–275. <https://doi.org/10.1109/ECS.2015.7124907>
6. Millerman, Arduino Color Recognition, <https://www.instructables.com/Arduino-Color-Recognition/>
7. Fattah F, Indra D, Mulyana S, Salim Y, As'ad I, Mude A (2021) Measurement of iodine levels in salt using color sensor. In: 2021 3rd East Indonesia conference on computer and information technology (EICoCIT), pp 410–414. <https://doi.org/10.1109/EICoCIT50028.2021.9431910>
8. Mohd Khairudin AR, Abdul Karim MH, Samah AA, Irwansyah D, Yakob MY, Zian NM (2021) Development of colour sorting robotic arm using TCS3200 sensor. In: 2021 IEEE 9th conference on systems, process and control (ICSPC 2021), pp 108–113. <https://doi.org/10.1109/ICSPC53359.2021.9689114>
9. Najmurrokhman A et al (2019) Design of a prototype of manipulator arm for implementing pick-and-place task in industrial robot system using TCS3200 color sensor and ATmega2560 microcontroller. *J Phys Conf Ser.* IOP Publishing, ISSN: 1742-6596. <https://doi.org/10.1088/1742-6596/1375/1/012041>
10. Singh AK, Balam NB, Kumar A, Kumar VA (2016) An intelligent color sensing system for building wall. In: 2016 International conference on emerging trends in communication technologies (ETCT), pp 1–4
11. Sung W, Chen G, Hsiao S (2023) Voice guidance system for color recognition based on IOT. *Comput Syst Eng* 45(1):839–855
12. Raikar MM et al (2020) Software defined internet of things using lightweight protocol. *Procedia Comput Sci* 171:1409–1418, ISSN 1877-0509
13. Raikar MM, Meena SM (2021) SSH brute force attack mitigation in Internet of Things (IoT) network: an edge device security measure. In: 2021 2nd international conference on secure cyber computing and communications (ICSCCC), pp 72–77
14. Raikar MM, Desai P, Kanthi N, Bawoor S (2018) Blend of cloud and internet of things (IoT) in agriculture sector using lightweight protocol. *ICACCI*, pp 185–190
15. Woodstock TK, Karlicek RF (2020) RGB color sensors for occupant detection: an alternative to PIR sensors. *IEEE Sens J* 20(20):12364–12373. <https://doi.org/10.1109/JSEN.2020.3000170>
16. Vachálek J, Šíšmišová D, Vašek P, Fiřtka I, Slovák J, Simovec M (2021) Design and implementation of universal cyber-physical model for testing logistic control algorithms of production line's digital twin by using color sensor. *Sensors* 21(5):1842. <https://doi.org/10.3390/s21051842>
17. Dezaki ML, Hatami S, Zolfagharian A, Bodaghi M (2022) A pneumatic conveyor robot for color detection and sorting. *J Cogn Robot* 2:60–72, ISSN 2667-2413. <https://doi.org/10.1016/j.cogr.2022.03.001>
18. Anupama P, Kumar KVS, Valsalam SR, Harikrishnan G, Muralidharan V (2012) An intelligent reflective colour sensor system for paper and textile industries. In: 2012 sixth international conference on sensing technology (ICST), Kolkata, India, pp 481–485
19. Cai L, Liu Y, Liu Z, Yang C (2017) Color recognition and dynamic decision-making model of 6 axis of industrial robot based on embedded system. In: 2017 29th Chinese control and decision conference (CCDC), Chongqing, China, pp 2836–2841. <https://doi.org/10.1109/CCDC.2017.7978995>
20. Hazza MHFA, Bt Abu Bakar AN, Adesta WYT, Taha AH (2017) Empirical study on AGV guiding in indoor manufacturing system using color sensor. In: 2017 5th international symposium on computational and business intelligence (ISCBI), Dubai, United Arab Emirates, pp 125–128. <https://doi.org/10.1109/ISCBI.2017.8053558>
21. Bak N, Chang BM, Choi K (2020) Smart block: a visual block language and its programming environment for IoT. *J Comput Lang* 60

# Design of a Compact Dual-Band Antenna with Meandered Slotted Patch and U-slotted Defected Ground Plane



Avisankar Roy, Surajit Mukherjee, Tapas Tewary, Smarajit Maity, and Sunandan Bhunia

**Abstract** A compact meandered slot-loaded rectangular microstrip patch antenna with a U-slotted defected background structure for dual-band working operation is presented in this article. The dual band has been obtained by cutting the rectangular slots and spur lines on the metallic patch. A U-like shaped slot has been incorporated in the ground metallic layer causing the reduction of the first resonant frequency significantly which indicates the achievement of 93% compactness concerning a conventional rectangular antenna. The effective equivalent inductance and capacitance of the microstrip patch are altered by slots in the ground backside plane, and the resonant frequency changes as a result. The fabricated structure of the proposed fabricated antenna resonates at 1.6 GHz and 6.1 GHz indicating the appropriateness for radio astronomy and radiolocation applications, respectively. The antenna depicts the gain of 2 dBi and 4 dBi for 1.6 GHz and 6.1 GHz frequencies. The overall physical dimension of the proposed antenna structure is only 54 mm × 42 mm × 1.524 mm.

**Keywords** Microstrip patch antenna · Compact · Dual band · Spur lines · Defected ground structure

---

A. Roy · S. Mukherjee  
Haldia Institute of Technology, Haldia, West Bengal, India

T. Tewary · S. Maity  
Academy of Technology, Bandel, West Bengal, India

S. Bhunia (✉)  
Central Institute of Technology, Kokrajhar, Assam, India  
e-mail: [bhuniasunandan@gmail.com](mailto:bhuniasunandan@gmail.com)

## 1 Introduction

Recent trends in wireless communication demand better infrastructure in the mobile environment. Internet of Things (IoT) is an important aspect of this current scenario. In the case of the transportation system through the land, vehicular communication has an important role. The smart driving technology needs to interact between the moving vehicles as well as static objects present outside. Also, the geolocation of any vehicle has an important aspect in the field of product distribution. Both systems should be present in modern vehicles. This demand also needs to fulfil another aspect. The communication system must be compact such that it can be fitted well in the vehicles as well as can carry by the commuter/ driver with ease. An antenna is an important part of the system. It needs to have properties like lightweight, easy integration capabilities, low cost, and low profile to achieve acceptability. Microstrip antenna possesses the above characteristics. Hence, widely used for systems that need to compact and multiband operate. Researchers have been working in the field of compact microstrip-printed antennas.

The compactness of a microstrip antenna can be realized in different ways. Researchers have proposed those in many works of literature for a few decades. The proposed techniques include cutting slots on the patch, using the shorting pin, etching ground plane with regular and irregular shapes, etc. [1–12]. The patch has a few regular rectangular slots that cause the surface current distribution to change and lengthen the current path on the patch towards the radiating edge, lowering the resonant frequency [1, 2]. Cutting the notch on the patch and shorted wall produce the lower resonant frequency along with the first higher resonant frequency generated for conventional antenna and hence dual band operation has been achieved [3]. The two current path have been formed due to incorporation of the notch. One produces the first higher resonant frequency and is the basic normal patch current directed towards the patch's radiating edge; however, other current path follows around the notch and consequently generates new lower resonant frequency. The resonant frequency is significantly lowered by a C-shaped ring structure within a half-wavelength slot on the patch antenna, and by comparing with the conventional patch almost 50% size reduction has been achieved [4]. In some literature, dual frequency operation with reduced-size microstrip antenna has been realized by incorporating cross-shaped slots on the patch, spur lines, rectangular slots on ground, stacked structure with aperture coupled feeding, etc. [5–8]. In article [9], a meandering slot has been engraved on the patch with infinite ground plane structure to achieve dual-band operation and about 86.5% size reduction has been proposed. From the simulated current distribution on patch, current path length has been found, and predicted resonant frequencies have been calculated. Some research article has shown that the use of slots on the ground plane can decrease the resonant frequency considerably [10]. Any kind of slot perturbation on the ground plane is defined as defected ground structure (DGS). An equivalent parallel RLC-tuned circuit can be considered in series with the transmission line to realize the effect of DGS, and hence the total effective capacitance and inductance of the antenna have changed, so that the resonant frequency has

been also changed, respectively [11, 12]. Some recent work on dual band microstrip patch antenna design includes as a metamaterial-configured electromagnetic bandgap structure has been incorporated into a square patch to achieve dual-band operation on 3.6 and 5.8 GHz [13], A miniaturized microstrip ring antenna with a multi-ring etched back ground plane and double ring radiators has been developed for GPS L1 and L2 band [14], and for LTE applications in LTE bands 41 (2.5 to 2.7 GHz) and 42 (3.3 to 3.8 GHz), a dual-band microstrip antenna with high band of dipole element and low band of patch element has been developed [15].

The antenna presented in this article is a miniaturized dual band rectangular microstrip printed patch antenna with meandering slots on the radiating layer and a U-shaped slotted defected ground layer. Due to the meandering slots on patch, the antenna radiates at 2.2 GHz and 6.4 GHz. The radiating resonant frequencies have been changed to 1.6 GHz and 6.1 GHz after the addition of a U-shaped slot in the ground plane. After getting the comparison with the usual reference rectangle-shaped microstrip printed antenna resonating at 1.6 GHz, approximately 93% compactness has been achieved due to the U-shaped slot's presence on the ground layer, which causes a significant decrease in the first resonant frequency.

## 2 Design Parameters and Techniques

A rectangular microstrip patch with dimension of  $18 \text{ mm} \times 14 \text{ mm}$  has been taken as a reference antenna where relative permittivity  $\epsilon_r$  has been taken as 3, thickness of the substrate has been taken as 1.524 mm and resonant frequency has been considered as 5.8 GHz. To consider the ground backside plane of the patch radiator to be infinite, it has been assumed to be three times larger than the upper patch. The proposed structure has the total dimension as  $54 \text{ mm} \times 42 \text{ mm}$ . The antenna was constructed on an Arlon AD 300A substrate having loss tan ( $\tan \delta$ ) of 0.002 to validate the experiment. Figure 1 depicts the dimension of the reference patch antenna.

To realize the dual-band operation some meandered rectangular slots have been etched out over the metallic radiating element. Due to the slots, the surface current patch length has been changed and lower frequency has been generated. The antenna dimensions with slotted patch have been demonstrated in Fig. 2.

In a microstrip patch antenna, the backside ground plane serves as a path for the signal to return, and the slots on the ground produce the discontinuity in the signal returning path. This results in a slow wave effect that causes the resonant frequency to decrease in value. On the ground plane, a U-like shaped slot has also been placed alongside the slotted patch. The first resonant frequency has been significantly reduced as a result of this modification. Figure 3 indicates the structure of the modified ground plane after the inclusion of the slot with dimension.

The step-by-step structural variation of the proposed patch antenna starting from the reference patch antenna has been given in Fig. 4. The proposed design was created in order to conduct the measurement, and Fig. 5 depicts an exact picture of the presented design.

**Fig. 1** Dimensions of the reference antenna with infinite ground plane

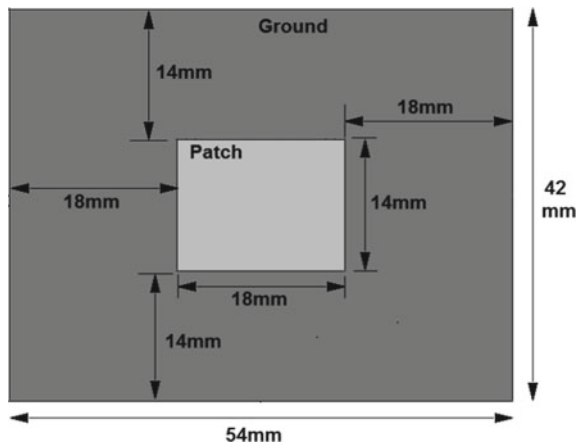
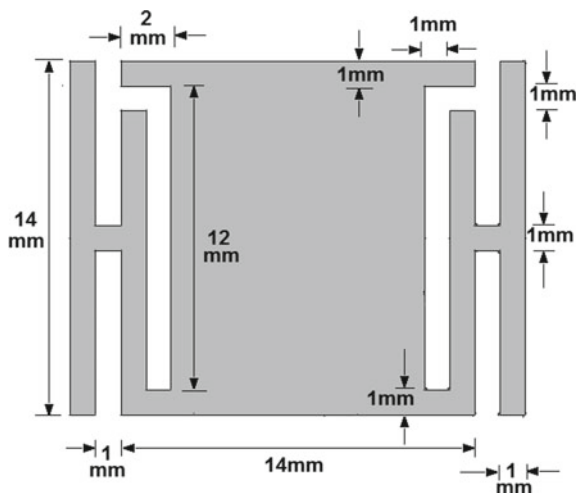


**Fig. 2** Dimensions of meandered slotted patch

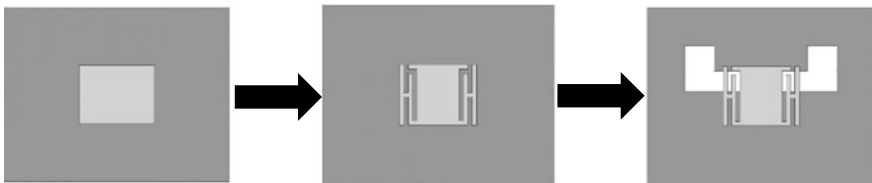
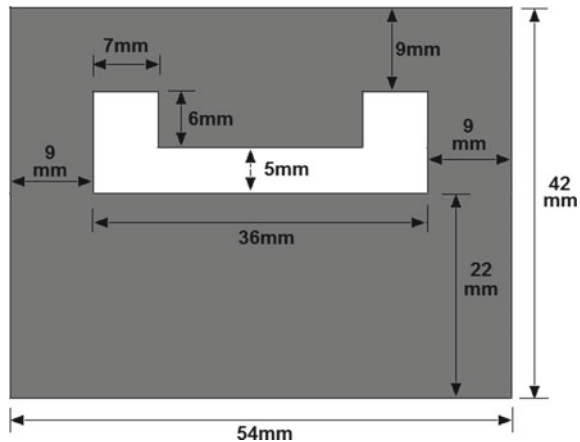


### 3 Results by Simulation and Measurement

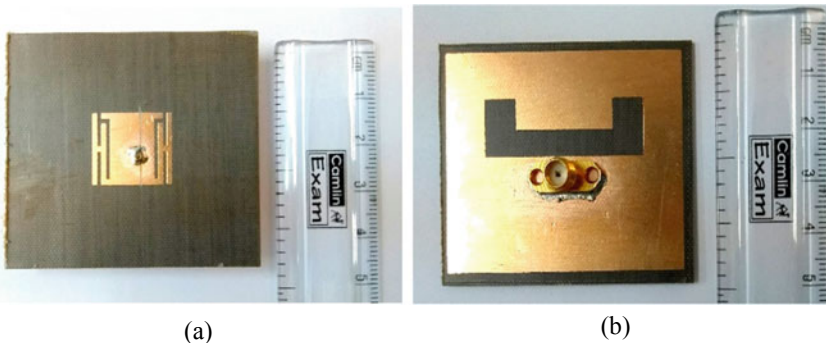
All the antenna structures have been designed and simulated in HFSS software. The fabricated prototype antennas have been analysed using Anritsu VNA, and the radiation characteristics have been measured inside an anechoic chamber. The measurement results indicate that the reference antenna has the resonant frequency at 5.5 GHz. Antenna with slotted patch only shows the measured frequencies as 2.2 GHz and 6.4 GHz. The measured resonant frequencies of the proposed structure with slotted patch and slotted ground plane have been obtained as 1.6 GHz and 6.1 GHz. The resonant frequencies, S11 in dB, and bandwidth are shown in Table 1.

For both 1.6 GHz and 6.1 GHz, the gain of the suggested antenna was found to be 3dBi. Figures 6 and 7 depict the simulated and measured frequency vs. S11 graph

**Fig. 3** U slotted ground plane with dimension



**Fig. 4** Structural modification steps towards antenna design

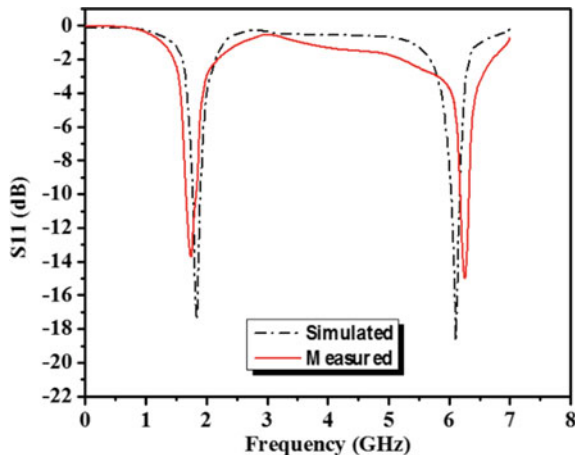
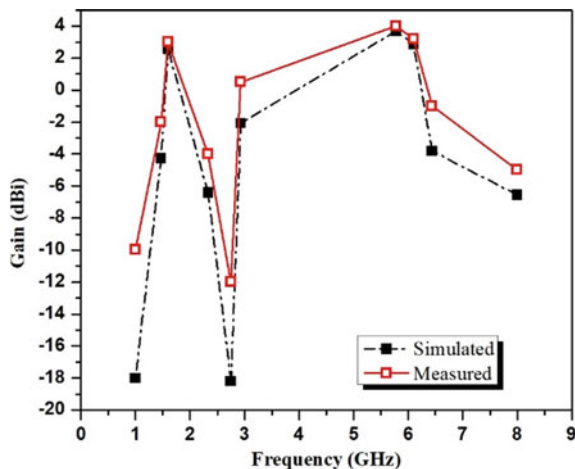


**Fig. 5** **a** Radiating element with slot (top layer) and **b** slotted ground plane (bottom layer) of the fabricated prototype antenna

and the variation of the antenna gain with respect frequency graph of the suggested antenna, respectively. The radiation pattern and simulated surface current distribution for 1.6 GHz and 6.1 GHz of the proposed antenna have been demonstrated in Fig. 8 and Fig. 9. It has been determined that the proposed antenna is nearly 93% more compact than the standard antenna that resonates at 1.6 GHz.

**Table 1** Simulated and measured data of the antennas

Type of the design		Resonant Fr (GHz)	S11 in dB	BW in MHz, %
Reference antenna	Simulated	5.6	-24	200, 3.57
	Measured	5.5	-25	200, 3.63
Antenna with slotted patch	Simulated	2.25	-17	40, 1.75
		6.74	-17	90, 1.26
	Measured	2.2	-20	70, 3.18
		6.4	-17	90, 1.4
Antenna with slotted patch and slotted ground	Simulated	1.7	-17	80, 4.7
		6	-19	90, 1.5
	Measured	1.6	-14	70, 4.37
		6.1	-15	80, 1.3

**Fig. 6** Frequency versus S11 plot of the proposed designed antenna**Fig. 7** Variation of gain with frequency of the proposed designed antenna

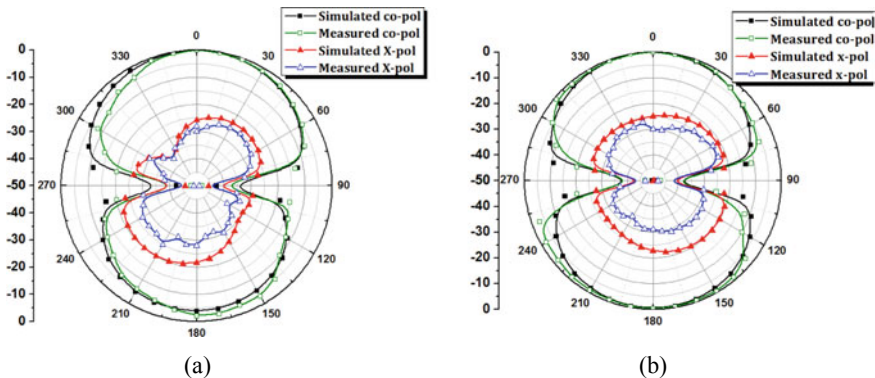


**Fig. 8** Radiation characteristics of the proposed design at **a** 1.6 GHz and **b** 6.1 GHz

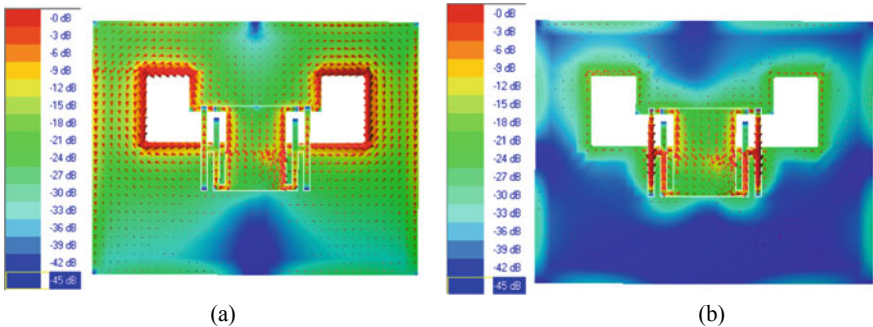


**Fig. 9** Simulated surface current orientation of the proposed antenna at **a** 1.6 GHz and **b** 6.1 GHz

## 4 Conclusion

In this literature, a small dual-band slotted rectangular microstrip patch antenna design has been put forth. A U-shaped slot in the ground layer has been incorporated to decrease the first resonant frequency more. It has been determined that the proposed antenna's resonating frequencies are 1.6 GHz and 6.1 GHz. The gain of the antenna for both resonating frequencies has been achieved as 3 dBi. The simulated results have been validated with the measured values. The outcomes show that the suggested antenna structure is suitable for radio astronomy and radiolocation applications.

## References

- Bhunia S, Sarkar D, Biswas S, Sarkar PP, Gupta B, Yasumoto K (2008) Reduced size small dual and multi-frequency Microstrip antenna. *Microw Opt Technol Let* 50:961–965

2. Bhunia S, Sarkar PP (2009) Reduced sized dual frequency microstrip antenna. *Indian J Phys* 83:1457–1461
3. Mishra A, Singh P, Yadav NP, Ansari JA (2009) Compact shorted microstrip patch antenna for dual band operation. *Progress Electromagnet Res C* 9:171–182
4. Chen RH, Lin YC (2011) Miniaturized design of microstrip-fed slot antennas loaded with C-shaped rings. *IEEE Antenn Wirel Propag Lett* 10:203–206
5. Chatterjee S, Chowdhury SK, Sarkar PP, Chanda Sarkar D (2013) Compact microstrip patch antenna for microwave communication. *Indian J Pure Appl Phys* 51:800–807
6. Chakraborty U, Kundu A, Chowdhury SK, Bhattacharjee AK (2014) Compact dual-band microstrip antenna for IEEE 802.11a WLAN application. *IEEE Antenn Wirel Propag Lett* 13:407–410
7. Sharma AK, Mittal A, Reddy BVR (2015) Slot embedded dual-band patch antenna for WLAN and WiMAX applications. *Electron Lett* 51(8):608–609
8. Roy A, Bhunia S, Chanda Sarkar D, Sarkar PP, Chowdhury SK (2017) Compact multi frequency strip loaded microstrip patch antenna with spur-lines. *Int J Microw Wirel Technol* 9(5):1111–1121
9. Roy A, Bhunia S, Sarkar DC, Sarkar PP (2017) Slot loaded compact microstrip patch antenna for dual band operation. *Progress Electromagnet Res C* 73:145–156
10. Sarkar S, Das Majumdar A, Mondal S, Biswas S, Sarkar D, Sarkar PP (2011) Miniaturization of rectangular microstrip patch antenna using optimized single-slotted ground plane. *Microw Optic Technol Lett* 53(1):111–115
11. Elftouh H, Touhami NA, Aghoutane M, Amrani SE, Tazon A, Boussouis M (2014) Miniaturized microstrip patch antenna with defected ground structure. *Progress Electromag Res C* 55:25–33
12. Roy A, Bhunia S, Chanda Sarkar D, Sarkar PP (2020) Compact wideband meandered slotted multi frequency microstrip antenna. *Wirel Personal Comm* 115(2):1769–1782
13. Smyth BP, Iyer AK (2021) Low-profile uniplanar dual-band and dual-polarized microstrip patch antenna using embedded MTM-EBGs. *IEEE Trans Antenn Propag* 69(7):3645–3653
14. Yuan J, Chen ZD, Li Y (2021) A compact dual-band microstrip ring antenna using multi ring ground for GPS L1/L2-band. *IEEE Antenn Wirel Propag Lett* 20(12):2250–2254
15. Yang SJ, Duan W, Liu YY, Ye H, Yang H, Zhang XY (2022) Compact dual-band base-station antenna using filtering elements. *IEEE Trans Antenn Propag* 70(8):7106–7111

# Performance Analysis of Energy Harvesting-Based Relay-Assisted CR Network Under Co-channel Interference Environment



Dipak Samanta, Jayanta Kumar Bag, Chanchal Kumar De,  
and Abhijit Chandra

**Abstract** In wireless radio frequency (RF) networks, efficient spectrum utilization is a promising technique. Energy harvesting (EH) from wireless environment is also very challenging issue. In this paper, a performance analysis of multi relay-based CR network has been proposed in presence of co-channel interference (CCI) environment. Here, the secondary nodes in the form of corresponding secondary transmitter (SU-Tx) along with secondary relay (SR) modules can harvest energy from the primary transmitter as well as CCI. In our model, a strategic yet adaptable relay protocol is defined as adaptive hybrid relay (AHR) mode, and this reflects a switching between amplification forward (AF) or decode forward (DF) mode of operation depending on the successfully decoding activities of relays. Successful decoding of relays occurs when the SINR of an individual relay exceeds a threshold SINR value. Considering energy harvesting conditions, the power control policies at specific transmitter nodes, i.e., (SU-Tx) and (SR), are taken care of in a suitable manner. We investigate the outage performance for secondary receiver and develop a closed-form mathematical equation for the proposed system model. An AF and DF mode have been compared with our proposed AHR model in terms of secondary outage probability. Here, we discuss the effect of numbers of relay, energy harvesting efficiency factor, and decoding threshold SINR on secondary outage probability. Finally, Monte-Carlo simulations have been used to validate all of the analytical closed-form equations.

**Keywords** Cognitive radio · Amplification forward (AF) · Decode forward (DF) · Adaptive hybrid relay (AHR) · Energy harvesting (ED) · Co-channel interference (CCI)

---

D. Samanta (✉) · J. Kumar Bag · C. Kumar De  
Department of ECE, Haldia Institute of Technology, Haldia 721657, West Bengal, India  
e-mail: [dipak.ecehit@gmail.com](mailto:dipak.ecehit@gmail.com)

A. Chandra  
Department of IEE, Jadavpur University, Kolkata 700032, West Bengal, India

## 1 Introduction

Spectral shortage is a major problem in wireless communication domains. The availability of our natural resources as an electromagnetic radio spectrum is limited and is congested daily with an increase in wireless devices and applications. Most spectra are underutilized due to the inflexibility of static allocation of spectra by primary users (PU), i.e., licensed users. Unlicensed users are called secondary users, and they can use the primary spectrum band to transmit signals by controlling interference constraints levels for the PU. Dynamic allocation of this spectrum is urgently needed to overcome this situation of underutilized problems for crowded users. Cognitive radio technology in wireless communications is the master solution for this underutilized spectral problem [1, 2]. Energy harvesting (EH) from radio frequency (RF) signal is a promising solution for powering wireless systems. In [3], the authors proposed and analyzed a dual-hop model based on RF energy harvesting. Wireless energy harvesting and information processing approach using AF relay mode have been illustrated here. In [4], the author focuses on energy harvesting from multiple PUs (primary users) signal. In [5], the authors evaluated the effectiveness of the decode forward (DF) and amplification forward (AF) protocols for multi-hop EH-based relay networks. Authors in [6] have investigated various relay allocating techniques and assessed the outage performance. The authors gave the idea of a dual-hop spectrum sharing scheme on the basis of the DF relaying method. Here, it is presumed that the cognitive relay is furnished with multiple antennas. In the presence of multiple primary users and multi-antenna-based relays network, the outage probability analysis formulas for proactive and reactive relay selective arrangements have been derived in [7]. The outage and throughput evaluation of the RF energy harvesting-assisted DF relay-based CR network have shown in [8]. In [9–11], the authors analyzed outage performance for multi-hop relay-assisted cognitive radio networks with all secondary nodes turned on dedicated power beacon following the time switching relay (TSR) protocol. In [12], the performance of cognitive wireless networks is evaluated in a MIMO environment while maintaining the interference threshold between the primary destination and the CSI. In [13], an adaptive joint underlay/overlay mode of transmission using multi-antenna-based proactive DF relay has been proposed to improve the spectrum utility in a CR network. The outage performance of the full-duplex relay-based CR network in the presence of numerous primary users and numerous destinations has been proposed in [14]. In [15], the authors have analyzed the effect of co-channel interference (CCI) along with feedback delay in multi-antenna-based AF relay networks. Antenna selection schemes are being studied in energy harvesting-based decode forward relays system. The authors in [16] have examined the effectiveness of the amplify-and-forward relaying strategy for small cell uplinks using multi-antenna-based relays. Whereas in [17], the authors considered primary co-channels that are not identical interference in cluster-based multi-hop cognitive networks. CCI is the interference a user experiences from a user in an adjacent cell that uses same frequency. CCI can be used as an alternative energy source for low-energy-powered communication devices in wireless networks.

The authors in [18] evaluated the impact of CCI on the secondary network of the dual-hop relay system considering the Nakagami m fading channel. In the above-mentioned works, a typical scenario has not been considered, where adaptive relay selection scheme co-exists with energy harvesting at the secondary source and relays in presence of CCI. The Joint underlay/overlay mode of transmission in cognitive radio network has been proposed in [19]. Here, closed-form expression of secondary outage incorporate with energy harvesting circuit in secondary transmitter from CCI environment has not been considered.

In this paper, to increase the spectrum utility, the adaptive hybrid relay (AHR)-based underlay CR network has been proposed, where the secondary transmitter and relays harvest energy from CCI and PU radio frequency (RF) signal using energy harvesting technique, which is not considered in [19]. Here, AHR is the combination of AF and DF relay protocol which can switch in between depending on the channel condition. The closed-form expression of secondary outage performance of AHR relay-based CR network has been derived and compared with the conventional AF and DF mode in different conditions. In this scenario, secondary source (SU-Tx) communicates with secondary destination (SU-Rx) via multiple adaptive hybrid relays (SR) in presence of CCI including primary transmitter (PU-Tx) and primary receiver (PU-Rx). The relays as well as secondary source are furnished with energy harvesting circuits and rechargeable battery. Both can obtain energy from the source signal and interference from the primary transmitter, CCI, and use this energy for advancing the received signal to the destination.

The key contributions of this paper are as follows:

- The outage performance of secondary user in underlay cognitive radio network using AHR relay scheme has been investigated in presence of CCI environment.
- The closed-form analytical expression of SU outage has been evaluated in underlay CR network using EH circuit at secondary transmitters (i.e., SU-Tx, SR) with maintaining maximum allowable transmit power policy at secondary transmitters.
- A comparative study among AF, DF, and AHR in the context of outage performance has been reflected.
- The impact of number of relays, energy harvesting efficiency factor, and decoding threshold SINR on SU outage performance has been indicated.
- The analytical closed-form expressions have been validated using MATLAB simulation test bed.

The remaining part of this article is structured as follows: Section 2 describes the proposed system model and the essential assumption, Sect. 3 deals with the energy harvesting policy and corresponding power allocation strategies at secondary transmitters, i.e., both secondary transmitter (SU-Tx) and secondary relay (SR); secondly, performance analysis of AF, DF, and AHR mode is carried out. In Sect. 4, the mathematical computation including closed-form equation is established. The analytical and simulation result are addressed in Sect. 5. Finally, Sect. 6 briefly describes the conclusion of the paper.

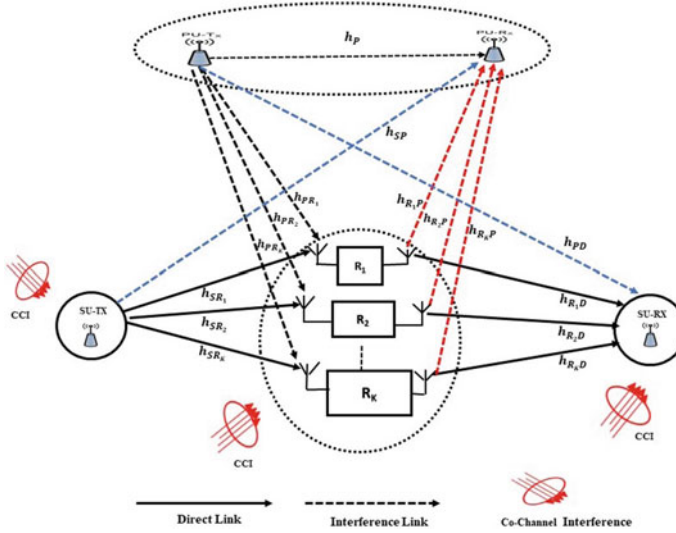


**Fig. 1** System model

## 2 System Model and Basic Assumption

The system configuration which is depicted in Fig. 1 is a proposed cognitive radio network model which consists of one primary user (PU), one secondary transmitter (SU-Tx), single secondary receiver (SU-Rx/D), and multiple relays ( $R_k; k = 1, 2, \dots, K$ ). Now, it is considered that the (SU-Tx), (SU-Rx/D), and ( $R_k; k = 1, 2, \dots, K$ ) have a single transmitting and receiving antenna. Considering higher shadowing effects, the direct link between (SU-Tx) and (SU-Rx) has been neglected here. All the relays are in AHR mode, that is, in adaptive selection mode, those can switch as a combination of AF and DF protocol depending on the channel quality. In this system model, we consider the effects of CCI at secondary transmitter, relays, and secondary receiver. Additionally, all the secondary nodes get affected by the transmitted signal from PU-Tx, as an interference source. The impact of interference at primary receiver by the transmitted signal from SU-Tx and SRs also addressed here. This has been assumed that the secondary source and all relays are partially powered by collecting energy from ambient RF sources through EH circuits presented at these nodes. Here, whole communication process is carried out using time switching protocol (TSP) in dual-hop mode. The important steps of the TSP protocol for information processing and energy harvesting at the relay are shown in Fig. 2. In Fig. 2,  $T$  is the total considered time that is necessary to travel information from the secondary source to the secondary destination node through relays, where  $\tau T$  ( $0 \leq \tau \leq 1$ ) is the fraction of the total time that secondary source and relays use for energy harvesting.

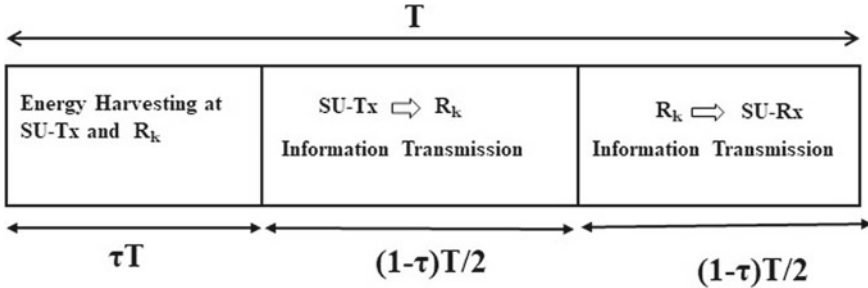


**Fig. 2** TSP protocol for energy harvesting and information processing

In the first time slot of transmission, SU-Tx sends signal to relay ( $R_k; k \in 1, 2, \dots, K$ ) under the condition of transmit power to ensure the interference to the primary user does not exceed the threshold constrained power ( $I_P$ ). During the second time slot, the relay uses the AHR relay protocol to transfer received signals to the secondary destination while keeping the interference threshold at  $I_P$ .

According to the adapted hybrid relay (AHR) protocol, if the relay can decode the received signal effectively, then DF scheme is followed, else the AF scheme is continued. In this model, the channel path coefficients are presumed to be zero mean, unit variance independent non-identical Rayleigh distribution type as well as all noise factors are considered as additive white Gaussian noise (AWGN) with variance  $N_0$ . Channel coefficients are denoted as follows:  $h_p$  denotes the channel path coefficient for PU-Tx to PU-Rx,  $h_{SR_k}$  ( $k = 1, 2, \dots, K$ ) represents channel coefficient for SU-Tx to  $k$ th relay ( $R_k$ ),  $h_{PR_k}$  ( $k = 1, 2, \dots, K$ ) is for PU-Tx to  $k$ th relay ( $R_k$ ),  $h_{SP}$  is used to represent the channel coefficient for SU-Tx to PU-Rx,  $h_{R_{kD}}$  ( $k = 1, 2, \dots, K$ ) is the channel coefficient for  $k$ th relay ( $R_k$ ) to SU-Rx,  $h_{PD}$  signifies the channel coefficient for PU-Tx to SU-Rx. Here,  $h_{C_n R_k}$  and  $h_{C_n D}$  are channel coefficient from  $n$ th CCI source to  $k$ th relay and SU-Rx, respectively. The relay is chosen in such a way that it will improve the end-to-end SINR of the SU-Tx to SU-Rx channel path. Secondary sources (SU-Tx) and relays have the capability to choose transmitted power amount which is varied between constrained transmitting power and energy harvesting power. All the channel power gains, denoted by  $g_x$ , follow an exponential nature distribution with a mean of  $\lambda_x$ , where  $x$  signifies appropriate channel link indicator suffix from each nodes. The exact link parameters are shown in Table 1.

The power distribution at secondary sources (SU-Tx) and relays is described in the following section.

### 3 Energy Harvesting and Power Allocation Strategies

The theory described here is employed to explore the power allocation strategy for SU-Tx and  $SR_k$ .

**Table 1** Channel gain with parameter List

Path-channel gain indicator with parameter list

Path-link	Channel gain	Parameter
PU-Tx-SU-Tx	$g_{PS}$	$\lambda_{PS}$
PU-Tx-SU-Rx	$g_{PD}$	$\lambda_{PD}$
$n$ th CCI-SU-Tx	$g_{C_nS}$	$\lambda_{C_nS}$
PU-Tx-R <sub>K</sub>	$g_{PR_k}$	$\lambda_{PR_k}$
SU-Tx-R <sub>K</sub>	$g_{SR_k}$	$\lambda_{SR_k}$
$n$ th CCI-R <sub>K</sub>	$g_{C_nR_k}$	$\lambda_{C_nR_k}$

Let us consider, total time taken to transmit the data packets from SU-Tx to the SU-Rx is  $T$ . Initially, fraction time  $\tau$  of  $T$  is reserved for harvesting energy at SU-Tx and SR. The remaining time ( $T - \tau$ ) is used for data transmission in this dual-hop communication process.

Energy harvested at SU-Tx is expresses as

$$E_S^H = \eta\tau \left( P_p g_{PS} + \sum_{n=1}^N P_C g_{C_nS} \right) \quad (1)$$

Here,  $P_p$  is denoted for the transmitted power by PU-Tx, and  $P_C$  is the power transmitted by single CCI node. The efficiency factor for the EH circuit at each node is defined by  $\eta$ .

Transmitted power at SU-Tx due to this harvested energy is given by

$$P_S^H = \left( \frac{E_S^H}{\frac{T-\tau}{2}} \right) \quad (2)$$

The transmission power of the SU-Tx must be regulated so that the PU does not receive significant interference from the SU's communication. Therefore, the SU-Tx transmit power should meet the PU receiver's interference power restriction, which is stated as

$$P_S^T = \left( \frac{I_P}{|h_{SP}|^2} \right) \quad (3)$$

where  $I_P$  is the threshold value of interference power at primary receiver PU-Rx.

Let  $P_S$  be the power transmitted by SU-Tx during different mode of operation can be written as

$$P_S = \min(P_S^T, P_S^H) \quad (4)$$

Energy harvested at secondary relays  $\text{SR}_k$  is given by

$$E_R^H = \eta \tau \left( P_S g_{\text{SR}_k} + P_p g_{\text{PR}_k} + \sum_{n=1}^N P_C g_{C_n R_k} \right) \quad (5)$$

Transmitted power at each relay of  $\text{SR}_k$  due to energy harvesting is given by

$$P_R^H = \left( \frac{E_R^H}{\frac{T-\tau}{2}} \right) \quad (6)$$

Similarly, in order to prevent the PU from experiencing too much interference from the SU's transmission, the  $\text{SR}_k$  transmission power must be controlled. As a result, the transmission power of  $\text{SR}_k$  must fulfill the interference power limitation of the PU receiver, which is given as

$$P_{R_k}^T = \min_{k=1,2,\dots,K} \left( \frac{I_P}{|h_{R_k P}|^2} \right) \quad (7)$$

Let  $P_R$  be the power transmitted by each relay of  $\text{SR}_k$  during different mode of operation can be written as

$$P_R = \min(P_{R_k}^T, P_R^H) \quad (8)$$

The secondary source (SU-Tx) and relays  $\text{SR}_k$  must maintain the interference power threshold ( $I_P$ ) with regards to the primary network. The mathematical expression of received signal at  $k$ th relay is given as follows:

$$y_{R_k}(t) = \sqrt{P_S} h_{S R_k} x_s(t) + \sqrt{P_p} h_{P R_k} x_p(t) + \sum_{n=1}^N \sqrt{P_C} h_{C_n R_k} x_c(t) + n_0(t) \quad (9)$$

The SINR through SU-Tx to  $k$ th relay is expressed as follows:

$$\gamma_{\text{SR}_k} = \frac{P_S |h_{S R_k}|^2}{P_p |h_{P R_k}|^2 + \sum_{n=1}^N P_C |h_{C_n R_k}|^2 + N_0} \quad (10)$$

The received signal at destination SU-Rx coming from  $k$ th relay is given as

$$y_D(t) = \sqrt{P_R} h_{R_k D} x_r(t) + \sqrt{P_p} h_{P D} x_p(t) + \sum_{n=1}^N \sqrt{P_C} h_{C_n D} x_c(t) + n_0(t) \quad (11)$$

The SINR through  $\text{SR}_k$  to  $D$  is expressed as

$$\gamma_{R_k D} = \frac{P_R |h_{R_k D}|^2}{P_p |h_{P D}|^2 + \sum_{n=1}^N P_C |h_{C_n D}|^2 + N_0} \quad (12)$$

where  $x_p(t)$ ,  $x_s(t)$ ,  $x_r(t)$ , and  $x_c(t)$  are the transmitting signals from PU-Tx, SU-Tx, SR<sub>k</sub>, and co-channel transmitter, respectively. Here,  $n_0(t)$  considers to be AWGN receiver noise with power spectral density  $N_0$ .

## 4 Performance Analysis of AHR Relay Protocol

The AHR scheme adaptively changes between AF and DF mode depending upon channel condition. DF mode is applicable, if and only if relays decode the incoming signal successfully. This scheme utilizes all the relay to work effectively, which in term makes the system performance better than the conventional AF and DF. Therefore, relay allocating scheme is performed to choose the best link via the set of relays from source to destination.

The process of decoding at R<sub>k</sub> succeeds only when  $\gamma_{SR_k} > \mu_{th}$ , i.e., *DF* protocol is continued, otherwise *AF* protocol is pursued. Where  $\mu_{th}$  is the threshold predefined SINR for successful decoding decision at the relay.

The DF relay scheme [7] defines a subset  $\delta$  of  $k_1$  relays out of  $K$  relays that can properly decode the received signal. Thus, the set can be described as  $\delta = \{\forall k \in (1, 2, \dots, k_1); \gamma_{SR_k} \geq \mu_{th}\}$ . The relays  $k_1$  effectively decodes the input signal when  $\gamma_{SR_{k_1}} > \mu_{th}$ . Now, these  $k_1$  relays of subset  $\delta$  are participated in transmission from relays to destination in *DF* mode. Remaining  $(K - k_1)$  count of relays operates in AF mode to transmit the message from relays to destination.

Therefore, the probability for a relay to operate in the AF scheme can be expressed as

$$\begin{aligned} P^{AF} &= \Pr(\gamma_{SR_k} < \mu_{th}) \\ &= \Pr\left(\frac{P_S |h_{SR_k}|^2}{P_p |h_{PR_k}|^2 + \sum_{n=1}^N P_C |h_{C_n R_k}|^2 + N_0} < \mu_{th}\right) \end{aligned} \quad (13)$$

For determining the cumulative distribution function (CDF) of Eq. (13), we assume that  $|h_{SR_k}|^2$  is denoted as independent exponentially distributed random variable (RV)  $X_1$  with the PDF  $f_{X_1}(x_1) = \frac{1}{\lambda_1} \exp(-\frac{x_1}{\lambda_1})$  and  $(P_p |h_{PR_k}|^2 + \sum_{n=1}^N P_C |h_{C_n R_k}|^2 = \sum_{n=1}^{N+1} P_T |h_{n R_k}|^2)$  where let  $P_p = P_C = P_T$  is represented as gamma distributed RV  $X_2$  with the PDF  $f_{X_2}(x_2) = \frac{(x_2)^{n-1} \exp(-\frac{x_2}{\lambda_2})}{\Gamma(n) \lambda_2^n}$ , since all channel power gains are independent identical exponential distribution with equal parameter of distribution, (i.e.,  $\lambda_{PR_k} = \lambda_{C_n R_k} = \lambda_2$ ). Here,  $\lambda_1$  and  $\lambda_2$  consider as parameter of the distribution for respective  $X_1$ ,  $X_2$  random variables. So Eq. (13) can be rewritten as

$$\begin{aligned}
P_{\text{AF}} &= \Pr\left(\frac{P_S X_1}{P_T X_2 + N_0} < \mu_{\text{th}}\right) \\
&= \int_{x_2=0}^{+\infty} \int_{x_1=0}^{\frac{(P_T \mu_{\text{th}} x_2 + \mu_{\text{th}} N_0)}{P_S}} f_{X_1}(x_1) f_{X_2}(x_2) dx_1 dx_2 \\
&= \int_{x_2=0}^{+\infty} \int_{x_1=0}^{\frac{(P_T \mu_{\text{th}} x_2 + \mu_{\text{th}} N_0)}{P_S}} \frac{1}{\lambda_1} \exp(-\frac{x_1}{\lambda_1}) f_{X_2}(x_2) dx_1 dx_2 \\
&= \int_{x_2=0}^{+\infty} \left[1 - \exp\left(-\frac{(P_T \mu_{\text{th}} x_2 + \mu_{\text{th}} N_0)}{P_S \lambda_1}\right)\right] f_{X_2}(x_2) dx_2 \\
&= 1 - \exp\left(-\frac{\mu_{\text{th}} N_0}{P_S \lambda_1}\right) \left(\frac{P_S \lambda_1}{P_S \lambda_1 + \mu_{\text{th}} P_T \lambda_2}\right)^n
\end{aligned} \tag{14}$$

On the other hand, the probability for a relay operated in the DF scheme can be expressed as

$$\begin{aligned}
P_{\text{DF}} &= \Pr(\gamma_{\text{SR}_k} \geq \mu_{\text{th}}) \\
&= 1 - P_{\text{AF}} \\
&= \left[\exp\left(-\frac{\mu_{\text{th}} N_0}{P_S \lambda_1}\right) \left(\frac{P_S \lambda_1}{P_S \lambda_1 + \mu_{\text{th}} P_T \lambda_2}\right)^n\right]
\end{aligned} \tag{15}$$

As per our proposed model,  $k_1$  number of relays out of  $K$  relays are operated in DF mode. The probability distribution of successfully decoded  $k_1$  relays out of total relays follows the binomial distribution, with parameters  $P_{\text{AF}}$ ,  $P_{\text{DF}}$ , and  $K$ . The outage probability for AHR scheme is depended on outage performance of the corresponding relays for AF and DF mode (i.e.,  $P_{\text{O}}^{\text{AF}}$ ,  $P_{\text{O}}^{\text{DF}}$ ). By the law of probability, the average outage probability for AHR scheme can be described as

$$P_{\text{O}}^{\text{AHR}} = \sum_{k_1=0}^K C_{k_1}^K (P_{\text{DF}})^{k_1} (P_{\text{O}}^{\text{DF}})^{k_1} (P_{\text{AF}})^{K-k_1} (P_{\text{O}}^{\text{AF}})^{K-k_1} \tag{16}$$

Where  $P_{\text{O}}^{\text{AF}}$  and  $P_{\text{O}}^{\text{DF}}$  are denoted as outage probabilities for AF, DF scheme at each relay, respectively. So in the following section, analysis of outage probabilities for AF, DF scheme at each relay is described, respectively.

#### 4.1 Outage Analysis for AF Protocol for Single Relay

The received signal at the relay is amplified and transferred to the secondary destination using the AF relaying method. The AF scheme has the advantages of being easy to implement and having a low-computational load on the relay. But due to this amplification process, the additive noise causes serious problem. The instantaneous end-to-end SINR from secondary source to SU-Rx via  $k^{\text{th}}$  relay can be written as [20]:

$$\gamma_k^{\text{AF}} = \frac{\gamma_{\text{SR}_k} \gamma_{\text{R}_k \text{D}}}{1 + \gamma_{\text{SR}_k} + \gamma_{\text{R}_k \text{D}}} \quad (17)$$

The end-to-end outage probability using AF relay scheme is expressed as

$$P_O^{\text{AF}} = \Pr(\gamma_k^{\text{AF}} \leq \gamma_{\text{th}}^s) \quad (18)$$

where  $\gamma_{\text{th}}^s = 2^{2R_s} - 1$  denotes the outage threshold at the SU-Rx. Let us consider the transmission rate of SU is  $R_s$ .

For calculating the CDF of Eq. (18),  $\gamma_{\text{SR}_k}$  and  $\gamma_{\text{R}_k \text{D}}$  are considered as random variables  $M$ ,  $P$ , respectively. Then,  $\gamma_k^{\text{AF}}$  can be expressed as

$$\gamma_k^{\text{AF}} = \frac{MP}{1 + M + P} \quad (19)$$

$$F_{\gamma_k^{\text{AF}}}(\gamma_{\text{th}}^s) = \Pr\left(\frac{MP}{1 + M + P} \leq \gamma_{\text{th}}^s\right) \quad (20)$$

The probability in Eq. (20) is calculated using two integration as follows [20, 21]:

$$\begin{aligned} F_{\gamma_k^{\text{AF}}} &= \int_{m=0}^{\gamma_{\text{th}}^s} \int_{p=0}^{+\infty} f_M(m) f_P(p) dm dp + \int_{m=\gamma_{\text{th}}^s}^{\infty} \int_{p=0}^{\frac{(m+1)\gamma_{\text{th}}^s}{m-\gamma_{\text{th}}^s}} f_M(m) f_P(p) dm dp \\ &= \underbrace{\int_{m=0}^{\gamma_{\text{th}}^s} \int_{p=0}^{+\infty} f_M(m) f_P(p) dm dp}_{S} + \underbrace{\int_{m=\gamma_{\text{th}}^s}^{\infty} \int_{p=0}^{\frac{(m+1)\gamma_{\text{th}}^s}{m-\gamma_{\text{th}}^s}} f_M(m) f_P(p) dm dp}_{T} \end{aligned} \quad (21)$$

Where  $f_M(m)$  and  $f_P(p)$  are the PDF of respective random variables  $M$ ,  $N$ . Here,  $M$  is expressed as

$$M = \frac{P_S |h_{\text{SR}_k}|^2}{P_p |h_{\text{PR}_k}|^2 + \sum_{n=1}^N P_C |h_{C_n \text{R}_k}|^2 + N_0} \quad (22)$$

For calculating the value of CDF for random variable  $M$ ,

$$\begin{aligned} F_M(m) &= \Pr(M \leq m) \\ &= \Pr\left(\frac{P_S |h_{\text{SR}_k}|^2}{P_p |h_{\text{PR}_k}|^2 + \sum_{n=1}^N P_C |h_{C_n \text{R}_k}|^2 + N_0} \leq m\right) \end{aligned} \quad (23)$$

we assume that  $|h_{\text{SR}_k}|^2$  is denoted as independent exponentially distributed random variable (RV)  $X_1$  with the PDF  $f_{X_1}(x_1) = \frac{1}{\lambda_1} \exp(-\frac{x_1}{\lambda_1})$  and  $(P_p |h_{\text{PR}_k}|^2 + \sum_{n=1}^N P_C |h_{C_n \text{R}_k}|^2 + N_0) = \sum_{n=1}^{N+1} P_T |h_{n \text{R}_k}|^2$  where  $P_p = P_C = P_T$  is represented as gamma

distributed RV  $X_2$  with the PDF  $f_{X_2}(x_2) = \frac{(x_2)^{n-1} \exp(-\frac{x_2}{\lambda_2})}{\Gamma(n)\lambda_2^n}$ , since all channel power gains are independent identical exponential distribution with equal parameter of distribution, (i.e.,  $\lambda_{PR_k} = \lambda_{C_iR_k} = \lambda_2$ ). Here,  $\lambda_1$  and  $\lambda_2$  consider as parameter of the distribution for respective  $X_1, X_2$  random variables. So Eq. (23) can be rewritten as

$$\begin{aligned} F_M(m) &= \Pr\left(\frac{P_S X_1}{P_T X_2 + N_0} < m\right) \\ &= \int_{x_2=0}^{+\infty} \int_{x_1=0}^{\frac{(P_T m x_2 + m N_0)}{P_S}} f_{X_1}(x_1) f_{X_2}(x_2) dx_1 dx_2 \\ &= \int_{x_2=0}^{+\infty} \int_{x_1=0}^{\frac{(P_T m x_2 + m N_0)}{P_S}} \frac{1}{\lambda_1} \exp(-\frac{x_1}{\lambda_1}) f_{X_2}(x_2) dx_1 dx_2 \\ &= \int_{x_2=0}^{+\infty} \left[1 - \exp\left(-\frac{(P_T m x_2 + m N_0)}{P_S \lambda_1}\right)\right] f_{X_2}(x_2) dx_2 \\ &= 1 - \exp\left(-\frac{m N_0}{P_S \lambda_1}\right) \left(\frac{P_S \lambda_1}{P_S \lambda_1 + m P_T \lambda_2}\right)^n \end{aligned} \quad (24)$$

The PDF random variable  $M$  can be expressed as

$$\begin{aligned} f_M(m) &= \frac{d(F_M(m))}{dm} \\ &= \exp\left(-\frac{N_0}{P_S \lambda_1} m\right) \left(1 + \frac{P_T \lambda_2}{P_S \lambda_1} m\right)^{-(n+1)} \left(\frac{N_0}{P_S \lambda_1} + \frac{N_0 P_T \lambda_2}{P_S^2 \lambda_1^2} m + \frac{P_T \lambda_2}{P_S \lambda_1} n\right) \end{aligned} \quad (25)$$

Assuming  $\frac{P_T \lambda_2}{P_S \lambda_1} = X$ ,  $\frac{N_0 P_T \lambda_2}{P_S^2 \lambda_1^2} = Y$ ,  $\frac{N_0}{P_S \lambda_1} = Z$ , the Eq. (25) can be written as

$$f_M(m) = \exp(-Zm) (1 + Xm)^{-(n+1)} (Z + Ym + Xn) \quad (26)$$

The random variable  $P$  can be expressed as

$$P = \frac{P_R |h_{R_k D}|^2}{P_p |h_{PD}|^2 + \sum_{n=1}^N P_C |h_{C_n D}|^2 + N_0} \quad (27)$$

For determining the value of CDF for  $P$  random variable,

$$\begin{aligned} F_P(p) &= \Pr(P \leq p) \\ &= \Pr\left(\frac{P_R |h_{R_k D}|^2}{P_p |h_{PD}|^2 + \sum_{n=1}^N P_C |h_{C_n D}|^2 + N_0} \leq p\right) \end{aligned} \quad (28)$$

we assume that  $|h_{RkD}|^2$  is denoted as independent exponentially distributed RV  $X_3$  with the PDF  $f_{X_3}(x_3) = \frac{1}{\lambda_3} \exp(-\frac{x_3}{\lambda_3})$  and  $(P_p |h_{PD}|^2 + \sum_{n=1}^N P_C |h_{C_n D}|^2 = \sum_{n=1}^{N+1} P_T |h_{xD}|^2)$  where  $P_p = P_C = P_O$  is represented as gamma distributed RV  $X_4$  with the PDF  $f_{X_4}(x_4) = \frac{(x_4)^{n-1} \exp(-\frac{x_4}{\lambda_4})}{\Gamma(n) \lambda_4^n}$ . Since each channel power gain follows identical exponential distribution with equal distribution of parameter, (i.e.,  $\lambda_{PD} = \lambda_{C_n D} = \lambda_4$ ). Here,  $\lambda_3$  and  $\lambda_4$  consider as parameter of the distribution for respective  $X_3, X_4$  random variables.

$$P = \frac{P_R X_3}{P_O X_4 + N_0} \quad (29)$$

$$\Pr\left(\frac{P_R X_3}{P_O X_4 + N_0} \leq \gamma_{th}^s\right) \quad (30)$$

$$\begin{aligned} F_P(p) &= \int_{x_4=0}^{+\infty} \int_{x_3=0}^{\frac{(P_O p x_4 + p N_0)}{P_R}} f_{X_3}(x_3) f_{X_4}(x_4) dx_3 dx_4 \\ &= \int_{x_4=0}^{+\infty} \int_{x_3=0}^{\frac{(P_O p x_4 + p N_0)}{P_R}} \frac{1}{\lambda_3} \exp(-\frac{x_3}{\lambda_3}) f_{X_4}(x_4) dx_3 dx_4 \\ &= \int_{x_4=0}^{+\infty} \left[ 1 - \exp\left(-\frac{(P_O p x_4 + p N_0)}{P_R \lambda_1}\right) \right] f_{X_4}(x_4) dx_4 \\ &= 1 - \exp\left(-\frac{p N_0}{P_R \lambda_3}\right) \left(\frac{P_R \lambda_3}{P_R \lambda_3 + p P_O \lambda_4}\right)^n \end{aligned} \quad (31)$$

The PDF for random variable P being expressed as

$$\begin{aligned} f_P(p) &= \frac{d(F_P(p))}{dp} \\ &= \exp\left(-\frac{p N_0}{P_R \lambda_3}\right) \left(1 + \frac{p \lambda_4 P_O}{P_R \lambda_3}\right)^{-(n+1)} \left(\frac{N_0}{P_R \lambda_3} + \frac{N_0 P_O \lambda_4}{P_R^2 \lambda_3^2} p + \frac{P_O \lambda_4}{P_S \lambda_3} n\right) \end{aligned} \quad (32)$$

After considering  $\frac{P_O \lambda_4}{P_R \lambda_3} = A$ ,  $\frac{N_0 P_O \lambda_4}{P_R^2 \lambda_3^2} = B$ ,  $\frac{N_0}{P_R \lambda_3} = C$ , Eq. (32) is written as

$$f_P(p) = \exp(-Cp) (1 + Ap)^{-(n+1)} (C + Bp + An) \quad (33)$$

The solution of integration under  $S$  notation in Eq. (21) can be expressed as

$$\begin{aligned} S &= \int_{m=0}^{\gamma_{\text{th}}^s} \int_{p=0}^{+\infty} f_M(m) f_P(p) dm dp \\ &= \int_{m=0}^{\gamma_{\text{th}}^s} \exp(-Zm)(1+Xm)^{-(n+1)}(Z+Ym+Xn) dm \end{aligned} \quad (34)$$

Applying the approximation of  $n+1 \approx n$ ,  $(1+\alpha x)^{-n} = \exp(-n\alpha x)$ . Consider  $Z+nX=S$

$$\begin{aligned} S &= \int_{m=0}^{\gamma_{\text{th}}^s} \exp(-(Z+nX)m)(Z+Ym+Xn) dm \\ &= \int_{m=0}^{\gamma_{\text{th}}^s} \exp(-Sm)(Ym+S) dm \\ &= -\frac{\exp(-\gamma_{\text{th}}^s S)(\gamma_{\text{th}}^s SY + S^2 + Y) + S^2 + Y}{S^2} \end{aligned} \quad (35)$$

In Eq. (21), the solution of integration under  $T$  notation can be written as [22]:

$$\begin{aligned} T &= \int_{m=\gamma_{\text{th}}^s}^{\infty} \int_{p=0}^{\frac{(m+1)\gamma_{\text{th}}}{m-\gamma_{\text{th}}^s}} f_M(m) f_P(p) dm dp \\ &= \int_{m=\gamma_{\text{th}}^s}^{\infty} \int_{p=0}^{\infty} f_M(m) f_P(p) dm dp \\ &= \int_{m=\gamma_{\text{th}}^s}^{+\infty} \exp(-Sm)(Ym+S) dm \\ &= \int_{m=\gamma_{\text{th}}^s}^{\infty} \exp(-Sm)(Ym+S) dm \\ &= \frac{Y \exp(\frac{S^2}{Y})}{S^2} \cdot \Gamma \left( 2, S\gamma_{\text{th}}^s + \frac{S^2}{Y} \right) \end{aligned} \quad (36)$$

After putting the value of  $S$  and  $T$  in Eq. (21), the CDF of  $\gamma_k^{\text{AF}}$  is

$$F_{\gamma_k^{\text{AF}}} = \left[ \left( -\frac{\exp(-\gamma_{\text{th}}^s S)(\gamma_{\text{th}}^s S Y + S^2 + Y) + S^2 + Y}{S^2} \right) + \left( \frac{Y \exp \frac{S^2}{Y}}{S^2} \cdot \Gamma \left( 2, S \gamma_{\text{th}}^s + \frac{S^2}{Y} \right) \right) \right] \quad (37)$$

So, the expression of Eq. (37) is the outage probability of  $k$ th relay using AF relay scheme.

## 4.2 Outage Analysis for DF Protocol for Single Relay

The DF relay scheme [7] defines that a relay successfully decodes the incoming signal before transmission to secondary destination. The relay effectively decodes the input signal when  $\gamma_{SR_k} > \mu_{\text{th}}$ . The received SINR at destination from  $k$ th relay can be expressed as

$$\gamma_D^{\text{DF}} = \gamma_{R_k D} \quad (38)$$

As probability for a relay operated in the DF scheme can be expressed as  $P^{\text{DF}}$ , mathematically outage probability using DF relay scheme is formulated as [23]:

$$\begin{aligned} P_O^{\text{DF}} &= \Pr(\gamma_D^{\text{DF}} \leq \gamma_{\text{th}}^s) P^{\text{DF}} \\ &= \Pr\left(\frac{P_R |h_{R_k D}|^2}{P_p |h_{PD}|^2 + \sum_{n=1}^N P_C |h_{C_n D}|^2 + N_0} \leq \gamma_{\text{th}}^s\right) P^{\text{DF}} \end{aligned} \quad (39)$$

where  $\gamma_{\text{th}}^s = 2^{2R_s} - 1$  denotes the outage threshold at the SU-Rx. Here,  $R_s$  is considering the transmission rate of SUs.

For calculating the CDF of equation  $\Pr(\gamma_D^{\text{DF}} \leq \gamma_{\text{th}}^s)$ ,  $|h_{R_k D}|^2$  is denoted as independent exponentially distributed RV  $X_3$  with the PDF  $f_{X_3}(x_3) = \frac{1}{\lambda_3} \exp(-\frac{x_3}{\lambda_3})$  and  $(P_p |h_{PD}|^2 + \sum_{n=1}^N P_C |h_{C_n D}|^2 = \sum_{n=1}^{N+1} P_T |h_{x D}|^2)$  where  $P_p = P_C = P_O$  is represented as gamma distributed RV  $X_4$  with the PDF  $f_{X_4}(x_4) = \frac{(x_4)^{n-1} \exp(-\frac{x_4}{\lambda_4})}{\Gamma(n) \lambda_4^n}$ . Since each channel power gain follows identical exponential distribution with equal distribution of parameter, (i.e.,  $\lambda_{PD} = \lambda_{C_n D} = \lambda_4$ ). Here,  $\lambda_3$  and  $\lambda_4$  consider as parameter of the distribution for respective  $X_3$ ,  $X_4$  random variables.

$$P = \frac{P_R X_3}{P_O X_4 + N_0} \quad (40)$$

$$\Pr\left(\frac{P_R X_3}{P_O X_4 + N_0} \leq \gamma_{\text{th}}^s\right) \quad (41)$$

$$\begin{aligned} F_P(\gamma_{\text{th}}^s) &= \int_{x_4=0}^{+\infty} \int_{x_3=0}^{\frac{(P_O \gamma_{\text{th}}^s x_4 + \gamma_{\text{th}}^s N_0)}{P_R}} f_{X_3}(x_3) f_{X_4}(x_4) dx_3 dx_4 \\ &= \int_{x_4=0}^{+\infty} \int_{x_3=0}^{\frac{(P_O p x_4 + \gamma_{\text{th}}^s N_0)}{P_R}} \frac{1}{\lambda_3} \exp(-\frac{y}{\lambda_3}) f_{X_4}(x_4) dx_3 dx_4 \\ &= \int_{x_4=0}^{+\infty} \left[1 - \exp\left(-\frac{(P_O p x_4 + \gamma_{\text{th}}^s N_0)}{P_R \lambda_1}\right)\right] f_{X_4}(x_4) dx_4 \\ &= 1 - \exp\left(-\frac{\gamma_{\text{th}}^s N_0}{P_R \lambda_3}\right) \left(\frac{P_R \lambda_3}{P_R \lambda_3 + \gamma_{\text{th}}^s P_O \lambda_4}\right)^n \end{aligned} \quad (42)$$

The PDF for random variable  $P$  being expressed as

$$f_P(\gamma_{\text{th}}^s) = \exp\left(-\frac{\gamma_{\text{th}}^s N_0}{P_R \lambda_3}\right) \left(1 + \frac{\gamma_{\text{th}}^s \lambda_4 P_O}{P_R \lambda_3}\right)^{-(n+1)} \left(\frac{N_0}{P_R \lambda_3} + \frac{N_0 P_O \lambda_4 \gamma_{\text{th}}^s}{P_R^2 \lambda_3^2} + \frac{P_O \lambda_4 n}{P_S \lambda_3}\right) \quad (43)$$

After applying the value of  $\Pr[\gamma_D^{\text{DF}} \leq \gamma_{\text{th}}^s]$  and  $P^{\text{DF}}$ , the solution of the outage probability in DF relay scheme in Eq. (39) expressed as

$$\begin{aligned} P_O^{\text{DF}} &= \left[1 - \exp\left(-\frac{\gamma_{\text{th}}^s N_0}{P_R \lambda_3}\right) \left(\frac{P_R \lambda_3}{P_R \lambda_3 + \gamma_{\text{th}}^s P_O \lambda_4}\right)^n\right] \\ &\quad \times \left[\exp\left(-\frac{\mu_{\text{th}} N_0}{P_S \lambda_1}\right) \left(\frac{P_S \lambda_1}{P_S \lambda_1 + \mu_{\text{th}} P_T \lambda_2}\right)^n\right] \end{aligned} \quad (44)$$

The solutions of  $P_O^{\text{AF}}$  and  $P_O^{\text{DF}}$  for single relay-based system are applied in Eq. (16) to find the the close form of outage probability for AHR scheme, so the expression is written as

$$\begin{aligned}
P_O^{\text{AHR}} &= \sum_{k_1=0}^K C_{k_1}^K (P_{\text{DF}})^{k_1} (P_O^{\text{DF}})^{k_1} (P_{\text{AF}})^{K-k_1} (P_O^{\text{AF}})^{K-k_1} \\
&= \sum_{k_1=0}^K C_{k_1}^K \left\{ \exp\left(-\frac{\mu_{\text{th}} N_0}{P_S \lambda_1}\right) \left( \frac{P_S \lambda_1}{P_S \lambda_1 + \mu_{\text{th}} P_T \lambda_2} \right)^n \right\}^{k_1} \\
&\quad \times \left[ \left\{ 1 - \exp\left(-\frac{\gamma_{\text{th}}^s N_0}{P_R \lambda_3}\right) \left( \frac{P_R \lambda_3}{P_R \lambda_3 + \gamma_{\text{th}}^s P_O \lambda_4} \right)^n \right\} \right. \\
&\quad \times \left. \left\{ \exp\left(-\frac{\mu_{\text{th}} N_0}{P_S \lambda_1}\right) \left( \frac{P_S \lambda_1}{P_S \lambda_1 + \mu_{\text{th}} P_T \lambda_2} \right)^n \right\} \right]^{k_1} \\
&\quad \times \left\{ \exp\left(-\frac{\mu_{\text{th}} N_0}{P_S \lambda_1}\right) \left( \frac{P_S \lambda_1}{P_S \lambda_1 + \mu_{\text{th}} P_T \lambda_2} \right)^n \right\}^{K-k_1} \\
&\quad \times \left[ \left\{ -\frac{\exp(-\gamma_{\text{th}}^s S) (\gamma_{\text{th}}^s S Y + S^2 + Y) + S^2 + Y}{S^2} \right\} \right. \\
&\quad \left. + \left\{ \frac{Y \exp \frac{S^2}{Y}}{S^2} \cdot \Gamma \left( 2, S \gamma_{\text{th}}^s + \frac{S^2}{Y} \right) \right\} \right]^{K-k_1}
\end{aligned} \tag{45}$$

Depending on the working mode of relays, AHR scheme shows two extreme conditions; these are as follows:

*Condition 1:* In AHR scheme, it is assumed that decoding SINR for all the relays ( $K$ ) is below the threshold decoding SINR ( $\mu_{\text{th}}$ ), so all relays operated in AF mode. In this case, number of DF operated relays ( $k_1$ ) is zero. Applying Eqs. (16) and (37) to determine the outage performance at secondary receiver for this case is expressed as

$$\begin{aligned}
P_O^{\text{AHR}} &= (P_{\text{AF}})^K (P_O^{\text{AF}})^K \\
&= \left[ \left\{ \exp\left(-\frac{\mu_{\text{th}} N_0}{P_S \lambda_1}\right) \left( \frac{P_S \lambda_1}{P_S \lambda_1 + \mu_{\text{th}} P_T \lambda_2} \right)^n \right\}^K \right. \\
&\quad \times \left. \left\{ -\frac{\exp(-\gamma_{\text{th}}^s S) (\gamma_{\text{th}}^s S Y + S^2 + Y) + S^2 + Y}{S^2} \right\} \right. \\
&\quad \left. + \left\{ \frac{Y \exp \frac{S^2}{Y}}{S^2} \cdot \Gamma \left( 2, S \gamma_{\text{th}}^s + \frac{S^2}{Y} \right) \right\} \right]^K
\end{aligned} \tag{46}$$

*Condition 2:* In this case, all relays ( $K$ ) are considered to be in DF mode because the decoding SINR for relays is above the threshold decoding SINR ( $\mu_{\text{th}}$ ). Number of DF operated relays ( $k_1$ ) are now  $K$ . With the help of Eqs. (16) and (44), the outage performance at the secondary receiver in this scenario is as follows:

$$\begin{aligned}
P_O^{\text{AHR}} &= (P_{\text{DF}})^K (P_O^{\text{DF}})^K \\
&= \left[ \left\{ \exp\left(-\frac{\mu_{\text{th}} N_0}{P_S \lambda_1}\right) \left( \frac{P_S \lambda_1}{P_S \lambda_1 + \mu_{\text{th}} P_T \lambda_2} \right)^n \right\}^K \right. \\
&\quad \times \left[ \left\{ 1 - \exp\left(-\frac{\gamma_{\text{th}}^s N_0}{P_R \lambda_3}\right) \left( \frac{P_R \lambda_3}{P_R \lambda_3 + \gamma_{\text{th}}^s P_O \lambda_4} \right)^n \right\} \right. \\
&\quad \times \left. \left. \left\{ \exp\left(-\frac{\mu_{\text{th}} N_0}{P_S \lambda_1}\right) \left( \frac{P_S \lambda_1}{P_S \lambda_1 + \mu_{\text{th}} P_T \lambda_2} \right)^n \right\} \right]^K \right] \quad (47)
\end{aligned}$$

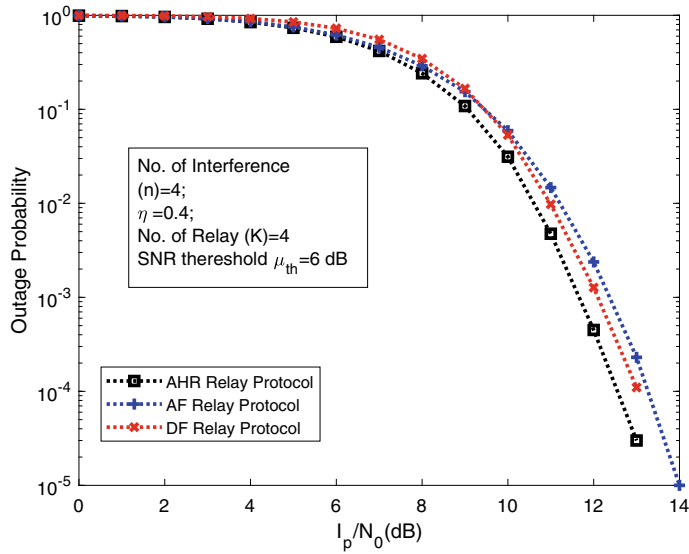
## 5 Result and Discussion

This section summarizes the outcomes of the results analysis conducted using the MATLAB Simulation testbed, as well as a brief comments based on the results. The numerical results presented here show how the suggested relay-assisted AHR relay protocol improved performance during spectrum access.

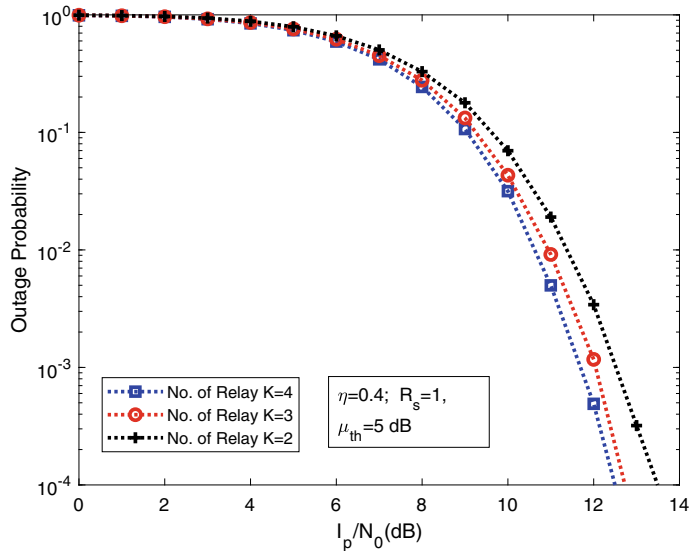
Figure 3 shows the comparison of outage performance at destination between AF, DF, and adaptive hybrid relay scheme (AHR). In this figure, it has been shown that with the same number of relays ( $K=4$ ), AHR scheme achieves better outage performance than individual outage performance of AF scheme and DF scheme, respectively, which implies that the AHR scheme is highly efficient than individual DF and AF schemes working at a time. The working principle of AHR protocol is dynamic depending upon the decoding procedure of the received signal at relays. The successfully decoded signal follows DF protocol, else AF protocol is maintained. Every relay takes part in this process, which improves the relay diversity numbers to select the best one. Finally, this scheme of adaptive control increases the system performance with respect to other two individual schemes.

Figure 4 shows the outage probability at secondary receiver (D) versus  $I_p/N_0$  under AHR protocol. The outage analysis at the secondary receiver (D) has been investigated for various numbers of relays  $K$  (i.e.,  $K = 2, 3, 4$ ). It is observed that the outage performance at destination is improved with increasing number of relays. This indicates that the increase in diversity is causing outages to improve.

In Fig. 5, it depicts the outage probability at the secondary receiver (D) versus  $I_p/N_0$  under the AHR protocol, with the parameters such as  $R_s = 1$  bit/sec/Hz held constant. The performance of a secondary outage in an AHR network with a fixed number of relays ( $K = 4$ ) is investigated using various energy harvesting efficiency factors ( $\eta$ ) (i.e.,  $\eta = 0.2, 0.4, 0.6$ ). The result also concludes that the increasing energy harvesting efficiency factor ( $\eta$ ) gives good outage performance. Because of higher energy harvesting efficiency factor ( $\eta$ ), the amount of harvested energy at SU transmitter and SU relays is more, so highly powered signals are transmitted from these nodes to their desired destination. The effect of noise and interference is reduced at the secondary destination due to the highly powered received signal.



**Fig. 3** Comparison of outage performance w.r.t  $I_p/N_0$  under AF, DF, and AHR mode



**Fig. 4** Comparison of outage performance w.r.t  $I_p/N_0$  under AHR mode with varying  $K = 2, 3, 4$

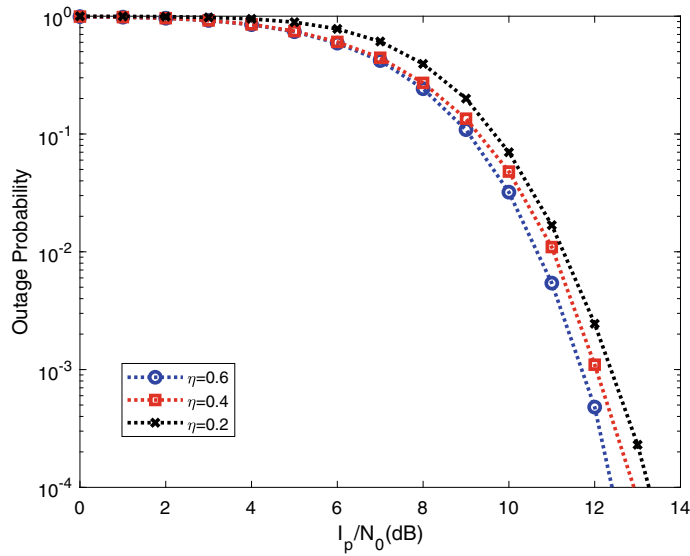


**Fig. 5** Comparison of outage performance w.r.t  $I_p/N_0$  under AHR mode with fixed  $K = 4$  varying  $\eta = 0.2, 0.4$ , and  $0.6$

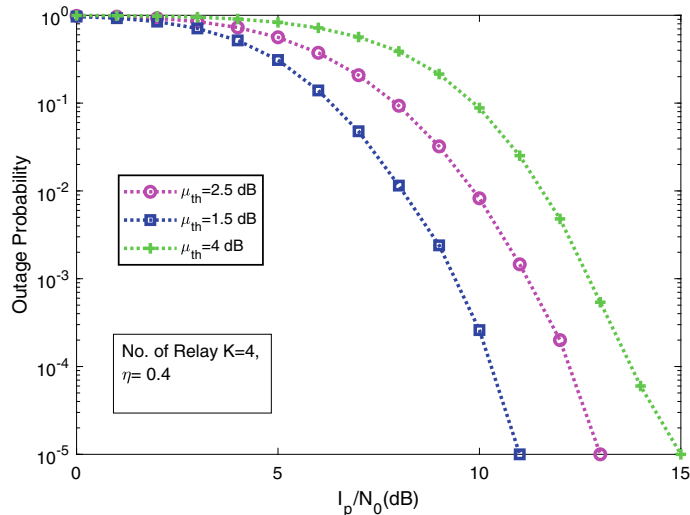


**Fig. 6** Comparison of outage performance w.r.t  $I_p/N_0$  under AHR mode varying  $\mu_{th} = 2.5$  dB, 1.5 dB, 4 dB with fixed  $K = 4$

The outage probability at the secondary receiver ( $D$ ) against  $I_p/N_0$  under the AHR protocol with fixed relays ( $K = 4$ ) is represented in Fig. 6. Using various decoding threshold SINR ( $\mu_{\text{th}} = 2.5 \text{ dB}, 1.5 \text{ dB}, 4 \text{ dB}$ ), the performance of secondary receiver outage in the AHR scheme with fixed number of relays ( $K = 4$ ) is explored. The outcome of figure is reflected that decreasing of the decoding threshold SINR ( $\mu_{\text{th}}$ ) provides a good outage performance.

## 6 Conclusion

We have proposed and analyzed the AF, DF, and AHR relay protocol for cognitive radio network in presence of co-channel interference including energy harvesting scenario at each secondary nodes. The outcomes of this work specify the adaptive nature of AHR relay mode, and this in turn improves the spectrum utility in a CR network. This proposed model smartly varies between AF or DF mode of operation based on the successfully decoding activities of relays in a co-channel interference-based environment. A comparison between all the modes of transmission has been discussed showing a better outage result in the AHR protocol. The effect of several interference sources on the evaluation of secondary outage performance has been accessed in an organized manner. At last, AHR relay-based CR network provides significant advantage in term of secondary outage performance under the environment of energy harvesting from CCI sources together with PU transmitter RF signals.

## References

- Mitola J, Maguire GQ (1999) Cognitive radio: making software radios more personal. *IEEE Pers Commun* 6(4):13–18
- Force S (2002) Spectrum policy task force report. *Fed Commun Comm ET Docket* 02 135
- Sharma S, Dhar Roy S, Kundu S (2020) Secure communication with energy harvesting multiple half-duplex DF relays assisted with jamming. *Wire Netw* 26(2):1151–1164
- Liu Y, Mousavifar SA, Deng Y, Leung C, Elkashlan M (2015) Wireless energy harvesting in a cognitive relay network. *IEEE Trans Wire Commun* 15(4):2498–2508
- Mao M, Cao N, Chen Y, Zhou Y (2015) Multi-hop relaying using energy harvesting. *IEEE Wire Commun Lett* 4(5):565–568
- Vashistha A, Sharma S, Bohara VA (2014) Outage analysis of a multiple-antenna cognitive radio system with cooperative decode-and-forward relaying. *IEEE Wire Commun Lett* 4(2):125–128
- De CK, Kundu S (2016) Proactive and reactive DF relaying for cognitive network with multiple primary users. *Radioengineering* 25(3):475
- Gu Y, Aissa S (2015) RF-based energy harvesting in decode-and-forward relaying systems: ergodic and outage capacities. *IEEE Trans Wire Commun* 14(11):6425–6434
- Poornima S, Babu A (2018) Performance analysis of energy harvesting cognitive relay networks with primary interference. *Telecomm Syst* 68(3):445–459
- De CK, Kundu S (2014) Adaptive decode-and-forward protocol based cooperative spectrum sensing in cognitive radio with interference at the secondary users. *Wire Pers Commun* 79(2):1417–1434

11. Saha A, Bhattacherjee SS, De CK, De D (2017) Cooperative spectrum sharing with multi-antenna based adaptive hybrid relay in presence of multiple primary users. *J Inf Optim Sci* 38(6):857–871
12. Huang Y, Al-Qahtani F, Zhong C, Wu Q (2013) Outage analysis of spectrum sharing relay systems with multi-secondary destinations in the presence of primary user's interference. IEEE, pp 1–6
13. Samanta D, Kumar Bag J, De Kumar C, Chandra A (2021) A smart spectrum utilization approach using multiantenna-based cognitive relays in cognitive radio network. *Int J Commun Syst* 34(1):4671
14. Samanta D, De CK, Chandra A (2022) Performance analysis of full-duplex multi-relaying energy harvesting scheme in presence of multi-user cognitive radio network. *IEEE Trans Green Commun Netw*
15. Mondal S, Roy S, Kundu S (2022) On performance of multihop energy harvesting CRN in the presence of co-channel interferers. *Int J Electron Lett* 10(1):1–15
16. Merino HW, Camara CE, de Almeida C (2019) Uplink spectral efficiency for small-cells with dual-hop amplify-and-forward relaying at 28 ghz. *IET Commun* 13(5):496–504
17. Nam PM, Duy TT, Ca PV (2019) Performance of cluster-based cognitive multihop networks under joint impact of hardware noises and non-identical primary co-channel interference. *TELKOMNIKA Telecommun Comput Electron Contr* 17(1):49–59
18. Hussein JA, Ikki SS, Boussakta S, Tsimenidis C (2017) Impact of co-channel interference on an underlay cognitive radio network over nakagami-m fading channels. IEEE, pp 1–7
19. Bag JK, Samanta D, De CK, Chandra A (2022) Outage analysis of joint underlay/overlay CR network. In: Proceedings of the 3rd international conference on communication, devices and computing. Springer, pp 537–550
20. Molu MM, Xiao P, Khalily M, Zhang L, Tafazolli R (2017) A novel equivalent definition of modified bessel functions for performance analysis of multi-hop wireless communication systems. *IEEE Access* 5:7594–7605
21. Papoulis A, Pillai SU (2002) Probability, random variables, and stochastic processes. Tata McGraw-Hill Education, Europe
22. Gradshteyn IS, Ryzhik IM (2014) Table of integrals, series, and products. Academic press, USA
23. Tran H, Zepernick H-J, Phan H (2013) Cognitive proactive and reactive DF relaying schemes under joint outage and peak transmit power constraints. *IEEE Commun Lett* 17(8):1548–1551

# Author Index

## A

- Abhijit Chandra, 617, 685  
Abo-Khalil, Ahmed G., 245, 409  
Aishikée Mishra, 189  
Ajay Parmar, 43  
Aloke Saha, 189  
Alpana Barman, 347  
Amitava Nag, 633  
Amiya Karmakar, 149  
Ananya Mandal, 189  
Angana Chakraborty, 57  
Angshuman Majumdar, 367  
Angsuman Sarkar, 333  
Anirban Chatterjee, 449  
Anirudh Kulkarni, 665  
Anitesh Anand, 217  
Anjali Chauhan, 303  
Anwesha Banerjee, 401  
Apratim Mitra, 609  
Archana Sahai, 95  
Arif Ahmed Sekh, 57  
Arijit Chatterjee, 401  
Arpan Adhikary, 583  
Arun Raj, 379  
Asha Ambhaikar, 323  
Ashis Kumar Dhara, 23  
Asish Bera, 521  
Avisankar Roy, 677  
Avishhek Das, 647  
Ayatullah Faruk Mollah, 11  
Ayesha Begum, 657

## B

- Bansal, Ramesh C., 245, 409

## Banza, Banza B., 409

- Brijmohan Lal Sahu, 563  
Buddhadeb Pradhan, 289

## C

- Chakravarthi, M. B., 657  
Chanchal Dey, 33, 177  
Chanchal Kumar De, 217, 391, 617, 685  
Chernenkaya Ludmila, V., 597  
Cinu C. Kiliroor, 463

## D

- Debasis De, 217  
Debasis Maji, 23  
Deepikasri, N., 275  
Dibyendu Chowdhury, 125, 303  
Dipak Samanta, 617, 685  
Durbadal Mandal, 379, 427, 647

## E

- Elisabeth Thomas, 309  
Emon Asad, 11  
Evuri Brahma Reddy, 1

## F

- Farooqui, U. K., 83

## G

- Gagan Kumar Sahoo, 159  
Gautam Sarkar, 23

**G** Gopi Ram, 427

## I

Indranil Dey, 229

## J

Jagannath Samanta, 391, 531  
 Jayanta Kumar Bag, 685  
 Jaydeb Bhaumik, 547  
 Jeyachidra, J., 503  
 Jheelam Mondal, 113  
 Joyoshri Goswami, 189

## K

Kalyan Sundar Kola, 449  
 Kamabu, Tsongo P., 409  
 Kandi Venkata Narasimha Reddy, 1  
 Kapil Kumar Gupta, 83  
 Katta Uday Kiran, 263  
 Keshav Kashyap, 521  
 Kingshuk Chatterjee, 197  
 Kisalaya Chakrabarti, 333  
 Kumar, S. N., 309  
 Kushal Roy, 367

## L

Leeladhar Malviya, 43  
 Le, Van Huyen, 491  
 Logesh, T., 503

## M

Madhubala, T., 275  
 Madhu Paswan, 217  
 Madhusudan Maiti, 125  
 Madiba, T., 409  
 Mahesh Chandra Govil, 263  
 Mamata Dalui Chakraborty, 521  
 Manas Mishra, 217  
 Manas Pandey, 303  
 Mandal Nabanita, 477  
 Manikandan, A., 275  
 Mantar Singh Mandloi, 43  
 Manvendra Singh, 263  
 Mayobo, Mowene G., 409  
 Mbukani, Mwana W. K., 409  
 Mbungu, Nsilulu T., 245, 409  
 Md. Sarfaraj Alam Ansari, 263  
 Meena, S. M., 665  
 Meenaxi M. Raikar, 665

Mou Das Mahapatra, 33, 177  
 Moupalii Sen, 401  
 Mugdhatanu Dev Goswami, 633  
 Musibono, Eyul'Anki D., 409  
 Muskan Singh, 83

## N

Namrata Dhanda, 83, 95  
 Nandhini, K., 503  
 Niladri Biswas, 531  
 Nimay Chandra Giri, 583  
 Niranjan Polai, 217

## P

Paramita Dey, 197  
 Parimal Acharjee, 347  
 Pitam Chakrabarti, 139  
 Poornaiah Billa, 657  
 Prabir Saha, 531  
 Pranabendu Giri, 531  
 Prasad, G. M., 359  
 Preeti Chandrakar, 563  
 Pritam Kumar Mukhopadhyay, 401  
 Psarag Jyoti Kalita, 633  
 Puja Sarkar, 633

## R

Rajani Kanta Mudi, 33, 177  
 Rajat Verma, 83, 95  
 Rajesh Dutta, 149  
 Rajesh Mukherjee, 521  
 Rajib Kar, 427, 647  
 Raj Kumar Maity, 391, 531  
 Rajrup Saha, 647  
 Rambabu Busi, 657  
 Ramya, R., 275  
 Ranjani, P., 503  
 Ritu Rani De, 33, 177  
 Ritwiz Singh, 521  
 Rohini Basak, 69  
 Rohit Sasmal, 531  
 Ruby, D., 503

## S

Sachindeb Jana, 333  
 Saheli Pal, 401  
 Saikat Acharyya, 69  
 Sakshi Pandey, 95  
 Sanchita Saha, 633  
 Santigopal Pain, 347

- Sapana Ranwa, 439  
Sarode Tanuja, 477  
Satish Kumar, 427  
Satyanarayana Talam, 657  
Seshagiri Rao Ambati, 229  
Shamba Chatterjee, 139  
Shatabhiswa Goswami, 189  
Shibendu Mahata, 33, 177  
Shilpa Yadav, 95  
Shipu Das, 289  
Shreerupa Biswas, 439  
Shreya Basu, 401  
Siddaraj Hubballi, 665  
Siddhartha Chatterjee, 583  
Sima Das, 583  
Singh, J. K., 359  
Siti, Mukwanga W., 409  
Sk Sahnawaj, 609  
Smarajit Maity, 677  
Sohini Ghosh, 289  
Solanki Mitra, 583  
Som Sagar, 463  
Sourav Das, 531  
Sourav Mandal, 69  
Souvik Dutta, 347  
Souvik Maiti, 23  
Sridhar Pilli, 229  
Srinjoy Sarkar, 289  
Stobak Dutta, 401  
Subhadeep Paul, 125  
Subhadip Dutta, 289  
Subham Mohanty, 159  
Subhankar Joardar, 57, 113  
Subhas Chandra Saha, 125  
Subhashree Choudhury, 159  
Sucheta Das, 139  
Sudakshina Kundu, 149  
Suddhendu DasMahapatra, 303  
Sudipta Sahana, 289, 401  
Sudipto Dhar, 289  
Sumaili, J., 409  
Sunandan Bhunia, 677  
Sunen Chakraborty, 197  
Surajit Mukherjee, 677  
Sutapa Bhattacharya, 583  
Swani Sundara Didde, 463  
Sweta Bijali Maity, 391
- T**  
Tapan Maity, 531  
Tapas Tewary, 677  
Thu, Dung Nguyen Thi, 597  
Tilak Mukherjee, 367, 657  
Tirthadip Sinha, 547  
Tripathy, S. K., 359  
Tshikala, Kiseya F., 409  
Tungadio, Diambomba H., 409
- U**  
Ujjwal Tripathi, 43  
Umamaheswari, G., 503
- V**  
Vanita S. Buradkar, 323  
Vinayak Merawade, 665
- Y**  
Yash Deshpande, 665